

**The prediction and back analysis
of excavation behaviour
in Oxford Clay**

by

**Nicholas David Pierpoint
MEng (Sheffield)**

Vol. II

**A thesis submitted to
The University of Sheffield
Department of Civil and Structural Engineering
for the degree of Doctor of Philosophy**

June 1996



6. Experimental results

6.1 Introduction

The experimental work was designed, as described in Chapter 5, to determine the *in situ* stress-strain response of Oxford Clay when subjected to the stress changes equivalent to those imposed by the Elstow excavation. Because of the limited number of specimens, the approach used was to carry out multiple-stage stress path tests consisting of constant p' and constant q stress probes originating from the same initial stress state, while attempting to reproduce the *in situ* stress state and the stress history of the deposit.

In this chapter the characteristic features of the stress-strain response of the soil are discussed. These are primarily the non-linearity and anisotropy.

The material stiffness non-linearity is most noticeable in the small strain range of 0.001% to 0.1% axial strain. This response was captured using local instrumentation in the form of non-contacting proximity transducers (see section 5.4.7) but their accuracy was not sufficient to conclude whether the maximum soil stiffness was recorded. However, an upper bound to the stiffness response was provided by recording the shear wave travel velocity through the specimen using bender elements to calculate the very small strain shear stiffness at less than 0.001% strain.

The soil behaviour is, at least, influenced by the factors discussed in section 5.1 and, consequently, the influence of stress level, imposed stress path and stress history is discussed.

The conclusions regarding the *in situ* soil stiffness have been drawn from a limited number of extended multiple-stage stress path tests and the validity of this approach is discussed by comparing the stress-strain response of the specimen along stress paths repeated at the beginning and the end of a particular test.

The current research work has been supplemented by experimental results obtained at the time of the Elstow excavation and these results have been included in this chapter to show the soil response during undrained shearing.

6.2 Stress path testing carried out as part of Elstow site investigation

6.2.1 Summary of tests

A series of 8 consolidated undrained triaxial tests, summarised in Table 6.1, were carried out in the stress path apparatus at the University of Sheffield at the time of the Elstow site investigation (Hird *et al.*, 1987). All tests were carried out on specimens of unweathered Oxford Clay. Half of the specimens were trimmed from the block samples taken as described in section 3.7.2. Both vertically and horizontally orientated specimens were formed. The trimming process took 8 hours, first using a wire saw and then a sharp knife, and required extreme care to avoid fracturing the block. The remaining specimens were from tube samples of approximately 100mm internal diameter. Although apparently undisturbed sections of the extruded sample were chosen to prepare specimens for testing, it was noted during the Elstow site investigation that the Mazier technique used to obtain the tube samples often caused excessive sample disturbance.

The tests were carried out in a Bishop and Wesley type hydraulic stress path cell modified to measure specimen strains locally in the central region using non-contacting proximity transducers (Sangamo type DT18M and DT19M). Two pairs of transducers on opposite sides of the specimen measured the axial strain and one pair measured the radial strain across the specimen diameter. The pore water pressures occurring in the specimens during the undrained shearing were measured at the base and also at the mid-height using a miniature pressure transducer. The specimen volume change during consolidation was measured directly by an Imperial College type volume change unit. Full details of the stress path cell and the local strain instrumentation are given in Yung (1987).

The local strain measurement system and the calibration procedures were less sophisticated than those used in the present work. Consequently, for a 95% confidence interval, the maximum possible error was about 0.009% and the largest probable random was about 0.003%

| Test name | Date | Sample number | Specimen origin | Specimen orientation | | Bulk density | Water content | |
|-----------|-----------|-----------------------|-----------------|----------------------|------------|-------------------|---------------|-------|
| | | | | Vertical | Horizontal | | Initial | Final |
| | | | | | | Mg/m ³ | % | % |
| Y1 | 25-Feb-87 | E/BT3/6.3/M12 | Tube | 3 | | 1.86 | 28.7 | 28.0 |
| Y2 | 24-Mar-87 | E/BT5/11.85-12.72/M12 | Tube | 3 | | 1.85 | 30.8 | 30.1 |
| Y3 | 07-Apr-87 | E/BT5/11.85-12.72/M22 | Tube | 3 | | 1.86 | 29.7 | 29.2 |
| Y4 | 05-May-87 | E/BT5/11.85-12.72/M31 | Tube | 3 | | 1.86 | 28.6 | 28.3 |
| Y5 | 01-Jun-87 | E/EX18/24.019/BL1/H | Block | | 3 | 1.85 | 28.0 | 28.5 |
| Y6 | 19-Jun-87 | E/EX18/24.019/BL1/V | Block | 3 | | 1.85 | 27.2 | 26.3 |
| Y7 | 08-Jul-87 | E/EX18/23.923/BL/H | Block | | 3 | 1.88 | 27.1 | 29.0 |
| Y8 | 27-Jul-87 | E/EX18/23.923/BL/V | Block | 3 | | 1.86 | 27.1 | 28.7 |

Table 6.1 - Summary of stress path tests carried out at the time of the Elstow site investigation

(Yung, 1987; Hird and Yung, 1987).

The back pressure system was flushed before, and during, placing of the specimen on the base pedestal to avoid trapping air. The specimens were generally subjected to a confining pressure of 100kPa under undrained conditions and the pore pressure response monitored over a 24 hour period in which the response equalised. The specimen was then conventionally saturated applying cell pressure and back pressure increments to maintain the specimen effective mean normal stress at its initial value. The specimen was consolidated isotropically to the required effective stress level. Undrained shearing was generally carried out at a constant stress rate, although for certain specimens (Table 6.2) this rate was increased between 0.1% and 1% axial strain in order to minimise testing times yet ensure an adequate definition of the stress-strain response both in the small strain region and as failure was approached.

| Test name | Initial effective stress | Initial B value | Final B value | Stress rate | | |
|-----------|--------------------------|-----------------|---------------|-------------|--------|------|
| | | | | 0-0.1% | 0.1-1% | >1% |
| | | | | kPa/hour | | |
| Y1 | 5.7 | 0.54 | 0.94 | 9.1 | 29.25 | 9.1 |
| Y2 | 67.4 | 0.61 | 0.97 | 16.8 | 27.9 | 30 |
| Y3 | 67.9 | 0.98 | 1.00 | 6.8 | 11.3 | 23.5 |
| Y4 | 80.3 | 0.90 | 0.98 | 5 | 5 | 5 |
| Y5 | 57.7 | 0.55 | 0.98 | 5 | 5 | 5 |
| Y6 | 72.8 | 0.57 | 0.98 | 5 | 5 | 5 |
| Y7 | 86.2 | 0.31 | 1.00 | 5 | 5 | 5 |
| Y8 | 83.0 | 0.16 | 0.99 | 5 | 5 | 5 |

Table 6.2 - Summary of initial specimen effective stress and shearing loading rate

6.2.2 Interpretation of undrained behaviour in stress path tests

Recalling the constitutive relationships presented in section 2.2,

$$\begin{bmatrix} \delta\epsilon_v \\ \delta\epsilon_s \end{bmatrix} = \begin{bmatrix} \frac{1}{K'} & \frac{1}{J'_{qv}} \\ \frac{1}{J'_{ps}} & \frac{1}{3G'} \end{bmatrix} \cdot \begin{bmatrix} \delta p' \\ \delta q \end{bmatrix} \dots\dots\dots (6.1)$$

For undrained loading, $\delta\epsilon_v = 0$, and thus,

$$\frac{\delta q}{\delta p'} = \frac{-J'_{qv}}{K'} \dots\dots\dots (6.2)$$

If the soil behaviour is assumed to be elastic the degree of anisotropy can be assessed from the gradient of the stress path in an undrained triaxial test. This may be interpreted in terms of the parameter, α , introduced by Graham and Houlsby (1983) for cross-anisotropic soil discussed in the following chapter (the value of α^2 represents the ratio of the Young's moduli, E'_h/E'_v).

$$\frac{\delta q}{\delta p'} = \frac{-J'_{qv}}{K'} = \frac{-J'}{K'} = -\frac{3\alpha^2 E^*}{\frac{2\alpha^2 - 2\alpha v^* - 2 + 2v^*}{\alpha^2 E^*}} = -\frac{3\alpha^2 E^*}{\alpha^2 - 4\alpha v^* + 2 - 2v^*}$$

$$\frac{\delta q}{\delta p'} = -\frac{3(\alpha^2 - 4\alpha v^* + 2 - 2v^*)}{2(\alpha^2 - \alpha v^* - 1 + v^*)} \dots\dots\dots (6.3)$$

where, v^* is an equivalent Poisson's ratio for cross-anisotropic soil

Equation 6.3 may be written as a quadratic in α as shown in equation 6.4,

$$\left(2\frac{\delta q}{\delta p'} + 3\right)\alpha^2 + \left(-2v^*\frac{\delta q}{\delta p'} - 12v^*\right)\alpha - 2\frac{\delta q}{\delta p'} + 2v^*\frac{\delta q}{\delta p'} + 6 - 6v^* = 0 \dots\dots\dots (6.4)$$

which may be solved to give the degree of anisotropy in terms of the stress path gradient and v^* as shown in equation 6.5,

$$\alpha = \frac{v^*\left(\frac{\delta q}{\delta p'} + 6\right) \pm \sqrt{(v^* - 2)^2\left(\frac{\delta q}{\delta p'}\right)^2 + 6(2v^* - 1)(v^* + 1)\left(\frac{\delta q}{\delta p'} + 3\right)}}{2\left(\frac{\delta q}{\delta p'}\right) + 3} \dots\dots\dots (6.5)$$

For a soil which is stiffer in the horizontal direction,

$$\alpha > 1, \infty > \frac{\delta q}{\delta p'} > -\frac{3}{2} \dots\dots\dots (6.6)$$

For a soil which is stiffer in the vertical direction,

$$0 < \alpha < 1, \infty > \frac{\delta q}{\delta p'} > 3 \dots\dots\dots (6.7)$$

The limits imposed on the undrained stress path direction by cross-anisotropic elasticity as described by equations 6.6 and 6.7 are shown digrammatically in Figure 6.1.

In a conventional undrained triaxial test the stress path will not be vertical unless the soil being tested is isotropically elastic. In general, the deviatoric and volumetric responses are coupled and it is not possible to determine the effective deviatoric stiffness from the stress-strain response.

$$\frac{\delta q}{\delta \epsilon_s} = 3G_u = \frac{3G'J'_{qv}J'_{ps}}{(J'_{qv}J'_{ps} - 3K'G')} \dots\dots\dots (6.8)$$

In order to compare the drained and undrained moduli therefore, values must be assumed for the volumetric stiffness and coupling stiffness. The response may be simplified by assuming the coupling stiffness are the same as shown in equation 6.9.

$$\frac{\delta q}{\delta \varepsilon_s} = 3G_u = \frac{3G'J'^2}{(J'^2 - 3K'G')} = 3G' \left[\frac{1}{1 - 3G' \left(\frac{K'}{J'^2} \right)} \right] \dots\dots\dots (6.9)$$

However, equation 6.10 shows that the stress-strain curve is still linked with the coupling stiffness and therefore a direct comparison may not be drawn between the undrained and drained deviatoric stiffness coefficients.

$$\frac{\delta q}{\delta \varepsilon_s} = 3G' \left[\frac{1}{1 + \left(\frac{\delta p'}{\delta q} \right) \cdot \left(\frac{3G'}{J'} \right)} \right] \dots\dots\dots (6.10)$$

Similarly, for cross-anisotropic soil, a direct comparison of Young's moduli from drained and undrained tests is not possible and therefore the anisotropy factor may not be determined in this way. Only through using the gradient of the stress path is it possible to obtain information regarding the degree of anisotropy from undrained stress path tests.

6.2.3 Undrained stress path test results

The stress path test results have been presented by Hird *et al.* (1987) and will only briefly be summarised here. The further analyses carried out as part of the present research involved,

- the interpretation of the undrained effective stress paths, as described in 6.2.2, to infer a degree of anisotropy from the soil response,
- determining the undrained deviatoric stiffness to make a qualitative comparison with the stiffness response obtained from the constant p' stress paths carried out as part of the current research.

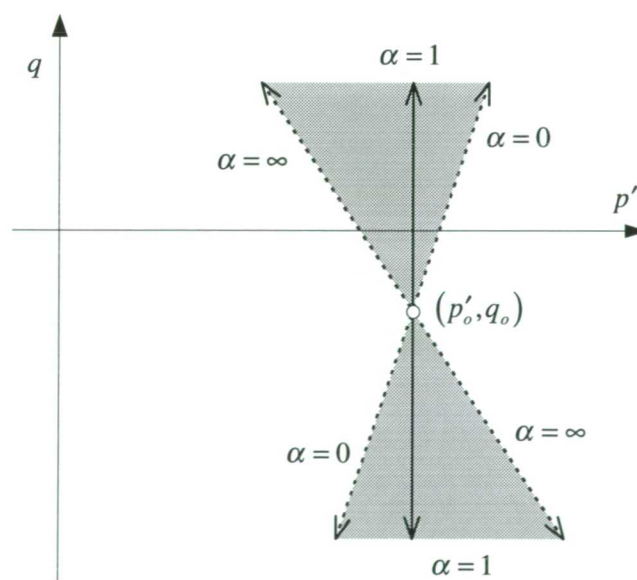


Figure 6.1 - Region of allowable effective stress paths for constant volume deformation of cross-anisotropic elastic soil

The undrained effective stress paths are shown in Figure 6.2. It is seen that the specimen response is erratic in tests Y1, Y2 and Y3. This is due to these tests being carried out at a loading rate which was varied in steps as the strain level increased (see Table 6.2). For the remaining tests, which included all the block sample specimens, the choice of a constant loading rate significantly improved the response. The smoothness of the undrained stress path is indicative of the quality of the measured stress-strain behaviour and accordingly analysis was concentrated on these tests.

The stress-strain responses of both the horizontally and vertically orientated specimens are shown in Figure 6.4 as deviator stress against triaxial shear strain for small and large strain levels. The volumetric strain response shown as an inset on this figure is that recorded locally by the axial and radial proximity transducers. This shows that the specimen deformed with uniform strains in the central region of the specimen up to approximately 100kPa but that after this point the local measurements no longer reflected the undrained response (the zero volumetric strain condition of a Poisson's ratio of approximately 0.5, as shown in Figure 6.3, is generally maintained up to this point). The stress-strain response in all cases is noticeably non-linear and the horizontally orientated specimens record the stiffest response. The undrained tangent Young's moduli implied by the stress-strain response are shown in Figure 6.5. Although it is not possible to accurately resolve the stiffness moduli at the smallest strain levels, the ratio of horizontal to vertical undrained Young's moduli is approximately 2 up to a stress change of 80kPa. Beyond this stress change the vertically orientated specimens experience greater plastic straining as failure is approached and the specimen stiffness falls rapidly.

An alternative interpretation of the degree of anisotropy of the specimens may be calculated using the initial stress path direction as previously described in section 6.2.2. The gradient of each stress path in Figure 6.2 is shown against change in deviator stress in Figure 6.6. For all the vertically orientated specimens, the stress path is inclined left of vertical indicating, as expected, that the soil is stiffer in the horizontal direction. This is confirmed by the positive gradient of the stress path followed by the horizontally orientated specimens. Using equation 6.5, the implied anisotropy factor, α^2 , the ratio of the horizontal to vertical drained Young's moduli, was calculated for a suitable range of possible Poisson's ratio values of 0.1 to 0.3. As shown in Figure 6.7, this suggests a ratio of between 2.5 and 4 for vertically orientated specimens.

The stress-strain response of the soil specimens interpreted as tangent deviatoric stiffness values and shown Figure 6.8 against triaxial shear strain. For the reasons described in section 6.2.2 comparisons with the drained deviatoric stiffness moduli presented in later sections must be approached with care.

There is no trend evident linking the deviatoric stiffness with the mean effective normal stress and thus the stiffness response normalised with the initial effective mean normal stress, p'_o , shown in Figure 6.9 shows a less unified view of the data. The implication is that either the dependence of the soil stiffness on the current stress level is minimal under initially isotropic stress conditions, or that the effect of the initially higher p' is cancelled by the possibly greater sample disturbance in the case of the Mazier tube samples.

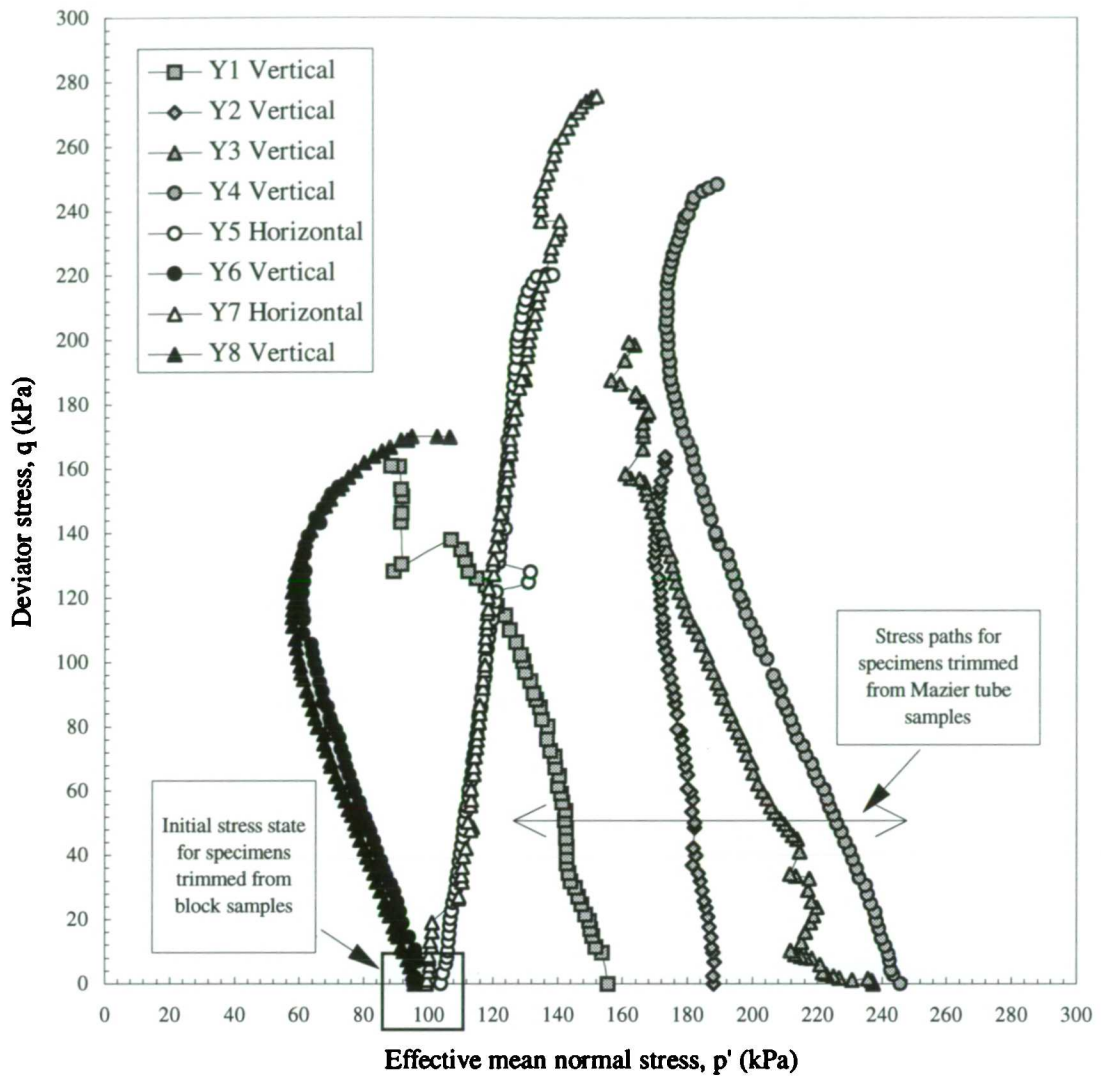


Figure 6.2 - Undrained stress path response

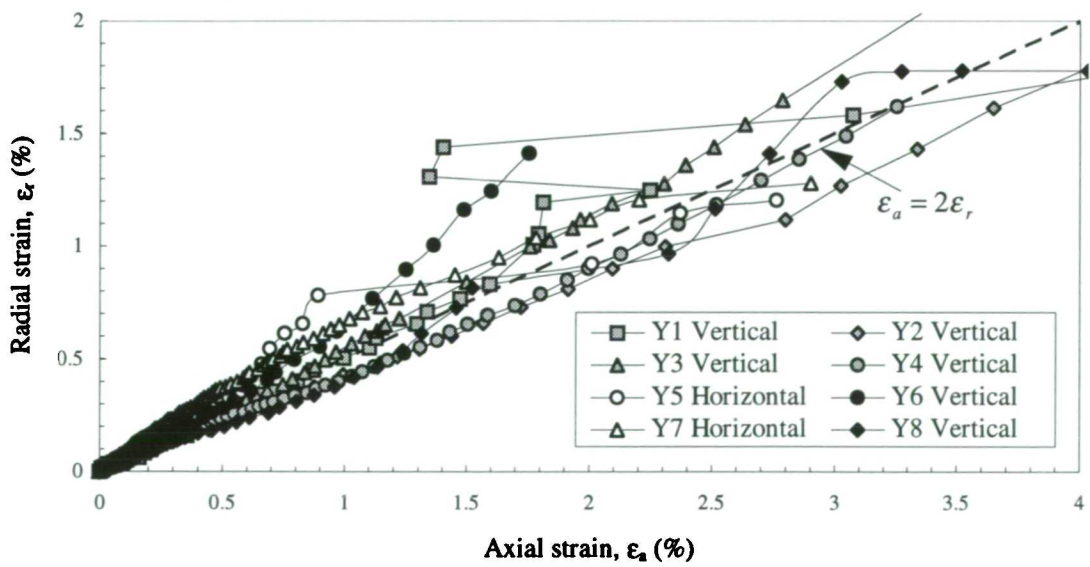


Figure 6.3 - Uniformity of strains in undrained stress path tests

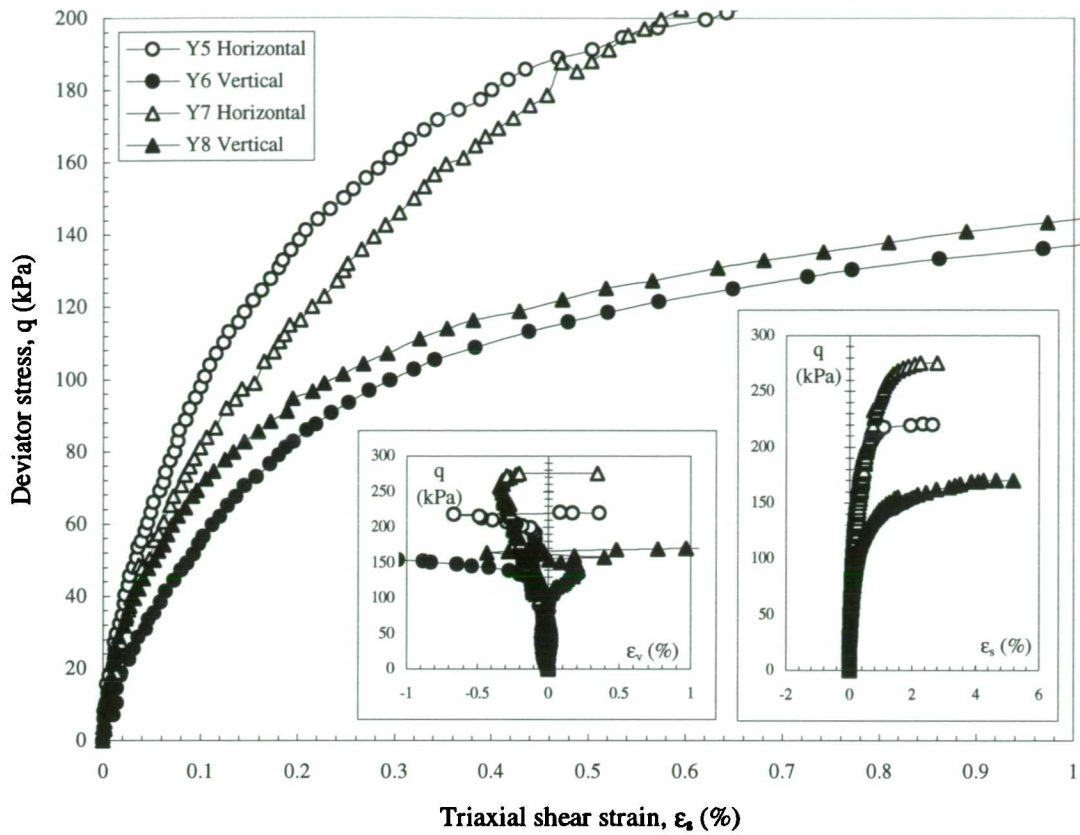


Figure 6.4 - Deviator stress vs. triaxial shear strain for horizontally and vertically orientated specimens trimmed from block samples

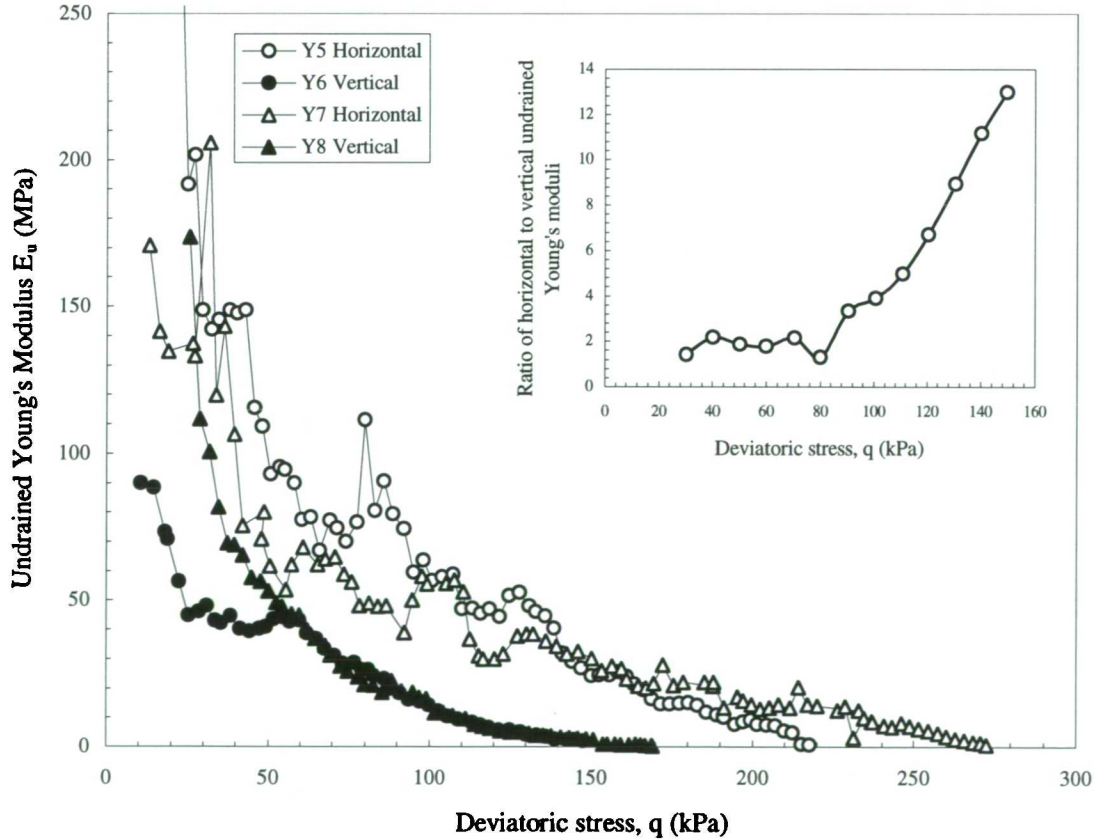


Figure 6.5 - Horizontal and vertical Young's moduli derived from stress path tests on specimens trimmed from block samples

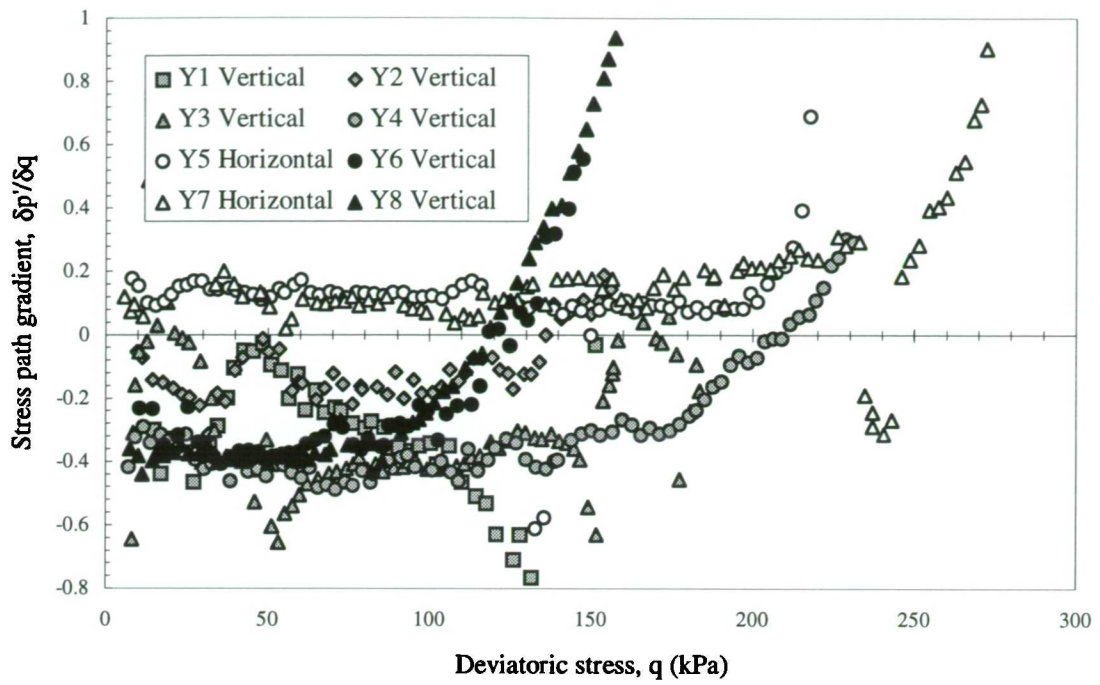


Figure 6.6 - Gradient of the stress paths recorded in each undrained stress path test

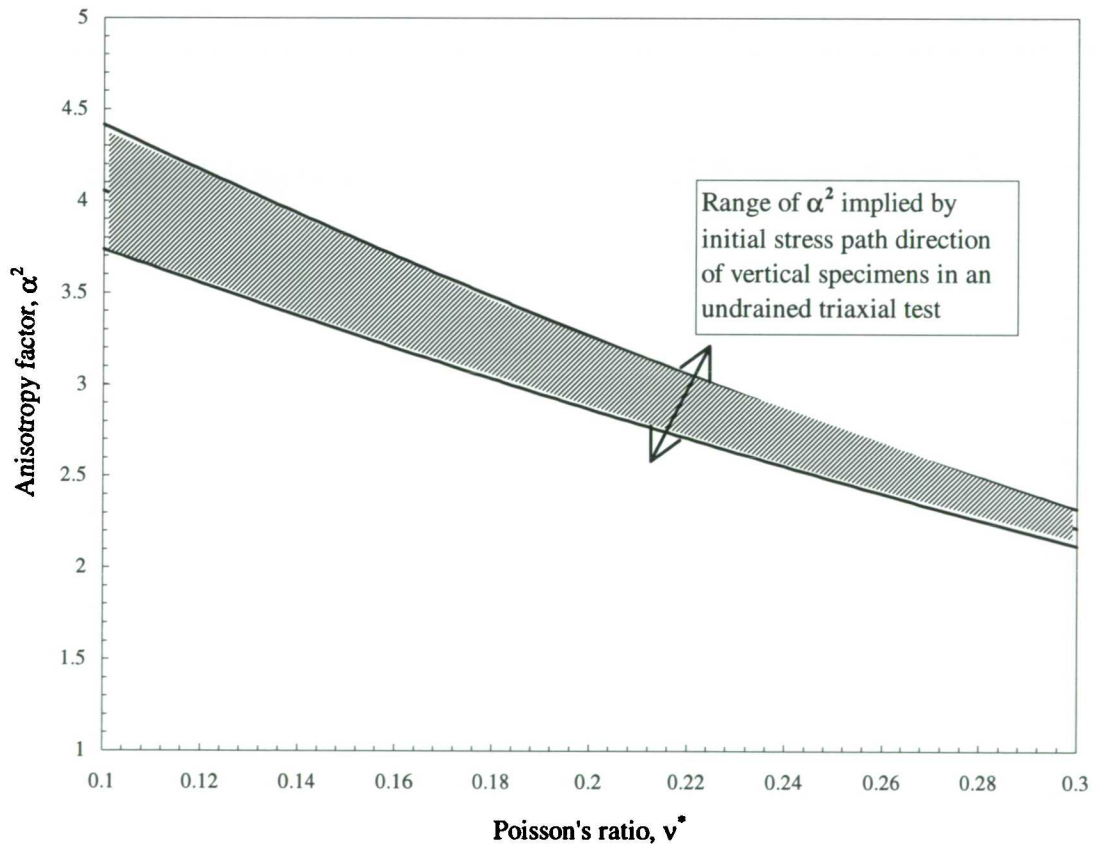


Figure 6.7 - Anisotropy factor implied from the gradient of undrained triaxial stress paths and an assumed variation of Poisson's ratio

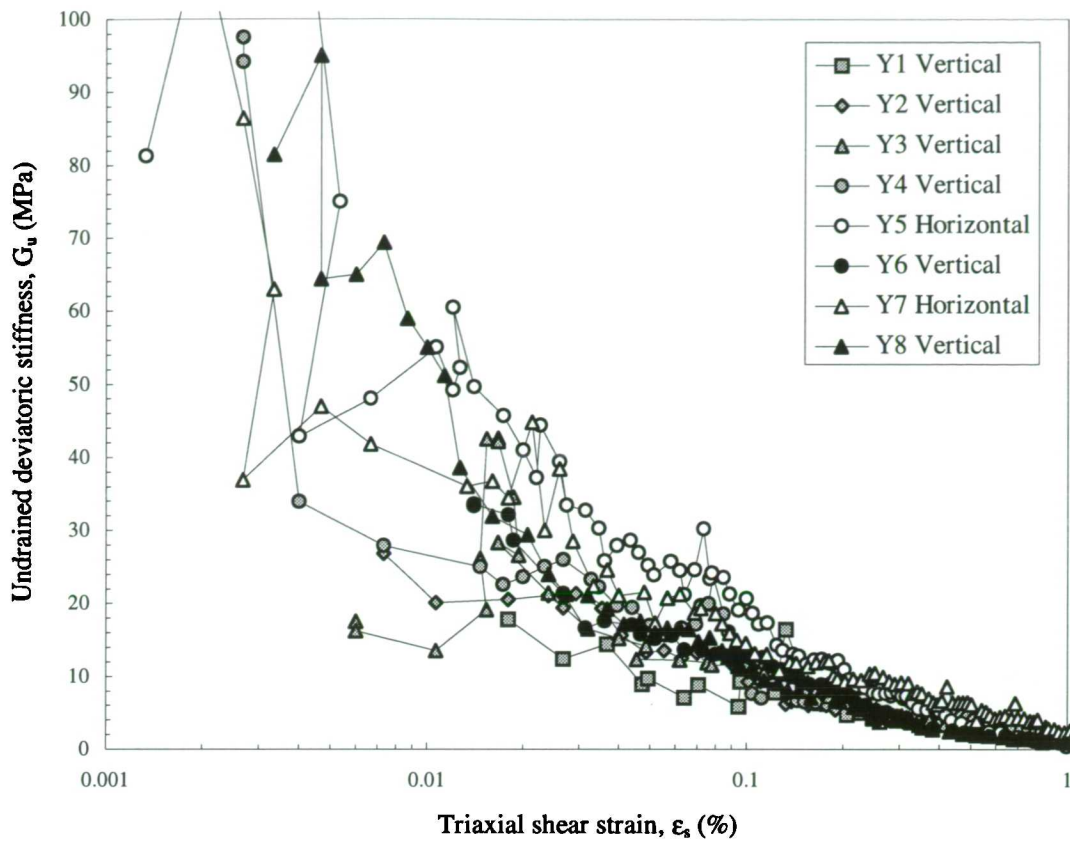


Figure 6.8 - Undrained deviatoric stiffness against triaxial shear strain for all undrained stress path tests

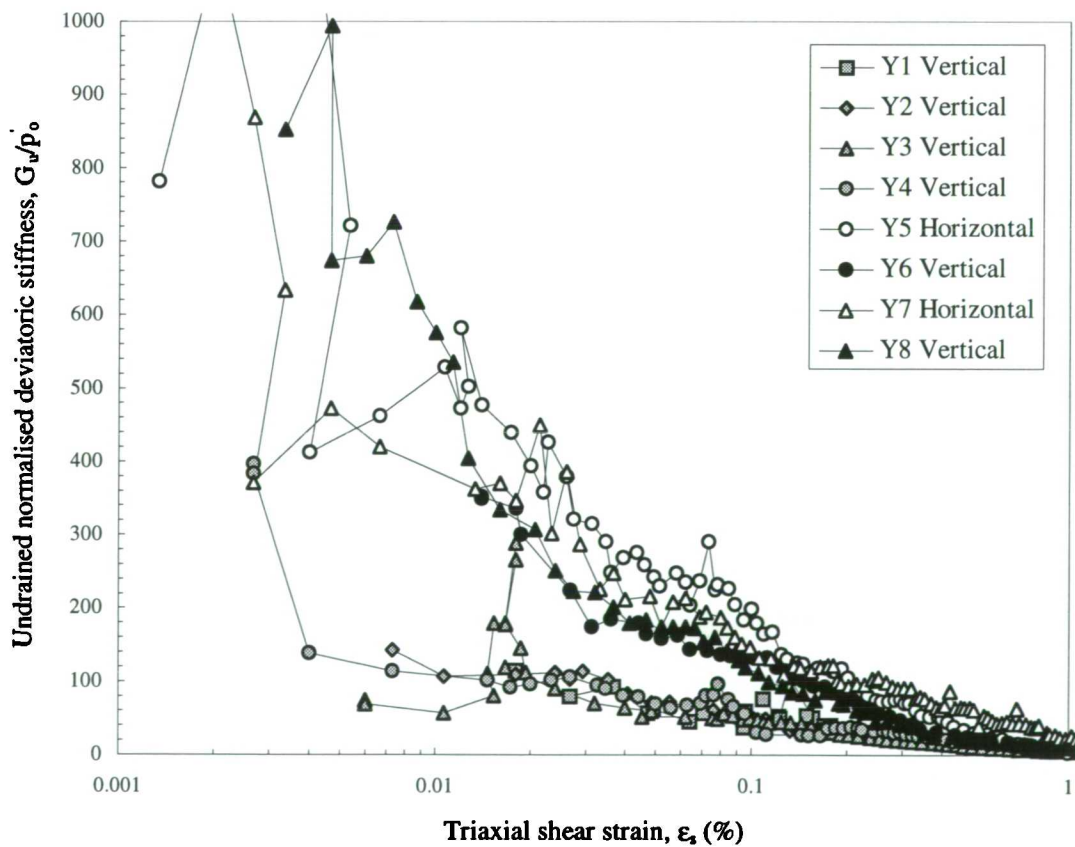


Figure 6.9 - Undrained deviatoric stiffness normalised with the initial effective mean normal stress, against triaxial shear strain for all undrained stress path tests

6.3 Stress path testing in current research programme

6.3.1 Summary of stress paths

A series of nine stress path tests was carried out on specimens trimmed from block samples of Oxford Clay. Each test consisted of multiple stress paths in order to obtain the maximum data from the limited material available, as described in section 5.3.2. Four of the tests were stopped prematurely: one because a number of local axial strain targets became detached and three because the load cell failed. Six of the tests were carried out on an existing stress path cell with the remainder on an identical apparatus commissioned during the current research. A system of bender elements was installed in each stress path cell which provided seismic wave travel velocity measurements in three of the tests (see section 6.5).

The soil tested was either unweathered or weathered Lower Oxford Clay from block samples stored since the Elstow excavation, or unweathered Lower Oxford Clay from block samples obtained from the Kempston Pit of the London Brick Company situated half a mile away from the Elstow site (see section 5.2).

A summary of the specimens in each of the stress path tests is given in Table 6.3 and each test is discussed below in section 6.3.3.

| Test | Block sample | Origin | Degree of weathering | Depth (m) | Initial water content (%) |
|------|-------------------|--------------|----------------------|-----------|---------------------------|
| T01 | E/EX15 25.640 /BL | Elstow | Unweathered | 4.86 | 25.9 |
| T02 | E/EX15 25.640 /BL | Elstow | Unweathered | 4.86 | 25.8 |
| T03 | E/EX17 24.910 /BL | Elstow | Unweathered | 5.59 | 28.6 |
| T04 | KEMP/21.5/ BL 1 | Kempston Pit | Unweathered | 9.0 | 29.0 |
| T05 | KEMP/21.5/ BL 1 | Kempston Pit | Unweathered | 9.0 | 27.5 |
| T06 | KEMP/21.5/ BL 1 | Kempston Pit | Unweathered | 9.0 | 27.5 |
| T07 | E/EX9 29.185 /BL | Elstow | Weathered | 1.315 | 29.4 |
| T08 | E/EX9 29.185 /BL | Elstow | Weathered | 1.315 | 28.5 |
| T09 | KEMP/21.5/ BL 1 | Kempston Pit | Unweathered | 9.0 | 26.6 |

Table 6.3 - Origins of stress path test specimens

6.3.2 Determining *in situ* effective stress state

It was assumed that, throughout the sampled depth of the Oxford Clay, the *in situ* stress state lay on the limit state of passive failure (as described in section 5.3.2) and that an angle of friction based on the frictional *compressive* strength of the Elstow deposit (Figure 3.5) could be used. To check experimentally the validity of this assumption the following aspects of the experimental programme could be considered:

- In each stress path test an initial confining pressure was applied under undrained conditions until a positive pore water pressure response was recorded. From this the initial suction within the specimen could be deduced. The B value indicating the degree of saturation was also recorded as a measure of the confidence in the estimated initial suction. The initial

specimen suction inferred from the increase in confining pressure, and the associated B value, from each test are presented in section 6.3.3.

- A series of high pressure oedometer tests was performed as described in section 5.8. This provided an indication of the previous vertical overburden pressure and was designed to show whether the soil deposit was as heavily overconsolidated as reported. The results of three high pressure oedometer tests are shown in Figure 6.10. It is apparent that the pressure, although increased to the system limits, was not sufficient to precisely show the onset of yield associated with the past maximum overburden pressure. Using this figure, an estimate using Casagrande's construction suggests a past maximum overburden pressure of 7-10MPa had been experienced. This corresponds to a previous maximum level of overburden of 700-1000m (assuming a water table at the surface and an average bulk unit weight of 2.0Mg/m^3). The level, suggested by Jackson and Fookes (1974) of 500m (see section 3.3.2) is not significantly at odds with this value. The results give no reason to doubt the assumption that the *in situ* stress state lies on or close to the passive failure limit state. Burland *et al.* (1979) show an example of a less heavily overconsolidated clay deposit in which the upper 4.0m depth was at passive failure. Bond and Jardine (1995) show an intact London Clay deposit with an OCR of 20 to 40 which is assumed to be at passive failure.

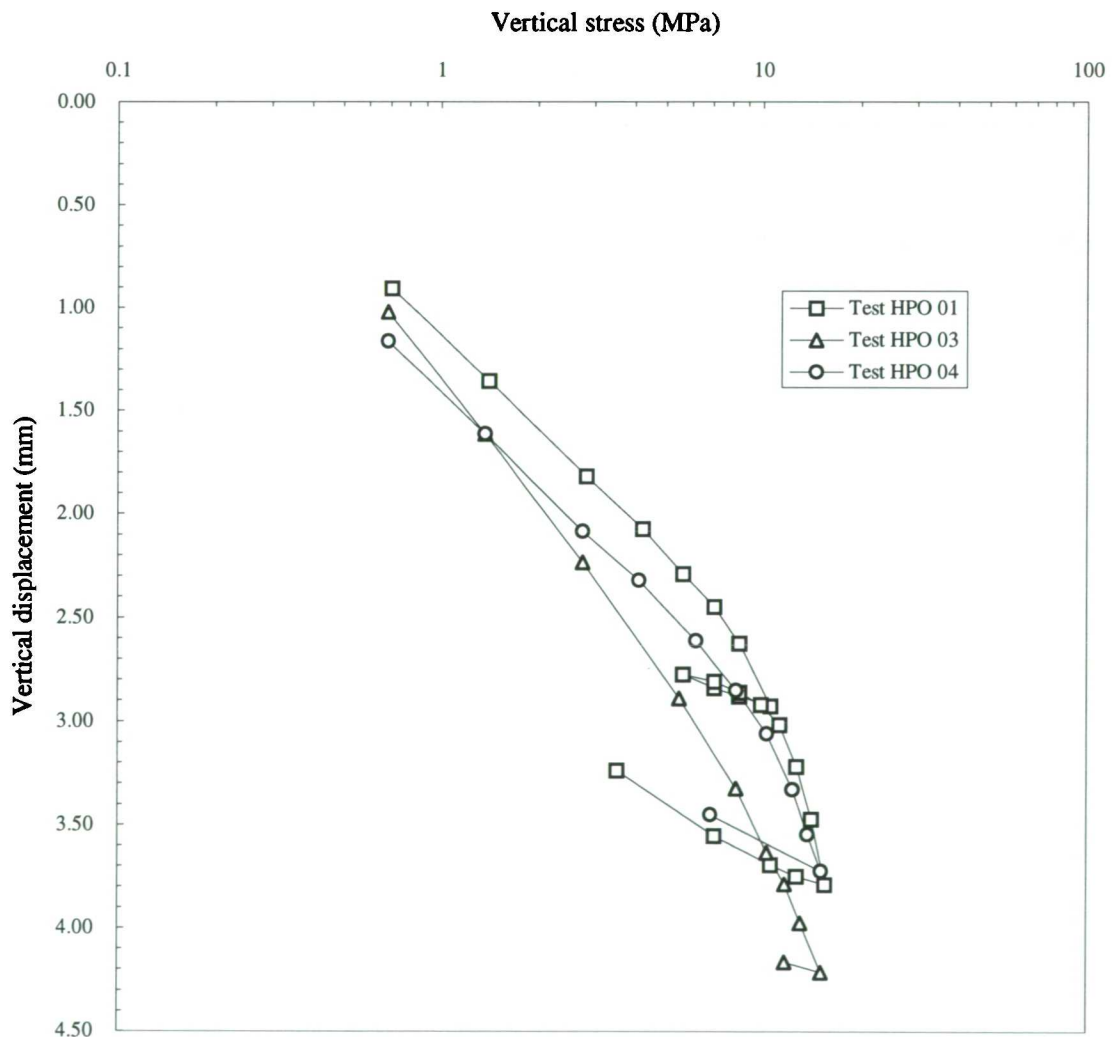


Figure 6.10 - Summary of all high pressure oedometer tests

- A series of filter paper suction tests (Chandler and Gutierrez, 1986) were carried out as described in section 5.9. The results of these tests are shown in Figure 6.11. As described in section 5.9 the calibrated filter paper suction is plotted with respect to time to give an indication of the possible error in its value. The figure shows that the suctions for the Elstow block samples, at 250-300kPa, from tests SUC01 and SUC02 are significantly greater than the approximately 60kPa suction recorded in test SUC03 for the Kempston Pit block sample.

It was initially planned to perform a suction test prior to each stress path test to provide an estimate of the *in situ* effective mean normal stress which could be combined with the known *in situ* vertical stress to obtain an *in situ* state in $p'-q$ stress space. The high values recorded in the initial suction tests, however, corresponded to apparently unreasonable values of K'_o which exceeded K'_p . The first stress path of test T02 (described in section 6.3.3) was carried out at $p'=250\text{kPa}$, equal to the suction recorded in the corresponding filter paper test. The specimen for test T02 was trimmed from a block sample taken from 4.6m depth and using an estimated effective vertical stress, an *in situ* K'_o of greater than 7 is calculated (suggesting a failure state close to the tension cut-off). The test failed prematurely while attempting to reinstate an appropriate initial stress state at an equivalent K'_o of 2.79. The results of the filter paper tests on the Elstow block samples do not concur well with the lower suctions estimated from the application of confining pressure in the associated stress path tests on specimens from the same block samples. The *in situ* effective mean normal stresses estimated from the initial stage of the triaxial tests are in the range 50-100kPa. It is possible that the triaxial test specimen could no longer maintain its suction during the trimming process or during setting up and coming into contact with the free water in the back pressure system. The use of the fuse-wire technique

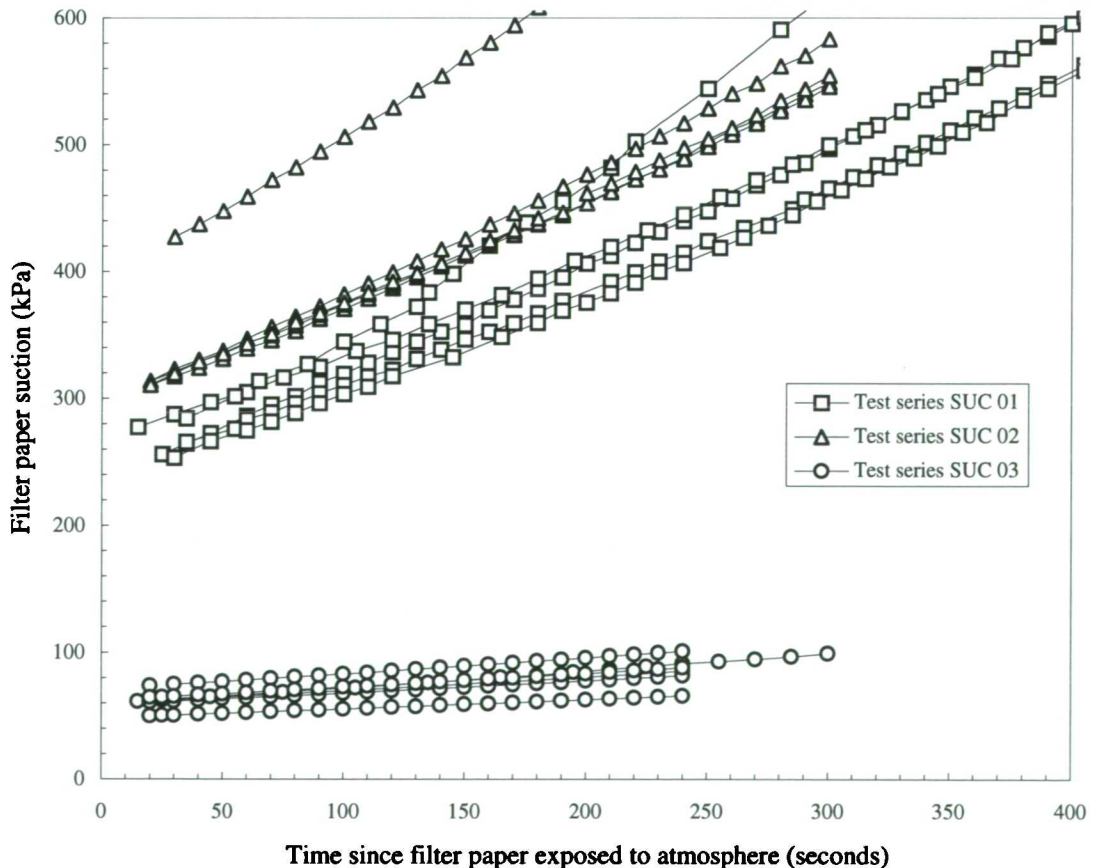


Figure 6.11 - Results of filter paper suction tests

(Burland and Maswoswe, 1982) could have prevented the specimen coming into contact with free water, although this technique was not used for the reasons stated in section 5.5.3.

Since there was considerable uncertainty about the *in situ* stress state it was decided to abandon the suction measurements and proceed with the stress path tests using a range of initial effective mean normal stress which would cover the likely range encountered throughout the deposit. The initial deviator stress level was chosen conservatively to correspond with a passive frictional strength of $\phi' = 25^\circ$ as discussed in section 5.3.2.

6.3.3 Test descriptions

Each test is summarised individually in Table 6.4 to Table 6.11, and the entire experimental programme is summarised in Table 6.12. The following sections describe each test in more detail. This involves detailing the name and type of each stress path carried out using the sign convention defined in Figure 6.12. This discussion is provided since it is essential to analyse the results of the tests in the knowledge of any peculiarities in the setting up of the specimens, or in the testing procedures.

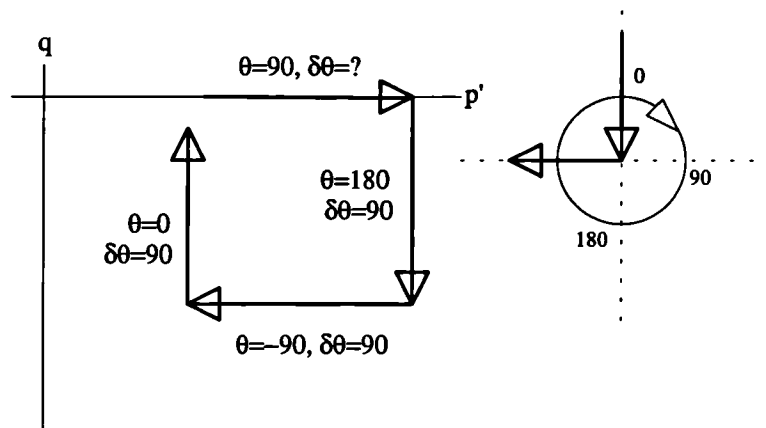


Figure 6.12 - Sign convention used in stress path direction

The stress paths shown individually for each test in the following figures are summarised diagrammatically in Figure 6.13.

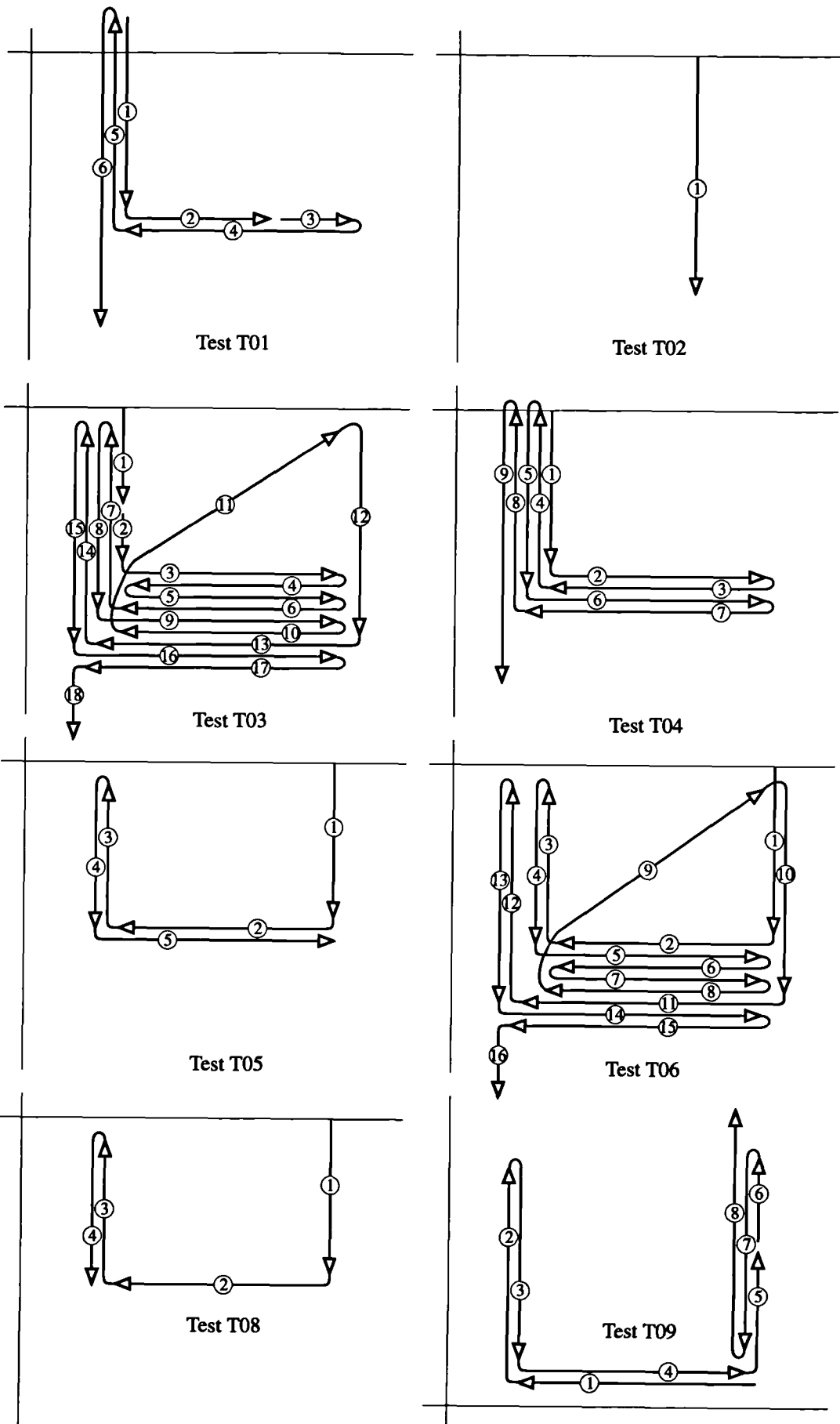


Figure 6.13 - Figurative representation of stress paths carried out in p' - q space for each stress path test

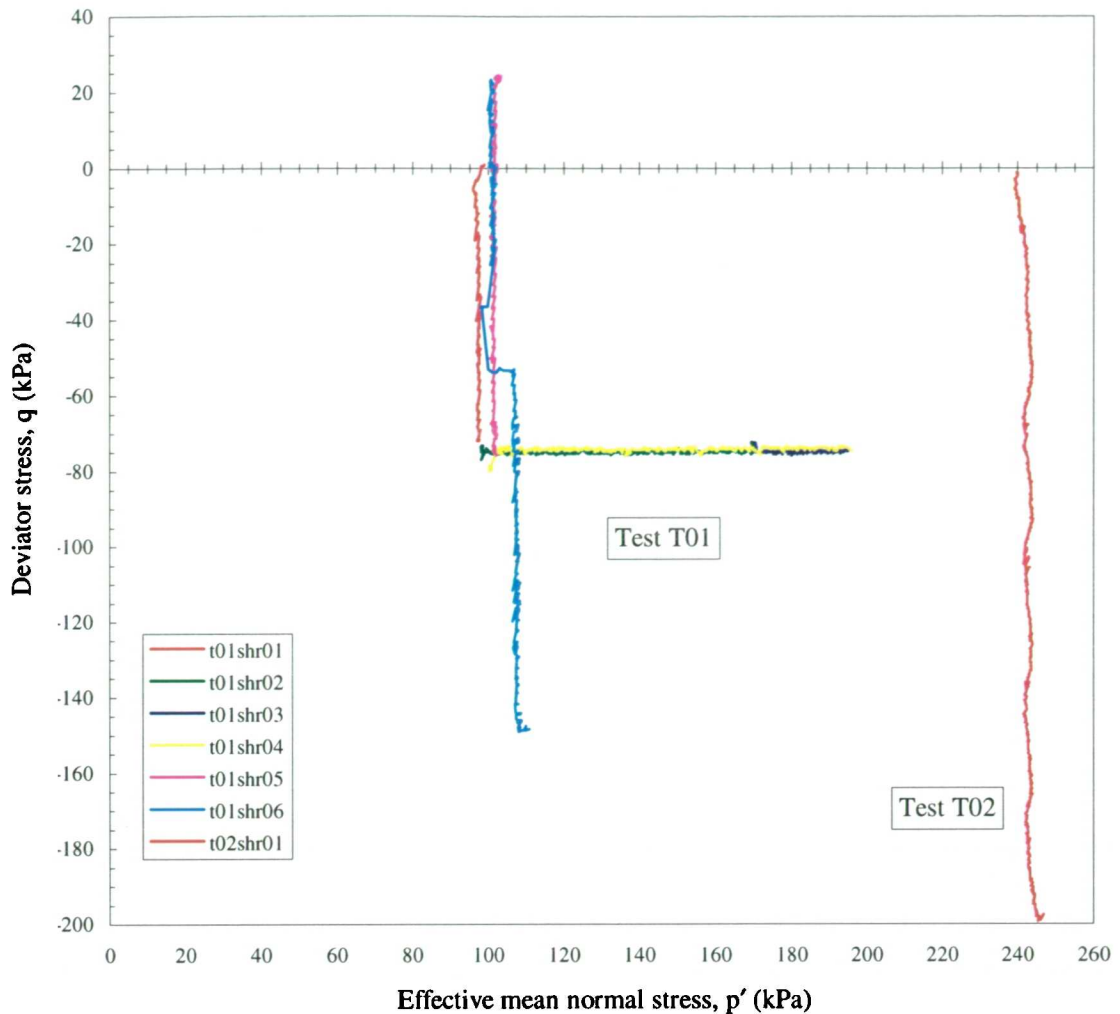


Figure 6.14 - Stress paths performed in tests T01 and T02

TEST T01

The test specimen was trimmed from an unweathered Oxford Clay block sample (E/EX15 25.640 /BL) taken from 4.86m depth at the Elstow site as described in section 5.2.1. It was noted during the trimming process that the specimen seemed to dry out very quickly in the temperature and humidity controlled environment of the laboratory. It was subsequently decided that a locally more humid environment would be provided by placing wet towels in the vicinity of the sample. The trimming process proved to be arduous and time consuming and became more difficult as the sample continued to dry out. The specimen required patching locally with remoulded soil and it was evident that fissures were opening up as the specimen dried.

The trimming process continued over two days. The first day was required to separate the block sample into quarters for further storage with the specimen trimming taking place on the second day after the block was originally exposed. As each section of the original block sample was exposed the sections of soil were continually resealed to prevent excessive drying.

The test was set up following the standard procedures outlined in section 5.5.2 with the following differences. The back pressure system was not adequately flushed before mounting the specimen nor was the miniature pore water pressure probe completely de-aired prior to testing. The incomplete flushing caused large discrepancies between the volume change measured locally on the specimen with that recorded by the volume change unit attached to the

back pressure line, and also required a large back pressure to achieve a suitable degree of saturation of the specimen.

Once the specimen had been set up in the cell, an initial confining pressure of 100kPa was applied under undrained conditions and the specimen was left for 24 hours to equilibrate. The pore pressure measured at the top and bottom of the specimen (10-15kPa) indicated an initial effective stress within the specimen of 85-90 kPa. The initial mid-height pore pressure measurement did not concur with these values, giving a lower value probably due to the insufficient initial deairing of the transducer. Specimen saturation initially proceeded, however, at an effective stress of 10kPa leading to swelling of the specimen but provided a final B value of 0.96 after simultaneously increasing the cell pressure and back pressure equally to a back pressure of 390kPa. Consolidation was carried out after a step increase in cell pressure (B=0.99) to an initial effective stress of approximately 100kPa. The load cell was connected and the system left once more to allow the small stress changes imposed during connection to equilibrate. Immediately prior to shearing, however, a leak developed in the back pressure system. The drainage lines to the specimen were closed, the cell pressure removed and the cell top removed to fix the leak before repressurising the system. This operation lasted less than an hour and it was assumed that the suctions developed within the specimen due to unloading would have been maintained and, since the specimen was already close to full saturation, disturbance to the specimen would have been minimal. The mid-height pore water pressure probe showed full recovery to the previous value before the drainage valves were reopened to the back pressure.

The effective stress paths followed during the stress path probe stages are shown in Figure 6.14 and the details of these paths are given in Table 6.4.

During the first stress path, t01shr01 (or 'path 1'), a local strain target became detached and axial strain measurements were subsequently based on one side of the specimen only. This was not thought to be a significant error since the local and endcap axial strain measurements were in very good agreement previously and the endcap measurements were self-consistent suggesting a uniform specimen response to loading. During the final stress path, path 6, taking the specimen to failure, it was noticed that there were jumps in the external axial strain readings indicating slippage of the top cap / load cell suction connection. These jumps also affected the local strain measurements. This was probably due to the slight tilting of the specimen changing the alignment of the proximity transducers and their targets. The endcap axial strains were not affected by these jumps and the stress-strain response was interpreted in terms of these

| Stage name | Date | Δt_h (hours) | q_o (kPa) | p'_o (kPa) | Δq (kPa) | $\Delta p'$ (kPa) | ϑ (°) | $\Delta \vartheta$ (°) |
|------------|-----------|-------------------------|----------------|-----------------|---------------------|----------------------|--------------------|---------------------------|
| t01pre | 11-Jun-92 | - | 0.0 | | 0.0 | | 90° | 90° |
| t01sat | 14-Jun-92 | - | 0.0 | 7.5 | 0.0 | 10.8 | 90° | 0° |
| t01con | 23-Jun-92 | - | 0.0 | 16.7 | 0.0 | 76.7 | 90° | 0° |
| t01cct | 02-Jul-92 | 189.5 | 4.3 | 96.1 | -2.0 | -0.1 | 90° | 0° |
| t01shr01 | 03-Jul-92 | 26.7 | -3.5 | 96.7 | -68.4 | 0.5 | 180° | 90° |
| t01shr02 | 06-Jul-92 | 22.7 | -77.1 | 98.1 | 2.9 | 72.6 | 90° | 270° |
| t01shr03 | 10-Jul-92 | 27.4 | -75.0 | 170.7 | -0.1 | 24.0 | 90° | 0° |
| t01shr04 | 11-Jul-92 | 2.2 | -75.0 | 195.8 | -0.7 | -92.2 | 270° | 180° |
| t01shr05 | 17-Jul-92 | 43.9 | -75.4 | 101.6 | 97.1 | 0.2 | 0° | 90° |
| t01shr06 | 22-Jul-92 | 33.8 | 22.8 | 100.6 | -171.4 | 10.3 | 180° | 180° |

Table 6.4 - Summary of stress path test T01

measurements.

TEST T02

The specimen for test T02 was trimmed from the remains of the block used for test T01 (E/EX15 25.640/BL). The trimming process proceeded at a quicker pace than for T01 but still took approximately 5 hours to complete. After specimen preparation and setting up, a confining pressure of 100kPa was applied which caused the endcap axial strain measurements to go out of range straight away. At this time the cell pressure was removed and the system stripped down to put the endcap strain transducers back in range before a confining pressure was applied again. Following the application of confining pressure, the measured pore pressure was raised to measurable values (average 14kPa) and suggested an initial specimen effective stress of 86kPa. Specimen saturation was carried out with two undrained increases in cell pressure producing a final B value of 0.97. The specimen was isotropically consolidated to an effective stress of 250kPa before shearing commenced.

Unfortunately the specimen failed as the estimated *in situ* stresses were being restored as the stress path overshot the target values, and so only a single stress path was performed. This effective stress path is shown with those for test T01 in Figure 6.14 and the path description is given in Table 6.5.

| Stage name | Date commenced | Δt_h hours | q_o kPa | p'_o kPa | Δq kPa | $\Delta p'$ kPa | ϑ ° | $\Delta \vartheta$ ° |
|------------|----------------|-----------------------|--------------|---------------|-------------------|--------------------|------------------|-------------------------|
| t02pre | 15-Aug-92 | - | 0.0 | - | 0.0 | - | 90° ? | 90° ? |
| t02sat | 24-Aug-92 | - | 0.0 | 58.3 | 0.0 | 17.0 | 90° | 0° |
| t02con | 28-Aug-92 | - | 0.9 | 79.7 | -2.4 | 160.7 | 90° | 0° |
| t02shr01 | 05-Sep-92 | 195.2 | -1.4 | 239.9 | -197.5 | 5.8 | 180° | 90° |

Table 6.5 - Summary of stress path test T02

TEST T03

The test specimen was prepared from a block sample taken from the Elstow excavation in the Lower Oxford Clay at a depth of 5.6m (E/EX17 24.910 /BL). The trimming process was carried out in only 2.5 hours but trimmings taken during this time showing that the specimen moisture content at its periphery apparently reduced by 1% every 1.5 hours as shown in Figure 6.15.

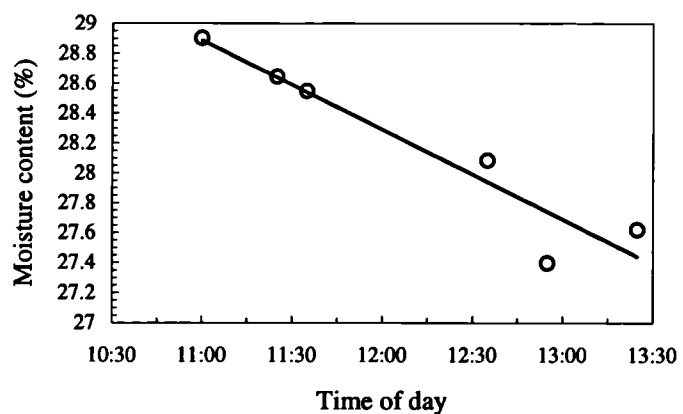


Figure 6.15 - Reduction in specimen moisture content during trimming of soil specimen for test T3

Following the application of 160kPa of confining pressure the initial effective mean normal stress was calculated as 140kPa, although the corresponding B value from a subsequent increase in cell pressure (100 kPa) was only 0.23. The cell pressure and back pressure were increased incrementally and simultaneously with periodic checks on the B value until a B value of 0.91 was attained.

A step consolidation stage was then applied increasing p' from 100kPa to 150kPa and Figure 6.16 shows the specimen volume change during this stage calculated from both local measurements and the volume change unit. This figure also shows the dissipation of excess pore water pressure as recorded by the mid-height pore water pressure probe for which the response is far more rapid. A similar response was recorded for the stepped consolidation stage

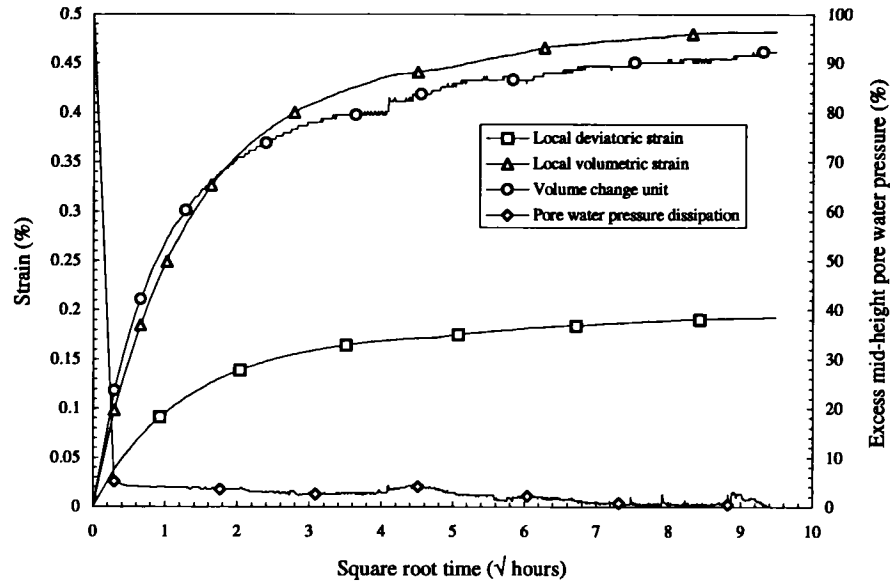


Figure 6.16 - Pore pressure response during isotropic consolidation in test T03

| Stage name | Date commenced | Δt_h hours | q_o kPa | p'_o kPa | Δq kPa | $\Delta p'$ kPa | ϑ ° | $\Delta \vartheta$ ° |
|------------|----------------|-----------------------|--------------|---------------|-------------------|--------------------|------------------|-------------------------|
| t03pre01 | 30-Oct-92 | 0.0 | 0.0 | ? | 0.0 | ? | 0° ? | 90° ? |
| t03conf01 | 02-Nov-92 | -0.3 | 0.0 | ? | 0.0 | ? | 90° ? | 90° ? |
| t03sat01 | 03-Nov-92 | 27.7 | 0.0 | 140.4 | 0.0 | 77.1 | 90° | 0° |
| t03sat02 | 05-Nov-92 | 38.5 | 0.0 | 217.8 | 0.0 | -139.0 | 270° | 180° |
| t03sat03 | 09-Nov-92 | 94.7 | 0.0 | 83.3 | 0.0 | 11.3 | 90° | 180° |
| t03sat04 | 11-Nov-92 | 75.4 | 0.0 | 101.6 | 0.0 | 49.2 | 90° | 0° |
| t03shr01 | 17-Nov-92 | 112.8 | 1.1 | 150.0 | -42.5 | 0.8 | 180° | 90° |
| t03shr02 | 20-Nov-92 | 35.3 | -84.0 | 150.8 | -28.4 | -5.0 | 180° | 0° |
| t03shr03 | 24-Nov-92 | 87.5 | -115.8 | 146.5 | -0.5 | 70.7 | 90° | 270° |
| t03shr04 | 30-Nov-92 | 61.4 | -115.7 | 215.5 | 0.5 | -58.8 | 270° | 180° |
| t03shr05 | 07-Dec-92 | 104.6 | -117.1 | 154.5 | 0.3 | 53.7 | 90° | 180° |
| t03shr06 | 13-Dec-92 | 98.2 | -114.3 | 209.0 | 0.0 | -49.5 | 270° | 180° |
| t03shr07 | 18-Dec-92 | 47.7 | -114.5 | 158.4 | 93.2 | -3.2 | 0° | 90° |
| t03shr08 | 04-Jan-93 | 363.4 | -14.4 | 153.9 | -100.8 | 3.7 | 180° | 180° |
| t03shr09 | 10-Jan-93 | 82.3 | -115.8 | 154.8 | -0.8 | 57.1 | 90° | 270° |
| t03shr10 | 16-Jan-93 | 77.4 | -118.1 | 216.8 | -0.6 | -54.3 | 270° | 180° |
| t03shr11 | 21-Jan-93 | 53.5 | -117.5 | 161.7 | 101.9 | 51.5 | 45° | 135° |
| t03shr12 | 28-Jan-93 | 54.9 | -16.4 | 209.1 | -98.0 | 1.9 | 180° | 135° |
| t03shr13 | 02-Feb-93 | 53.6 | -117.2 | 209.6 | 0.6 | -48.6 | 270° | 90° |
| t03shr14 | 07-Feb-93 | 63.3 | -117.8 | 161.7 | 102.5 | -4.7 | 0° | 90° |
| t03shr15 | 12-Feb-93 | 49.4 | -15.3 | 156.9 | -99.1 | 3.0 | 180° | 180° |
| t03shr16 | 17-Feb-93 | 51.0 | -115.5 | 159.4 | -0.2 | 50.7 | 90° | 270° |
| t03shr17 | 19-Feb-93 | 1.5 | -115.8 | 209.6 | 0.0 | -47.4 | 270° | 180° |
| t03shr18 | 24-Feb-93 | 49.1 | -117.2 | 153.9 | -57.7 | 11.5 | 180° | 270° |

Table 6.6 - Summary of stress path test T03

of test T02. It would seem that the mid-height pore water pressure probe was not recording the true specimen pore water pressure. One explanation is that the recorded pressures were influenced by the proximity of the filter paper drains on the specimen periphery. Alternatively, the fissure system may have allowed a more direct connection between the back pressure supply and the location of the mid-height pore pressure transducer. In subsequent stress path probing stages, the recorded effective stress paths are therefore possibly erroneous as excess pore water pressures would not have been recorded. In the stepped consolidation stages of all the other stress path tests, however, the volumetric response and the dissipation of excess pore water pressure were consistent.

The shearing stages of the stress path test consisted of a sequence of 17 constant p' and constant q stress paths and a single diagonal stress path as shown in Figure 6.17. The details of each of these paths are given in Table 6.6.

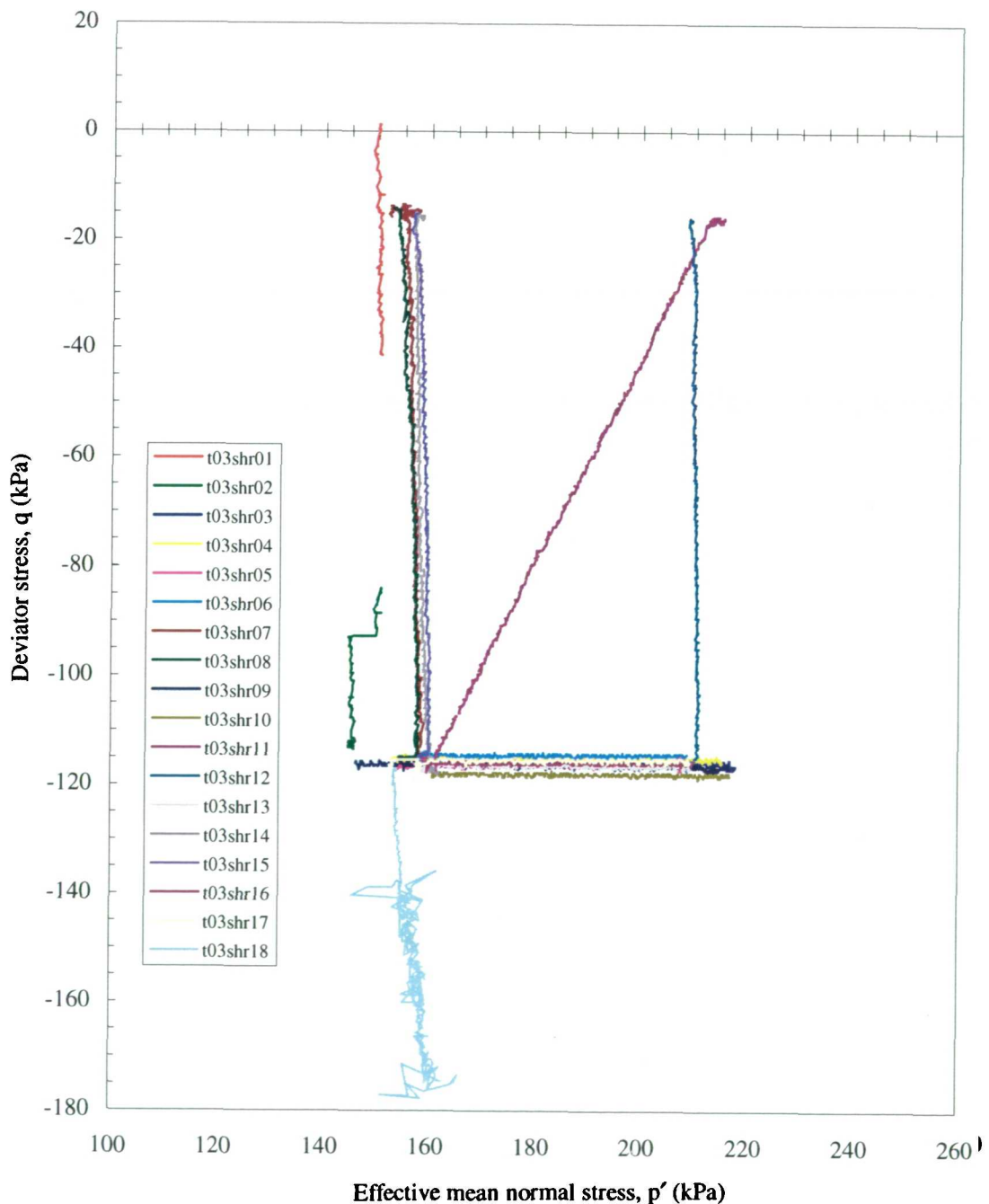


Figure 6.17 - Stress paths performed in test T03

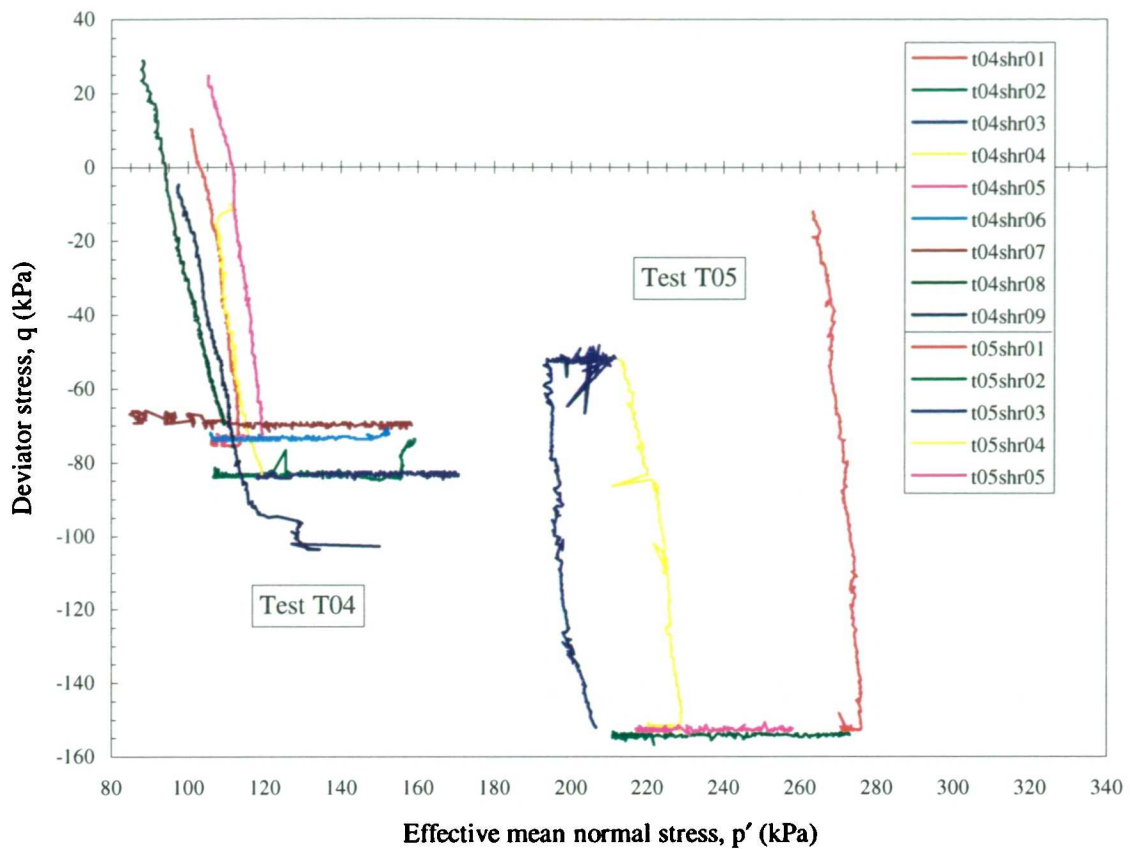


Figure 6.18 - Stress paths performed in tests T04 and T05

TEST T04

The specimen for this test was trimmed from a block sample (KEMP/BL1/21.5) of unweathered Oxford Clay taken from a freshly excavated slope at the Kempston Pit at 21.5mAOD (see section 5.2.2). The specimen was initially trimmed using a bandsaw to a rectangular prism of approximately the desired dimensions before final trimming by hand. This greatly speeded up the trimming process reducing the final hand trimming to 1 hour.

Upon application of the confining pressure, a leak developed at the connection of an endcap transducer and the cell base. The cell pressure was removed with all drainage valves closed and the leak fixed before reapplying the cell pressure. It was then noticed that there was a further leak at the mid-height pore water pressure transducer connection and, once more, the cell had to be depressurised and stripped down. The subsequent application of confining pressure showed that saturation was complete ($B=0.99$) and the sample was then consolidated to an effective mean normal stress of 100 kPa.

The stress path probing stage of the test continued over 9 stress paths which are shown in Figure 6.18 and described in Table 6.7. At the end of the fourth stress path the top cap suction connection failed. At this time the deviator stress was only -10kPa and it was not thought that the specimen was unduly damaged; testing therefore continued. However, the local axial strain targets had become detached and the cell pressure had to be removed under undrained conditions in order to re-affix them. Following reapplication of the cell pressure the mid-height pore pressure showed a recovery to its previous value.

When the specimen failed the mid-height pore pressure transducer connection also failed and was left for several hours in this condition. Consequently, free water came in contact with the

specimen and caused unrecorded swelling. The final measured water content therefore did not accurately reflect the end of test conditions.

Bender element tests were carried out during test T04.

| Stage name | Date commenced | Δt_h (hours) | q_o (kPa) | p'_o (kPa) | Δq (kPa) | $\Delta p'$ (kPa) | ϑ (°) | $\Delta\vartheta$ (°) |
|------------|----------------|-------------------------|----------------|-----------------|---------------------|----------------------|--------------------|--------------------------|
| t04pre01 | 16-Mar-93 | - | 0.0 | ? | - | - | - | - |
| t04con01 | 23-Mar-93 | - | 0.0 | 21.7 | - | 60.1 | 90° | 180° |
| t04shr01 | 02-Apr-93 | - | 10.0 | 101.0 | -85.7 | 11.8 | 180° | 180° |
| t04shr02 | 07-Apr-93 | 51.0 | -84.0 | 106.6 | 0.1 | 38.3 | 90° | 270° |
| t04shr03 | 16-Apr-93 | 167.5 | -83.5 | 170.8 | -0.3 | -38.1 | 270° | 180° |
| t04shr04 | 22-Apr-93 | 80.2 | -83.1 | 119.3 | 72.9 | -8.5 | 0° | 90° |
| t04shr05 | 29-Apr-93 | 129.4 | 23.9 | 105.2 | -97.7 | 14.1 | 180° | 180° |
| t04shr06 | 05-May-93 | 76.5 | -73.8 | 106.5 | 0.6 | 33.1 | 90° | 270° |
| t04shr07 | 15-May-93 | 155.2 | -69.3 | 157.3 | -0.3 | -45.7 | 270° | 180° |
| t04shr08 | 08-Jun-93 | 320.6 | -69.8 | 109.6 | 98.8 | -21.4 | 0° | 90° |
| t04shr09 | 18-Jun-93 | 154.9 | -5.4 | 97.3 | -97.5 | 52.8 | 180° | 180° |

Table 6.7 - Summary of stress path test T04

TEST T05

The specimen for this test was trimmed from a block sample of unweathered Oxford Clay taken from the Kempston Pit adjacent to the location of the test T04 specimen (KEMP/BL1/21.5). The specimen was trimmed almost to its final dimensions directly on the band saw with only minor hand trimming subsequently to remove smearing effects, as described in section 5.5.1. This allowed the specimen to be ready for setting up in the stress path cell within only 15 minutes of being exposed from its protective storage seal. The test was conducted in the newly commissioned second stress path cell.

A confining pressure of 400kPa was applied but the mid-height pore pressure transducer showed no response and the cell pressure was removed under undrained conditions in order to reattach the transducer. After equalisation under the confining pressure the initial effective mean normal stress within the specimen was approximately 145kPa. As the specimen came under equilibrium at this stress a local axial target became detached and it was decided to strip the cell down again under undrained conditions. Upon reapplication of the confining pressure another target fell off and the cycle had to be repeated. At this stage all the axial targets were secured to the supporting perspex rings with a fillet of Araldite and this prevented the problem reoccurring in this cell. The confining pressure was applied for the third time ($B=0.95$) followed by a stepped change in the cell pressure from 100 to 200kPa allowing consolidation to a back pressure of 400kPa. Before the stress path probe stages could commence the back pressure and cell pressure had to be lowered simultaneously by 50kPa to provide a sufficient pressure for the remaining test stages.

Five stress path probes were carried as shown in Figure 6.18. The details of these stress paths are given in Table 6.8. This test ended prematurely due to the failure of the load cell at the end of stress path 5. Since the test was stress controlled, and due to insufficient fail-safe measures, the control program interpreted the load cell failure as a change of stress to be corrected for and consequently caused the specimen to be rapidly brought to passive failure. Subsequently,

additional checks and controls were incorporated into the control program to prevent a recurrence of this problem.

| Stage name | Date commenced | Δt_h (hours) | q_o (kPa) | p'_o (kPa) | Δq (kPa) | $\Delta p'$ (kPa) | ϑ (°) | $\Delta \vartheta$ (°) |
|------------|----------------|-------------------------|----------------|-----------------|---------------------|----------------------|--------------------|---------------------------|
| t05conf01 | 18-Jun-93 | - | 0.0 | ? | - | - | - | - |
| t05conf02 | 22-Jun-93 | - | 0.0 | ? | - | - | - | - |
| t05conf03 | 29-Jun-93 | - | 0.0 | ? | - | - | - | - |
| t05conf04 | 09-Jul-93 | - | 0.0 | ? | - | - | - | - |
| t05con01 | 14-Jul-93 | - | 0.0 | 164.9 | 0.0 | 82.7 | 90° | 0° |
| t05sat02 | 02-Aug-93 | - | -11.6 | 267.2 | -0.9 | -2.6 | - | - |
| t05shr01 | 03-Aug-93 | 3190.4 | -12.1 | 263.3 | -140.9 | 12.7 | 180° | 90° |
| t05shr02 | 09-Aug-93 | 50.1 | -154.2 | 273.0 | -0.4 | -51.6 | 270° | 90° |
| t05shr03 | 15-Aug-93 | 80.5 | -152.1 | 206.6 | 100.1 | -12.8 | 0° | 90° |
| t05shr04 | 08-Sep-93 | 504.9 | -52.1 | 212.3 | -100.5 | 16.5 | 180° | 180° |
| t05shr05 | 14-Sep-93 | 74.2 | -152.8 | 217.1 | 0.7 | 40.3 | 90° | 270° |

Table 6.8 - Summary of stress path test T05

TEST T06

The test specimen was trimmed from the same block as the test T04 specimen (KEMP/BL1/21.5) using an identical process to test T05 allowing the trimming process to be completed very rapidly.

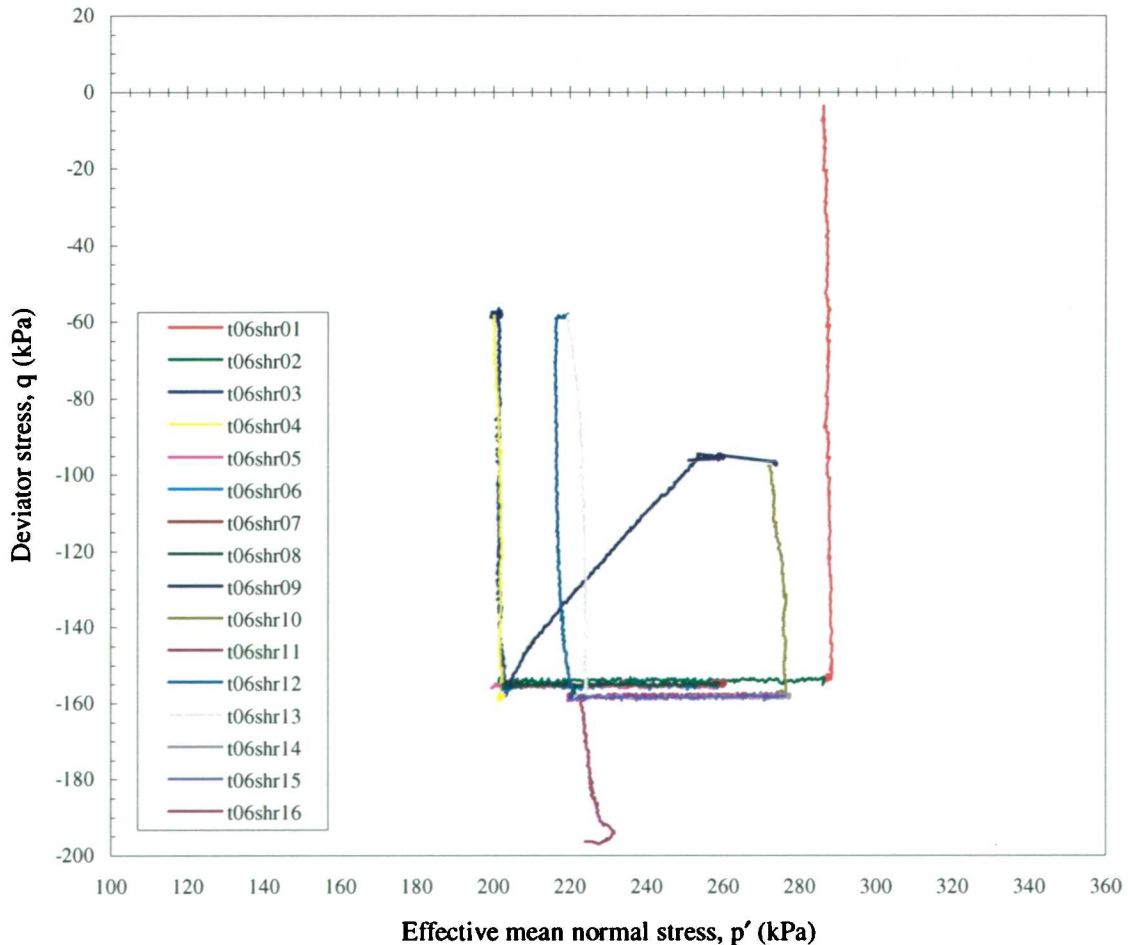


Figure 6.19 - Stress paths performed in test T06

Upon application of the initial confining pressure of 400kPa, the initial effective mean normal stress was approximately 90kPa. A further undrained application of confining pressure confirmed a suitable degree of saturation ($B=0.97$). The specimen was then allowed to consolidate isotropically to 200kPa under a stepped change in stress. Problems were encountered during test T04 due to incomplete specimen drainage during the stress path probe stages, and the step consolidation stage was used to infer a suitable testing rate as described in section 6.4.7.

This was the only test, other than test T03, in which a full complement of stress path probes were carried out. They consisted of a sequence of 15 constant p' and constant q stress paths and a single diagonal stress path as shown in Figure 6.19. The details of each of these paths are given in Table 6.9.

Unfortunately, early in the test series, during stress path 3, one of the local axial strain targets became detached. Up to this point the average endcap strains and the average local axial strains were in very good agreement (Figure 6.25; Figure 6.26; Figure 6.27) and the use of the endcap strains in interpreting the stress-strain response was considered. The specimen volumetric strain was computed using the local radial strains and either the endcap axial strains or the single set of local axial strain measurements (Figure 6.28). It was found that the former were in closer agreement with the measurements of the volume change unit attached to the back pressure system. It was therefore decided that the specimen response for this test would be based on the endcap axial strain response in association with the local radial strains. In the early stages of the test, although the average endcap axial strain was effectively the same as the average local axial strain response the axial strains measured on either side of the specimen were significantly different. This discrepancy can be explained by considering the distance of both the endcap

| Stage name | Date commenced | Δt_h (hours) | q_o (kPa) | p'_o (kPa) | Δq (kPa) | $\Delta p'$ (kPa) | ϑ (°) | $\Delta \vartheta$ (°) |
|------------|----------------|-------------------------|----------------|-----------------|---------------------|----------------------|--------------------|---------------------------|
| t06pre01 | 02-Jul-93 | - | 0.0 | - | 0.0 | - | - | - |
| t06conf01 | 08-Jul-93 | - | 0.0 | - | 0.0 | - | - | - |
| t06sat01 | 09-Jul-93 | - | 0.0 | 90.7 | 0.0 | 7.4 | - | - |
| t06con01 | 13-Jul-93 | - | 0.0 | 102.3 | 0.0 | 69.5 | 90° | 90° ? |
| t06sat02 | 02-Aug-93 | - | -3.2 | 286.7 | -1.8 | -0.9 | - | - |
| t06shr01 | 03-Aug-93 | 462.5 | -3.8 | 286.3 | -149.5 | 2.1 | 180° | 90° |
| t06shr02 | 10-Aug-93 | 49.9 | -153.3 | 286.4 | -1.6 | -81.3 | 270° | 90° |
| t06shr03 | 16-Aug-93 | 72.4 | -158.3 | 203.1 | 99.9 | -2.4 | 0° | 90° |
| t06shr04 | 08-Sep-93 | 487.3 | -58.7 | 200.2 | -100.1 | 1.7 | 180° | 180° |
| t06shr05 | 14-Sep-93 | 75.2 | -156.1 | 199.5 | 0.7 | 53.5 | 90° | 270° |
| t06shr06 | 20-Sep-93 | 85.0 | -155.0 | 259.7 | -1.3 | -52.4 | 270° | 180° |
| t06shr07 | 26-Sep-93 | 85.3 | -155.3 | 203.3 | 0.4 | 51.3 | 90° | 180° |
| t06shr08 | 02-Oct-93 | 81.4 | -155.1 | 258.9 | -0.4 | -50.8 | 270° | 180° |
| t06shr09 | 08-Oct-93 | 82.1 | -155.0 | 204.6 | 59.4 | 49.1 | 45° | 135° |
| t06shr10 | 14-Oct-93 | 88.3 | -98.0 | 272.3 | -60.5 | 3.8 | 180° | 135° |
| t06shr11 | 19-Oct-93 | 71.5 | -157.9 | 276.3 | -0.7 | -50.0 | 270° | 90° |
| t06shr12 | 24-Oct-93 | 74.4 | -158.7 | 220.8 | 99.4 | -4.5 | 0° | 90° |
| t06shr13 | 30-Oct-93 | 74.1 | -58.7 | 219.4 | -100.5 | 4.6 | 180° | 180° |
| t06shr14 | 05-Nov-93 | 74.6 | -159.0 | 221.7 | 1.3 | 48.4 | 90° | 270° |
| t06shr15 | 10-Nov-93 | 74.0 | -158.2 | 276.1 | -1.0 | -46.7 | 270° | 180° |
| t06shr16 | 16-Nov-93 | 73.0 | -159.4 | 223.1 | -37.2 | 1.0 | 180° | 270° |

Table 6.9 - Summary of stress path test T06

targets and the local axial proximity transducer targets from the centre of the specimen. The local axial targets, being further from the specimen centreline, are affected more by tilting of the specimen than are the endcap measurements. Moreover, the degree of tilt may be greater in the central region of the specimen's length than at its ends. These factors necessitated the difference in approach to that used for test T01, in which the axial strain was calculated from the proximity transducers on one side of the specimen after one of the axial targets became detached on the opposite side.

Bender element tests were carried out during test T06.

TEST T07

This test was carried out on a specimen trimmed on the band saw from a block sample of weathered Lower Oxford Clay taken from the Elstow excavation (E/EX9 29.185/BL). The test was carried out in the second stress path cell.

Following application of confining pressure the inferred initial effective mean normal stress within the specimen was approximately 200 kPa. Although this test provided information on the consolidation characteristics of the weathered material, the load cell failed during the first stress path probe and the test had to be abandoned. There are, consequently, no stress path probe data presented for test T07, although a series of bender element tests were carried out in the initial stages from which stiffnesses could be inferred (see section 6.5).

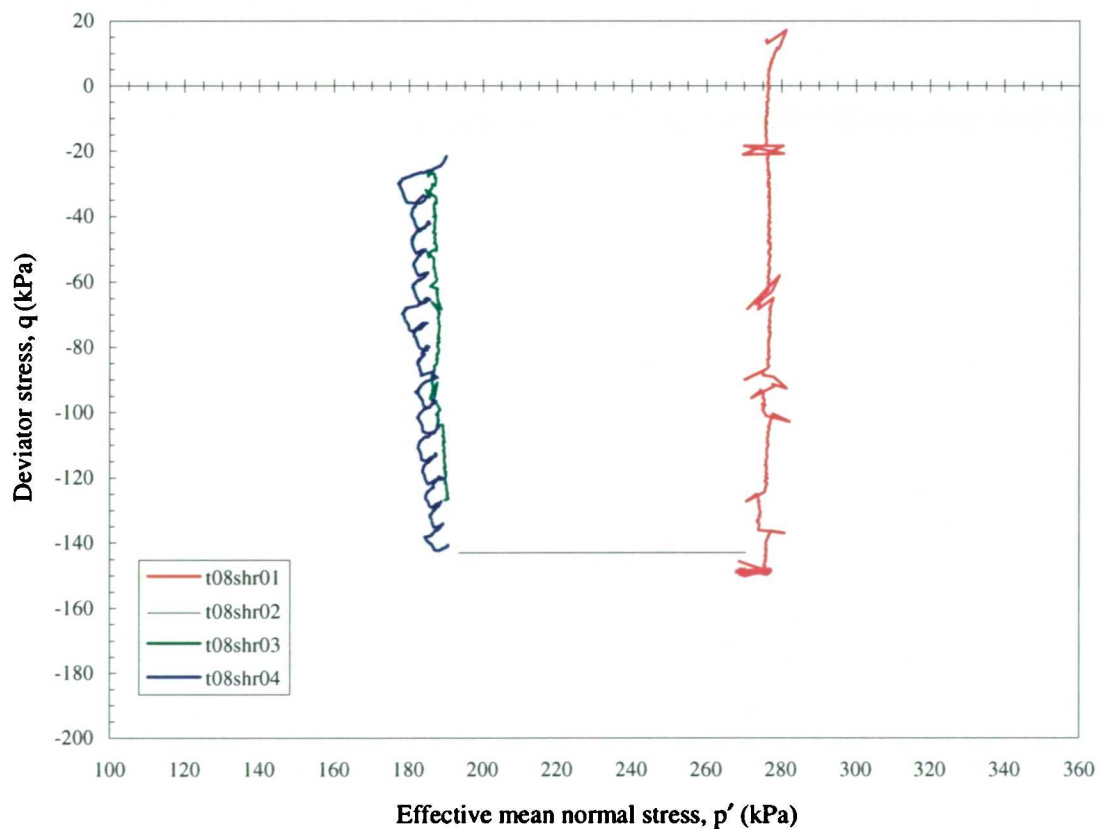


Figure 6.20 - Stress paths performed in test T08

| Stage name | Date | Δt_h hours | q_o kPa | p'_o kPa | Δq kPa | $\Delta p'$ kPa | ϑ ° | $\Delta \vartheta$ ° |
|------------|-----------|-----------------------|--------------|---------------|-------------------|--------------------|------------------|-------------------------|
| t08conf01 | 26-Nov-93 | - | 0.0 | ? | 0.0 | - | - | - |
| t08sat01 | 29-Nov-93 | - | 0.0 | 235.5 | 0.0 | -34.0 | 90° | 180° |
| t08con01 | 03-Dec-93 | - | 0.0 | 201.5 | 0.0 | 0.0 | 90° | 0° |
| t08shr01 | 13-Dec-93 | 237.8 | 14.0 | 276.0 | -163.3 | -0.3 | 180° | 90° |
| t08shr02 | 06-Jan-94 | 466.3 | -149.0 | 267.6 | 0.0 | -70.0 | 270° | 90° |
| t08shr03 | 14-Mar-94 | 1543.3 | -127.0 | 189.8 | 99.8 | -3.0 | 0° | 90° |
| t08shr04 | 29-Sep-94 | 4725.6 | -21.8 | 190.0 | -127.1 | -3.4 | 180° | 180° |

Table 6.10 - Summary of stress path test T08

TEST T08

The specimen for this test was trimmed from the same block of weathered Oxford Clay from the Elstow Pit, and in the same manner, as for test T07. The test was also carried out in the second stress path cell.

Following application of confining pressure the inferred initial effective mean normal stress with the specimen was 233 kPa. The specimen was saturated by simultaneously increasing the cell pressure and back pressure until the back pressure was 350kPa and the cell pressure was 200kPa greater. The drainage valves to the specimen were open during this time allowing the specimen to swell to a p' of 200kPa. The B value was found to be 0.92 from a subsequent increase in cell pressure of 80kPa. The drainage valves were reopened allowing the specimen to isotropically consolidated to a p' of 280kPa.

The stress path probe stages of the test proceeded for four stress paths as shown in Figure 6.20 and described in Table 6.10. At the end of the final stage, t08shr04, one of the three stepper motor controllers failed reducing the oil pressure in the lower chamber to zero and rapidly bringing the specimen to failure in extension.

Problems were also discovered with the transducer response transmitted via the AIU which caused the control system to correct for apparent pressure jumps (e.g. t04shr04 in Figure 6.20). This led to poor definition of the stress-strain curves as discussed in section 6.4.2.

TEST T09

This test was carried out on a specimen trimmed from the remaining unweathered Oxford Clay block sample obtained from the Kempston Pit and used for tests T04 and T06 (KEMP/BL1/21.5). The specimen was trimmed using the band saw technique previously referred to and, after setting up, was subjected to an initial confining pressure of 300kPa. After equilibrium had been attained, the initial effective mean normal stress within the specimen was 155kPa. The cell pressure and back pressure were raised slowly and simultaneously with the drainage valves open until a back pressure of 425kPa and a cell pressure of 625kPa were attained. At this point the saturation of the specimen was tested for a rise in cell pressure of 60kPa, and a B value of 0.997 was obtained. The specimen was then allowed to consolidate isotropically, to the back pressure of 425kPa, producing a p' of 260kPa.

On attempting to connect the load cell it was realised that a non-uniform deformation had occurred during consolidation and the surface of the top cap and the base of the load cell suction connection were slightly off parallel. It was not possible to provide a suitable suction connection between the rubber sleeve of the suction connector and the sides of the load cell. It

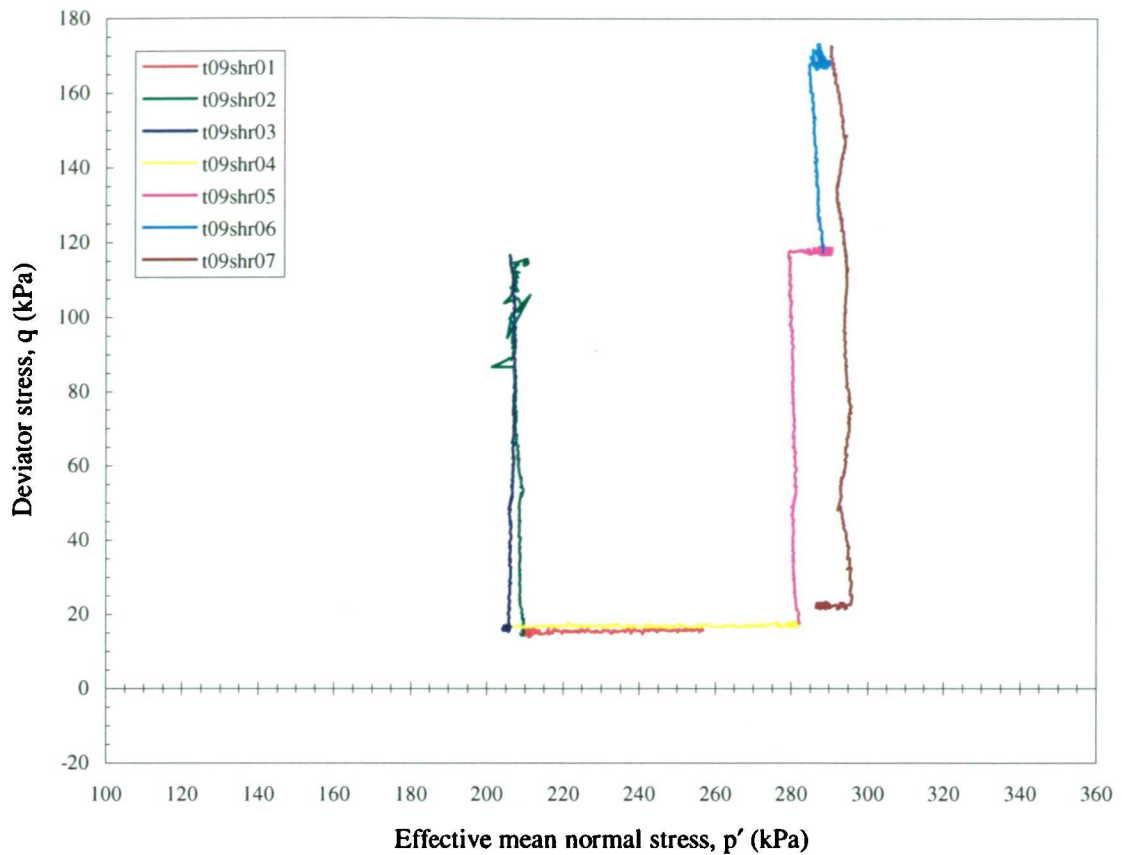


Figure 6.21 - Stress paths performed in test T09

was decided to continue with the test by carrying out the stress path stages under positive deviator stresses.

The stress path probe stages of the test extended over eight stress paths. These are shown in Figure 6.21 and described in Table 6.11. The test was terminated prematurely since, in the final stress path, both endcap transducers had gone out of range and a local axial strain target had become detached. With no accurate method to measure the axial strain it was decided to abandon the test and bring the specimen to active failure. However, during the final loading path the load cell oil seal started to leak and the recorded stresses were erroneous.

| Stage name | Date | Δt_h (hours) | q_o (kPa) | p'_o (kPa) | Δq (kPa) | $\Delta p'$ (kPa) | ϑ (°) | $\Delta \vartheta$ (°) |
|------------|-----------|-------------------------|----------------|-----------------|---------------------|----------------------|--------------------|---------------------------|
| t09sat01 | 26-Nov-93 | - | 0.0 | ? | - | - | 90° | ? |
| t09shr01 | 14-Dec-93 | 422.1 | 15.6 | 256.6 | 0.3 | -39.1 | 270° | 180° |
| t09shr02 | 06-Jan-94 | 511.9 | 15.6 | 209.4 | 98.8 | -1.8 | 0° | 90° |
| t09shr03 | 14-Jan-94 | 128.3 | 116.2 | 205.8 | -100.4 | 0.2 | 180° | 180° |
| t09shr04 | 21-Jan-94 | 105.1 | 16.6 | 207.2 | -0.3 | 64.1 | 90° | 270° |
| t09shr05 | 31-Jan-94 | 155.5 | 17.5 | 282.1 | 99.5 | -3.0 | 0° | 270° |
| t09shr06 | 23-Feb-94 | 484.8 | 117.3 | 288.1 | 50.1 | -3.7 | 0° | 0° |
| t09shr07 | 16-Mar-94 | 477.4 | 172.6 | 290.3 | -149.6 | 5.4 | 180° | 180° |
| t09shr08 | 28-Mar-94 | 187.4 | 22.7 | 291.1 | 509.5 | 10.1 | 0° | 180° |

Table 6.11 - Summary of stress path test T09

A summary of the entire testing programme is shown in Table 6.12

| Test series | Start date | End date | Number of stress paths | Soil type | p' (kPa) | Comments |
|-------------|-------------|-------------|------------------------|-----------|------------|---|
| T01 | 12 Jun 1992 | 27 Jul 1992 | 9 | Old | 100 | Useable trial test Target detached |
| T02 | 17 Aug 1992 | 11 Sep 1992 | 1 | Old | 250 | Premature failure |
| T03 | 1 Nov 1992 | 26 Feb 1993 | 18 | Old | 150 | Full test |
| T04 | 17 Mar 1993 | 21 Jun 1993 | 10 | New | 100 | High excess pore water pressures |
| T05 | 21 Jun 1993 | 18 Sep 1993 | 5 | New | 200 | Load cell failure |
| T06 | 9 Jul 1993 | 10 Nov 1993 | 16 | New | 200 | Full test Target detached |
| T07 | 27 Oct 1993 | 22 Nov 1993 | 0 | W.O.C | 200 | Load cell failure |
| T08 | 24 Nov 1993 | 29 Sep 1994 | 4 | W.O.C. | 200 | Pressure failure |
| T09 | 11 Nov 1993 | 5 Apr 1994 | 7 | New | 200 | Triaxial compression Load cell failure |

Table 6.12 - Summary of stress path tests

6.4 Interpretation of stress path tests

6.4.1 Introduction

The stress path tests described in section 5.3.2 were designed to determine the *in situ* stiffness response of the soil as accurately as possible. This required determining the deviatoric, volumetric and coupling stiffnesses from constant p' and constant q stress paths. The sequence of loading in the test was required to ensure that the stiffnesses were determined from stress paths on soil with a similar stress history. All the loading paths undertaken to reinstate the initial stress state were also fixed as constant p' or constant q stress paths. This allowed an assessment of the influence of the sense and degree of stress path rotation and the sensitivity of the stiffness parameters to the simplified modelling of the assumed geological stress history.

It was hoped that the following four aspects of the soil behaviour in relation to the *in situ* soil stiffness could be investigated during the experimental programme:

- the influence of the recent stress history effect described in chapter 2.4.2. This involved looking at the effect on the stress-strain response along a given path of different recent stress histories. (The similarity of the previous stress path was interpreted by Stallebrass (1990a) in terms of the stress path length, the length of the initial holding period at a constant stress state, and the rotation of stress path.)
- the feasibility of the multi-stage stress path testing method by comparing the stiffness response along repeated stress paths during the course of a test series and noting any change in the behaviour.
- the influence of the choice of the *in situ* stress state on the stress-strain response of the soil. This involved looking at the influence of both the effective mean normal stress and the deviator stress since it was thought that the anisotropic stress state was close to passive failure throughout the heavily overconsolidated deposit (see section 3.4.3)
- the relative stiffness characteristics of the two sources of Oxford Clay used in the testing programme: the block samples taken at the site investigation for the Elstow excavation and kept in storage since 1987 (see section 3.7.2) and the fresh block samples taken from the Kempston Pit to provide addition testing material for the current research (see section 5.2.2).

6.4.2 Quality of stress control

The control of the stress paths depended on how steady the supply pressure was, and how small a pressure increment could be applied by the stepper motors. A typical example of the stress control by the stepper motors for the constant q and the constant p' stress paths is shown in Figure 6.22 and Figure 6.23 respectively. These figures show that the total stress paths could be followed to an accuracy of approximately ± 0.5 kPa.

Due to the nature of the stepper motor control system, the specified stress path generally forms an upper or lower bound to the actual stress path, depending on whether the applied pressures are increasing or decreasing (see section 5.4.9). If this effect is not allowed for when specifying a stress path, there is a possibility of an initial jump in the stress control of 2-3 kPa (see Figure 5.18), which affects the most important initial small strain response of the soil. To compensate for this effect, the control algorithm follows a stress path 1 kPa higher or lower than the actual required stress path as necessary, preventing any initial irregularities in the stress control.

Following the consolidation stage, the back pressure was not controlled by the associated stepper motor, but rather assumed to remain constant. The variation in the supply to the back pressure system during four typical stress paths from test T06 is shown in Figure 6.24. The back pressure varied by 3-5 kPa during a stress path of approximately 80 hours. An active stepper motor control on this system would have prevented such a drift but would have caused short term variations of ± 0.5 kPa, rather than the 0.1-0.2 kPa recorded. It is not known which method would have produced the better overall control.

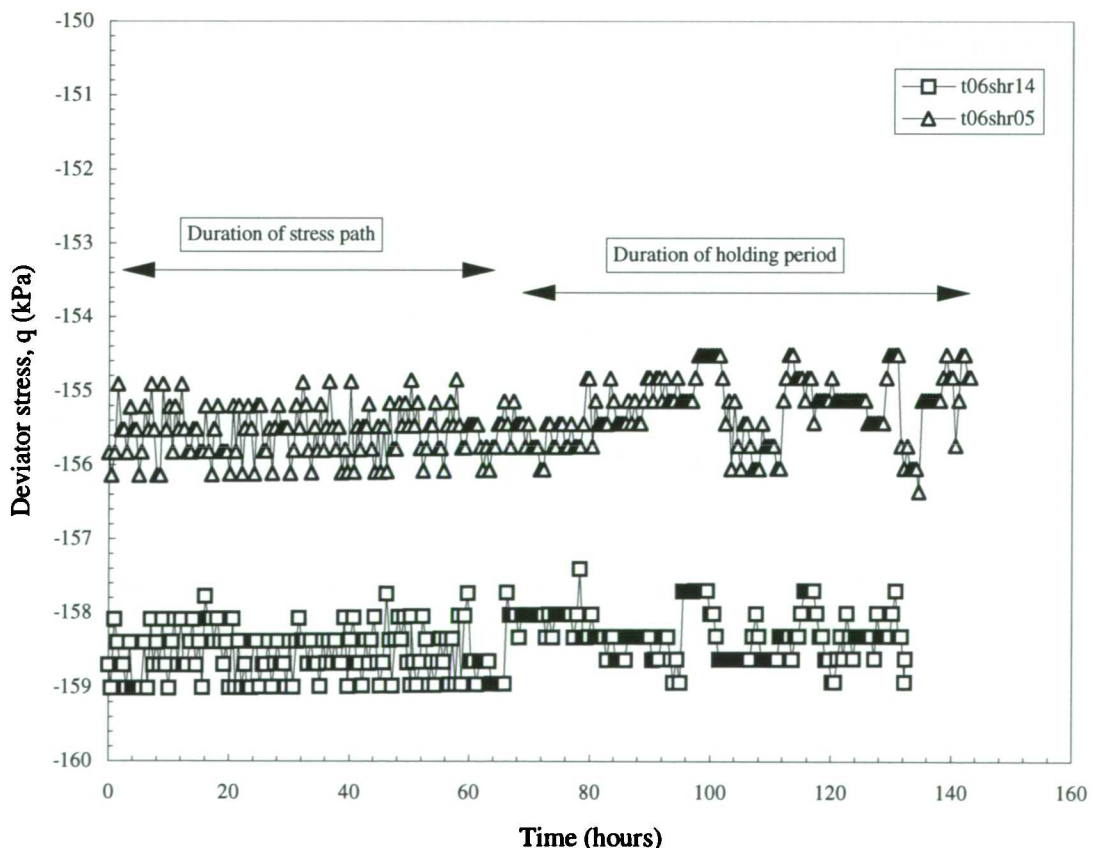


Figure 6.22 - Typical control of deviator stress for constant q stress paths

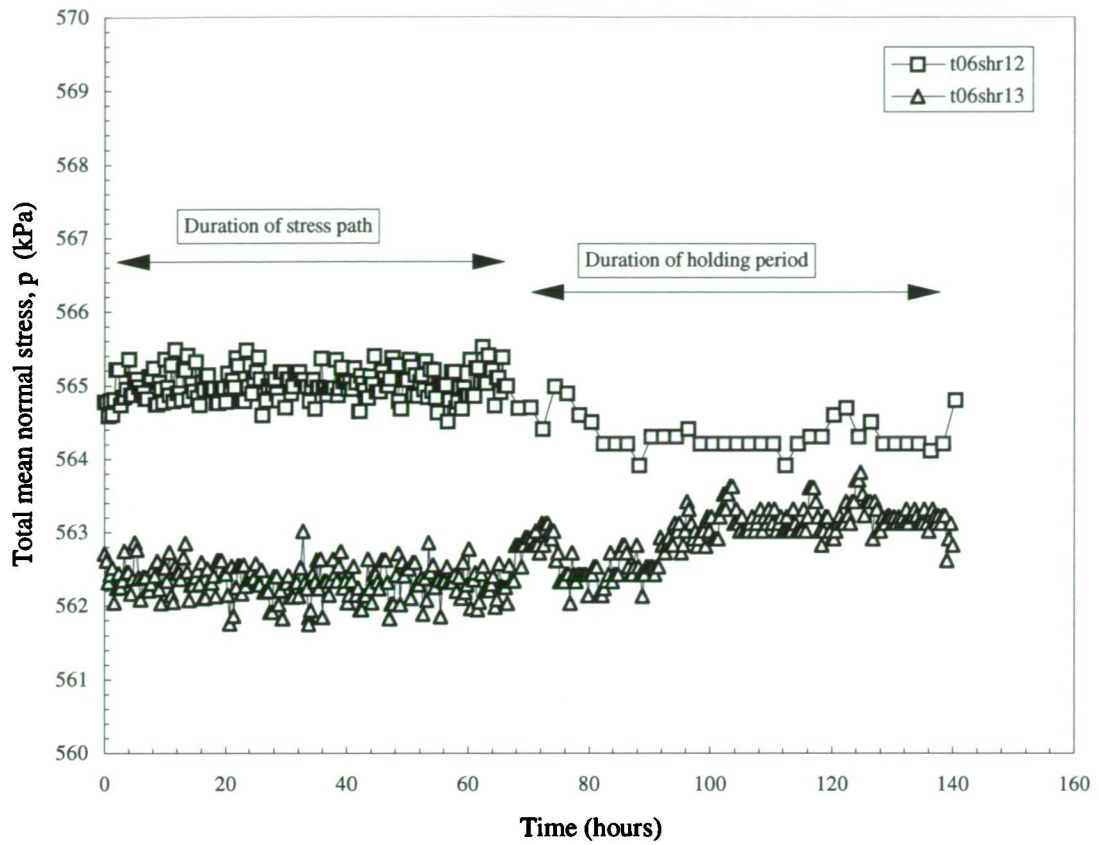


Figure 6.23 - Typical control of mean normal stress for constant p' stress paths

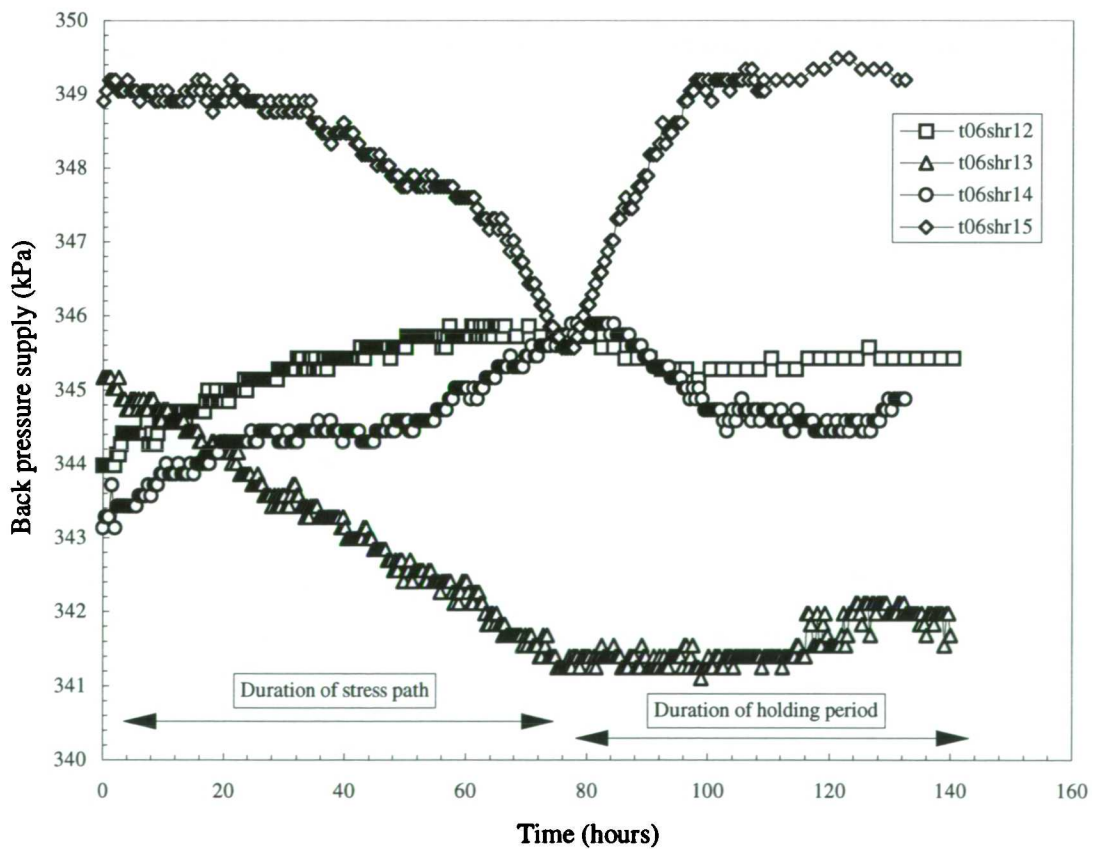


Figure 6.24 - Typical variation in the back pressure supply during stress path tests

It was realised during the course of the tests in the second stress path cell that the quality of stress control was lower than for the first stress path cell. Thus the results of tests T05, T07 and T08 are of an inferior quality to those of tests T01, T02, T03, T04, T06 and T09.

6.4.3 Quality of the strain measurements

The measurement of axial strain in the stress path cell was carried out in three ways, as described in section 5.4.7. Figure 6.25 shows the axial strain response, measured locally on the specimen and also by the endcap transducers, upon the initial application of confining pressure in stress path test T06. A higher, and less uniform, axial strain is recorded by the endcap transducers than by the local measurements which is probably due to the bedding errors at the specimen ends (see section 2.3). For the same test, Figure 6.26 shows the axial strain response, including the external measurement on the base pedestal, for the first stress path probe. It is seen that the endcap measurements and the local measurements have a very similar average strain although the difference between the readings on either side of the specimen is greater in the case of the local measurements. The external measurements show that there was a large increase in strain at approximately -40kPa deviator stress which was probably due to slippage at the suction connection to the load cell. During the next stage of the test, shown in Figure 6.27, there was a similar average response from all methods of axial strain measurement, although the greatest difference between the readings on either side of the specimen occurred with the local measurements.

The similarity between the endcap and local measurements strain measurements was apparent in the later stages of every stress path test. It can be concluded that for these multi-stage stress path tests, after the first stress path probe, the average local and endcap measurements are very similar. The endcap measurements may be thought superior for they showed a more uniform response on either side of the specimen, but the local measurements may have been recording a true non-uniform deformation in the central region of the specimen. For this system the compliance of the load cell is seen to be minimal and, were it not for their poor resolution, the external measurements could possibly have returned a similar specimen response for the later stages, assuming no slippage of the endcap suction connection took place.

The uniformity of the specimen response and the degree of bedding error at the specimen ends was may also checked by comparing the volumetric strain measured externally, using the volume change unit connected to the back pressure drainage line, with that calculated using the axial and radial strains for a right-cylinder specimen. Figure 6.28 directly compares the two methods of calculating the volumetric strain for three typical stress paths and the initial step consolidation stage of test T06. It is seen that a greater volumetric strain was recorded by the volume change unit than by the local strains during the step consolidation stage which is attributable to bedding and seating errors at the specimen ends. During the subsequent stress paths the external and local volumetric strain measurements compare almost exactly showing that the specimen was deforming relatively uniformly.

As described in 6.4.2, the quality of stress control was lower in cell 2 than in cell 1. The consequence of this was that, although the local strain measurements were of greater resolution in cell 2, the recorded stress-strain curves showed frequent irregularities. The determination of accurate and appropriate tangent stiffnesses from such curves was problematic.

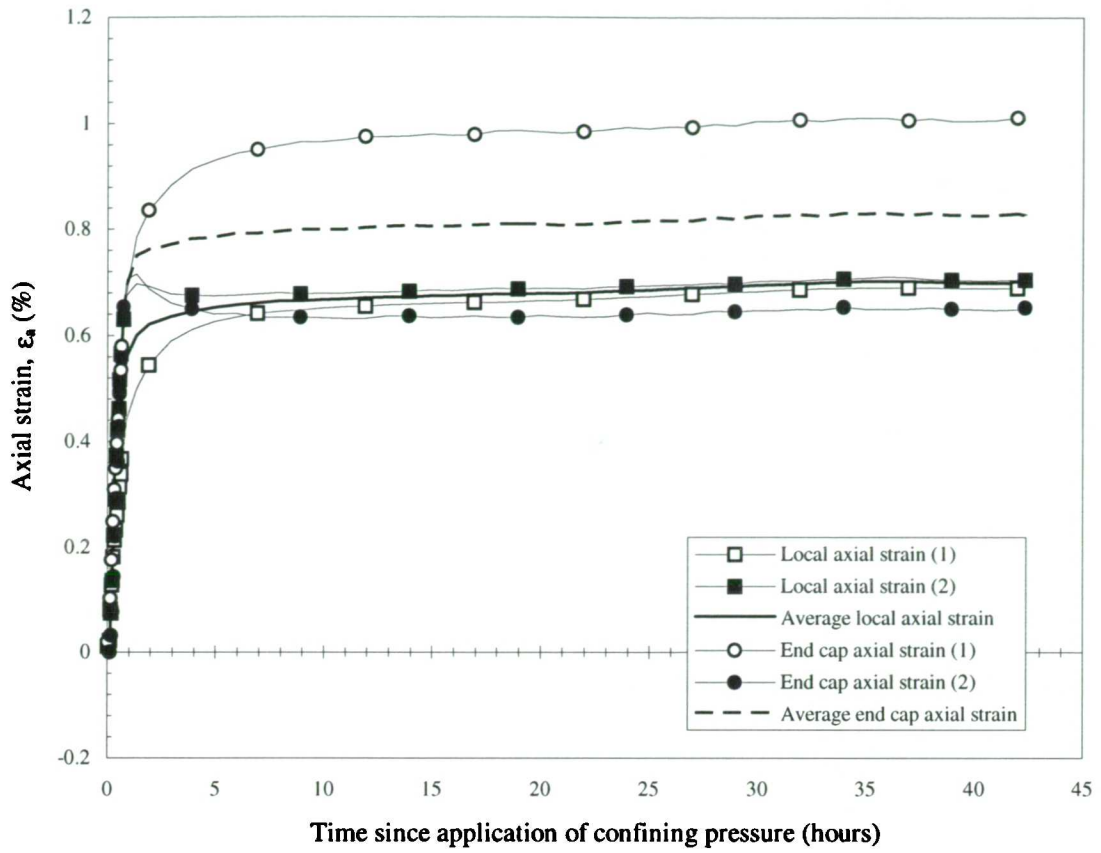


Figure 6.25 - Local and endcap axial strain response during initial loading of test T06

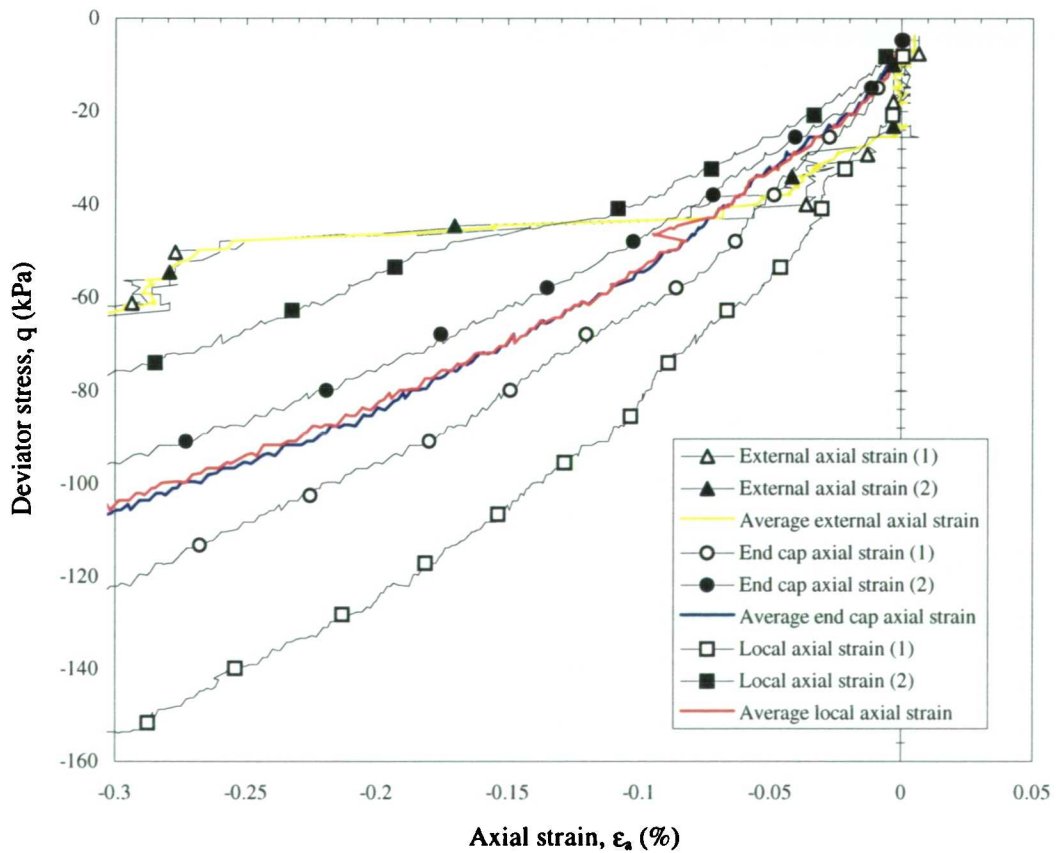


Figure 6.26 - Comparison of axial strain measurements in stress path t06shr01

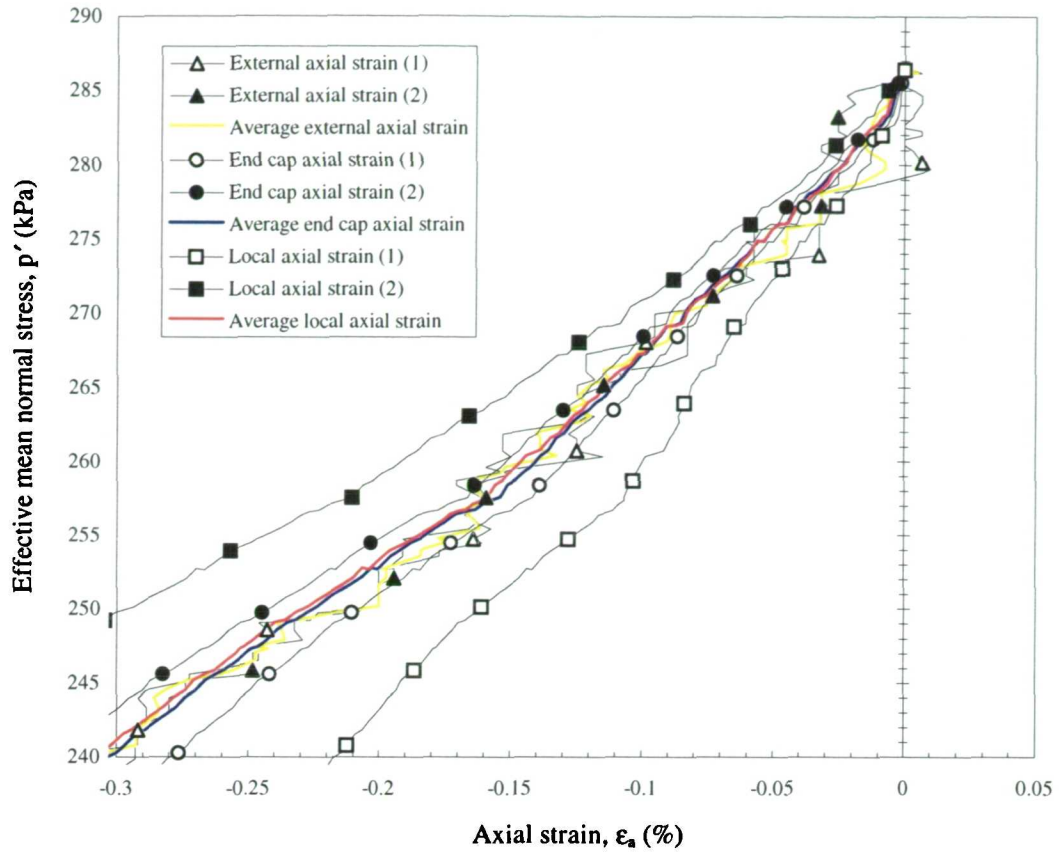


Figure 6.27 - Comparison of axial strain measurements in t06shr02

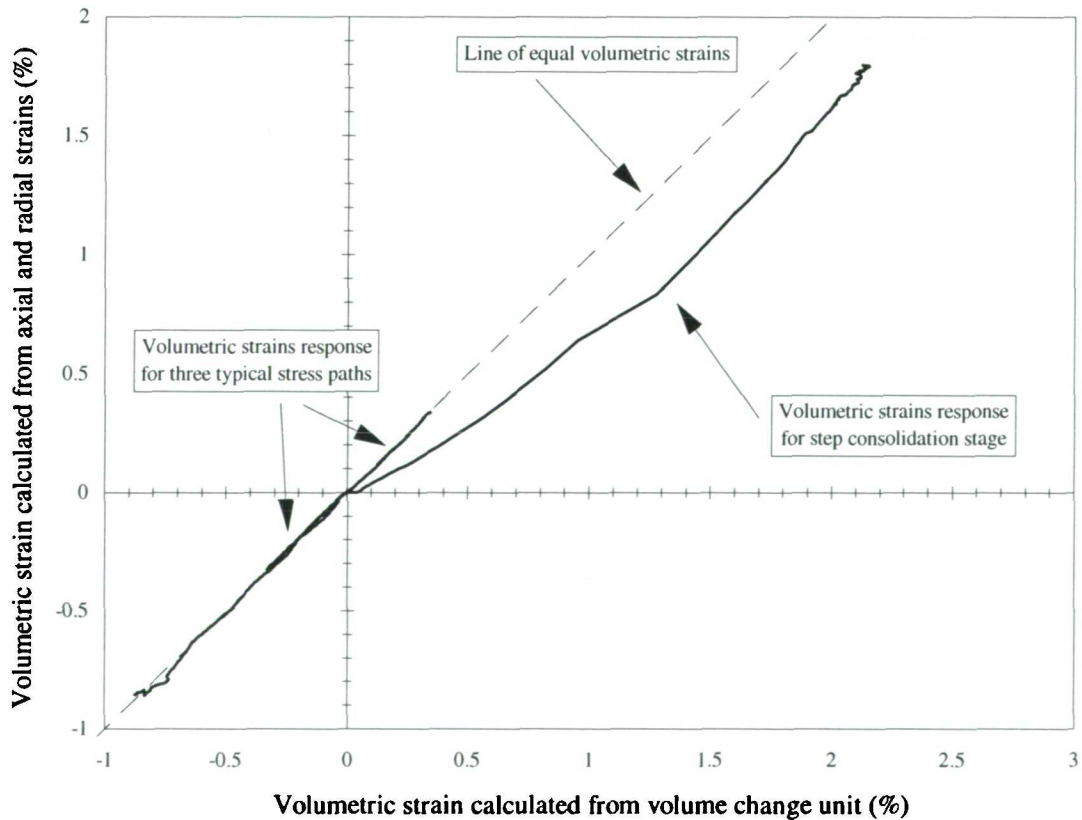


Figure 6.28 - Comparison of volumetric strain calculated by local strain measurements and by the volume change unit connected to the back pressure line

6.4.4 Possibility of multi-path testing

In principle, all the stiffness parameters required for the constitutive model (described later in Chapter 7) could be obtained from a single multi-stage test. However, for the multi-stage stress path testing method to be valid it was required to show that there was no change in the stiffness characteristics of the soil specimen from the initial to the final stages of the test. This has been checked using the results of tests T03 and T06 since these both ran to completion and contained several repeats of constant p' and constant q stress paths.

In test T03 the constant p' paths 8 and 15, and paths 7 and 14 can be compared, each pair of paths having the same recent stress history. The stress-strain response of paths 8 and 15, and of 7 and 14, shown in Figure 6.29, and the associated interpreted tangent stiffnesses, shown in Figure 6.30, are reasonably similar. The initial response of path 14 is slightly stiffer than that of path 7 which may be attributable to the higher residual strain rate at the onset of path 14 as discussed in section 6.4.5.

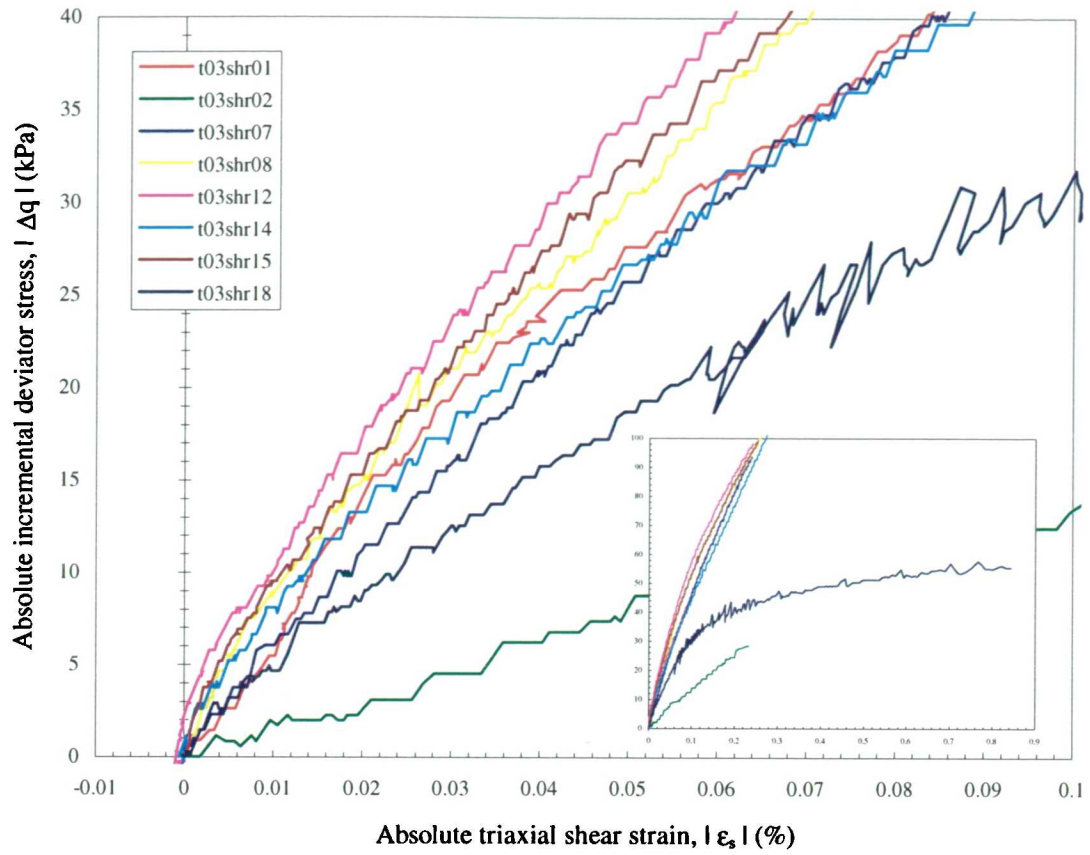
Next the constant q stress paths, 3, 9 and 16 sharing the same recent stress history can be compared. The stress-strain responses and the interpreted tangent stiffnesses, shown in Figure 6.31 and Figure 6.32 respectively, show a close agreement between the responses of paths 9 and 16 but path 3 had a less stiff response. Path 3, however, continued after a relatively short holding period (35 hours) from the end of path 2 resulting in a relatively large residual strain rate at the onset of path 3, as discussed in section 6.4.5.

The constant q stress paths 4, 6, 10, and 17 can also be compared. Paths 4, 6 and 10 all exhibit a very similar stress-strain response, as shown in Figure 6.31. The stress-strain response of path 17 is significantly different and this is discussed in section 6.4.5.

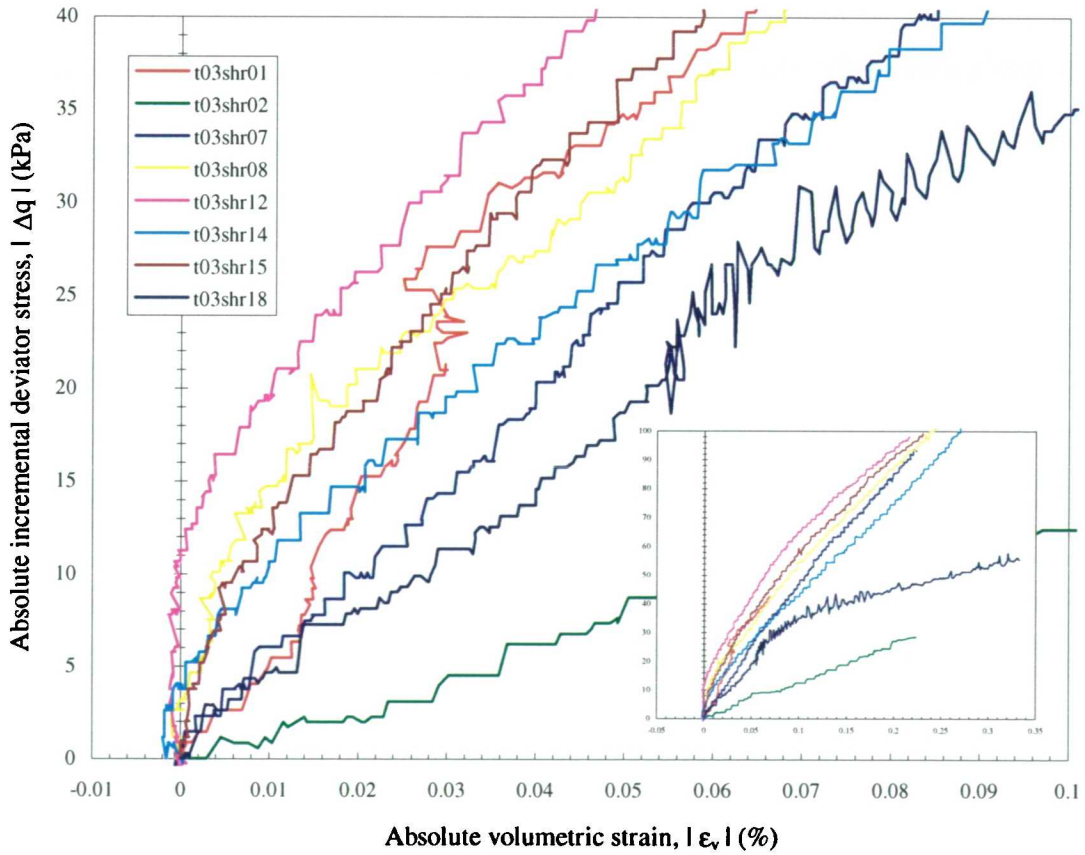
For test T06 the stress-strain response is shown for the constant p' stress paths in Figure 6.33 and for the constant q stress paths in Figure 6.34. The interpreted tangent stiffnesses are shown in Figure 6.35 and Figure 6.36 respectively. The pairings for the constant p' stress paths are 3 and 12 (increasing q following a 90° rotation), and also 4 and 13 (decreasing q following a 180° rotation). No noticeable differences in the stress-strain responses are evident. In Figure 6.35 path 3 apparently shows a less stiff response. However, Figure 6.33 shows that path 3 has an initially stiff response which is not adequately captured on a log strain plot. Although the holding periods were similar for both paths 3 and 12, the stresses during the previous holding period (for path 2) were poorly controlled and, consequently, the strain rate did not decay smoothly. The influence of the relatively high strain rate at the end of path 2 on the subsequent stress-strain response is explained below in section 6.4.5. Also, the stresses in the initial stages of path 3 were poorly controlled such that a slight fall in the effective mean normal stress produced negative volumetric strains (Figure 6.33(b)).

The repeat stress paths for the constant q stress paths were 6, 8 and 15 (decreasing p' following a 180° rotation); 5 and 14 (increasing p' following a -90° rotation); 2 and 11 (decreasing p' following a 90° rotation). Again the differences between the results are small. The greatest difference is seen between paths 2 and 11 and is explained in terms of a difference in the length of the approach path (see section 6.4.5).

The results of tests T03 and T06 suggest the multi-stage stress path testing technique is viable for obtaining numerous stiffness data from a single Oxford Clay soil specimen.



(a)



(b)

Figure 6.29 - Stress-strain response for constant p' stress paths in test T03

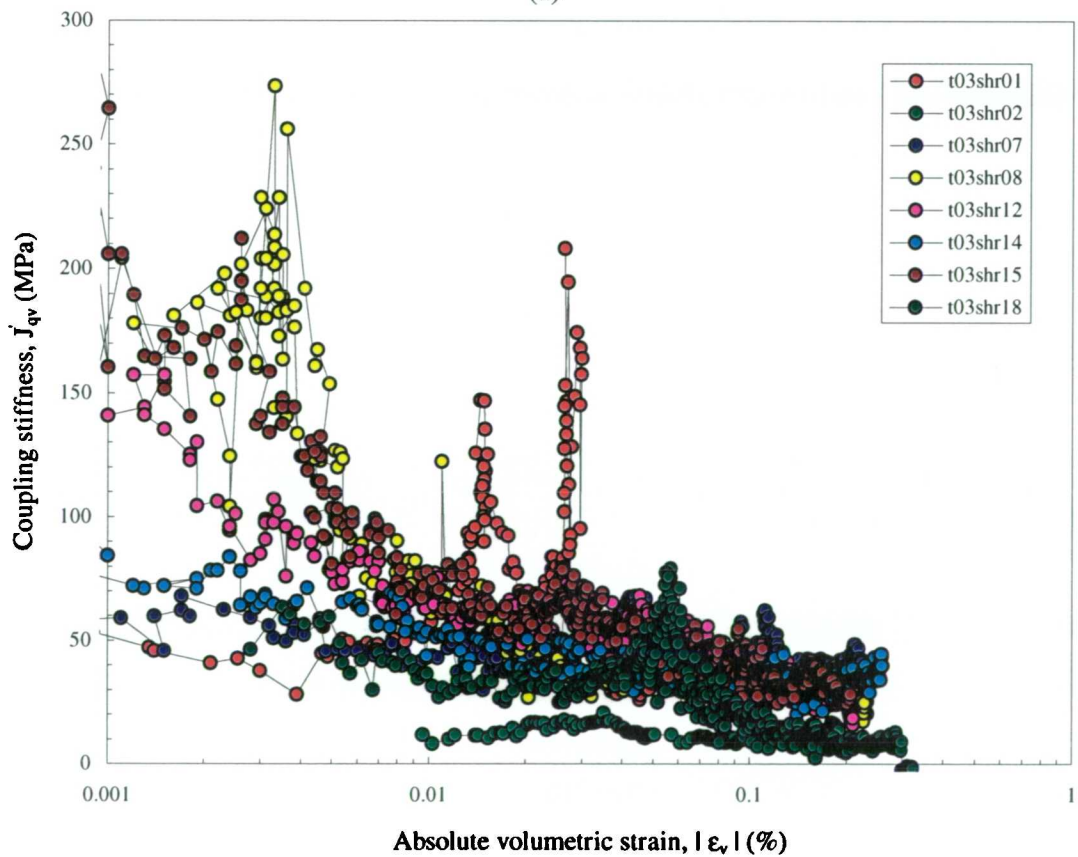
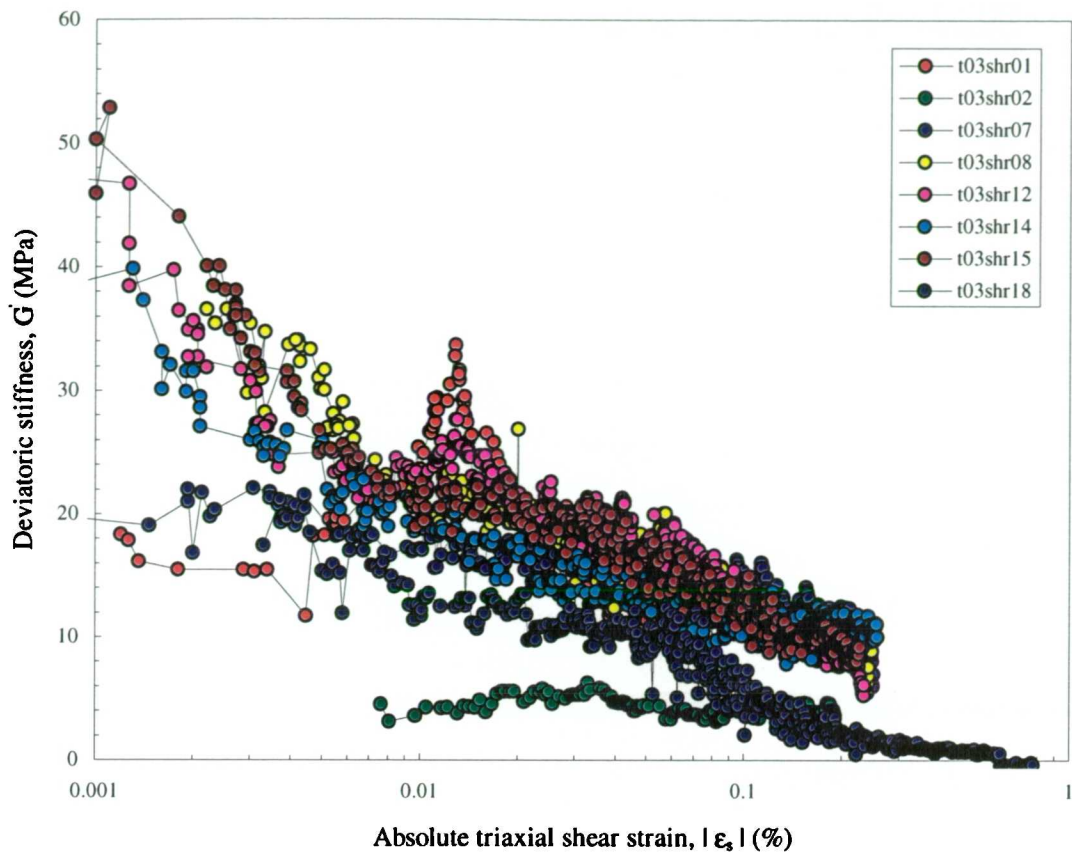
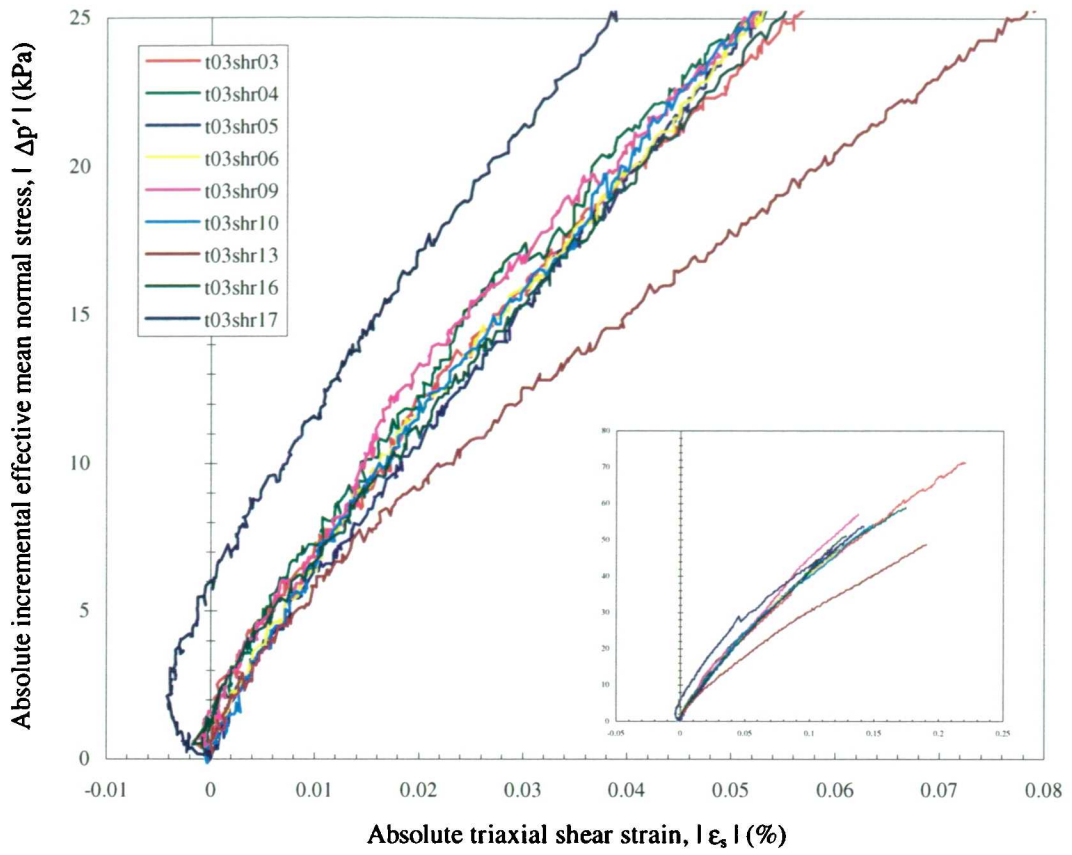
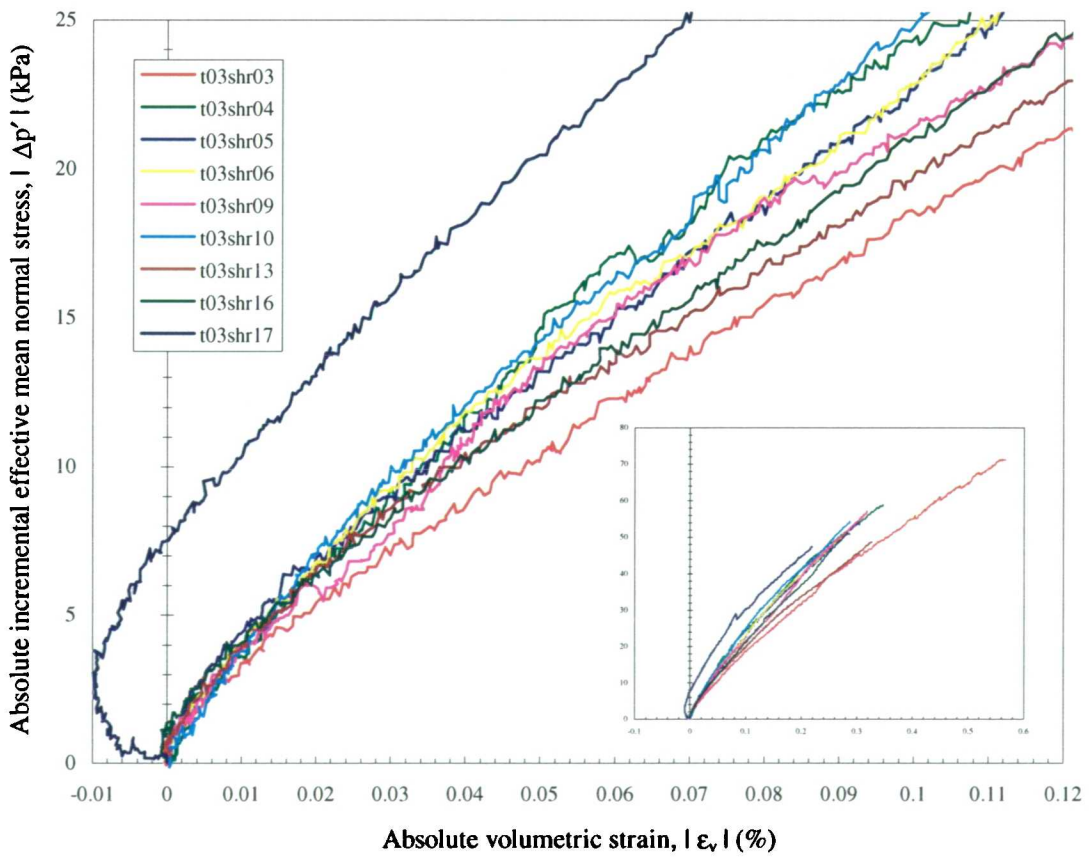


Figure 6.30 - (a) Deviatoric stiffness response against triaxial shear strains and (b) coupling stiffness response for deviator stresses and volumetric strains against volumetric strains for constant p' stress paths of test T03

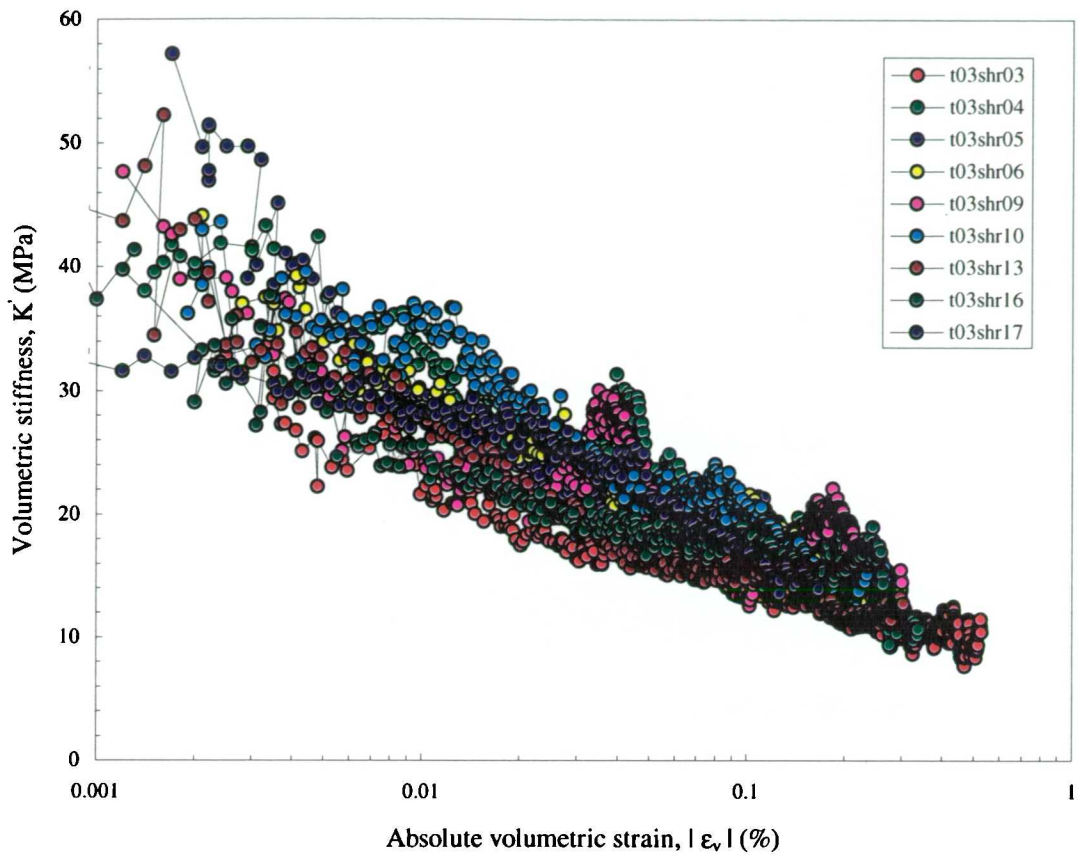


(a)

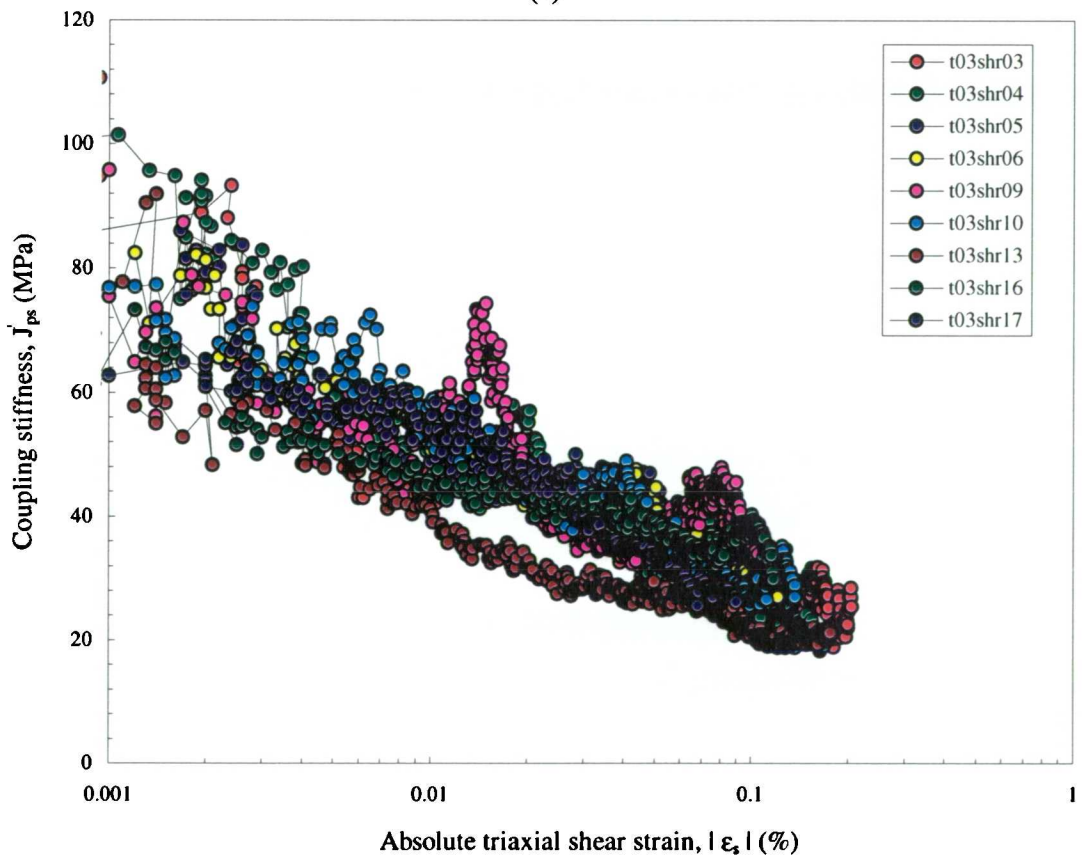


(b)

Figure 6.31 - Stress-strain response of constant q stress paths in test T03



(a)



(b)

Figure 6.32 - (a) Volumetric stiffness response against volumetric strain and (b) Coupling stiffness response of effective mean normal stresses and triaxial shear strains against triaxial shear strains for constant q stress paths of test T03

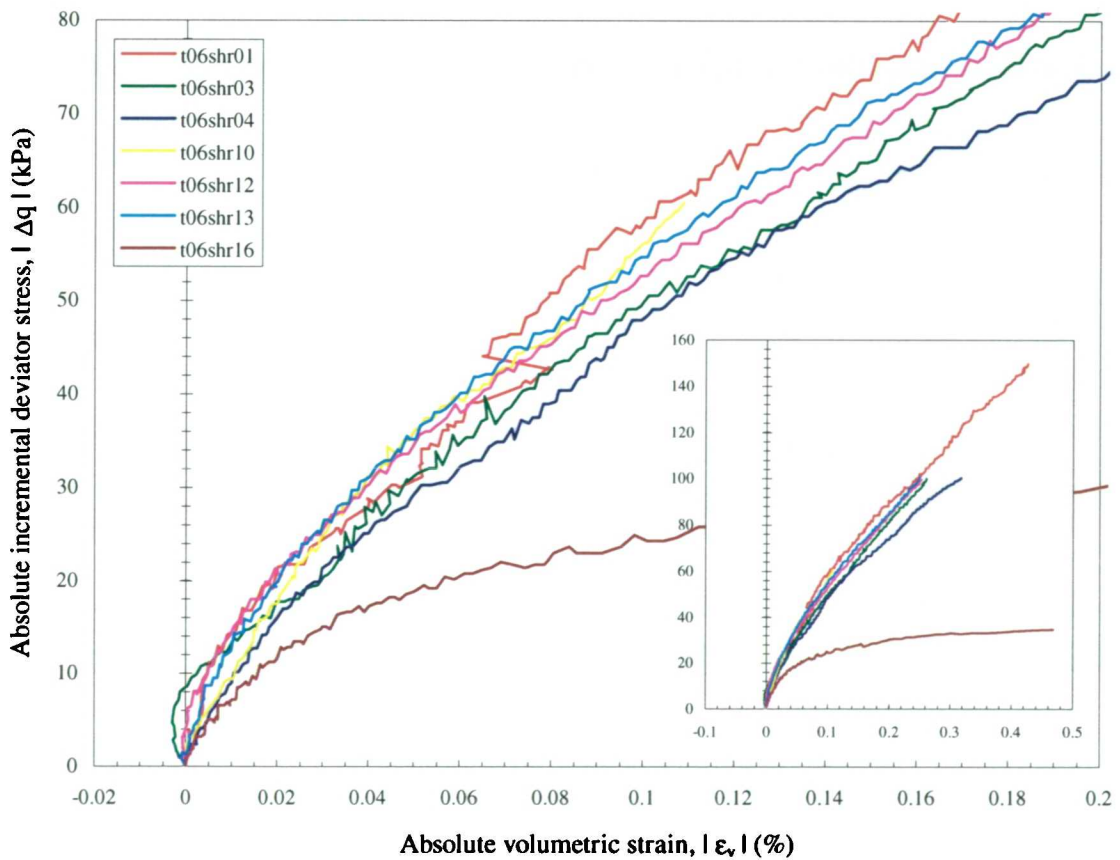
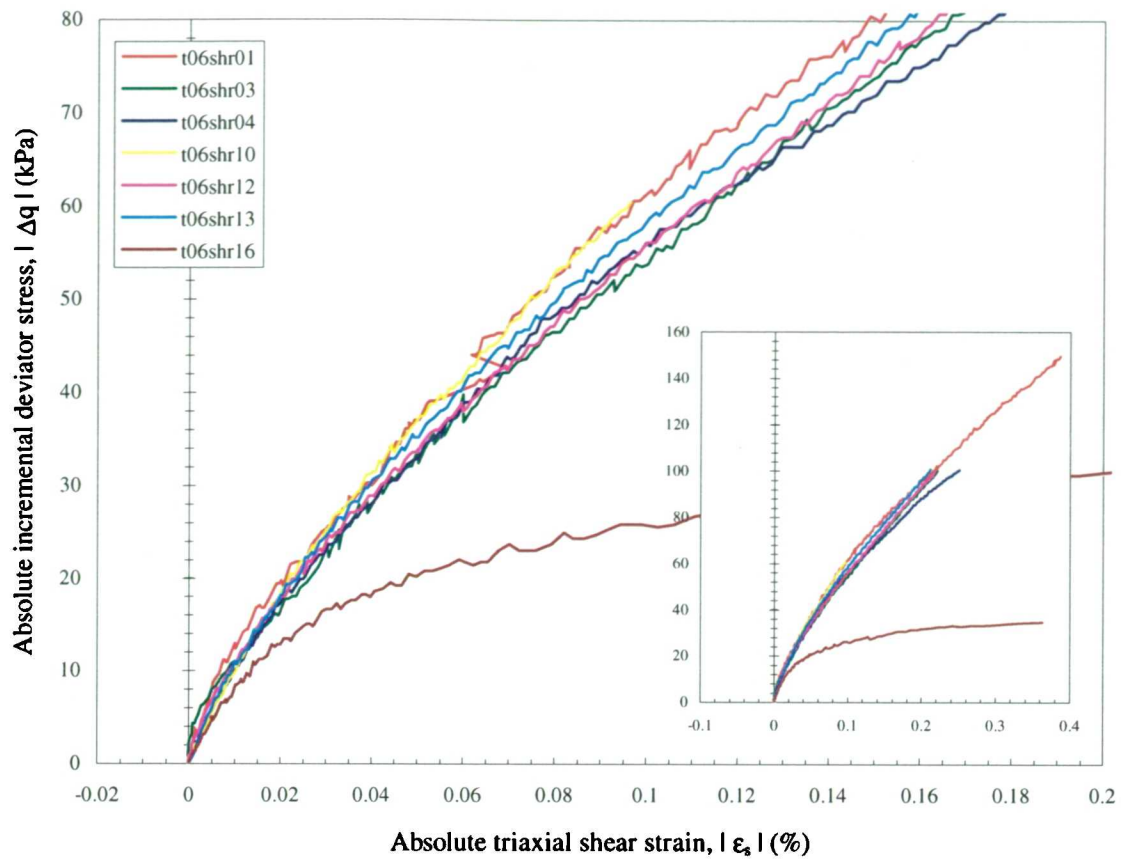
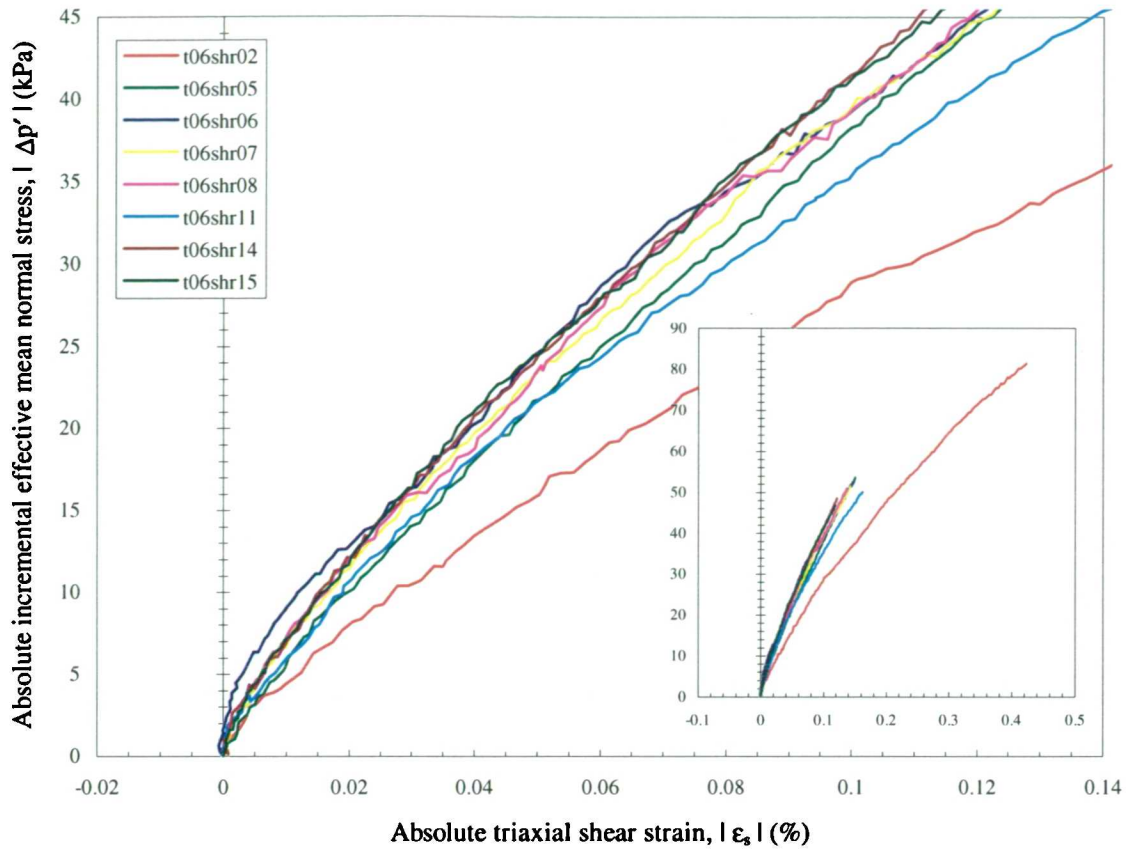
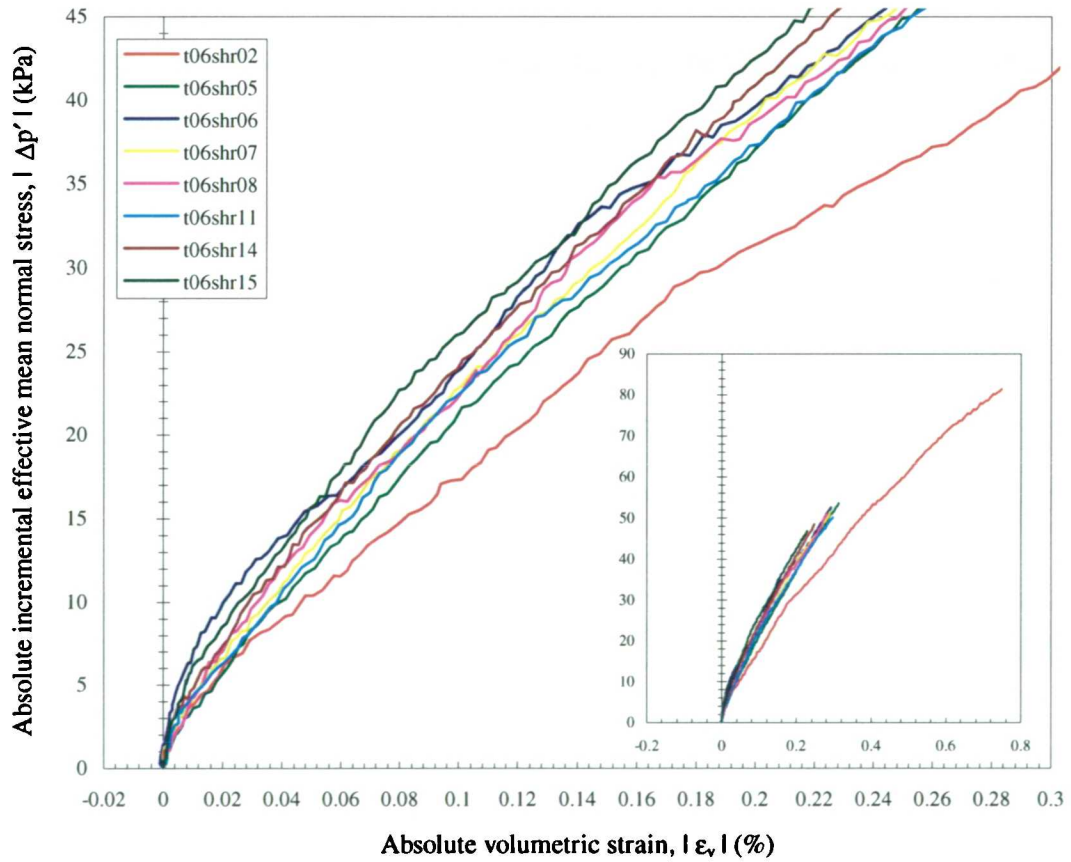


Figure 6.33 - Stress-strain response of constant p' stress paths in test T06



(a)



(b)

Figure 6.34 - Stress-strain response for constant q stress paths in test T06

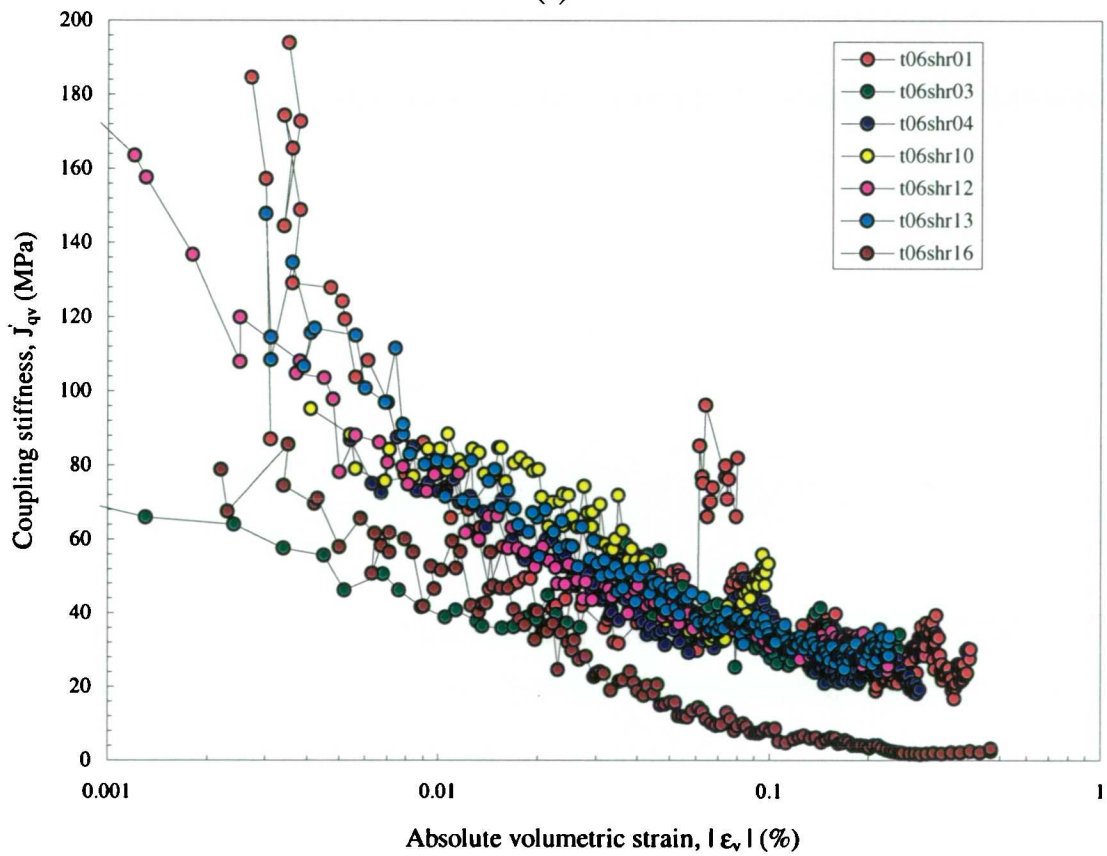
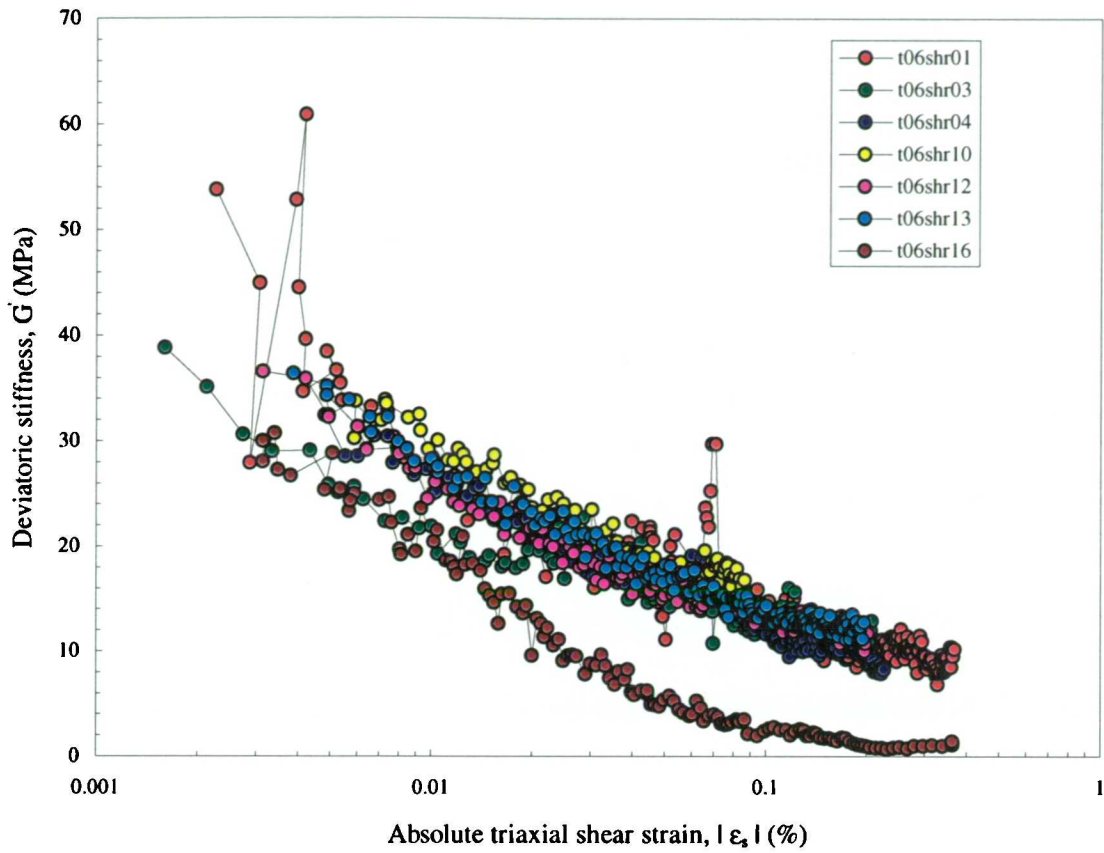
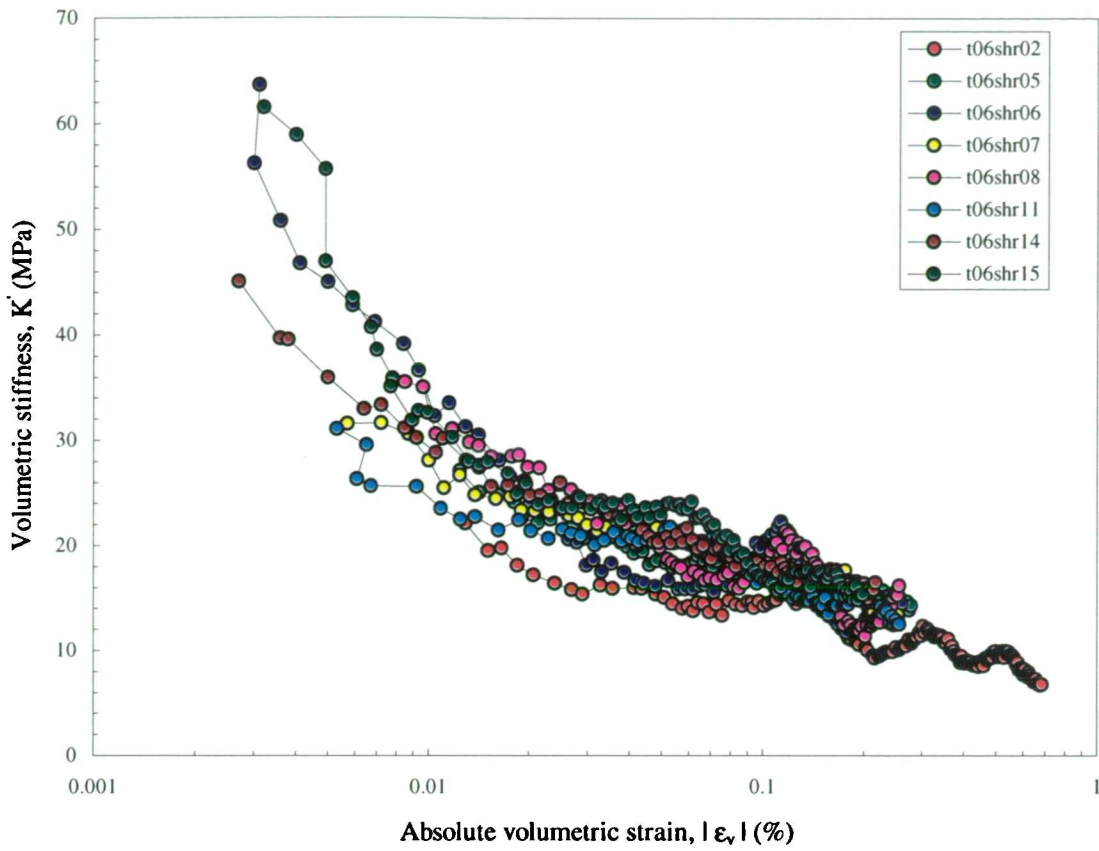
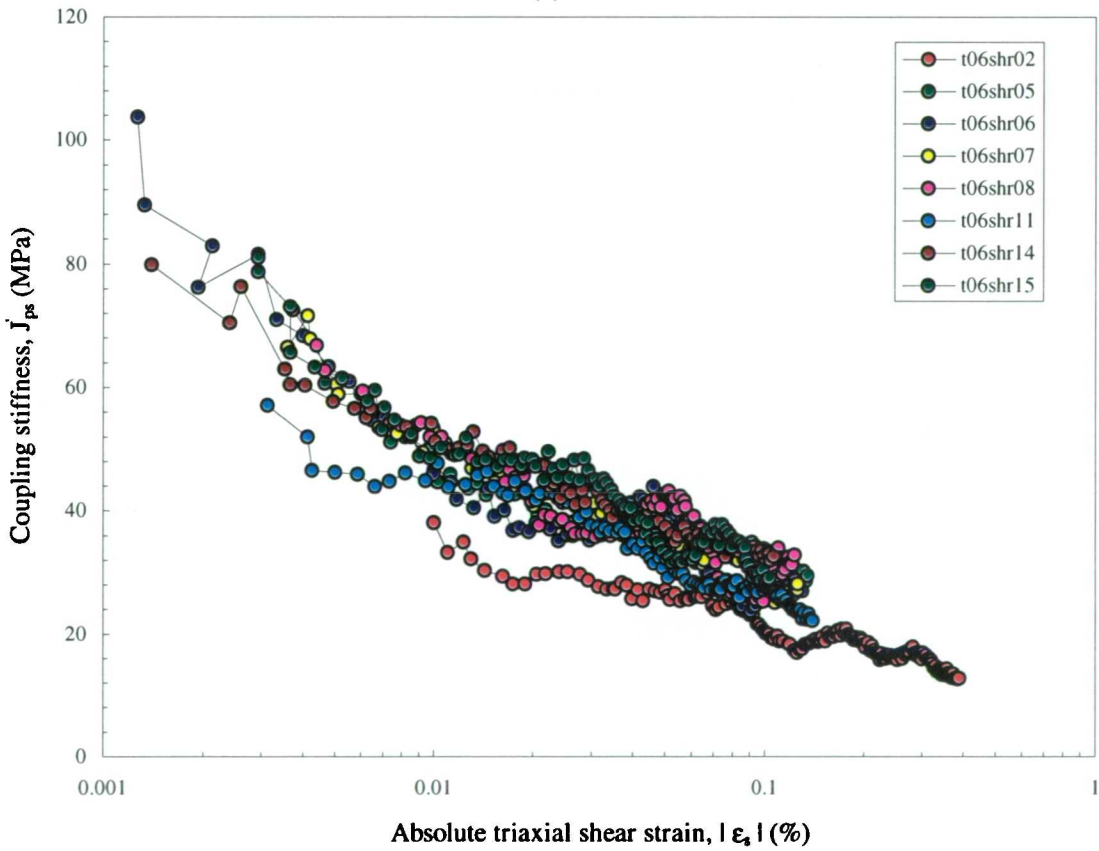


Figure 6.35 - (a) Deviatoric stiffness response against triaxial shear strains and (b) coupling stiffness response for deviator stresses and volumetric strains against volumetric strains for constant p' stress paths of test T06



(a)



(b)

Figure 6.36 - (a) Volumetric stiffness response against volumetric strain and (b) Coupling stiffness response of effective mean normal stresses and triaxial shear strains against triaxial shear strains for constant q stress paths of test T06

6.4.5 Influence of recent stress history

It was hoped to provide an interpretation of the influence of recent stress history in terms of physical effects rather than express them simply as a function of stress state holding period, approach path length, and stress path rotation. Any recent stress history effect must be caused by an alteration to the soil state which persists as a new stress path is applied. This would include the following aspects:

- preferential alignment of the soil particles in response to the previously applied stresses
- incomplete consolidation
- creep
- the formation of additional or stronger bonds e.g. cementation between particles, or thixotropic ageing (Mitchell, 1960)

The last three aspects are transient and their influence can broadly be categorised as ‘ageing’ effects. These are listed in their approximate order of occurrence although clearly there is a degree of overlap. Schmertmann (1991) reviewed many results in the literature in which the effect on soil of maintaining constant effective stress was to invariably increase both its strength and its stiffness over a period of time. Schmertmann argued that it was the mechanical features of ageing which dominated the ageing process over an engineering time scale since none of his examples showed evidence of chemical bonding or other cohesion effects. One effect was that of secondary compression (creep) strains resulting in the rearrangement of soil particles into slightly denser structures and, for sands, this resulted in an increased frictional resistance and hence higher stiffness (e.g. Mesri *et al.*, 1990). For clay soils, Schmertmann suggested that there was the additional aspect of the plate-like clay particles tending to disperse into a more disorganised structure increasing the frictional mobilisation capability of the soil. He continued to show that this ageing effect could be similarly brought about by reducing the strain rate in a triaxial compression test. During such a test, the slower the strain rate of the soil specimen, the greater its stiffness. Further examples of these effects were given in section 2.4.2.

Following the application of a particular stress path in the laboratory a soil specimen experiences both volumetric and deviatoric creep strains depending on the stress path orientation and the degree of soil anisotropy. The change in stress path which produces the most dramatic reversal in the preferred volumetric and deviatoric behaviour of the soil will extract the stiffest response. Conversely, a stress path which reinforces the preferred volumetric and deviatoric creep behaviour will lead to the least stiff response. However, after a prolonged holding period the soil may not be undergoing much creep and the subsequent behaviour may not be preferentially affected by this factor. In this case, the densification and dispersive aspects described by Schmertmann (1991) may lead to an increase in stiffness regardless of the stress path direction.

The possible influence of the soil strain rate over a relatively short timescale is demonstrated qualitatively in Figure 6.37 which shows the strain rate and stiffness characteristics of two stress paths starting from an identical initial stress state and having experienced an identical stress history. One stress path continues in the same direction as the approach path whilst the

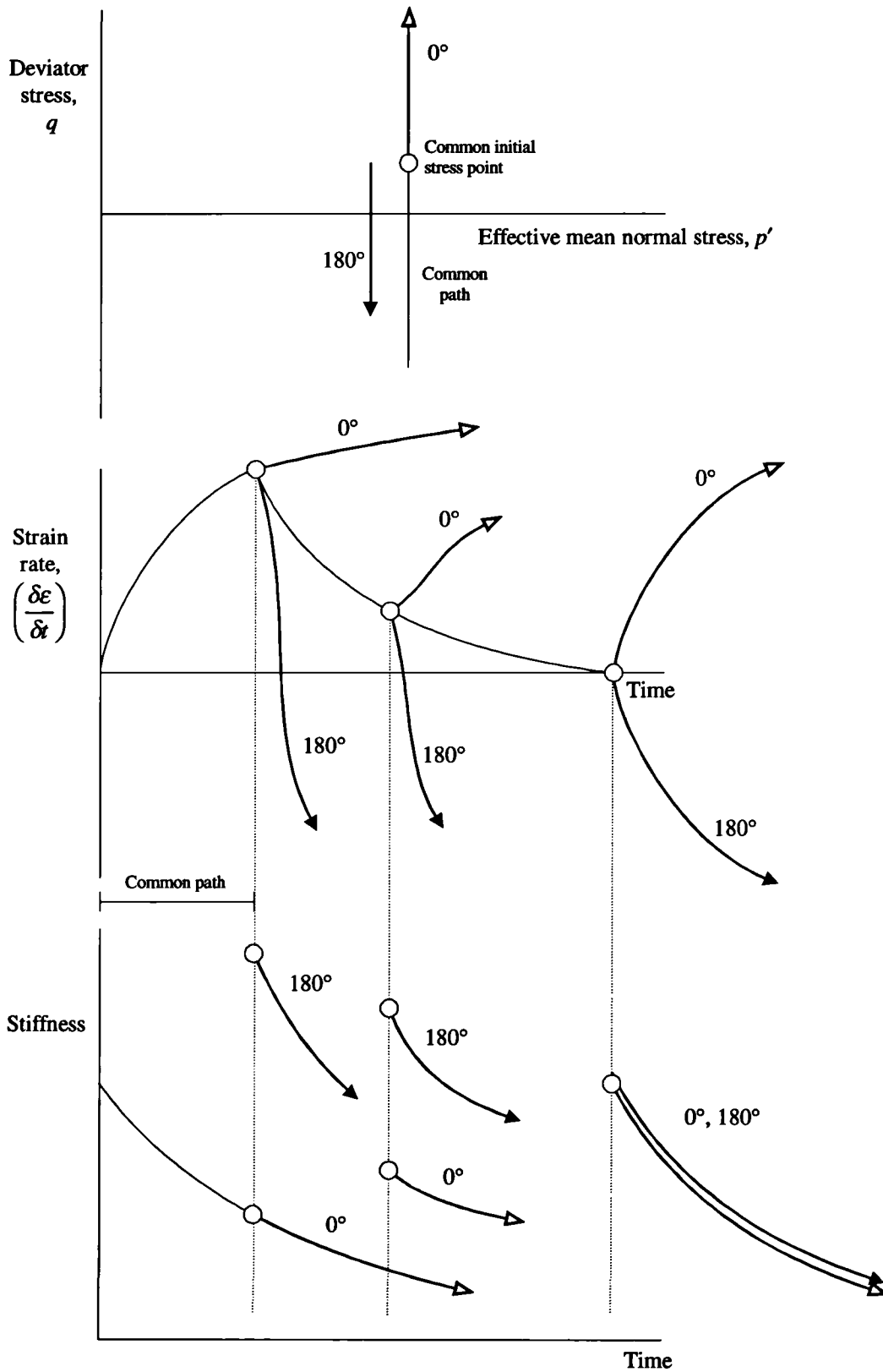


Figure 6.37 - Qualitative figure showing the influence of holding period and soil creep on subsequent loading stress paths

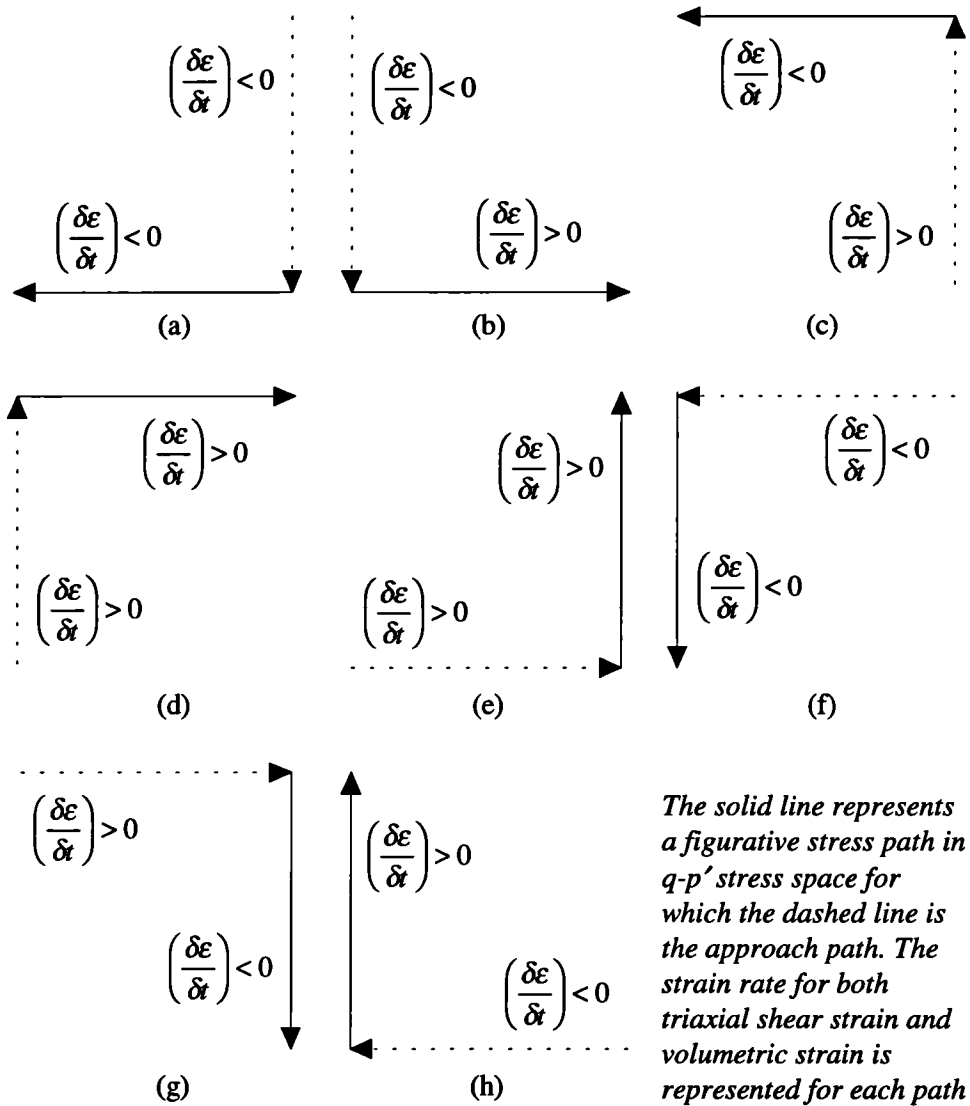
second continues in the opposite direction. The stiffness characteristics of each stress path are shown against time for three different holding periods. The first case is for zero holding period. For the continuation path the effect is not noticeable since from the soil's perspective there has been no change in the loading regime. For the stress path reversal, the soil exhibits a large increase in stiffness since the loading must act to reverse the residual strain rate of the soil. For the second case, the stress paths proceed after a holding period long enough to allow some degradation in the strain rate, although it is still significant. Again, the stress path reversal causes an increase in stiffness although of a reduced magnitude as compared with that for zero holding period. For the continuation path, however, the soil also exhibits an increase in stiffness since the strain rate must now be increased again before the low soil stiffness, as at the end of the previous stress path, is produced. The third case is for an extensive holding period in which the creep rate has effectively reduced to zero. Whether the subsequent stress path is a continuation path or a reversal path, the rate of increase of strain will be similar for each case and therefore the initial stiffness for both paths will be the same. Figure 6.37 addresses the influence of strain rate alone. If the approach path causes significant structural changes to the soil then, even after an extended holding period, the soil will exhibit a stiffness response dependent on the stress path rotation – a permanent recent stress history effect. Qualitatively, it seems reasonable to assume that as the degree of overconsolidation increases the soil structure becomes more resistant to minor stress changes. For example, the particle structure that developed in the Oxford Clay due to its deposition 450 million years ago and subsequent removal of 500m overburden would be less affected by the relatively small stress changes experienced during the triaxial test than would a soft normally consolidated deposit.

Figure 6.38 generalises the effect shown in Figure 6.37 for the remaining constant p' and constant q stress path directions. The figures (a) to (h) show the sign of the generalised strain rate during each particular stress path direction. For a triaxial test this generalised strain may be deviatoric strain or volumetric strain. The figure assumes that the strain increment and the stress increment are of the same sign although this is only necessarily true for elastic behaviour. The inset table on the figure describes each stress path rotation and the effect on the soil stiffness if loading continues before the strain rate has decayed significantly. For example, (a) shows a constant p' approach path with decreasing q for which the triaxial shear strain and volumetric strain rates are negative. The applied constant q stress path with decreasing p' will also experience a negative generalised strain rate. The stress path rotation therefore has the effect of producing a reduced stiffness compared with the stiffness that would have been expected had the holding period been extended so that the generalised strain rate had effectively reduced to zero. The inset table summarises the effect in terms of the approach path stress path direction and the rotation relative to the subsequent stress path. This shows that for a constant p' stress path, a positive (clockwise) rotation produces a greater stiffness for the same short holding period than a negative rotation. Conversely, for a constant q stress path, a positive rotation produces a lesser volumetric or deviatoric stiffness for the same short holding period than a negative rotation. It follows from this that a constant p' stress path following isotropic swelling to an overconsolidated state will have a less stiff response in extension than in compression, with the opposite being true following isotropic compression.

Evidence to support this hypothesis may be obtained from the experimental programme in terms of:

- differences in the stiffness response of interrupted stress paths attributable to the residual strain rate

- comparisons of the stiffness response along a particular stress path direction with a similar approach path direction but with different holding periods
- comparisons of the stiffness response of different stress path rotations for constant p' and constant q stress paths at different initial stresses, assuming that the initial stress state has a lesser influence and may be considered separately.



| Figure | ϑ | $\delta\vartheta$ | Effect on stiffness |
|--------|-------------|-------------------|---------------------|
| (a) | 180° | 90° | ↓ |
| (b) | 180° | -90° | ↑ |
| (c) | 0° | -90° | ↑ |
| (d) | 0° | 90° | ↓ |
| (e) | 90° | -90° | ↓ |
| (f) | 270° | -90° | ↓ |
| (g) | 90° | 90° | ↑ |
| (h) | 270° | 90° | ↑ |

For $\Delta p' = 0$ stress paths,
 $G(+\Delta\vartheta) > G(-\Delta\vartheta)$

For $\Delta q = 0$ stress paths,
 $G(-\Delta\vartheta) > G(+\Delta\vartheta)$

Figure 6.38 - Effect of strain rate on soil stiffness following a change in stress path direction

There are three cases in the experimental programme in which the stress path was a continuation of the previous stress path: in test T01 the constant q path 3 continued in the increasing p' direction following path 2 after a holding period of 27.4 hours; in test T03 the constant p' path 2 continued in the decreasing q direction following a very short (1.5 hour) holding period after path 1; in test T09 the constant p' stress path 6 continued in the increasing q direction following path 5 and an extended earlier holding period after path 4 in which the strain rate had reduced to a very low level.

In both the constant p' path of T01 and the constant q path of T03, the continuation of the loading direction following a short holding period resulted in relatively low stiffnesses with a fairly linear stress-strain response as shown for test T01 in Figure 6.39, and previously in Figure 6.31 and Figure 6.32 for test T03. The strain rates recorded for the stress paths in test T03 are shown in Figure 6.41. In test T09 a rather different effect was noted in that the stress-strain responses of paths 5 and 6, for which the interpreted tangent stiffnesses are shown in Figure 6.40, were very similar. After allowing an extended constant stress holding period of 484 hours the subsequent stress-strain response was very similar to that of the previous stress path which suffered a -90° rotation following a holding period of 155 hours at the end of path 4. The different responses for the constant p' continuation paths in test T01 and test T09 show the importance of the holding period and the residual strain rate when considering the effect of recent stress history on the stiffness of heavily overconsolidated Oxford Clay.

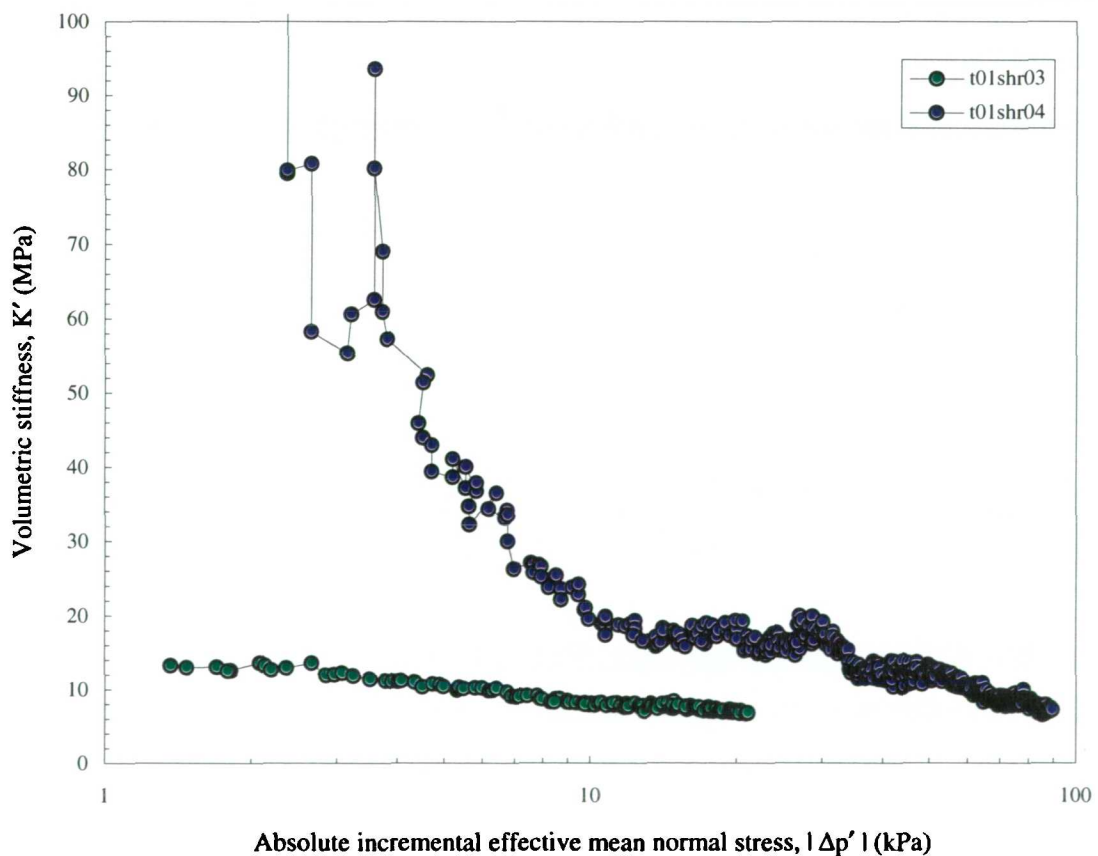


Figure 6.39 - Volumetric stiffness recorded in constant q stress paths of test T01

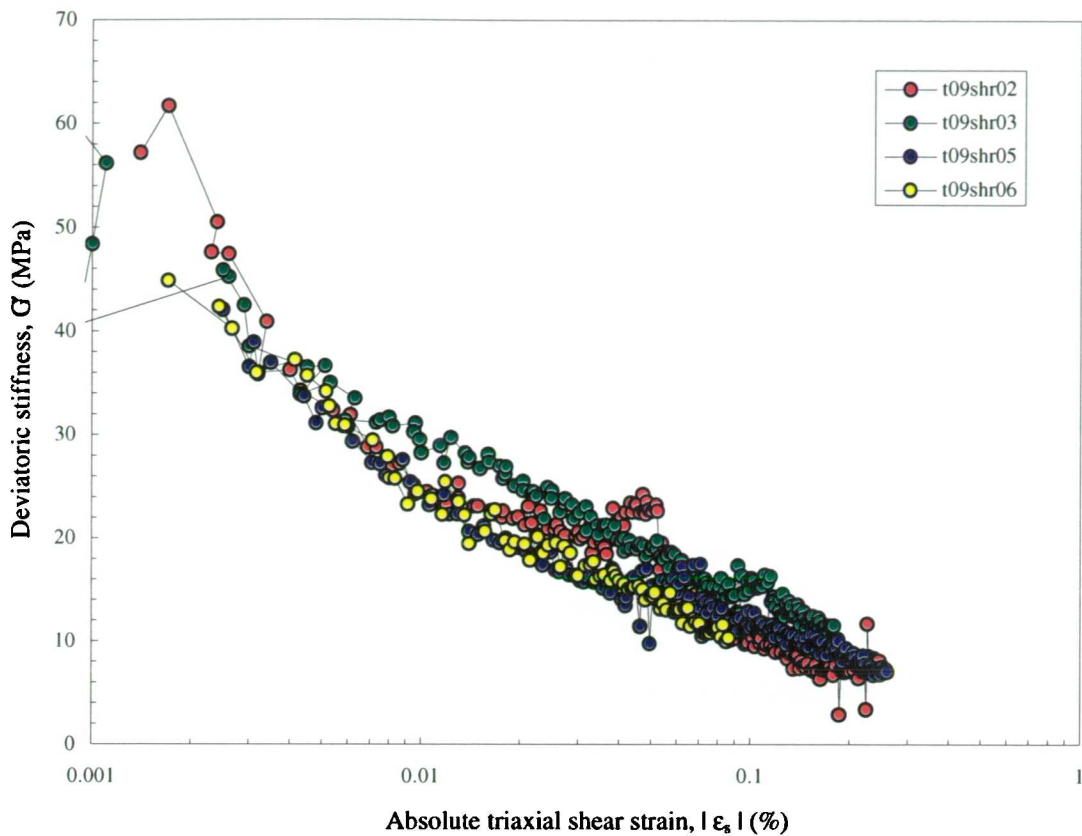


Figure 6.40 - Deviatoric stiffness recorded in constant p' stress paths of test T09

As described in section 6.4.4, the constant q stress paths 4, 6, 10, and 17 in test T03 each share a 180° reversal in stress path following a constant q stress path with increasing p' . The stress paths 4, 6 and 10 all exhibit a very similar stress-strain response whereas path 17 differs significantly, as shown in Figure 6.31. This will now be explained in terms of residual creep rates. The holding periods for paths 4, 6 and 10 were 61.4, 98.2 and 77.4 hours respectively with approach path lengths of 70.7, 53.7 and 57.1 kPa respectively. It was observed that the residual strain rates due to an approach path length greater than 50kPa reduced to similar values after 60 hours. The strain rates at the end of the approach paths, shown in Figure 6.41 (c) and (d), are $<0.0002\%$ / hour for triaxial shear strains and $<0.0004\%$ / hour for volumetric strains. The strain rate at the start of path 17, however, with the shorter holding period of 1.5 hours was 0.003% / hour and 0.006% / hour for triaxial shear strain and volumetric strain respectively. These high residual creep rates combined with the slow loading rates used produced reversals in the initial portion of the stress-strain responses shown for path 17 in Figure 6.31. The strain rates during both the stress path probing stage and the holding period stage are shown in Figure 6.42 on a continual time scale which shows the change in the direction of straining. The volumetric and coupling stiffnesses for these stress paths are shown in Figure 6.43 (a) and (b) respectively. In these figures the stiffness is plotted against the change in effective mean normal stress to show the influence of the residual creep rate. The convergence of these paths occurs after a stress change of 20-30kPa, suggesting a limit to the effect.

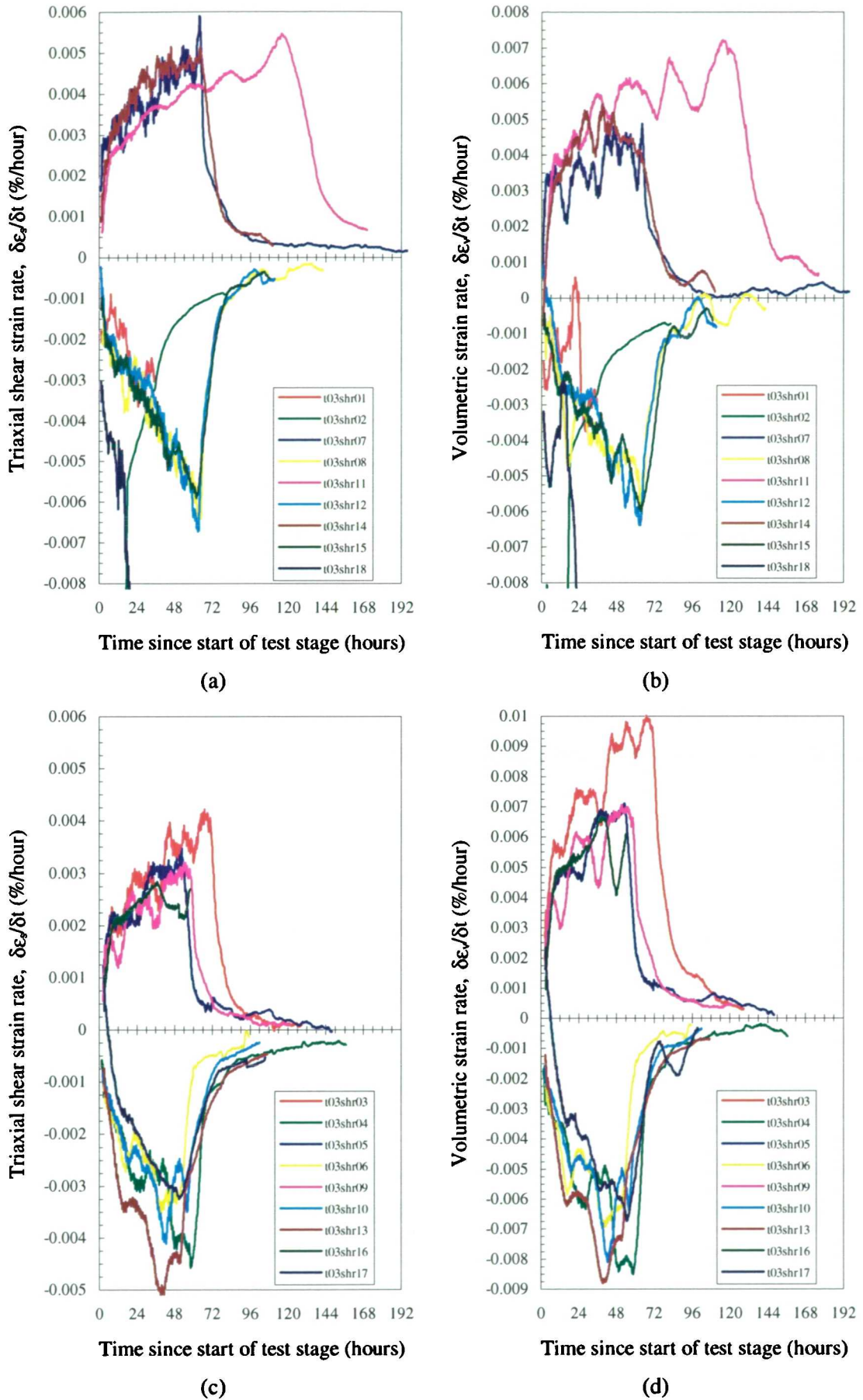


Figure 6.41 - Strain rate during stress paths of test T03

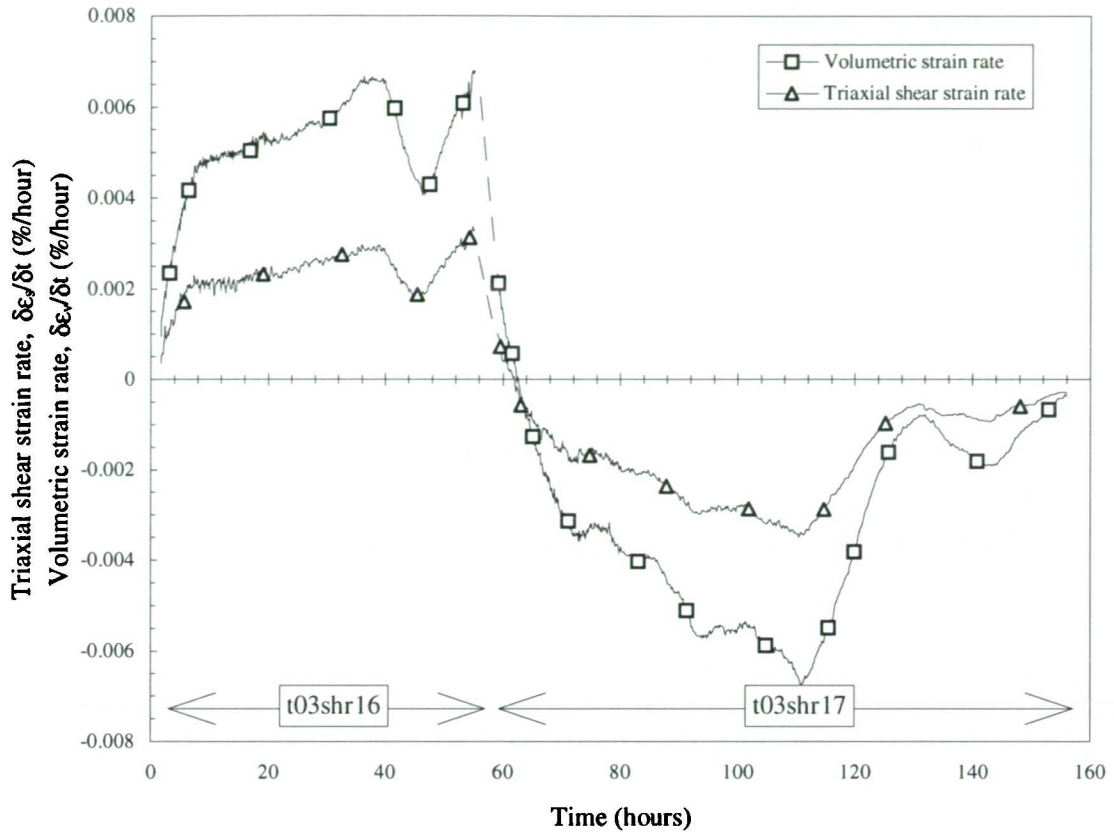


Figure 6.42 - Variation in strain rate during a 180° path reversal in test T03

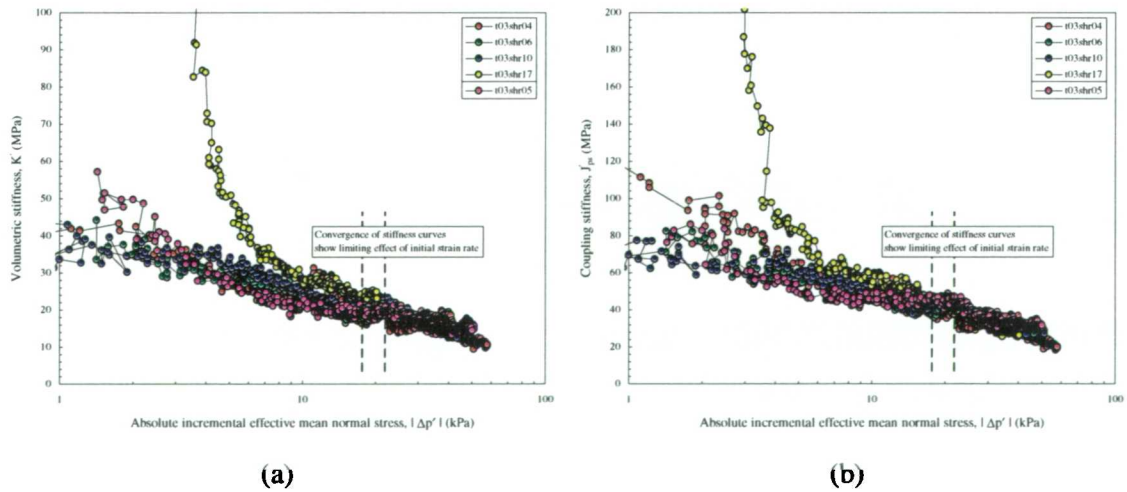


Figure 6.43 - Stiffness moduli for constant p' stress paths following a 180° path reversal

As described in section 6.4.4, there is a difference in the stress-strain response of paths 2 and 11 in test T06. Although paths 2 and 11 were the same (decreasing p' following a 90° rotation), the stress-strain response was different and may be explained by differences in the stress history for each path. The approach path length for path 2 was 150kPa whereas the approach path length for path 11 was 60kPa; additionally, the holding period for path 2 was shorter. The sign of both the triaxial shear strain and volumetric strain rates were similar for both the approach path and the subsequent stress path (corresponding to case (a) in Figure 6.38) and consequently any residual strain rate prior to the path rotation would act to reduce the material stiffness in the following path relative to a similar path with a lesser initial residual strain rate. The difference in strain rate of path 2 from all other paths is clearly shown in Figure 6.44 (c) and (d).

In test T03 paths 7 and 14 were the same (constant p' stress paths following a 90° rotation). The stress-strain response, shown in Figure 6.29, show that the initial response of path 7 was slightly less stiff than that for path 14. In both cases the approach paths were 50kPa in length and the holding periods were 47.7 and 63.3 hours respectively. Using the approach of Figure 6.38(h), such a stress path rotation should produce a stiffer response as the holding period is shortened. This may be connected to the higher strain rate at the end of approach path 13 than for path 6 as shown in Figure 6.41. Although the holding periods were similar for each path, a greater strain rate was attained during the loading stage of path 13 and the rate of strain rate decay was less than that of path 6 such that the residual strain rates were greater at the onset of path 14 than of path 7. In this example, it was not sufficient for the stress paths to have similar approach paths and holding periods for additionally the approach paths have to be of sufficient length such that the final stiffness and strain rate are equal if, as in this case, the strain rates at the onset of the path are not equal.

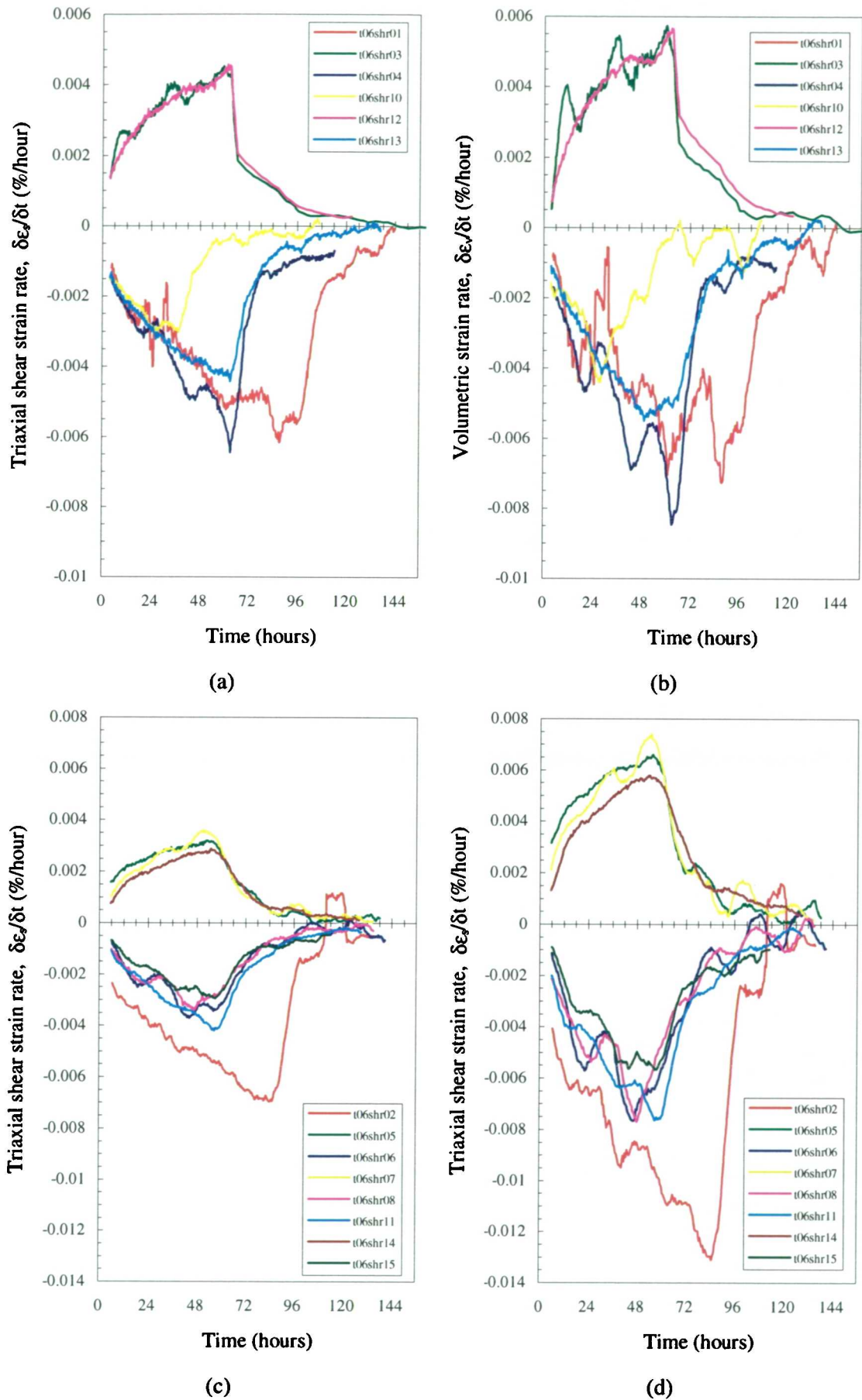


Figure 6.44 - Strain rate during stress paths of test T06

6.4.6 Influence of effective mean normal stress

The influence of the effective mean normal stress on the small strain stiffness response of the soil may generally be quantified as follows:

- by comparing results from appropriate paths from the same multi-stage stress path test having the same recent stress history but carried out at different effective mean normal stresses. Unfortunately, a suitable stress path was not incorporated into the experimental programme since the multi-stage stress path tests were designed to determine appropriate stiffness parameters at a given initial stress state.
- by comparing results from stress paths of similar stress history in different tests. Although comparisons may be carried out between the present stress path tests, only the initial stress path starting from an isotropically consolidated state might properly gauge the influence of the effective mean normal stress, for all the other stress paths commenced at different deviatoric stresses.

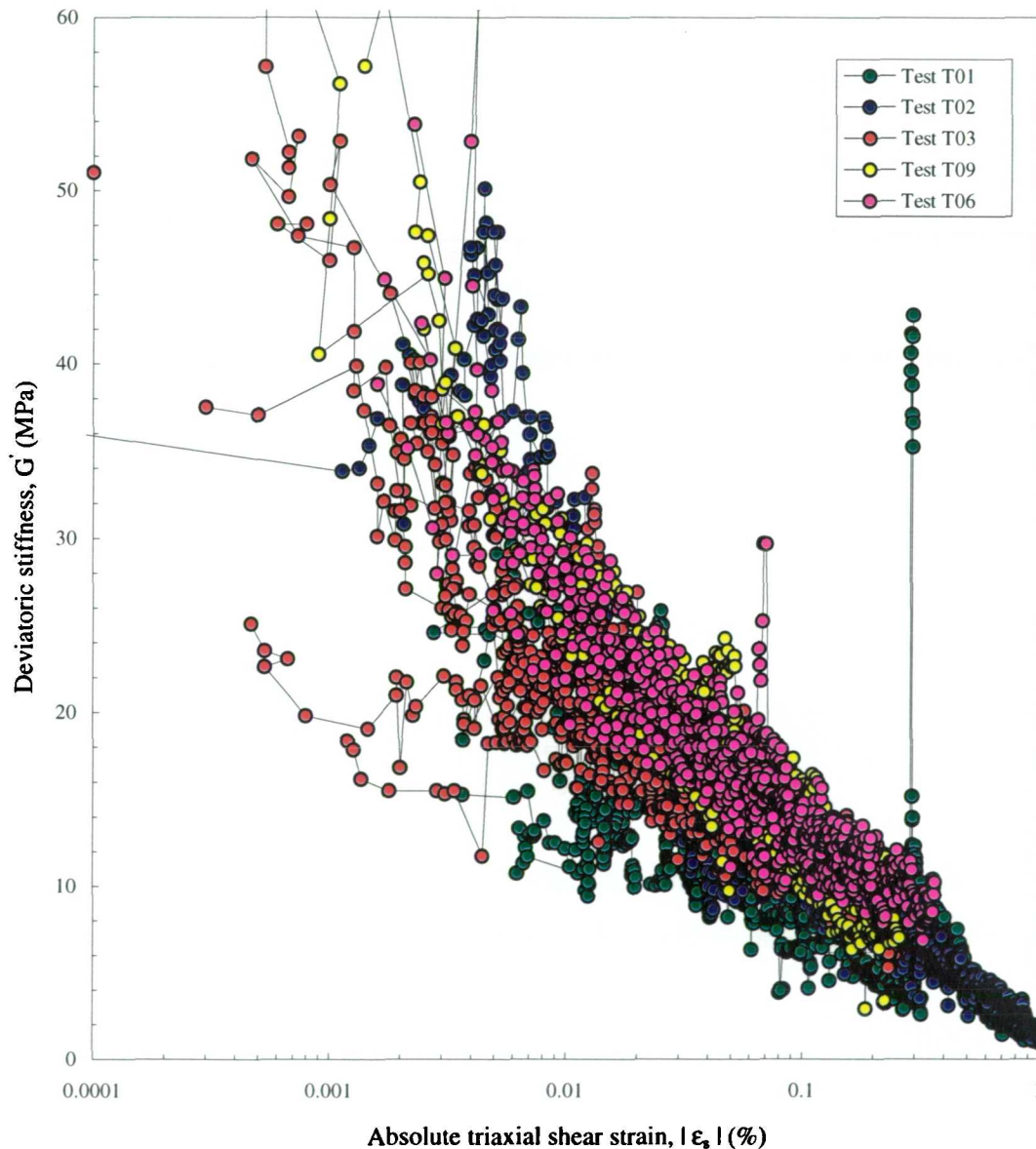


Figure 6.45 - Combined stiffness response of tests T01, T02, T03, T06 and T09 showing the deviatoric stiffness response against triaxial shear strain

Considering the above limitations, the influence of the effective mean normal stress on the stress-strain response of the soil may be seen in Figure 6.45 which shows the average range of tangent deviatoric stiffness recorded in stress tests T01, T02, T03, T06 and T09. No clear trend is apparent although the average deviatoric stiffness response of test T06 is perhaps approximately 5MPa greater than the average response of test T03 for constant p' stress paths which are offset by approximately 70kPa.

There is also no recordable difference in the magnitude of stiffness recorded on tests carried out on specimens trimmed from either the Elstow or the Kempston Pit block samples. The magnitude and decay with strain level of the deviatoric tangent stiffness recorded in test T02 (for a specimen trimmed from an Elstow block sample) is similar to the range of data observed in test T06 (for a specimen trimmed from a Kempston Pit block sample) which was carried out at similar effective mean normal stress.

6.4.7 Effect of loading rate

The choice of loading rate for the stress path tests was governed by the necessity of achieving drained conditions so as to ensure constant p' and constant q stress paths. Where it is not possible to ensure fully drained conditions, a loading rate must be chosen such that any undissipated excess pore pressure should be of a small enough magnitude that the required results from the test are not significantly affected.

There was not sufficient time in the experimental programme to carry out a parametric study on the influence of testing time and it was initially decided to carry out all the tests at a stress rate similar to that adopted in previous studies carried out on London Clay (Richardson, 1988). A nominal rate of axial stress change of 1kPa/hour was chosen, resulting in a stress rate of 1.5kPa/hour for the constant p' stress paths and 1kPa/hour for the constant q stress paths.

For tests T01, T02 and T03, on specimens trimmed from block samples from the Elstow site, the pore water pressure at mid-height was at all times the same as that recorded at the specimen ends. However, when testing specimens from the fresh block samples obtained from the Kempston Pit, in test T04 onwards, it was noticed that a significant excess pore water pressure was generated at the mid-height of the specimen. At this stage the testing rate was re-evaluated.

The choice of loading rate in triaxial tests has traditionally been based on times to failure (Bishop and Henkel, 1962). However, another approach has recently been proposed by Cherrill (1990) to provide a method of determining the loading rate for stress paths which may be far from failure, as in the present case.

Cherrill's method for drained triaxial tests is based on equation 6.11.

$$\bar{u} = \mu' \sigma_c \dots\dots\dots (6.11)$$

where, \bar{u} = excess pore water pressure

$$\sigma_c = \text{characteristic stress defined as, } \sigma_c = \left(\frac{d\sigma_a}{dt} \right) \cdot t_{100}$$

and $\left(\frac{d\sigma_a}{dt} \right)$ is the rate of axial loading,

and t_{100} is defined in the usual way.

The parameter μ' is a parameter which varies according to the type of test, the degree of overconsolidation of the soil specimen, and the drainage conditions. Choosing suitable values

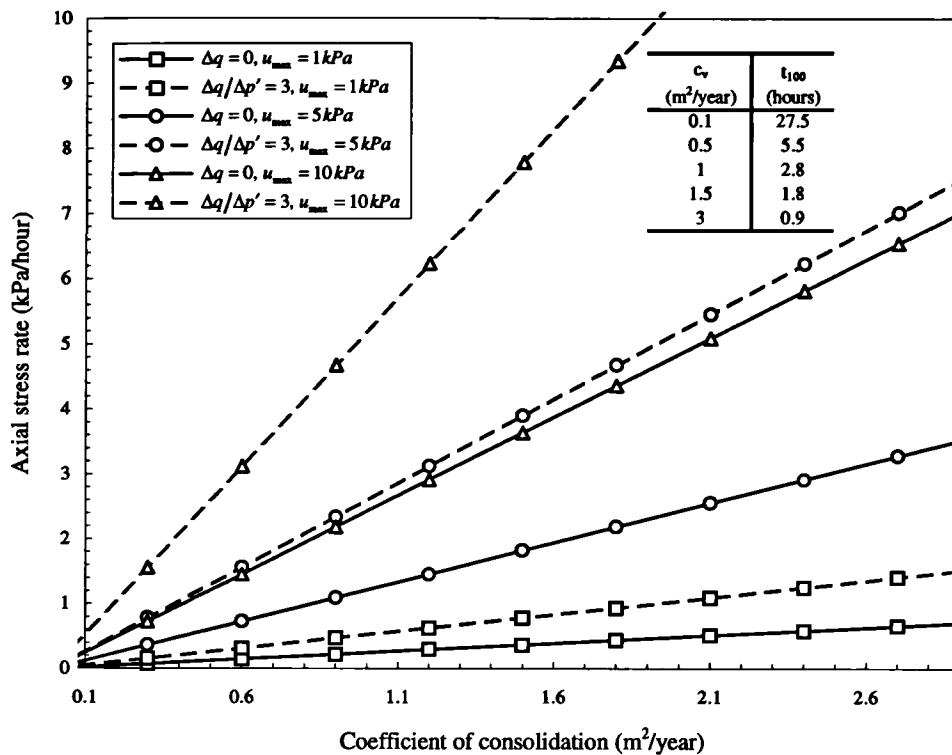


Figure 6.46 - Determination of axial stress rate following Cherrill (1990)

for an overconsolidated soil specimen with all-round drainage using filter paper drains, the required axial stress rates to produce excess pore water pressures at the mid-height of the specimen of 1, 5, and 10kPa respectively are shown as a function of coefficient of consolidation in Figure 6.46 during isotropic compression and constant stress rate triaxial compression/extension stress paths.

The procedure presently adopted to determine a suitable loading rate was, therefore, to carry out a step consolidation stage and calculate t_{100} , from which $\left(\frac{d\sigma_a}{dt}\right)$ could be determined for a specified maximum excess pore water pressure.

From the literature, a range for the coefficient of consolidation of Oxford Clay is summarised in Table 6.13 with the corresponding consolidation times for all round drainage in 100x200mm triaxial specimens.

| Source | c_v ($m^2 / year$) | t_{100} (hours) |
|------------------------------|------------------------|-------------------|
| Elstow site investigation | 0.4-2.9 (0.7-1.3) | 0.9-6.9 |
| Burland <i>et al.</i> (1977) | 0.5-1.0 | 2.8-5.5 |
| Jackson and Fookes (1974) | 0.27-0.41 | 6.7-10.2 |
| <i>Current research</i> | <i>0.2-1.8</i> | <i>2.1-13.7</i> |
| Test T01 | 1.53 | |
| Test T02 | 1.79 | |
| Test T03 | 1.15 | |
| Test T05 | 0.15 | |
| Test T06 | 0.28 | |
| Test T08 | 0.48 | |
| Test T09 | 0.24 | |

Table 6.13 - Coefficient of consolidation of unweathered Oxford Clay

As shown in Table 6.13, during the current research, the coefficient of consolidation was found to vary over a considerable range. There is a clear distinction between the consolidation characteristics of the specimens prepared from the Elstow block samples and those prepared from the Kempston Pit block samples. Test T01, T02, and T03 (Elstow material) recorded coefficients of consolidation at the high end of the range, whilst in tests T05, T06, and T09 (Kempston Pit material) the recorded values were at the low end of the range. The test T08 specimen (weathered Oxford Clay from Elstow) also recorded a relatively low coefficient of consolidation. The lower rates of consolidation for the specimens trimmed from the Kempston Pit block samples explain the relatively high excess pore water pressures recorded in the later tests. For example, in stress path test T06, the step consolidation stage led to a t_{100} of 9.8 hours. To maintain approximately drained conditions, for an excess pore water pressure of 1kPa, the required rate of change of axial stress is 0.07kPa/hour. Such a testing rate was obviously impractical, leading to excessive testing times (2 months for a single 100kPa length stress path), and it was decided that the nominal rate of axial stress change of 1kPa would be retained as the lowest feasible testing rate. For the above example, such a loading rate would be expected to produce a maximum excess pore water pressure at the mid-height of the specimen during constant q stress paths of 14.7kPa, but the actual maximum excess pore water pressure encountered during testing was sometimes twice this value (see, for example, Figure 6.47). However, because of the time constraints it was decided that such excess pore water pressure generation would have to be tolerated and consequently the same testing rate was used in all the stress path tests to allow meaningful comparisons between tests.

The testing rates required in such low permeability materials may undermine the applicability of drained stress path tests on specimens as large as 100x200mm. A compromise must be made between the test durations being feasible and the specimen size being large enough to be

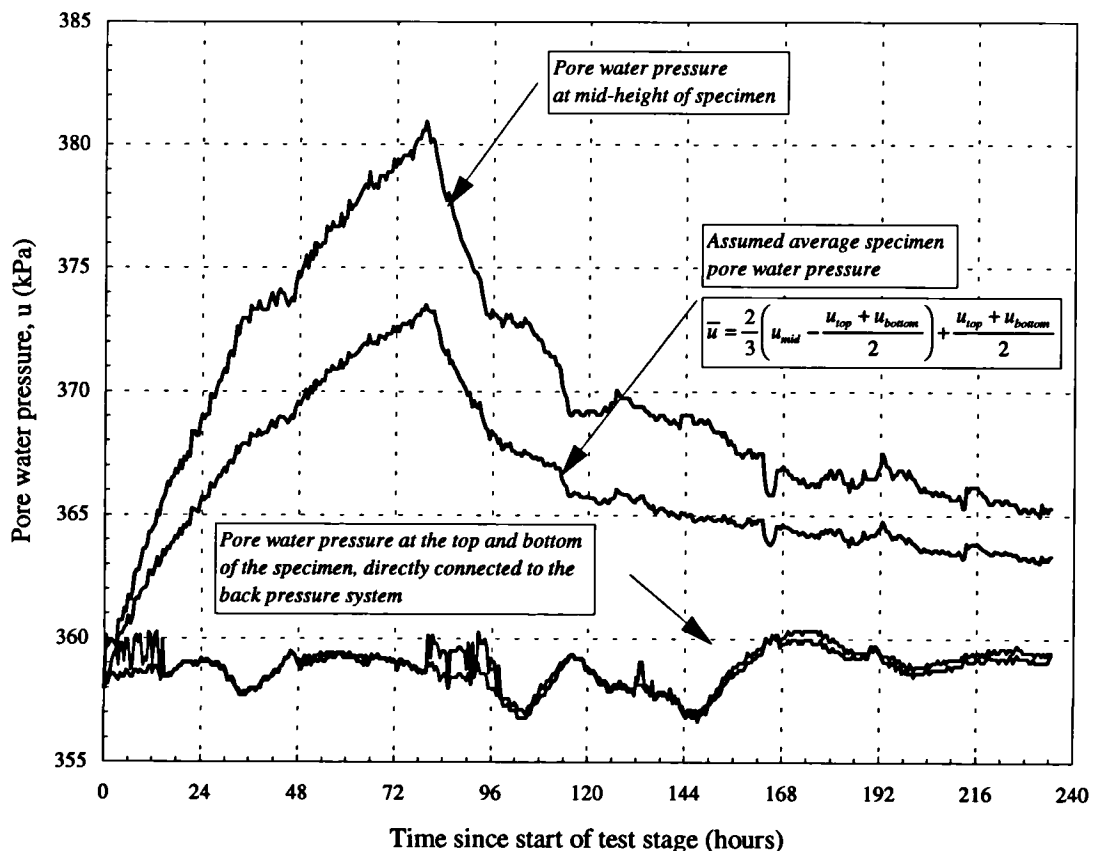


Figure 6.47 - Pore water pressure response for stress path 4 in test T09

representative. At very low loading rates the stiffness of the soil could be expected to be affected in the following ways:

- Creep strains within the soil, often regarded as a separate subsequent response following strains due to changes in effective stress, will have a far more significant role on the strains incurred due to the stress path loading. There are two possibly and opposing effects: firstly, additional creep strains could lead to a less stiff response; secondly, the creep strains could lead to mechanical ageing (Schmertmann, 1991) and a stiffening of the response (see section 6.4.5).
- Because the strain rate within the soil will always be relatively low, the soil will respond similarly to a soil maintained at constant stress for a certain holding period before the path continued. This will tend to produce a more stiff response.

The effect of loading rate is illustrated in Figure 6.48 in which stress paths 3 and 7 are otherwise identical except that stress path 3 was carried out 1kPa / hour and stress path 7 was carried out at 0.25kPa / hour. A stiffer small strain response was recorded for stress path 7 where the maximum strain rate was significantly lower than during the other paths.

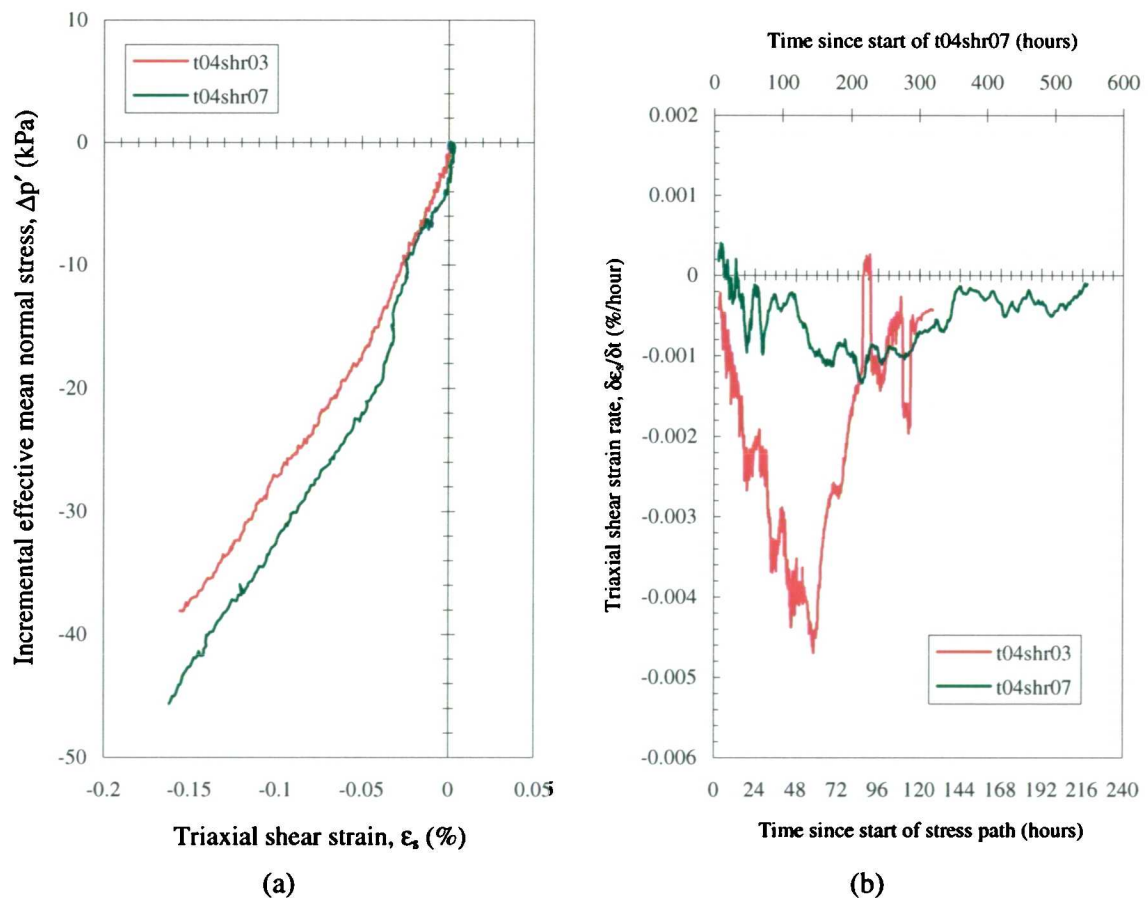


Figure 6.48 - Stress-strain response strain rate for two constant q stress paths in test T04, demonstrating the influence of loading rate on stiffness

6.4.8 Comparison of failure stresses

The final stress state for those specimens which attained passive failure (tests T01, T02, T03, T04 and T06) is shown in q - p' space in Figure 6.49. Included on this figure are purely frictional failure states with the angle of internal friction varying parametrically between 20° and 45° . Only test specimens T03 and T06 were brought to failure following the constant q unloading stress path from the estimated *in situ* stress state; test specimens T01, T02 and T04 were brought to failure from an initially isotropic stress state. If the failures are interpreted as being purely frictional, specimens T02, T04 and T06 failed at friction angles of 28° to 34° , and tests T03 failed at relatively high friction angle of 40° . The stress state of test specimen T01 at failure was approaching the point where a tensile stress would have been present. The results do not produce consistent evidence as to the location of the failure envelope of the unweathered Oxford Clay.

The two extremes in the measured maximum mobilised angle of friction occurred for tests T01 and T02. However, both of these test specimens were trimmed from the same block sample obtained from the Elstow excavation. This would suggest that the differences in failure angles of friction are not solely attributable to differences in the Elstow and Kempston Pit material (although tests T04 and T06 on material derived from the Kempston Pit failed at similar mobilised angles of friction).

A possible explanation of the variation in failure states may be that the effective stress state recorded in the test was not representative of the stress state in the region of the specimen where failure was initiated. Although the deviator stress is recorded directly from the load cell, the effective mean normal stress relies on the mid-height miniature pore water pressure

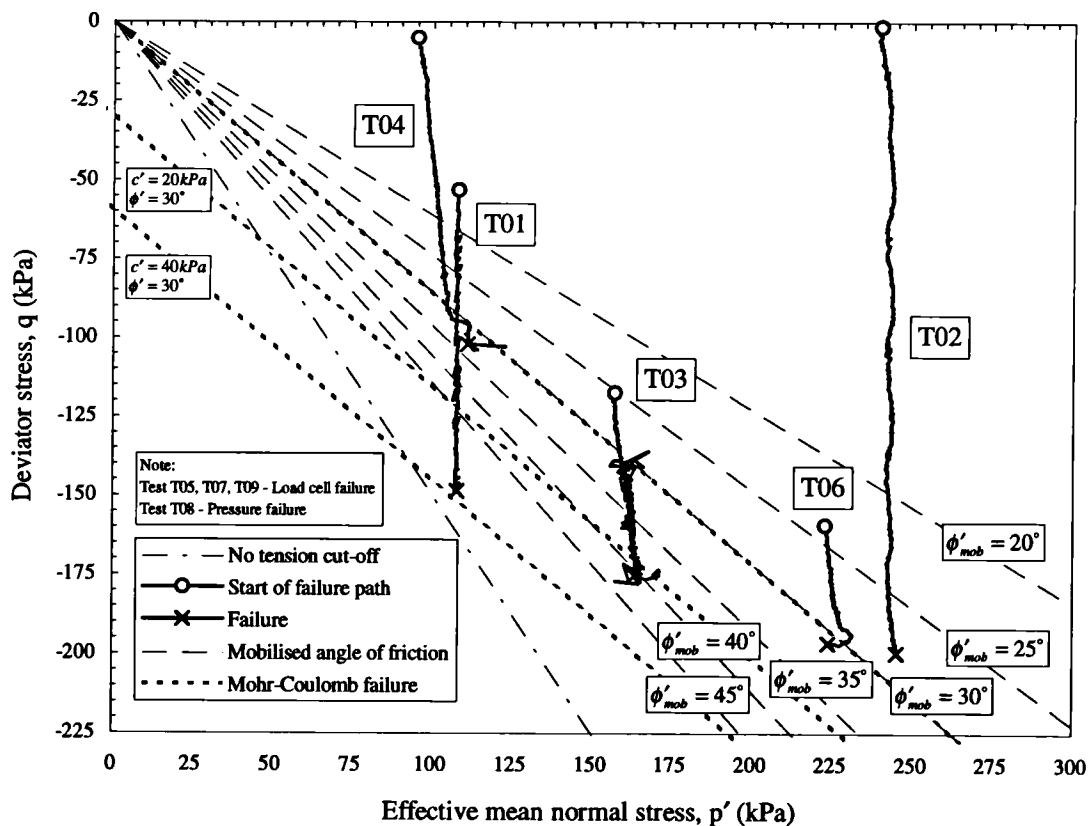


Figure 6.49 - Passive failure states of specimens in stress path tests T01, T02, T03, T04 and T06

transducer. It was seen in section 6.3.3 that the mid-height pore water pressure probe could not always be relied on to accurately describe the pore water pressure in the central third of the specimen. This was attributed to either the proximity of the specimen side drains or to the influence of the specimen's fissure system. A heavily overconsolidated clay would be expected to dilate as its stress state approached failure. This would tend to produce negative excess pore water pressures and cause a corresponding increase in p' . The influence of the specimen's cross-anisotropic nature would also tend to increase p' as q was reduced (see section 6.2.2). Relatively large excess pore water pressures were recorded at the mid-height of the specimen in test T04 and, consequently, the effective stress path to failure shown on Figure 6.49 is inclined to the vertical. If the specimen pore water pressure had been calculated based on the back pressure measurement, the resulting vertical effective stress path would have increased the apparent mobilised angle of friction at failure from 34° to 40° . If a similar increase in p' with reducing q is assumed for test T01 as for test T04, the mobilised angle of friction at failure for test T01 reduces from the almost tensile failure to the still relatively high but more reasonable value of 46° . These large values of mobilised angle of friction appear more reasonable if a degree of cohesion is assumed. It is shown in Figure 6.49 that assuming a cohesion of 25–40kPa i.e. as reported in the literature (Table 3.1), reduces the slope of the failure envelope significantly.

Schmertmann (1991) argued that through mechanical ageing processes, higher strengths would be observed in specimens carried out at relatively low rates of loading (see section 6.4.5). For the tests described here, however, all stress paths were carried out at the same rate and consequently this should not have affected the failure states.

6.4.9 Relative levels of stiffness and strain

For tests T03, T06 and T09, the 4 stiffness parameters derived from both the constant p' and constant q stress paths are combined for each test in Figure 6.50, Figure 6.51, and Figure 6.52 respectively. Although these figures contain results for a variety of stress histories, the conclusions from each test are generally similar.

- Both coupling stiffnesses are numerically greater than either the volumetric stiffness or the deviatoric stiffness.
- The volumetric stiffness and the deviatoric stiffness are numerically very similar.
- At small strains, the coupling stiffness parameters are not the same as each other. J'_{qv} is numerically greater than J'_{pv} and possesses a higher degree of non-linearity.
- The coupling stiffnesses converge to a common value at larger strains.

The difference in the coupling stiffnesses highlights fundamental features of the soil's behaviour as described later in section 7.4. Similarity of the coupling stiffnesses is a necessary condition for both cross-anisotropic elasticity and associated plastic straining. The results therefore suggest that the soil is behaving plastically from the onset of loading and that the plastic strains are initially non-associated. As loading continues, the plastic strains become increasingly associated.

Further information on the fundamental soil response may be obtained from the relative levels of deviatoric strain and volumetric strain. The strain paths recorded for each stress path probe in tests T03 and T06 are shown in Figure 6.53 and Figure 6.54 respectively. In an isotropic elastic material, there would be no volumetric straining during a constant p' stress path and the strain path would plot horizontally. In the current tests, however, the magnitude of volumetric

strain was similar to the magnitude of deviatoric strain. Such volumetric straining along constant p' stress paths could be explained by anisotropic elastic material behaviour. A prerequisite of this type of behaviour is that the strain path should be a straight line and any deviation from a straight line is indicative of plastic straining (Atkinson, 1975). On Figure 6.53 and Figure 6.54 a slight curvature of the initial portion of these strain paths is evident. The greatest curvature is found for paths 2,12, and 14 in test T03, and for path 3 in test T06. In all these cases the residual strain rate in the specimen before the onset of the path (shown in Figure 6.41 and Figure 6.44 respectively) was relatively high, affecting the subsequent response as described in section 6.4.5. It should be noted that the strain paths are plotted for small strains and that small deviations from the specified stress path caused by the limitations of the control system produce oscillations in the strain path response.

For the constant q stress paths, an isotropic elastic material would undergo purely volumetric strains whereas Figure 6.53 and Figure 6.54 show deviatoric strains approximately half the magnitude of the volumetric strains for these paths. The strain paths shown for the constant q stress paths are relatively linear for both tests T03 and T06 although there is a reversal in the strain path for path 17 in test T03 as discussed in section 6.4.5.

In conclusion, the strain paths show that for a moderate and monotonic change in stress, the deviatoric and volumetric strains could be explained within a cross-anisotropic elastic framework. However, the unequal coupling stiffnesses suggest that the behaviour is truly inelastic in which case the linear strain paths suggest associated flow.

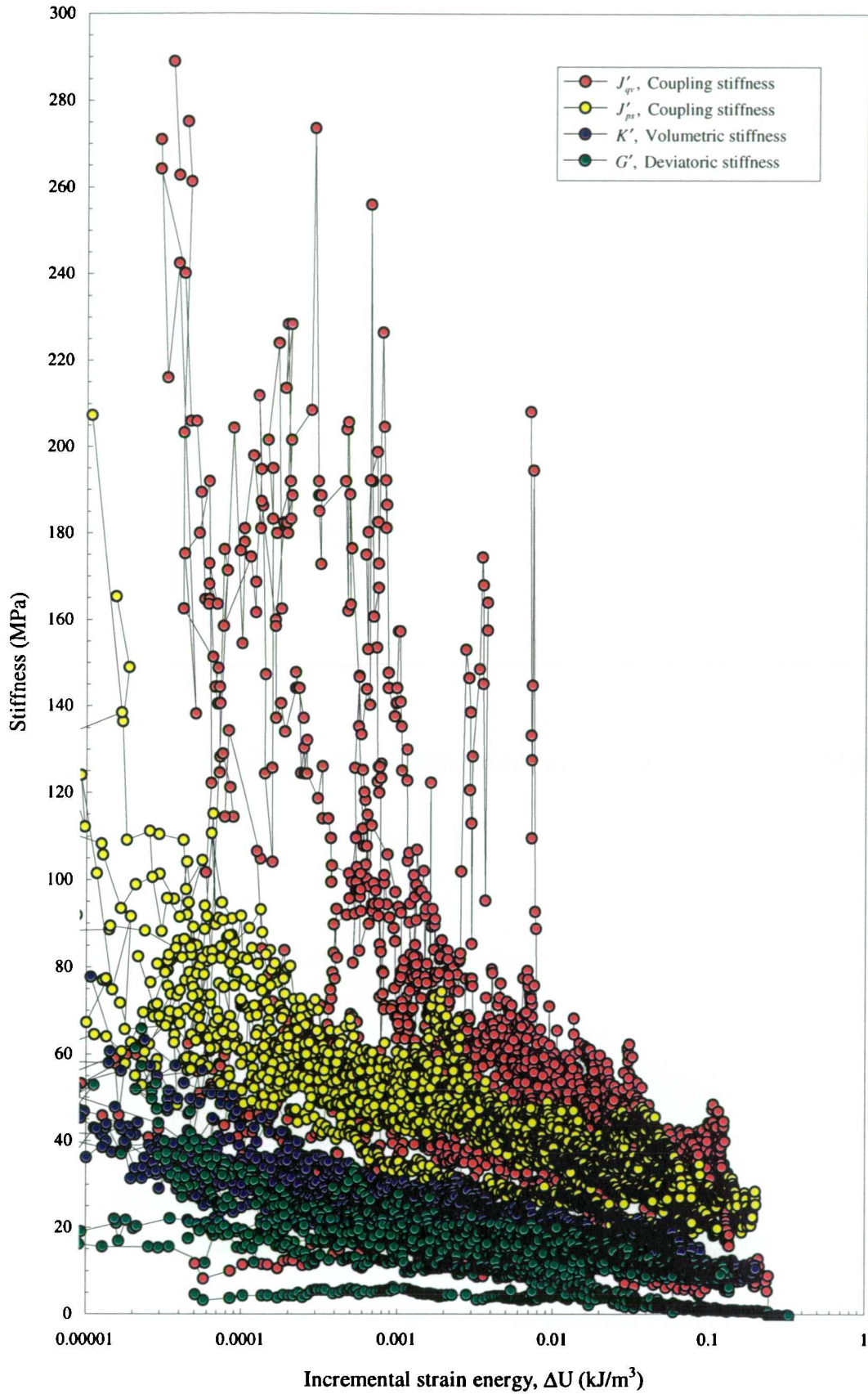


Figure 6.50 - Comparison of all derived stiffness parameters against incremental strain energy for test T03

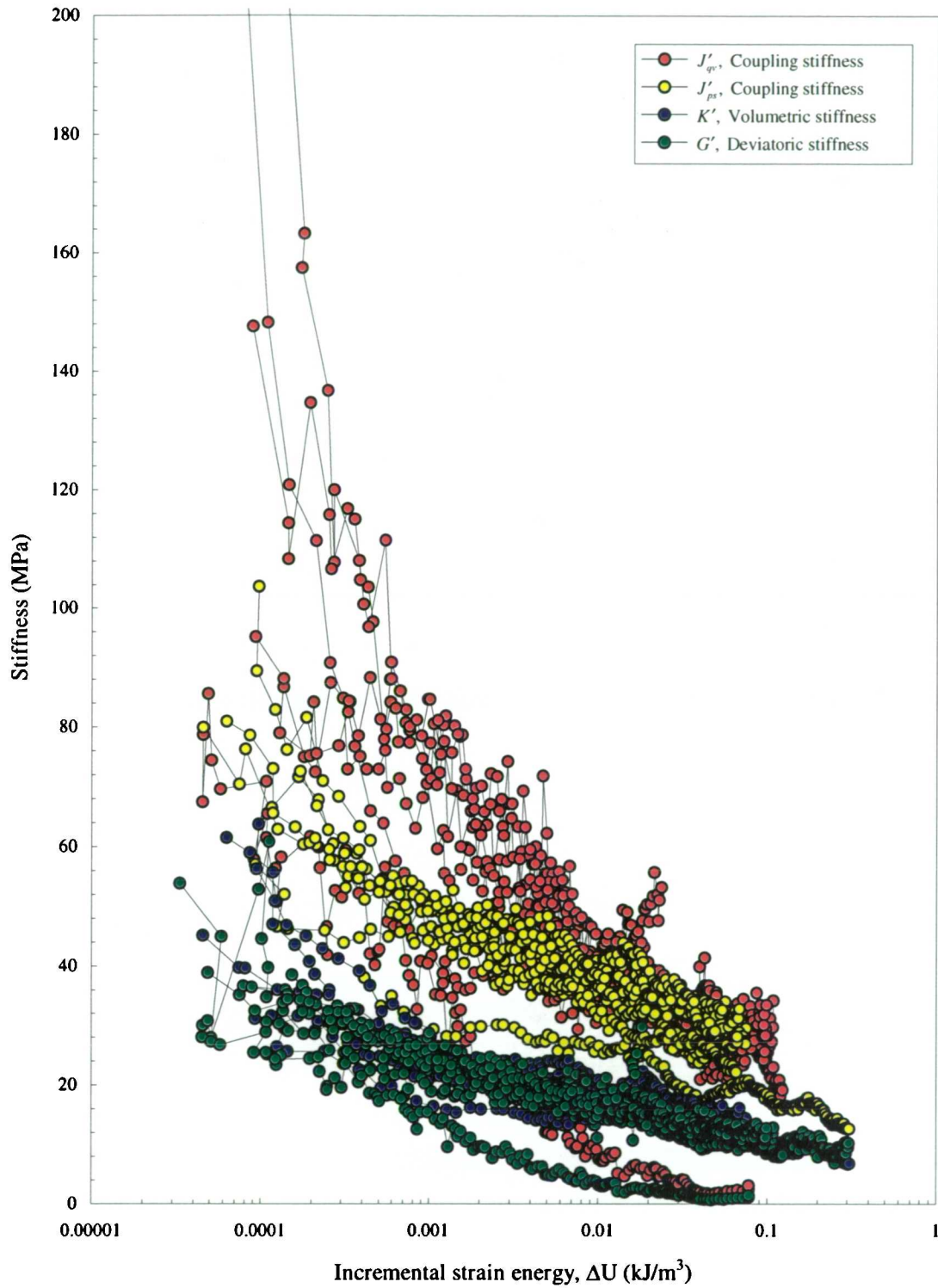


Figure 6.51 - Comparison of all derived stiffness parameters against incremental strain energy for test T06

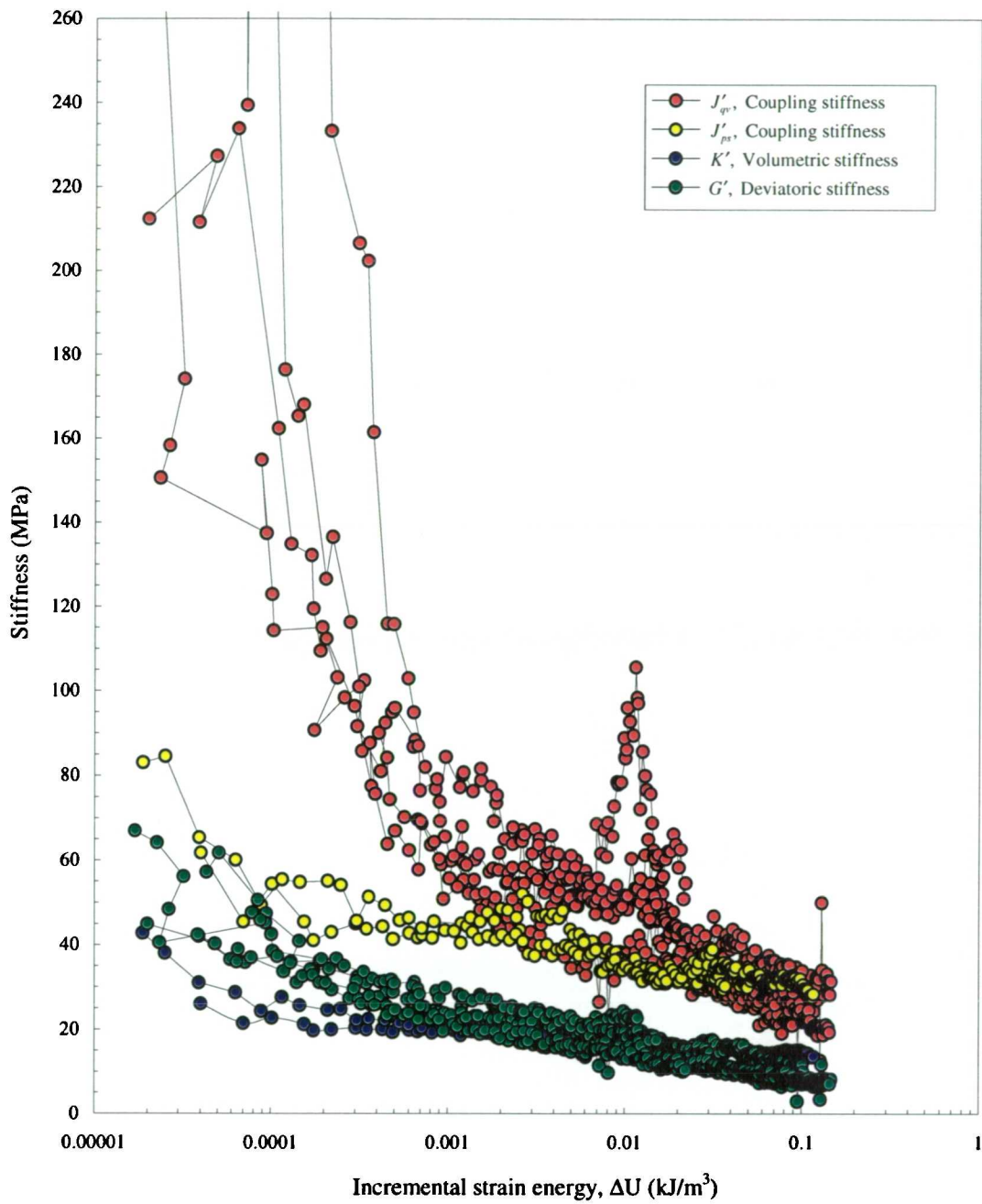


Figure 6.52 - Comparison of all derived stiffness parameters against incremental strain energy for test T09

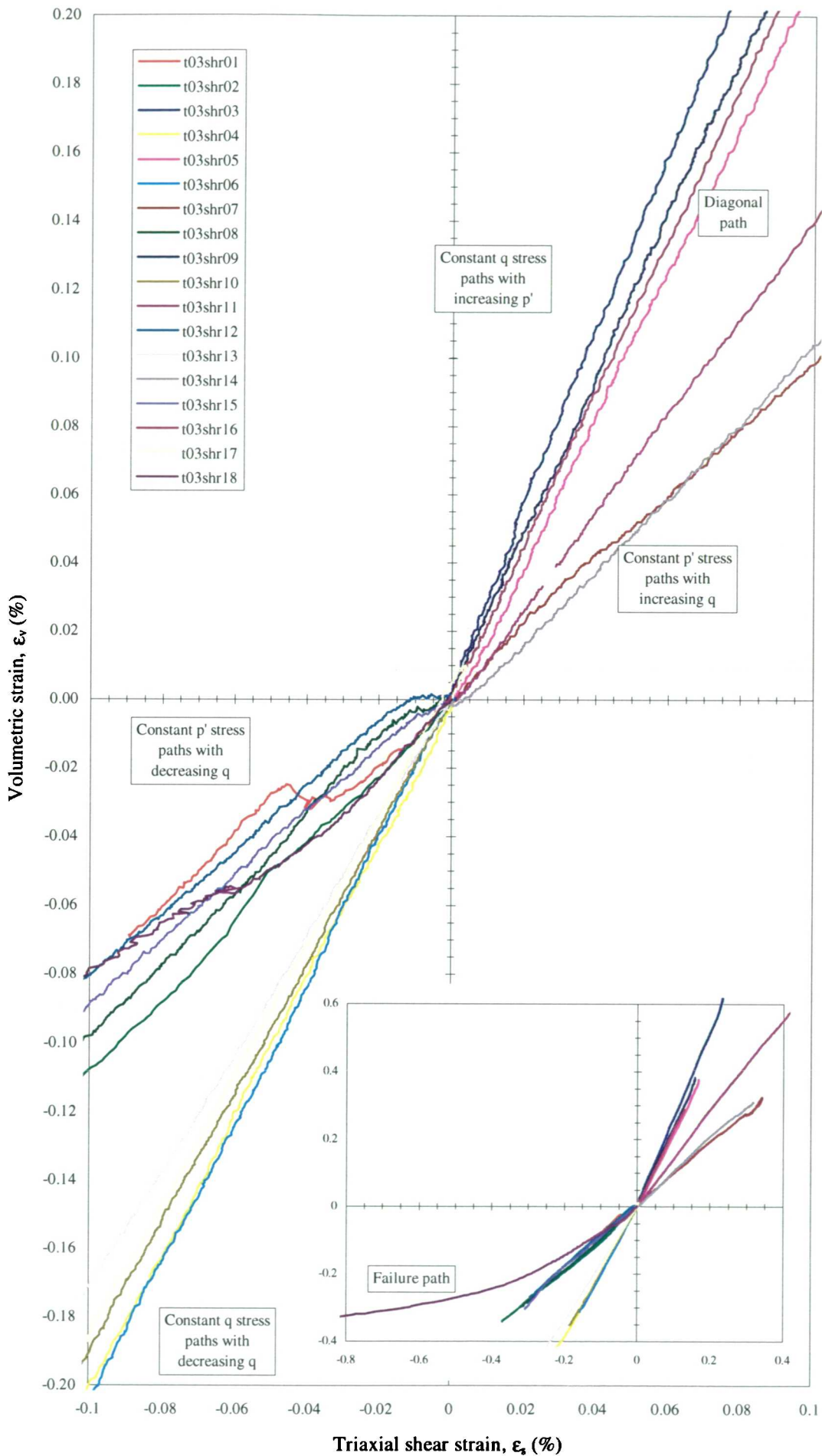


Figure 6.53 - Strain response of test T03 as triaxial shear strain vs. volumetric strain

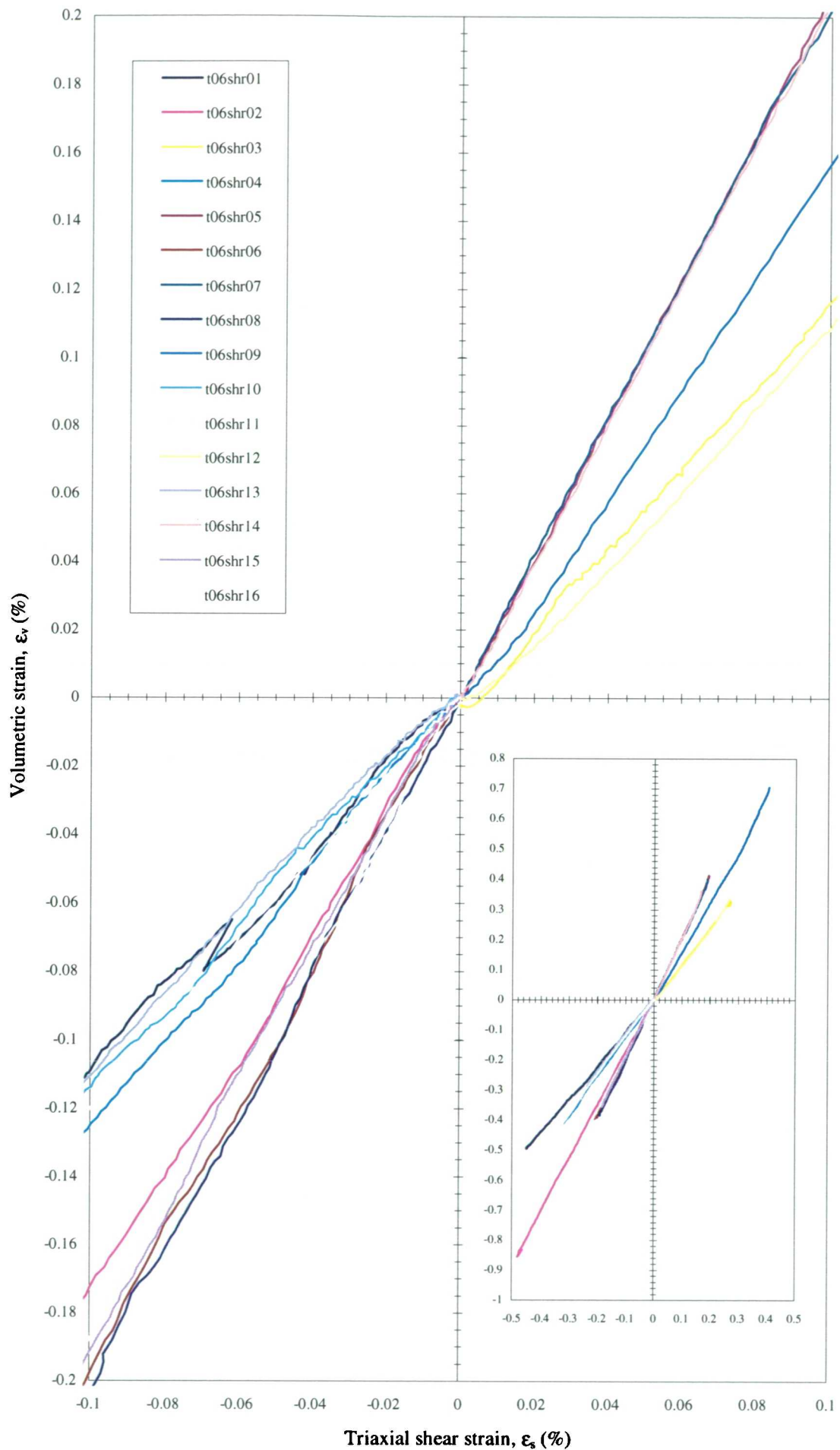


Figure 6.54 - Strain response of test T06 as triaxial shear strain vs. volumetric strain

6.4.10 Strain energy contours

In choosing the length of each stress path two conflicting requirements were considered:

1. The stress path had to be long enough to ensure that each stiffness parameter could be interpreted over the full small strain range and that the non-linearity of the response could be adequately described.
2. The stress path length had to minimise the level of straining and the consequent disturbance to the specimen caused by the multi-stage testing technique.

It was found that a stress path length of 100kPa was sufficient for the constant p' stress paths to describe satisfactorily the specimen's non-linearity. The stress path length for the constant q stress paths was selected to involve the same level of incremental strain energy as for the constant p' stress paths. Contours of equal strain energy are shown for test T03 and test T06 in Figure 6.55 and Figure 6.56 respectively. A similar level of strain energy is incurred for a stress change of 60kPa on a constant q unloading stress path as for a stress change of 100kPa on a constant p' loading stress path.

The degree of anisotropy represented by the strain energy contours may be examined by plotting contours of equal strain energy for a linear cross-anisotropic elastic material (Georgiannou, 1988). The incremental strain energy under triaxial conditions may be derived from equation 2.35 giving,

$$\Delta U = \frac{\Delta\sigma_h}{E_v} [\Delta\sigma_h - 2\nu_{vh}\Delta\sigma_v] + \frac{2\Delta\sigma_v}{E_v} \left[\frac{E_v\Delta\sigma_v}{E_h} (1 - \nu_{hh}) - \Delta\sigma_h \nu_{vh} \right] \dots\dots\dots (6.12)$$

where the subscripts v and h represent the horizontal and vertical directions

Equation 6.12 may be interpreted in terms of the equivalent elastic parameters determined from a triaxial test following Graham and Houlsby (1984) as discussed in later in section 7.4. The parameters E^* , ν^* and α^2 represent the Young's modulus, Poisson's ratio and the degree of anisotropy (the ratio of horizontal to vertical Young's moduli) respectively of a cross-anisotropic elastic body. The strain energy may therefore be represented by equation 6.13.

$$\Delta U = \frac{\Delta\sigma_h}{E^*} \left[\Delta\sigma_h - \frac{2\nu^*\Delta\sigma_v}{\alpha} \right] + \frac{2\Delta\sigma_v}{E^*} \left[\Delta\sigma_v \frac{(1-\nu^*)}{\alpha^2} - \Delta\sigma_h \frac{\nu^*}{\alpha} \right] \dots\dots\dots (6.13)$$

A specific strain energy contour may be plotted by solving equation 6.13 for either the horizontal or vertical stress,

$$\Delta\sigma_v^2 \left[2 \frac{1-\nu^*}{\alpha^2} \right] + \Delta\sigma_v \left[-\frac{4\nu^*\Delta\sigma_h}{\alpha} \right] + [\Delta\sigma_h^2 - \Delta UE^*] = 0 \dots\dots\dots (6.14)$$

$$\Delta\sigma_v = \frac{\frac{4\nu^*\Delta\sigma_h}{\alpha} \pm \sqrt{\left(\frac{4\nu^*\Delta\sigma_h}{\alpha}\right)^2 - 8\frac{1-\nu^*}{\alpha^2}(\Delta\sigma_h^2 - \Delta UE^*)}}{4\frac{1-\nu^*}{\alpha^2}} \dots\dots\dots (6.15)$$

Strain energy contours are plotted in q - p' stress space in Figure 6.57 for which the ratio of horizontal to vertical Young's moduli is increased from 1 (isotropic) to 5 at a constant Poisson's ratio of 0.2. The contours are elliptical and are increasingly elongated and orientated along the deviatoric stress axis as the degree of anisotropy increases. The value of Poisson's

Incremental deviator stress, Δq (kPa)

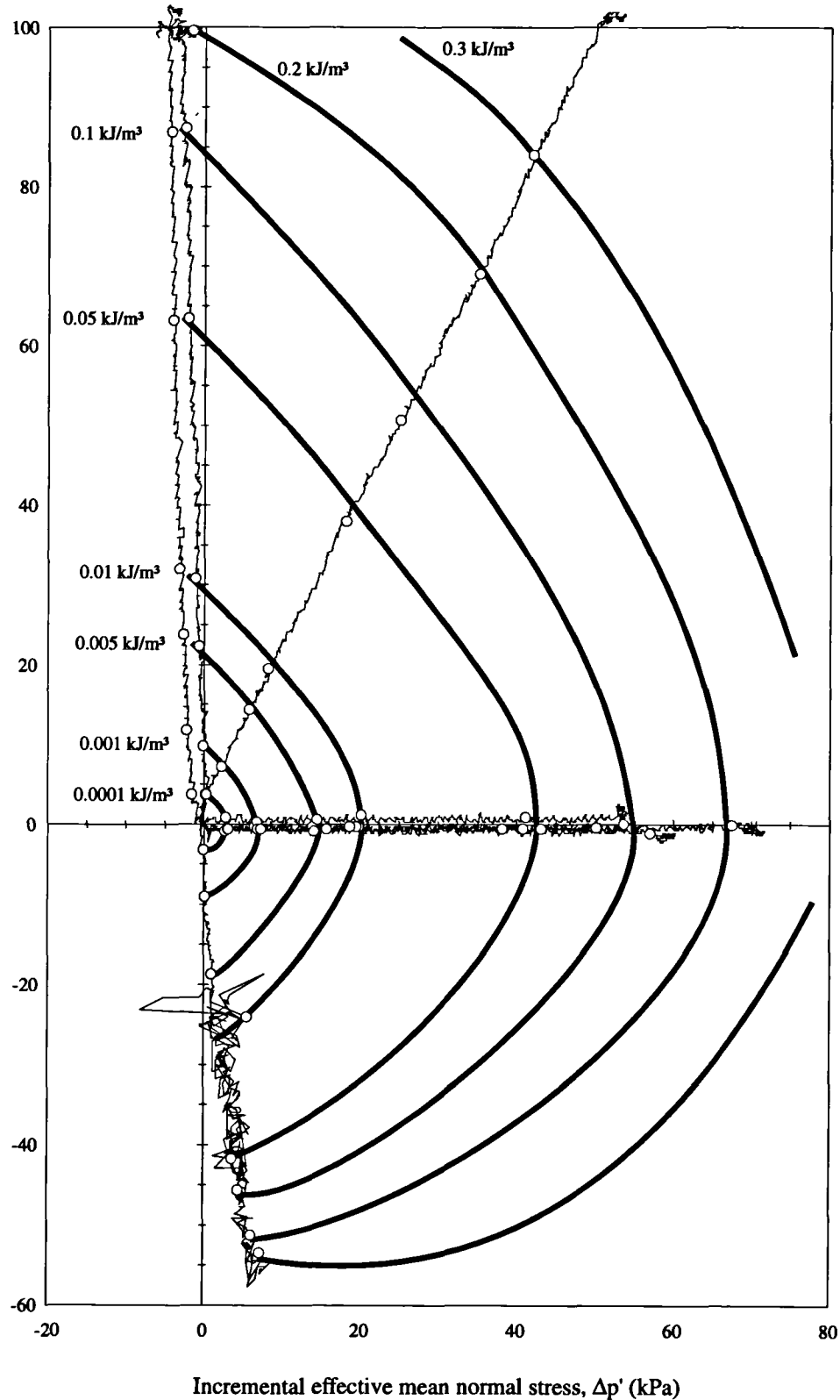


Figure 6.55 - Contours of strain energy around initial stress point in test T03

ratio has relatively less influence on the shape of the strain energy contours compared with the degree of anisotropy (Figure 6.58). The strain energy contours are, however, only symmetrical about both the q and p' axes when Poisson's ratio is zero.

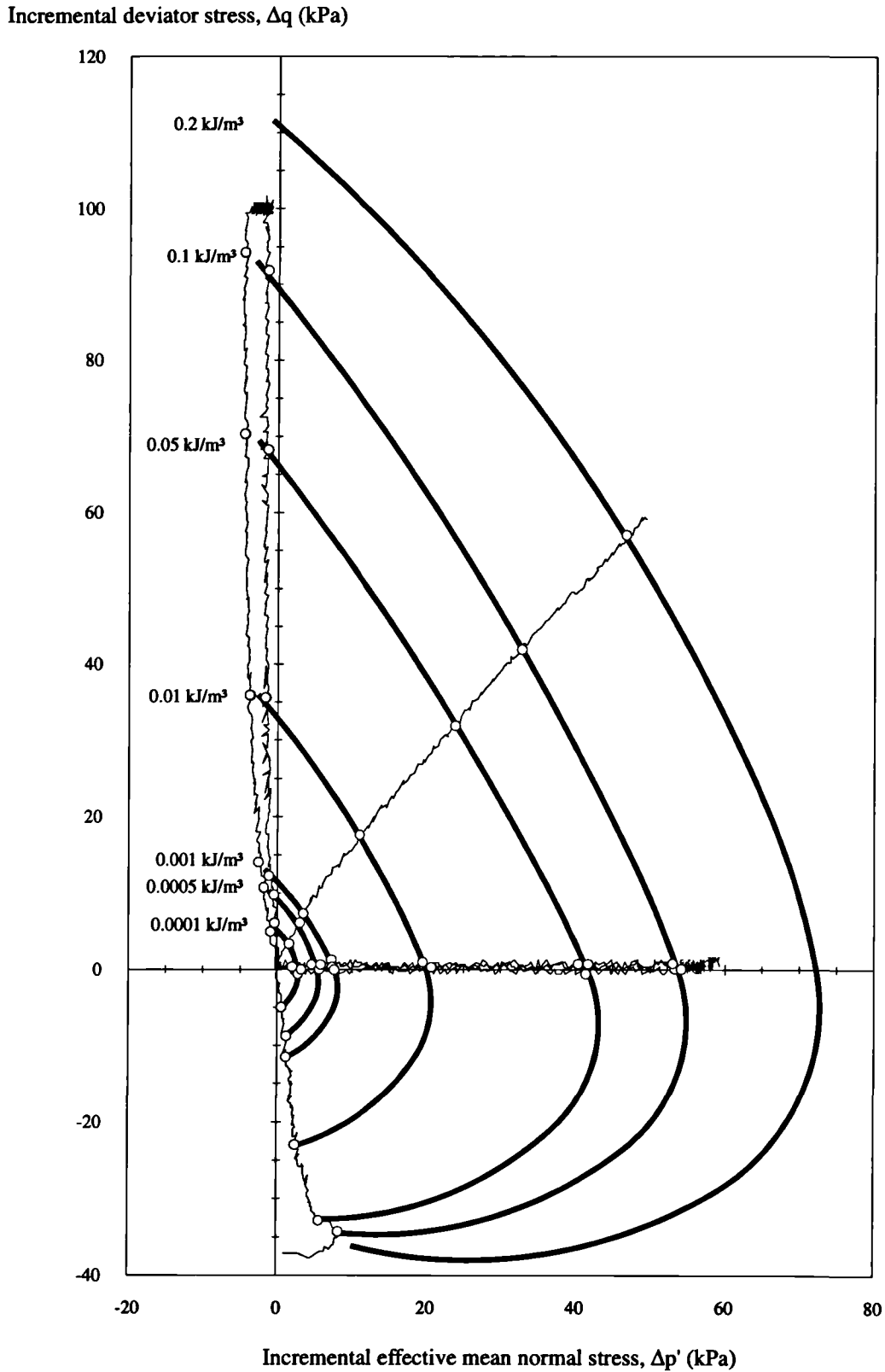


Figure 6.56 - Contours of strain energy around initial stress point in test T06

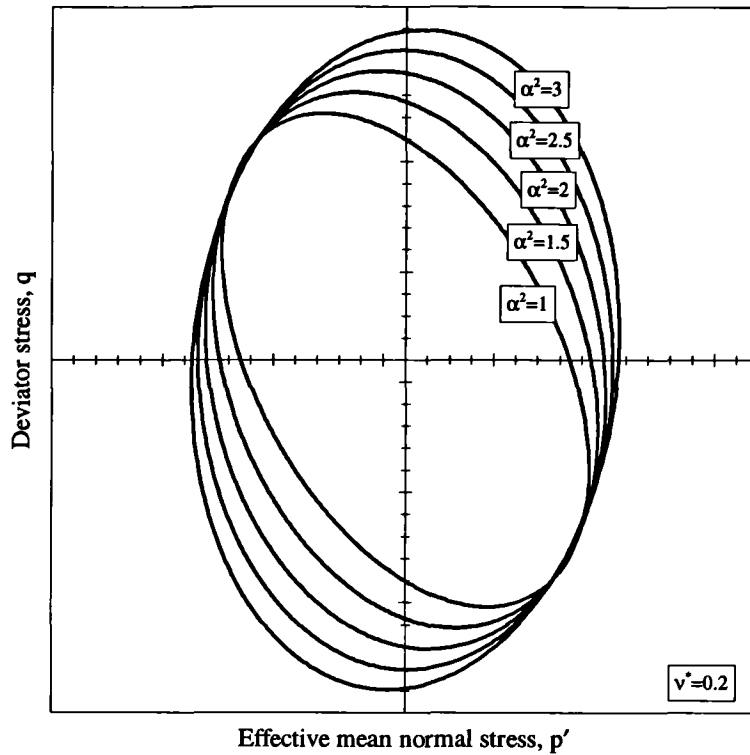


Figure 6.57 - Strain energy contours for a linear cross-anisotropic elastic material showing the influence of the degree of anisotropy for a constant Poisson's ratio

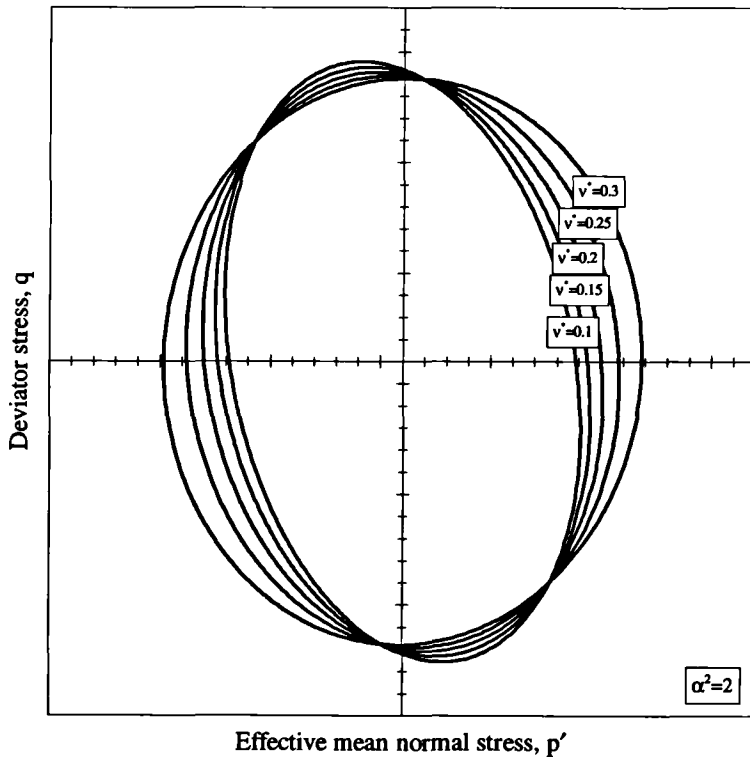


Figure 6.58 - Strain energy contours for a linear cross-anisotropic elastic material showing the influence of Poisson's ratio for a constant degree of anisotropy

The strain energy contours for cross-anisotropic elastic material ($\alpha^2 > 2$) are qualitatively similar to the low strain energy (inner) contours recorded for tests T03 and T06 (Figure 6.55 and Figure 6.56 respectively). At larger strain energies the contours become deformed and are concentrated in the direction of the passive failure surface indicating the softer response in this region as plastic strains develop. For increasing q and p' , however, the elliptical shape is retained. The shape of the contours reveals a highly anisotropic material which, when monotonically loaded from its *in situ* stress state, deforms similarly to an elastic material at small strains, and at larger strains for stress path probes directed away from its passive failure surface.

6.5 Dynamic testing using bender elements

6.5.1 Performance of bender element system

Bender elements were installed in both of the stress path cells and, although they were constructed similarly, the performance of each set was very different. Most significantly there was generally more noise encountered in cell 1 (with consequently less clear traces) but greater electromagnetic interference in cell 2 (causing a coupling between the transmitter and receiver elements).

The Gould 1425 digital oscilloscope, amplifier, and the two function generators (described in section 5.7.2) were used throughout the experimental programme and no problems with them were encountered.

In stress path test T06 it was found that the quality of the traces improved dramatically during the early stress path probing stages of the test, although the test apparatus and procedures remained unchanged. This was probably due to poor initial soil-element contact at the receiver and transmitter elements which improved after consolidation and several stress path cycles.

In stress path test T07, in the second stress path cell, there was a very high degree of electromagnetic coupling between the transmitter and receiver bender elements causing an instant response at the receiver element when the function generator triggered a step wave in the transmitter element. Although the degree of electrical shielding of the system was investigated it was not possible to remove this effect. (see section 6.5.4).

6.5.2 Characterising aspects of the bender element trace

Almost all bender element tests were carried out using a pulsed step wave input. However, three series of tests were carried out using a pulsed sine wave input. Within each test series the frequency of the sine wave pulse was varied in the range 0.5kHz to 50kHz as described in section 5.7.3. It was hoped that, although the form of the bender element response would be different for each input frequency, the waves would have a common starting point which would signify the arrival of the shear wave. A shear wave arrival time could be deduced by visual inspection and this was compared to that derived from the wave spectral and correlation analysis techniques described in section 2.6.5.

A typical bender element test result for cell 1 is shown in Figure 6.59. This figure shows two square wave inputs (with a positive and a negative voltage step respectively) and the corresponding bender element output on which the point of first deflection, and subsequent maxima and minima are labelled. The inset shows undulations in the bender element trace between the main maxima and minima. All points were consistent between bender element tests and therefore not attributed to system noise. Similarly, a typical bender element test result for a square wave input in cell 2 is shown in Figure 6.60. A number of differences are immediately evident:

- the magnitude of the response in cell 2 is larger than in cell 1 for the same amplification
- the voltage trace at the receiver is smoother in cell 2 than in cell 1
- the relative amplitude of the higher frequency (<0.5ms) and the lower frequency (>0.5ms) components is significantly greater in the cell 1 trace than in the cell 2 trace

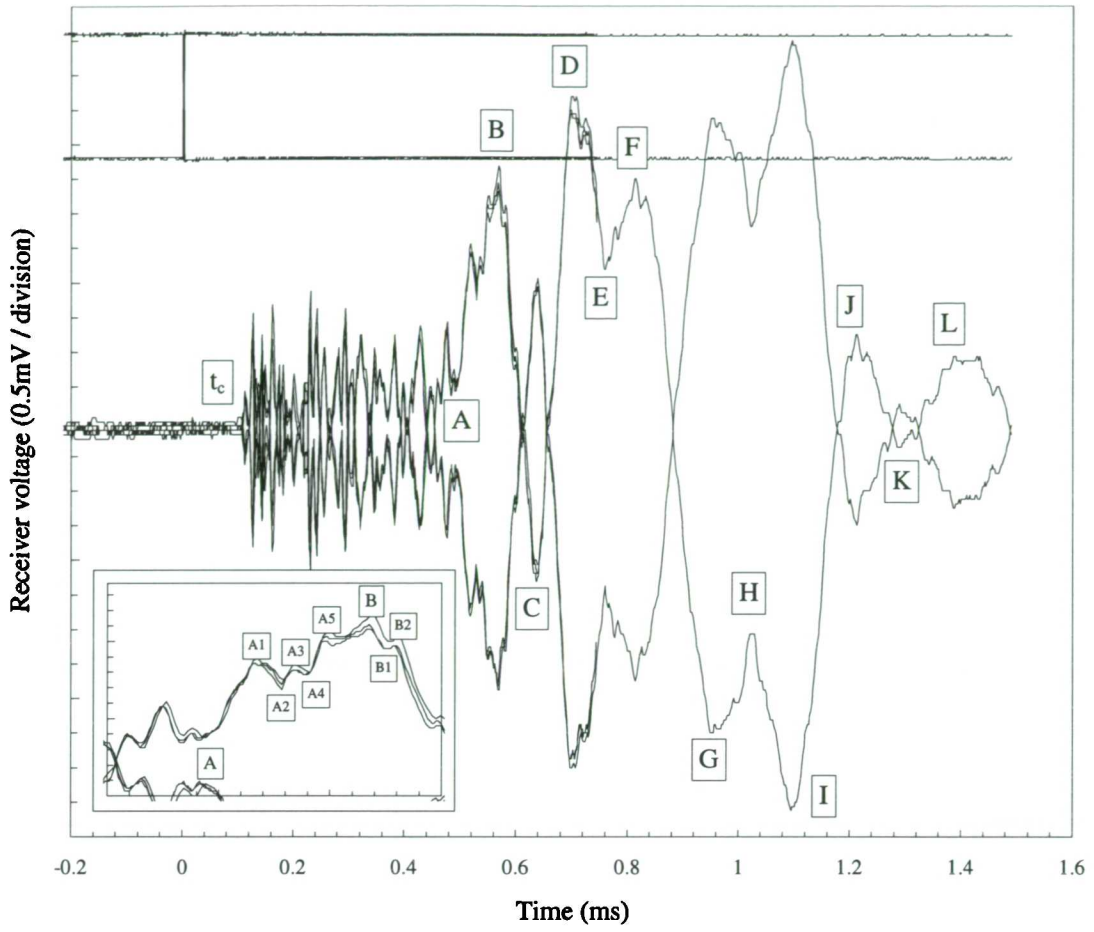


Figure 6.59 - Typical bender element test result for a square wave input using the cell 1 apparatus.

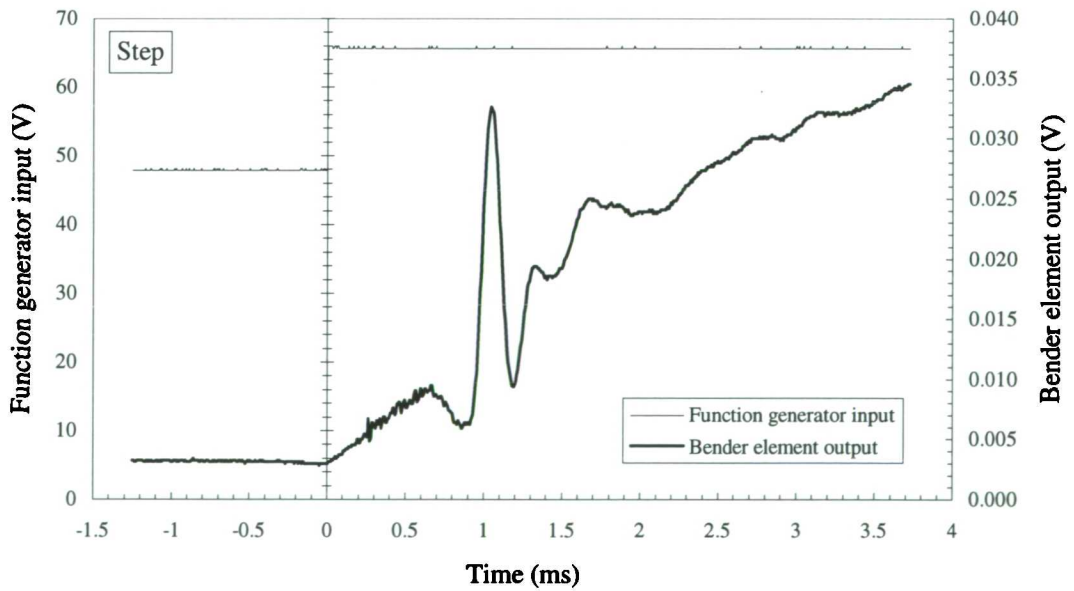


Figure 6.60 - Typical bender element test result for a square wave input using the cell 2 apparatus.

Initially considering the cell 1 bender element response, the first point of interest on the received trace is the point of first deflection, t_c , which corresponds to the arrival of the fastest (primary) component of the waveform. This time of arrival corresponds to the velocity of a compressive wave pulse in water. Although the bender elements are set up to have a shear connection to the soil specimen, the connection is not perfect and allows the travelling wave pulse to contain many separate components, travelling at different frequencies and wavelengths. The bender element construction is such that the dominant transmitted and received components are due to shear waves propagating vertically with a particle movement in the horizontal plane. The compression wave component of the trace travels at a speed approximately equal to the speed of a compression wave in water since the soil is fully saturated and the water phase is generally stiffer than the soil particle phase. The speed of a compression wave in water is equal to the speed of sound in water. Although the exact value varies with temperature and pressure, for the conditions within a stress path cell, it is equal to 1483 m/s (Rice and Walsh, 1956). At the corresponding arrival time, t_c , in Figure 6.59, there is an initial small deflection before the arrival of a larger pulse. This section of the figure has been transformed in Figure 6.61, in which the bender element receiver voltage is plotted against the associated wave velocity. This figure shows that the initial deflection of the received signal corresponds to an impossible wave velocity (greater than 1483 m/s). The reason for this initial deflection is not known but it was a common feature on all the traces from cell 1 and is not attributable to errors in the specimen length, the arrival time measurement accuracy, or in the specimen density measurement.

Receiver bender element output (V)

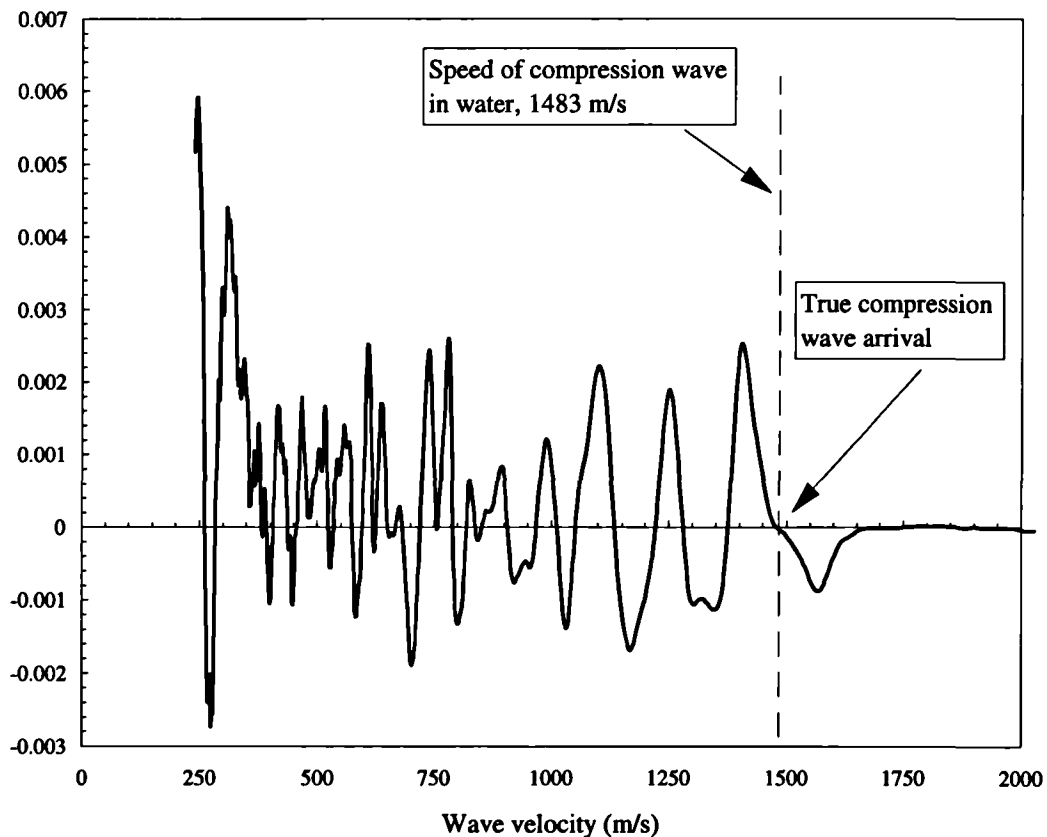


Figure 6.61 - Typical bender element trace receiver output against wave velocity showing wave velocities greater than that of the compression wave arrival

The methodology of the bender element tests (see section 5.7.3) included transmitting waves with an increasing or a decreasing voltage (positive step or negative step). Inspection of Figure 6.59 shows that the two traces produced by opposite polarity input steps are exactly opposite along the entire response. The positive and negative step inputs were intended to separate the shear and compressive components of the bender element trace, since only the shear components were thought to reverse in direction with the driving pulse. In fact, all aspects of the wave form reverse polarity. Sánchez-Salineró *et al.* (1986) showed that the additional wave components due to near-field effects (see below and section 2.6.4) are dependent on the initial shear wave excitation direction. Consequently, the near-field and shear components all reverse when the input function is reversed. However, this does not explain the reversal in the initial high frequency wave components representing the incident water compression wave. This is perhaps due to the physical configuration of the bender element tip. A compression wave, to be detected, must move the tip of the receiving bender element laterally. A perfect compression wave would be incident a 90° to the bender element tip. The increase in water pressure either side of the element would be equal resulting in no net effect on the element. However, if the receiver bender element was slightly out of alignment, a plane compressive wave would be incident on one side of the element before the other causing a net increase in pressure along one edge and the element would deflect. Similarly, a slightly out of alignment transmitter element would, instead of a plane wave, transmit either an initially compressive or initially expansive pressure wave.

The high frequency waves subsequent to time t_c are due to reflections of the initial wave pulse and continue until they are interrupted at point A on Figure 6.59 by the arrival of a lower frequency wave. Viggiani and Atkinson (1995a) argued that, for a square wave input within the geometry defined by the triaxial apparatus, the portion of the wave response from A to B characterises the near-field effect (see section 2.6.4). The bender elements were initially aligned in the triaxial cell such that an increase in voltage at the transmitter would correspond to the same sign of tip displacement for an increase in voltage at the receiver. This would suggest that the point of first reversal, B, at approximately 0.56ms would be taken as the shear wave arrival.

Considering the bender element tests with a square wave input in cell 2, although there is an immediate deflection due to an electrical coupling, the general form of response is similar to that in cell 1. If the effect of the immediate change in slope of the received trace is accounted for, the first point of reversal in the received trace occurs at approximately 0.9ms.

To account for the discrepancy between the responses in the two cells, and to isolate the true arrival of the shear wave, two techniques were employed:

1. the sending of sine wave pulses of differing frequencies and comparison of the output traces with the result of a step wave input. Although the form and frequency of the output will be dependent on the input wave frequency, the arrival of the shear wave should not be affected. It was anticipated that this approach would be extended to include numerous other wave types but this was not possible due to time constraints.
2. performing wave spectral and correlation analyses on the transmitted and received waveforms to locate any similarities in the frequency components, as described in section 2.6.5

The use of a number of different frequency sine waves, in addition to the square wave is illustrated in two series of bender element tests from stress path test T06. These are shown in Figure 6.62 and Figure 6.63 respectively.

When studying these figures to locate the true shear wave arrival, it is required to locate a common point on each curve at which there is a wave deflection. If a particular wave crest translates as the sine wave input frequency varies then it must represent a slower component. When parametrically varying the frequency of sine waves there are a number of limiting factors which must be considered:

- The lower the frequency, the less energy input to the soil and the less chance there is of generating a detectable shear wave arrival.
- The near-field terms are governed by equation 6.16, in which low values of R result in a higher near-field effect (see section 2.6.4). Consequently, a low frequency input will be more likely to propagate the near field component to the receiver than a higher frequency input.

$$R = \frac{d}{\lambda} = \frac{fd}{v_s} \dots\dots\dots (6.16)$$

where , d = specimen length
 λ = wavelength of the shear wave
 f = frequency of the shear wave
 v_s = shear wave velocity

It was seen in section 2.6.4 that, for shear wave propagation in an ideal isotropic elastic three-dimensional medium, the near-field component was separated from the shear wave component for values of R greater than about 4.

- The higher the frequency the shorter the necessary response time of the piezoceramic. There is a limiting frequency at which the bender elements can not react quickly enough to the applied voltage changes. Consequently, no movement of the tip occurs and a shear wave is not produced.
- The higher the frequency, the greater the chance of 'overshooting' (Jovicic *et al.*, 1996). This effect is due to the bender element being physically unable to follow the rate of displacement prescribed by input from the function generator . This may be due to either a poorly built bender element or due to a large discrepancy between the stiffness of the bender element and the soil. The effect may be quantified using the self-monitoring element described by Dyvik and Madshus (1984) although this technique was not employed here. Overshooting tends to result in discontinuities in the bender element input response which are recorded by the receiving element. Also, the bender element displacement may not be planar such that a degree of torque is introduced producing additional wave components.

It should be noted that a square wave is essentially made up of an infinite range of frequencies from very low to very high and is, therefore, affected by both near-field components and overshooting. The initial vertical slope of the square wave input is not followed by the bender element and the rapid rise time may result in overshooting and oscillating about the final tip displacement.

Considering the time range in Figure 6.62 corresponding to the possible shear wave arrival, it is seen that, at frequencies less than 3kHz, the arrivals of the transmitted waves were of very low amplitude and could not be accurately detected. For frequencies greater than 20kHz (the limiting frequency), no response was detected at the receiver element. At 20Hz a repeatable response was detected which was unlike that any other frequency. This showed large amplitude compression wave arrivals, and was possibly due a form of resonance in the bender element. For a range of frequencies between 3 and 10kHz, the received waveform is relatively clear. An initial displacement corresponding to the near-field component of the square wave input at 0.5ms is evident up to a frequency of 8kHz.

The traces in Figure 6.63 similarly represent both stepped wave and sine wave input functions for a separate bender element tests series from stress path test T06. Again, the received traces for the 5kHz and 10kHz sine wave inputs, and the point of first reversal in the received traces for the square wave inputs suggest a shear wave arrival time of approximately 0.56ms.

The square wave and sine wave bender element tests presented for this test might appear to suggest a shear wave arrival of approximately 0.56ms. However, an alternative interpretation may be seen when the bender element readings are viewed at a lower resolution but at a larger time base. The square wave input bender element tests at a larger time base in Figure 6.63 show a large departure in the received trace at approximately 0.83ms. The magnitude of this response is greater than that at the point of first reversal and is in the same direction as the step of the square wave input. Figure 6.64 shows again a selection of the sine wave traces from Figure 6.62 but this time with the corresponding input trace. Plotting the bender element tests in this way clearly shows the passing of the transmitted shear wave at the receiver element for low frequencies and suggests an arrival time of 0.83ms (the same as for the square wave input in Figure 6.63). At 2kHz the shear wave is still clear although the additional wave component at 0.5ms is apparent. As the frequency increases, the magnitude of this additional component increases until, at 4kHz, it is greater than the shear component recorded for an input frequency of 1kHz.

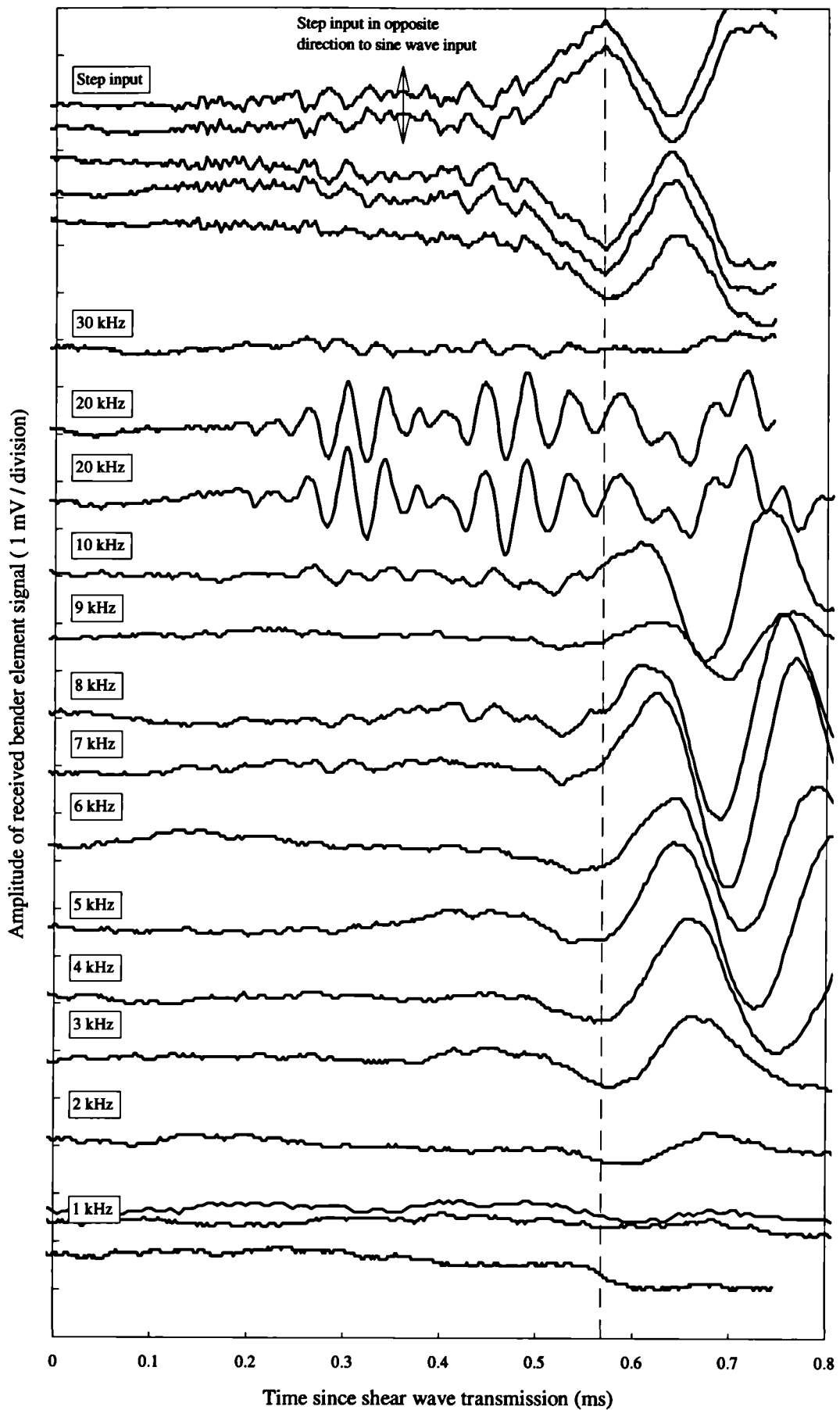


Figure 6.62 - Bender element output from sine wave and square wave input during test T06 (stage 10, $q = -98\text{kPa}$, $p' = 275\text{kPa}$) showing initial deflections at receiver

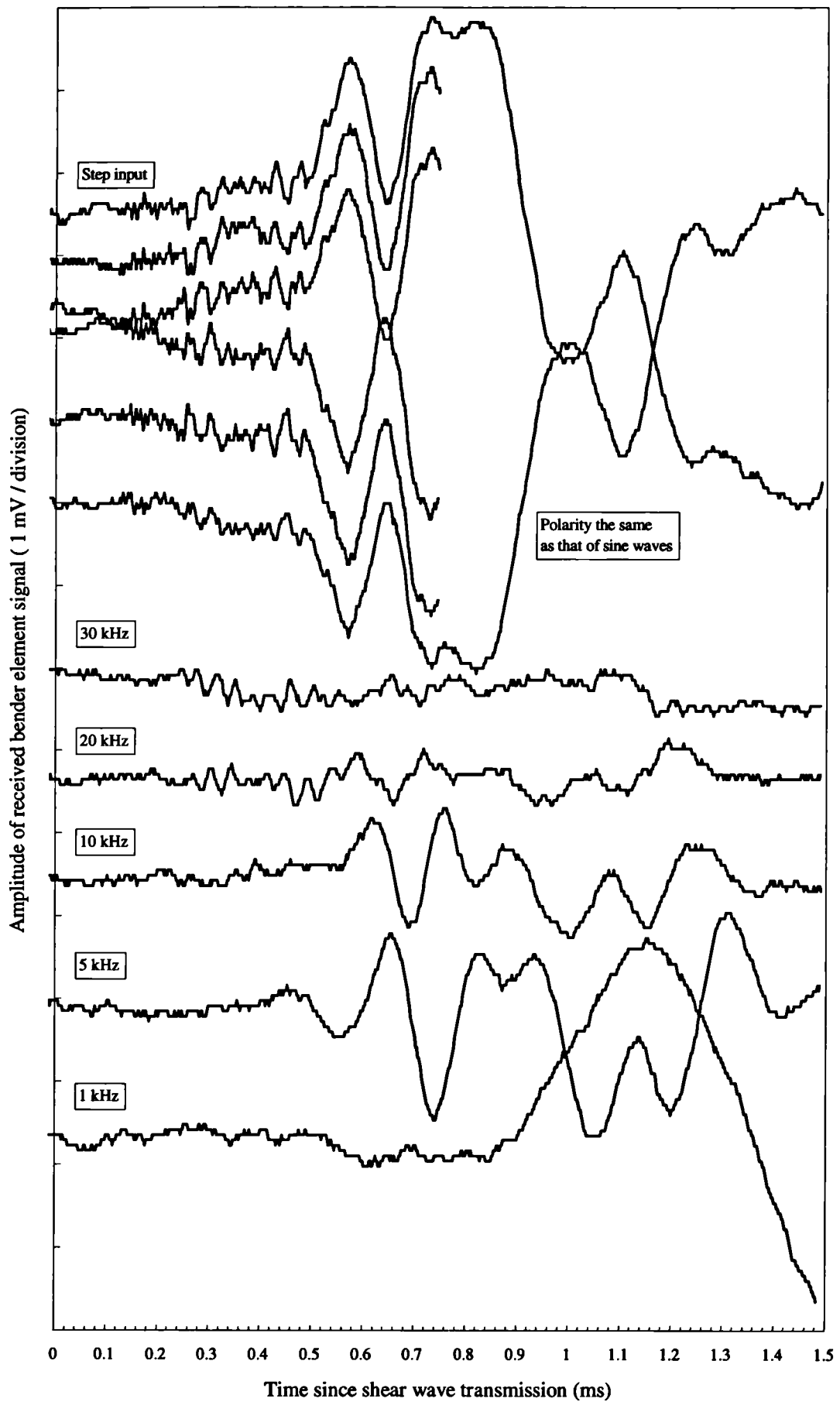
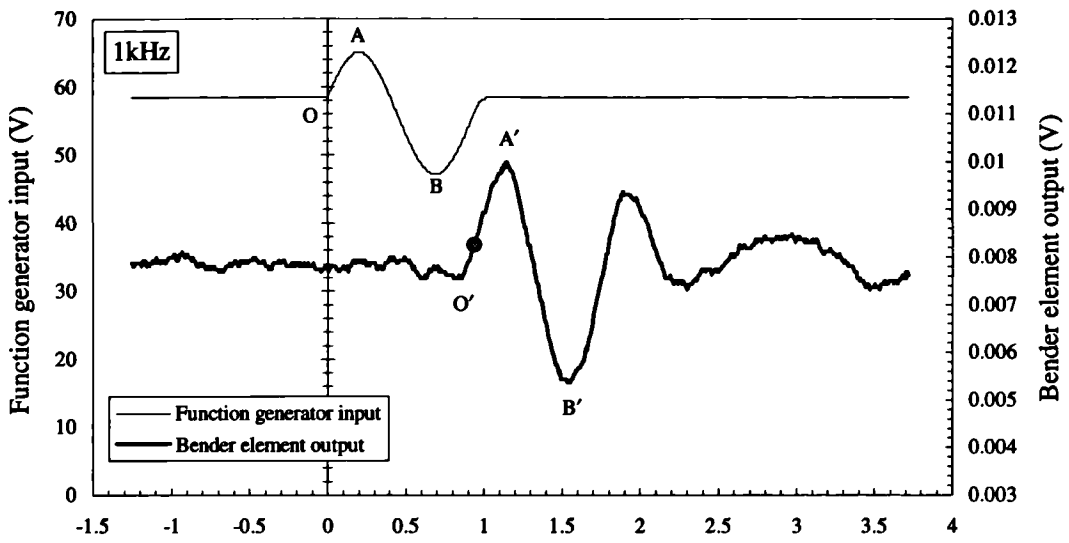
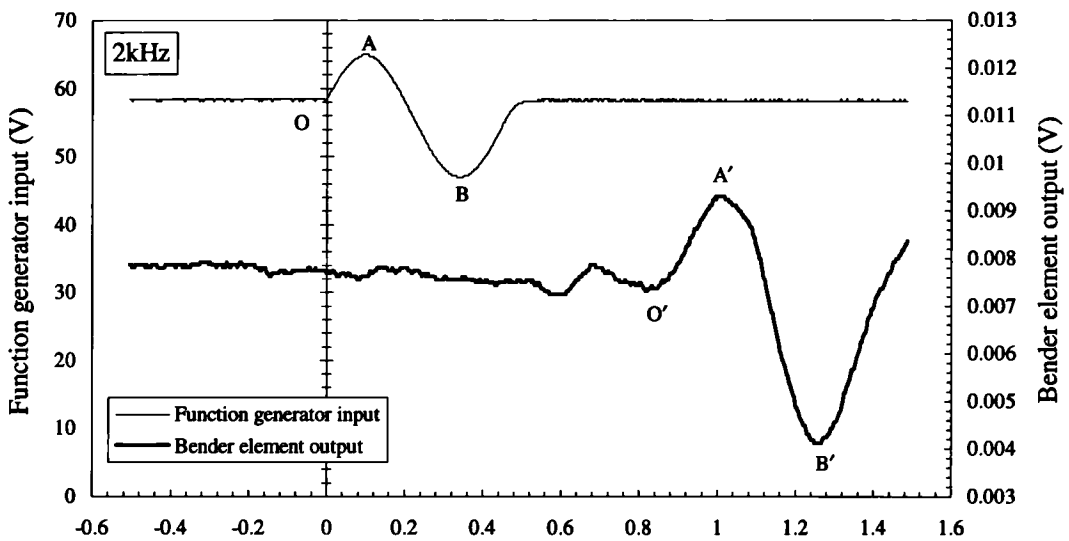


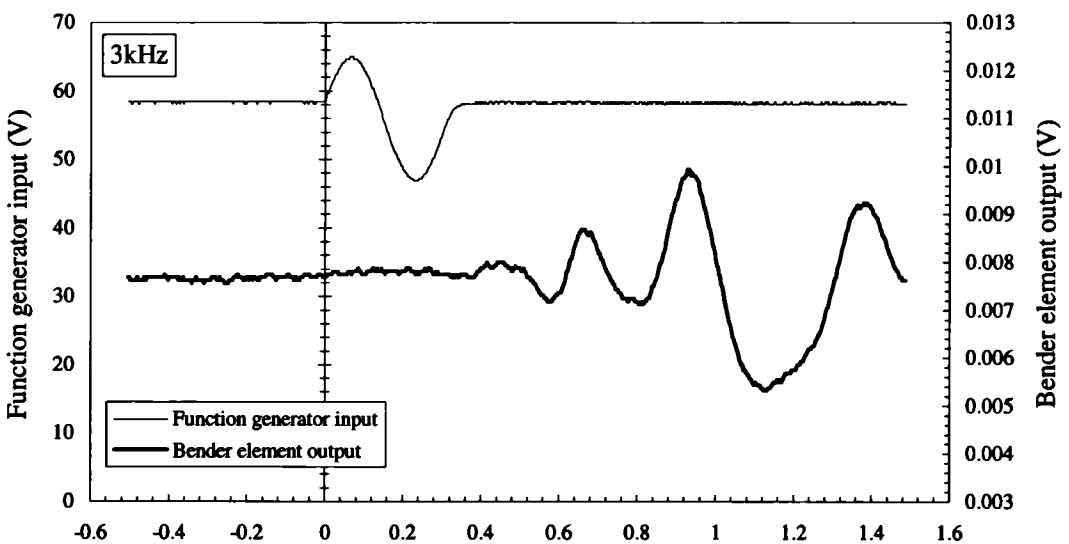
Figure 6.63 - Bender element output from sine wave and square wave input during test T06 (stage 10, $q = -132\text{kPa}$, $p' = 275\text{kPa}$) showing largest deflections at receiver



(a)

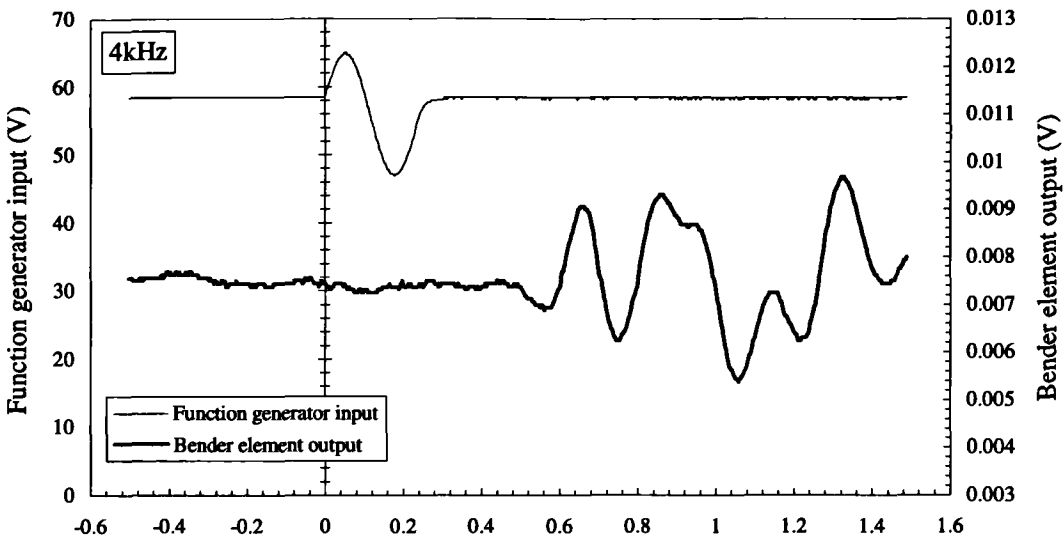


(b)

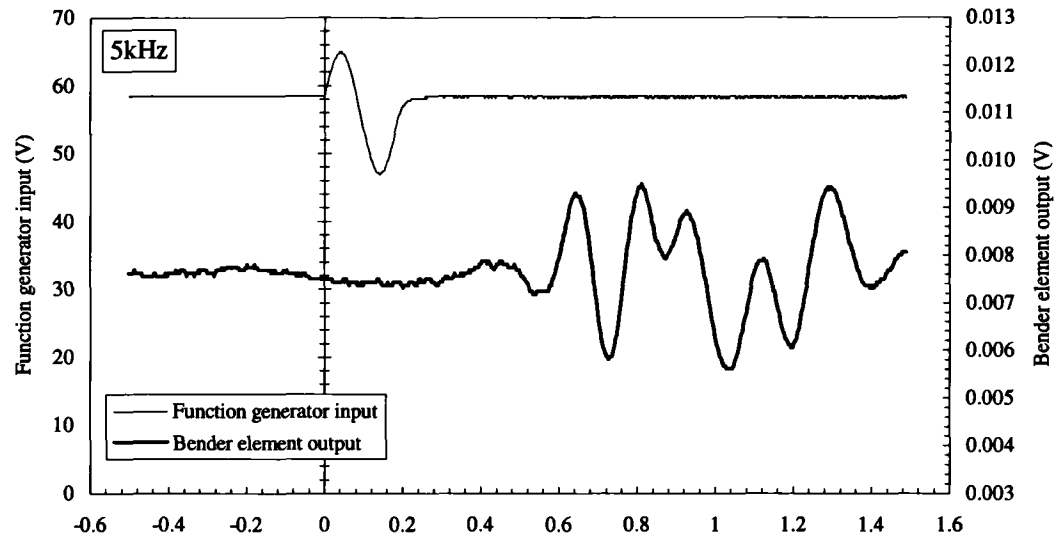


(c)

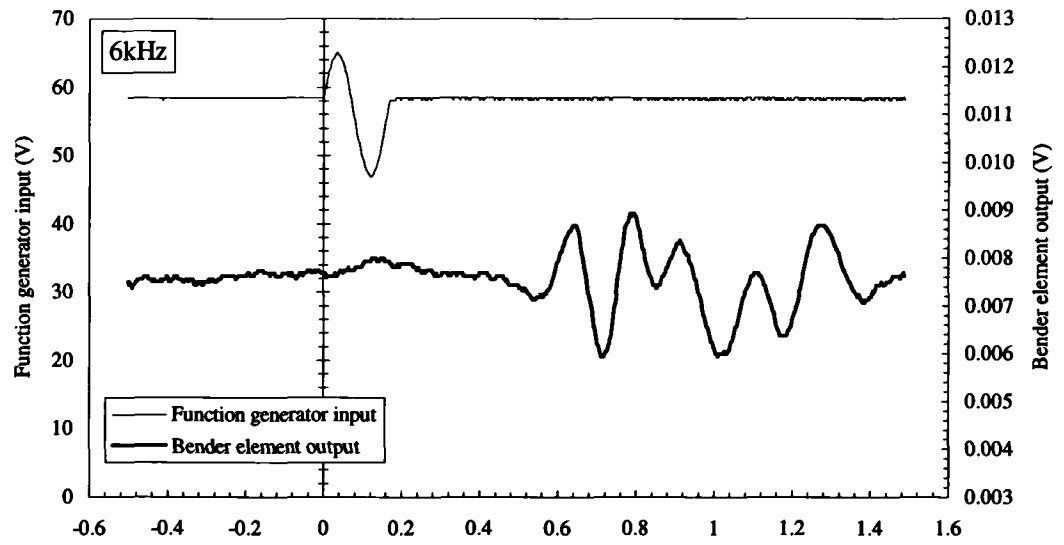
continued...



(d)



(e)



(f)

Figure 6.64 - Bender element output from sine wave input for Figure 6.62 results

The set of traces shown in Figure 6.65 and Figure 6.66 were obtained during stress path test T07 in cell 2. The bender element tests shown in Figure 6.65 all correspond to sine wave inputs, and in Figure 6.66, the stepped wave input response of Figure 6.60 has been superposed. The effect of the electromagnetic coupling of the input and output traces in cell 2 was much less for the sine wave inputs than for the square wave inputs. The effect was slightly more noticeable at lower input frequencies for the sine wave responses, although much less than for the stepped wave input response. Despite these problems, the passing of the shear wave is clearly detected. On Figure 6.65, the sections of the trace which vary with frequency (and as such not the initial shear wave arrival) are easily identifiable and on Figure 6.66 this may be allied with the square wave input which suggest an arrival of 0.92-0.94ms at the first reversal of the shear wave.

A selection of the sine wave bender element tests shown in Figure 6.65 are represented in Figure 6.67. In this case, as the frequency increases an additional wave component is not recorded as was the case in the cell 1 tests shown in Figure 6.64. At lower frequencies the near field effect is more noticeable than at higher frequencies as expected. For an input frequency of 0.75kHz, the output trace is barely distinguishable, although for 1kHz the response is well defined. For input frequencies less than 5kHz the near-field effect coincides with and obscures the shear wave arrival. An input frequency of 5kHz, however, is high enough to eliminate near-field effects and low enough to allow the transmitter element to respond without overshooting.

The wave components arriving at approximately 0.5ms in the cell 1 bender element tests shown here are clearly exhibiting an effect not evident in the cell 2 tests. There are a number of possible explanations for these differences:

- In cell 1 of the high frequency components associated with compression waves are more significant. This indicates a misalignment of the bender elements and shows that the bender elements in cell 1 are capable of receiving wave components other than pure shear. As described in section 2.6.4, in a two-phase medium there is potential for two forms of compression wave. It is possible that some of the wave components detected in the current tests are secondary compression waves. The secondary components of the recorded waves are of similar magnitude to the shear wave component and greater than the primary compression component. This may be due to the frequency of the primary compression component being very high resulting in the bender element being unable to accurately describe the response. The true magnitude of the primary compressive component may therefore be greater than that recorded. The secondary compression wave would be expected to be both frequency dependent and out-of-phase with the shear wave. This was the case in the current tests.
- The overshooting effect may be more severe for the cell 1 bender elements than for the cell 2 bender elements and, even for relatively low frequencies, the bender elements may not be capable of smoothly following the function generator input function. This would result in the transmission of unpredictable additional wave components through the soil specimen.
- The additional wave component may be part of the near-field effect, but the dimensions of each bender element and the test specimen in both cases were approximately the same and consequently a similar near-field component would be expected. Also, none of the examples of near-field components presented in Chapter 2 show a similar response to that seen here.

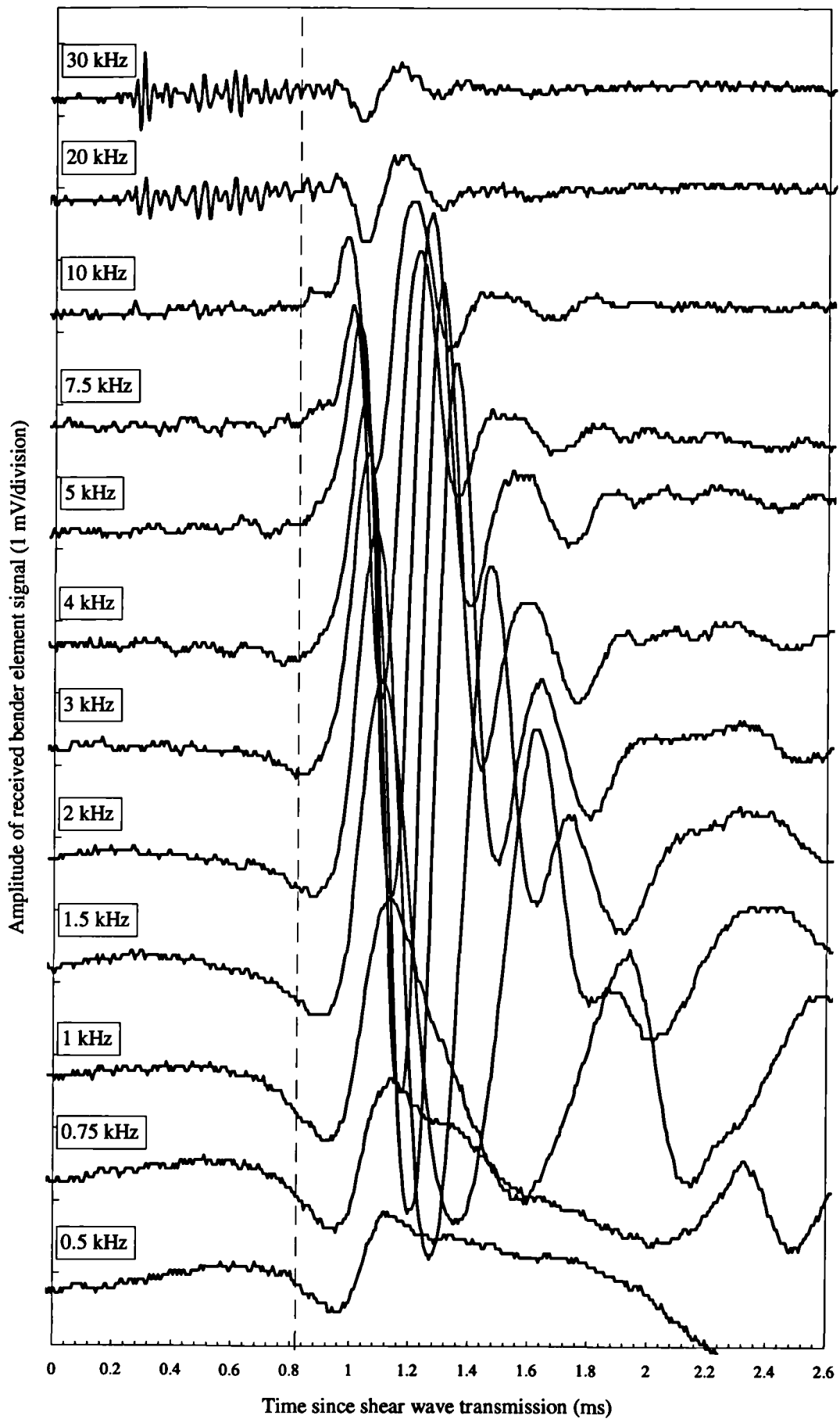


Figure 6.65 - Bender element response to varying frequency sine wave input for a bender element test series in stress path test T07 ($p' = 276\text{kPa}$)

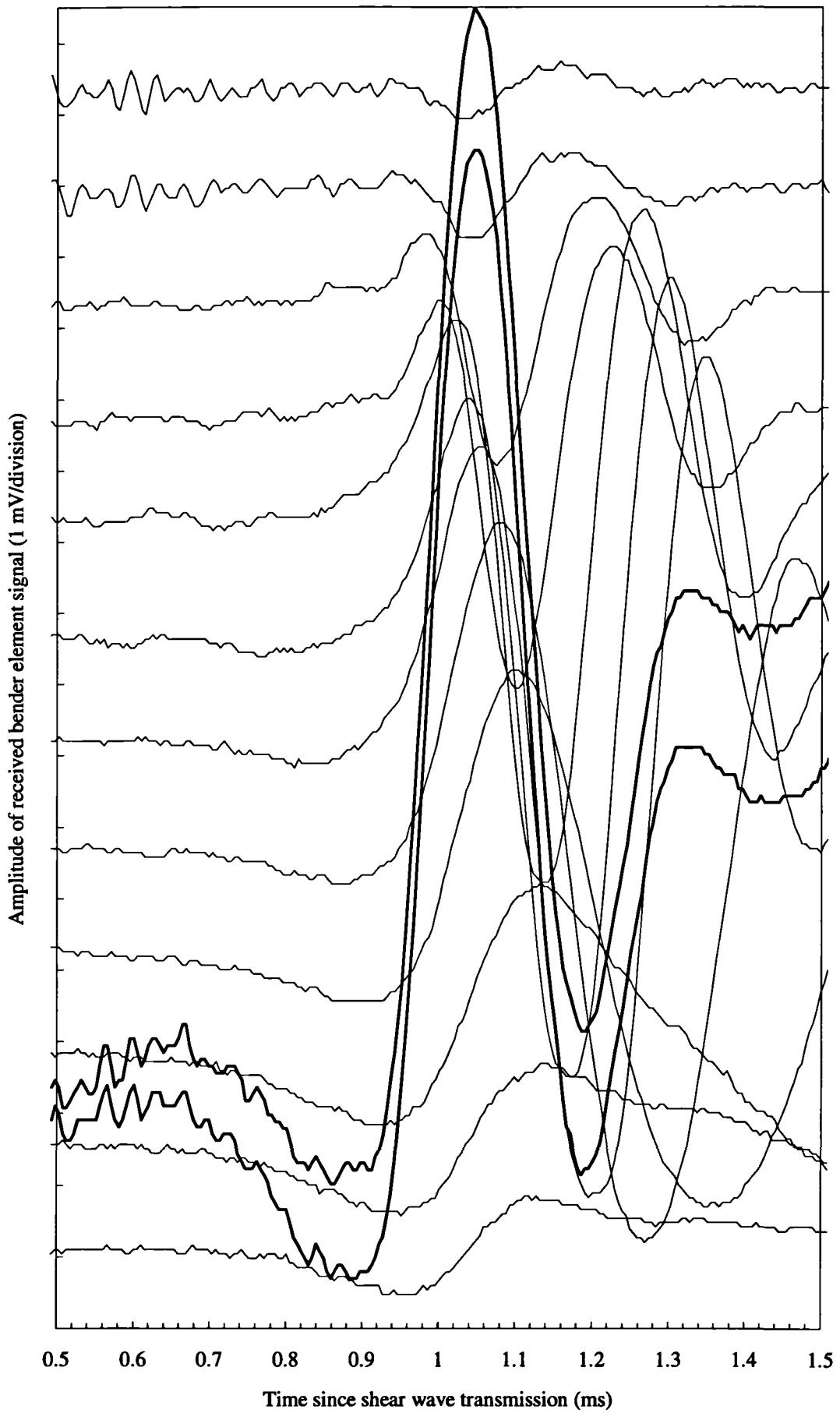
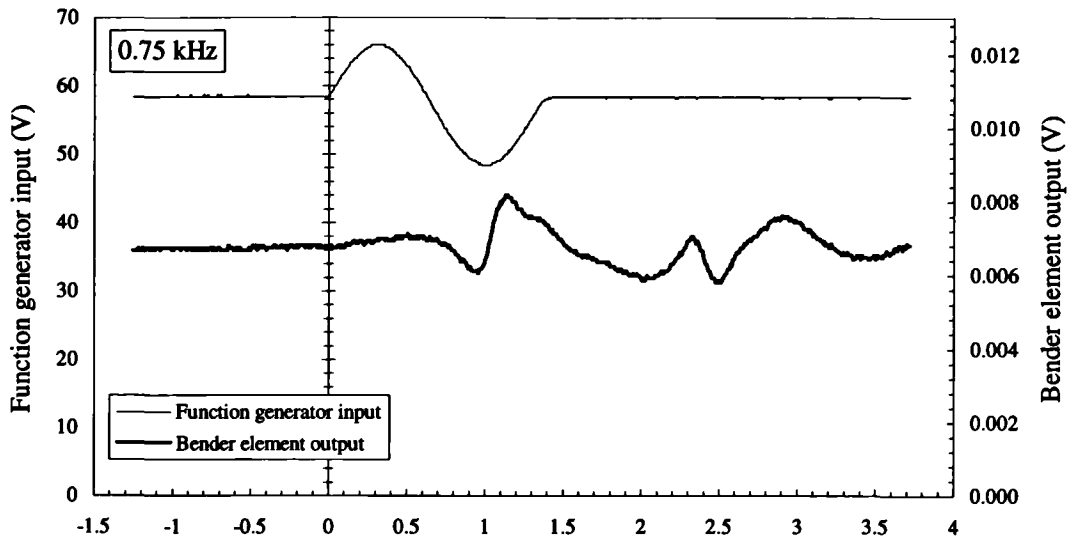
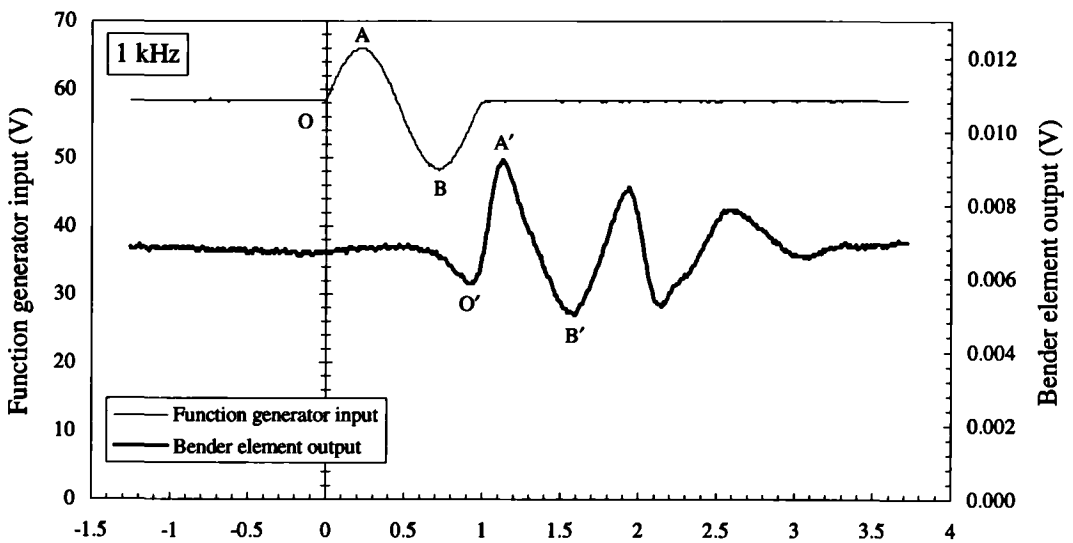


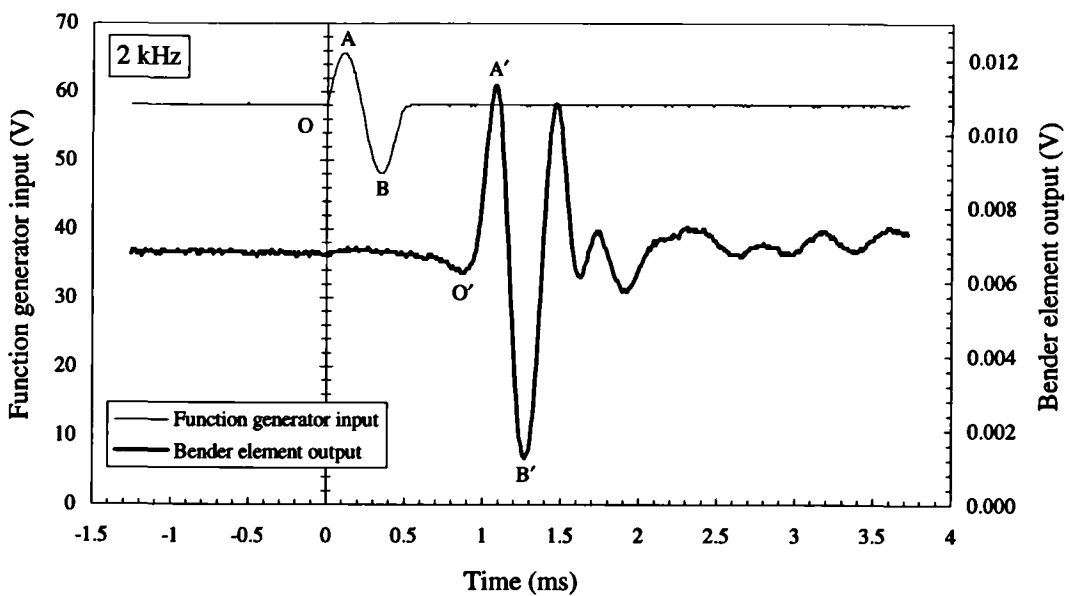
Figure 6.66 - Comparison of square wave and variable frequency sine wave input for a bender element test series in stress path test T07 ($p' = 276\text{kPa}$)



(a)

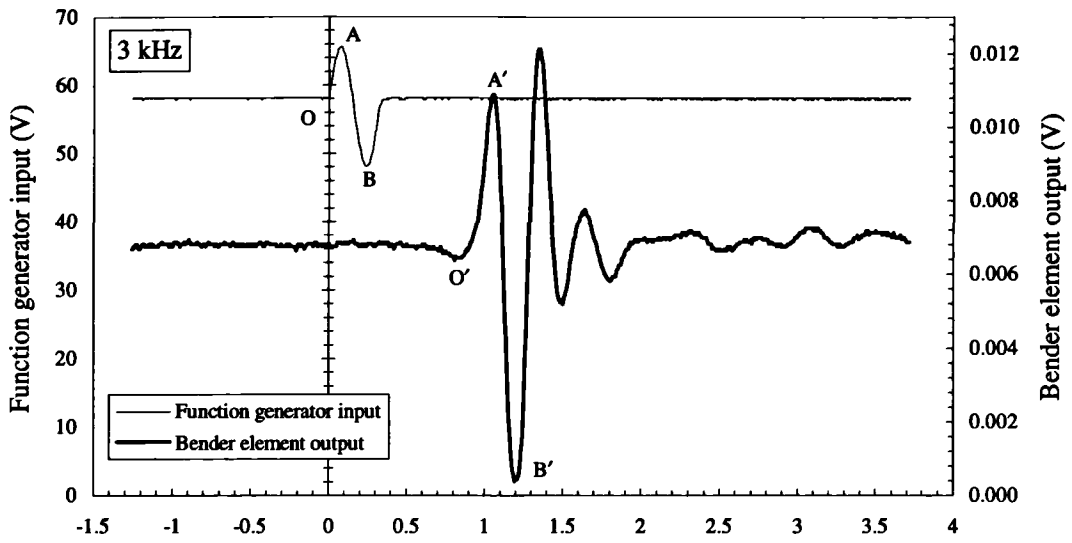


(b)

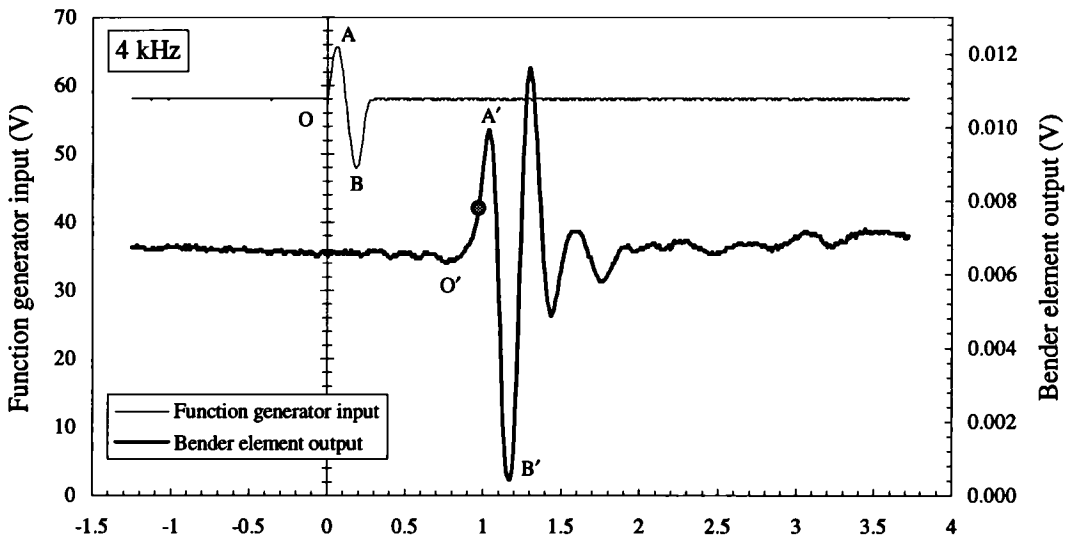


(c)

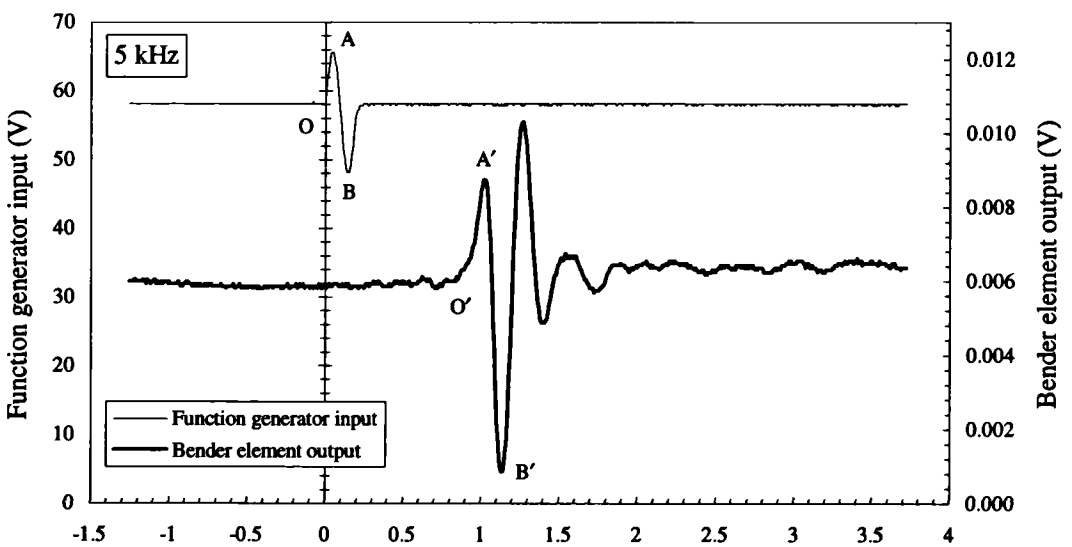
continued...



(d)



(e)



(f)

Figure 6.67 - Bender element output from sine wave input for Figure 6.65 results

6.5.3 Correlation analyses

The identification of wave arrival times in section 6.5.2 may be compared with the arrivals indicated by comparisons of the spectral analysis functions of the transmitted and received bender element signals. Correlation and spectral methods are used extensively in waveform analysis (see section 2.6.5) and were applied to bender element traces by Viggiani (1992). Although numerous techniques are available to analyse wave forms, the most physically understandable are the correlation theorems. Consider two waveforms such as the typical transmitted and received bender element traces:

$$\left. \begin{array}{l} g(t) = \text{Transmitted waveform} \\ h(t) = \text{Received waveform} \end{array} \right\} \text{voltage amplitude vs. time} \dots\dots\dots (6.17)$$

The *correlation* of these functions, denoted by $Corr(g, h)$, is defined by equation 6.18,

$$Corr(g, h) = \int_{-\infty}^{+\infty} g(t + \tau)h(t) dt \dots\dots\dots (6.18)$$

The correlation is a function of τ , which is called the *lag*. The maximum absolute value of this function specifies the time shift that would have to be imposed on the first trace to give the 'best fit' if it was superimposed on the output trace.

Although solutions do exist for equation 6.18 with waveforms expressed as amplitude vs. time, it is more usual to use equivalent functions in the frequency domain. For numerical manipulation the functions may be represented as Fourier series in which the waveform is represented by an infinite series of increasingly insignificant trigonometrical functions as shown in Figure 6.68.

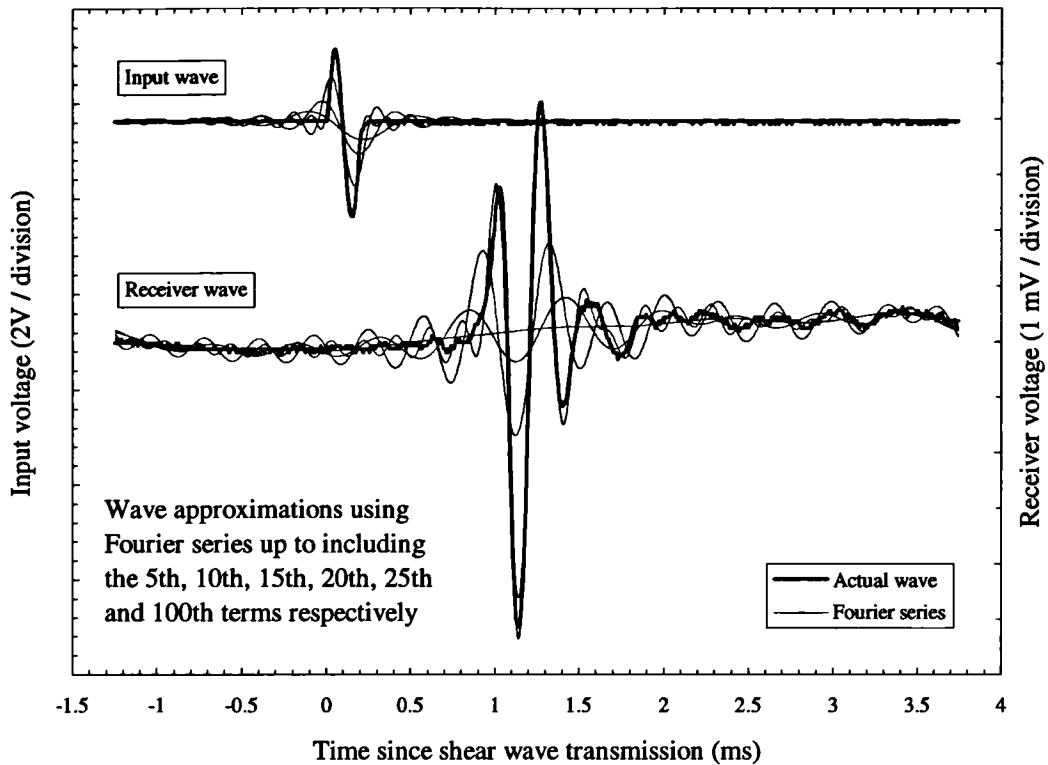


Figure 6.68 - Using Fourier series to approximate typical input and receiver bender element voltage time responses

A convenient algorithm for calculating the Fourier series functions is found through using the fast Fourier transform (FFT) to return the equivalent waveforms represented in the frequency domain such that in equation 6.19,

$$\left. \begin{aligned} G(f) &= FFT[g(t)] \\ H(f) &= FFT[h(t)] \end{aligned} \right\} \text{amplitude vs. frequency} \dots\dots\dots (6.19)$$

The Fourier transform of the cross-correlation function may be calculated by multiplying the Fourier transform of one waveform by the complex conjugate of the Fourier transform of the other as in equation 6.20.

$$Corr(g,h) = G(f).H^*(f) \dots\dots\dots (6.20)$$

The cross-correlation function is generally a series of real numbers which may be plotted against the imposed time shift. The maximum absolute value of this function is taken to represent the arrival of the transmitted wave at the receiver.

This analysis has been implemented as a module in a computer program to automate the process of analysis once a bender element test has been carried out. Correlation functions for the results shown in Figure 6.62 for sine wave inputs are plotted in Figure 6.69 (the analysis may not be used for square wave input tests since the shape of the input and output bear no relation). For frequencies up to 6kHz, the maximum of the cross-correlation function is in the range 0.88-0.9ms, and this matches the arrival of the later wave component (thought to be the shear wave). For higher frequencies the results are ambiguous. The presence of the additional wave components complicates the interpretation and high correlations are shown for 0.58-

0.60ms and 0.62-0.64ms (out-of-phase). The results of Figure 6.70 based on Figure 6.63 are less clear and the 1, 5, 10 and 20kHz input waveforms each show the maximum absolute correlation in different places none of which coincide with the stepped wave output peaks and troughs. These traces may be of too poor quality to effectively make the correlation function physically reasonable. A clearer picture emerges from the spectral analysis in Figure 6.71 which is based on the results of Figure 6.66. In this case the maximum correlations are all seen at approximately 0.90-1.0ms. This coincides well with both sine wave and stepped wave input responses.

In spectral analysis errors may be incurred due to the change in frequency ('spreading') of the driving pulse as it travels through the specimen (Brignolo and Gotti, 1992). Figure 6.72(a) shows an example of an input sine wave and an artificially generated output pulse and (b) shows the correlation functions for a series of such waves. The artificial output in each case is equal in amplitude and waveform to the input, although at decreased frequency. The imposed time lag is known and may be compared to the correlation of attenuated output. As the relative drop in frequency increases so the error in the correlation increases suggesting a probable error in the arrival time for these idealised functions of 0.02 to 0.1ms. This is a similar variation to that of Figure 6.71 and is probably indicative of the accuracy of this application of spectral analysis.

Further correlation analyses may be carried out manually using corresponding points on both the input and output curves for the sine wave inputs shown in Figure 6.67 and Figure 6.65. The interval times between points O, A and B on the input trace and the corresponding points O', A' and B' on the received trace have been calculated where possible and are shown in Table 6.14 and Table 6.15 respectively. For the cell 2 traces, point O' is located at the point of first reversal and is consequently affected by the near-field components in those tests with lower input frequencies. For the cell 1 traces, point O' may only be identified on the lower frequency traces.

The potential for identifying the shear wave velocity from interval times or from spectral analyses depends on the degree of similarity between the transmitted and received waveforms. The average frequency of the received waveform (calculated using the time interval A'-B') is shown in Table 6.14 and Table 6.15. For input frequencies up to 5kHz the received frequency is of a similar magnitude. However, for higher frequencies the output is considerably different from the input and, consequently, the waveform correlation and spectral analysis methods of interpretation suffer. The predicted O' value has been calculated as half the time interval A'-B' before point A' and therefore represents the arrival time associated with the average wavelength of the received waveform.

The spreading and alteration of the waveform as it travels through the specimen, and the difference between the function generator signal and the actual transmitted waveform lead to the differences between, the predicted O' time and the measured point of first arrival, O'. The predicted O' times are generally greater than the measured point O' times and thus occur significantly within the rise of the passing shear wave, as shown by the shaded circle in Figure 6.67(a) and Figure 6.67(e) for example.

| f_{in} (Hz) | f_{out} (Hz) | O' (ms) | predicted O' (ms) | A-A' (ms) | B-B' (ms) |
|------------------|-------------------|------------|-------------------------|--------------|--------------|
| 1 | 1.23 | 0.85 | 0.94 | 0.95 | 0.86 |
| 2 | 2.000 | 0.84 | 0.88 | 0.91 | 0.91 |
| 3 | 2.59 | 0.81 | 0.83 | 0.86 | 0.89 |

**Table 6.14 - Analysis of sine wave input bender element test
for stress path test T06 in cell 1**

| f_{in} (Hz) | f_{out} (Hz) | O' (ms) | predicted O' (ms) | A-A' (ms) | B-B' (ms) |
|------------------|-------------------|------------|-------------------------|--------------|--------------|
| 0.5 | - | 0.96 | - | - | - |
| 0.75 | - | 0.94 | - | - | - |
| 1 | 1.16 | 0.92 | 0.91 | 0.91 | 0.84 |
| 1.5 | 2.00 | 0.90 | 0.97 | 0.95 | 0.88 |
| 2 | 2.70 | 0.87 | 0.99 | 0.98 | 0.92 |
| 3 | 3.30 | 0.84 | 0.97 | 0.98 | 0.96 |
| 4 | 3.94 | 0.84 | 0.97 | 0.97 | 0.98 |
| 5 | 4.45 | 0.83 | 0.96 | 0.98 | 0.99 |
| 7.5 | 4.66 | 0.83 | 0.94 | 0.97 | 1.00 |
| 10 | 4.66 | 0.83 | 0.91 | - | - |
| 20 | 4.66 | - | 0.88 | - | - |
| 30 | 4.88 | - | 0.88 | - | - |
| Step | 3.41 | 0.87-0.91 | 0.97 | - | - |
| Step | 3.53 | 0.87-0.91 | 0.97 | - | - |

**Table 6.15 - Analysis of sine wave input bender element test
for stress path test T07 in cell 2**

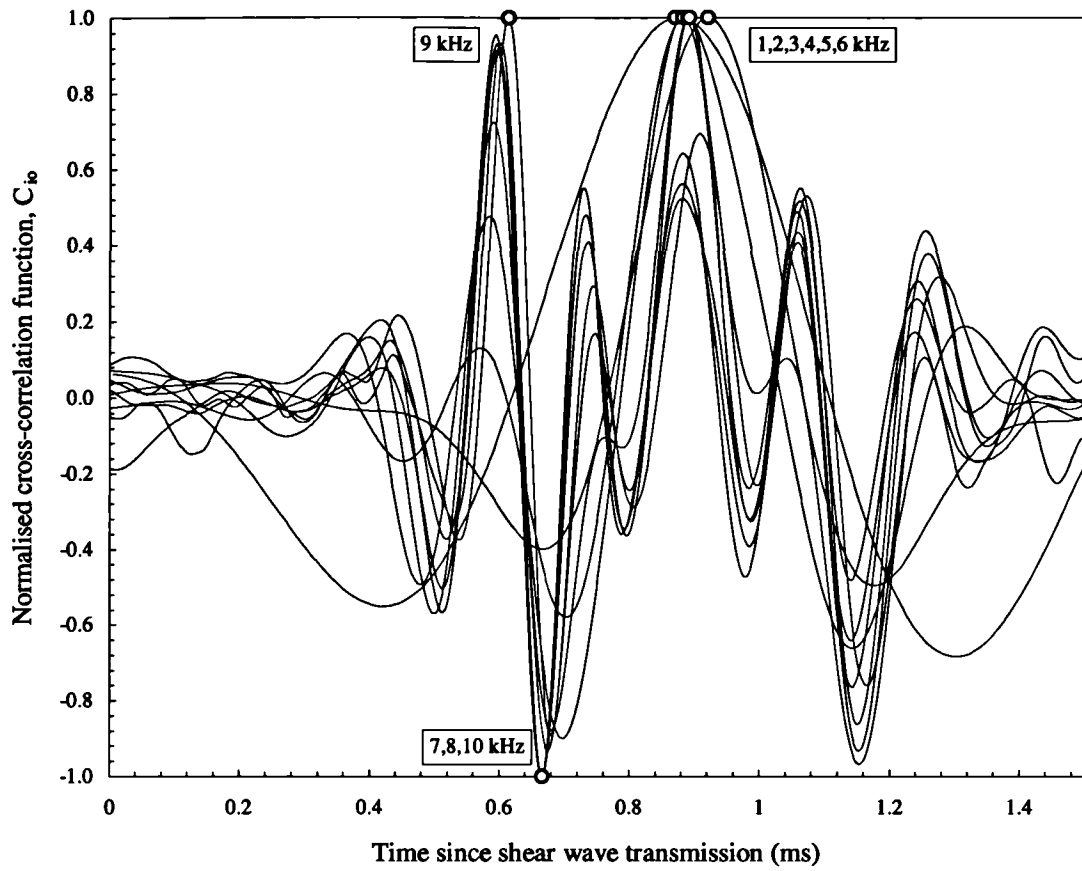


Figure 6.69 - Cross-correlation coefficient for bender element traces in Figure 6.62

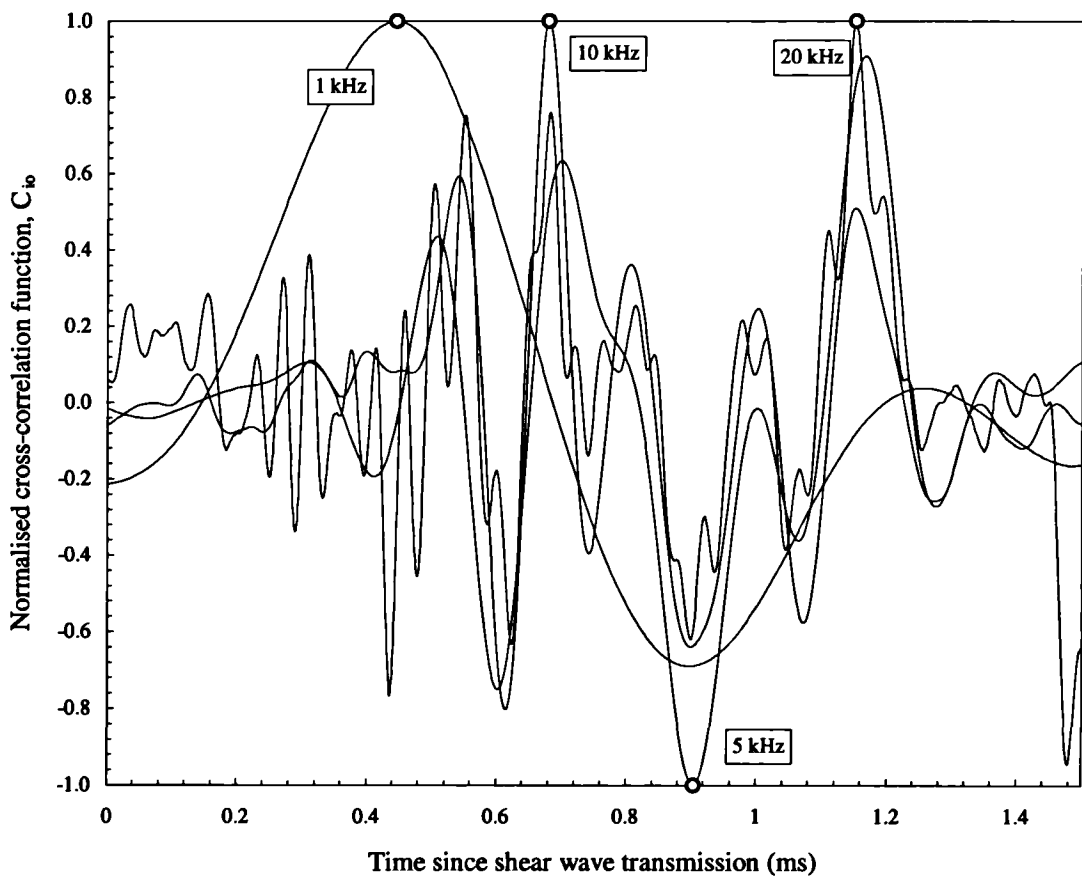


Figure 6.70 - Cross correlation coefficients for bender element traces in Figure 6.63

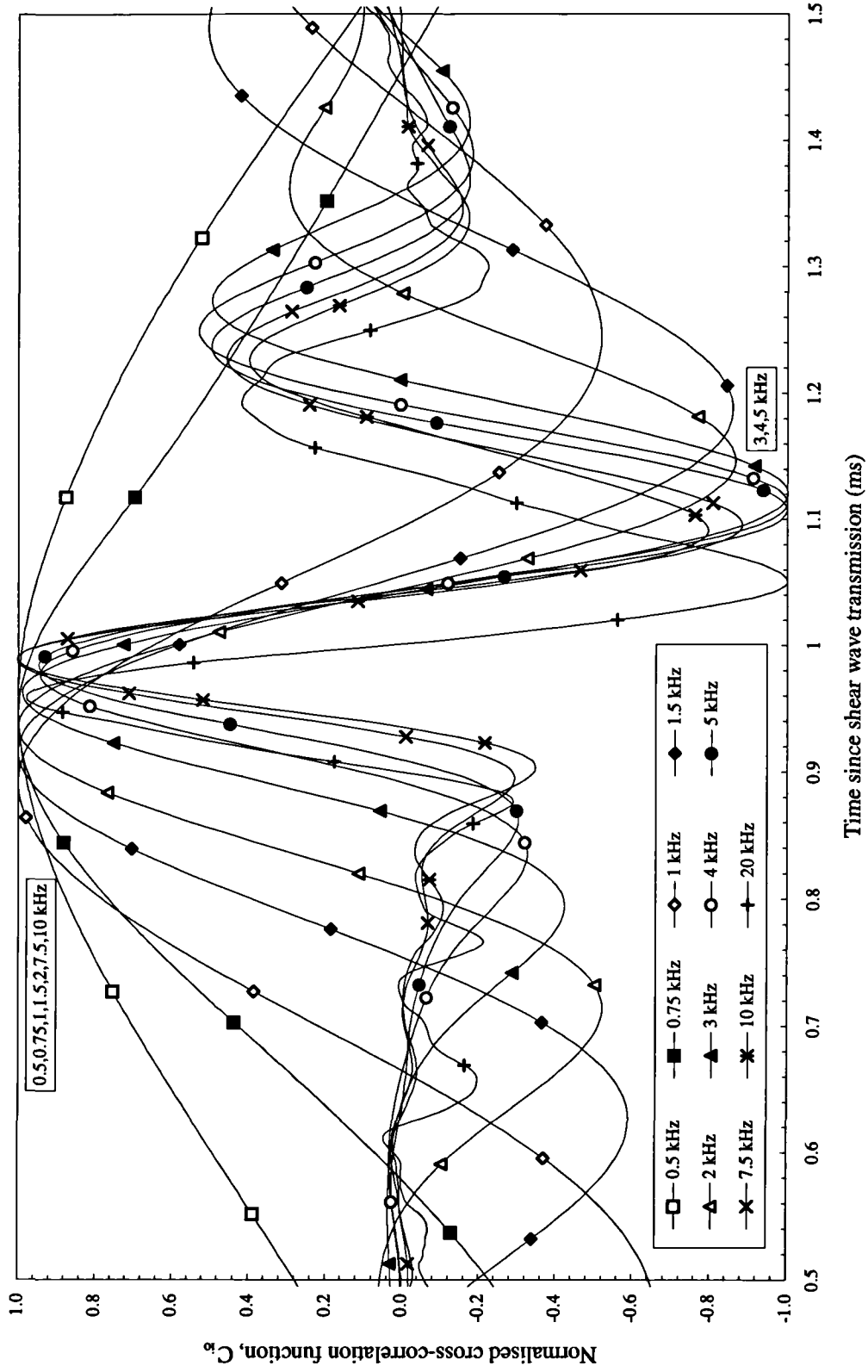
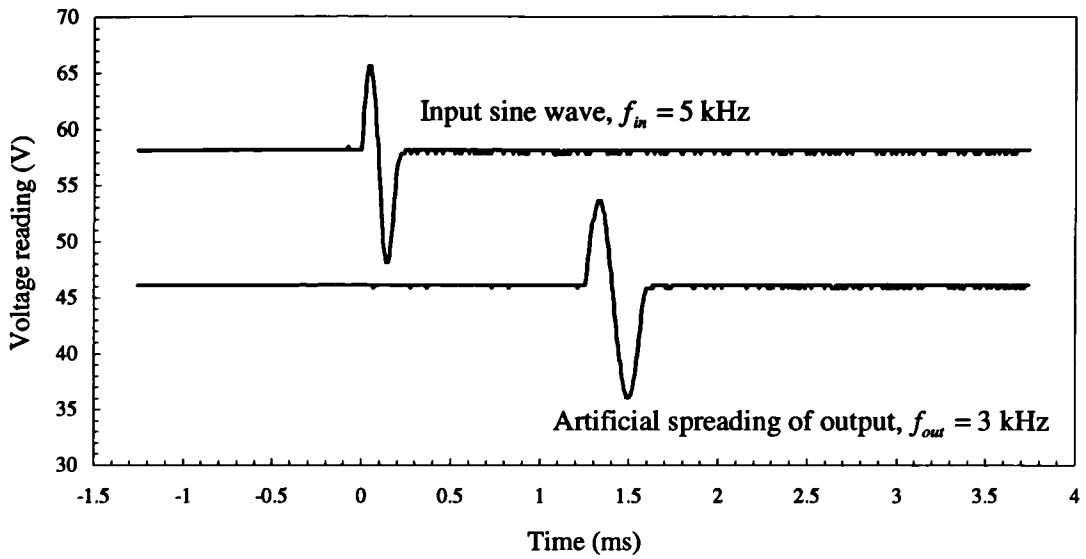
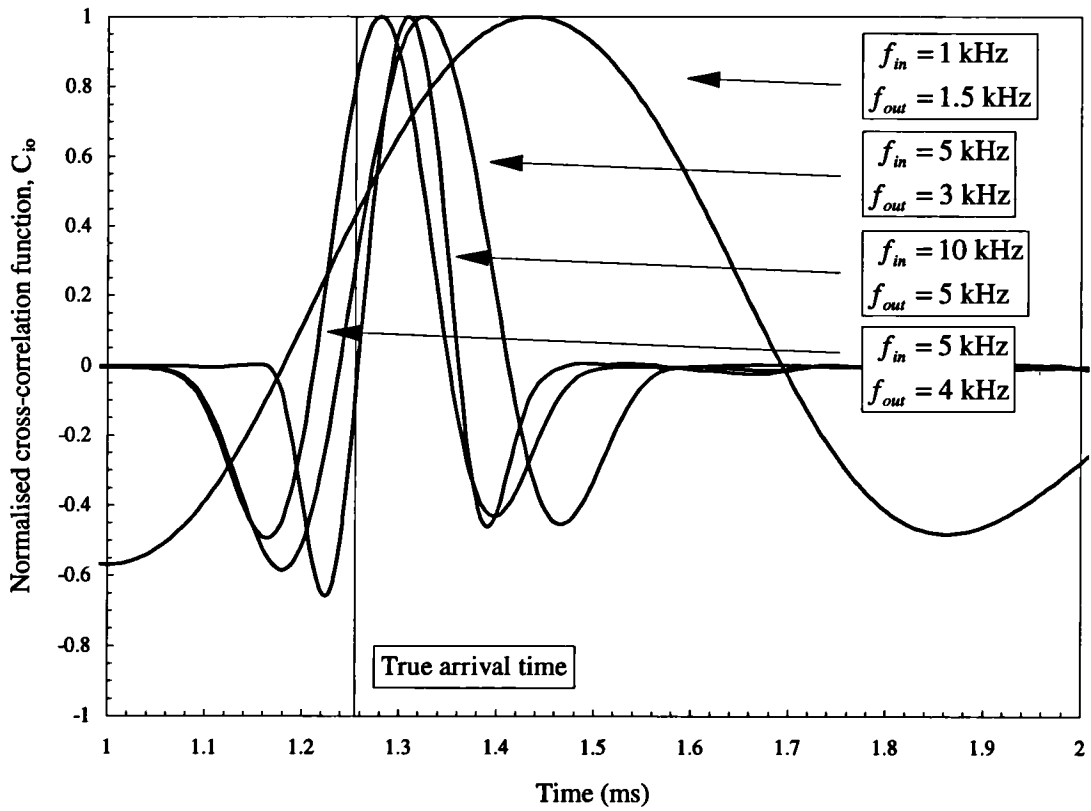


Figure 6.71 - Cross correlation coefficients for bender element traces shown in Figure 6.65



(a)



(b)

Figure 6.72 - Effect of attenuation of input wave during propagation from input to receiver, (a) example of ideal input and receiver functions incorporating attenuation from 5 kHz to 3 kHz, (b) normalised cross correlation coefficients for a series of artificial analyses incorporating attenuation

6.5.4 Comparison of static and dynamic measurements

The aim of using the bender elements was to find an upper limit to the deviatoric stiffness expressed by the maximum shear modulus, G_o . This would possibly correspond to a true elastic stiffness as discussed in Chapter 2.

The most comprehensive series of bender element tests was carried out during stress path test T06, and for each received trace the travel velocity of each successive identifiable peak or trough was converted to a shear stiffness using equation 6.21 (see also section 2.6.3)

$$G = \rho v_s^2 \dots\dots\dots (6.21)$$

For example, Figure 6.73 shows the change in the received waveform along two consecutive constant q stress paths as the effective mean normal stress just increased and then decreased between 200 and 260kPa. It is interesting to note on this figure the degree of similarity in the region of the traces before the region of the lower frequency wave component at approximately 0.6-0.8ms. This section of the trace has been attributed to compression wave components. It is seen that these, relatively minor, high frequency aspects of the trace (even those superposed on the region of the shear wave arrival) occur at the same time on all waveforms. In a saturated medium it would not be expected that the compression waves would be affected by the pressure changes associated with a triaxial test. The final section of the trace from 0.6-0.8ms translates as p' is increased or decreased, suggesting a soil stiffness dependent on p' . This region of the trace has been attributed to either near-field components or secondary compression components (see section 6.5.2). Unfortunately, the limited time base of these traces prevents the variation in the later shear wave arrival to be examined. Viggiani (1992) suggested that the near-field components and the shear wave components were dependent on p' to a similar degree, and the variation of the shear stiffness with p' may, therefore, be estimated from the variation calculated by using equation 6.21 for these earlier components. This 'apparent' stiffness has been calculated for points along all the constant q and constant p' stress paths in test T06. The dependence of the calculated stiffness of p' and q is shown in Figure 6.74(a) and (b) respectively. The upper and lower sets of data in these figures represent the stiffnesses associated with the first and second reversal of the received waveform respectively. It is clear that the calculated stiffness is dependent on p' . The change in stiffness with p' calculated from either the first or second reversal is the same and, if a similar variation may be assumed for the shear stiffness, Figure 6.74(a) suggests a variation of the shear stiffness with p' of the form shown in equation 6.22.

$$\Delta G_o = a. \Delta p' \dots\dots\dots (6.22)$$

where, $100 < a < 150$

The response also shows an increase in G_o of the order of 10MPa over the duration of the tests, suggesting that the cyclic straining was having a measurable effect on the soil behaviour which was not detected by the local small strain instrumentation.

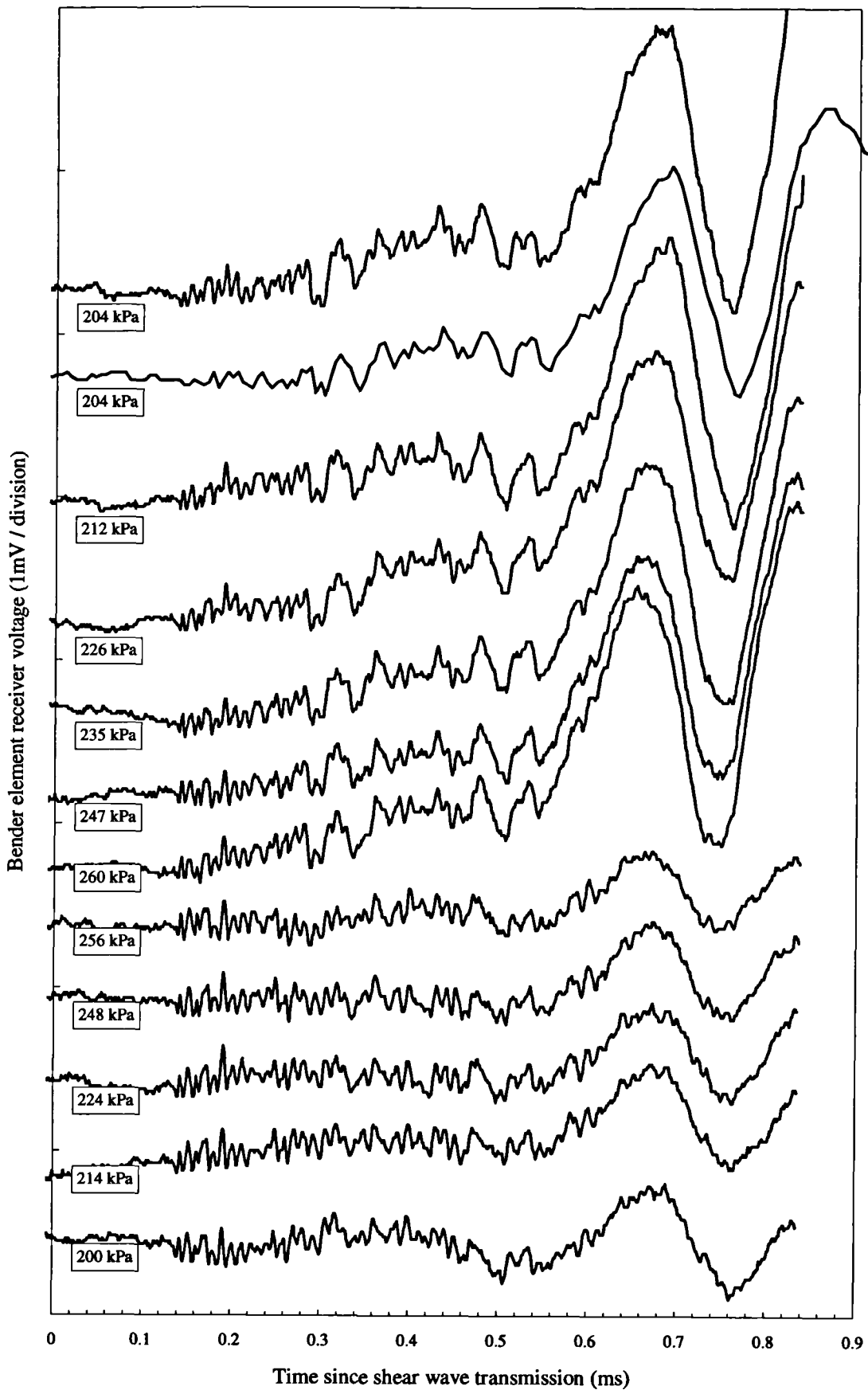
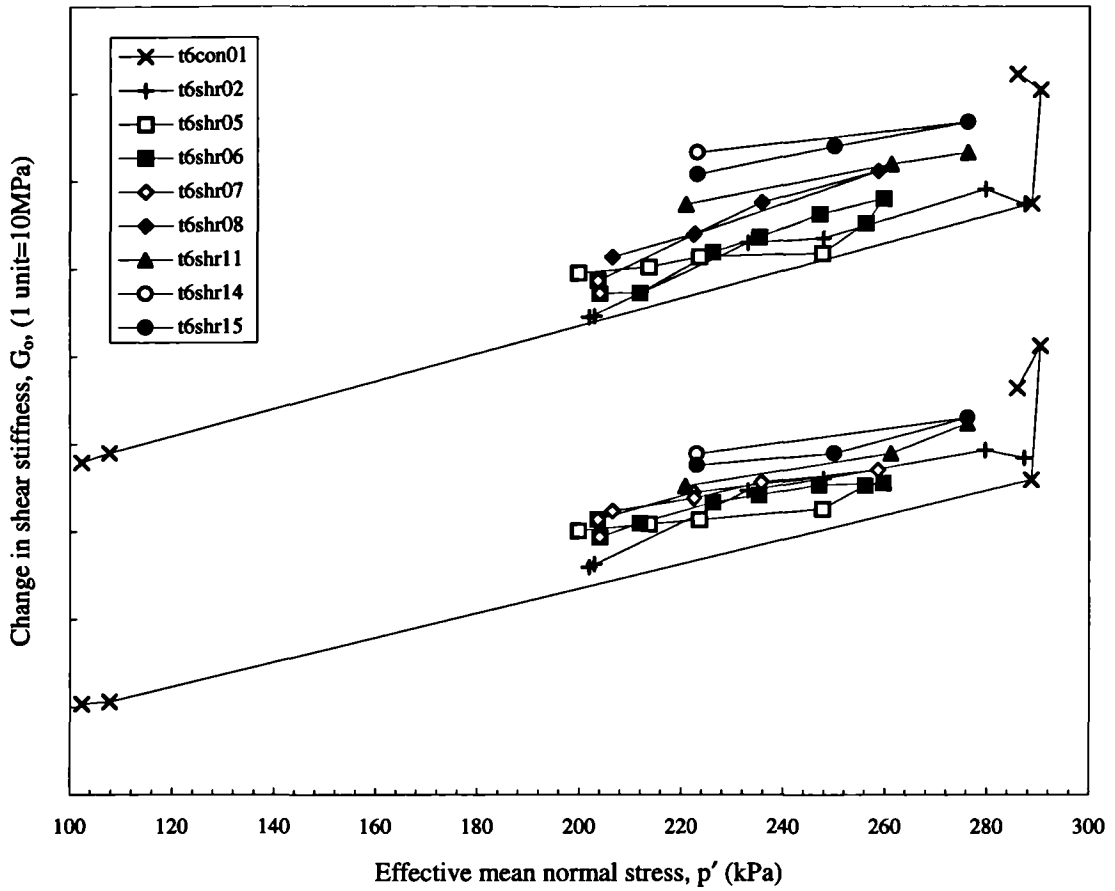
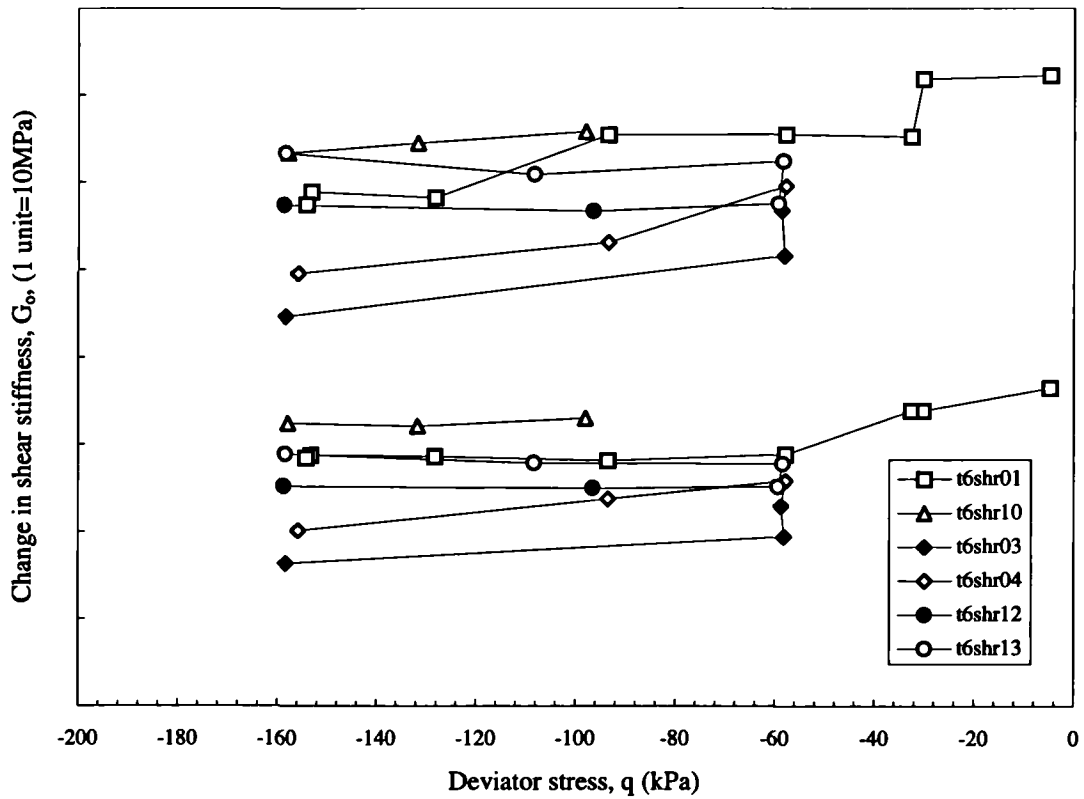


Figure 6.73 - Change in form of received bender element waveform trace during two consecutive constant q stress paths as p' increases from 200kPa to 260kPa and returns again to 200kPa.



(a)



(b)

Figure 6.74 - Changes in shear stiffness interpreted from bender element tests during (a) constant q , and (b) constant p' stress paths of test T06 (two separate groupings of results represent interpretation based on different sections of the trace - see text)

The results for the variation of the shear stiffness along the constant p' stress paths suggest that changes in the level of deviator stress bear no relation to changes in the maximum shear modulus. The shear wave travel velocity through a particulate material is influenced by the rigidity of the available wave travel pathways and therefore on the degree to which the particles are forced together. It is an increase in p' rather than q which is likely to affect the interparticle compression and, therefore, the dependence of the shear stiffness on p' rather than q seems qualitatively correct. A number of relationships between pressure and shear stiffness were given in section 2.7. The majority of relevant test data for overconsolidated clays exist for London clay and the numerical parameters shown in equation 6.16 based on equation 2.28 were determined by Viggiani (1992).

$$G_o = 400p'^{0.76}R_o^{0.25} \dots\dots\dots (6.23)$$

For the 200kPa range of p' shown in Figure 6.74(a), an increase in shear stiffness of 35 and 45MPa is calculated by equation 6.16 for overconsolidation ratios of 20 and 50 respectively. This compares reasonably well with the rise of 30MPa shown for the same figure.

The interpreted shear modulus from the bender element tests may be compared to the deviatoric stiffness calculated from the local strain instrumentation in the stress path tests. The deviatoric stiffness recorded in stress path test T06 is shown against triaxial shear strain in Figure 6.35(a). The magnitude of shear strain imposed in a bender element test is probably less than 0.001% (see section 2.6.2), which is beyond the accuracy of the local measurements. Therefore, to compare static and dynamic measurements, the deviatoric stiffness must be extrapolated back to an appropriate strain level. From Figure 6.35(a), a deviatoric stiffness of approximately 50-60MPa may be extrapolated to a triaxial shear strain of 0.001%. The interpretation of the sine wave traces shown in Figure 6.65 and Figure 6.66 suggest the shear wave arrival was at approximately 0.85ms. This corresponds to a shear stiffness of approximately 75-85MPa which is about 50% greater than the static measurements. Such discrepancies between the static and dynamic measurement of shear stiffness may be due to the following:

- Experimental error may be appreciable in either of the measurements. The careful calibration procedures make this unlikely for the stress path cell instrumentation. Although no actual calibration process was performed for the bender element apparatus as a whole, the oscilloscope was calibrated using the function generator to send waveforms of set frequency and amplitude.
- Non-linearity in the stress-strain response is still significant below the measurement accuracy of the stress path cell instrumentation. However, the use of the LDT local strain device (Tatsuoka and Shibuya, 1992, Tatsuoka and Kohata, 1995) allows continuous measurement of the stiffness response from 0.0001% to 1% axial strain (see section 2.5.2) and results obtained for a stiff overconsolidated clay using such instrumentation (Mukabi *et al.*, 1994a and b) suggest that, at strain levels of <0.002%, the stress-strain response is practically linear.
- The local strain instrumentation and the bender element apparatus may be measuring different aspects of the soil stiffness. For a cross-anisotropic soil the shear stiffness measured dynamically is dependent on the orientation of the transmitting and receiving elements as described in section 2.6.4. Although the shear wave transmission will involve particle movement in many orientations, the dominant motion in the present case will be particle movement in the horizontal plane with vertical wave propagation. Thus the system

records the shear stiffness in the vertical plane, G_{hv} . Only in an isotropic soil would this shear stiffness be the same as that in the horizontal plane, G_{hh} , and also equal to the deviatoric stiffness, G' , measured in triaxial apparatus. Using the simplified cross-anisotropic parameters proposed by Graham and Houlsby (1983) (presented later in Chapter 7) a relationship between the deviatoric and shear moduli is given in Figure 6.75. This figure shows that for a cross-anisotropic material with $\alpha^2 = 2$, the stiffness recorded in a bender element test may be 50% higher than the corresponding deviatoric stiffness interpreted from static strain measurements in a triaxial cell. This would explain the discrepancy in the present case.

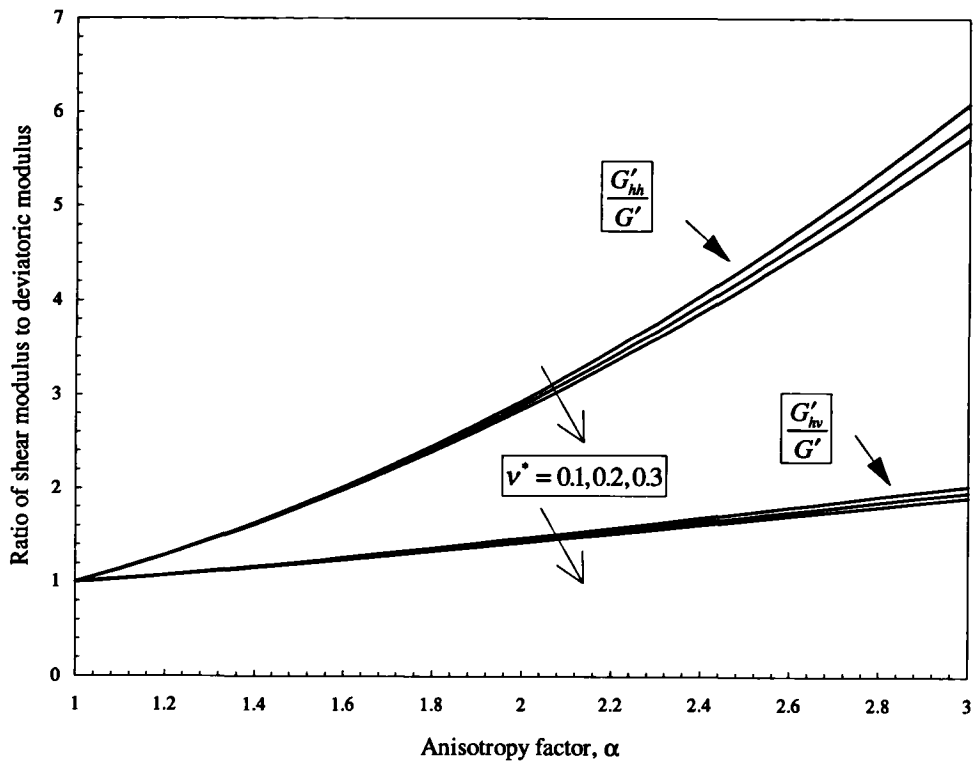


Figure 6.75 - Shear and deviatoric stiffness for a cross-anisotropic soil

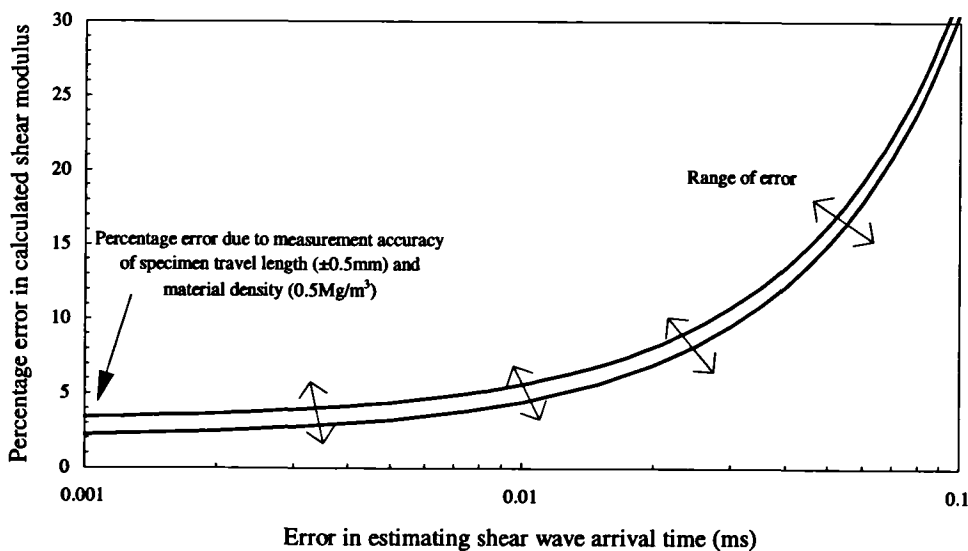


Figure 6.76 - Percentage error in the calculation of dynamic shear modulus due to experimental errors in bender element tests



7. Numerical model development

7.1 Introduction

A constitutive model was required to apply the deformation characteristics obtained from the laboratory testing programme, Chapter 6, to the simulation of the excavation process at the Elstow site described in Chapter 3.

This chapter describes the formulation and implementation of cross-anisotropic elastic constitutive relations, in which material non-linearity is incorporated through dependency on the cumulative incremental strain energy. An outline of the model has previously been presented by Hird and Pierpoint (1994).

A brief summary of elasticity theory is presented as a background to the formulation of the model and the methods used to determine the model input parameters from triaxial stress path tests are described.

The validation of the model consisted of checking its mathematical correctness and using it to simulate specimen response along additional stress paths incorporated into the experimental programme.

7.2 Requirements of a constitutive model

Simplicity in numerical models has been strongly advocated (Wroth and Houlsby, 1985), particularly when they are required as a tool for engineering analyses. The degree of complexity of a model is not always obvious, however. The criterion used to express the complexity is often the number of model parameters required, but it is also helpful to rate the model in terms of how easily each of the parameters may be quantified. A model should therefore be rated on the number and type of laboratory and/or field tests that are required to sufficiently define the model.

It may be said that a model should be as simple as possible, but not too simple. In other words, a model should be simple to understand and to implement while predicting a realistic soil response. It has long been realised that non-linearity and anisotropy are essential features of soil behaviour (Burland, 1989; Atkinson and Sällfors, 1991). The incorporation of small strain non-linearity into numerical analyses has significantly improved the quality of predictions of ground movements around engineering structures as described in section 2.3. This form of non-

linearity, the dependence of stiffness moduli on strain, must be considered a key feature of the modelling process. In a heavily overconsolidated deposit, the soil may be several times stiffer in the horizontal direction than in the vertical direction (see section 6.2.3) and in such circumstances it is desirable to incorporate the anisotropic nature of the deposit.

The non-linearity of the soil stiffness moduli may be defined within an elastic or an inelastic constitutive model. For soils which exhibit material non-linearity, the irrecoverability of strain is usually an accompanying characteristic. This effect is conveniently incorporated into constitutive models within the framework of plasticity. A number of these models have been described in section 2.7 and such models would be essential for modelling problems where loading was principally non-monotonic or involved large strain levels. However, even in a monotonic loading situation, the choice of an elastic or plastic model will affect the solution. In a plastic response, the principal strain increments coincide with the direction of the principal stresses, whereas in an elastic response the principal strain increments and the principal stress increments coincide. When the changes of stress are in the direction of the principal stresses (e.g. in a triaxial test), the elastic and plastic models might be able to produce the same response, but when the principal stresses are free to rotate (e.g. during excavation), the form of displacement will differ in each case. The application of an elasticity formulation to practical problems is therefore limited to cases in which the level of plastic straining is at a minimum. In heavily overconsolidated clay deposits, the soil structure has been well defined by a history of several hundred metres of overburden and such soils have traditionally been characterised as elastic. For these soils it might be reasonable to apply elasticity theory to monotonic loading deformation analyses (Jardine *et al.*, 1991; Burghignoli *et al.*, 1991). However, care is still required since, as described in section 2.4.2, even the small strain response of heavily overconsolidated clays has been shown to exhibit irrecoverability of strains and, therefore, an inelastic character.

7.3 Application of the theory of elasticity

Hooke's law of elasticity theory (*Ut tensio sic vis* - Hooke, 1676), may be generalised in three dimensions (with axes x, y and z) and written as:

$$\begin{bmatrix} \epsilon_x \\ \epsilon_y \\ \epsilon_z \\ \gamma_{xy} \\ \gamma_{yz} \\ \gamma_{zx} \end{bmatrix} = \begin{bmatrix} \alpha_{11} & \alpha_{12} & \alpha_{13} & \alpha_{14} & \alpha_{15} & \alpha_{16} \\ \alpha_{21} & \alpha_{22} & \alpha_{23} & \alpha_{24} & \alpha_{25} & \alpha_{26} \\ \alpha_{31} & \alpha_{32} & \alpha_{33} & \alpha_{34} & \alpha_{35} & \alpha_{36} \\ \alpha_{41} & \alpha_{42} & \alpha_{43} & \alpha_{44} & \alpha_{45} & \alpha_{46} \\ \alpha_{51} & \alpha_{52} & \alpha_{53} & \alpha_{54} & \alpha_{55} & \alpha_{56} \\ \alpha_{61} & \alpha_{62} & \alpha_{63} & \alpha_{64} & \alpha_{65} & \alpha_{66} \end{bmatrix} \cdot \begin{bmatrix} \sigma_x \\ \sigma_y \\ \sigma_z \\ \tau_{xy} \\ \tau_{yz} \\ \tau_{zx} \end{bmatrix} \dots\dots\dots (7.1)$$

This represents a material that possesses no planes of symmetry and results in 36 coefficients relating stress to strain. The most useful definition of elasticity is that the material behaviour is recoverable. The principles of thermodynamics require the existence of an elastic strain energy function during reversible cycles of changes of state under constant temperature (Love, 1927). The existence of this function requires symmetry in the constitutive matrix such that,

$$\alpha_{ab} = \alpha_{ba} \dots\dots\dots (7.2)$$

This reduces the number of independent coefficients from 36 to 21 as shown in equation 7.3

$$\begin{bmatrix} \epsilon_x \\ \epsilon_y \\ \epsilon_z \\ \gamma_{xy} \\ \gamma_{yz} \\ \gamma_{zx} \end{bmatrix} = \begin{bmatrix} \alpha_1 & \alpha_{12} & \alpha_{13} & \alpha_{14} & \alpha_{15} & \alpha_{16} \\ & \alpha_{22} & \alpha_{23} & \alpha_{24} & \alpha_{25} & \alpha_{26} \\ & & \alpha_{33} & \alpha_{34} & \alpha_{35} & \alpha_{36} \\ & & & \alpha_{44} & \alpha_{45} & \alpha_{46} \\ & & & & \alpha_{55} & \alpha_{56} \\ & & & & & \alpha_{66} \end{bmatrix} \begin{bmatrix} \sigma_x \\ \sigma_y \\ \sigma_z \\ \tau_{xy} \\ \tau_{yz} \\ \tau_{zx} \end{bmatrix} \dots\dots\dots (7.3)$$

Symmetrical matrix

Most natural materials show some behavioural symmetry and as the degree of symmetry increases, the number of independent parameters reduces. The consequence of this is that the degree of coupling between the respective normal and shear components of stress and strain is reduced (Lekhnitskii, 1963). A material that possesses three planes of elastic symmetry may be represented by equation 7.4. In this case there are just nine independent elastic coefficients and there is no longer a coupling between normal stresses and shear strains, between shear stresses and normal strains, or between shear stress and strains that are not in corresponding planes (see Figure 7.1). Such conditions could arise in a rock deposit in which three orthogonal joint planes exist which are aligned with the coordinate axes x, y and z. This is known as *orthotropic-anisotropy* or, alternatively, *orthotropy*.

$$\begin{bmatrix} \epsilon_x \\ \epsilon_y \\ \epsilon_z \\ \gamma_{xy} \\ \gamma_{yz} \\ \gamma_{zx} \end{bmatrix} = \begin{bmatrix} \frac{1}{E_x} & -\nu_{yx} & -\nu_{zx} & - & - & - \\ \frac{-\nu_{xy}}{E_x} & \frac{1}{E_y} & -\nu_{zy} & - & - & - \\ \frac{-\nu_{xz}}{E_x} & \frac{-\nu_{yz}}{E_y} & \frac{1}{E_z} & - & - & - \\ - & - & - & \frac{1}{G_{xy}} & - & - \\ - & - & - & - & \frac{1}{G_{yz}} & - \\ - & - & - & - & - & \frac{1}{G_{zx}} \end{bmatrix} \begin{bmatrix} \sigma_x \\ \sigma_y \\ \sigma_z \\ \tau_{xy} \\ \tau_{yz} \\ \tau_{zx} \end{bmatrix} \dots\dots\dots (7.4)$$

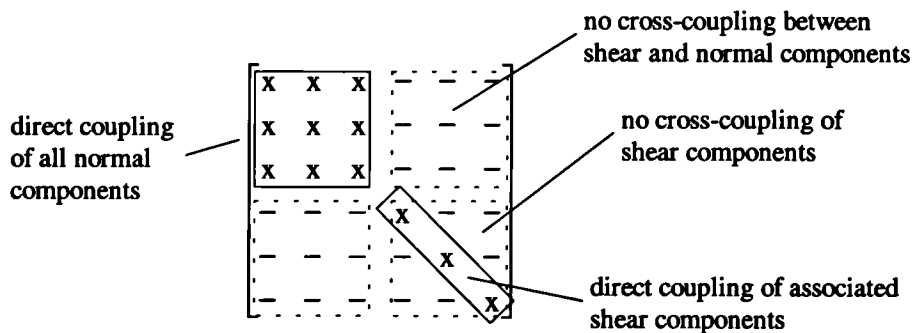


Figure 7.1 - Form of coupling between stress and strain components of constitutive matrix of cross-anisotropic elasticity

In sedimentary strata, it is common for a plane of symmetry to exist due to the depositional history. A soil deposit is often laterally extensive and has been subjected to purely one-dimensional movements. If a soil exhibits the same properties in any horizontal direction, being different from those in the vertical direction, it is said to be *cross-anisotropic* or *transversely*

isotropic. This form of anisotropy is represented in equation 7.5 in which the vertical axis is aligned with the y axis.

$$\begin{bmatrix} \epsilon_x \\ \epsilon_y \\ \epsilon_z \\ \gamma_{xy} \\ \gamma_{yz} \\ \gamma_{xz} \end{bmatrix} = \begin{bmatrix} \frac{1}{E_h} & \frac{-\nu_{vh}}{E_v} & \frac{-\nu_{hh}}{E_h} & - & - & - \\ \frac{-\nu_{hv}}{E_h} & \frac{1}{E_v} & \frac{-\nu_{hv}}{E_h} & - & - & - \\ \frac{-\nu_{hh}}{E_h} & \frac{-\nu_{vh}}{E_v} & \frac{1}{E_h} & - & - & - \\ - & - & - & \frac{1}{G_{hv}} & - & - \\ - & - & - & - & \frac{1}{G_{hv}} & - \\ - & - & - & - & - & \frac{1}{G_{hh}} \end{bmatrix} \begin{bmatrix} \sigma_x \\ \sigma_y \\ \sigma_z \\ \tau_{xy} \\ \tau_{yz} \\ \tau_{xz} \end{bmatrix} \dots\dots\dots (7.5)$$

- where, E_v = Young's modulus in vertical direction
- E_h = Young's modulus in horizontal direction
- G_{hv} = Shear modulus in any vertical plane
- G_{hh} = Shear modulus in any horizontal plane
- ν_{hv} = Poisson's Ratio of strain in vertical direction to applied strain in horizontal direction
- ν_{vh} = Poisson's Ratio of strain in horizontal direction to applied strain in vertical direction
- ν_{hh} = Poisson's Ratio of strain in horizontal direction to applied strain in orthogonal horizontal direction

Remembering that for an elastic material the compliance matrix is symmetric,

$$\frac{\nu_{hv}}{E_h} = \frac{\nu_{vh}}{E_v}, \dots\dots\dots (7.6)$$

and, since the material is isotropic on the horizontal plane,

$$G_{hh} = \frac{E_h}{2(1 + \nu_{hh})}, \dots\dots\dots (7.7)$$

there remain five independent elastic coefficients.

A material that is completely homogenous and equivalent in all directions is termed *isotropic*. Such a degree of symmetry reduces the number of independent elastic coefficients to two and is represented by equation 7.8.

$$\begin{bmatrix} \epsilon_x \\ \epsilon_y \\ \epsilon_z \\ \gamma_{xy} \\ \gamma_{yz} \\ \gamma_{xz} \end{bmatrix} = \frac{1}{E} \begin{bmatrix} 1 & -\nu & -\nu & - & - & - \\ -\nu & 1 & -\nu & - & - & - \\ -\nu & -\nu & 1 & - & - & - \\ - & - & - & 2(1+\nu) & - & - \\ - & - & - & - & 2(1+\nu) & - \\ - & - & - & - & - & 2(1+\nu) \end{bmatrix} \begin{bmatrix} \sigma_x \\ \sigma_y \\ \sigma_z \\ \tau_{xy} \\ \tau_{yz} \\ \tau_{xz} \end{bmatrix} \dots\dots\dots (7.8)$$

Isotropic soil behaviour may be encountered in carefully prepared laboratory specimens. However, it is the cross-anisotropic condition that is most prevalent in the field.

The cross-anisotropic compliance matrix may be inverted to obtain the **D** matrix associated with numerical analysis as shown in equations 7.9 and 7.10.

$$\sigma = \mathbf{D} \cdot \varepsilon \quad \dots\dots\dots (7.9)$$

$$\begin{bmatrix} \sigma_x \\ \sigma_y \\ \sigma_z \\ \tau_{xy} \\ \tau_{yz} \\ \tau_{zx} \end{bmatrix} = \frac{E_v}{(1 + \nu_{hh})(1 - 2\nu_{hh})} \cdot \begin{bmatrix} \frac{E_h}{E_v}(1 - \nu_{hh}) & \frac{\nu_{hh}^2}{\nu_{vh}} & \frac{E_h}{E_v}\nu_{hh} & - & - & - \\ \frac{\nu_{hh}^2}{\nu_{vh}} & (1 - \nu_{hh}) & \frac{\nu_{hh}^2}{\nu_{vh}} & - & - & - \\ \frac{E_h}{E_v}\nu_{hh} & \frac{\nu_{hh}^2}{\nu_{vh}} & \frac{E_h}{E_v}(1 - \nu_{hh}) & - & - & - \\ - & - & - & \frac{\nu_{hh}}{\nu_{vh}}\left(\frac{1 - 2\nu_{hh}}{2}\right) & - & - \\ - & - & - & - & \frac{\nu_{hh}}{\nu_{vh}}\left(\frac{1 - 2\nu_{hh}}{2}\right) & - \\ - & - & - & - & - & \frac{E_h}{E_v}\left(\frac{1 - 2\nu_{hh}}{2}\right) \end{bmatrix} \begin{bmatrix} \varepsilon_x \\ \varepsilon_y \\ \varepsilon_z \\ \gamma_{xy} \\ \gamma_{yz} \\ \gamma_{zx} \end{bmatrix} \quad \dots\dots\dots (7.10)$$

7.4 Interpreting soil response in triaxial tests in terms of elasticity

The incremental stress-strain behaviour of a soil in a triaxial system has been described in Chapter 2, and may be represented by equation 7.11 (Atkinson and Sällfors, 1991).

$$\begin{bmatrix} \delta\varepsilon_v \\ \delta\varepsilon_s \end{bmatrix} = \begin{bmatrix} \frac{1}{K'} & \frac{1}{J'_{qv}} \\ \frac{1}{J'_{ps}} & \frac{1}{3G'} \end{bmatrix} \cdot \begin{bmatrix} \delta p' \\ \delta q' \end{bmatrix} \quad \dots\dots\dots (7.11)$$

If functions are available for the four incremental moduli contained in equation 7.11, this equation is sufficient to represent the behaviour of soil in a triaxial system. These functions may be determined empirically, through curve-fitting of appropriate stress-strain curves, or analytically, by assuming that the material response is governed by a particular constitutive law. The formulation of such a constitutive law may be based on elasticity, plasticity or elastoplasticity. For an elastic formulation the constitutive matrix must be symmetric (see section 7.3). This is also a requirement of a plasticity solution in which the flow rule is associated (Atkinson, 1975).

Hence, $J'_{qv} = J'_{ps}$, and

$$\begin{bmatrix} \delta\varepsilon_v \\ \delta\varepsilon_s \end{bmatrix} = \begin{bmatrix} \frac{1}{K'} & \frac{1}{J'} \\ \frac{1}{J'} & \frac{1}{3G'} \end{bmatrix} \cdot \begin{bmatrix} \delta p' \\ \delta q' \end{bmatrix} \dots\dots\dots (7.12)$$

The cross-anisotropic elastic response shown in equation 7.5 may be interpreted in terms of incremental effective stresses in equation 7.13.

$$\begin{bmatrix} \delta\varepsilon_x \\ \delta\varepsilon_y \\ \delta\varepsilon_z \\ \delta\gamma_{xy} \\ \delta\gamma_{yz} \\ \delta\gamma_{zx} \end{bmatrix} = \begin{bmatrix} \frac{1}{E'_h} & \frac{-v'_{vh}}{E'_v} & \frac{-v'_{hh}}{E'_h} & - & - & - \\ \frac{-v'_{hv}}{E'_h} & \frac{1}{E'_v} & \frac{-v'_{hv}}{E'_h} & - & - & - \\ \frac{-v'_{hh}}{E'_h} & \frac{-v'_{vh}}{E'_v} & \frac{1}{E'_h} & - & - & - \\ \hline - & - & - & \frac{1}{G'_{hv}} & - & - \\ - & - & - & - & \frac{1}{G'_{hv}} & - \\ - & - & - & - & - & \frac{1}{G'_{hh}} \end{bmatrix} \cdot \begin{bmatrix} \delta\sigma'_x \\ \delta\sigma'_y \\ \delta\sigma'_z \\ \delta\tau'_{xy} \\ \delta\tau'_{yz} \\ \delta\tau'_{zx} \end{bmatrix} \dots\dots\dots (7.13)$$

The G parameters in equations 7.11 and 7.13 must not be confused with each other. In equation 7.11, G' represents the deviatoric response in triaxial stress space whilst in equation 7.13, G'_{hv} and G'_{hh} represent the coupling of shear stresses and shear strains. Since only normal stresses may be manipulated in a triaxial test, equation 7.13 reduces to equation 7.14.

$$\begin{bmatrix} \delta\varepsilon_x \\ \delta\varepsilon_y \\ \delta\varepsilon_z \end{bmatrix} = \begin{bmatrix} \frac{1}{E'_h} & \frac{-v'_{vh}}{E'_v} & \frac{-v'_{hh}}{E'_h} \\ \frac{-v'_{hv}}{E'_h} & \frac{1}{E'_v} & \frac{-v'_{hv}}{E'_h} \\ \frac{-v'_{hh}}{E'_h} & \frac{-v'_{vh}}{E'_v} & \frac{1}{E'_h} \end{bmatrix} \cdot \begin{bmatrix} \delta\sigma'_x \\ \delta\sigma'_y \\ \delta\sigma'_z \end{bmatrix} \dots\dots\dots (7.14)$$

For the axisymmetric conditions of a triaxial test, only vertical and horizontal stresses and strain may be measured as shown in equation 7.15.

$$\begin{bmatrix} \delta\varepsilon_a \\ \delta\varepsilon_r \end{bmatrix} = \begin{bmatrix} \frac{1}{E_v} & \frac{-2v_{vh}}{E_v} \\ \frac{-v_{vh}}{E_v} & \frac{1}{E_h} - \frac{v_{hh}}{E_h} \end{bmatrix} \cdot \begin{bmatrix} \delta\sigma'_a \\ \delta\sigma'_r \end{bmatrix} \dots\dots\dots (7.15)$$

Rewriting equation 7.11 in terms of axial and radial stress increments,

$$\delta\varepsilon_v = \delta p' \left(\frac{1}{K'} \right) + \delta q' \left(\frac{1}{J'_{qv}} \right) = \delta\sigma'_a \left(\frac{1}{3K'} + \frac{1}{J'_{qv}} \right) + \delta\sigma'_r \left(\frac{2}{3K'} - \frac{1}{J'_{qv}} \right) \dots\dots\dots (7.16)$$

$$\delta\varepsilon_s = \delta p' \left(\frac{1}{J'_{ps}} \right) + \delta q \left(\frac{1}{3G'} \right) = \delta\sigma'_a \left(\frac{1}{3J'_{ps}} + \frac{1}{3G'} \right) + \delta\sigma'_r \left(\frac{2}{3J'_{ps}} - \frac{1}{3G'} \right) \dots\dots\dots (7.17)$$

But, using equation 7.15

$$\delta\varepsilon_v = \delta\varepsilon_a + 2\delta\varepsilon_r = \delta\sigma'_a \left(\frac{1}{E'_v} - \frac{2\nu'_{vh}}{E'_v} \right) + \delta\sigma'_r \left(\frac{-2\nu'_{vh}}{E'_v} + \frac{2(1-\nu'_{hh})}{E'_h} \right) \dots\dots\dots (7.18)$$

$$\delta\varepsilon_s = \frac{2}{3}(\delta\varepsilon_a - \delta\varepsilon_r) = \delta\sigma'_a \left(\frac{2}{3E'_v} + \frac{2\nu'_{vh}}{3E'_v} \right) + \delta\sigma'_r \left(\frac{-4\nu'_{vh}}{3E'_v} - \frac{2(1-\nu'_{hh})}{3E'_h} \right) \dots\dots\dots (7.19)$$

Therefore, comparing similar terms in equations 7.16-7.17 and 7.18-7.19,

$$K' = \frac{E'_v E'_h}{E'_h(1-4\nu'_{vh}) + 2E'_v(1-\nu'_{hh})} \dots\dots\dots (7.20)$$

$$J'_{qv} = \frac{3E'_v E'_h}{2E'_h(1-\nu'_{vh}) + 2E'_v(1-\nu'_{hh})} \dots\dots\dots (7.21)$$

$$G' = \frac{3E'_v E'_h}{4E'_h(1+2\nu'_{vh}) + 2E'_v(1-\nu'_{hh})} \dots\dots\dots (7.22)$$

$$J'_{ps} = \frac{3E'_v E'_h}{2E'_h(1-\nu'_{vh}) - 2E'_v(1-\nu'_{hh})} \dots\dots\dots (7.23)$$

In the present case $J'_{qv} = J'_{ps} = J'$ since the response is being interpreted in terms of elasticity.

If strain dependent functions for the Young's moduli and Poisson's ratios could be deduced this would provide an elastic framework for the interpretation of soil response. However, Graham and Houlsby (1983) showed that in a conventional triaxial testing system only three independent elastic parameters may be determined and that, to independently establish the four elastic parameters in equation 7.14, tests must be carried out on horizontally orientated and vertically orientated specimens. There are numerous problems associated with testing horizontally orientated specimens in the triaxial apparatus (Saada, 1970), for example, the non-uniform response of laminated soils as shown in Figure 7.2. Even if the four parameters (E'_v, E'_h, ν'_{vh} and ν'_{hh}) could be determined, the fifth independent parameter (G'_{vh}) would remain unknown.

Therefore, Graham and Houlsby (1983) suggested a particular form of anisotropy such that all parameters could be obtained from triaxial tests on vertically orientated specimens. Of the three elastic parameters that may be derived from a standard triaxial test, two are required to represent isotropy leaving only one parameter through which to incorporate anisotropy. The isotropic case may be modified by multiplying the stiffness coefficients to increase the stiffness in a horizontal direction by an anisotropy factor, α . This results in a three parameter simplification of 5 parameter cross-anisotropic elasticity using:

$$E^*, \nu^*, \alpha$$

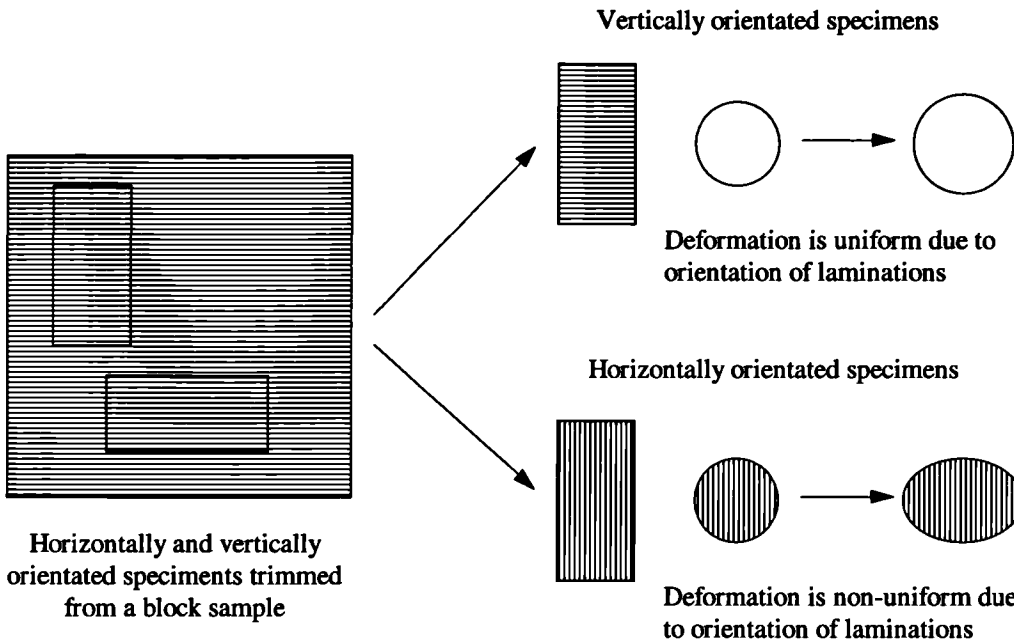


Figure 7.2 - Effect of lamination orientation in triaxial tests

such that

$$E_v = E^*, E_h = \alpha^2 E^*$$

$$v_{vh} = \frac{v^*}{\alpha}, v_{hh} = v^*$$

$$G_{hv} = \frac{\alpha E^*}{2(1+v^*)}, G_{hh} = \frac{\alpha^2 E^*}{2(1+v^*)}$$

The parameter α is therefore a quantitative measure of the degree of anisotropy as shown by the relations of equations 7.24 to 7.26.

for Young's moduli, $\frac{E'_h}{E'_v} = \alpha^2$ (7.24)

for Poisson's ratios, $\frac{v'_{hh}}{v'_{vh}} = \alpha$ (7.25)

and for shear moduli, $\frac{G'_{hh}}{G'_{hv}} = \alpha$ (7.26)

These parameters may be compared with the full description of cross-anisotropy shown in equation 7.13 to produce the simplified stress-strain relation of equation 7.27

$$\begin{bmatrix} \delta\epsilon_x \\ \delta\epsilon_y \\ \delta\epsilon_z \\ \delta\gamma_{xy} \\ \delta\gamma_{yz} \\ \delta\gamma_{zx} \end{bmatrix} = \frac{1}{E^*} \begin{bmatrix} \frac{1}{\alpha^2} & \frac{-v^*}{\alpha} & \frac{-v^*}{\alpha^2} & - & - & - \\ \frac{-v^*}{\alpha} & 1 & \frac{-v^*}{\alpha} & - & - & - \\ \frac{1}{\alpha^2} & \frac{-v^*}{\alpha} & \frac{1}{\alpha^2} & - & - & - \\ - & - & - & \frac{2(1+v^*)}{\alpha} & - & - \\ - & - & - & - & \frac{2(1+v^*)}{\alpha} & - \\ - & - & - & - & - & \frac{2(1+v^*)}{\alpha^2} \end{bmatrix} \begin{bmatrix} \delta\sigma'_x \\ \delta\sigma'_y \\ \delta\sigma'_z \\ \delta\tau'_{xy} \\ \delta\tau'_{yz} \\ \delta\tau'_{zx} \end{bmatrix} \dots\dots\dots (7.27)$$

and may be substituted into equations 7.20-7.23 to relate the volumetric, deviatoric and coupling stiffness moduli with the Graham and Houlsby type parameters as shown in equations 7.28-7.30.

$$K' = \frac{\alpha^2 E^*}{\alpha^2 - 4\alpha v^* + 2 - 2v^*} \dots\dots\dots (7.28)$$

$$G' = \frac{3\alpha^2 E^*}{4\alpha^2 + 8\alpha v^* + 2 - 2v^*} \dots\dots\dots (7.29)$$

$$J' = \frac{3\alpha^2 E}{2\alpha^2 - 2\alpha v^* - 2 + 2v^*} \dots\dots\dots (7.30)$$

By manipulating these relations K' , G' and J' may be converted into the parameters E^* , v^* and α as shown in equations 7.31-7.33.

$$E^* = 9 \frac{GJK}{GJ + 6GK + 3KJ} \dots\dots\dots (7.31)$$

$$v^* = -\frac{1}{2} \frac{(2GJ - 3KJ + 3GK)\alpha}{GJ + 6GK + 3KJ} \dots\dots\dots (7.32)$$

$$\alpha = \frac{1}{2} \frac{-2GJ + 3KJ - 3GK \pm 3\sqrt{4J^2G^2 + 12GJ^2K + 12G^2JK + 9K^2J^2 - 18JGK^2 - 63G^2K^2}}{12GK - 3KJ - 4GJ} \dots\dots\dots (7.33)$$

In this way the specimen response from a series of triaxial tests on vertically orientated specimens may be interpreted within the framework of cross-anisotropic elasticity, albeit in a simplified form.

7.5 'Model OC' - a constitutive model to represent the behaviour of the heavily overconsolidated Oxford Clay

In order to model excavation behaviour using CRISP, a new constitutive model that incorporated both non-linearity and anisotropy was required (see section 7.2). It was thought that an elastic model might be sufficient to describe the response to monotonic loading in the heavily overconsolidated Oxford Clay. The details of the model are described below.

7.5.1 Anisotropy implementation

The soil anisotropy is incorporated using the relations proposed by Graham and Houlsby (1983) and presented in section 7.4. The use of these relations allowed an elastic formulation in general stress space for which the required parameters could all be obtained from triaxial tests on vertical specimens. The compliance matrix in equation 7.27 may be inverted to provide the constitutive stiffness matrix (**D**) as shown in equation 7.34 and further in equation 7.35.

$$\delta\sigma' = \mathbf{D} \cdot \delta\varepsilon \quad \dots\dots\dots (7.34)$$

$$\begin{bmatrix} \delta\sigma'_x \\ \delta\sigma'_y \\ \delta\sigma'_z \\ \delta\tau'_{xy} \\ \delta\tau'_{yz} \\ \delta\tau'_{xz} \end{bmatrix} = \frac{E^*}{(1+\nu^*)(1-2\nu^*)} \cdot \begin{bmatrix} \alpha^2(1-\nu^*) & \alpha\nu^* & \alpha^2\nu^* & - & - & - \\ \alpha\nu^* & (1-\nu^*) & \alpha\nu^* & - & - & - \\ \alpha^2\nu^* & \alpha\nu^* & \alpha^2(1-\nu^*) & - & - & - \\ - & - & - & \alpha(1-2\nu^*)/2 & - & - \\ - & - & - & - & \alpha(1-2\nu^*)/2 & - \\ - & - & - & - & - & \alpha^2(1-2\nu^*)/2 \end{bmatrix} \begin{bmatrix} \delta\varepsilon_x \\ \delta\varepsilon_y \\ \delta\varepsilon_z \\ \delta\gamma_{xy} \\ \delta\gamma_{yz} \\ \delta\gamma_{xz} \end{bmatrix} \quad \dots\dots\dots (7.35)$$

7.5.2 Non-linearity implementation

The non-linearity of the model is based on the incremental strain energy. Incremental strain energy is described in section 2.7 and is represented again by equation 7.36.

$$\Delta U = \sum_0^{\varepsilon_v} \Delta p' \delta\varepsilon_v + \sum_0^{\varepsilon_s} \Delta q \delta\varepsilon_s \quad \dots\dots\dots (7.36)$$

The utilisation of the model in CRISP was predominantly for plane strain conditions so that,

$$\Delta U = \sum_0^{\varepsilon_1} (\sigma'_1 - \sigma'_{1e}) \delta\varepsilon_1 + \sum_0^{\varepsilon_3} (\sigma'_3 - \sigma'_{3e}) \delta\varepsilon_3 \quad \dots\dots\dots (7.37)$$

However, for the axisymmetric conditions of the triaxial test from which the input parameters are derived,

$$\Delta U = \sum_0^{\epsilon_a} (\sigma'_a - \sigma'_{a_0}) \delta \epsilon_a + 2 \sum_0^{\epsilon_r} (\sigma'_r - \sigma'_{r_0}) \delta \epsilon_r, \dots\dots\dots (7.38)$$

where $(\sigma_{a_0}, \sigma_{r_0})$ defines the initial stress state, (σ_a, σ_r) defines the new state and the subscripts a and r refer to axial and radial directions.

It was assumed that the relationships between the stiffness parameters used in the model and incremental strain energy were identical under axisymmetric and plane strain conditions.

7.5.3 Effect of loading direction

This model was designed to analyse monotonic loading situations, specifically the ground response due to excavation, but practical construction problems which appear monotonic may involve loading reversals in the soil caused by the construction sequence. This is illustrated in Figure 7.3 for a sloped excavation analysis under undrained conditions. The soil elements beneath the side slopes will be subject to a reversal in loading direction as excavation progresses. If the stress path loading direction is monitored for each soil element during each increment in the analysis, such a load reversal may be detected and a suitable stiffening of the response may be allocated to that element.

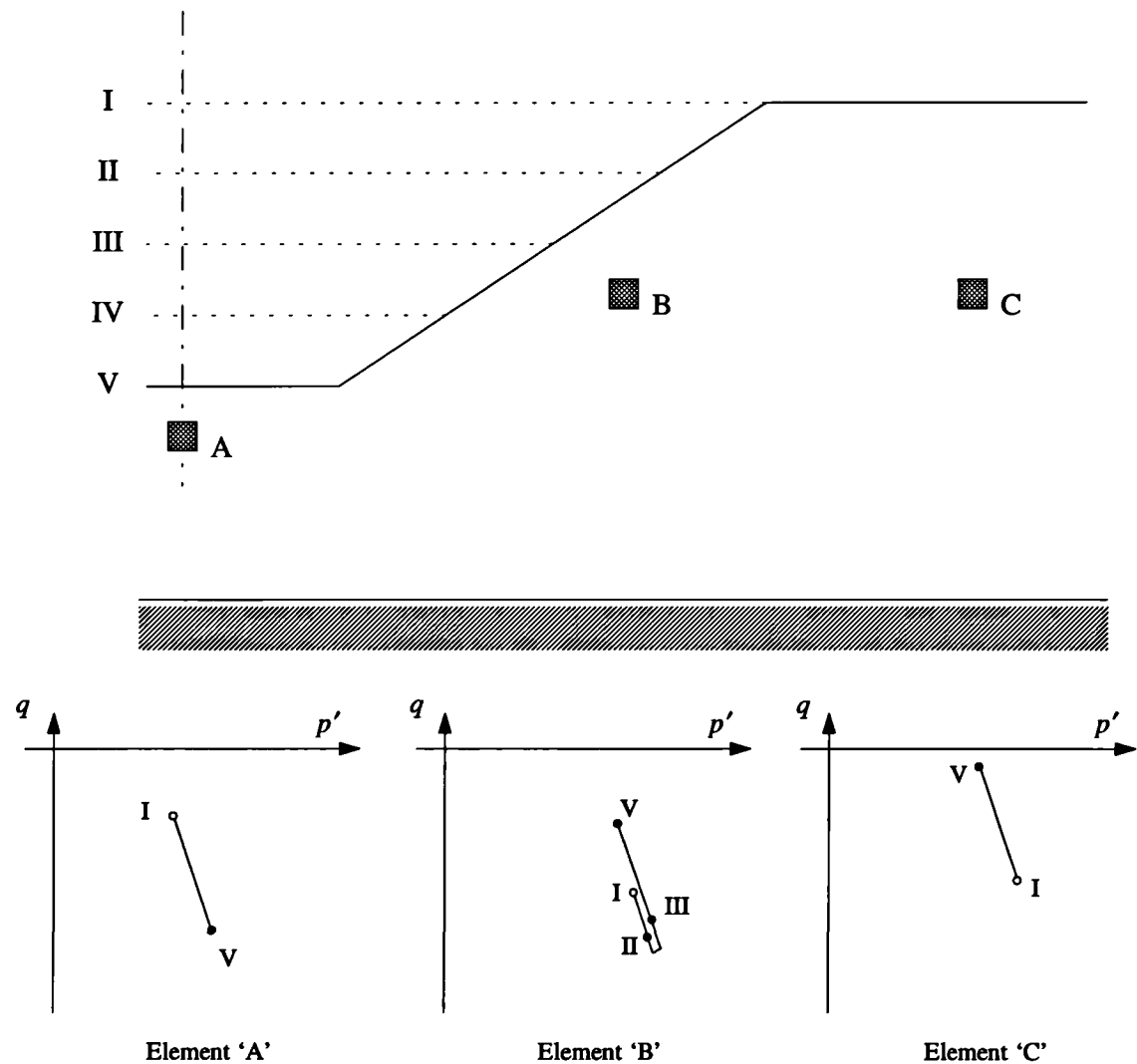


Figure 7.3 - Load reversals taking place during staged construction of an excavation

During an analysis an appropriate response for each soil element must be modelled, depending on its location. The approach to this problem by various authors has been discussed in Chapter 2. A similar approach to that of Jardine *et al.* (1991) has been adopted in the present work, although to prevent the need to discretize zones around the excavation, the model calculates appropriate stiffness parameters for a soil element based on the stress path increment direction. It is assumed that the ground in the vicinity of the excavation has experienced an identical stress history. Furthermore, it is assumed that the soil response to a stress probe from an initial stress state, (p'_i, q_i) , into quadrant A, B, C, or D in Figure 7.4, can be simulated by an elastic formulation which uses stiffness moduli derived from the bordering constant p' and constant q stress path directions. For example, the response of an element of soil whose stress state follows a path that enters quadrant 'A' is modelled using G' and J'_{qv} defined from the 'compression' path, and K' and J'_{ps} defined from the 'unloading' path.

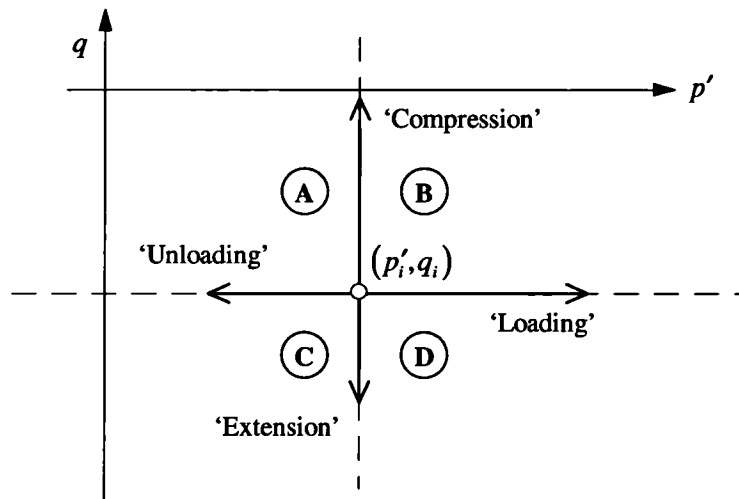


Figure 7.4 - Possible stress path probe directions from the *in situ* state

In order to calculate the stress path increment direction, the current stress state is compared to that of the previous one. The general stress state surrounding the excavation is reduced to an equivalent triaxial stress state by using the vertical and average horizontal stresses and ignoring the effect of principal stress rotation. The stress path increment direction should perhaps be calculated from the principal stress state for consistency with the triaxial conditions (from which the parameters were derived). However, for analyses in which the degree of principal stress rotation is large enough to cause the directions of the major and minor principal stresses to switch, determining changes in the current stress path direction in triaxial stress space becomes problematic and, consequently, the vertical and horizontal stresses are used.

If the stress path direction (in triaxial stress space) of a soil element, during a particular load increment, enters a different quadrant (Figure 7.4) from that during the previous load increment, then that soil element is said to have undergone a load reversal. The incremental strain energy at this point is then stored and used as a datum for subsequent load increments. This is clearly a somewhat crude attempt at modelling the complex stress-strain response of the soil elements at the side of an excavation, but it was hoped that it would suffice for the current application.

When attributing a load reversal to a soil element, care must be taken to ensure solutions exist for equations 7.31 to 7.33. For example, if the stress increment direction moved from 'A' to 'B' in Figure 7.4, and the datum for K' and J'_{ps} alone was reset, a real solution may not exist for

equation 7.33 if G' is small relative to K' . Consequently, a scheme for specifying load reversals must be adopted that ensures the relative magnitudes K', G', J'_{qv} , and J'_{ps} are always consistent. The approach adopted for the analysis of the Elstow excavation is described in section 8.8.

7.5.4 Selection of input parameters

As the model relies on the basis of the relationship between stiffness and incremental strain energy. This relationship had to be determined for each of the four stiffness moduli shown in equation 7.11 such that:

$$K', G', J'_{qv}, J'_{ps} = f(U) \dots\dots\dots (7.39)$$

The stiffness parameters were determined from the triaxial stress path tests described in Chapter 6. Several techniques for mathematically defining the tangent stiffness non-linearity were investigated, as described in sections 5.6.1 and 5.6.2, and an example plot of stiffness versus incremental strain energy, in which the non-linearity is described by a polynomial on a natural logarithmic scale, is shown in Figure 7.5. The experimental data in the figure come from path 12 in stress path test T06 (see Figure 6.35).

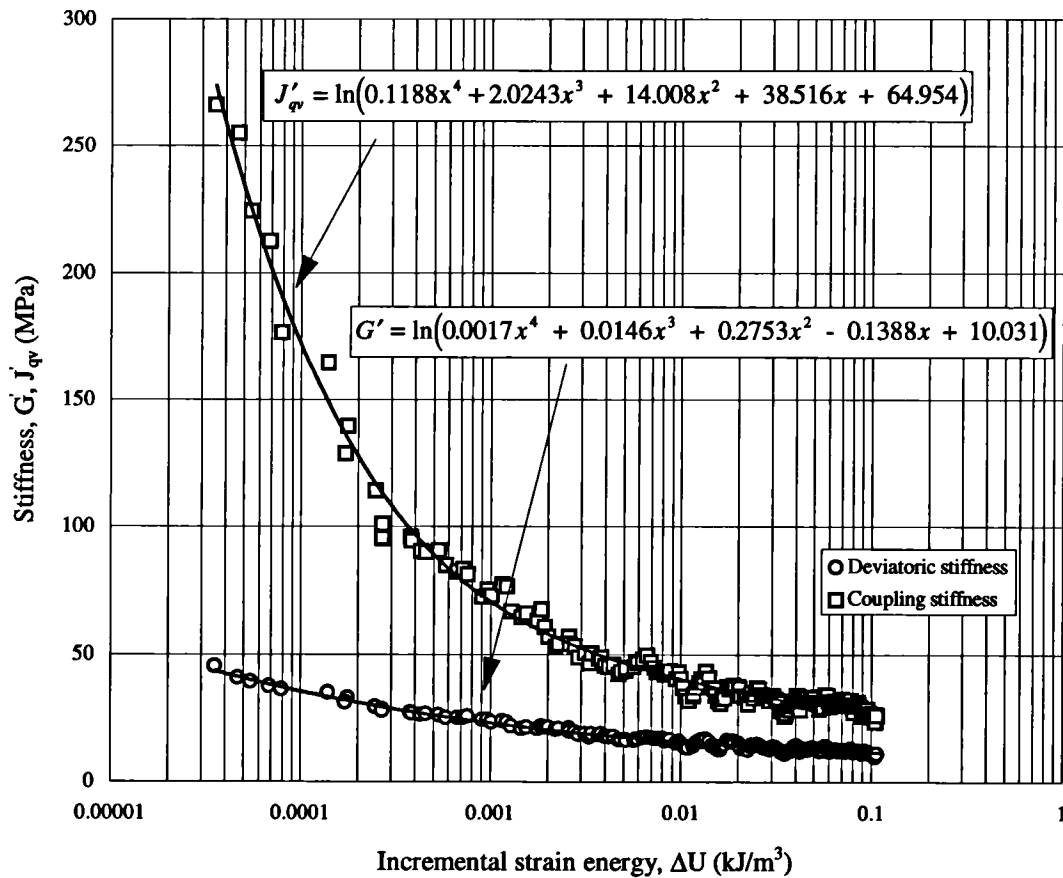


Figure 7.5 - Typical non-linear stiffness variation showing form of strain energy relationship

To form an elastic constitutive matrix, the coupling between volumetric and deviatoric responses must be represented by a single parameter (J'). This is calculated from the upper and lower bound coupling stiffnesses as shown in equation 7.40.

$$J' = J'_{ps} + \beta(J'_{qv} - J'_{ps}) \dots\dots\dots (7.40)$$

where, if the factor $\beta = 0$, $J' = J'_{ps}$

and if $\beta = 1$, $J' = J'_{qv}$

The value of β may be entered directly or, alternatively, may be calculated automatically from the current stress path direction as shown in Figure 7.6. However, it is shown in section 7.6 that the value of β has relatively little influence on the deformation response.

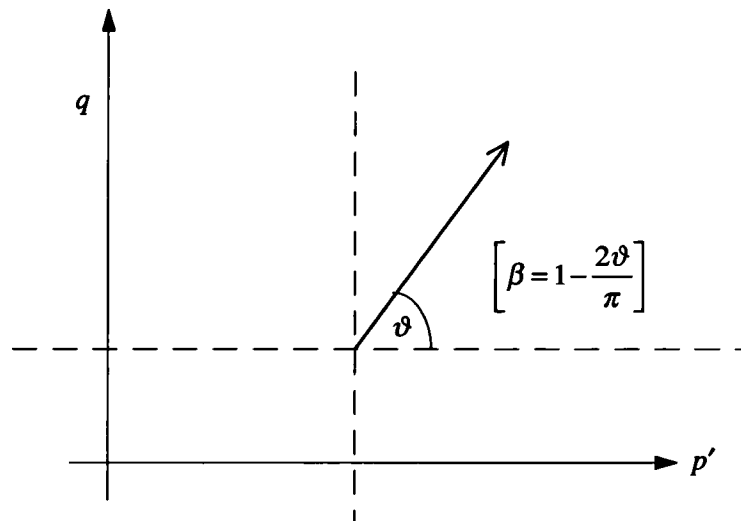


Figure 7.6 - Automated calculation of β to imply an elastic coupling stiffness

Although the natural variability of soil requires a certain level of redundancy in the determination of soil properties, in principle it is possible to determine all the parameters for this model from a single triaxial test using the multi-stage testing techniques described in section 5.3.2. Local instrumentation should be considered essential to capture the small strain response.

7.5.5 Implementation into finite element code

This model (Model OC) has been incorporated into the finite element program CRISP (Britto and Gunn, 1987). Full details of the implementation into the finite element code are given in Pierpoint (1996a) and Figure 7.7 shows a flow chart summary of the model operation.

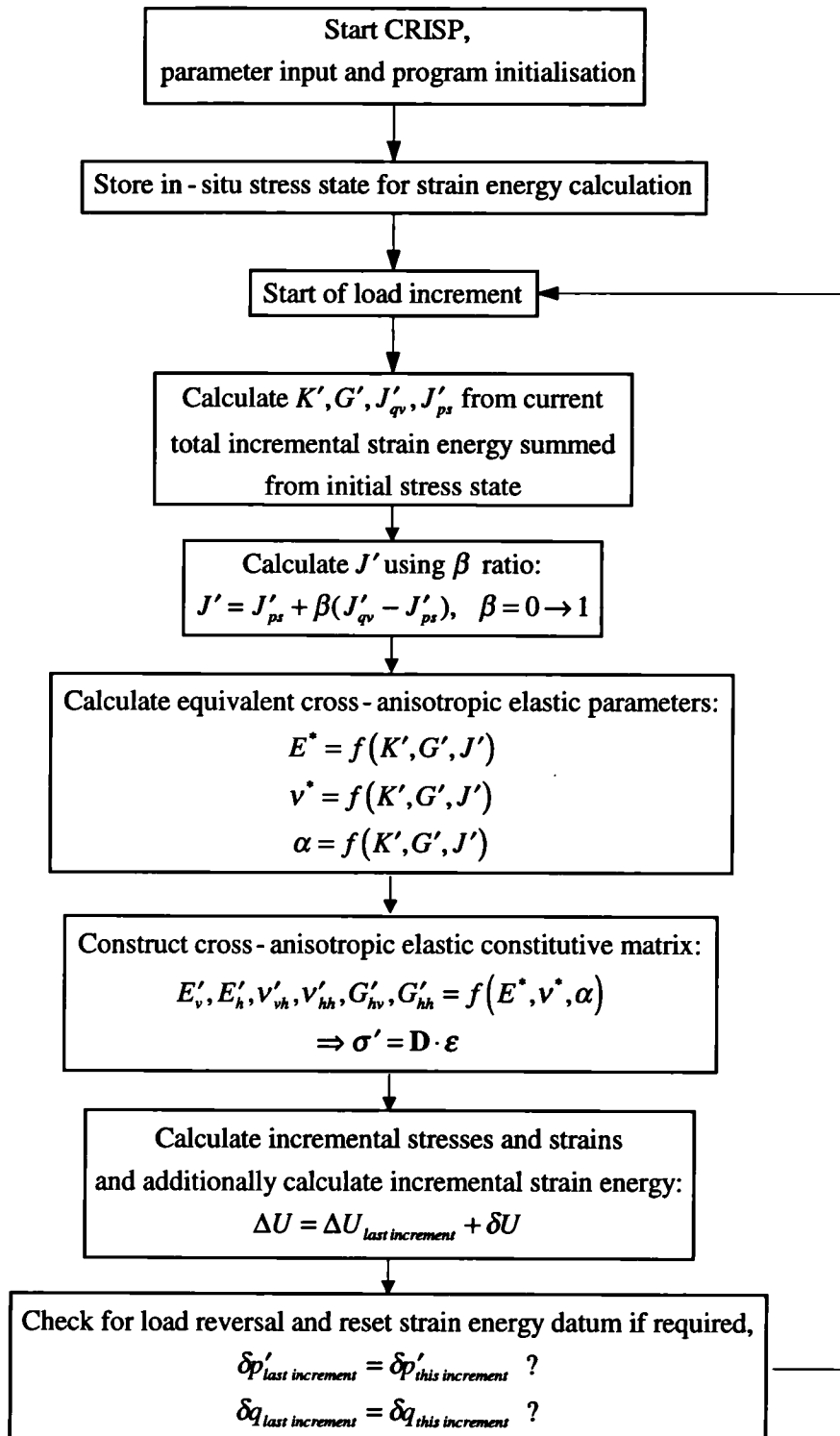


Figure 7.7 - Flowchart for 'Model O.C.'

7.6 Model validation

Aspects of validation include the checking of the correctness of computation and the checking of model performance against test data.

In addition to implementing the model into finite element code, the model has been implemented in a simplified form for analyses which do not warrant the sophistication of the finite element method. The program SingleCell calculates the response of a unit element under uniform stresses and strains in triaxial stress space, essentially solving equation 7.11 incrementally using tangent stiffnesses. This has been used to perform checks on the validity of the response of the CRISP implementation.

SingleCell is written in Microsoft VisualBasic for Applications and is linked to a series of Microsoft Excel for Windows spreadsheets. Figure 7.8 shows an example of a screen display. A stress path may be specified as a straight line from the initial to the final stress state, or as a series of stress increments to define an incrementally non-linear stress path. The material non-linearity is specified by selecting either a 'loading' or an 'unloading' condition for each of the stiffness moduli as required. Since the solution algorithm is not extended to general stress states, the solution procedure is straightforward and the requirement of specifying a symmetrical constitutive matrix is not a limitation. The program has therefore been used to investigate the influence of the form and degree of cross-coupling on the response of the triaxial specimens in the experimental programme.

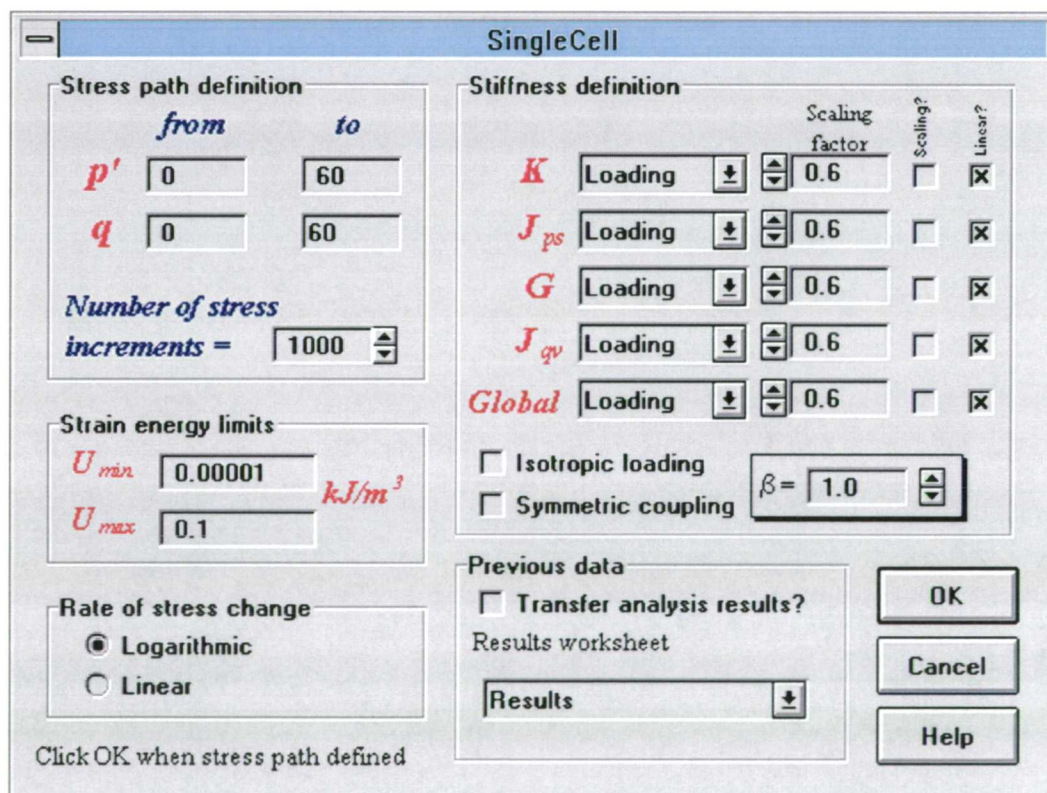


Figure 7.8 - SingleCell for Microsoft Windows 3.1

Initially, the model was tested to ensure that linear elastic model results could be duplicated; this was essentially to check that the constitutive matrix was correctly formulated. To check that the model behaviour could be strain dependent, analyses were then carried out using a simple stepped stiffness curve for which hand calculations could be compared.

A constant q and a constant p' stress path were simulated for triaxial conditions with CRISP using a suitably fine mesh (200 elements), although a single element would have been sufficient. These analyses incorporated stiffness non-linearity recorded in specific stress paths from the experimental programme, enabling the results of the analyses and the experimental data to be compared directly. This checked that the element response was identical to that intended. These analyses were also carried out with the SingleCell program and, as expected, produced identical results.

The stiffness parameters obtained from the constant p' and constant q triaxial stress paths must be capable of representing behaviour along more general stress paths. Two diagonal stress paths were incorporated into the experimental programme to provide data for validation purposes. They were included as part of tests T03 and T06 described in Chapter 6 and are shown in Figure 7.9. In both cases the stiffness non-linearity was determined from the stress-strain curves of two constant p' stress paths and one constant q stress path. The diagonal stress paths were designed to have gradients in total stress space of 2:1 for test T03 and 1:1 for test T06. Within each test all these paths originated from the same stress point, had identical approach paths and involved similar holding periods at the beginning (see section 6.3.3). The tangent stiffness response was evaluated for each path (see section 5.6.2) and described mathematically in terms of the total incremental strain energy. Since strain energy is less familiar than either deviatoric or volumetric strain, a comparison of these parameters for the validation stress paths is shown in Figure 7.10. The tangent stiffness parameters assumed for the validation analyses are given for test T03 and test T06 in Figure 7.11 and Figure 7.12 respectively. These figures each include a family of J' curves which represent the variation of the elastic coupling stiffness between the upper and lower bound specified by J'_{qv} and J'_{ps} respectively; the curves are generated by putting $\beta = 0, 0.1, \dots, 0.9, 1.0$ in equation 7.40.

Although the stress paths were carried out at a rate designed to ensure fully drained conditions within the specimen, an increase of pore water pressure was evident, particularly in the early stages of test T06 (see section 6.4.7). To allow for this effect, the actual non-linear effective stress path for each test was modelled directly. The use of a mid-height pore water pressure probe allowed the accurate determination of the pore water pressure within the central region of the specimen. The deviation of the actual and intended drainage conditions was tolerated in view of the exceptionally long test times that would have been necessary to eradicate it.

For each diagonal stress path, five validation analyses were carried out. All the analyses incorporated non-linearity but the form and degree of deviatoric and volumetric coupling varied in each case.

- a) *Non-linear isotropic elasticity*: the coupling stiffness, J' , in equation 7.12 was set to a suitably high value (1×10^{20} MPa) effectively eliminating any coupling.
- b) *Non-linear cross-anisotropic elasticity*: $J' = J'_{qv}$, i.e. the coupling stiffness set at the upper bound of the experimental response.
- c) *Non-linear cross-anisotropic elasticity*: $J' = (J'_{ps} + J'_{qv})/2$, i.e. the coupling stiffness was set at the average experimental response.
- d) *Non-linear cross-anisotropic elasticity*: $J' = J'_{ps}$, i.e. the coupling stiffness was set at the lower bound of the experimental response.

- e) *Non-linear cross-anisotropic non-associated plasticity*: $J'_{qv} \neq J'_{ps}$, i.e. the constitutive matrix is not symmetric such that the coupling between deviatoric stresses and volumetric strains is not the same as between volumetric stresses and deviatoric strains. This analysis could not be carried out in CRISP due to the solution technique requiring a symmetric matrix and so was only performed using SingleCell.

For test T03, the computed and measured strains for the diagonal path are compared in Figure 7.13 and Figure 7.14 where strain is plotted versus change of deviator stress and effective mean normal stress respectively. These results are presented in terms of the strain path in Figure 7.15. Similarly for test T06 these comparisons are shown in Figure 7.16, Figure 7.17 and Figure 7.18 respectively.

The cross-anisotropic model predictions (cases b, c, and d) are reasonably close to the experimental data and a significant improvement on the isotropic elastic prediction (case a). It can be seen that the model response is relatively insensitive to variation in the coupling stiffness for values of J' ranging between J'_{ps} and J'_{qv} . For test T03 there is practically no variation between the anisotropic analyses. For both test T03 and test T06, the inelastic analysis (case e) generally lies within the stress-strain response of the elastic analyses but is able to provide a marginally closer fit to the data at small strain levels (see for example Figure 7.18). The improvement in the prediction, however, is slight, and the simpler elastic analyses produce acceptable results.

The relations of equation 7.31, describing the anisotropy factor, α , and Poisson's ratio, ν^* , being quadratic, have two roots. One of these solutions must be disregarded since it represents impossible material properties, e.g. a negative value of α can produce a negative value of G'_{hv} . The variations of E^* , ν^* , and α , and the implied cross-anisotropic elastic parameters, with incremental strain energy are shown in Figure 7.19 and Figure 7.20 for test T03 and test T06 respectively. In these figures cross-anisotropic elastic analyses are presented in which the coupling stiffness is varied within the experimental range ($\beta = 0, 0.1, 0.2, \dots, 0.9, 1.0$).

The analysis with $\beta = 0$ for test T06 produces numerical instabilities in the solutions for α and ν^* ($= \nu'_{hh}$) at small strain energy levels ($< 0.0001 \text{ kJ/m}^3$) which have been removed from Figure 7.20.

It is seen that, particularly in test T06, there is significant variation in the elastic parameters over the range of coupling stiffness which would cause concern were it not for the associated small variations in the resultant stress-strain response. A feature of the test T06 cross-anisotropic parameters is that the implied Poisson's ratio is generally negative. This is both unfamiliar and unrealistic and is probably the consequence of attempting to model inelastic behaviour within an elastic framework.

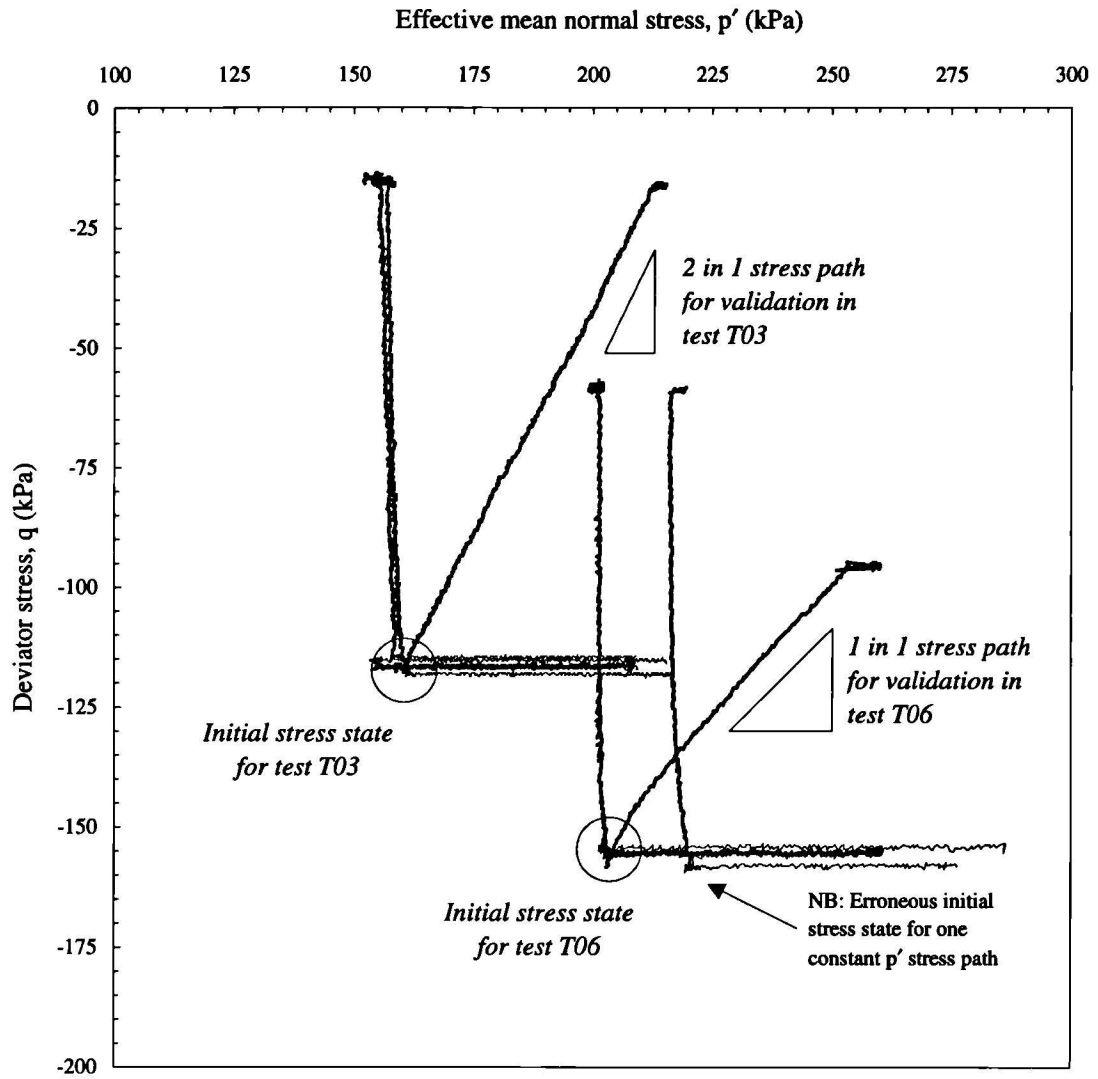


Figure 7.9 - Stress paths from test T03 and test T06 used for model validation analyses

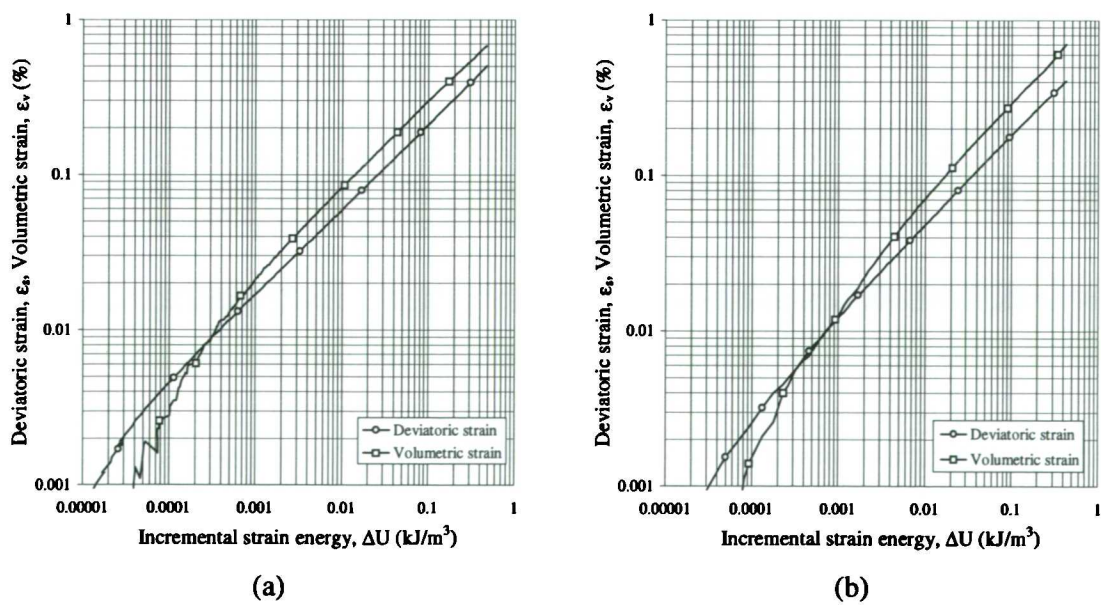


Figure 7.10 - Relationship between incremental strain energy and deviator strain and volumetric strain in (a) test T03 and (b) test T06

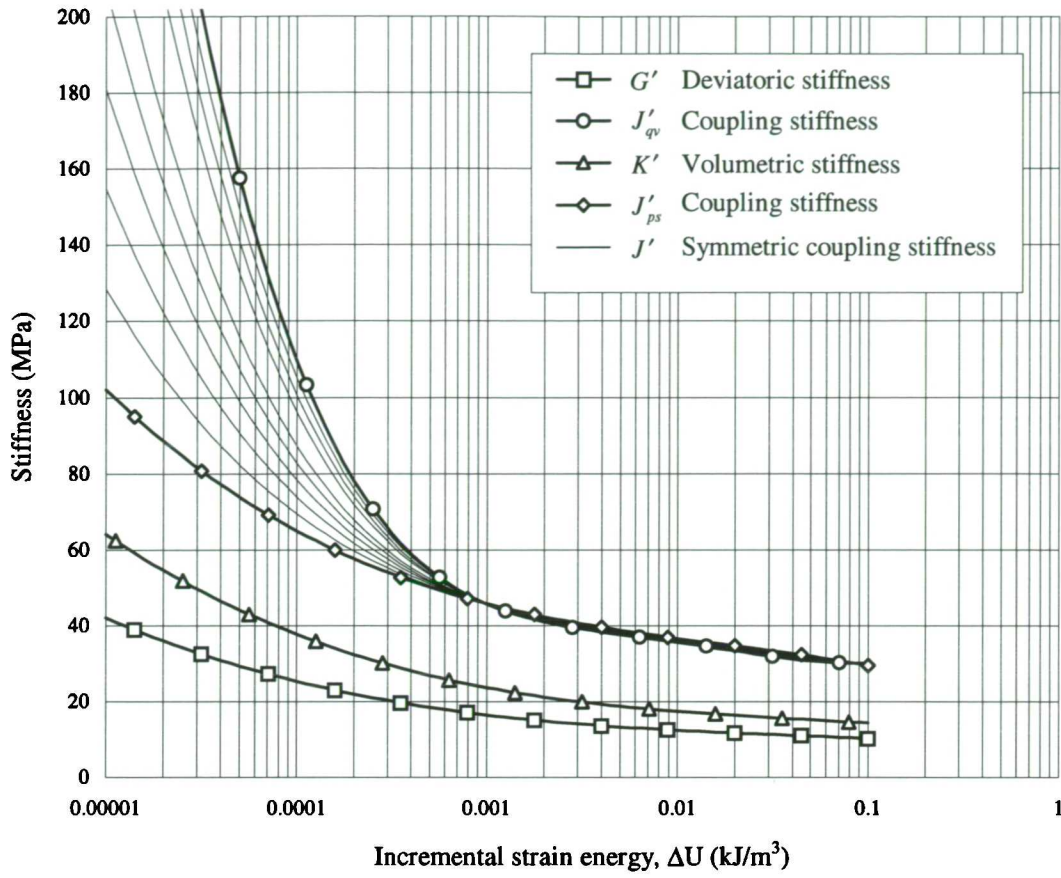


Figure 7.11 - Stiffness response of test T03 used for model validation analyses

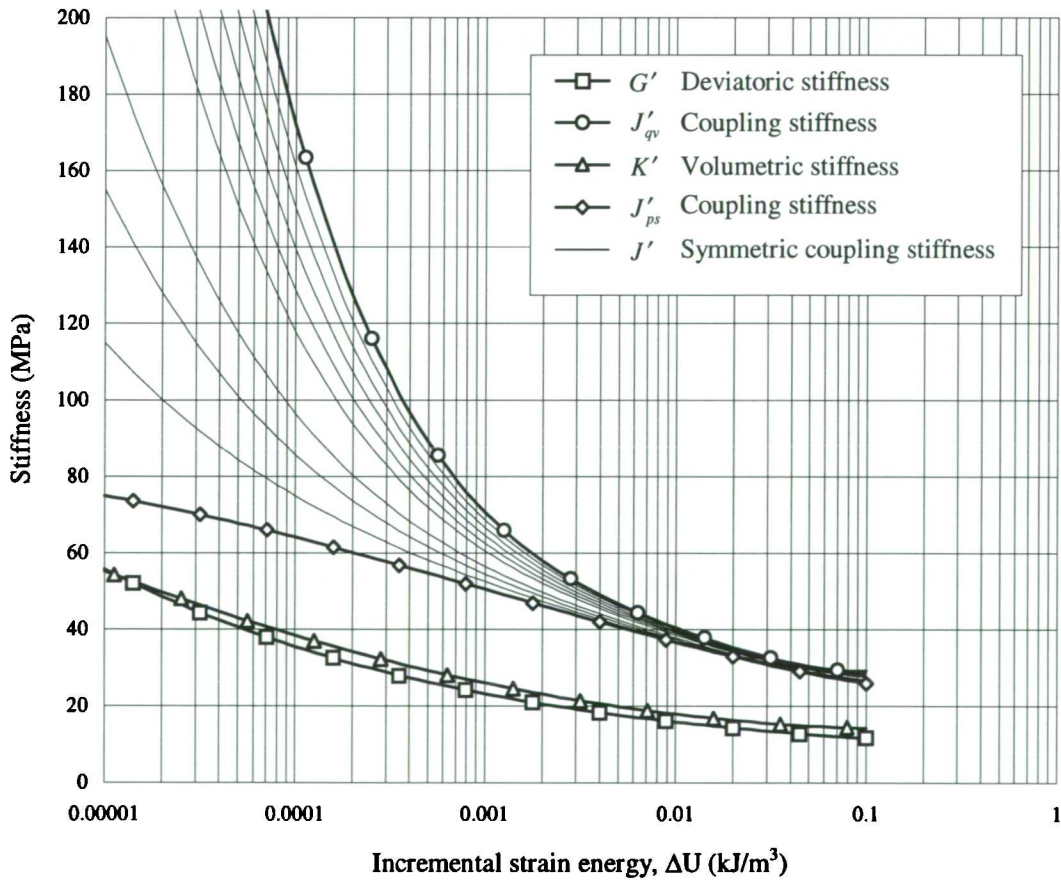
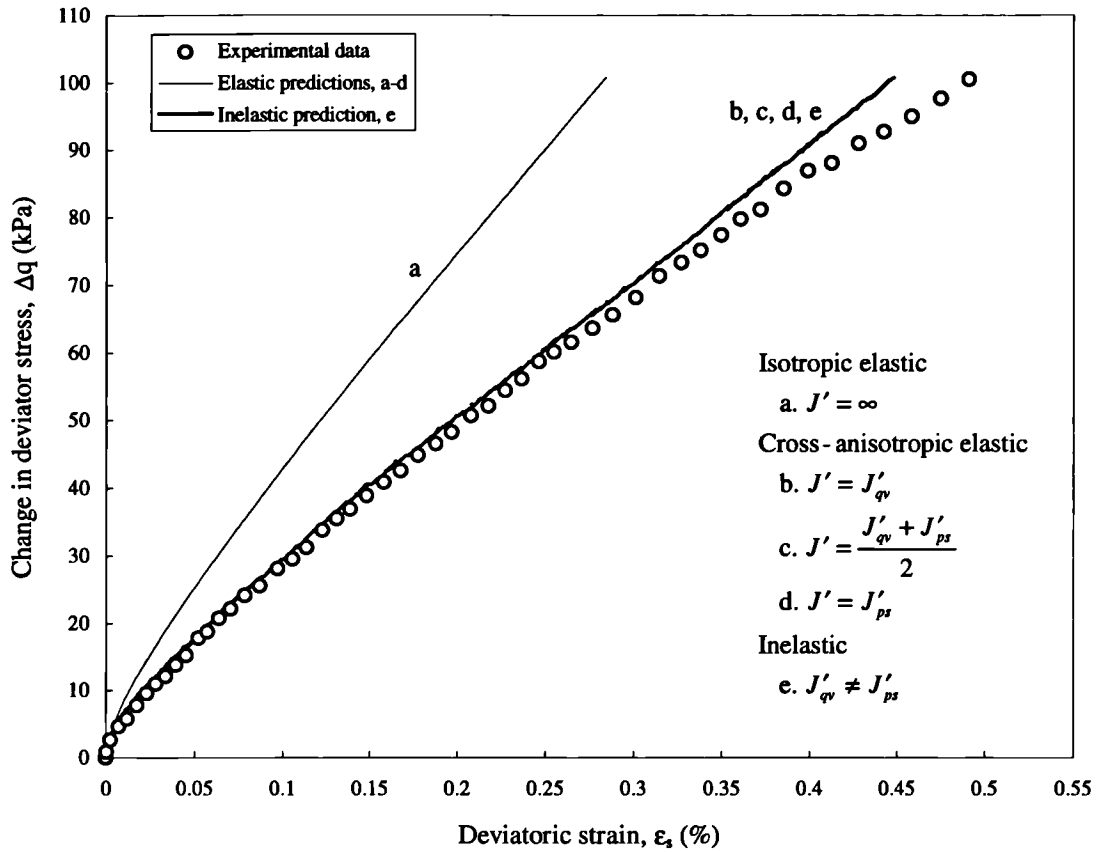
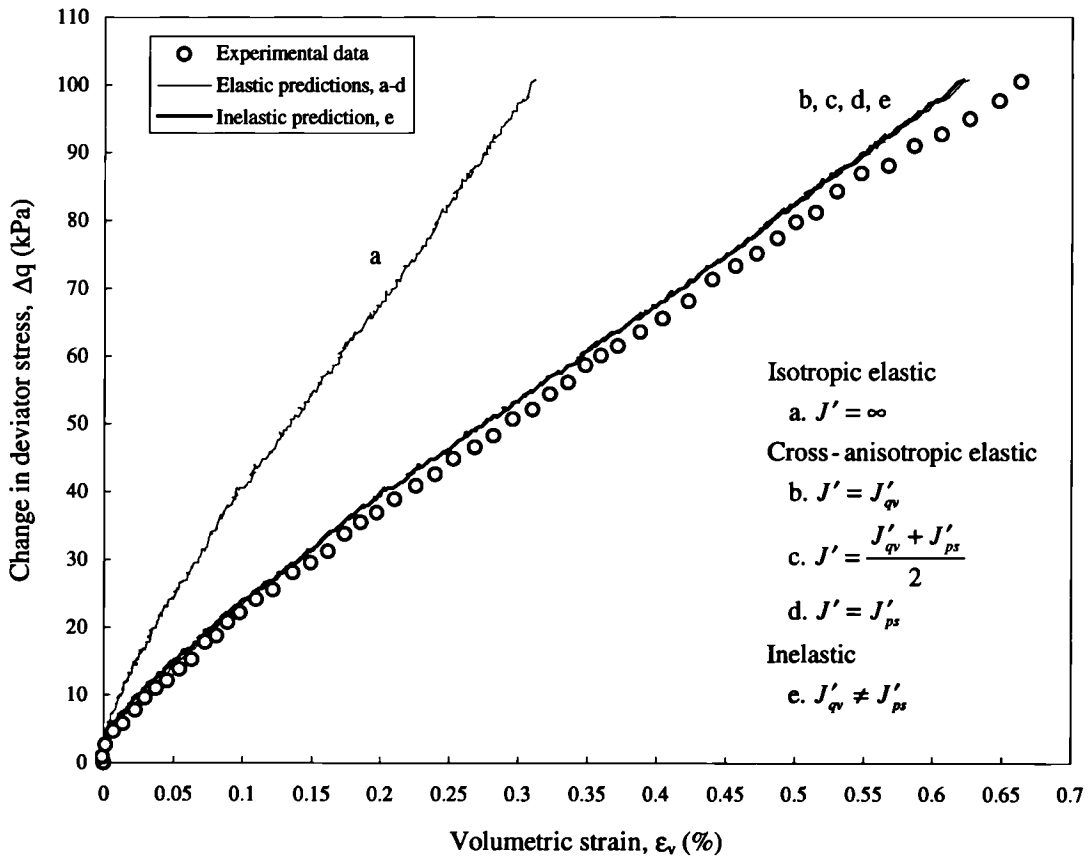


Figure 7.12 - Stiffness response of test T06 used for model validation analyses

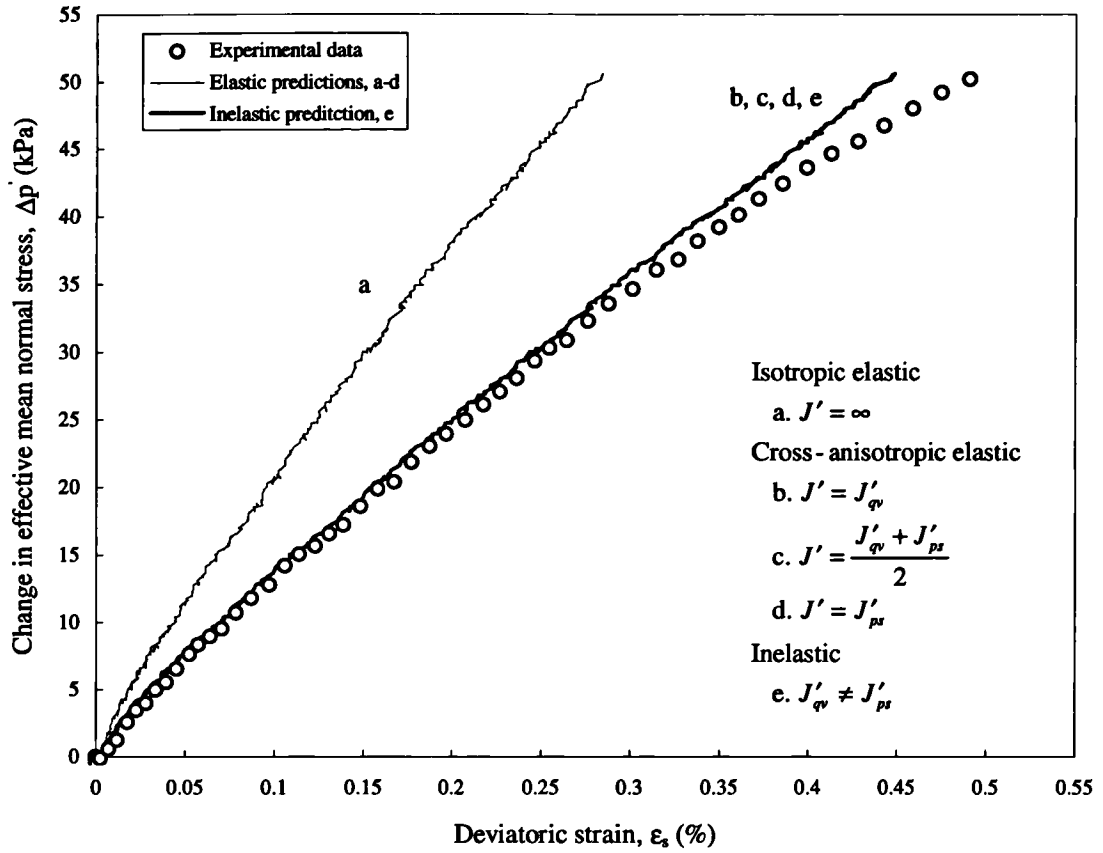


(a)

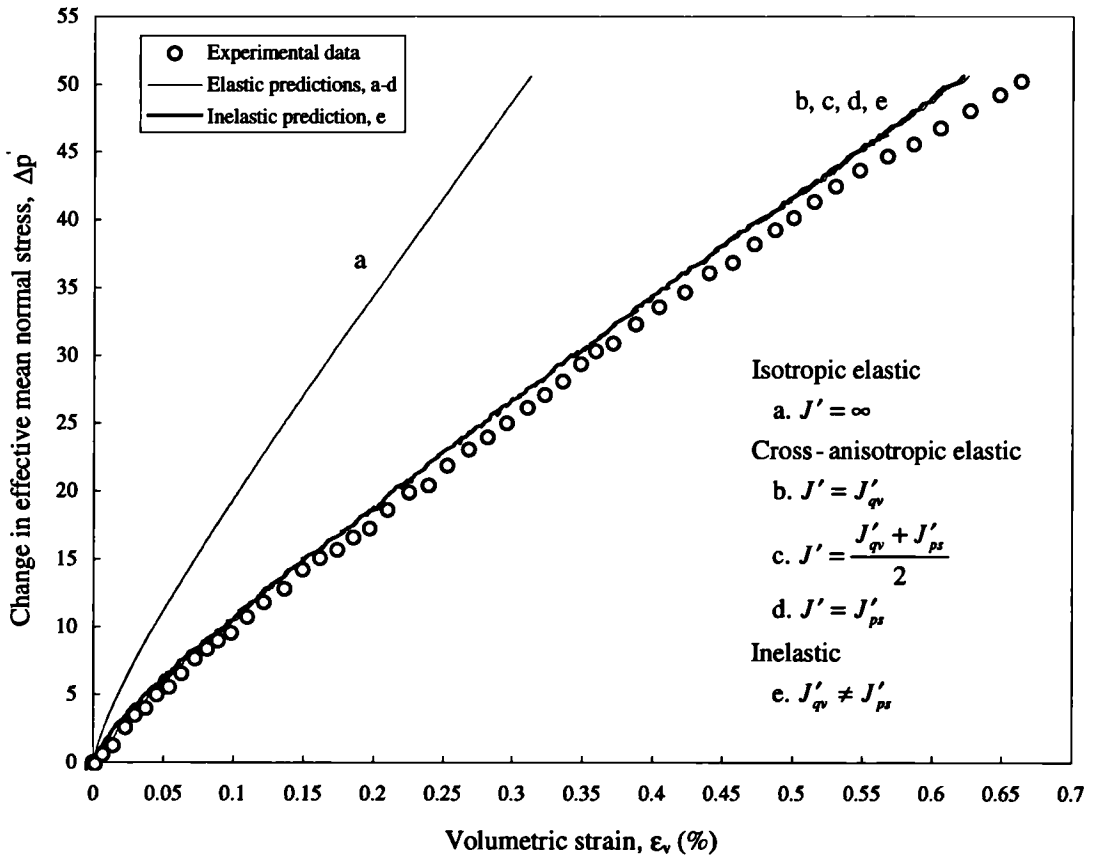


(b)

Figure 7.13 - Deviatoric and volumetric response due to change in deviator stress along diagonal validation stress path in test T03



(a)



(b)

Figure 7.14 - Deviatoric and volumetric response due to change in effective mean normal stress along diagonal validation stress path in test T03

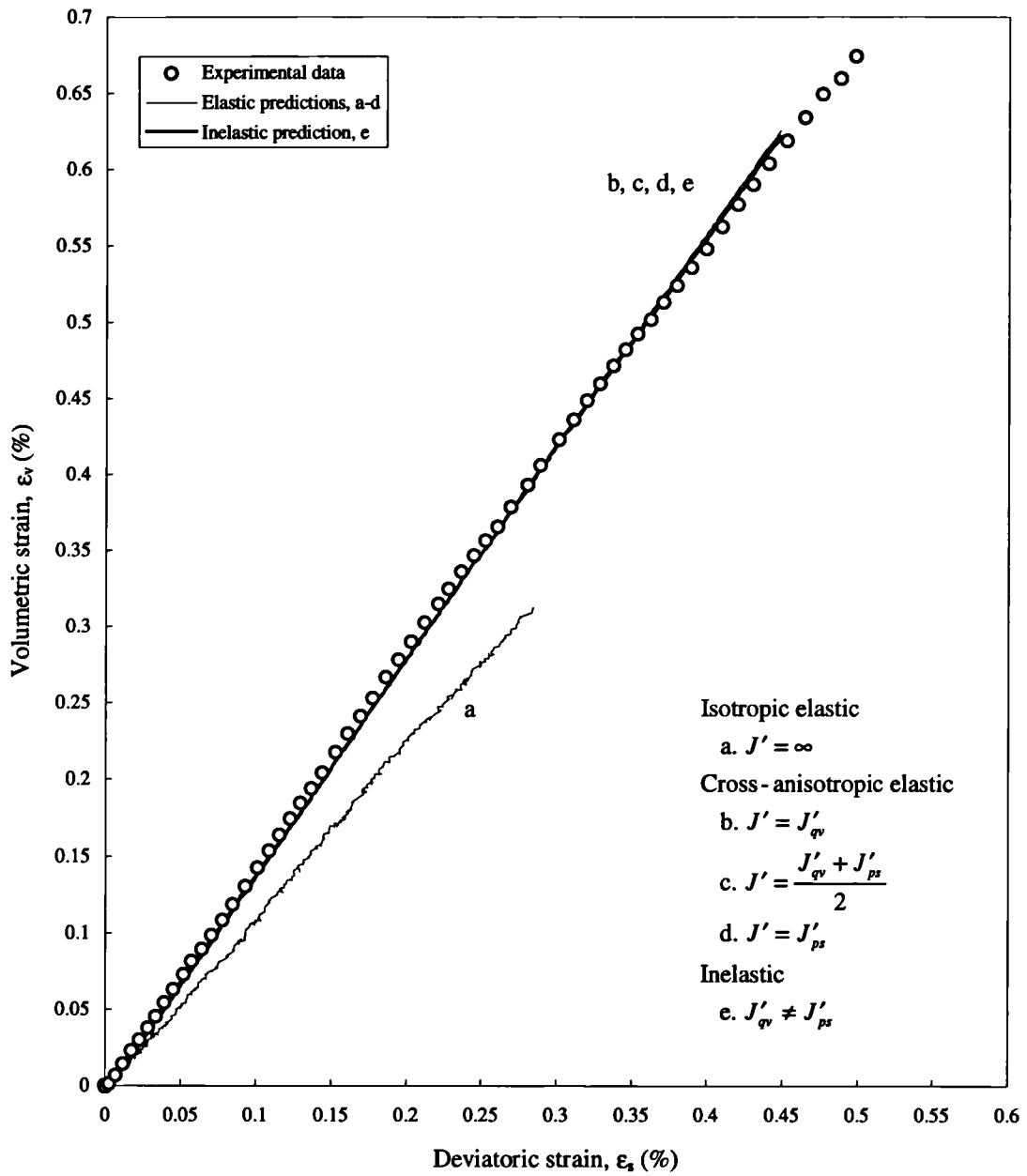
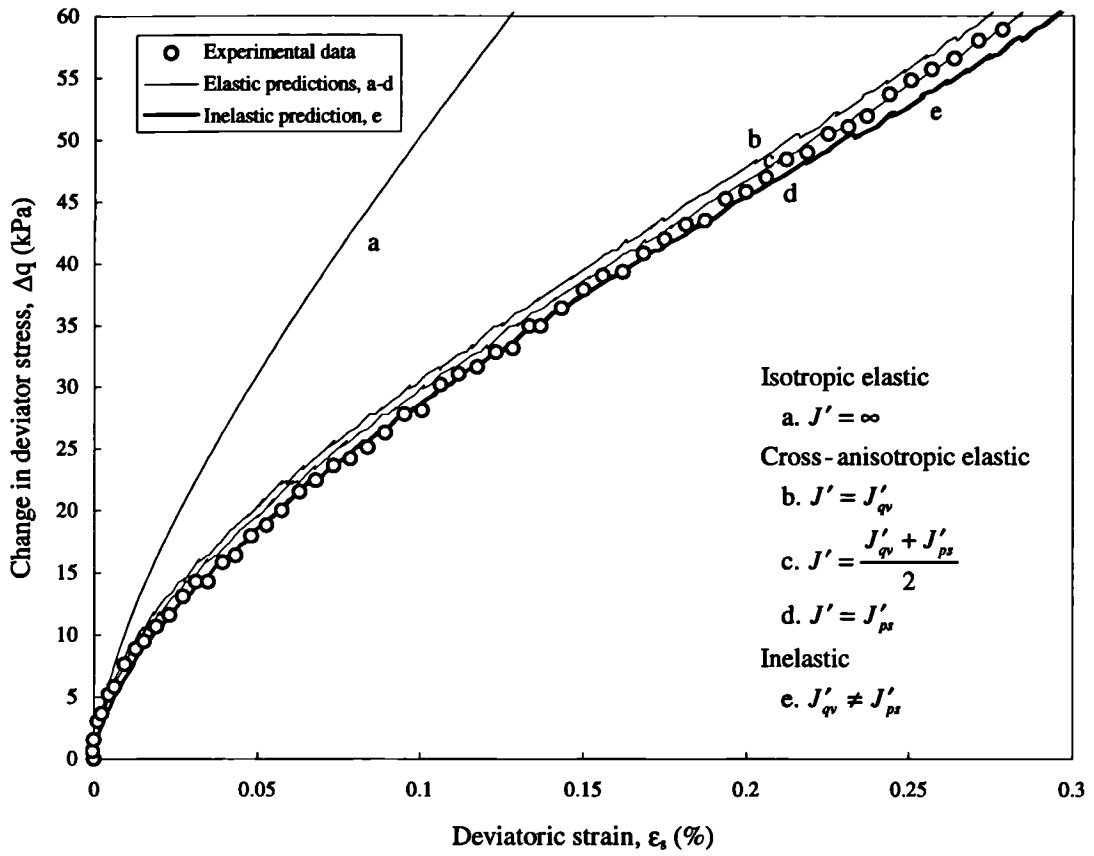
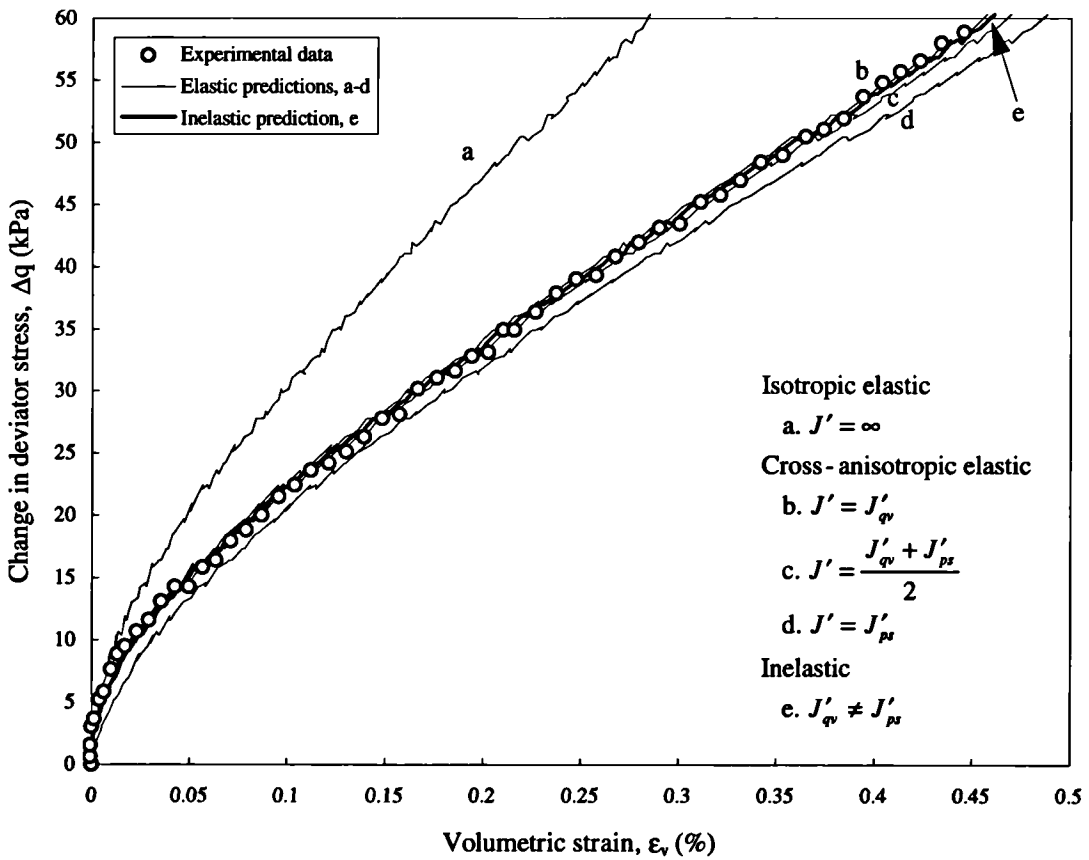


Figure 7.15 - Strain path response along diagonal validation stress path in test T03

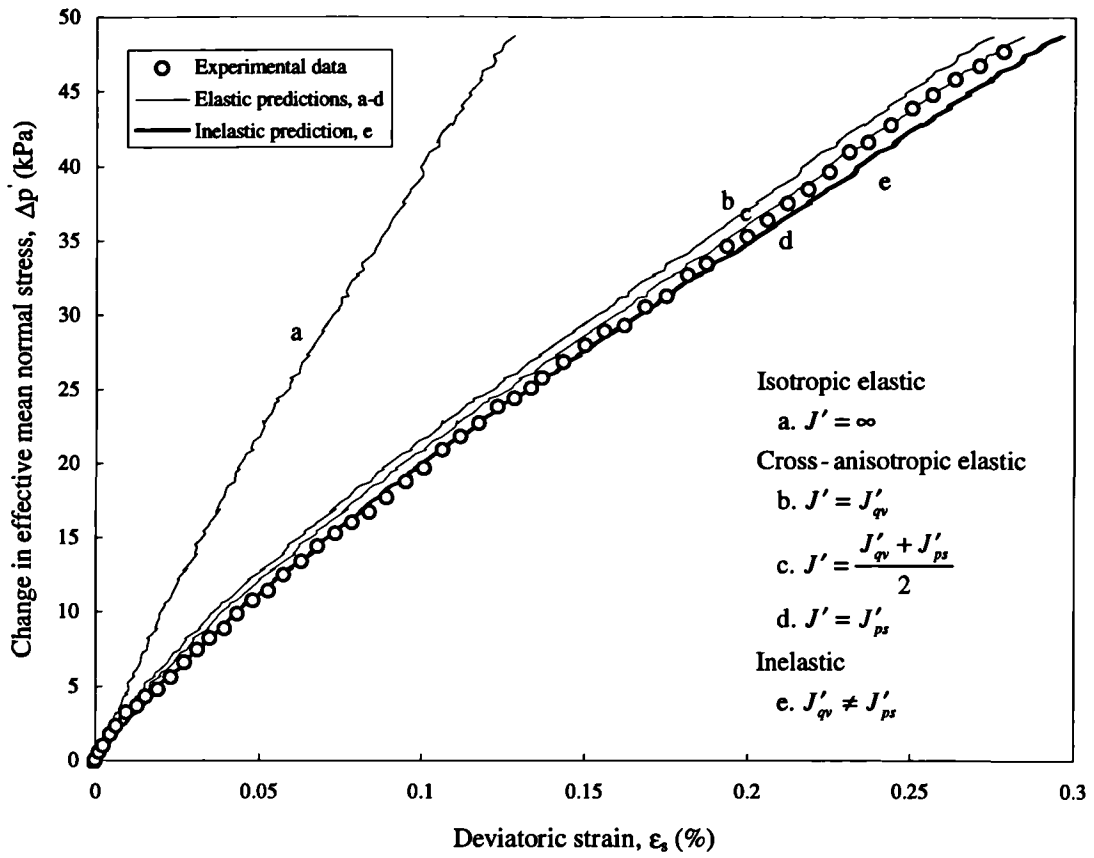


(a)

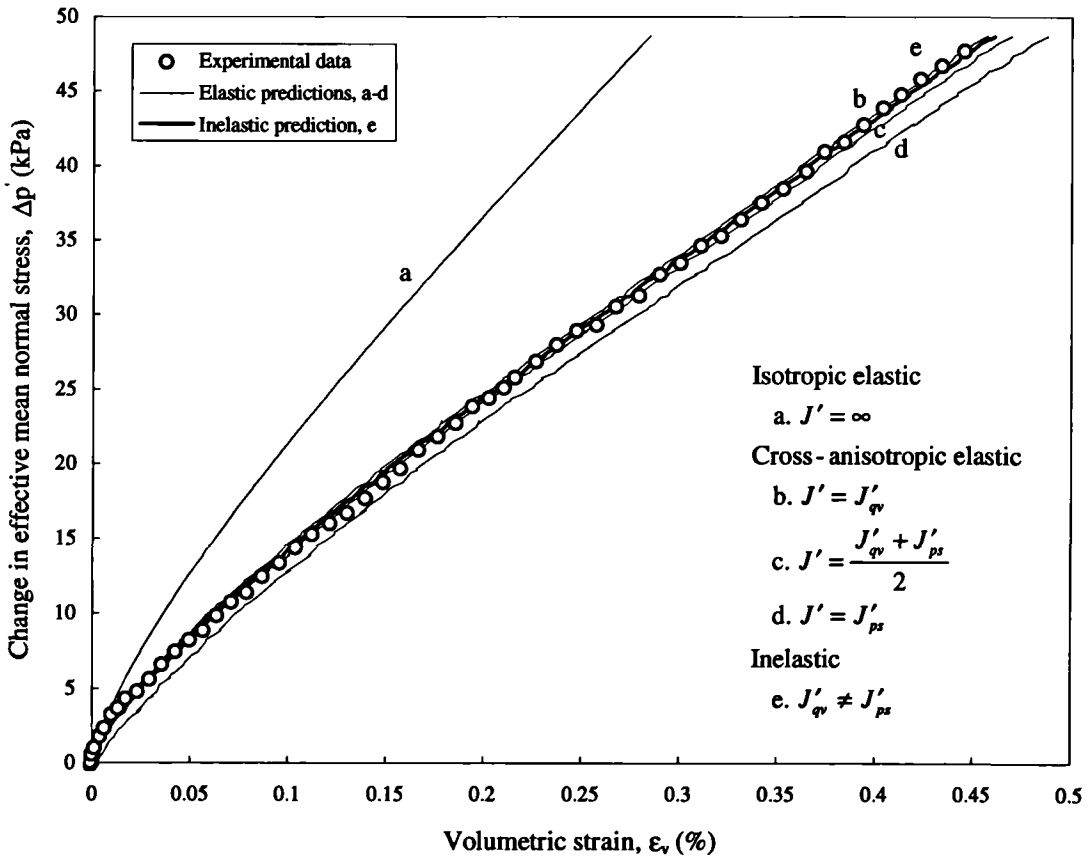


(b)

Figure 7.16 - Deviatoric and volumetric response due to change in deviator stress along diagonal stress validation stress path in test T06



(a)



(b)

Figure 7.17 - Deviatoric and volumetric response due to change in effective mean normal stress along diagonal validation stress path in test T06

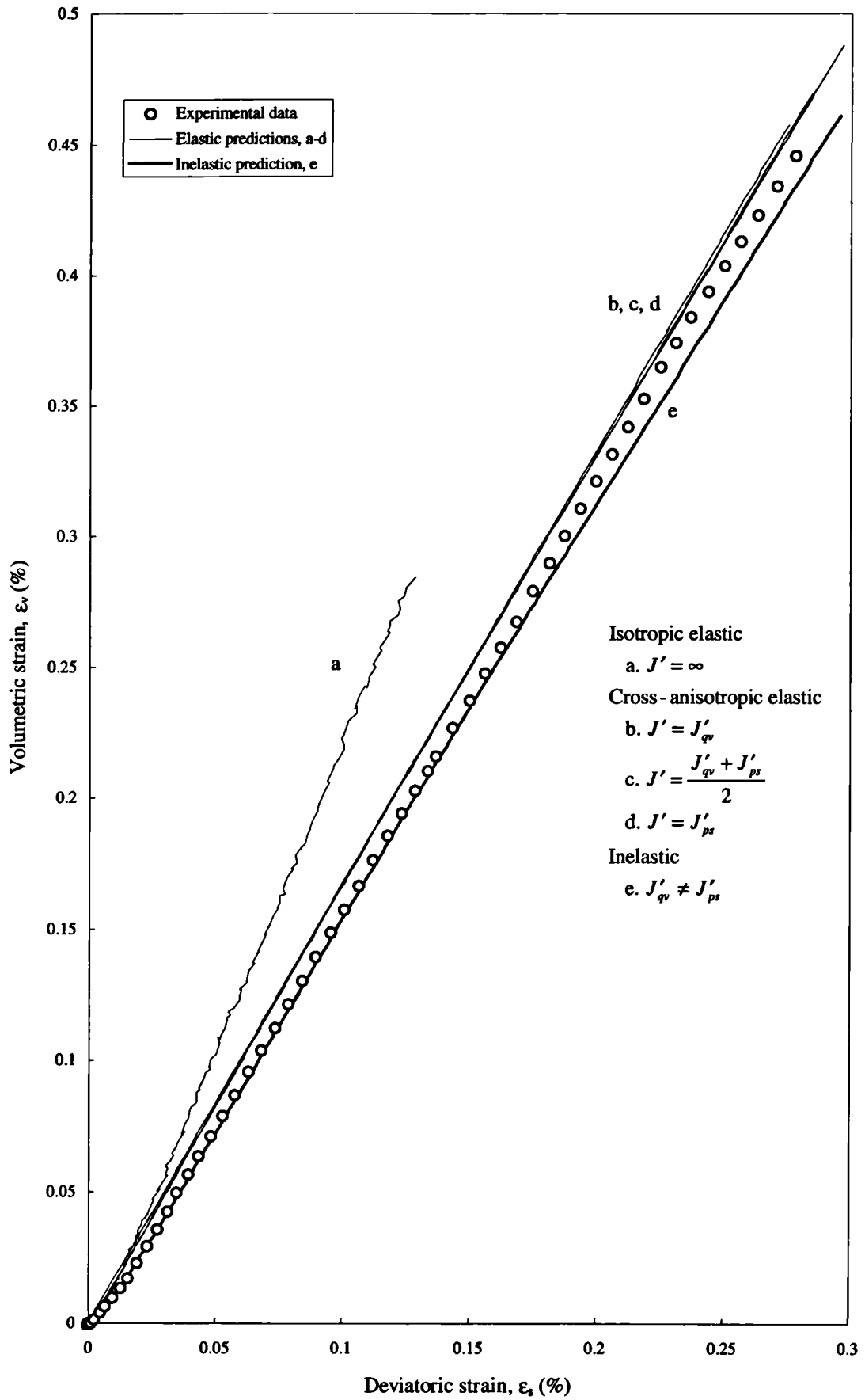


Figure 7.18 - Strain path response along diagonal validation stress path in test T06

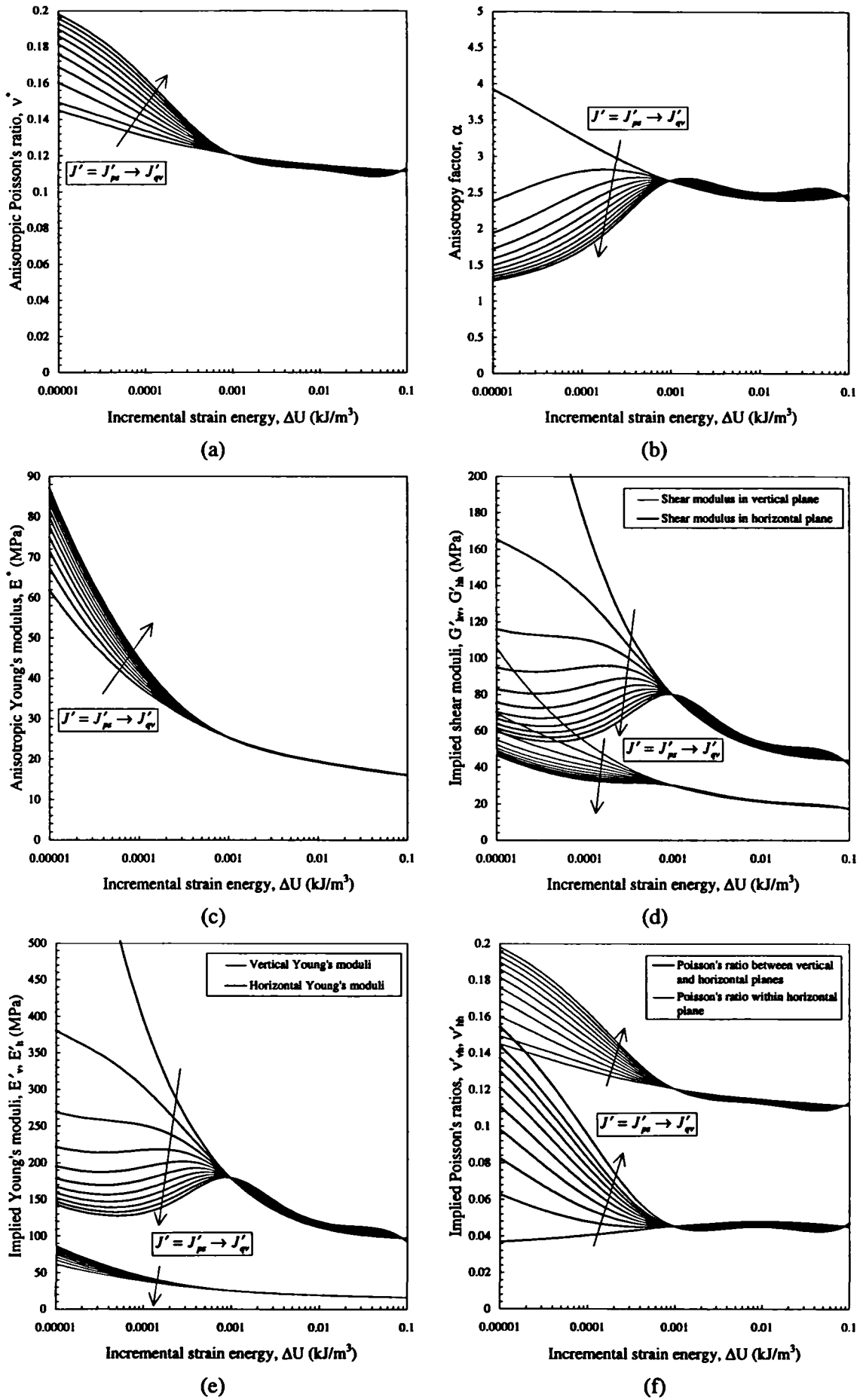


Figure 7.19 - Cross-anisotropic elastic parameters implied from test T03

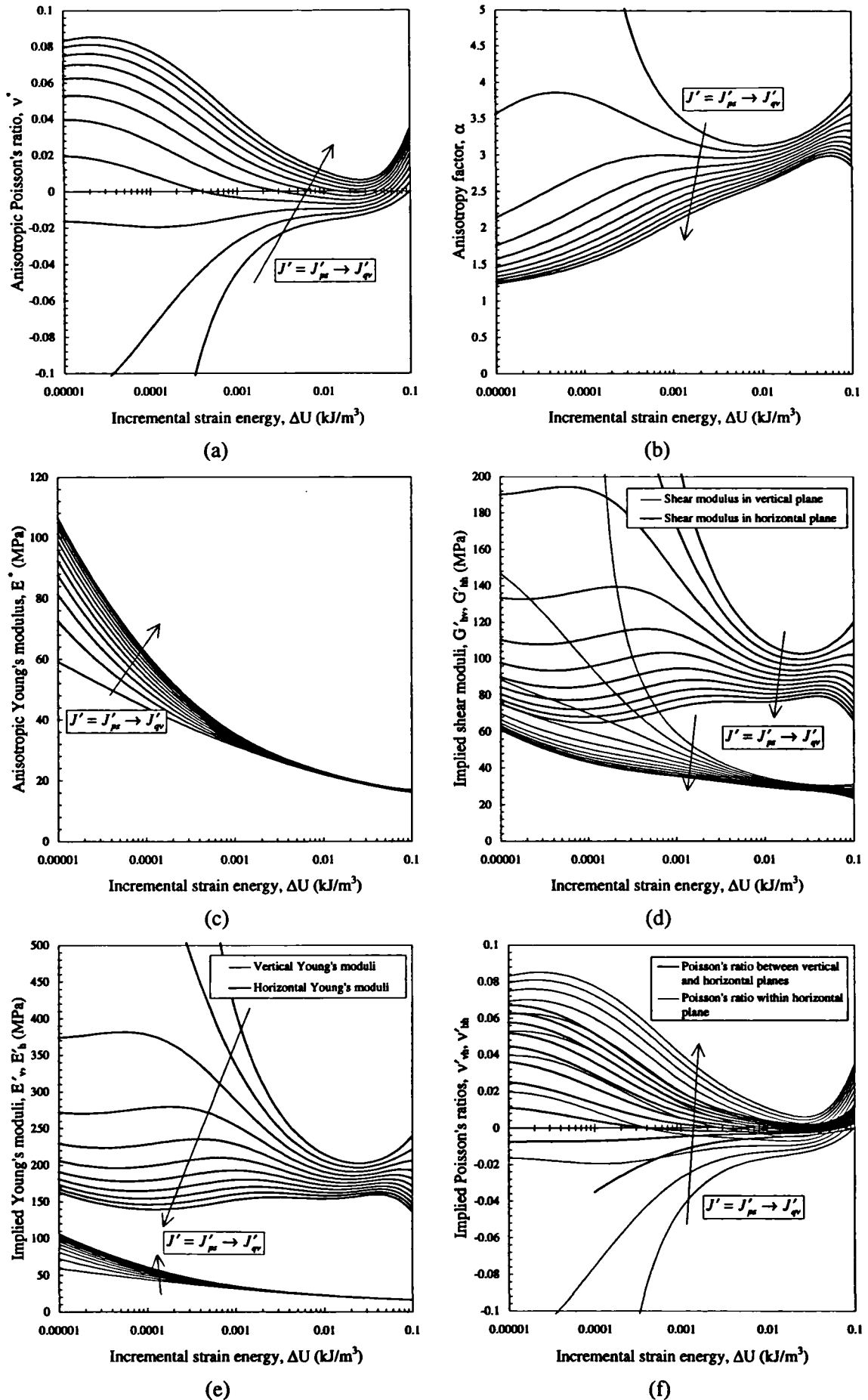


Figure 7.20 - Cross-anisotropic elastic parameters implied from test T06



8. Numerical modelling of Elstow excavation

8.1 Introduction

One of the primary goals of the research described in this thesis was to predict the ground behaviour at the Elstow site in response to the construction of the trial excavation. The Elstow excavation has been described in Chapter 3, and the interpreted ground response has been presented in Chapter 4. This chapter reports a prediction of the excavation behaviour using the non-linear cross-anisotropic elastic model described in Chapter 7, and parameters derived from the experimental results presented in Chapter 6.

An initial suite of numerical analyses was performed at the time of the excavation and these analyses are briefly reviewed. In these analyses stiffness non-linearity and linear cross-anisotropic elasticity were separately incorporated. It was necessary to repeat these initial analysis stages both to check the reliability of the new model and to ensure a consistent development of the modelling process.

As described below, the modelling process developed as increasing degrees of sophistication were incorporated into the analysis as follows:

1. Linear isotropic elasticity
2. Non-linear isotropic elasticity
3. Linear cross-anisotropic elasticity
4. Non-linear cross-anisotropic elasticity

The influence of the stress path direction is discussed both in terms of the previous stress path experienced prior to the *in situ* state, and the effect of reversals in the direction of loading caused by excavation. The influence the method of modelling the excavation sequence is also discussed.

Consolidation analyses of the excavation were not performed, but the influence of the degree of drainage in the Oxford Clay was investigated by varying the bulk modulus of water.

At each stage the efficacy of the finite element solution was dependent on a number of factors. The factors considered were the extent of the finite element mesh, the mesh discretisation, and the number of load increments used to describe the non-linearity.

After an initial attempt had been made at predicting the ground response due to excavation, the site instrumentation data were analysed. The comparison of the numerical prediction with the actual excavation response is discussed and is followed by an account of parametric studies performed on certain parameters controlling the model behaviour. An attempt was finally made to obtain a best fit to the instrumentation data by optimising the input parameters.

8.2 Previous modelling of the Elstow excavation

As part of the initial site investigation, a number of numerical analyses of the excavation were carried out using a modified version of CRISP (Mott MacDonald, 1987). These early analyses were used to provide an estimate of the ground displacements and the likely changes in pore water pressure, to aid in the positioning of the instrumentation (see section 3.6). It was envisaged that following excavation, once the actual ground response had been recorded, a back-analysis of the ground behaviour would be carried out to establish material parameters which could be used for the analysis of future structures on the site. This back-analysis had not been carried out, however, before the site investigation works were cancelled.

A series of linear isotropic elastic analyses was performed, but it was soon concluded that the soil's non-linearity and anisotropy had a significant effect on the ground behaviour. The CRISP program was therefore modified to incorporate the stiffness non-linearity of the Oxford Clay. A simple power law was incorporated to represent the incremental stress-strain response of an isotropic elastic material as shown in equation 8.1.

$$\Delta\sigma_1 - \Delta\sigma_3 = k\varepsilon^n \quad \dots\dots\dots (8.1)$$

where, k and n are material properties

This analytical model was fitted to triaxial test data of deviator stress against axial strain such that,

$$\Delta q = k\varepsilon_a^n \quad \dots\dots\dots (8.2)$$

and the tangential Young's modulus could therefore be related to the current strain level using equation 8.3.

$$E = \frac{\delta q}{\delta \varepsilon_a} = nk\varepsilon_a^{n-1} = \frac{nk}{\varepsilon_a} \quad \dots\dots\dots (8.3)$$

The stiffness was also normalised with respect to the undrained shear strength such that, if the undrained shear strength was modelled as increasing with depth, the soil stiffness correspondingly increased with depth.

The post peak strain softening response associated with the Oxford Clay was considered to be of secondary importance, and was consequently ignored in favour of modelling the clay as perfectly plastic with a Tresca yield criterion, with yield corresponding to the undrained shear strength of the soil.

The material parameters required to define the model were derived from a number of sources:

- For the Oxford Clay and near-surface deposits, the non-linear stress-strain response was obtained from the series of consolidated undrained small strain triaxial tests performed on vertical specimens from 6m depth, as described in section 6.2.

- The variation in undrained shear strength with depth was determined from both the conventional laboratory testing programme and from previous investigations in the area.
- *In situ* horizontal loading tests (Camkometer) described in section 3.4.3 containing unload-reload loops were used to assess the variation with depth of both the horizontal shear moduli and the undrained shear strength.
- In the strata below the Oxford Clay, only a very limited testing programme was carried out before the suspension of works. Information in the literature regarding the engineering properties of these layers was minimal and they were therefore modelled simply, using an isotropic linear elastic model. The stiffness parameters were determined from the unload-reload loops of the *in situ* horizontal loading tests. This resulted in a profile of increasing stiffness beneath the Oxford Clay down to the Blisworth Limestone. It was realised that the representation was fairly crude, but it was tolerated as deformations due to excavation were expected to be concentrated in the Oxford Clay.

It was originally hoped that the pressuremeter tests would provide a guide to the *in situ* stresses but, since they were apparently unsuccessful, a range of values for K'_o , between 1.8 and 2.4 was assumed, in line with values used for London Clay.

The Head material, the Oxford Clay, the Kellaways Clay and the Blisworth Clay were modelled as undrained; the Cornbrash and the Blisworth limestone strata were modelled as fully drained; the Kellaways Sand, being confined by the Oxford Clay above and the Kellaways Clay below, was assumed to be partially drained.

Comparison of these analyses with the instrumentation data available at that time showed that the displacements were generally overestimated. The horizontal displacements in particular were noted as exceeding the measured movements by up to 3 times.

A second set of non-linear analyses was then performed using the stiffness response for the Oxford Clay reported from the same series of small strain triaxial tests, but derived from the horizontally trimmed specimens. The small strain tests showed that specimens trimmed horizontally were initially stiffer (in terms of the undrained Young's moduli) by 2 to 4 times, and generally exhibited a more linear response than those trimmed vertically (see section 6.2.3). These analyses showed that, although the horizontal displacements could now be more accurately reproduced, the vertical displacements were significantly underestimated.

Thus, the inherent stiffness anisotropy of the Oxford Clay appeared to be having an important influence on the actual ground response due to excavation. A non-linear anisotropic model had not been incorporated into CRISP at that time, and further analyses were therefore performed with the available linear anisotropic elastic model. Although further analyses were limited by the suspension of the site investigation, a linear elastic anisotropic analysis, using secant stiffness values derived at 0.1% axial strain, representing a ratio of horizontal to vertical Young's moduli of 3, produced a displacement profile which was apparently much more in accord with the instrumentation results.

Although it would have been possible to optimise the linear cross-anisotropic elastic input parameters in the style of Cole and Burland (1972), the next logical step in the modelling process was to combine the effects of the anisotropy with the observed stiffness non-linearity.

Analyses were performed both with and without the plastic yield criterion and little difference between the results was found. It was also concluded that incorporating the effects of plasticity

had a relatively minor influence on the model performance. However, the role of plastic strains within the assumed yield surface could not be evaluated.

The following sections describe the work carried out as part of the present research in applying the model described in Chapter 7, in which both cross-anisotropy and stiffness non-linearity were incorporated within the framework of elasticity, to the Elstow excavation.

8.3 Mesh geometry

Numerous mesh configurations were tried until the final mesh design, shown in Figure 8.1, was chosen. It was decided that the soil profile was sufficiently horizontally uniform for the excavation to be treated as symmetric about the centreline, allowing only half the excavation to be modelled. It was further decided that the analyses could assume plane strain conditions, although such behaviour could only be confirmed once the instrumentation data had been examined.

It was anticipated that the measurable ground response would be concentrated to a large extent within the Oxford Clay strata to a horizontal distance of about three times the excavation depth. It was important, however, that the outer boundaries would have no influence upon the excavation response. The finite element grid extended horizontally 50m from the excavation centreline, to the most remote instrument location, and vertically to 30m to include the Blisworth limestone strata.

The final mesh configuration was relatively substantial, with 1232 grid nodes detailing a total of 1705 finite elements. The elements comprised 1084 linear strain triangles (3 vertices; 7 integration points) and 621 linear strain quadrilaterals (4 vertices; 9 integration points), resulting in a total of 13177 integration points. The stresses and strains within such elements vary linearly. It was not envisaged that a consolidation analysis would be necessary and the additional degrees of freedom that would have been needed were not incorporated.

The mesh was designed to simplify the subsequent analysis procedures. Element boundaries were aligned to coincide with the instrumentation locations, the geological boundaries, and excavation stages. During its construction, the excavation progressed in an even manner (see section 3.5.1). Detailed site records were kept and this allowed the excavation process to be modelled reasonably accurately. There were pauses in the excavation procedure at 3m, 5m and 7.5m before the final excavation depth of 10m was attained. These levels were included in the mesh geometry; the mesh was further subdivided to provide 20 layers of elements which could be removed during the analysis. Further discretisation was naturally based on providing more elements (integration points) where the largest changes in the ground stresses and strains were expected. It was found that it was the requirement of a smoothly varying pore water pressure response rather than a smoothly varying displacement response which governed the number of elements required in the analysis. Because it was the time required for thorough analysis of the results, rather than the actual computing time required to run an analysis, which was the limiting resource factor, a large number of elements, ensuring a precise solution was employed.

The finite element mesh was created using the mesh generation package FEMGEN (Femsys, 1992), and the complete CRISP geometry and main program input files were created using a computer program written during the current research.

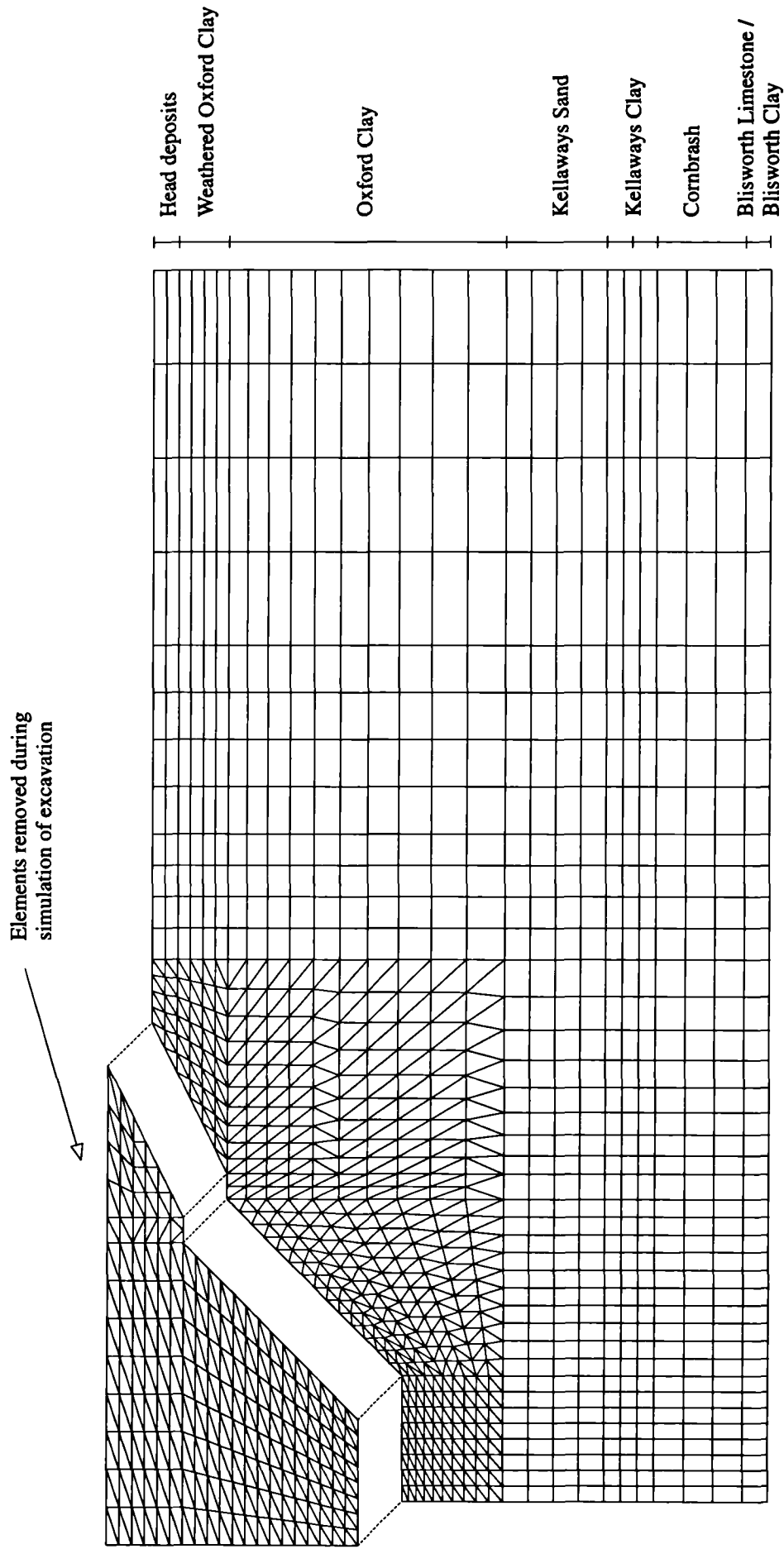


Figure 8.1 - Finite element mesh used for final CRISP analyses with non-linear cross anisotropic elastic model.

8.4 Material properties

The material properties of the soil strata were known at two contrasting levels of confidence. For the Oxford Clay, the stiffness response was known to a high degree of accuracy, from very small strains up to failure strains. The information on the lower strata was far more limited.

The Oxford Clay was modelled by the non-linear cross-anisotropic elastic model described in the previous chapter. The input parameters for this model were derived from the experimental programme described in Chapter 6. As described in section 7.5, the input for the model consists of two, complementary, non-linear stiffness relations, for increasing and decreasing stress levels respectively, for each of the four stiffness parameters in the constitutive relation of equation 7.11. In the experimental programme, a certain degree of redundancy was incorporated and allowed an average stiffness response to be formulated for the stress path loading directions shown in Figure 7.4. From the initial stress point, the stiffness response was investigated for constant p' stress paths, for both increasing q and decreasing q , and constant q stress paths for increasing p' . The constant q , decreasing p' stress path direction was not investigated in the experimental programme. If the holding period at constant stress did not affect the stress-strain behaviour, a relatively low stiffness from the end of the constant q , decreasing p' path approaching the assumed initial stress state could be used. However, the influence of the holding period was found to be comparable with that of the change in stress path direction and it was decided to use the same stiffness as for the constant q , increasing p' stress path to represent this threshold effect.

The stiffness relations for each loading direction used for the Oxford Clay are shown in Figure 8.6. Equations were fitted to plots of stiffness against the incremental strain energy and it was found that 3rd or 4th order polynomials fitted on a log scale were flexible enough to describe the variation adequately. Subsequently, a more flexible definition was found (equation 5.14 in section 5.6.2), but this was not used for the excavation predictions. Although the implementation of the model could have incorporated a stiffness variation dependent on the effective mean normal stress (e.g. equation 2.28), the experimental results were not thought to justify a specific normalisation procedure and consequently this feature was not incorporated into the analysis.

The effect of weathering on the stiffness response of the upper layers could not be adequately investigated and the same stiffnesses were adopted for the weathered and unweathered material.

Very little information was available at the time of the site investigation regarding the stiffness response of the soil strata below the Oxford Clay and no additional information could be obtained experimentally during the current research programme. It was thought that beneath the Oxford Clay the soil would generally experience small and very small strain levels and it was therefore expected that the response of the Kellaways strata (and those below) would be more reasonably described by data from *in situ* dynamic testing (Figure 3.10) rather than from conventional triaxial testing. It was recognised, however, that there was a large degree of uncertainty about the stiffness of these strata and, consequently, the stiffness was investigated parametrically to determine the influence on the overall excavation response.

The stiffness parameters used for the lower soil layers are shown in Table 8.1. This table includes the range of values used in the parametric study (see section 8.10). Linear cross-anisotropic stiffness moduli have been derived by assuming values for α^2 and ν^* of 3 and 0.25 respectively. Taking the derived *in situ* shear modulus as representative of the shear stiffness response in the vertical plane (vertical particle motion with horizontal propagation, see section

2.6.4), the four additional cross-anisotropic elastic parameters were derived using the relations described in section 7.4.

The material properties required in addition to the stiffness properties are the bulk unit weight of the soil (given in Table 8.2) and the bulk modulus of water (discussed in section 8.7).

| Strata | | G'_{insitu} MPa | G'_{hv} MPa | ν^* | α^2 | E^* MPa | E'_h MPa | E'_v MPa | ν'_{hh} | ν'_{vh} | G'_{hh} MPa | K' MPa |
|---|------|----------------------|------------------|---------|------------|--------------|---------------|---------------|-------------|-------------|------------------|-------------|
| Kellaways Sand | Min. | 65 | 65 | | | 94 | 281 | 94 | | | 113 | 102 |
| | Avg. | 143 | 143 | 0.25 | 3 | 207 | 620 | 207 | 0.25 | 0.14 | 248 | 224 |
| | Max. | 227 | 227 | | | 328 | 983 | 328 | | | 393 | 355 |
| Kellaways Clay | Min. | 50 | 50 | | | 72 | 217 | 72 | | | 87 | 78 |
| | Avg. | 142 | 142 | 0.25 | 3 | 204 | 613 | 204 | 0.25 | 0.14 | 245 | 222 |
| | Max. | 347 | 347 | | | 501 | 1503 | 501 | | | 601 | 543 |
| Cornbrash | Min. | 396 | 396 | | | 572 | 1715 | 572 | | | 686 | 619 |
| | Avg. | 1794 | 1794 | 0.25 | 3 | 2589 | 7768 | 2589 | 0.25 | 0.14 | 3107 | 2806 |
| | Max. | 4617 | 4617 | | | 6664 | 19992 | 6664 | | | 7997 | 7223 |
| Blisworth Limestone / Blisworth Clay | Min. | 142 | 142 | | | 204 | 613 | 204 | | | 245 | 222 |
| | Avg. | 347 | 347 | 0.25 | 3 | 501 | 1503 | 501 | 0.25 | 0.14 | 601 | 543 |
| | Max. | 396 | 396 | | | 572 | 1715 | 572 | | | 686 | 619 |

Table 8.1 - Cross-anisotropic elastic model parameters used to define soil strata below level of Oxford Clay

8.5 Initial stress state

For elastic analyses, such as those described here, it is changes in stress rather than the absolute stress levels that govern the soil behaviour. However, for an excavation analysis, elements are removed from the initial mesh during the analysis and the stresses within these elements are applied as loads to the new mesh boundary. The *in situ* stresses are, therefore, directly relevant to the analysis. The vertical stresses may be determined relatively accurately given a knowledge of the bulk unit weight of the soil strata and the initial pore water pressure regime. Determining the horizontal stress regime, however, is more problematic. In the previous numerical analyses (see section 8.2) a typical range for K'_o between 1.8 and 2.4 was used since the pressuremeter testing was apparently unsuccessful and produced K'_o values that revealed no trend with depth and which varied between 1 and 15. For the current research the pressuremeter test data has been re-examined as described in section 3.4.3 and, using an average response from each arm in a test, a vague trend with depth was evident (Figure 3.11). The corresponding K'_o predicted in this case was greater than that associated with passive failure and may be indicative of the problems associated with applying the pressuremeter testing system to stiff soils.

The value of K'_o was assumed to be constant with depth at 2.25, corresponding to $\phi'_{mob} = 22.6^\circ$ and representing an average of the previously assumed values. This was considered a reasonable value for such material and represented an average representation of that. In view of the uncertainty surrounding K'_o values as shown in Figure 3.12 and discussed in section 3.4.3, it was decided to conduct a parametric study with a much wider range of K'_o (from 1 to 5) than used in the previous analyses (see section 8.10).

The initial pore water pressure regime was clearly defined by the piezometer clusters and was presented in Figure 4.35. This suggested a water table at 29.6mAOD, 0.9m below the ground

surface. The pressure distribution was assumed to be hydrostatic, although the actual pressure in the Kellaways and Cornbrash strata was apparently sub-hydrostatic. It was assumed that this would have a relatively minor influence on the excavation behaviour. The pore water pressure conditions in the upper 0.9m of the head material, whether suction was maintained or lost, were shown to have a minor effect in initial analyses.

The parameters governing the initial stress states are given in Table 8.2.

| Strata | Depth (m) | Bulk density (kN/m ³) | K' _o | | |
|-----------------------|-----------|-----------------------------------|-----------------|------|------|
| | | | Min. | Avg. | Max. |
| Head | 1 | 17.80 | 1.0 | 2.25 | 5.0 |
| Weathered Oxford Clay | 3 | 18.53 | 1.0 | 2.25 | 5.0 |
| Oxford Clay | 14 | 17.55 | 1.0 | 2.25 | 5.0 |
| Kellaways Sand | 18 | 19.50 | 1.0 | 2.25 | 5.0 |
| Kellaways Clay | 20 | 19.50 | 1.0 | 2.25 | 5.0 |
| Cornbrash | 23.5 | 19.50 | 1.0 | 2.25 | 5.0 |
| Blisworth | 24.5 | 19.50 | 1.0 | 2.25 | 5.0 |

Table 8.2 - Modelling parameters governing the initial stress state

8.6 Simulation of excavation

The simulation of the excavation process in a finite element analysis would ideally be done by using a mesh consisting of many small elements so that as elements are 'removed' the implied loading to the remaining mesh is small, allowing an incremental non-linear analysis to be sufficiently precise. However, the use of a large number of, possibly thin, elements could lead to excessive solution times, or to numerical problems associated with finite elements of large aspect ratio. CRISP partially circumvents these problems by allowing the effect of element removal to be spread over a number of increments (Britto and Gunn, 1987). In CRISP, the process of element removal involves the immediate reduction of the element stiffness to zero followed by the application of the implied change of loading which is distributed over the, user-specified, number of subsequent increments. The nodal loads, **F**, equivalent to the removal of elements are calculated from equation 8.4.

$$\mathbf{F} = \int_v \mathbf{B}^T \boldsymbol{\sigma} d(\text{Vol}) - \int_v \mathbf{N}^T \mathbf{w} d(\text{Vol}) - \int_s \mathbf{N}^T \boldsymbol{\tau} d(\text{Area}) \tag{8.4}$$



Boundary forces



Self-weight loads



Nodal loads equivalent to element edge pressure loading

The Elstow excavation was simulated with 20 layers of 0.5m thick elements representing the 10m excavated depth. A study was carried out to determine the influence of the rate of removal of these elements on the overall modelled ground response and this is discussed in section 8.10.

8.7 Simulation of drainage conditions

As for the previous analyses, the Oxford Clay was assumed to be undrained. This was justified from the relatively low values of *in situ* permeability recorded (6x10⁻¹⁰ m/s, Table 3.3). The Kellaways Sand and the lower limestone strata were assumed to be fully drained since much

higher values of *in situ* permeability were recorded for these strata. The influence of the degree of drainage allowed in the Kellaways Sand was assessed parametrically and is discussed in section 8.10.

In CRISP an undrained analysis is modelled by incorporating a suitable value for the water bulk stiffness into the normal stress and strain terms of the **D** matrix. The bulk stiffness of water is approximately 2×10^6 kPa which may be specified directly in CRISP. For a non-linear analysis, however, where the soil stiffness is possibly changing over an order of magnitude, it is advantageous to specify the water bulk stiffness as a multiple of the soil bulk stiffness. This prevents numerical problems associated with performing calculations with large relative differences in stiffness. This is described by equation 8.5 in which *n* is a constant value, usually set between 50 and 500.

$$K_w = n K' \dots\dots\dots (8.5)$$

The required value *n* within this range is unknown but a value must be chosen that gives a reasonable approximation to undrained behaviour. The required change in pore water pressure is unknown but the change in volumetric strain is known and should be as close to zero as possible. As the bulk modulus of the water phase is increased to ensure undrained conditions, the possibility of numerically ill-conditioned equations increases. The volumetric strain occurring for a centreline element at the base of the excavation is shown in Figure 8.2 for a range of values for *n*. This figure represents an analysis in which the effect of 10m excavation in Oxford Clay is spread over 100 increments. To maintain the maximum volumetric strain below a nominal 0.001% strain, a bulk modulus of 500 times that of the soil skeleton was required. For a given constitutive model, undrained analyses should be carried out for a range of water stiffness values to determine the sensitivity of the results to the value selected and to determine when numerical instabilities start to occur. The results of such analyses are presented

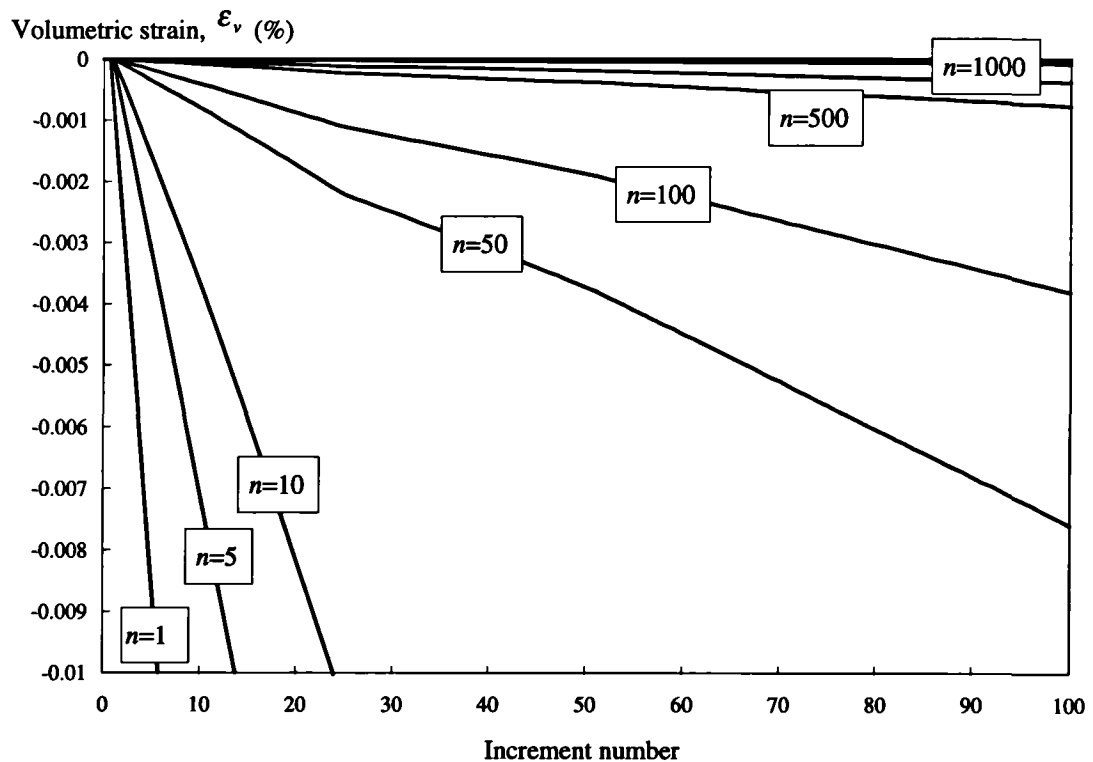


Figure 8.2 - Effect of varying bulk stiffness of water on the volumetric strain at the excavation base in a typical CRISP analysis

in section 8.10.

In the present non-linear analyses, it was not always possible to obtain a smoothly varying pore pressure regime. In such cases attempts were made to reduce the bulk modulus of the water phase, and to significantly increase the number of elements close to the loaded boundaries. There was still some oscillation, or unreasonable variation from integration point to integration point within elements, and this is indicative of numerical problems in the solution. It was found that calculating the average of the integration point values within an element, and taking the average value to apply at the element centroid, provided a smoothly varying pore water pressure field. The program was therefore modified so that the average element pore water pressure was sent as an additional output parameter to a separate computer file.

8.8 Influence of the stress path direction

Incorporated into the model implementation, described in Chapter 7, is the ability to interrogate the current stress path direction for each element and also to determine whether there has been a change in the stress path direction from the previous load increment (see section 7.5.3). At the start of an analysis a directionally dependent stiffness response is attached to each soil element depending on the loading direction incurred in the first loading increment. If a stress path reversal subsequently takes place, a different response is substituted. A change in the stress path direction is identified by comparing the stress path direction for each element in the two most recent load increments. In the excavation analyses, a reversal was deemed to have taken place if there had been a reversal in the direction of the change in deviator stress defined in triaxial stress space. A change from quadrant 'B' to quadrant 'A', for example, in Figure 7.4, does not constitute a load reversal. This approach was adopted to ensure a solution always existed for the constitutive relations as discussed in section 7.5.3. For the undrained analyses considered here the change in effective mean normal stress is constrained by the degree of anisotropy. Under these conditions, a load reversal definition based on the deviatoric stress increment direction is sufficient.

The effect of excavation on the deviatoric stress response is shown for a particular analysis in Figure 8.3 which shows the stress state after excavation has proceeded in steps down to the berm at 3m depth. It is seen that beyond the excavation crest and beneath the centre of the excavation, the soil is not expected to undergo any changes in the loading direction. Beneath the sides of the excavation, however, as layers are progressively removed, soil elements do undergo a change in the direction of loading. The actual stress path response for 6 elements at key points around the excavation is shown for a non-linear cross-anisotropic analysis in Figure 8.4. This analysis consisted of 100 load increments, each 0.5m thick layer of elements being removed in the course of 5 increments. All the stress paths have a consistently negative slope which is indicative of a cross-anisotropic response for soil that is stiffer horizontally than vertically (see section 6.2.2). At the base of the excavation, element 532 experiences a continual fall in deviator stress. Just beyond the excavation crest and remote from the excavation, elements 370 and 406 respectively experience a continual increase in deviator stress as the excavation progresses. At the excavation sides however, first element 931, and then element 700, are subject to a change in the loading direction as the excavation passes their respective elevations.

The model assigns stiffnesses as shown in Figure 8.5. In (a) the change in q associated with the elements highlighted in Figure 8.4 is shown for each load increment within the analysis, and the associated stiffness response is shown in (b). In the first increment of the analysis, every element is arbitrarily assumed to be unloading and the analysis adopts the stiffness curve

associated with this condition. After the first increment, however, the true stress path direction is known and the analysis continues with the elements outside the excavation plan area (370, 406) experiencing increasing q and the remaining elements experiencing decreasing q . The stiffness of elements 370 and 406 is reset at zero incremental strain energy. As excavation progresses the strain energy level increases and the soil stiffness corresponding falls. At increments 31, 70 and 84, elements 991, 700 and 673 respectively are subject to a change in the stress path direction from unloading to loading and the stiffness is reset in a similar manner to that of elements 370 and 406.

The initial assumption that every element is unloading has a negligible effect on the remaining analysis as long as the change in load in the first increment is small. An alternative approach would have been to carry out the first loading increment twice. The first time the loading direction for each element would be stored and subsequently used to determine the stiffness response during the second run of the analysis.

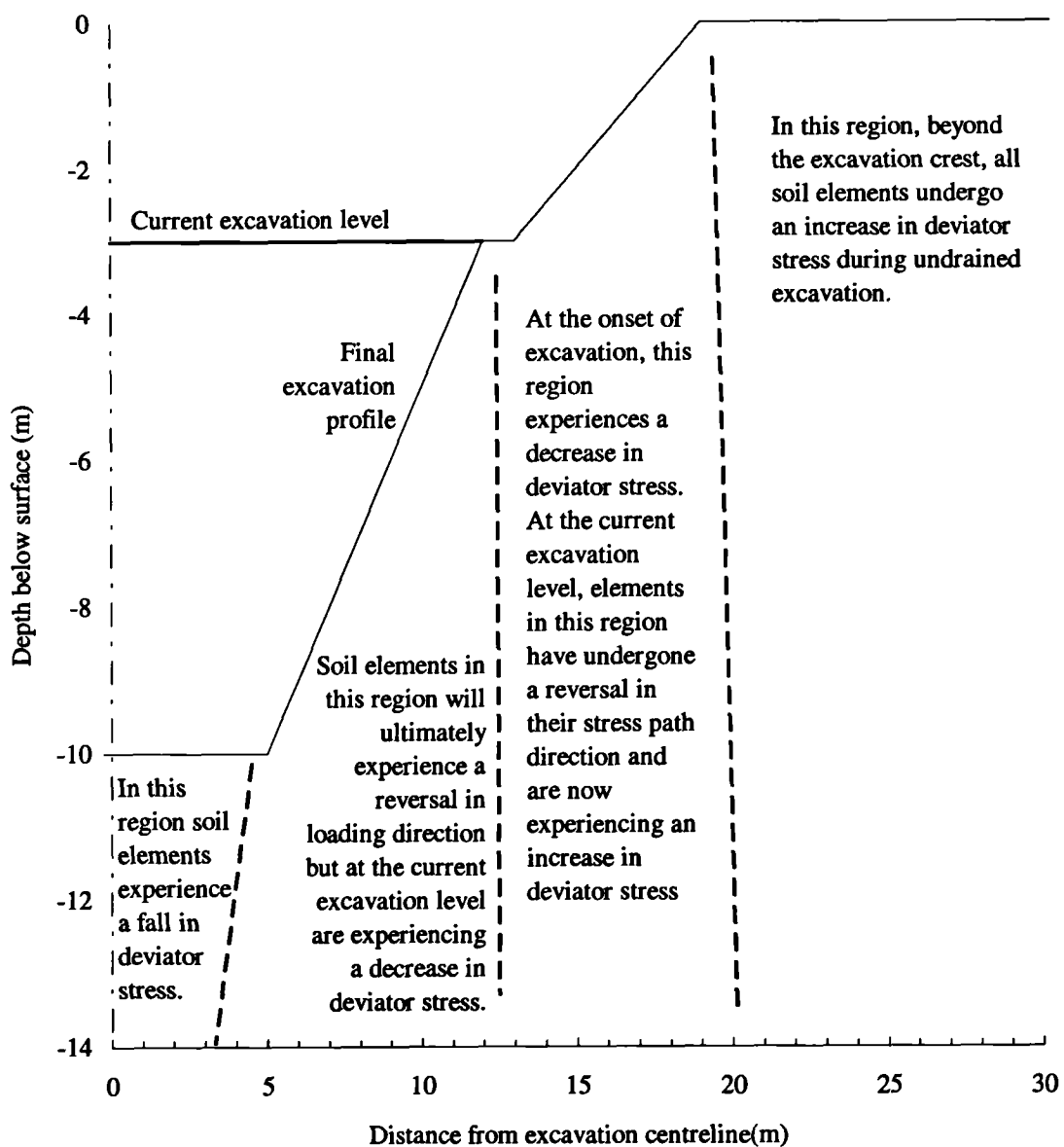


Figure 8.3 - The effect on the deviatoric stress experienced in different regions surrounding the excavation as the excavation level progresses.

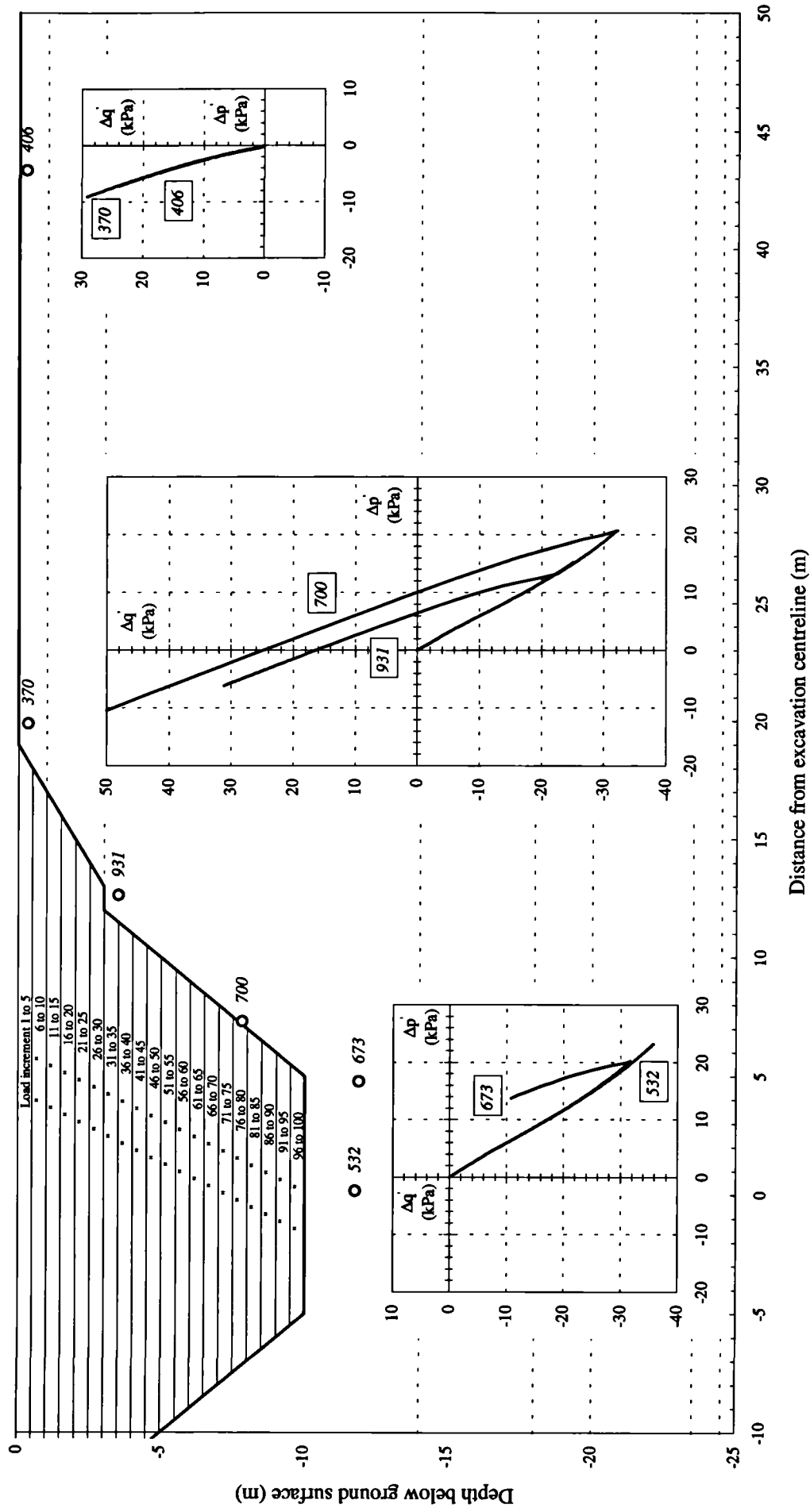
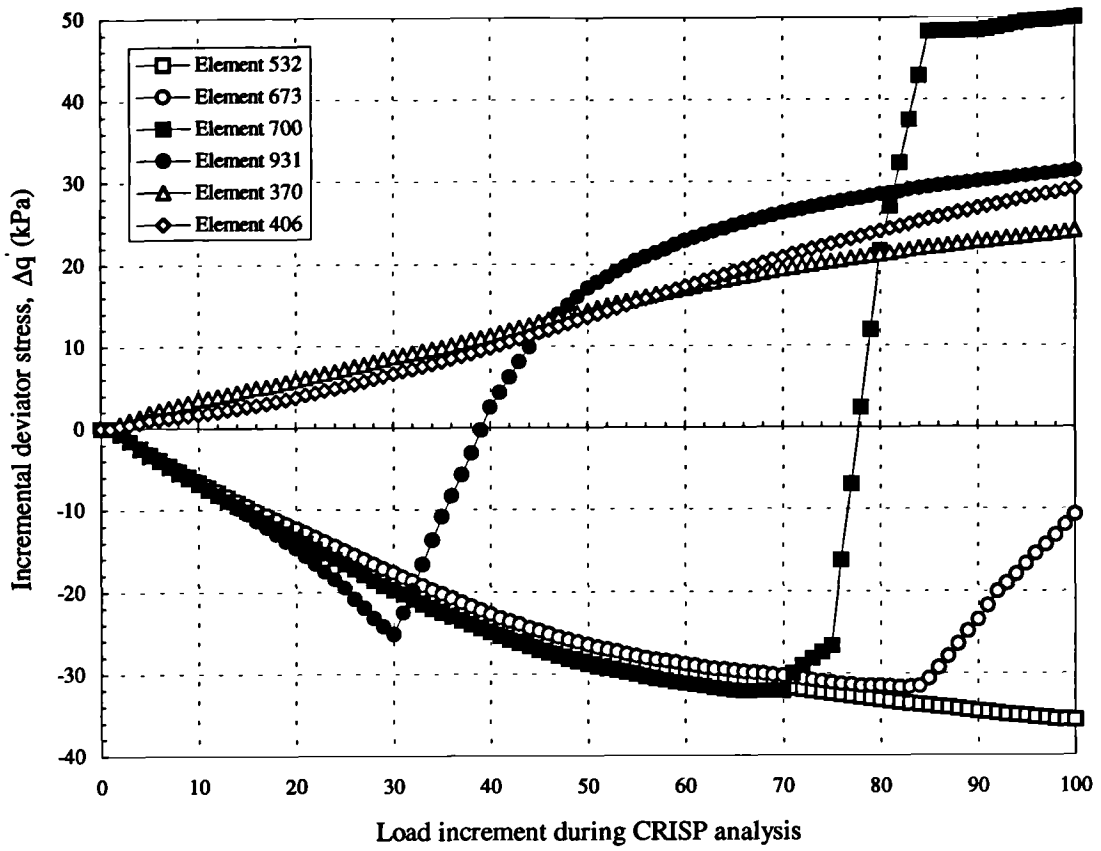
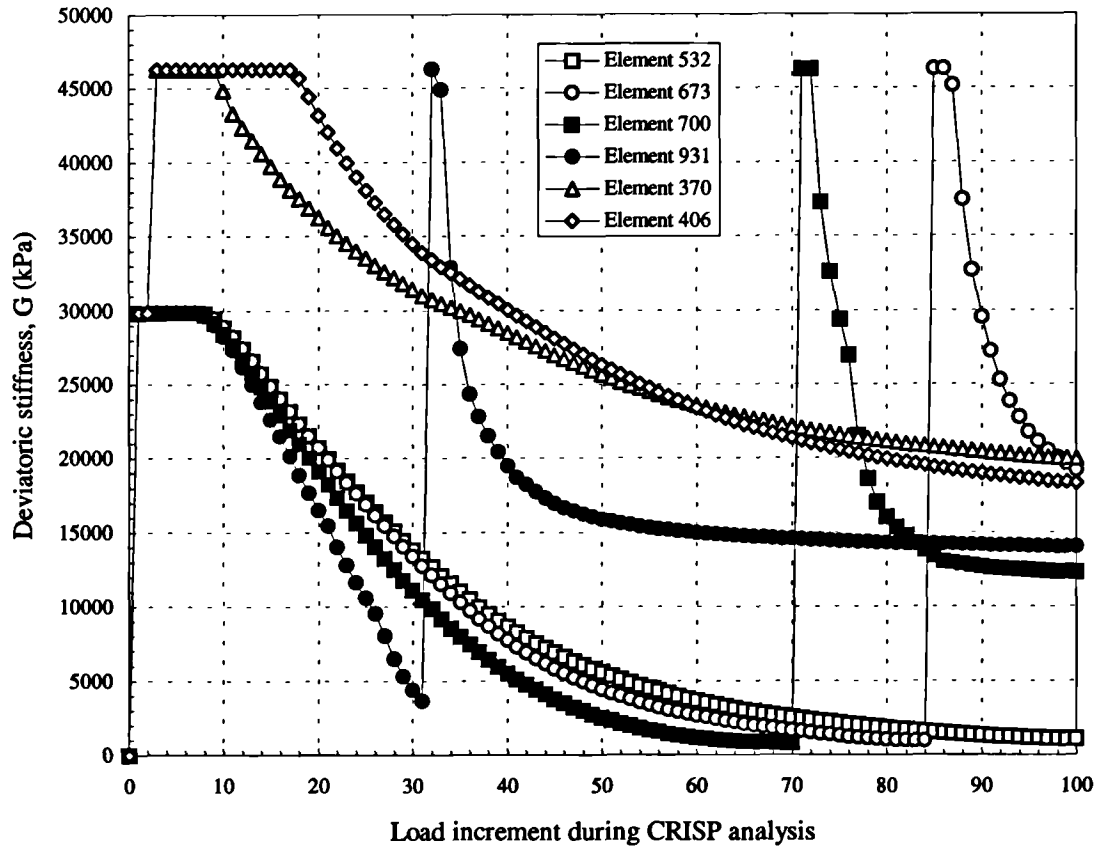


Figure 8.4 - Development of stress path during process of excavation



(a)



(b)

Figure 8.5 - Deviatoric stiffness response dependent on the stress path direction during the process of excavation

8.9 Methodology in the Elstow finite element analyses

8.9.1 Introduction

The methodology used in the analyses presented here was based on acceptance of the conclusion of the numerical analyses performed at the time of the excavation, namely that both anisotropy and non-linearity featured prominently in controlling the ground response. It was important, however, to provide a single best prediction of the excavation behaviour before the instrumentation data had been analysed and the actual ground behaviour following excavation had been determined. Genuine prediction provides the most realistic test for any modelling procedure. Thus, a single analysis will be presented as the prediction of the excavation response. This analysis incorporated a soil model for the Oxford Clay with a stress path dependent, cross-anisotropic, and non-linear stiffness response which was based on the experimental (laboratory) data. Additionally this analysis incorporated the best estimate of the material parameters and drainage characteristics for the remaining soil strata. It was hoped that parametric analyses to define the error bounds of this prediction would be available concurrently but time restraints meant that these were carried out following the initial comparison of the numerical prediction and the instrumentation data. This is unfortunate but does not detract from the validity of the original prediction.

All analyses subsequent to the interpretation of the instrumentation data must be considered part of the back analysis. A back analysis of field behaviour usually involves the manipulation of a particular constitutive model's input parameters to improve the representation of the field behaviour.

The behaviour of the cross-anisotropic elastic model described in the previous chapter is essentially governed by the eight non-linear stiffness relations required to describe the response in each quadrant of q - p' stress space. A complete back analysis would therefore consist of the integrated and simultaneous manipulation of the non-linearity in each equation. Such an analysis would be very involved, and not necessarily useful, since a number of combinations could perhaps provide an adequate fit to the data without being physically reasonable.

For the present work, the back analysis consisted of varying combinations of parameters for which a physical justification could be provided. For the non-linear model this approach resulted in assuming that the stress-strain responses from either or both of the constant p' and constant q stress path directions were in error due to the testing method being either inadequate or inappropriate or due to the soil specimen being disturbed. In these parametric analyses, the non-linear stiffness relations were modified by scaling each stiffness value by the same constant factor at each value of incremental strain energy.

8.9.2 Description of analyses carried out

The first analyses carried out on the excavation were linear isotropic elastic analyses designed to check the finite element mesh and to assess the modifications made to CRISP. These analyses determined the size of the required mesh, and the number and type of finite elements used.

Following the linear analyses and the final detailing of the geometry of the problem, a prediction of the excavation behaviour was carried out. This could be considered a genuine prediction since the instrumentation data from the excavation had not been analysed. In the prediction:

- the Oxford Clay, weathered Oxford Clay and head material were modelling using Model O.C., the non-linear cross-anisotropic elastic model implementation. The stiffness parameters were defined with respect to incremental strain energy, were dependent on the current stress path direction, and were sensitive to reversals in the direction of loading as shown in Figure 8.6. All strata beneath the Oxford Clay were modelled as linear cross-anisotropic elastic using the average *in situ* derived stiffness parameters given in Table 8.1.
- the Oxford Clay, Kellaways Clay and Blisworth strata were modelled as undrained, and the Kellaways Sand and Cornbrash strata as drained (using $n=500$ and $n=0$ respectively in equation 8.5).
- the excavation process was simulated through the removal of elements incrementally in 20, 0.5m deep layers. The non-linear analysis was carried out over 100 load increments with the

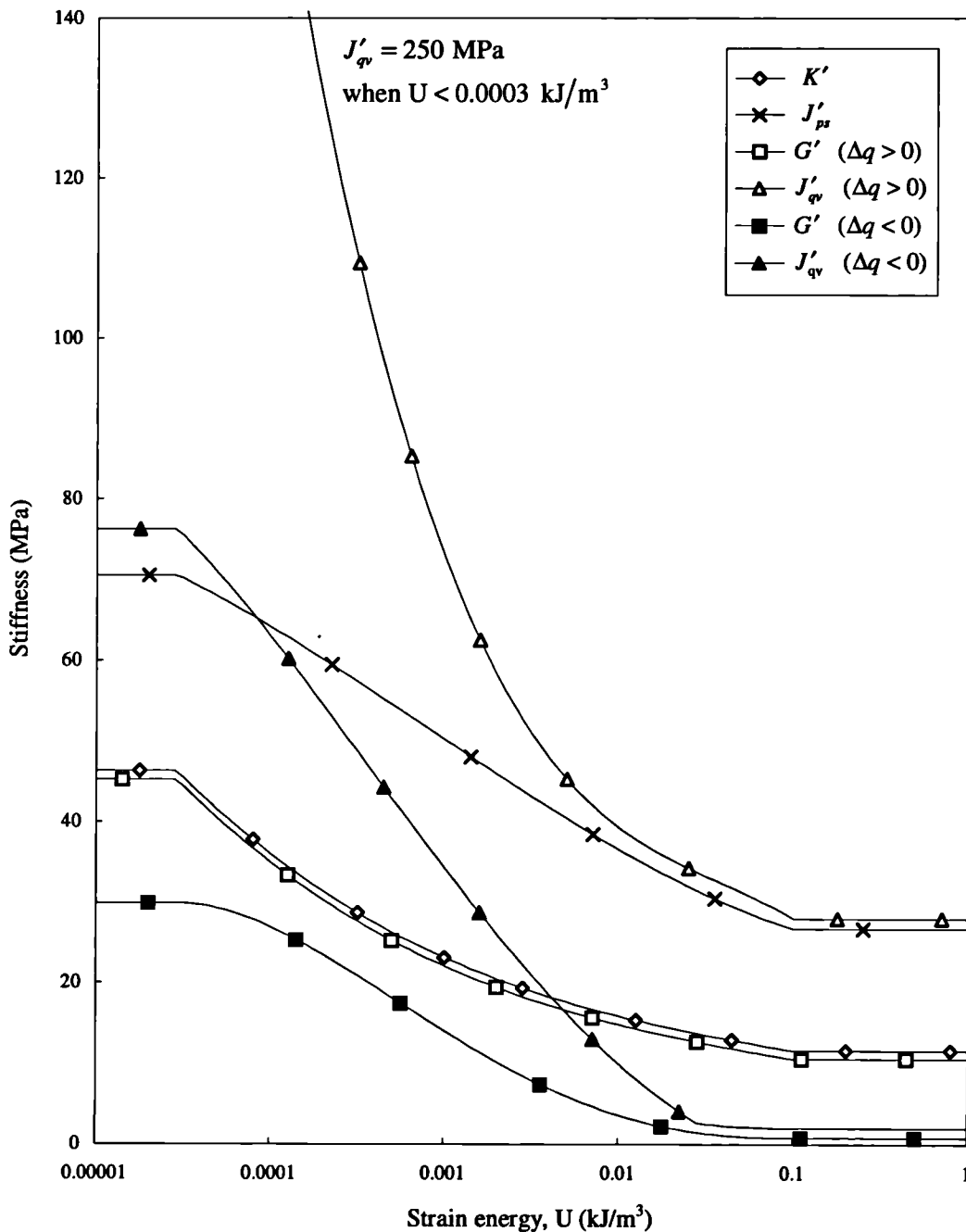


Figure 8.6 - Non-linear anisotropic elastic model input stiffness parameters

effect of each 0.5m excavation layer removal being spread out over 5 increments.

- the *in situ* stress state was defined based on: a water table 0.9m depth; a hydrostatic pressure distribution; a total vertical stress distribution from the bulk densities given in Table 8.2; a horizontal effective stress distribution using the average K'_o in Table 8.2.

The sensitivity of this model prediction to assumptions regarding J' was then investigated. The principal simplification of the experimental results was the implementation of cross-anisotropy into an elastic model by combining the two coupling stiffness parameters, J'_{qv} and J'_{ps} , into the single parameter J' . The first stage of the sensitivity analysis therefore consisted of varying the factor β in equation 7.40 globally over the range 0 to 1 (in each element this factor is more usually determined from the current stress path direction as shown in Figure 7.6). Additionally, the cross-anisotropic aspect of the model was removed by setting J' to a suitable high value (1×10^{20} MPa). The off-diagonal coupling stiffness terms in equation 7.12 were then effectively zero, making the soil response isotropic.

At this stage, the modelling process was halted and the analysis of the instrumentation data presented in Chapter 4 was carried out.

Subsequently, analyses were carried out to investigate the sensitivity of the prediction to stress path direction dependent stiffness. This required carrying out the following additional analyses:

- all stiffness parameters determined from the stress path in the experimental programme for increasing q ('compression' in Figure 7.4).
- all stiffness parameters determined from the stress paths in the experimental programme for decreasing q ('extension' in Figure 7.4).

Once the sensitivity of the model O.C. implementation had been investigated, other uncertainties could be investigated. This involved varying:

- the degree of drainage in the underlying sand and limestone strata, assuming that the Kellaways Sand and Cornbrash strata, although laterally extensive, were confined by the adjacent clay layers and consequently partially drained. Analyses were carried out by setting the factor n in equation 8.5 to 0, 5, 50, and 500.
- the value of K'_o in the Oxford Clay.
- the degree of anisotropy in the Oxford Clay.
- the linear elastic stiffnesses of the lower strata.
- the effect of the number of increments.
- the influence of the modelling of the construction process.

8.10 Results of numerical analyses of Elstow excavation

The prediction of the ground response to excavation, carried out without knowledge of the actual behaviour, has been plotted at the location of the field instruments. A coding of the genuine prediction and a number of variants of this analysis are shown in Table 8.3.

| Analysis | Description |
|----------|--|
| A01 | <i>The genuine prediction</i> - a non-linear cross-anisotropic analysis incorporating a stress path dependent stiffness and responding to reversals in the stress path direction |
| A04 | As A01, but with $\beta = 0; J' = J'_{ps}$ |
| A05 | As A01, but with $\beta = 0.5; J' =$ average of coupling stiffnesses |
| A06 | As A01, but with $\beta = 1; J' = J'_{qv}$ |
| A07 | As A01, but isotropic |

Table 8.3 - Description of excavation analyses

The instrumentation data for both horizontal and vertical movements are presented as the collection of data taken from time I to time S and covering the period following the completion of excavation to the end of the monitoring period. Due to the variability of the some of the responses (as discussed in section 4.2.2) it is helpful to view a range of data.

A vector displacement plot of the genuine prediction compared with the displacements at the combined inclinometer / extensometer instrument locations is shown in Figure 8.7.

For vertical displacements, groups of extensometers were located within the Oxford Clay at depths of 1.5m, 4.5m, 8m, 11m, 12.5m, and 14m below the ground surface (see section 3.6 and section 4.2.2). The measured ground response is compared with the cross-anisotropic and isotropic responses of Model O.C. in Figure 8.8 to Figure 8.13. The analyses A04, A05 and A06 are not included in these figures for clarity.

Beyond the excavation crest, the magnitude of settlement was generally underpredicted. This was particularly noticeable at shallow depths as shown in Figure 8.8, in which the settlement was underestimated by as much as 10mm, and in Figure 8.9. Similarly, the heave recorded within the plan area of the excavation was generally greater than that predicted and in some cases significantly so. The comparison was particularly poor at the base of the excavation. For example, at 11m depth, a heave of 22mm compares with a prediction of 7mm. At the base of the Oxford Clay (14m depth), however, the model prediction and the instrumentation data agree reasonably well. This perhaps suggests that the inability to correctly predict the vertical displacements lies mainly with the modelling of the Oxford Clay. Contrasting the isotropic and anisotropic model predictions, the main differences were seen adjacent to the excavation sides where horizontal stress changes had a dominating influence. This resulted in a deeper settlement trough for the isotropic prediction (see again Figure 8.8), although a convergence of the responses was evident at the excavation base and away from the excavation where stress changes were more one-dimensional.

The record of horizontal displacement was obtained from inclinometers located at section F ($x=0$); sections G and H ($x=\pm 4.5m$); section I and J ($x=\pm 12.5m$); sections K and L ($x=\pm 19m$);

sections M and N ($x=\pm 23.5\text{m}$); sections O and P ($x=\pm 34\text{m}$); sections Q and R ($x=\pm 49\text{m}$). (The section locations are shown in Figure 4.1 and the displacements at these locations are discussed in section 4.2.2). This ground response is compared with the cross-anisotropic and isotropic predictions of Model O.C. in Figure 8.14 to Figure 8.25. For sections F, Q, and R, the predicted horizontal displacement is zero which is a necessary consequence of the defined boundary conditions (Figure 8.14; Figure 8.24; Figure 8.25). The instrumentation data shown in these figures are the same as the average inclinometer profiles plotted in Chapter 4 to which reference may be made. The section G response has not been included since no instrumentation data were available at this location following completion of the excavation.

For horizontal displacements, the influence of incorporating cross-anisotropy was far more marked than for vertical displacements and also considerably improved the ability of the model to match the instrumentation data. Figure 8.14 shows the degree of scatter at the excavation centreline which must be accepted at all other measurement locations, being attributable principally to the inaccuracy of the inclinometers. This scatter was generally $\pm 1\text{-}2\text{mm}$ with greater variance in the upper 1-2m of the instrument as discussed in section 4.2.2. The form of the predicted response was typically the same as that shown in Figure 8.15: very small displacements below the Kellaways strata, increasing but still small displacements within the Kellaways strata, and much larger displacements in the Oxford Clay. The comparison with the instrumentation data at this location was relatively poor, although it improved when the anisotropic response was incorporated. This mismatch can justifiably be attributed to the lack of good quality data available for this instrument section. At sections I and J, in Figure 8.16 and Figure 8.17 respectively, both the quality of the prediction and the importance of incorporating anisotropy was clear. Similar conclusions may be drawn from sections K and L in Figure 8.18 Figure 8.19 respectively. Since it is the modelling of the Oxford Clay strata with which this work is principally concerned, it is possibly justified to translate the displacement response calculated for the Oxford Clay (to match the horizontal displacement at the base of the strata). This improves the comparison at section O in Figure 8.22. However, the quality of the data at these more remote single instrument sections is poor.

The influence of the choice of coupling stiffness within the range defined by the experimental programme is shown in terms of horizontal and vertical displacements in Figure 8.26 and Figure 8.27 respectively. In Figure 8.26, and in similar style figures to follow, the horizontal displacement profile is presented, for each instrument section not on the mesh boundary, on an offset horizontal scale. In Figure 8.27, and in similar style figures to follow, the parametric influence on the vertical displacement response is shown for each of the vertical levels where suitable extensometer data were available for comparison. It is seen that, for the prediction of the excavation behaviour (analysis A01), the stress path direction dependent β factor resulted in displacements near the upper bound of the range ($\beta = 1$). This is as expected since the $\beta = 1$ response is attributable to the constant p' stress path response in which the coupling stiffness is defined by J'_{ϕ} . The undrained stress paths in the Oxford Clay are defined and restricted by the imposed requirement of constant volume deformation. The stress paths (see for example Figure 8.4) are inclined to the left of vertical due to the anisotropic nature of the response but are still reasonably near vertical and therefore result in a β factor relatively close to 1.0.

The corresponding prediction of the change in pore water pressure for the above analyses is shown in Figure 8.28 in which the change in pore water pressure first presented in section 4.2.4 is shown at the limited locations where data were available: at the base of the excavation, at the toe of the excavation slope, and at the berm situated approximately halfway up the excavated

slope. No data concerning the pore water pressure are available beyond the excavation crest. The numerical predictions and the piezometer data agree very poorly. The comparison is best in (c) at the excavation berm, but the prediction still overestimated the change in pore water pressure by a factor of 2. It is evident in these figures that varying the degree of coupling using the β factor has only a limited influence on the pore water pressure response. In order to show that the choice of the bulk stiffness of water in these analyses was not having a significant affect, further analyses were carried out in which the degree of drainage of the Oxford Clay strata was increased (Figure 8.29), and in which the degree of drainage in the lower sand and limestone strata was reduced (Figure 8.30). It is clear that even assuming near drained conditions within the Oxford Clay, when $n=5$, the predicted pore pressure response within the Oxford Clay still significantly exceeds that recorded by the instrumentation. The reduction of drainage within the lower strata is, however, significant when contrasting this with the fully drained response assumed in the excavation prediction analysis. It seems that choosing n to be less than 5 for the Kellaways Sand and between 5 and 50 for the Cornbrash would reproduce the recorded change in pore water pressure at these elevations. The effect of such an alteration of the drainage characteristics on the deformation response is shown for these same analyses in Figure 8.31. The influence was minimal, although greater for vertical displacements than for horizontal displacements. The form and magnitude of the displacements varied little, even if the more permeable strata below the Oxford Clay were considered to be undrained.

During the experimental programme, the anisotropic stiffness non-linearity was determined in a manner that would permit predictions to be made for element stress paths in any direction from the *in situ* stress state (see section 5.3.2). Although the model implementation allocates the stiffness definitions dynamically as the excavation analysis proceeds, the effect of using a single (fixed) set of parameters was investigated. Figure 8.32 shows horizontal and vertical displacement contours, contrasting analyses in which the stiffness definition was dependent on the stress path direction with analyses in which the stiffness characteristics were fixed. Comparing (c) and (d) on this figure, the difference in applying the stiffness characteristics for either increasing or decreasing q is clear. The horizontal and vertical displacements in (d) far exceed those of (c) and compare very badly with the instrumentation data. It must be considered unrealistic to apply the stiffness characteristic appropriate for the unloading at the excavation base to the whole area of ground affected by the excavation. Comparing (a) and (c), the effect of incorporating stress path dependent stiffness is evident in that, although the general form of the displacement response was similar, the heave at the base of the excavation was 30-40% greater when the lower stiffness associated with unloading is taken into account. The magnitude of the horizontal deformation at the excavation sides also increased although this effect was counter balanced by the increase in stiffness associated with the stress path reversals experienced in this area.

The non-linearity in the material response is dealt with in CRISP through the incremental tangent stiffness approach. The results are, therefore, generally dependent on the number of increments over which an analyses is carried out and, for construction problems, on the rate and method of element removal/addition.

The effect of the first of these variables is presented in Figure 8.33 and Figure 8.34. The excavation prediction was carried out in 100 increments but here this is compared to 1, 2, 3, 4, 8, 20, 30, and 40 increment analyses. It is clear that even a 20 increment analysis is fairly close to the final solution. For analyses carried out in fewer increments than this, the form of the displacement response varied significantly, especially adjacent to the excavation where the stress path direction dependent stiffness had a greater influence.

The influence of the method of excavation is shown in Figure 8.35 and Figure 8.36. For a 100 increment analysis, the excavated elements were removed in 1, 2, 3, 4, and 8 layers, and the results compared to the actual prediction in which 20 layers were used. In all these cases, the change in stress was distributed evenly throughout the 100 increments, as described in section 8.6. These figures show that the method of modelling the excavation process had only a limited effect on the resulting deformation response. Although small, the effect was greatest at the sides of the excavation. This is as expected, since this was the region directly affected by the increased stiffness due to reversals in the stress path direction.

The influence of the stiffness of the lower strata is shown for horizontal and vertical displacements in Figure 8.37 and Figure 8.38 respectively. The actual prediction, using the average values presented in Table 8.1, is compared with two analyses which use the upper and lower bound of the stiffness values. The vertical displacement presented by the lower bound values is perhaps closer to the actual instrumented response in terms of heave at the base of the excavation, but the settlement beyond the excavated crest is not reproduced much better. Additionally, the horizontal displacements clearly show that these lower bound values produce excessive displacements below the Oxford Clay. The use of average values seems a reasonable decision for the excavation prediction with, if anything, higher values were required to reproduce the field response for lateral movement.

The effect of varying K'_o in the Oxford Clay strata is shown for horizontal and vertical displacements in Figure 8.39 and Figure 8.40 respectively. As expected, changing the value of K'_o has a much greater effect on the horizontal displacements than on the vertical displacements. The excavation sides are the most significantly affected.

To determine the variation in the predicted displacements corresponding to scatter in the experimental stiffness data, a series of analyses was carried out employing the range of data retrieved. Since the scatter in the experimental data was greater at small strains, the scaling of the stiffness data was biased towards this region (reducing exponentially to coincide with the large strain stiffnesses which were not altered). A general $\pm 25\%$ variation in all the small strain stiffnesses suggested a variation in the final excavation response of a maximum of $\pm 1\text{mm}$ for the horizontal displacement (Figure 8.41) and $\pm 0.5\text{mm}$ for the vertical displacement (Figure 8.42). This variation in displacement is neither very significant nor enough to explain the discrepancies between the predicted and actual ground movements.

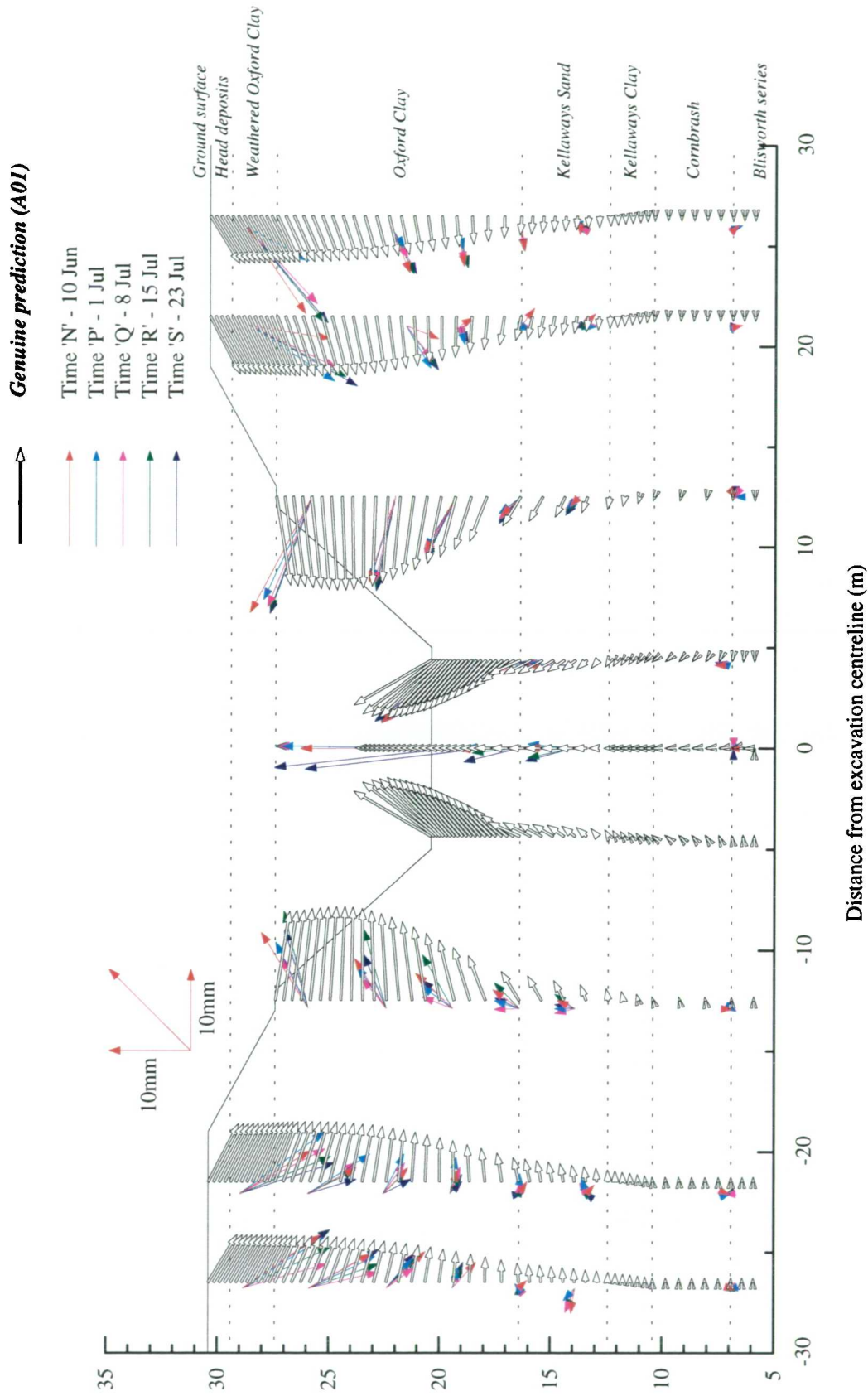


Figure 8.7 - Comparison of displacement vectors for the genuine prediction and the actual excavation behaviour

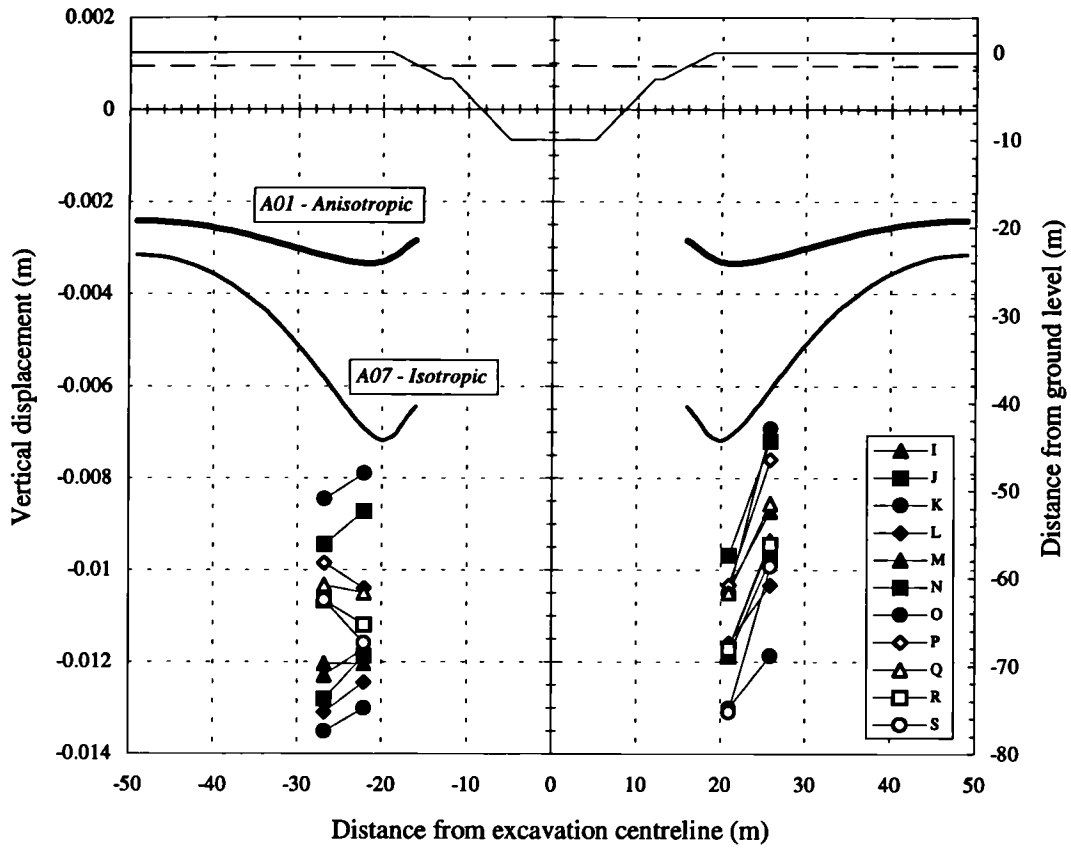


Figure 8.8 - Prediction of vertical displacement at 1.5m depth

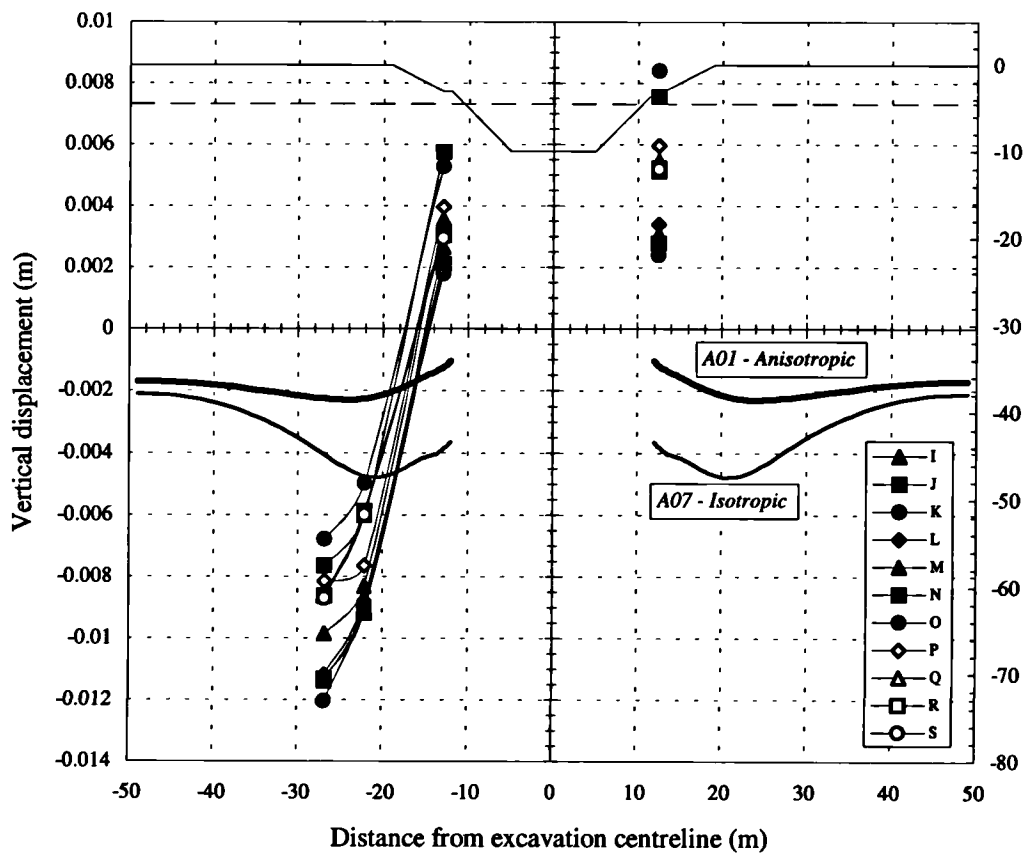


Figure 8.9 - Prediction of vertical displacement at 4.5m depth

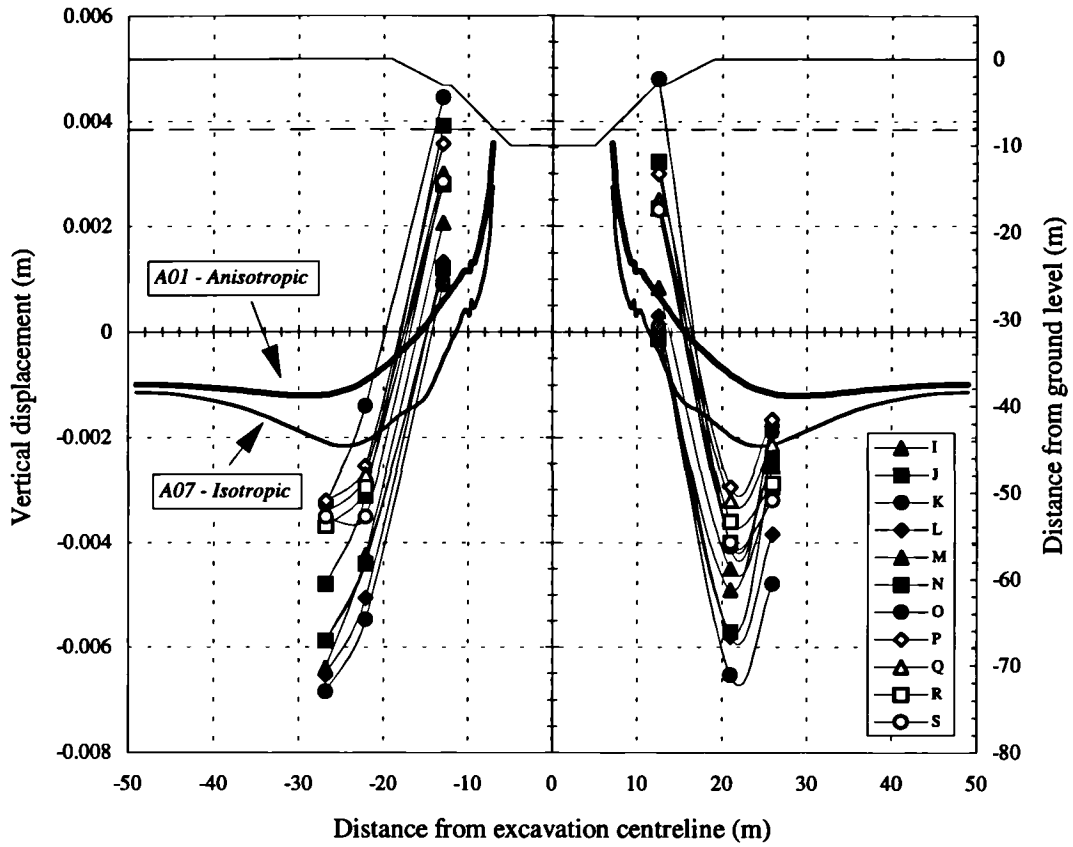


Figure 8.10 - Prediction of vertical displacement at 8m depth

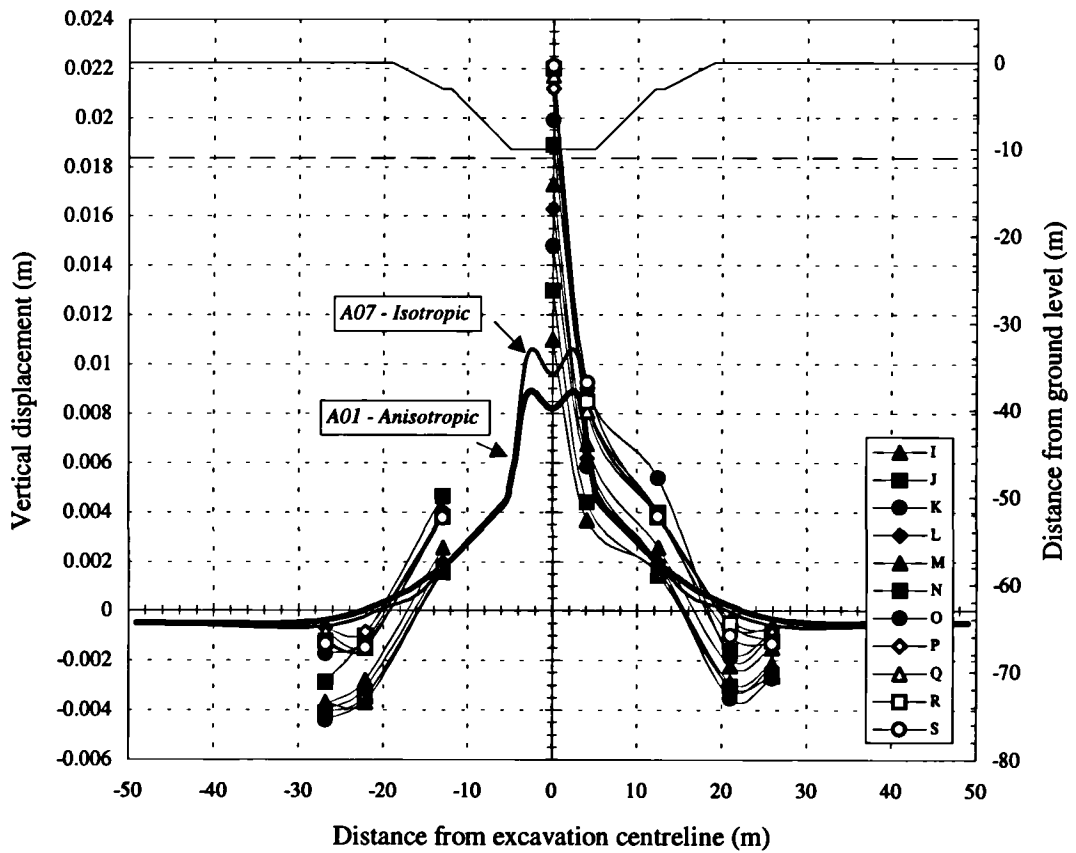


Figure 8.11 - Prediction of vertical displacement at 11m depth

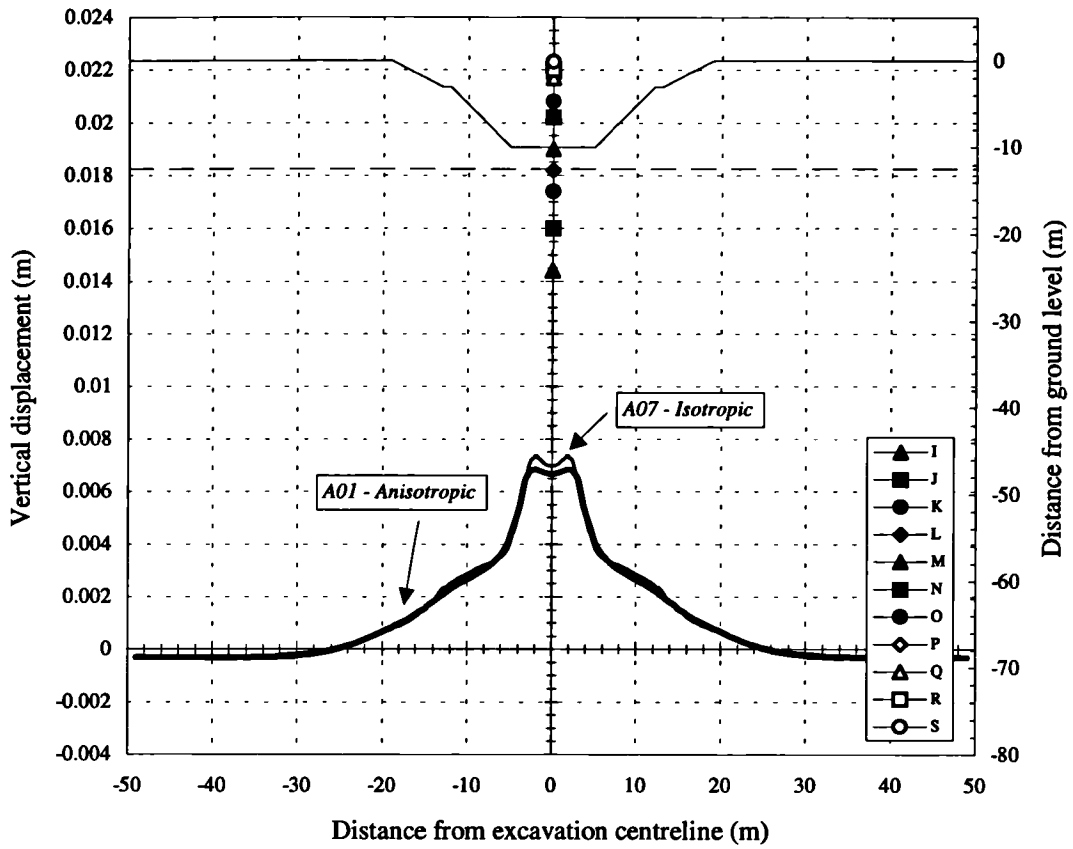


Figure 8.12 - Prediction of vertical displacement at 12.5m depth

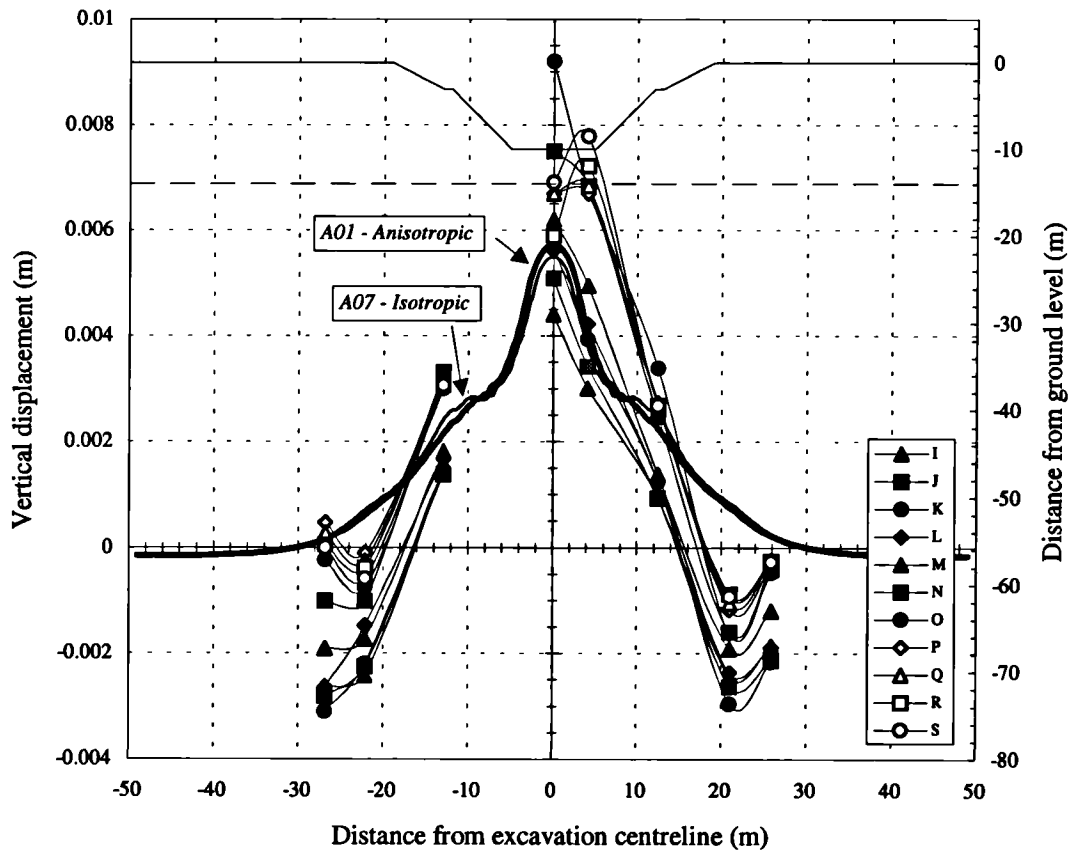


Figure 8.13 - Prediction of vertical displacement at 14m depth

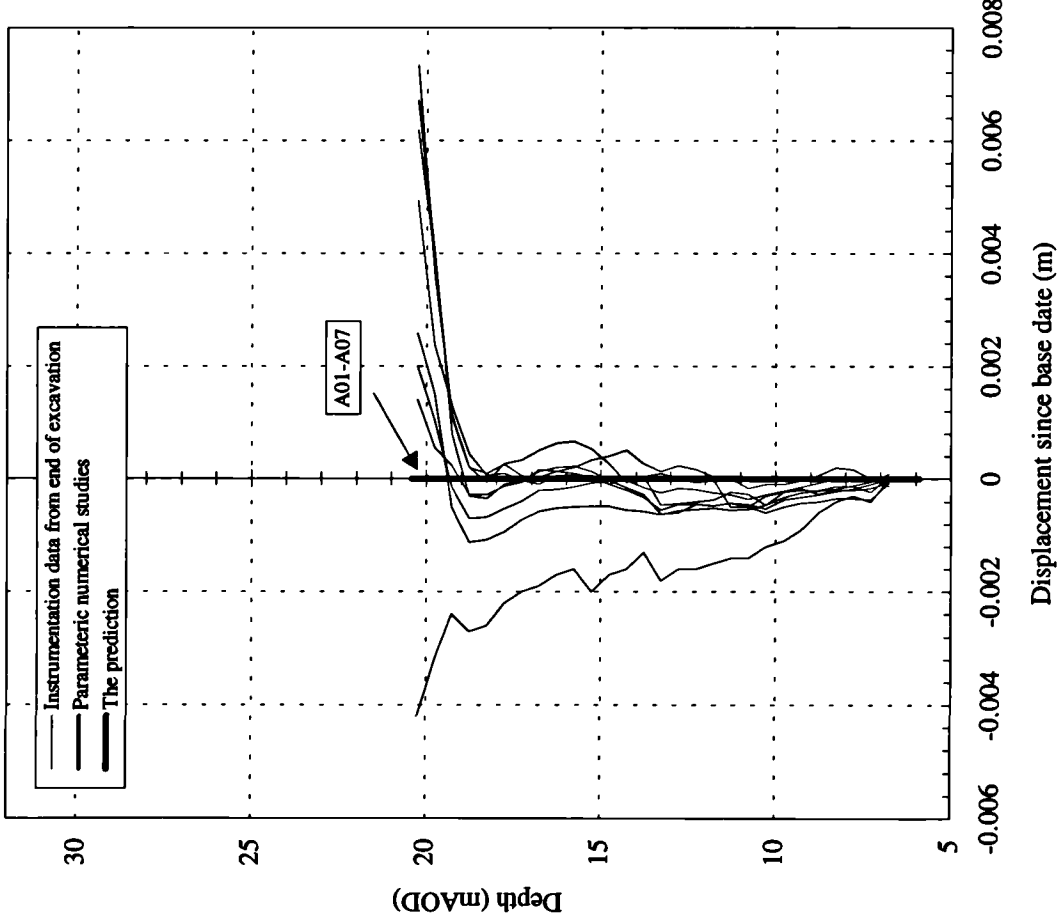


Figure 8.14 - Prediction of horizontal displacement at section F

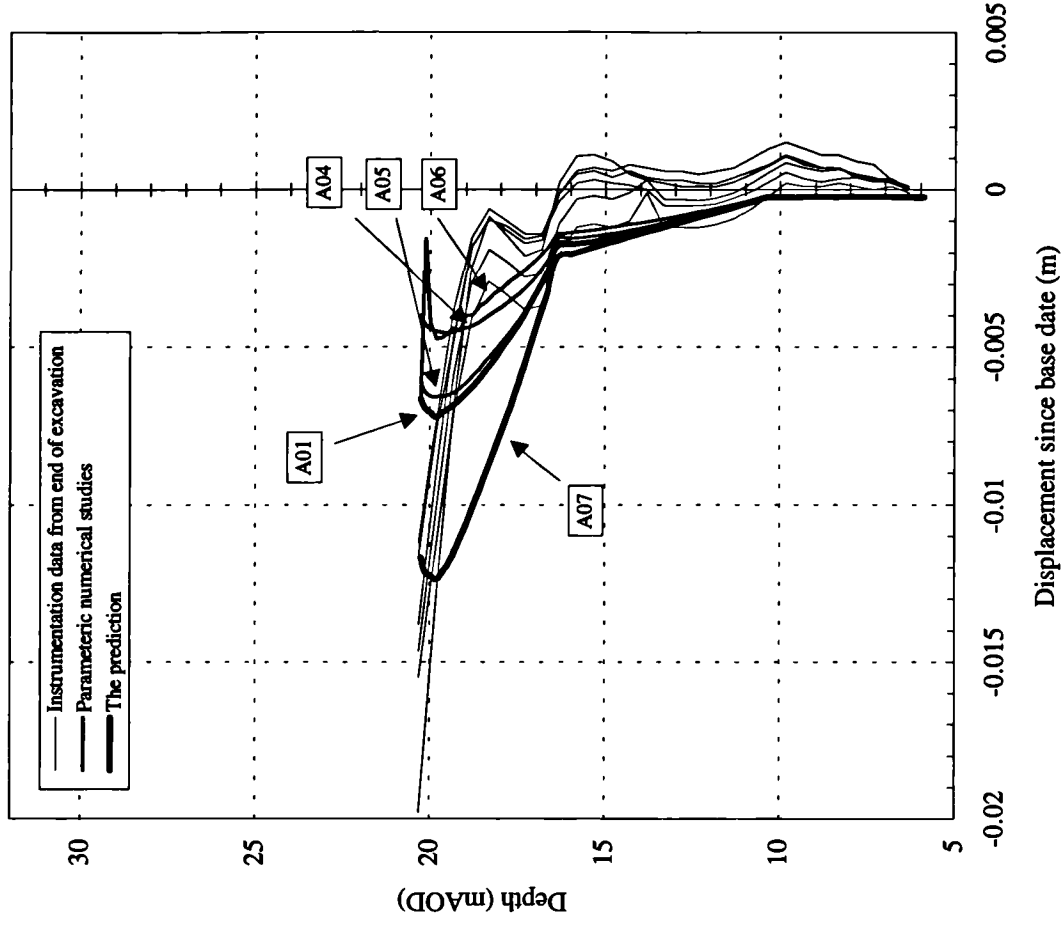


Figure 8.15 - Prediction of horizontal displacement at section H

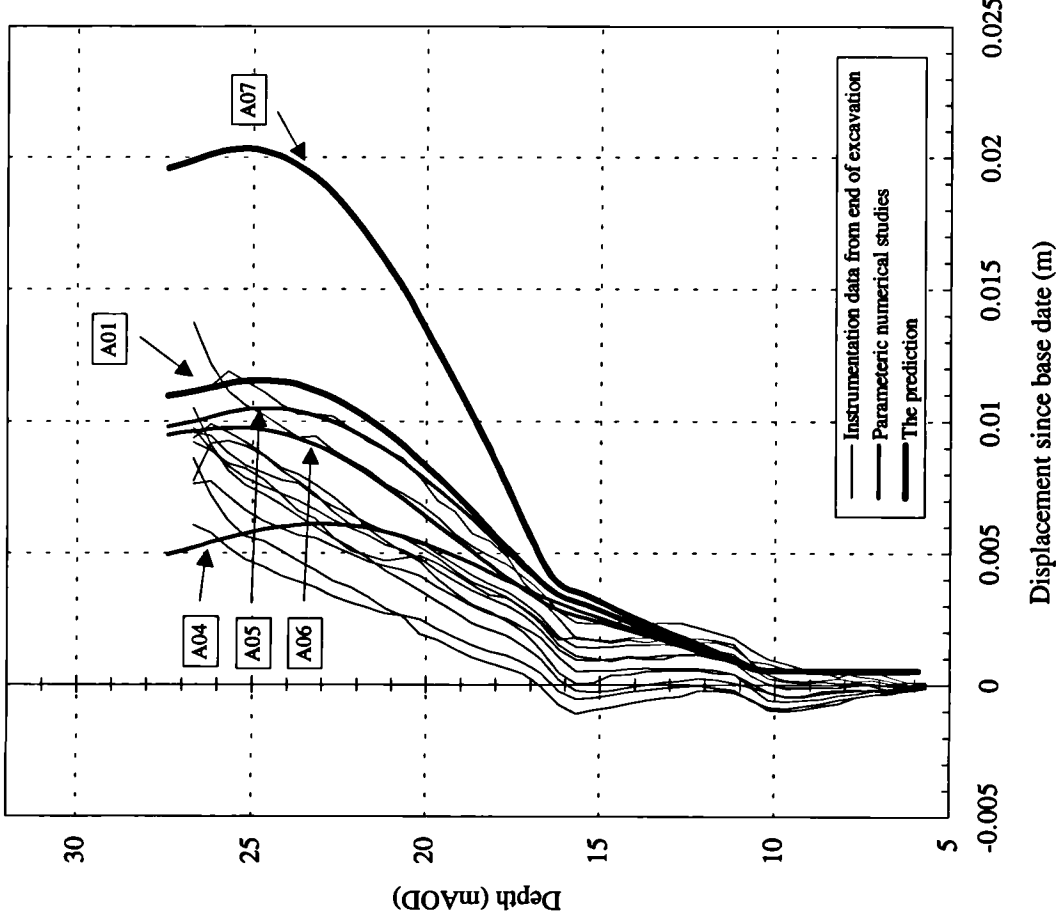


Figure 8.16 - Prediction of horizontal displacement at section I

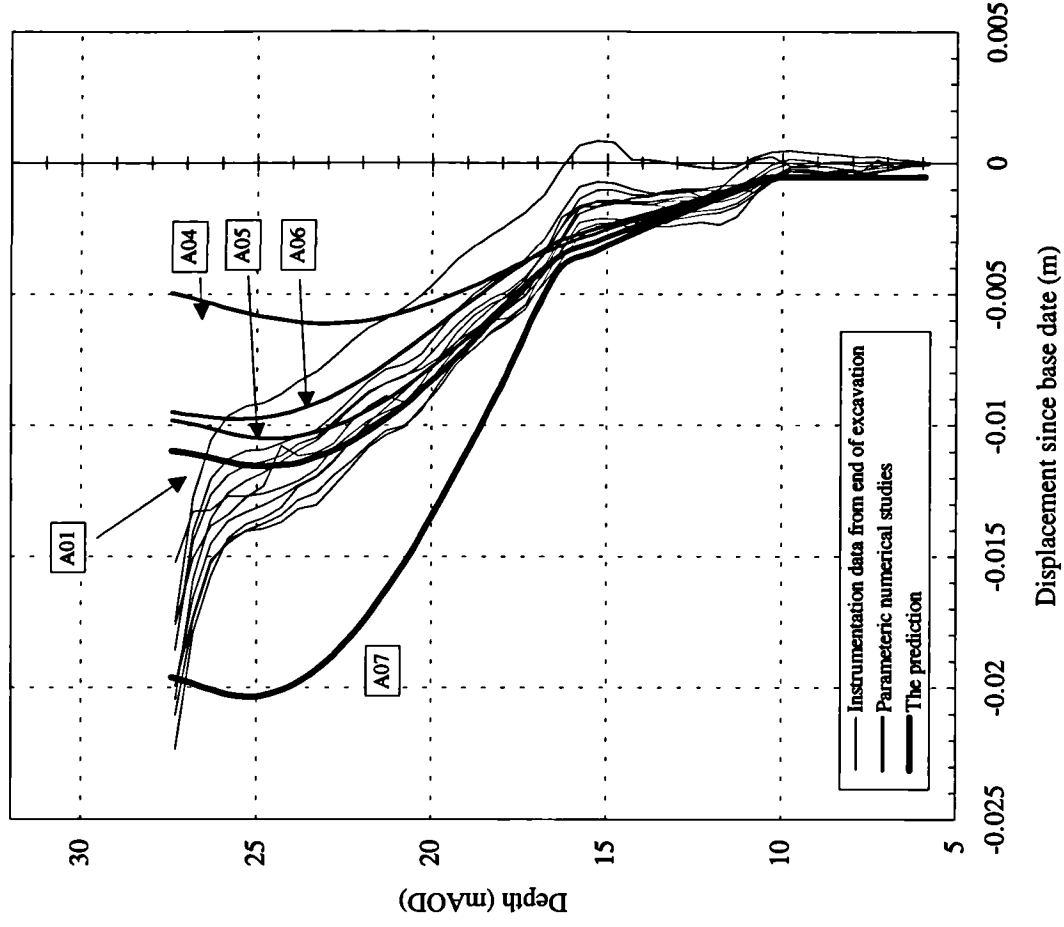


Figure 8.17 - Prediction of horizontal displacement at section J

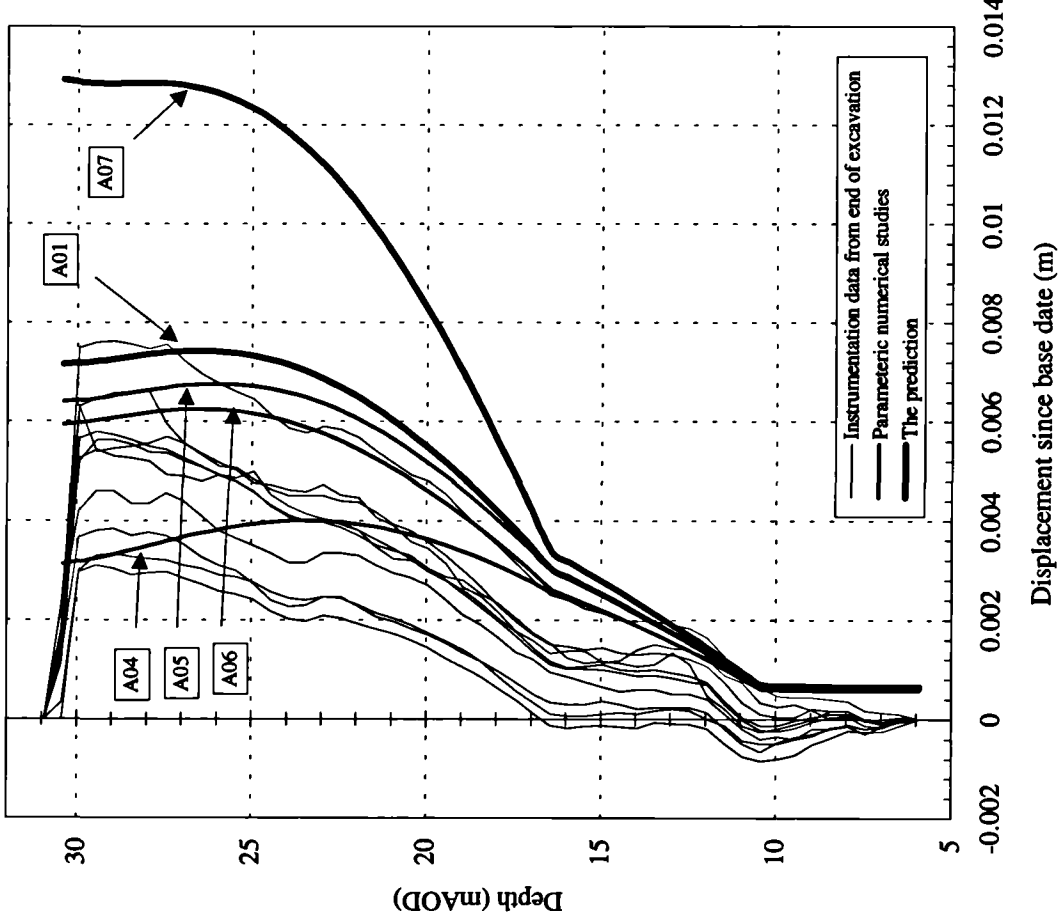


Figure 8.18 - Prediction of horizontal displacement at section K

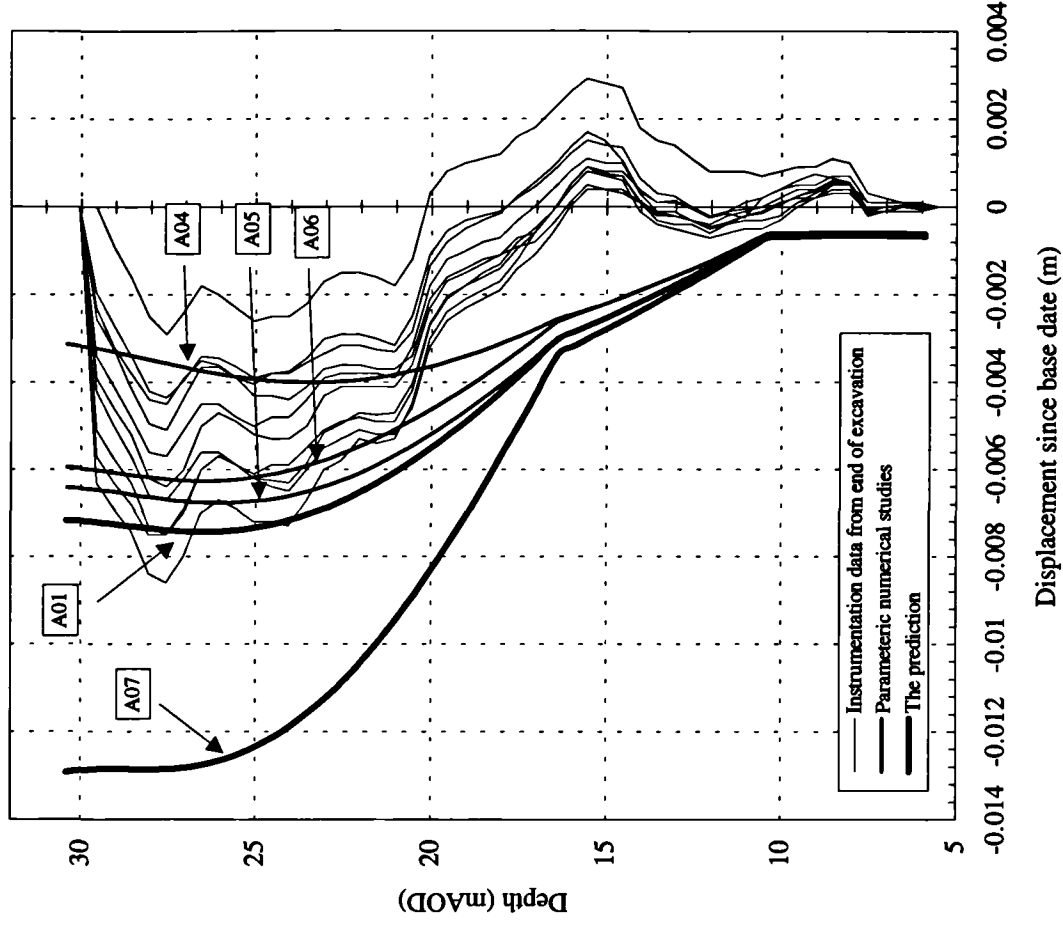


Figure 8.19 - Prediction of horizontal displacement at section L

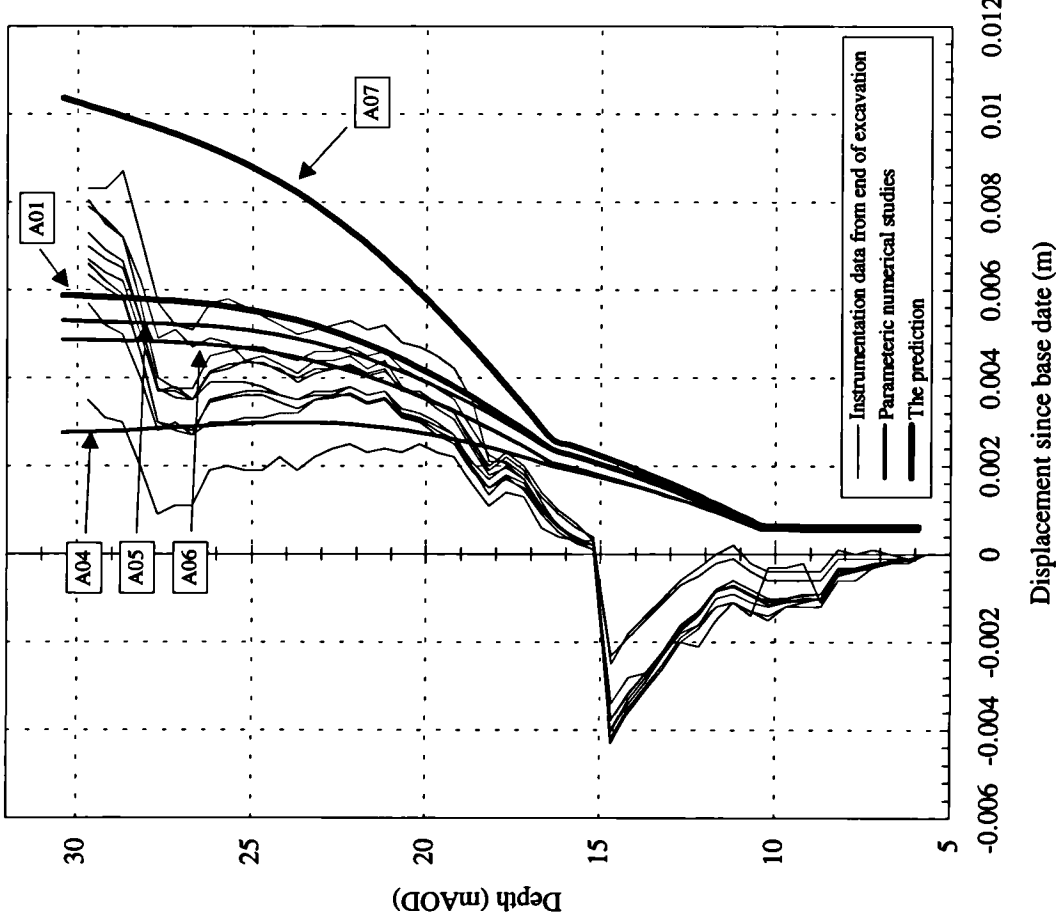


Figure 8.20 - Prediction of horizontal displacement at section M

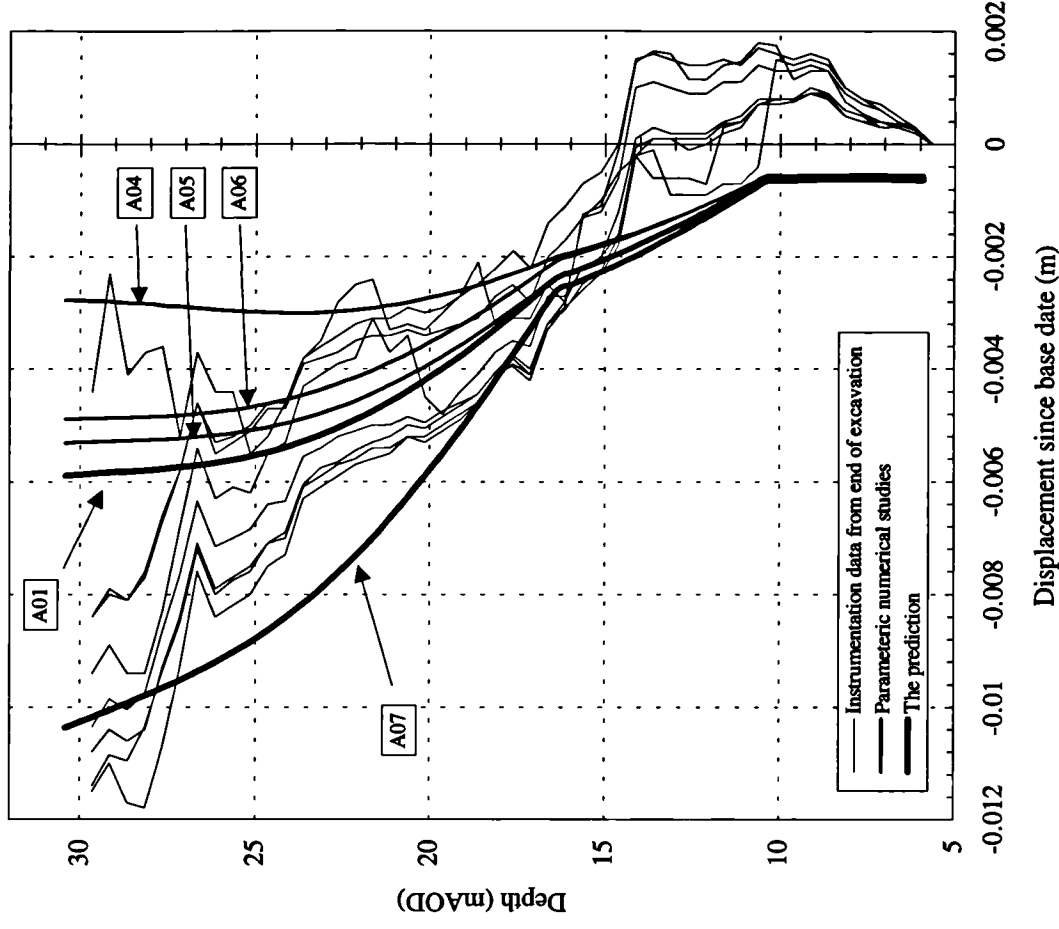


Figure 8.21 - Prediction of horizontal displacement at section N

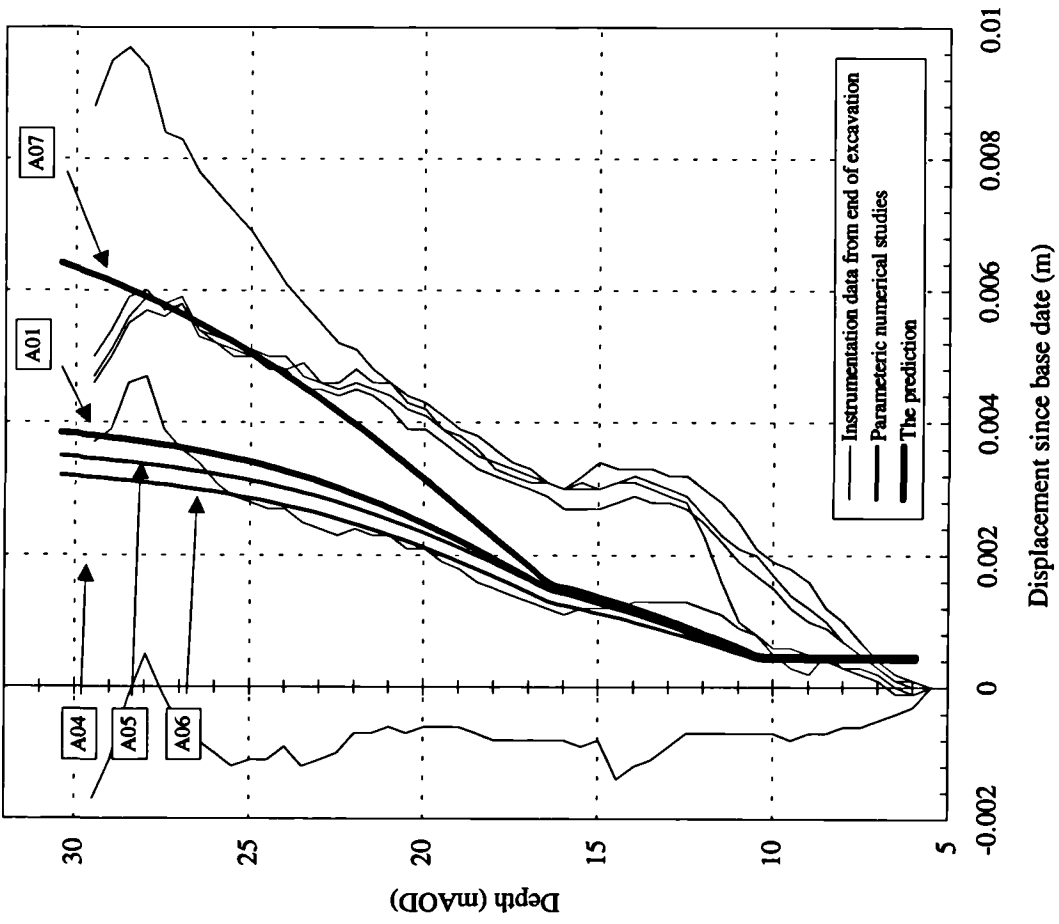


Figure 8.22 - Prediction of horizontal displacement at section O

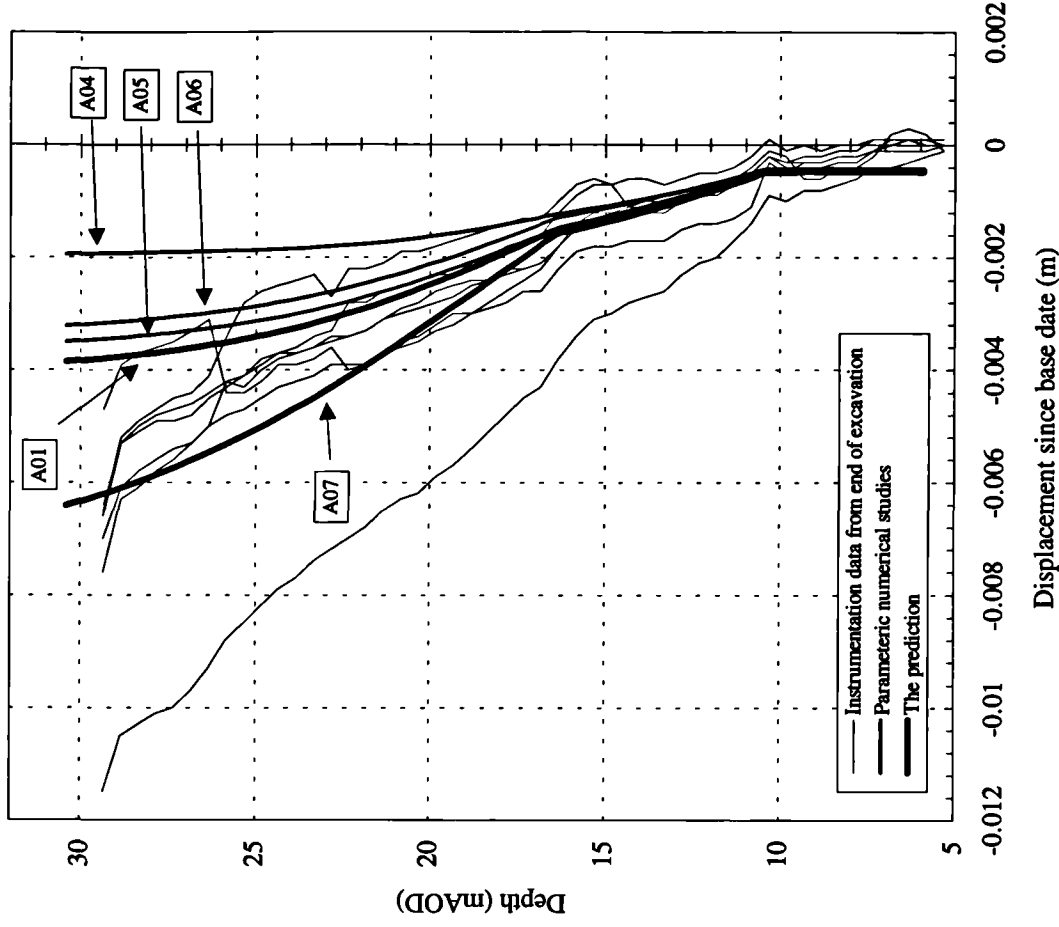


Figure 8.23 - Prediction of horizontal displacement at section P

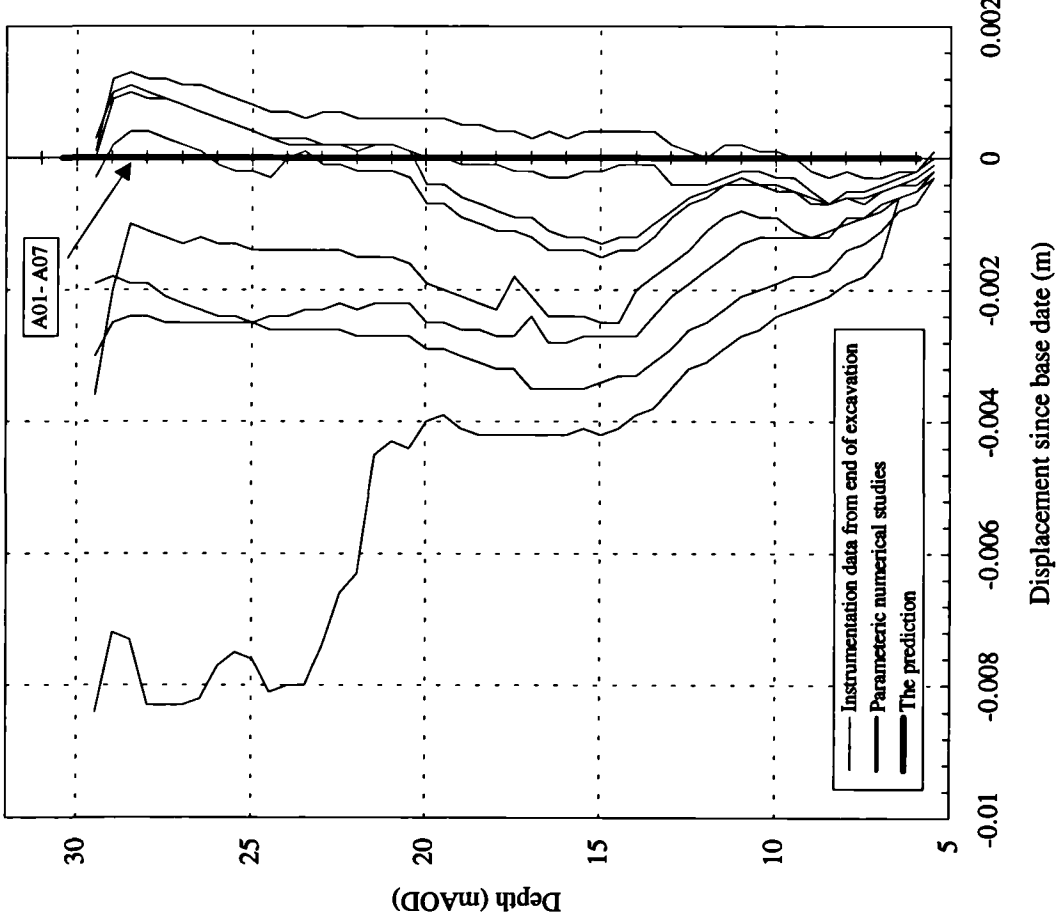


Figure 8.24 - Prediction of horizontal displacement at section Q

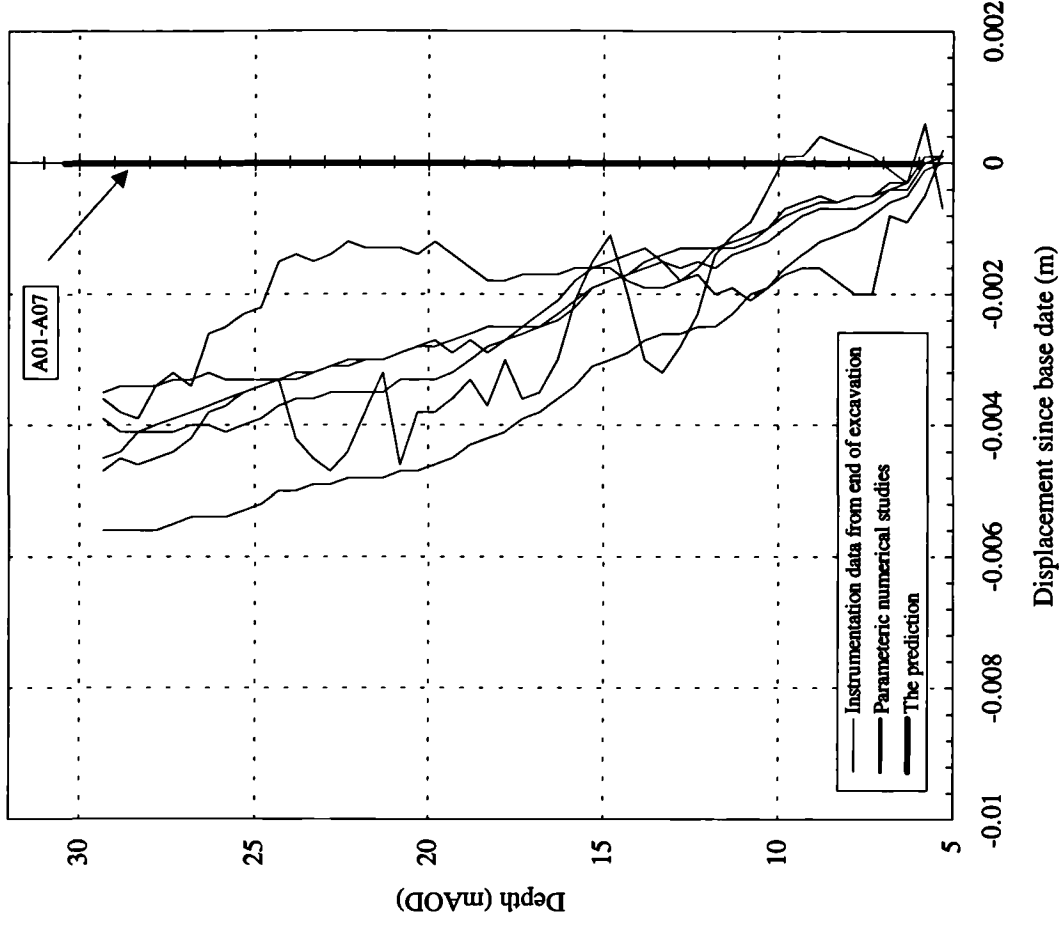


Figure 8.25 - Prediction of horizontal displacement at section R

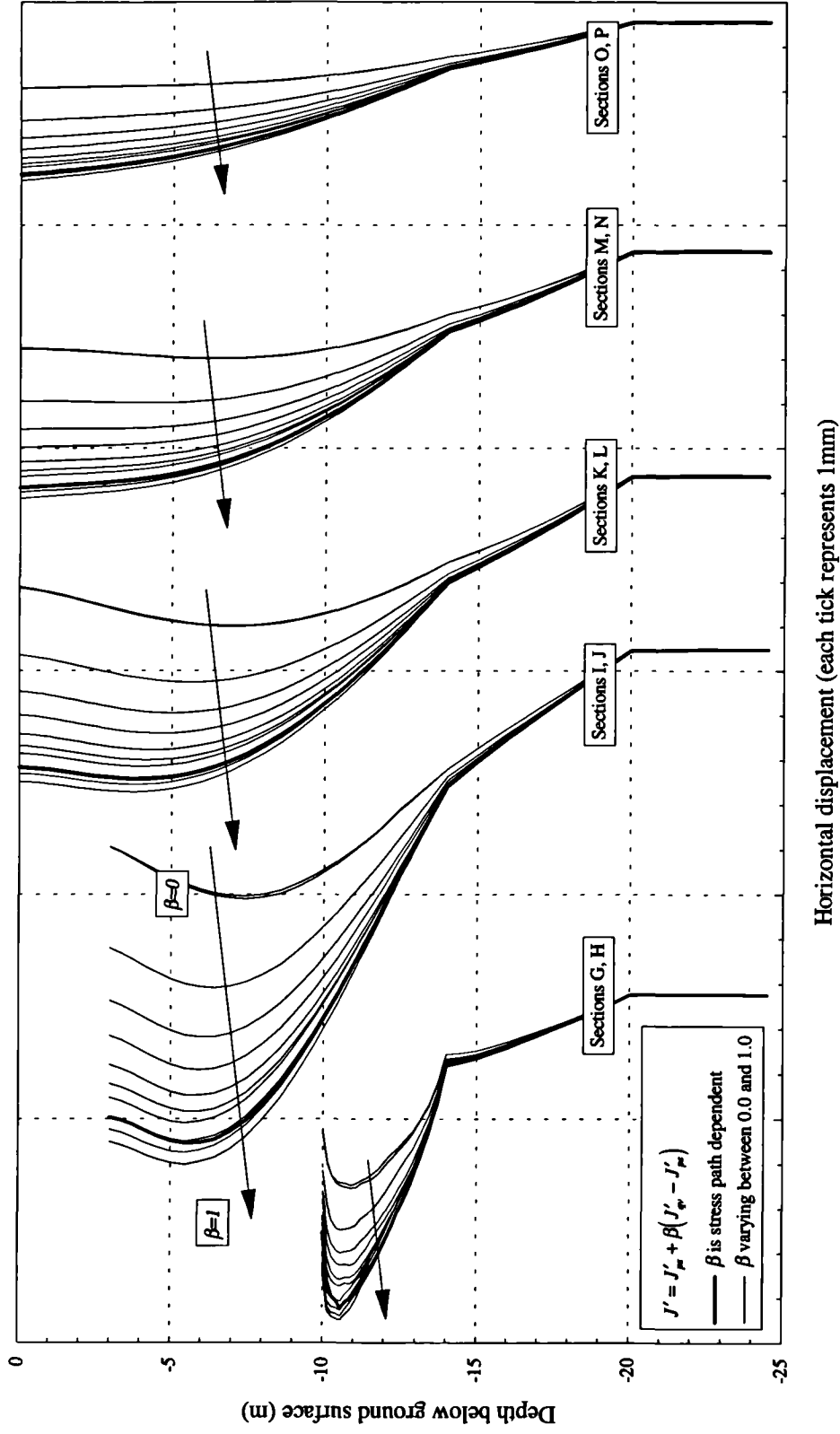


Figure 8.26 - Effect on non-linear cross-anisotropic model prediction of horizontal displacement when the degree of anisotropy is varied using the β parameter

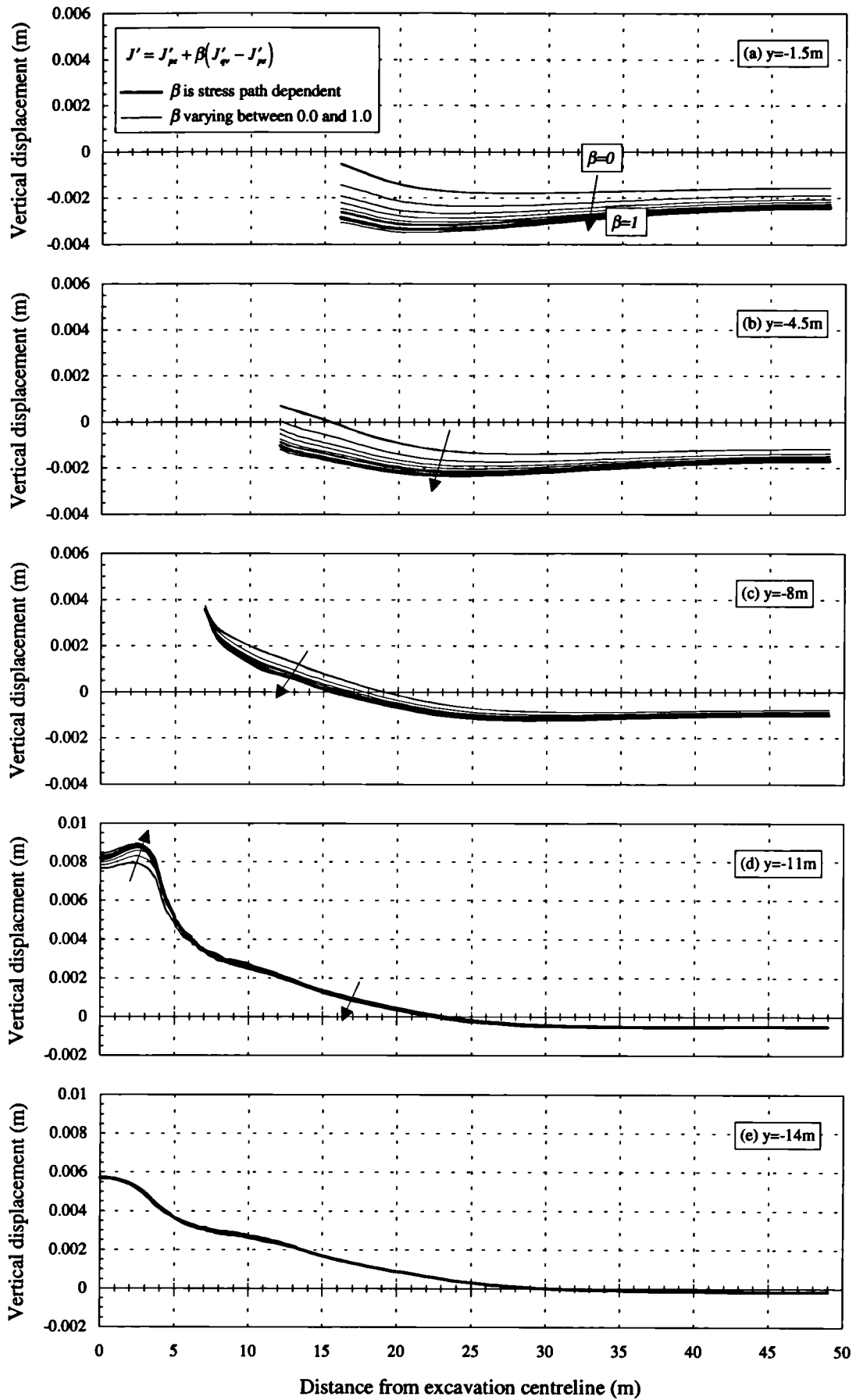


Figure 8.27 - Effect on non-linear cross-anisotropic model prediction of vertical displacement when the degree of anisotropy is varied using the β parameter

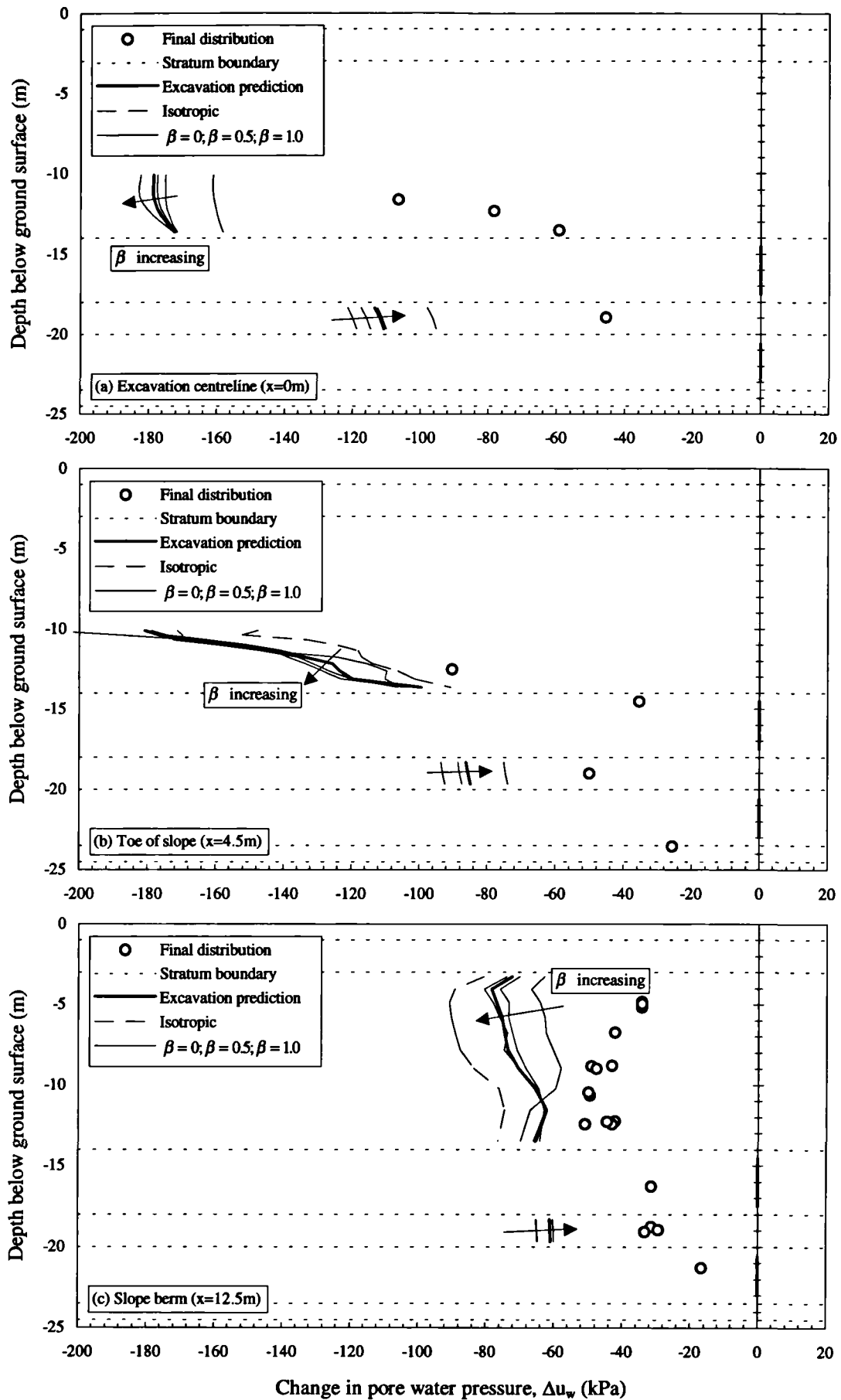


Figure 8.28 - The effect of the varying the coupling stiffness on the pore water pressure response in the non-linear cross-anisotropic elastic model

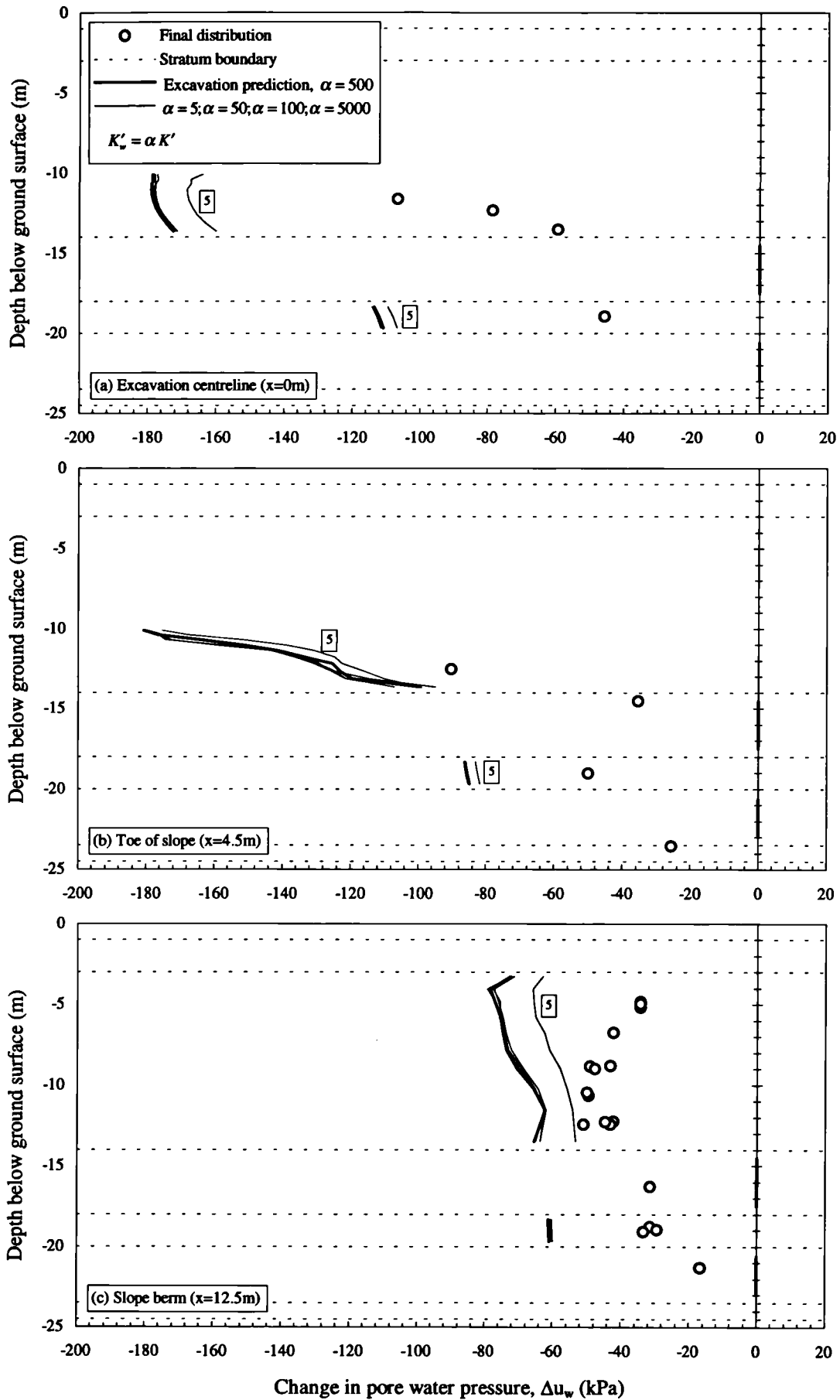


Figure 8.29 - The effect of varying the bulk stiffness of water in the Oxford Clay for pore water pressure response in non-linear cross-anisotropic elastic model

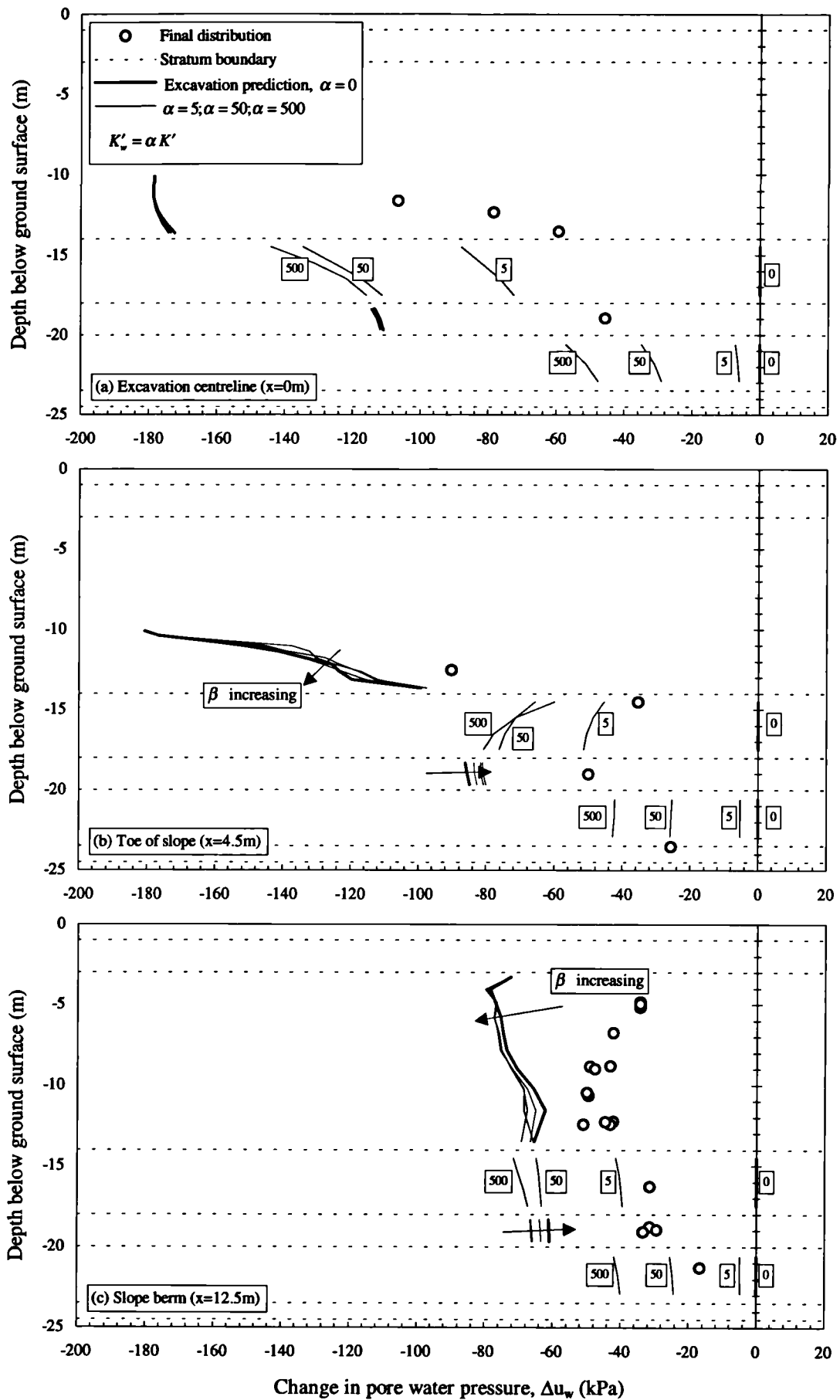
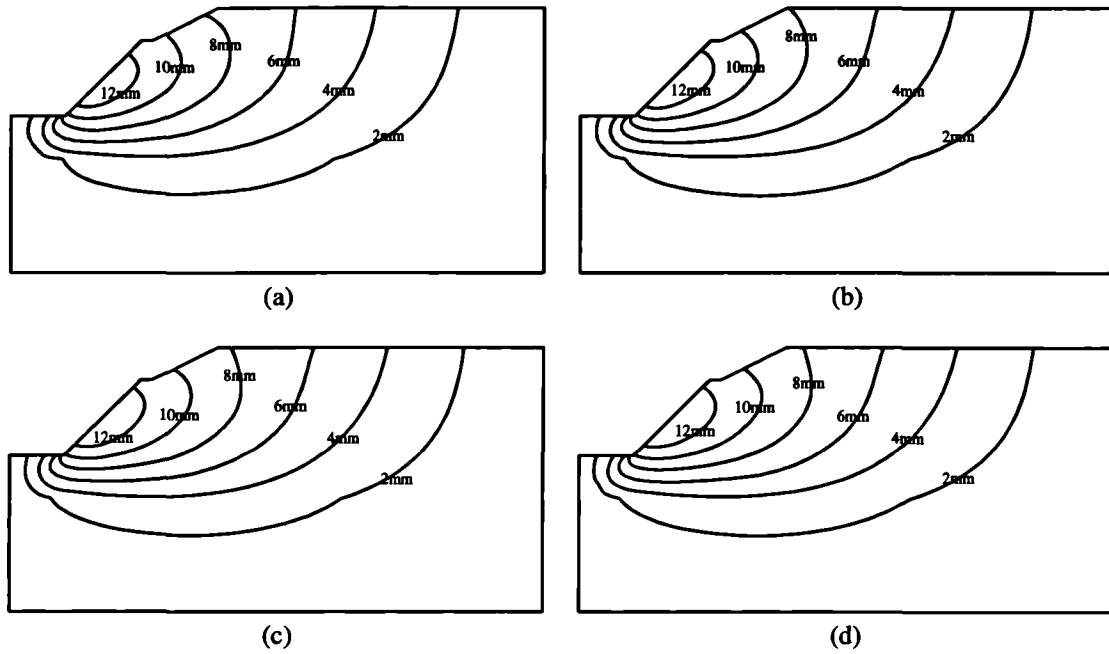
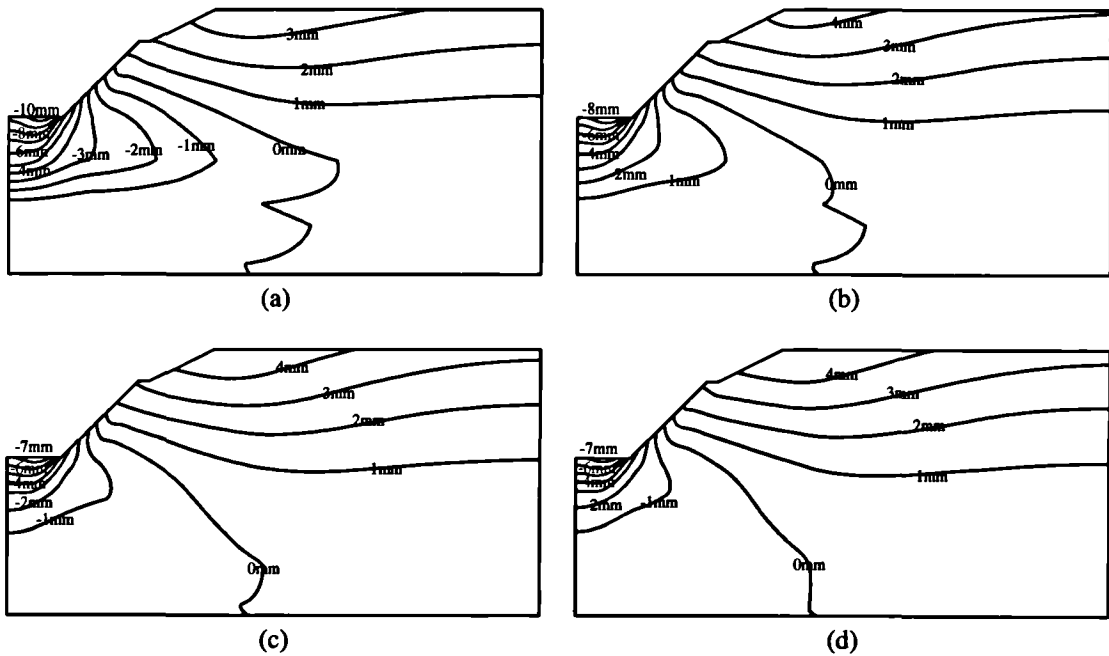


Figure 8.30 - The effect of varying the bulk stiffness of water in the soil strata below the Oxford Clay for the non-linear cross-anisotropic elastic model

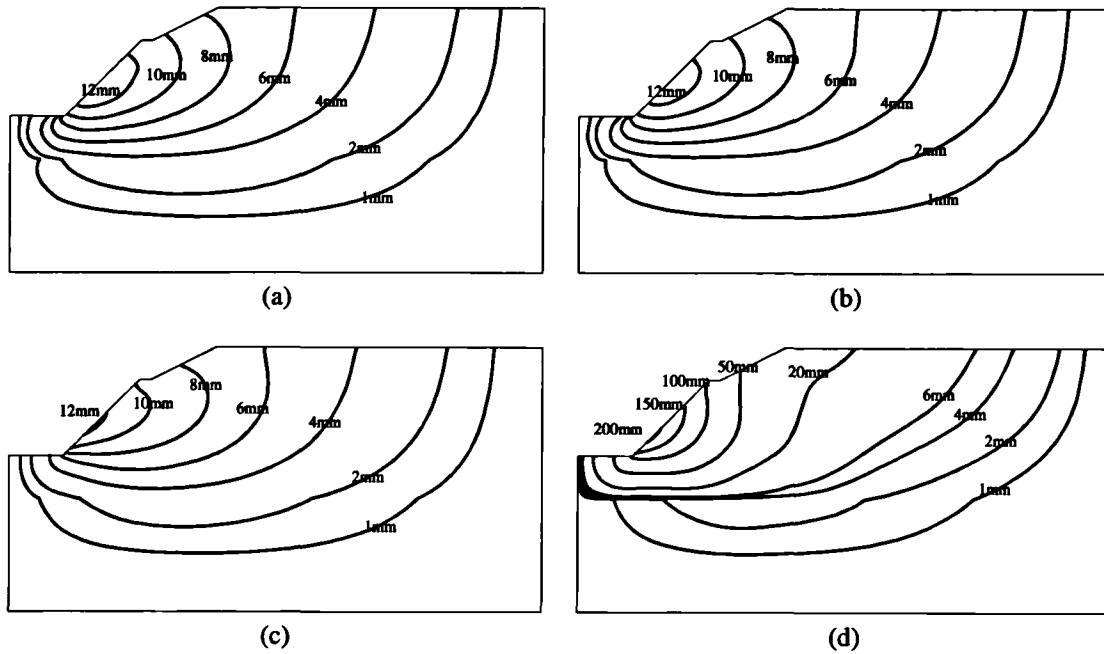


Horizontal displacement

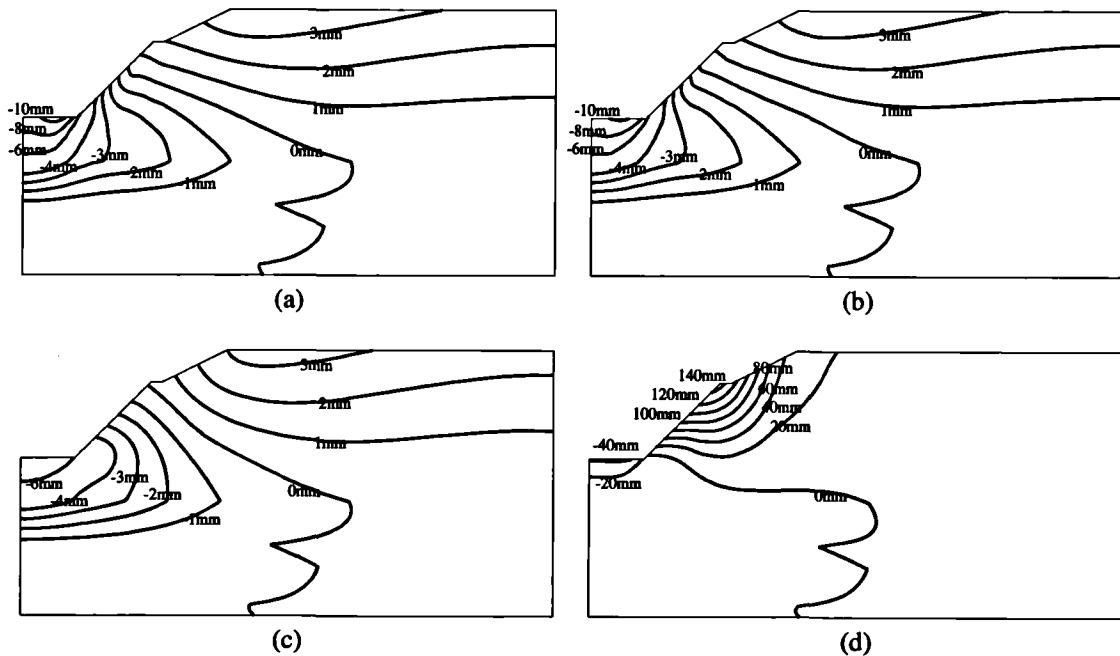


Vertical displacement

Figure 8.31 - The effect of the degree of drainage in the underlying sand and limestone layers on horizontal and vertical displacement following excavation when $n=500$ in Oxford Clay and Kellaways Clay and $n=0$ (b) $n=1$ (c) $n=50$ (d) $n=500$ in Kellaways Sand and limestone strata



Horizontal displacement



Vertical displacement

Figure 8.32 - The effect of the initial stress path direction on non-linear anisotropic elastic CRISP analyses of the excavation (a) stiffness characteristic applied dynamically dependent on the current stress path direction at element centroid (b) stress path direction at individual element integration points (c) stiffness characteristic associated with loading/compression stress path (d) stiffness characteristic associated with unloading/extension stress path.

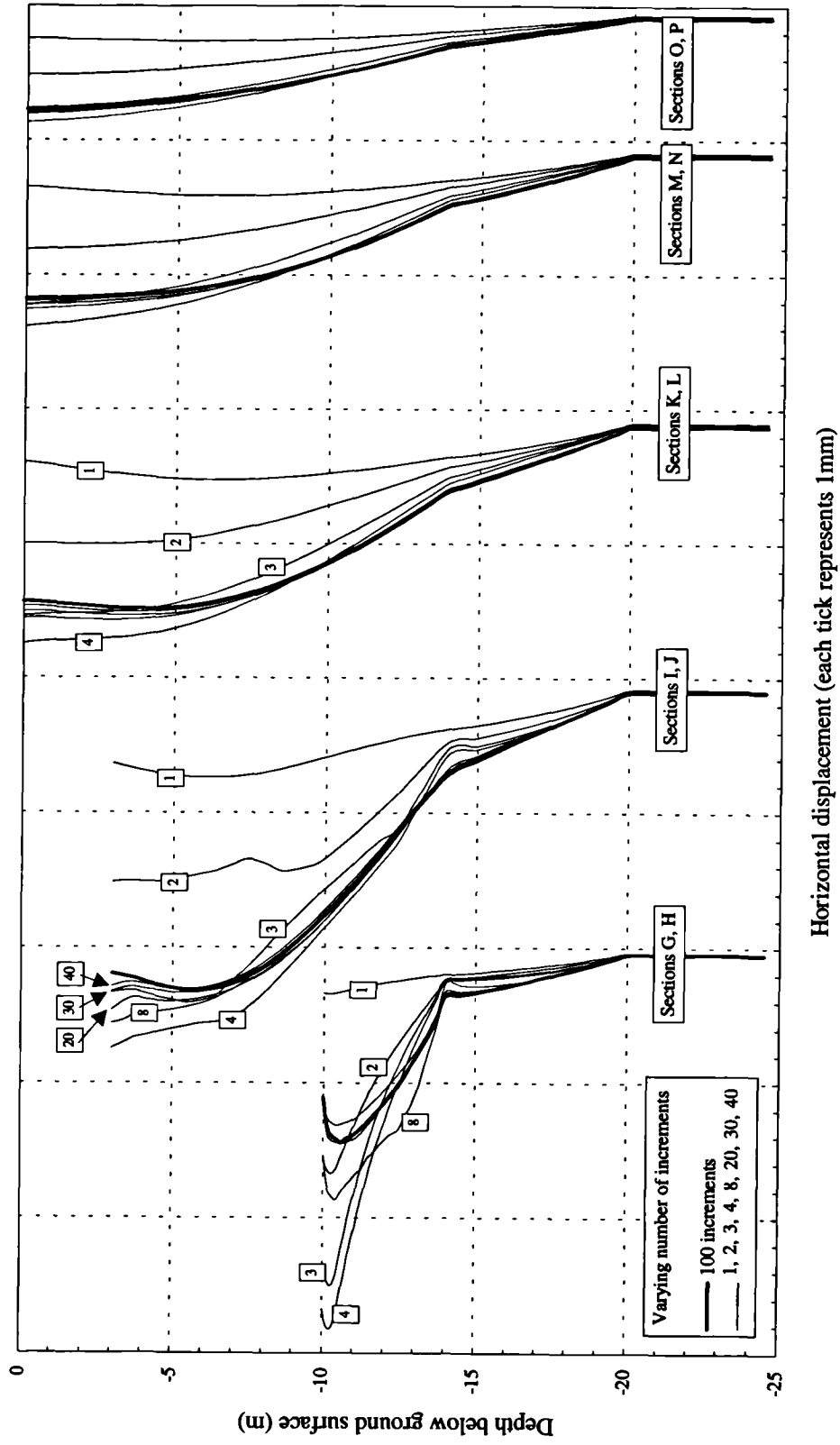


Figure 8.33 - Effect on non-linear cross-anisotropic model prediction of horizontal displacement when the number of increments per analysis is varied

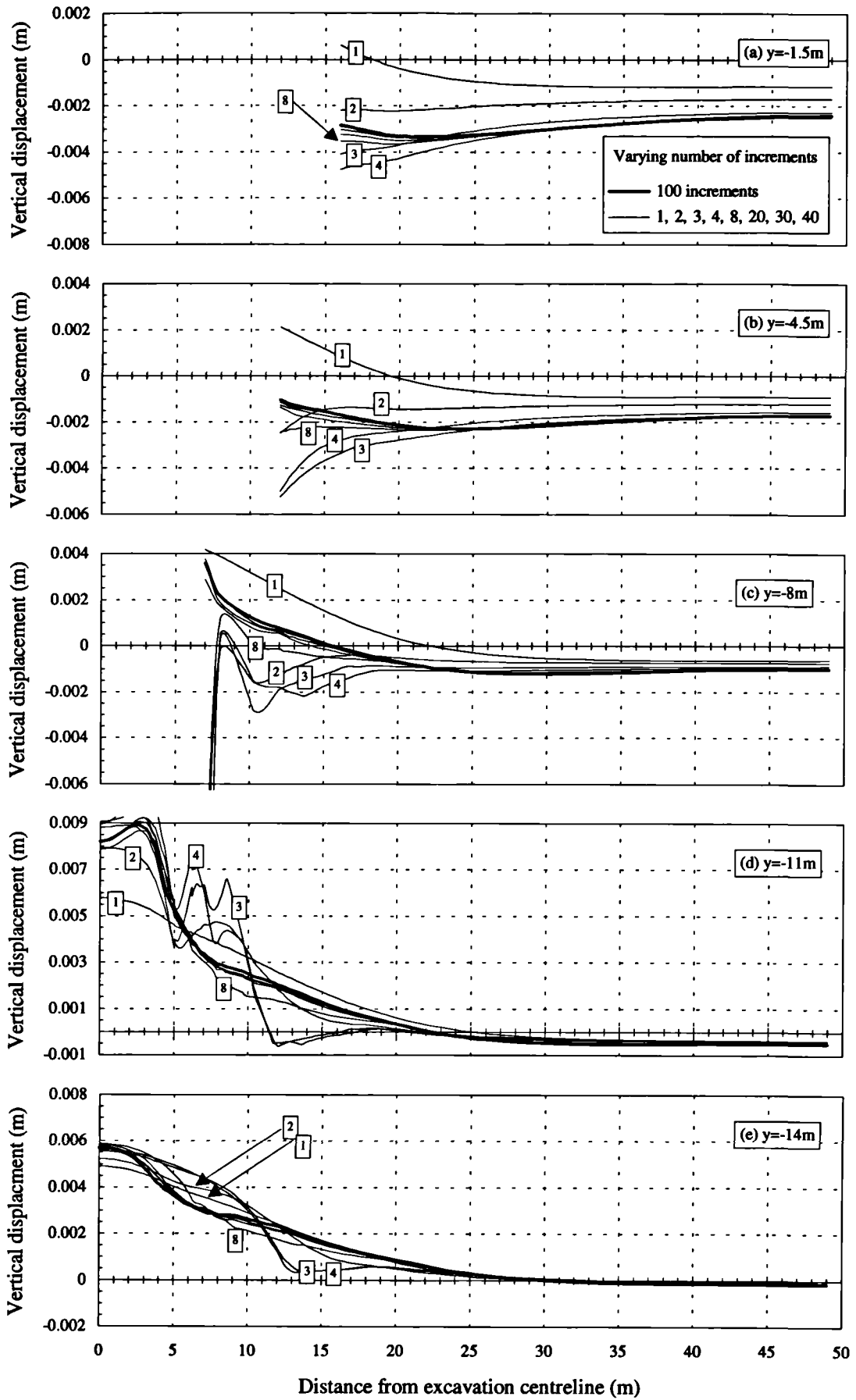


Figure 8.34 - Effect on non-linear cross-anisotropic model prediction of vertical displacement when the number of increments per analysis is varied

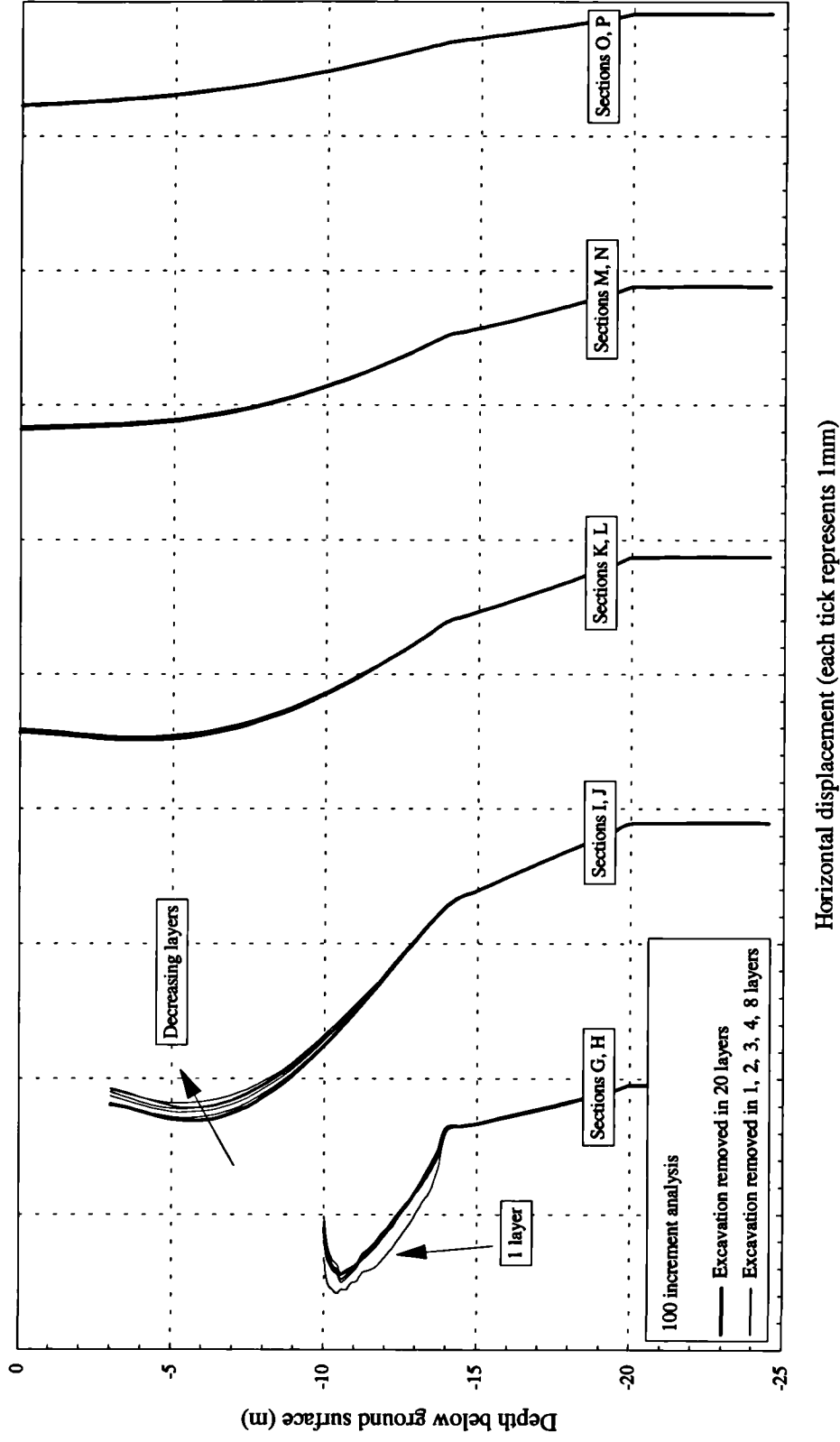


Figure 8.35 - Effect on non-linear cross-anisotropic model prediction of horizontal displacement when the effect of the excavation modelling process is altered

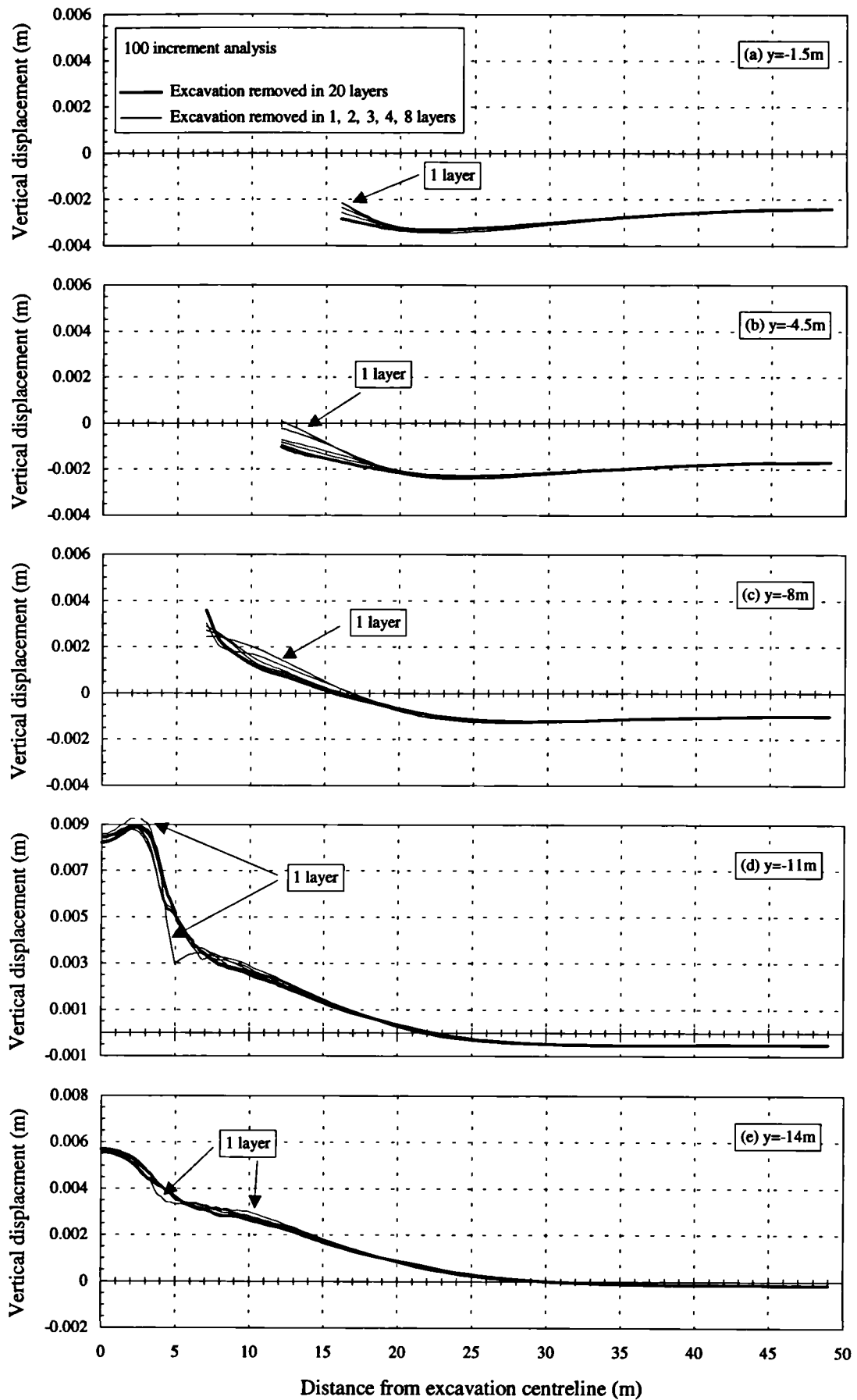


Figure 8.36 - Effect on non-linear cross-anisotropic model prediction of vertical displacement when the effect of the excavation modelling process is altered

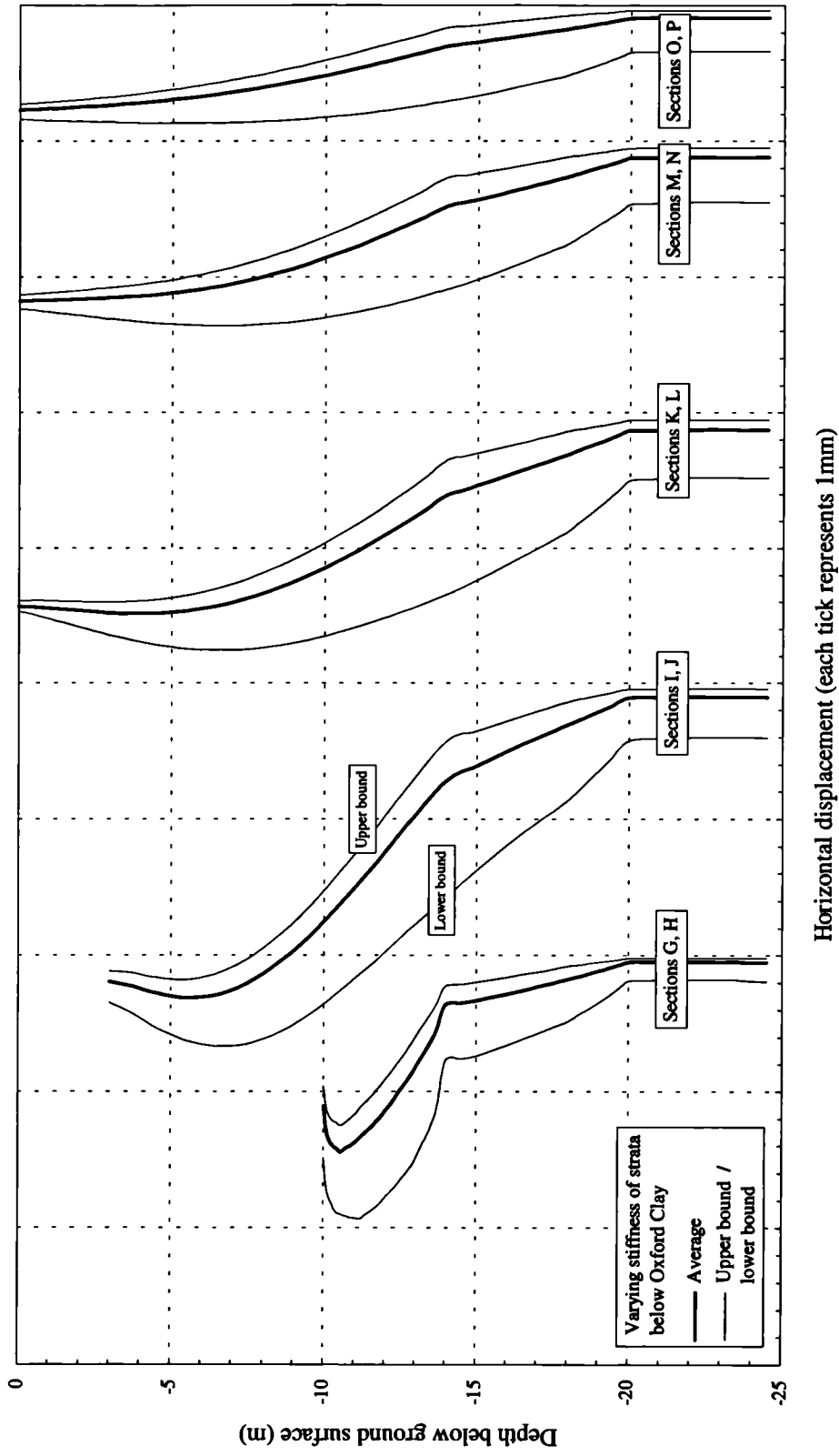


Figure 8.37 - Effect on non-linear cross-anisotropic model prediction of horizontal displacement when stiffness of the lower soil and rock strata is varied

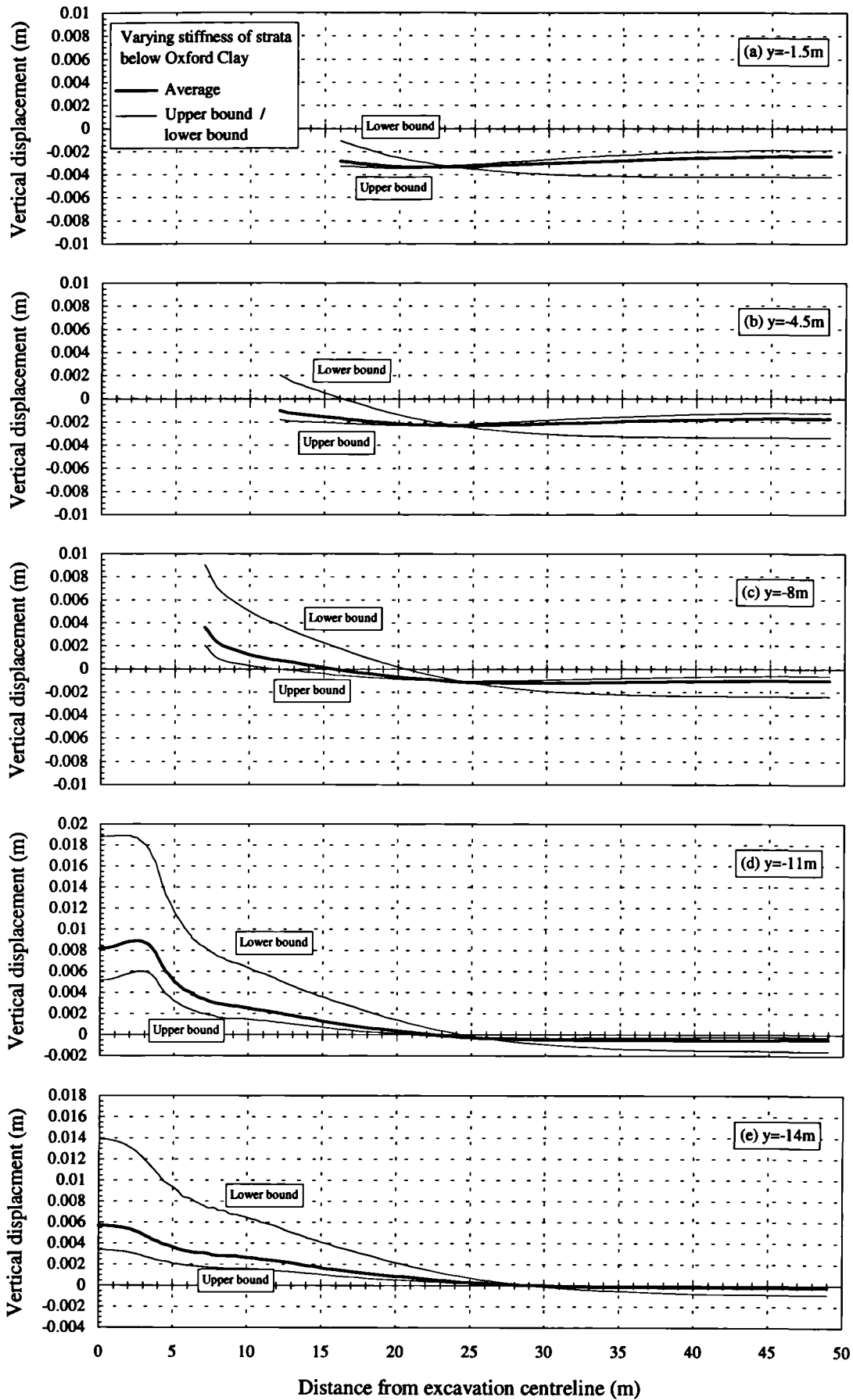
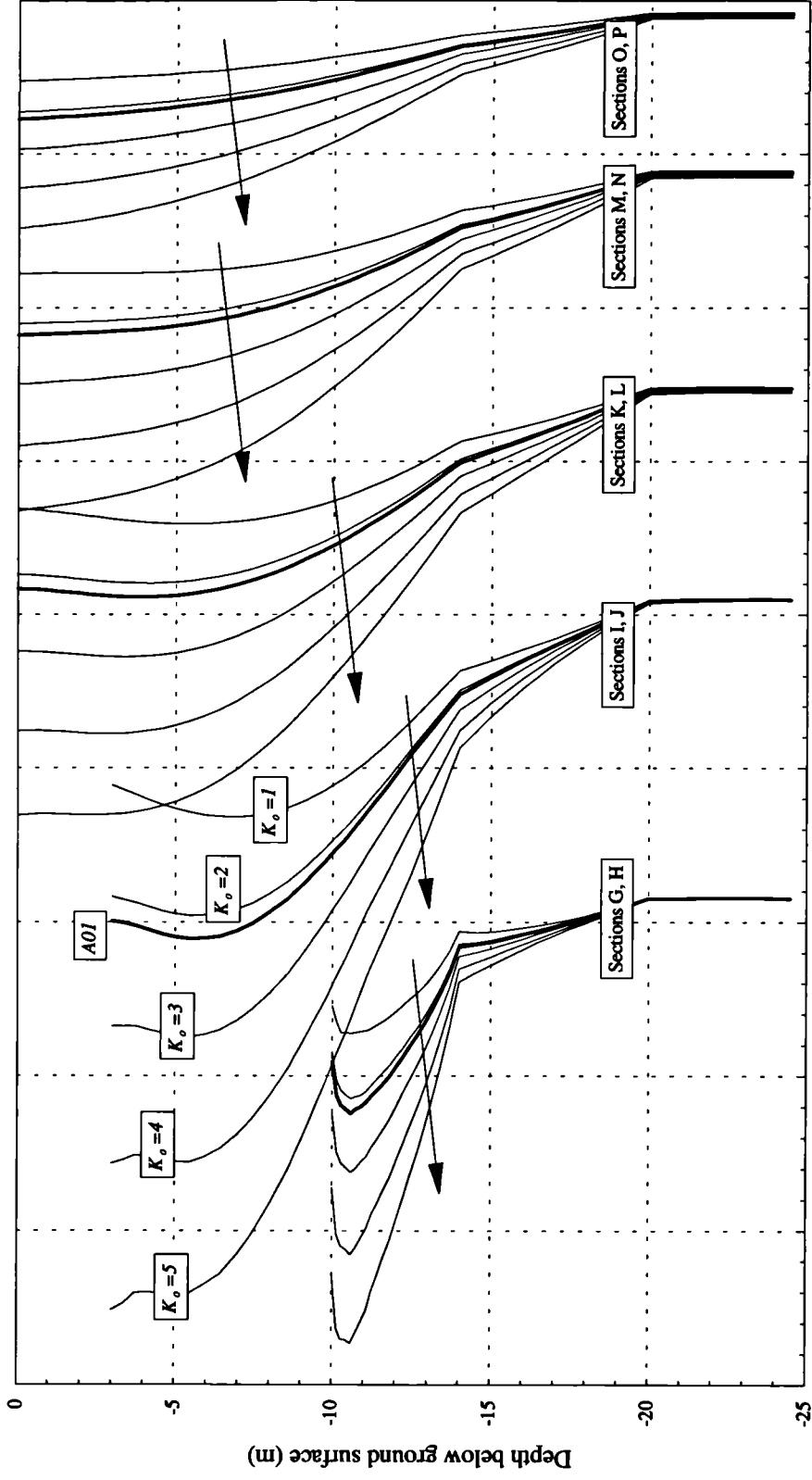


Figure 8.38 - Effect on non-linear cross-anisotropic model prediction of vertical displacement when stiffness of the lower soil and rock strata is varied



Horizontal displacement (each tick represents 1mm)

Figure 8.39 - Effect on non-linear cross-anisotropic model prediction of horizontal displacement when varying K_0 within the Oxford Clay

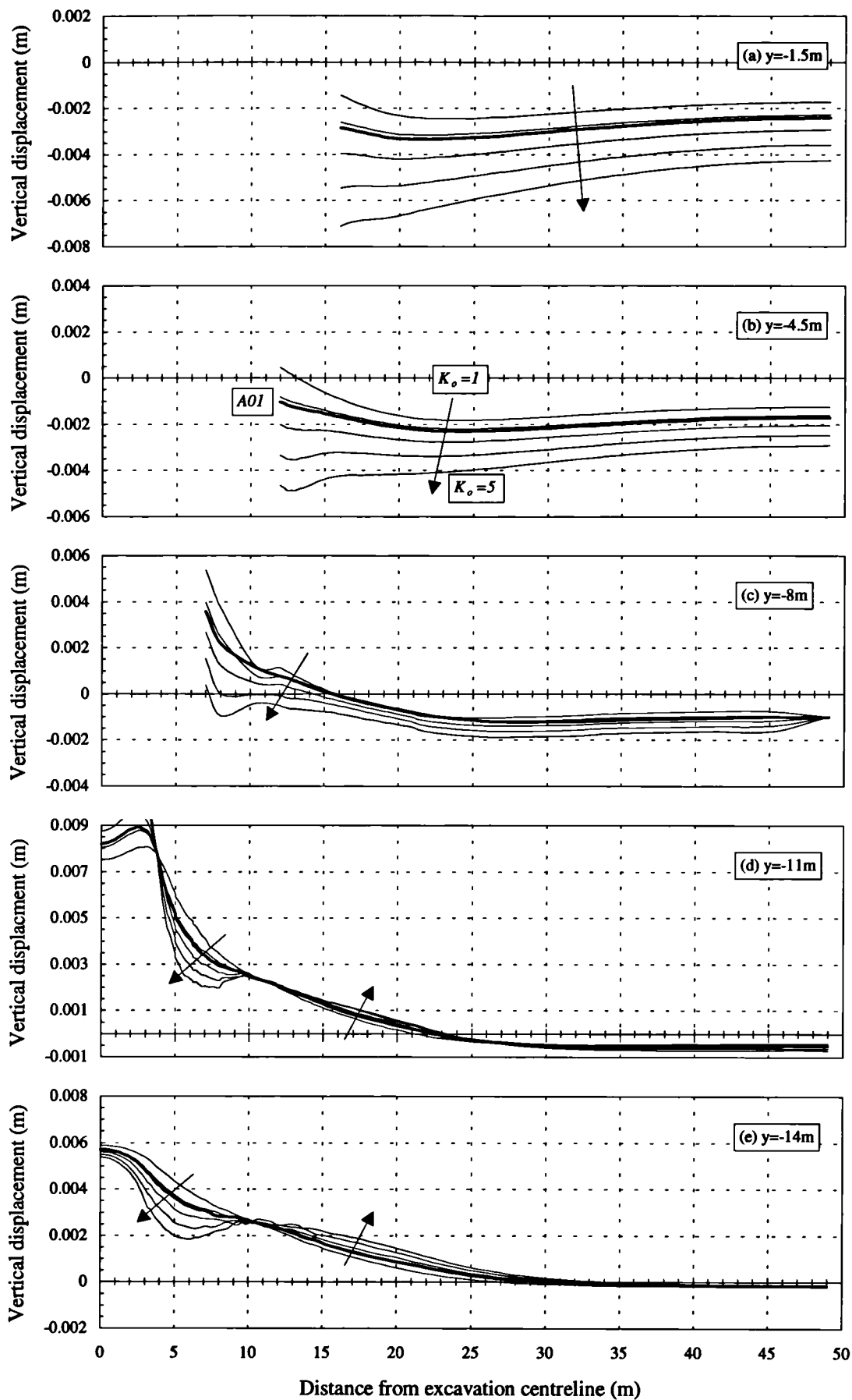


Figure 8.40 - Effect on non-linear cross-anisotropic model prediction of vertical displacement when varying K_o within the Oxford Clay

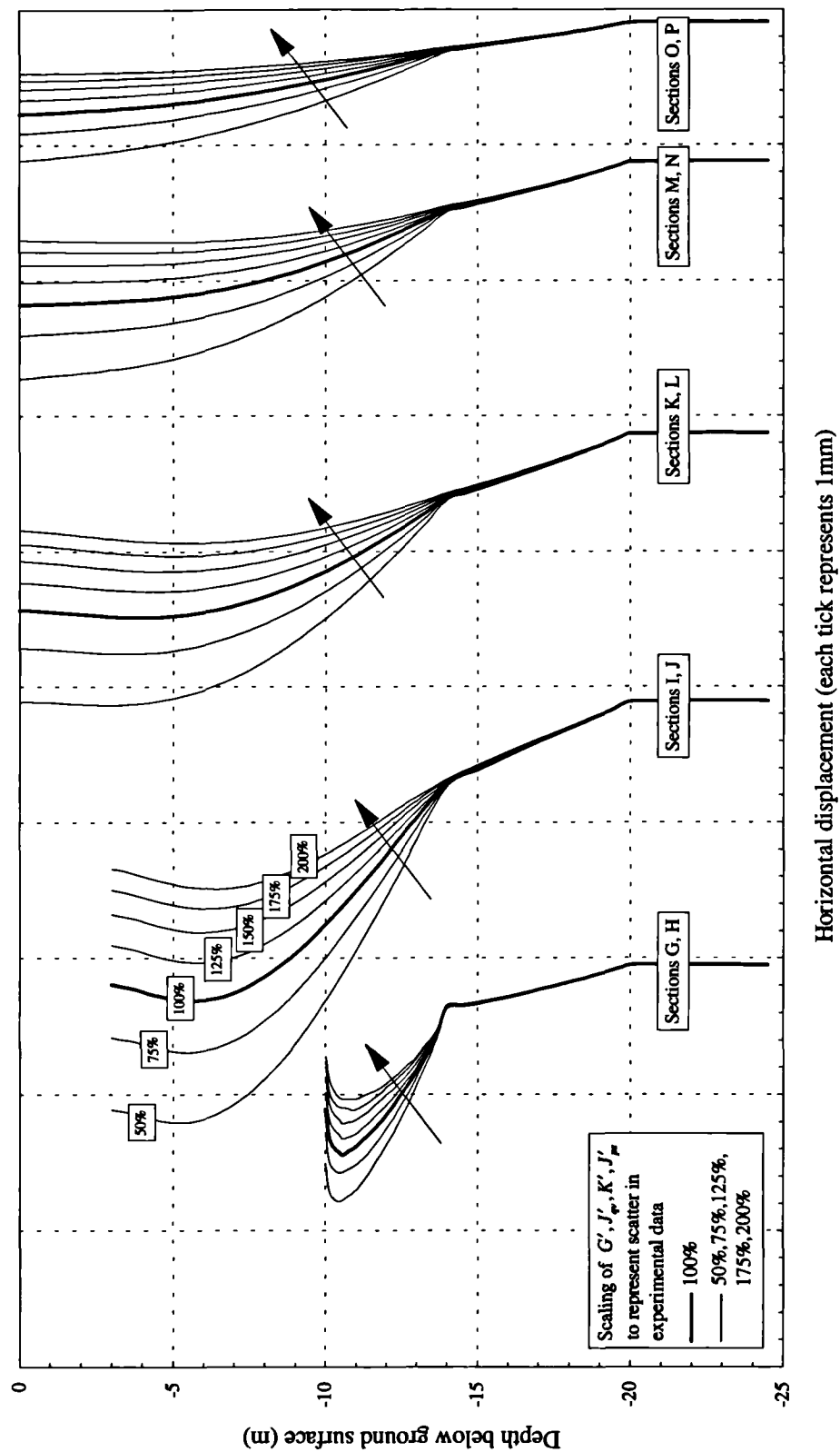


Figure 8.41 - Effect on non-linear cross-anisotropic model prediction of horizontal displacement when stiffness is varied over experimental range

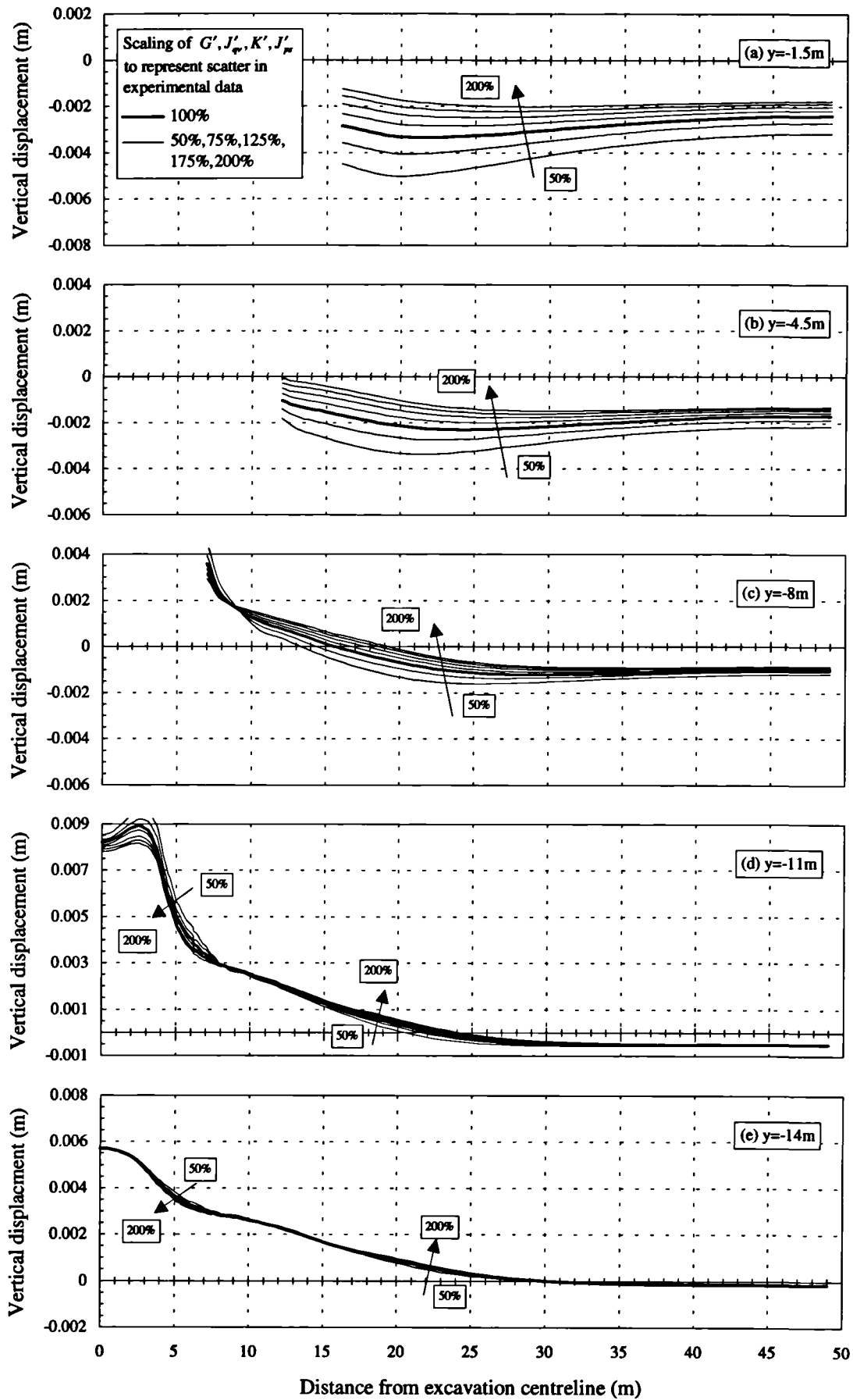


Figure 8.42 - Effect on non-linear cross-anisotropic model prediction of vertical displacement when stiffness is varied over experimental range

8.11 Back analysis of instrument data

As described in section 8.9.1, the back analysis was limited to varying stiffness parameters in a simple way associated with their method of determination. Consequently, this involved the following exploratory computations (example plots are presented for the stiffness parameters derived during increasing q or increasing p' stress paths although the conclusions are valid for the other quadrants of q - p' space):

- The deviatoric stiffness, G' , was scaled independently (Figure 8.43)
- The volumetric stiffness, K' , was scaled independently (Figure 8.44)
- The combined coupling stiffness, J' , was scaled independently (Figure 8.45)
- G' and J' (through J'_{qv}) were scaled simultaneously (Figure 8.46)
- K' and J' (through J'_{ps}) were scaled simultaneously (Figure 8.47)
- Finally, all parameters were scaled equally and simultaneously (Figure 8.48)

In this sequence of figures (Figure 8.43 to Figure 8.48), the influence of varying the model parameters is assessed in terms of the implied simplified cross-anisotropic parameters (E^* , ν^* , and α) in order to establish the likely effect on the model prediction. In each case, the specified parameter is varied over a range of values from half that to twice that of the original prediction. It should be noted that such scaling may produce physically unreasonable responses within an elastic constitutive framework. A number of conclusions can be drawn from these variational plots. When the deviatoric stiffness varied separately, E^* , ν^* , and α all vary considerably, but when this variation is combined with a similar variation in the coupling stiffness, α is practically constant. Similarly, when the volumetric stiffness and the coupling stiffness are scaled together, α varies little. This demonstrates that the anisotropic nature of the response is dependent on the ratio of the coupling stiffness to both K' and G' . This is shown in Figure 8.48, when all input parameters are scaled together, resulting in no change in α , and in Figure 8.45, when only J' is varied, in which a greater variation in α is recorded. The anisotropic Poisson's ratio, ν^* , varies considerably as one or two of the input parameters are scaled, although is constant when the parameters K' , G' and J' are scaled simultaneously in Figure 8.48. The least variation in ν^* is seen when only J' is scaled (Figure 8.45) suggesting that ν^* is largely dependent on the ratio of K' to G' . The anisotropic Young's modulus, E^* , is shown to be largely dependent on G' , slightly affected by the variation in J' , and affected very little by variation in K' .

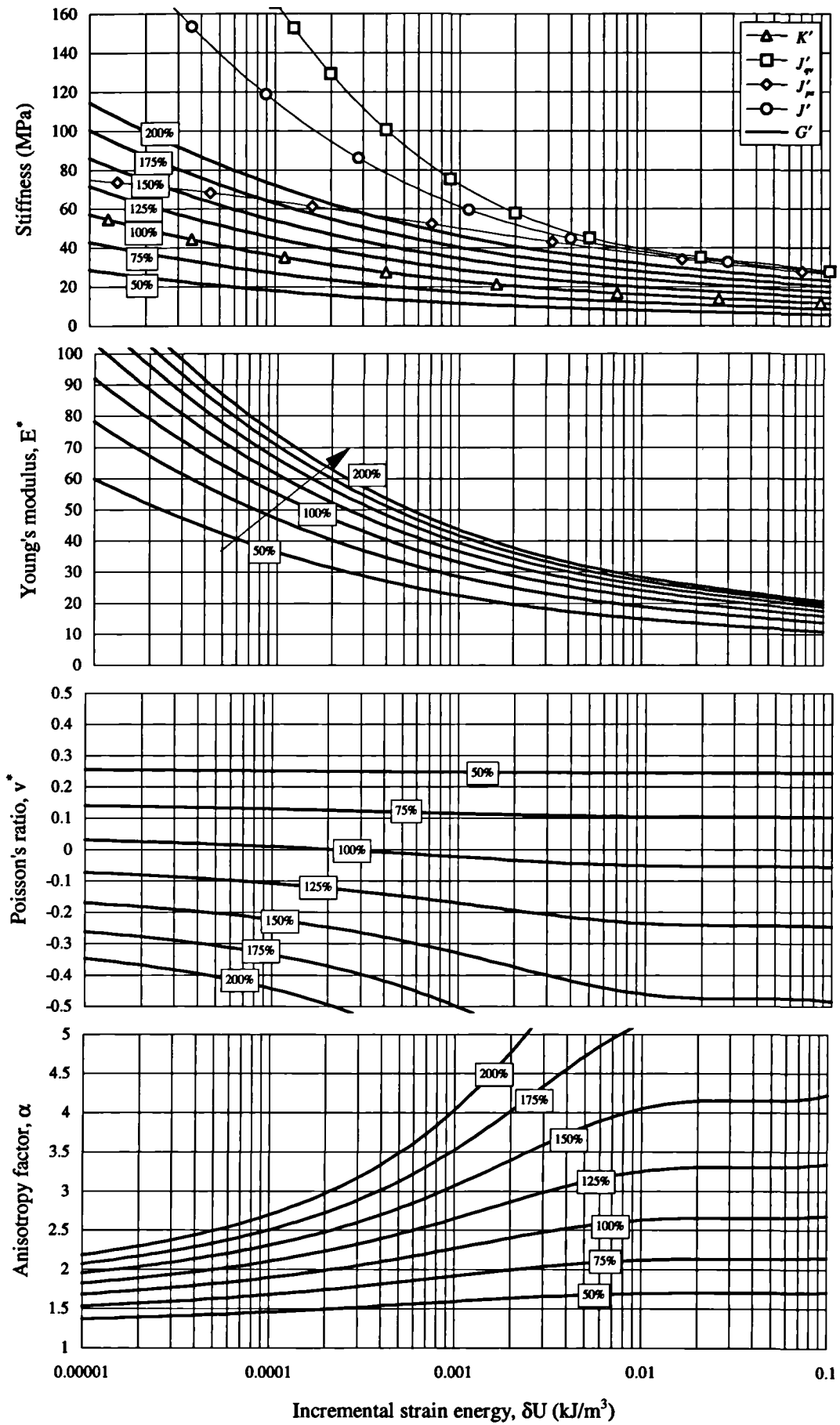


Figure 8.43 - Parametric influence of the deviatoric stiffness derived from constant p' , increasing q stress paths on the anisotropic elastic parameters

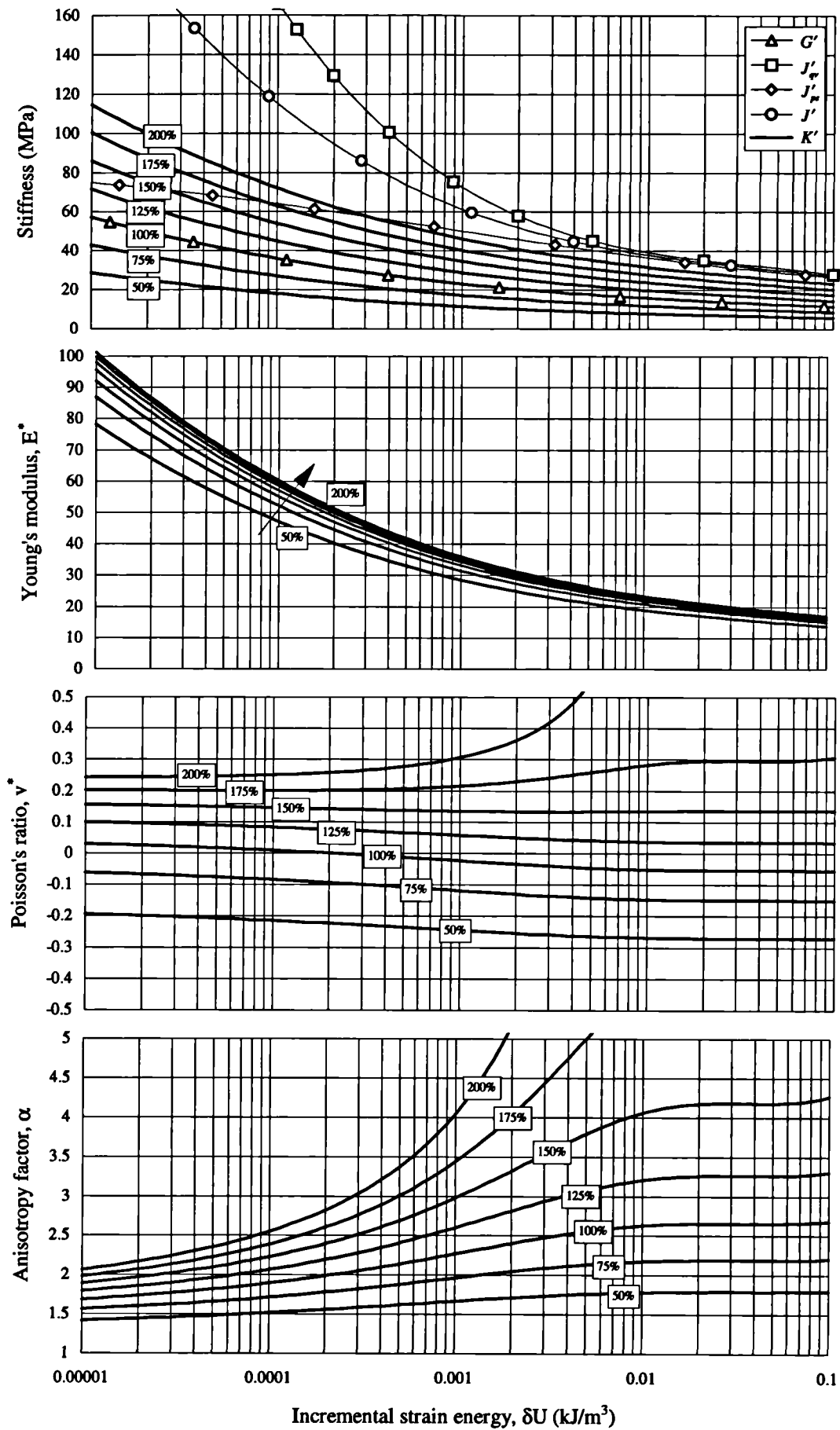


Figure 8.44 - Parametric influence of the volumetric derived from constant q , increasing p' stress paths on the anisotropic elastic parameters

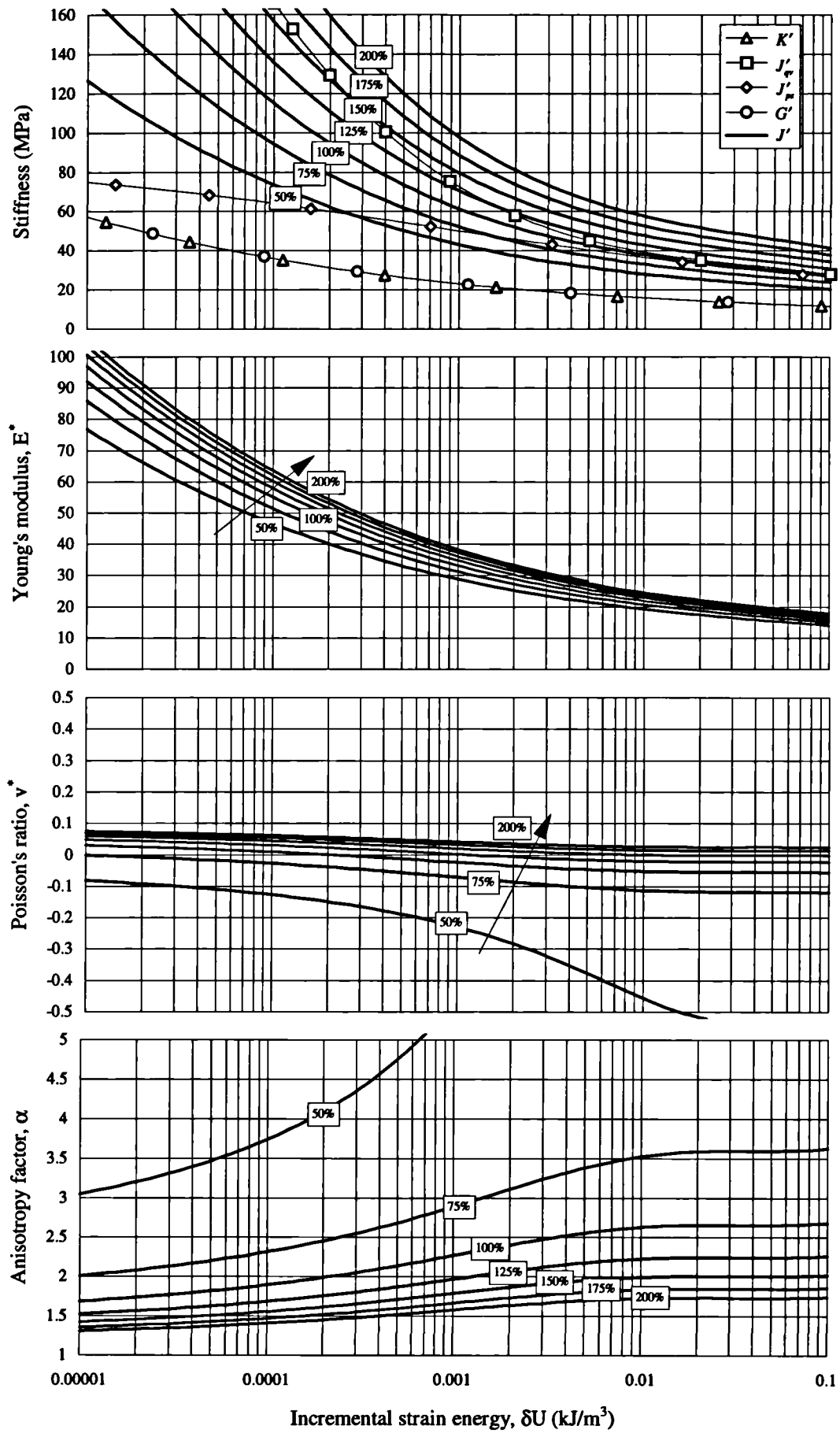


Figure 8.45 - Parametric influence of the combined coupling stiffness on the anisotropic elastic parameters

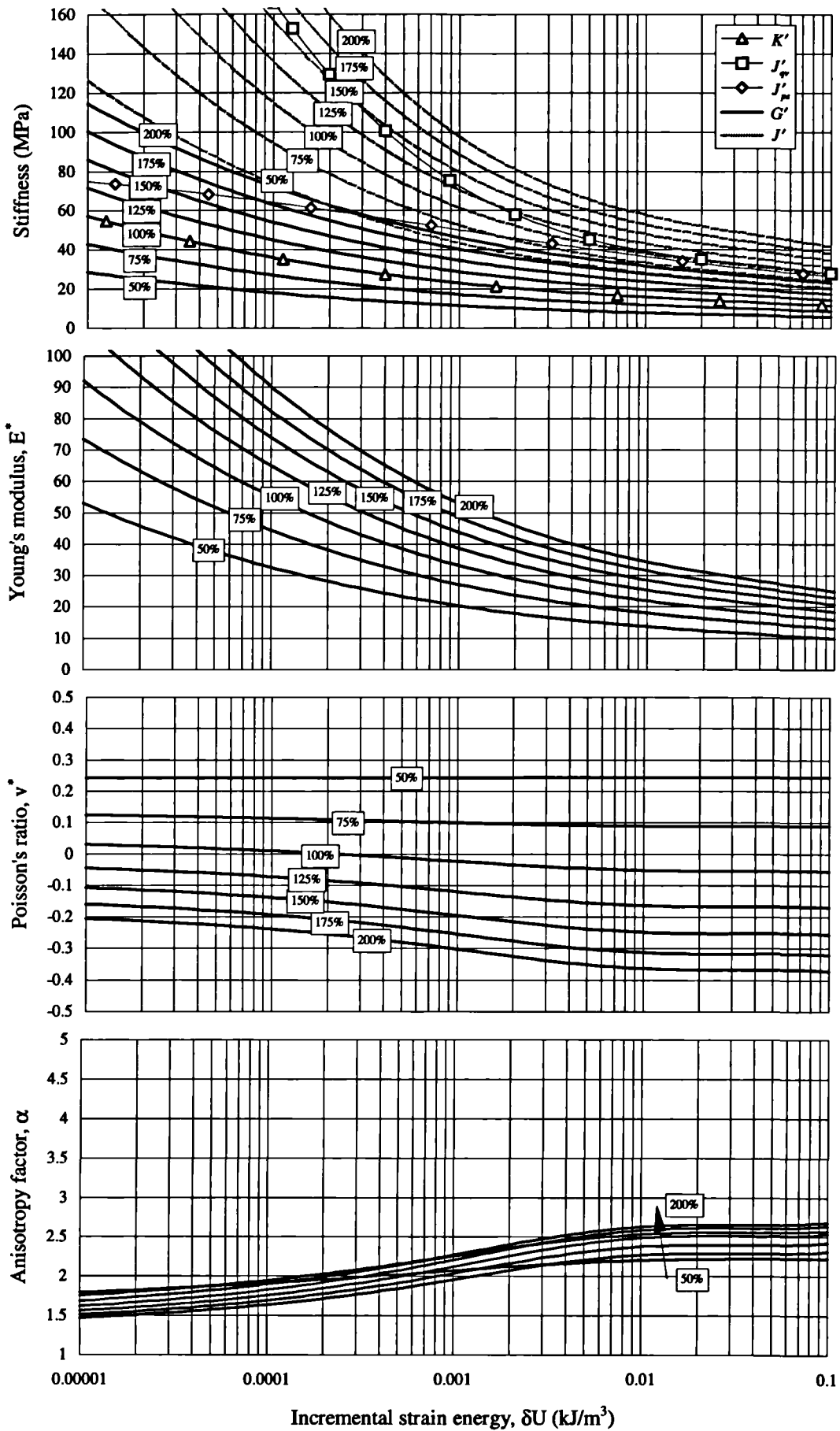


Figure 8.46 - Parametric influence of the deviatoric stiffness and coupling stiffness derived from constant p' , increasing q stress paths on the anisotropic elastic parameters

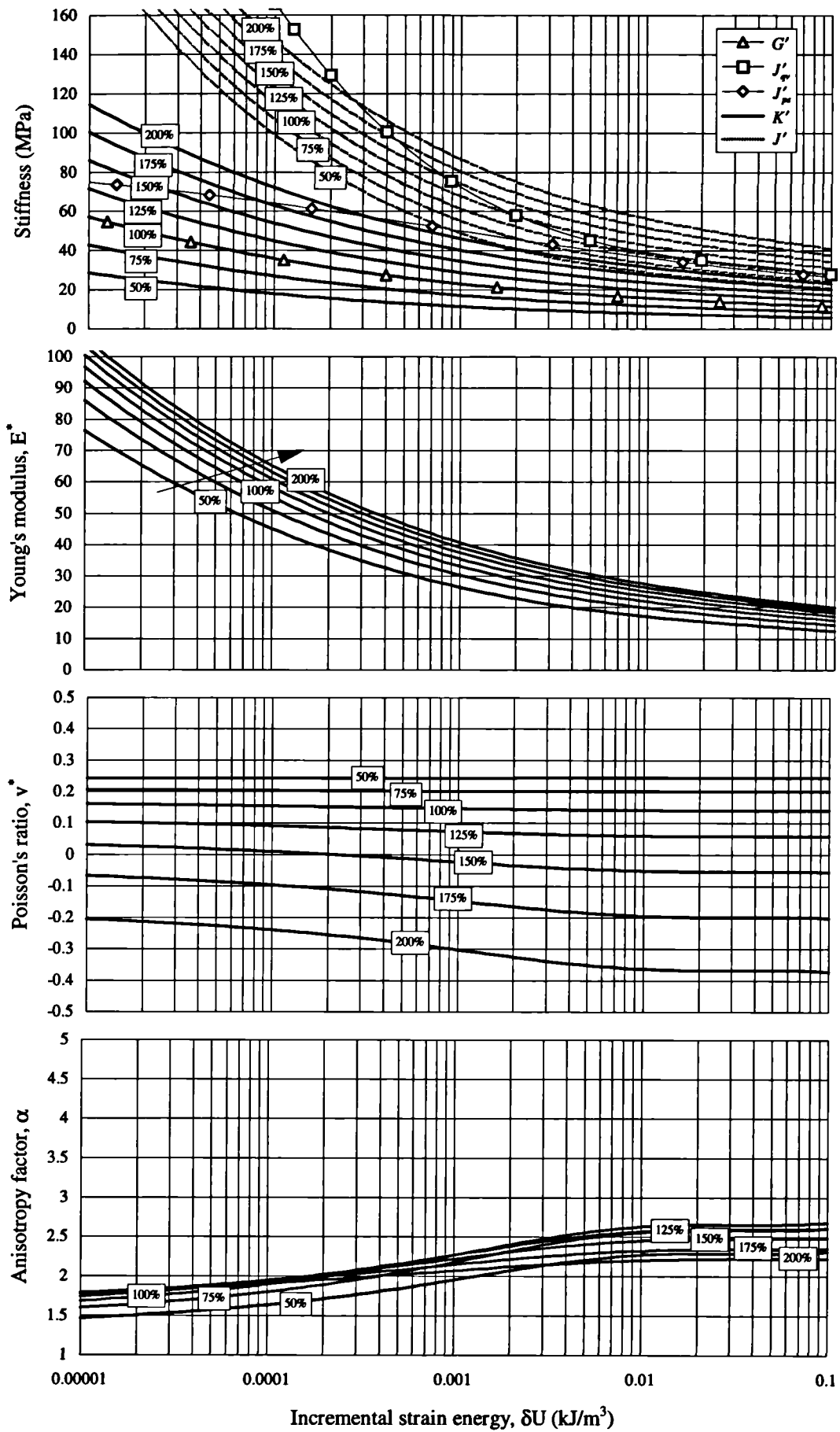


Figure 8.47 - Parametric influence of the volumetric stiffness and coupling stiffness derived from constant q , increasing p' stress paths on the anisotropic elastic parameters

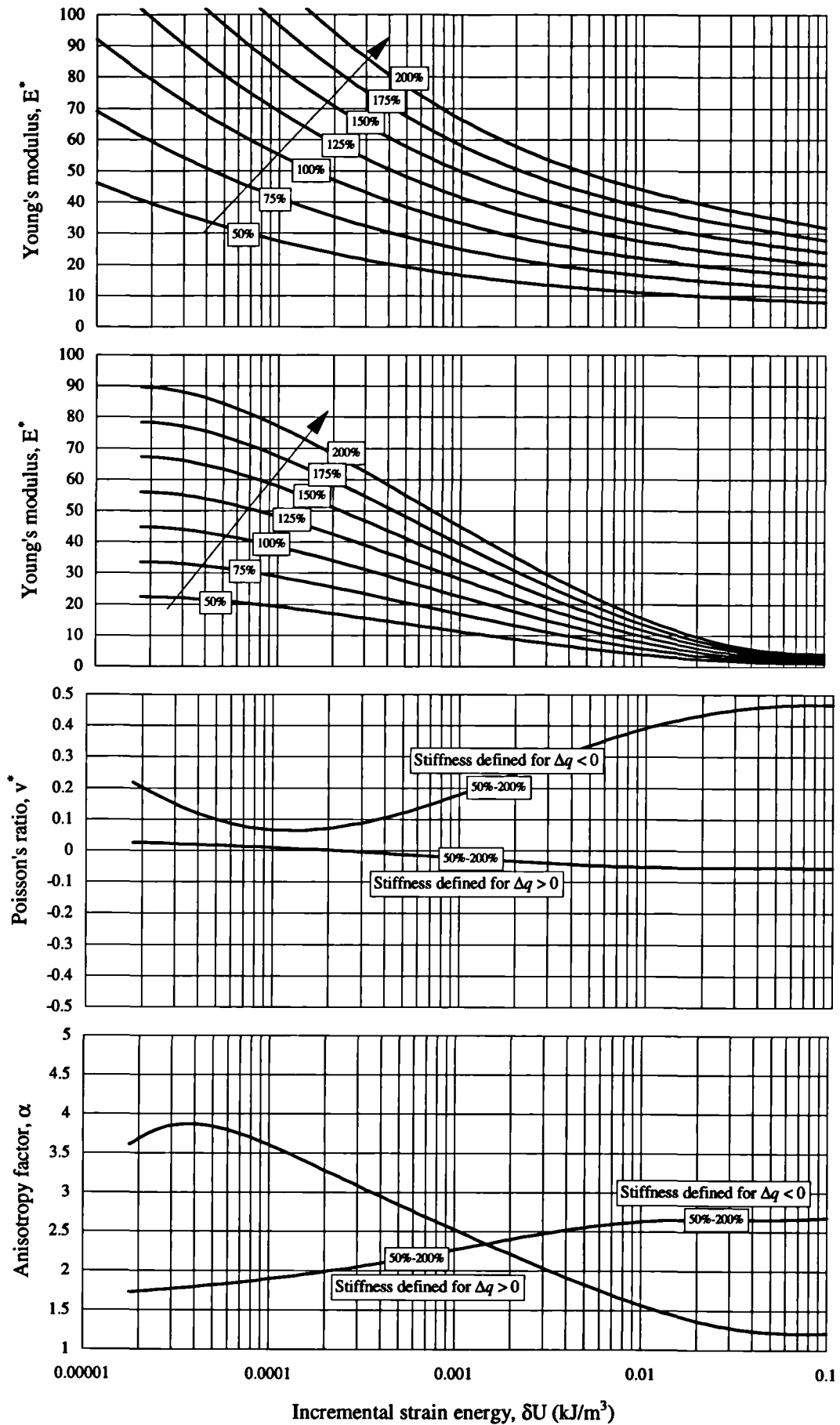


Figure 8.48 - Parametric influence of simultaneously varying all the stiffness parameters derived from the experimental programme on the anisotropic elastic parameters

Following this study, an attempt was made to optimise the input parameters to the model to produce a better general fit to the recorded excavation behaviour. Analyses were performed in which the stiffness parameters derived for increasing p' and q (Figure 8.49 and Figure 8.50), and those for decreasing p' and q (Figure 8.51 and Figure 8.52) were varied using a linear scaling factor. Also, an analysis was performed in which all stiffness parameters were scaled simultaneously (Figure 8.53 and Figure 8.54).

It is immediately clear from inspection of Figure 8.53 to Figure 8.52 that none of the above combinations of parameter manipulation is able to produce the combination of relatively large heave at the excavation base and settlement beyond the excavation crest. No individual cases showed any overall improvement over the genuine prediction. For example, if all stiffness parameters are reduced by 50%, a more realistic settlement at the excavation crest is calculated but the overall the vertical displacement profile is less satisfactory. Furthermore, the horizontal displacements are generally more than doubled within the Oxford Clay, which renders the predicted horizontal displacement profile less realistic.

Optimisations were also attempted for linear elastic analyses using both isotropic and cross-anisotropic stiffnesses. Figure 8.55 and Figure 8.56 show the horizontal and vertical displacement respectively comparing a number of linear isotropic elastic analyses to the genuine prediction, A01. Figure 8.57 shows the corresponding pore water pressure response. A range of G' was taken to cover the range encountered in the experimental programme, and analyses are shown for $G' = 10, 35$, and 60MPa. The resulting displacements vary considerably between analyses although, interestingly, the $G' = 35$ MPa analysis produces a response very similar to the non-linear cross-anisotropic elastic analysis proposed as the genuine prediction. A further analysis was carried out in which either a low ($G' = 10$ MPa) or a high ($G' = 60$ MPa) stiffness was assigned to elements of Oxford Clay depending whether they were 'unloading' or 'loading' respectively. The high stiffness value was assigned to elements experiencing a reversal in the loading direction during excavation. This analysis, labelled $G' = 10/60$ MPa, is also shown in Figure 8.55 and Figure 8.56 and also produces a similar response to the genuine prediction, A01. Figure 8.58 and Figure 8.59 show the horizontal and vertical displacement respectively for a series of linear cross-anisotropic elastic analyses in which $G' = 10$ MPa and $\alpha^* = 1$ (isotropic), 2, or 3. A contour plot of this data is shown in Figure 8.60. The most heavily cross-anisotropic analysis records displacements which are similar to those of the genuine prediction. Clearly, there are a number of combinations of parameters that can produce similar predictions for a variety of models. A similar conclusion was reached by Ng and Lings (1995) who obtained suitable predictions of a retaining wall problem using either a linear or a non-linear model. The key difference is that an appropriate stiffness or degree of anisotropy for a linear analysis may only be found in retrospect, whereas the non-linear stiffness variation may be obtained directly from suitable experimental data.

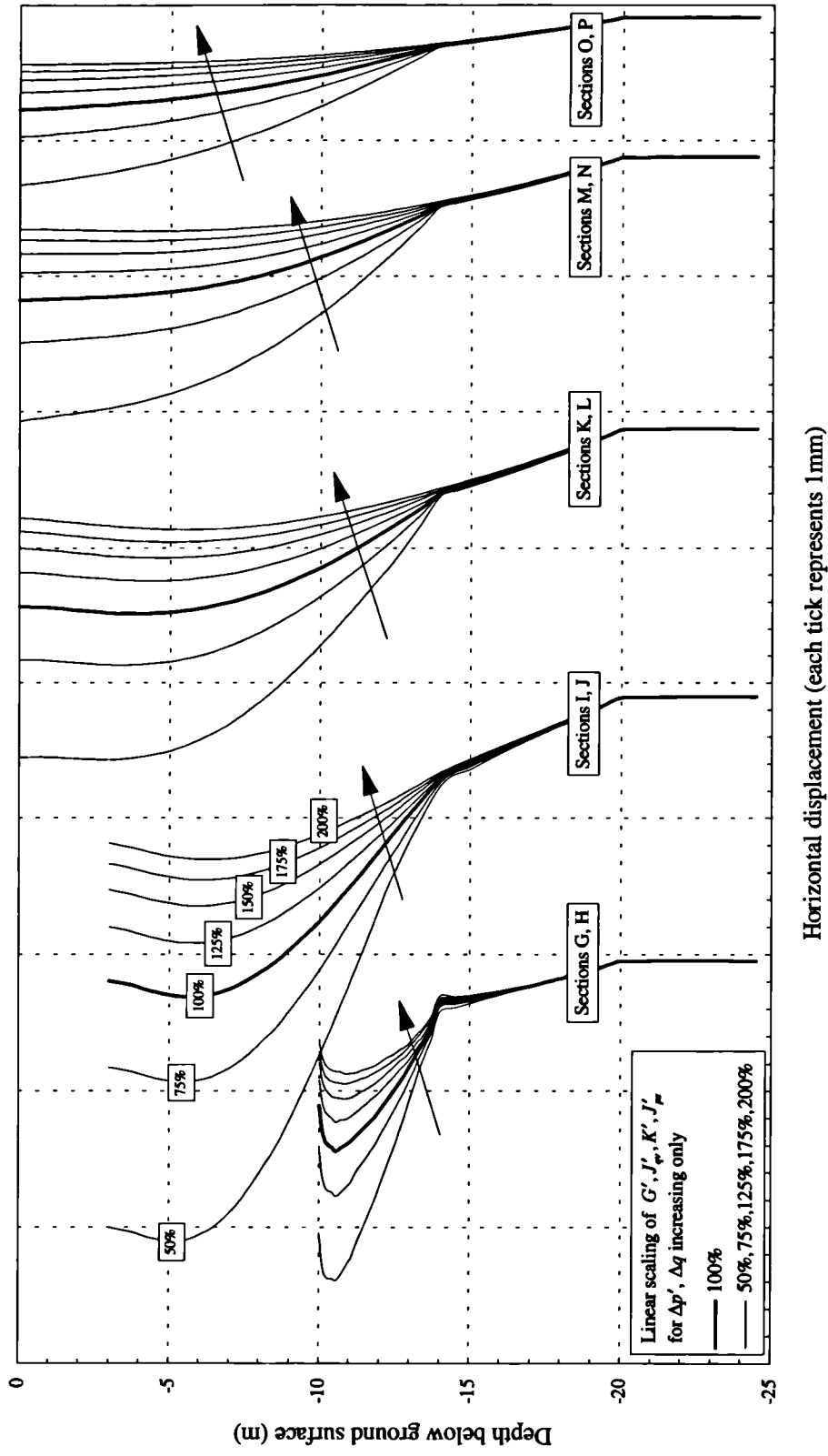


Figure 8.49 - Effect on non-linear cross-anisotropic model prediction of horizontal displacement when loading stiffness parameters only are scaled

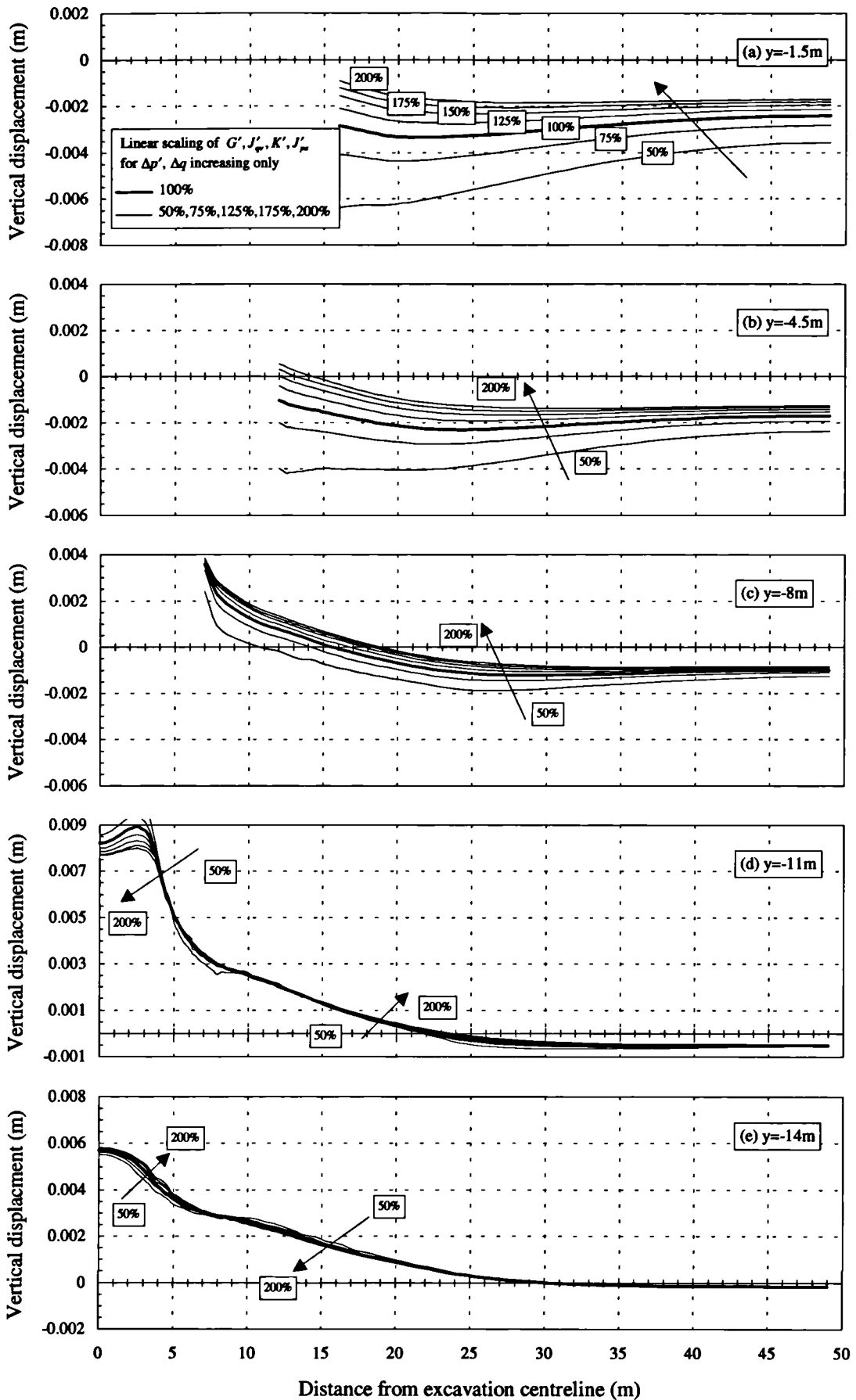


Figure 8.50 - Effect on non-linear cross-anisotropic model prediction of vertical displacement when loading stiffness parameters only are scaled

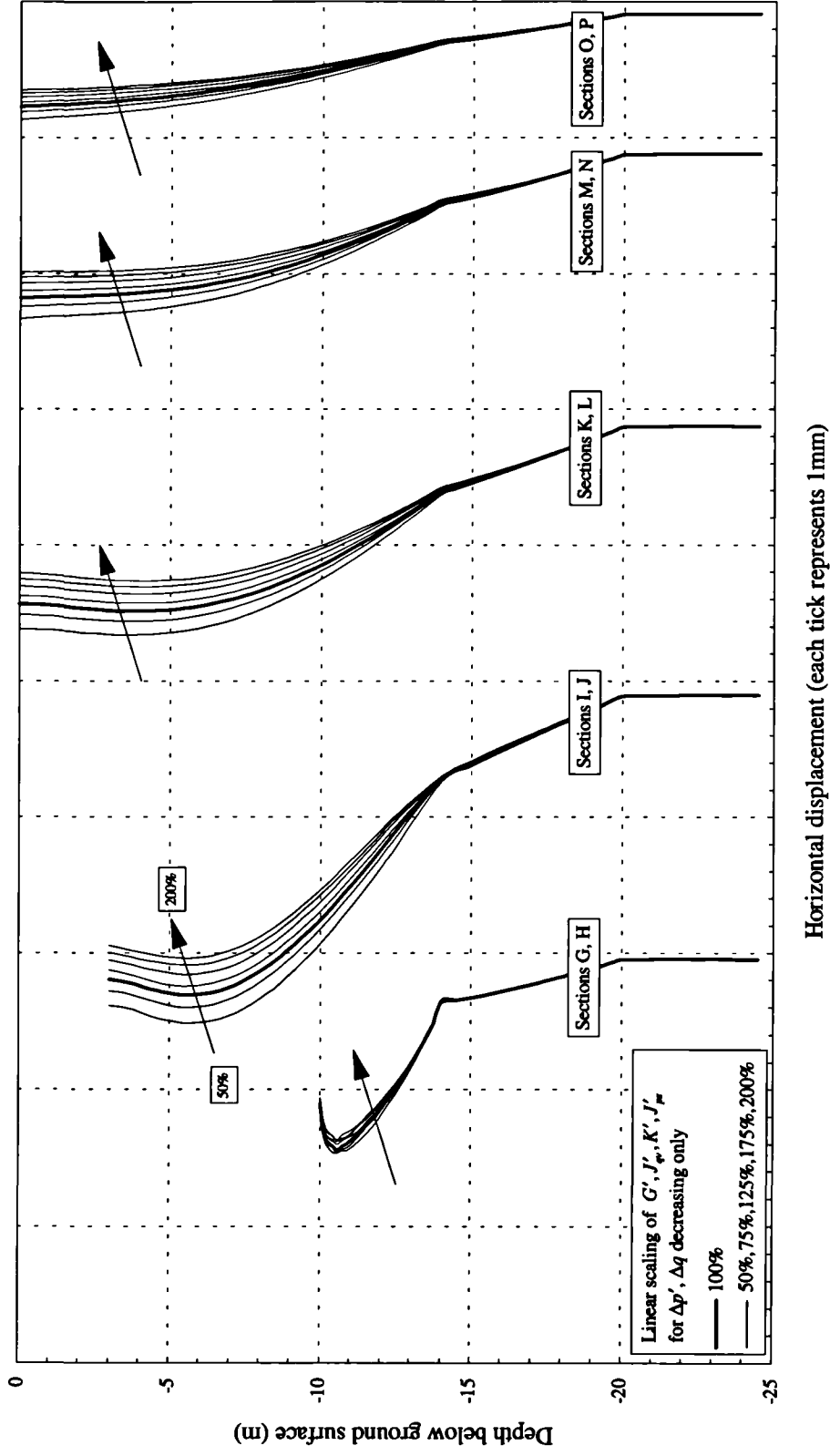


Figure 8.51 - Effect on non-linear cross-anisotropic model prediction of horizontal displacement when unloading stiffness parameters only are scaled

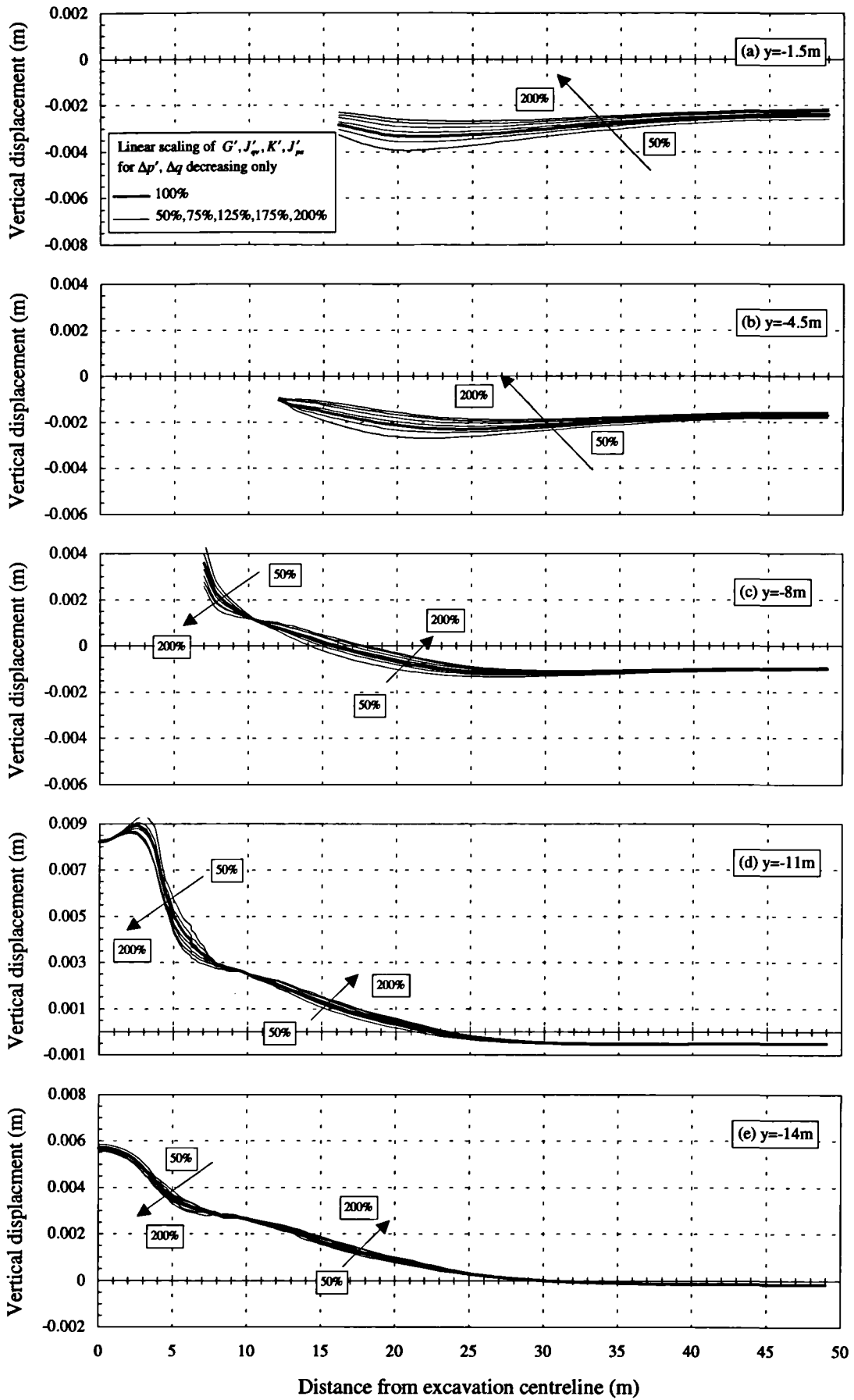


Figure 8.52 - Effect on non-linear cross-anisotropic model prediction of vertical displacement when unloading stiffness parameters only are scaled

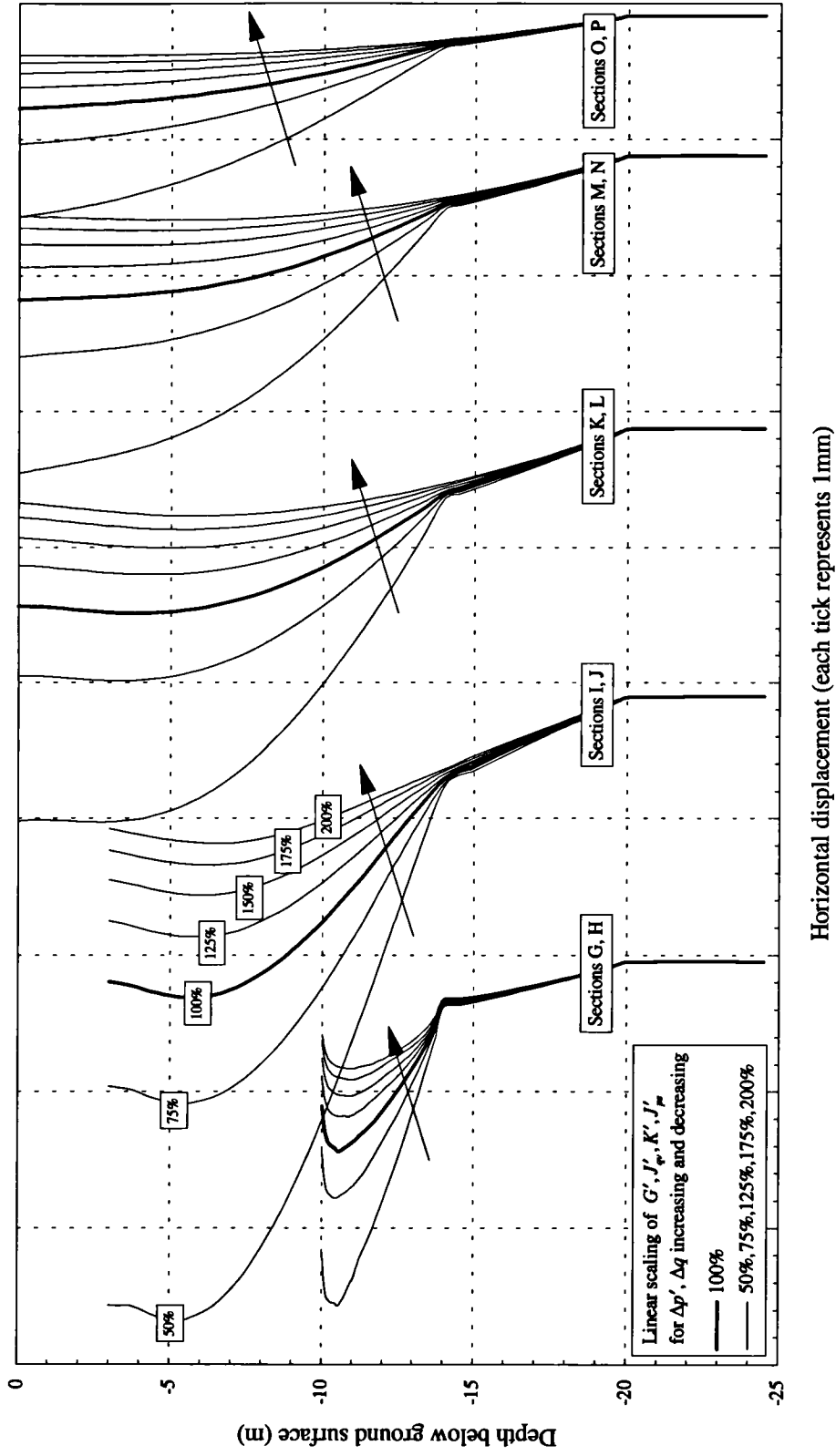


Figure 8.53 - Effect on non-linear cross-anisotropic model prediction of horizontal displacement when loading and unloading stiffness parameters are scaled

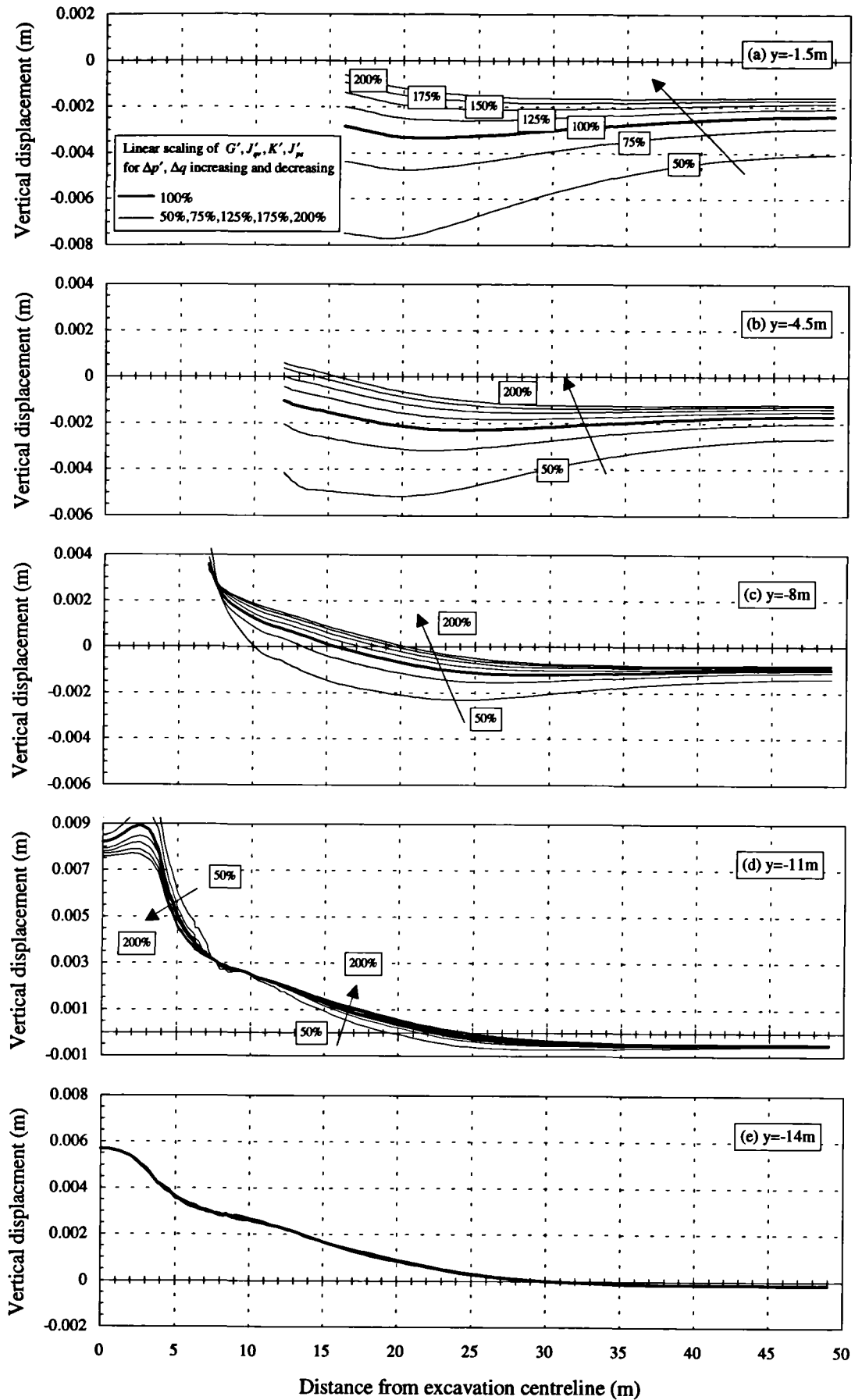


Figure 8.54 - Effect on non-linear cross-anisotropic model prediction of vertical displacement when loading and unloading stiffness parameters are scaled

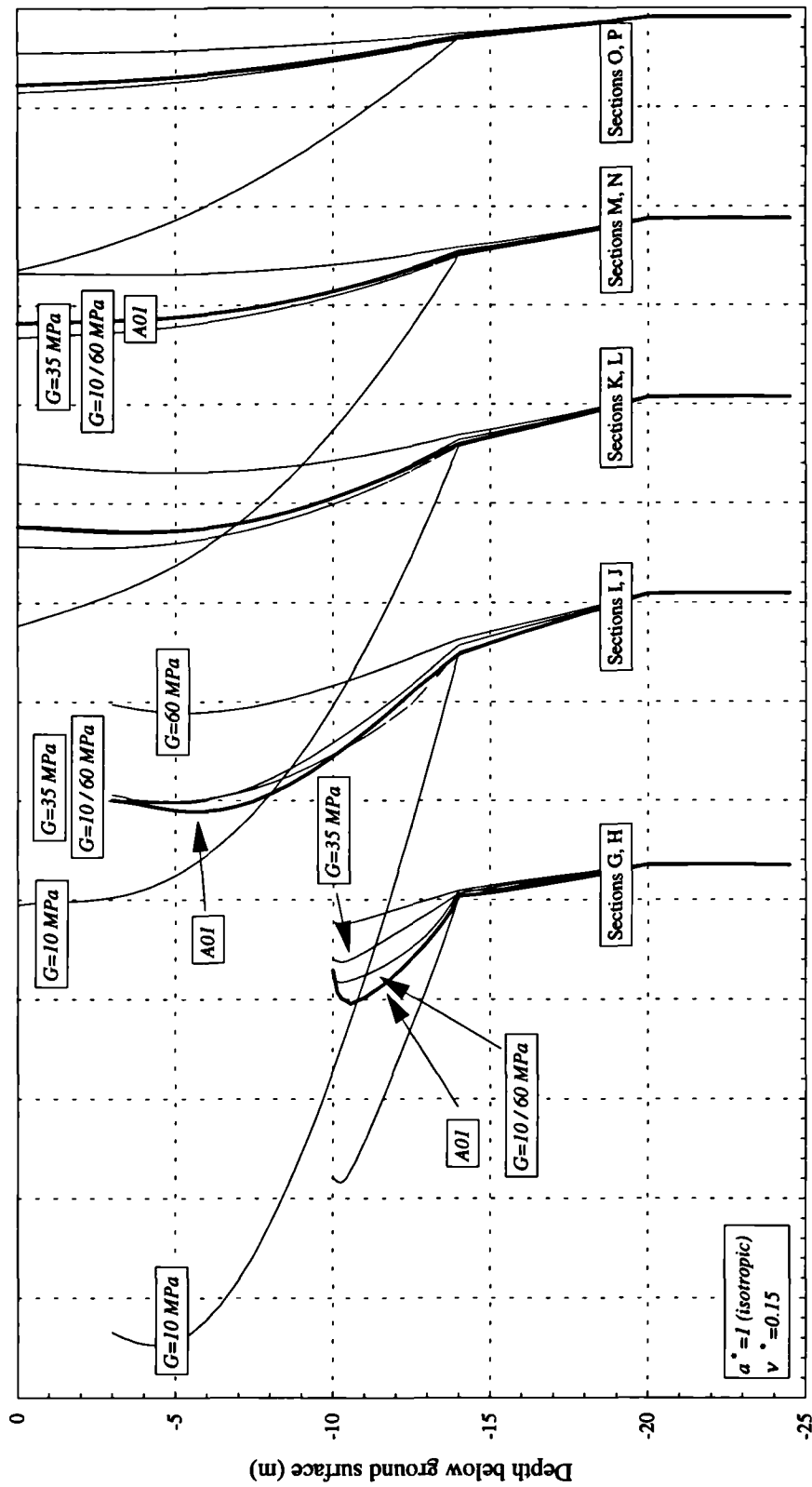


Figure 8.55 - Comparison of the genuine prediction of the excavation horizontal displacement with a series linear isotropic analyses for which G varies and with one analysis in G is set depending on the load increment direction

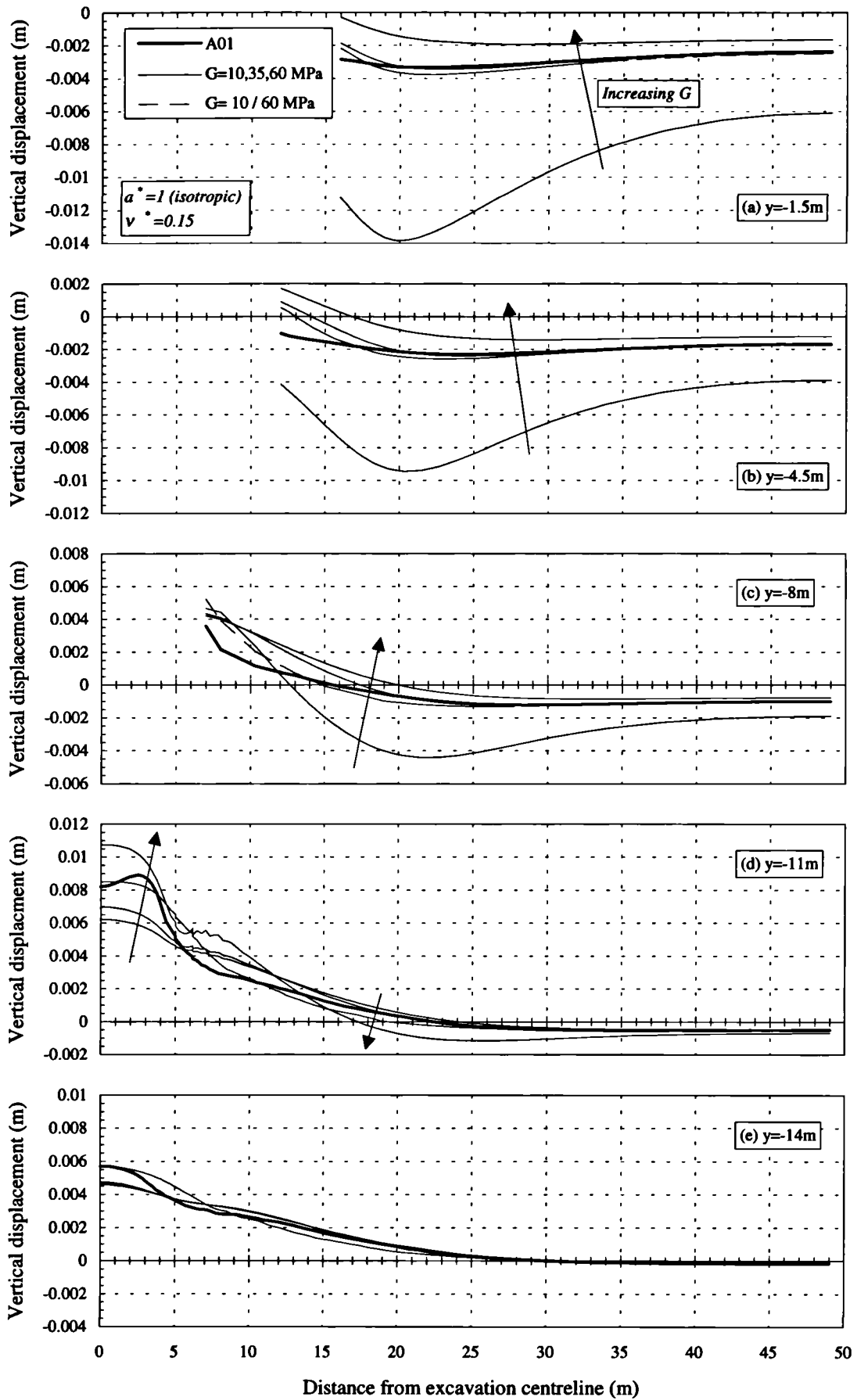


Figure 8.56 - Comparison of the genuine prediction of the excavation vertical displacement with a series linear isotropic analyses for which G varies

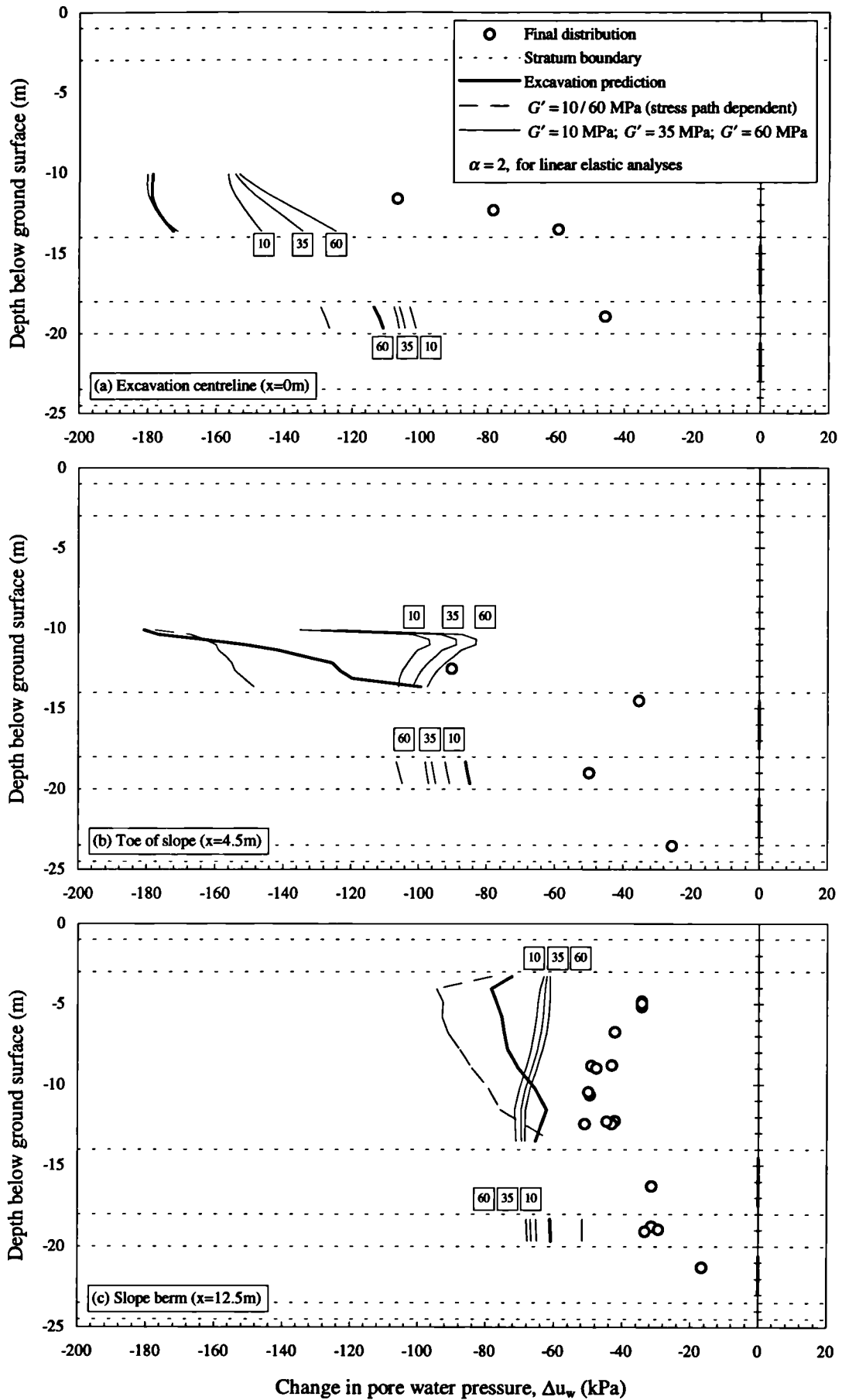


Figure 8.57 - Comparing the pore water pressure response of linear and non-linear cross-anisotropic elastic models

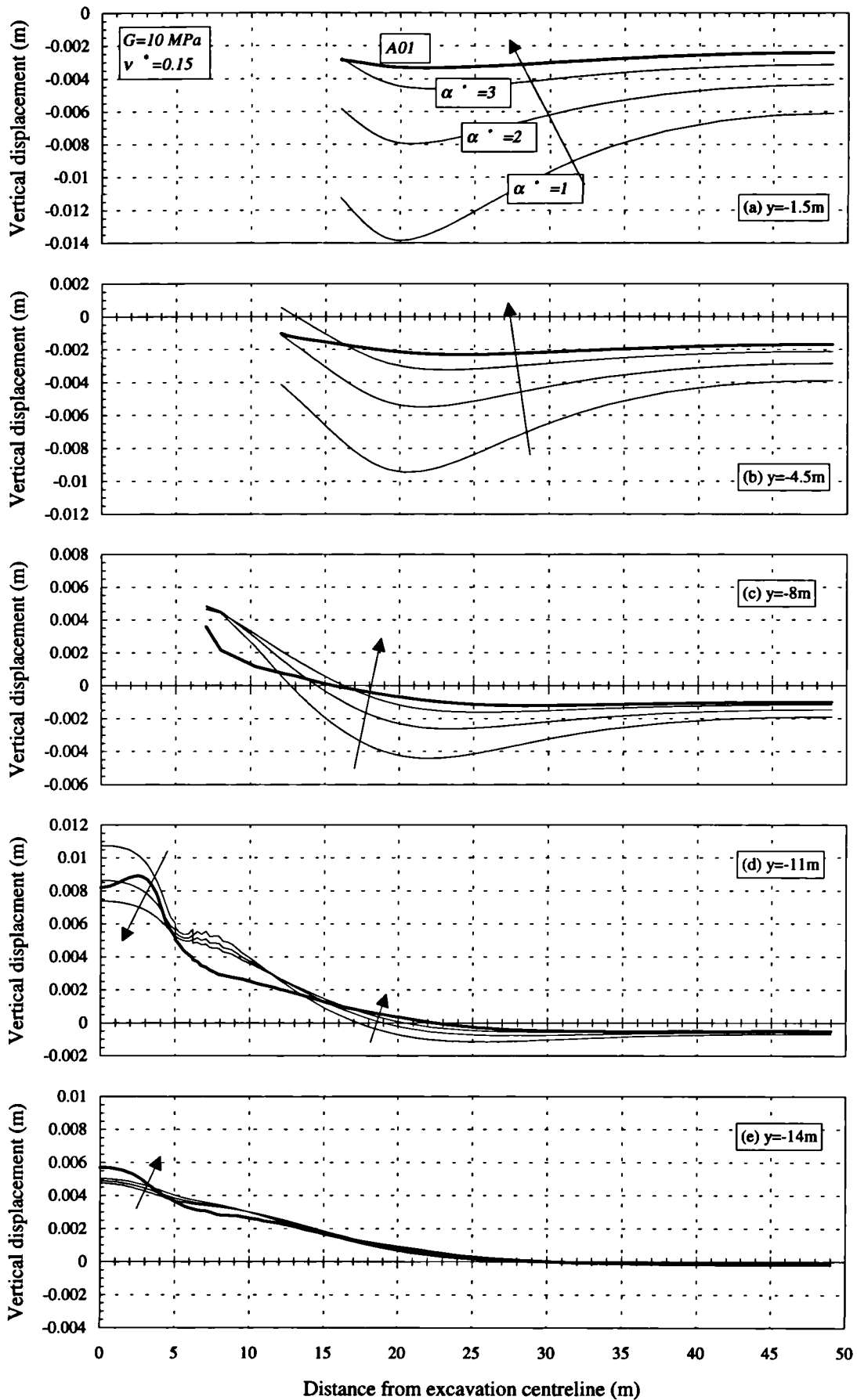


Figure 8.59 - Comparison of the genuine prediction of the excavation vertical displacement with a series of linear cross-anisotropic elastic analyses in which α^* varies

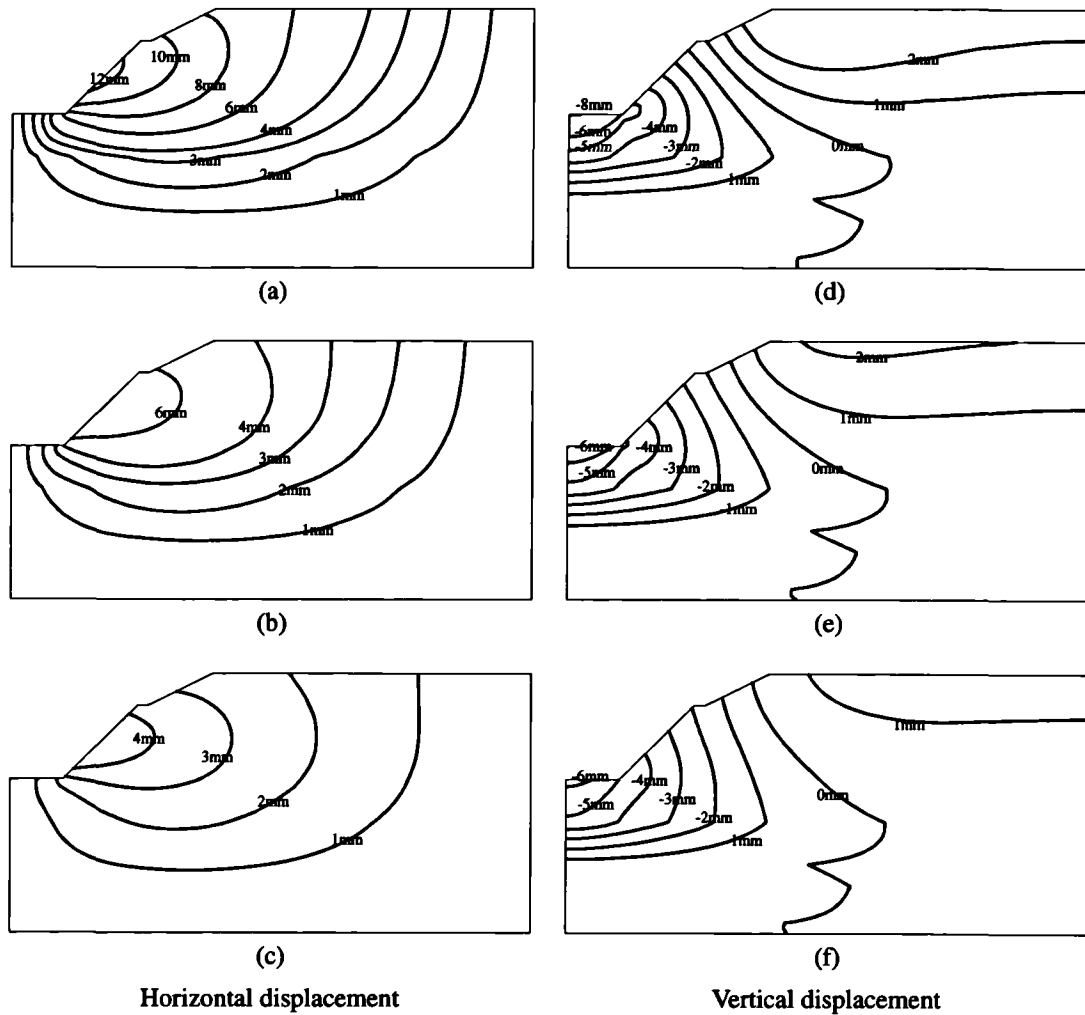


Figure 8.60 - The effect of the anisotropy factor on linear elastic CRISP analyses of the excavation, (a) $\alpha^*=1$, (b) $\alpha^*=2$, (c) $\alpha^*=3$ showing horizontal displacement, and in (d), (e), (f) showing vertical displacement



9. Conclusions

9.1 Introduction

This thesis has described the prediction of the ground response due to the construction of a large, open and unsupported excavation in Oxford Clay. The 10m deep excavation was instrumented and formed part of a full site investigation at Elstow, Hertfordshire, U.K.

The work has involved computer controlled triaxial stress path tests on high quality soil specimens trimmed from block samples. These tests were designed to define the anisotropy and the non-linearity of the stress-strain response. The use of local instrumentation and bender element apparatus allowed the soil stiffness to be investigated from very small strains.

The stress-strain relationships defined in the experimental programme were used in a non-linear cross-anisotropic elastic model based on the constitutive framework proposed by Graham and Houlsby (1983). This model was implemented in the finite element computer program CRISP and in the program SINGLECELL, which defined the unit element response. A prediction of the ground response was then made without any prior knowledge of the instrumented excavation response. Back analyses were then conducted in which the model parameters were varied parametrically to investigate their effect on the predicted behaviour.

The Elstow site investigation has been described, particularly in relation to the trial excavation. The instrumentation data have been analysed and presented in sufficient detail to allow qualitative interpretation and quantitative comparison with numerical results.

In this section, the main conclusions drawn in the preceding chapters are collected together and possible areas for future work are identified.

9.2 Excavation response

The Elstow site is situated on an outcrop of the stiff, heavily overconsolidated Lower Oxford Clay. The Clay overlies the Kellaways strata of sand and clay and, in turn, the Cornbrash and Blisworth limestones. Chapter 3 described the construction of the excavation that was carried out at Elstow to provide information on the ground's response to stress relief. Although the planned work was not completed, a large body of data was nevertheless obtained. Excavation took place from March until May 1987, at which time the site investigation was cancelled. The monitoring of the excavation continued, however, for a further 3 months. The Oxford Clay was thought likely to be the stratum most affected by the excavation and investigations were concentrated here. In particular, a study of the large and small scale ground structure was carried out through detailed logging. Trial pits constructed for this purpose were taken as the

excavation progressed and 5m long profiles of the excavation sides were logged. As part of the sampling operation, several block samples were retrieved which were used in the current experimental programme.

In Chapter 4, an analysis of the instrumentation data was presented, although the pore water pressure response had been analysed previously. It was found that the degree of variation between successive measurements of individual inclinometers made necessary an averaging of data for instruments installed at equal distances from the excavation centreline. The average response along these instrument section lines revealed clear trends in the behaviour. The in-plane horizontal displacements were negligible along the centreline of the excavation, and away from the centreline their development closely followed the excavation sequence. The maximum displacement was recorded soon after excavation was complete. The out-of-plane measurements (although less accurate than the in-plane measurements) were generally small and suggested that plane strain conditions existed for 10m on either side of the main instrumented section. The extensometer data conformed to the expected behaviour with heave developing at the base of the excavation, compensated by settlement beyond the excavation crest. At the berm, two-thirds of the way up the excavation sides, heave was initially recorded but later, as the excavation passed this level, settlement was recorded.

The inclinometer and extensometer readings were combined to calculate the magnitude of volumetric strain throughout the excavation. Although the accuracy of the technique was limited, it showed that there was volumetric expansion at the base of the excavation that was perhaps balanced by volumetric compression beyond the excavation crest. The volumetric expansion at the base of the excavation was thought to be due to the opening of fissures due to stress relief. Such opening of fissures was recorded in this location during the site investigation. It was also noticed that there was seepage into the excavation along pyritic bands and other discontinuities intersected by the sides of the excavation. It was thought possible that such seepage could have produced the slight volumetric compression recorded beyond the excavation crest.

The pore water pressure response recorded by the piezometers suggested that all strata were undrained during the monitoring period. Following an initial fall in piezometric level (corresponding to the removal of vertical stress during excavation), the level remained at a constant depressed value for the following 3 months. This was true for all piezometers in clay, sand, and limestone strata. This implication of undrained conditions was at odds with the response suggested by the displacement measurements.

The inclinometer, extensometer and piezometer data all suggested a symmetry to the ground response about both major axis of the excavation.

9.3 Stress path testing

In section 6.2, previous undrained tests on specimens of Oxford Clay from the Elstow site were re-analysed. This showed that the ratio of the undrained horizontal to vertical Young's modulus was approximately 2 throughout the small strain range (although up to 4 for the smallest stress changes). However, the undrained deviatoric stiffnesses derived in these tests could not be directly related to drained deviatoric stiffnesses because of the anisotropic material response. The degree of anisotropy, defined in terms of the parameter α (Graham and Houlsby, 1983), was calculated from the initial direction of the undrained stress path defined in q - p' space. The exact value varied with Poisson's ratio but the average value was approximately 3.

The undrained deviatoric stiffness obtained from these tests was also plotted normalised with respect to the initial effective mean normal stress. It was suggested that differences in the sampling technique (either tube samples or block samples) produced the apparent lack of a relationship. It could not be ascertained whether normalisation techniques were useful for interpreting the undisturbed soil stiffness.

The stress path tests carried out during the current work were designed to determine the *in situ* stress-strain response of Oxford Clay appropriate for predicting the ground response following excavation. By applying a series of constant p' and constant q stress paths the deviatoric and volumetric responses were investigated separately. This allowed not only the deviatoric and volumetric stiffness to be separately assessed, but also the coupling between these responses, described by the parameters J'_{qv} and J'_{ps} . The stiffness parameters were defined for stress path probes with a similar recent stress history (i.e. the approach paths were each of the same length and from the same direction, and the period of time at which the specimen was held at constant stress at the end of this path was similar). It was thought that, at small strains, the stress-strain response for any stress path direction could be predicted using the stiffnesses derived from the adjacent constant p' and constant q stress paths. Provision for testing this hypothesis was made by incorporating a diagonal stress path in two of the tests.

Since the supply of test material was limited, it was necessary to maximise the information that could be obtained from each soil specimen. A multi-stage testing technique was developed allowing all necessary stiffness parameters to be obtained from a single stress path test. This involved performing cycles of constant p' and constant q type stress paths such that an initial stress state (corresponding to a conservative estimate of the calculated *in situ* stress state) was approached from the same direction before carrying out a stress path probe from which stiffness parameters could be derived. A total of 9 stress path tests was carried out, although only 2 of these (tests T03 and T06) were carried out as intended to completion.

It was found that the deviatoric stiffness at small strains was significantly different for stress path probes in compression (increasing q) and those in extension (decreasing q). The effect of changes in the direction of the stress path, however, was found to be minimal. This is in contrast to data reported for reconstituted London Clay in which such a recent stress history effect was evident (Atkinson and Stallebrass, 1992). The deviatoric stiffnesses recorded for paths following a 90° or 180° change in the stress path direction, or where the stress path continued in the same direction, were similar at small strains, if there was sufficient period at which the specimen was held at constant stress to allow the specimen's strain rate to fall to insignificant values. It was possible to create a recent stress history effect if a very small holding period was allowed between stress paths. It is suggested that for Oxford Clay (and similarly heavily overconsolidated soils), where the stress changes imposed during laboratory testing are insufficient to cause significant alterations to the soil structure, recent stress history effects are mainly due to the residual strain rates in the soil following the previous stress path. These effects are therefore highly dependent on the duration of the holding period at which the specimen is held at constant stress before carrying out a subsequent stress path probe.

The influence of the residual strain rate in a test specimen was found to be significant in these tests because the requirement of fully drained conditions necessitated very slow loading rates. The creep rate of the soil was consequently relatively significant compared to the strain rates attained during a stress path. It was found that it was generally not possible to achieve fully drained conditions and therefore the constant p total stress paths resulted in slightly curved effective stress paths. It was realised that, for 100mm diameter specimens of low permeability

clay, the limits of the testing procedure were being reached. Two opposing factors had to be considered. Stress paths had to be carried out slowly enough to ensure adequate drainage and to accurately define the effective stress path, but not so slowly that the residual strain rate within the specimen significantly affected the stress-strain relation.

A system of bender elements was incorporated into the stress path apparatus allowing wave propagation tests. This work, and other research, has shown that the traditional bender element test with a square wave input is unsuitable for interpretation of the shear wave arrival. A sequence of traces is preferred, in which the frequency of a sinusoidal input is varied. This allows different aspects of the propagating wave to be identified and ensures a correct identification of the shear wave arrival. The installation in each of two stress path cells produced different characteristic traces. A near-field effect was evident in the traces from both cells. Additionally, in one cell, a secondary wave component was identified which was at first interpreted as the shear wave arrival. However, it was decided that the wave was travelling too fast to be a shear wave and that it was out-of-phase with the transmitted signal. It was suggested that this wave component was possibly the secondary compression wave described by Biot (1956a), or the consequence of the inability of the transmitter bender element to accurately follow the prescribed input function, or a further manifestation of the near-field effect.

The shear stiffness calculated from the shear wave travel velocity was approximately 50% higher than the deviatoric stiffness recorded at the smallest resolvable strains in the stress path tests. It was suggested that this difference could be attributable to the effect on wave propagation of a strongly cross-anisotropic soil. It was shown that, within the constitutive framework proposed by Graham and Houlsby (1983), the elastic shear stiffness recorded in bender element tests (G_w) could be 50% higher than the deviatoric stiffness (G') recorded at small strains under triaxial conditions.

A consistent variation of volumetric, deviatoric, or coupling stiffnesses with the initial effective mean normal stress was not apparent from the small strain data. A stiffness dependent on the effective mean normal stress is commonly assumed and has been demonstrated for many soils (see section 2.4.2). However, it was considered that, on the basis of the current data, it was unjustified to assume such a variation during the subsequent prediction of the ground response to excavation. The small strain stiffness of the soil was consequently assumed to be constant with depth within the Oxford Clay.

The Oxford Clay used for the stress path tests came from block samples taken during the Elstow site investigation and carefully preserved, and from newly taken block samples from the nearby Kempston Pit. The Kempston Pit block samples were taken from approximately the same depth as those from the Elstow excavation, although it was realised that the shallow regional dip may have resulted in the samples being taken from different geological sub-zones within the Oxford Clay. The moisture contents of both samples were similar, although the Kempston Pit samples were considerably easier to trim to obtain a triaxial specimen. During the trimming process, the Elstow block samples seemed to dry out more quickly and their fissures were more prominent than the Kempston pit samples. However, modelling of the excavation behaviour was mainly dependent on the stress-strain relation, and this was shown to be similar for soil taken from either location.

The relative magnitudes of the volumetric, deviatoric, and coupling stiffnesses indicate fundamental attributes of the soil response. The two coupling stiffnesses were numerically different at a given incremental strain energy level (serving as a generalised measure of deformation). This suggested that over the small strain range recorded in the current tests, the

specimen response was not elastic, and that a flow rule describing a plastic response must be non-associated. However, the inner strain energy contours plotted around the initial stress point of the stress path probes in tests T03 and T06 were of a shape and orientation similar to that which would be expected for a cross-anisotropic elastic material. At larger values of strain energy the contour shape reflected the development of plastic strains.

The failure states in extension of the stress path test specimens were within the bounds quoted in the literature but covered a wide range of mobilised angles of friction from 25° to approaching tension failure (test T01). Tests T03 failed at a relatively high mobilised friction angle of 40° , and Test T02, which was carried out on a specimen trimmed from the same block that as used for test T01, and tests T04 and T06 failed with $\phi'_{mob} = 28^\circ-34^\circ$. The failures at high stress ratio could also be explained assuming a degree of cohesion to the failure envelope. A further explanation of the high mobilised angles of friction was that the mid-height pore pressure probe did not accurately record the true specimen pore water pressure (perhaps due to the influence of fissures, or to the proximity of the specimen's filter paper drains), and that dilation produced unmeasured negative excess pore water pressures. Consequently, the specimen's effective mean normal stress would have been greater than that measured, allowing apparently higher frictional strengths to be achieved. Alternatively, the differences could have been purely attributable to experimental variation since differences in specimen quality were apparent during the trimming process. Interestingly, considering all stress path tests, although there was considerable variation in the frictional strength, the magnitude and non-linearity of stiffness at small strains were similar.

It was found that the stress path apparatus generally performed well. The load cell proved to be the least reliable component of the apparatus causing several failures during the testing programme. The limiting factor controlling the accuracy to which the stress-strain relation could be defined was the stress control rather than the strain measurements and consequently, the resolution of the stepper motors should be increase considerably. Alternatively, strain controlled testing could be implemented (in which a specific stress path could be applied through manipulating the cell pressure).

9.4 Non-linear anisotropic soil modelling

A cross-anisotropic non-linear elastic model has been implemented in CRISP. The formulation of the model accords with Graham and Houlsby (1983) with non-linearity introduced through the evaluation of incremental strain energy. Input parameters have been obtained for Oxford Clay from the triaxial stress path tests for constant q and constant p' stress paths with increasing and decreasing stress levels. It was shown that diagonal path response could be predicted very well using this technique, and that the influence of the coupling of the deviatoric and volumetric behaviour was significant. Although the validation checks were limited in scope, they suggested that the model would be capable of simulating behaviour along more general stress paths, as would occur around an excavation. This model, called *Model OC*, was applied to the prediction of the ground movements and pore water pressures due to construction of the Elstow excavation.

A genuine prediction was compared with the analysed excavation instrumentation data. The horizontal displacement field was predicted successfully but, although the general form of the vertical movements was predicted correctly, the magnitudes of the heave at the excavation base and the settlement beyond the excavation crest were underpredicted by as much as 2 to 3 times. On the other hand, the fall in pore water pressure following excavation was predicted to be

much larger than that recorded. It was suggested that the deficiencies in this prediction were related to the modelling of the Oxford Clay rather than to either the modelling of the lower strata or to the method of modelling the excavation process (to which the final prediction was relatively insensitive). The differences could not be accounted for by varying the model parameters over the range encountered within the experimental programme. Furthermore, it was not possible to manipulate the input parameters of the elastic model during the back analysis to provide a more accurate fit to the data. It was possible to manipulate the parameters to obtain better fits to particular aspects of the response, but the accuracy of the overall response reduced in such analyses. It was found, however, that the results of the non-linear analysis could be reproduced in an isotropic elastic analysis in which the shear stiffness was approximately half that recorded at small strains, or if high and low stiffnesses were assigned to loading and unloading regions respectively. The results could also be reproduced if the Oxford Clay were modelled as a strongly cross-anisotropic linear elastic material with a relatively low shear stiffness.

A significant feature of the back analysis and the parametric variation of the model parameters was that incorporating anisotropy into the soil response was at least as important as including the effects of stiffness non-linearity. A similar conclusion was reached by Simpson *et al.* (1996) for predicting settlements due to tunnelling in London Clay.

Although, the model was shown to perform well within the confines of triaxial stress space, extending the application of the model to the more complex conditions of the Elstow excavation was only partially successful. To account for the differences between the instrumented excavation response and the range of the model predictions, the deficiencies in the numerical modelling must be examined. An immediate criticism of the numerical modelling is that, although it was based on an elastic constitutive model, the soil response can only be considered elastic over a very limited strain range. This strain was certainly exceeded during excavation. The inclusion of incrementally non-linear plastic deformation from small strains may possibly improve the prediction.

The calculation of volumetric strains from the instrumentation displacement data suggested that volumetric expansion was taking place at the base of the excavation, and, possibly, corresponding volumetric compression was taking place beyond the excavation crest. Such volumetric effects (attributed to the influence of structural features within the soil) were not capable of being reproduced by the present model but may account for the major discrepancies between predicted and actual movements.

9.5 Further Work

9.5.1 Experimental

The influence of time related effects on stiffness parameters obtained in stress path tests warrants further attention. This would include an investigation of both the holding period and the effect of very slow loading rates on recorded stress-strain behaviour. For a heavily overconsolidated clay in which the multi-stage testing techniques described in this thesis might be applicable, a stress path similar to that shown in Figure 9.1 is suggested.

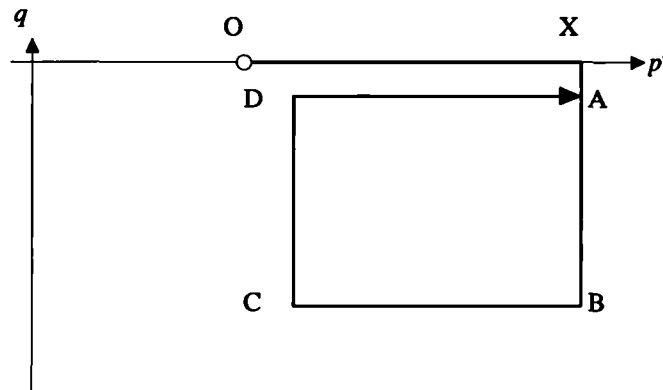


Figure 9.1 - Suggested multi-stage stress path test to investigate the influence of time on soil stiffness

A heavily overconsolidated soil specimen would be consolidated from O to X before being cycled through the series of stress paths from A-B-C-D at a constant loading rate. During each cycle, the holding period would be the same at each point (A-D). In subsequent cycles this holding period would be increased or decreased. The test could be continued until a degradation in the specimen stiffness was noticed (this would be checked by repeating a previous cycle of stress paths). The effect would be investigated for anticlockwise and clockwise stress path cycles, and for compression and extension stress states.

The anisotropy of the shear stiffness implied by the bender element measurements for the Oxford Clay requires further investigation. The relationship between the deviatoric stiffness and the cross-anisotropic shear stiffnesses also requires clarification, perhaps by propagating shear waves vertically, horizontally and obliquely through the specimen (for example, Bellotti *et al.*, 1996).

It was found that the bender element response was quite different in each of the two stress path cells, although the testing procedures and the soil type were similar in each case. It is suggested that this effect be investigated further, particularly the influence of the workmanship in the bender element production and the effect of misalignment on wave propagation.

The resolution of the load control system in the stress path cells needs to be improved further to match the greater resolution of the local strain measurements. The use of strain controlled testing is suggested to eliminate load reversals during the initial stages of a test. The resolution could be improved still further if a 16-bit A/D converted were installed into the system. However, this would only be suitable in a strain controlled test or in a stress controlled test with an order of magnitude improvement in stress control.

Further investigation of the Oxford Clay is required to investigate more fully the influence of initial isotropic and anisotropic stress state on the stiffness of the natural soil. The stress-strain response of the soil is presently ill-defined between the limits of the small strain instrumentation and the dynamic measurements of the bender element apparatus. A general improvement in the overall measurement accuracy will allow the relative magnitudes of the deviatoric, volumetric, and coupling stiffnesses to be quantified at very small strains. Of particular interest would be whether the magnitudes of the coupling stiffnesses coincided at such strain levels as would be expected for an elastic material response (see Figure 9.2). (Suitable testing material may be readily obtained from brick pits such as Kempston Pit with permission from the London Brick Company.)

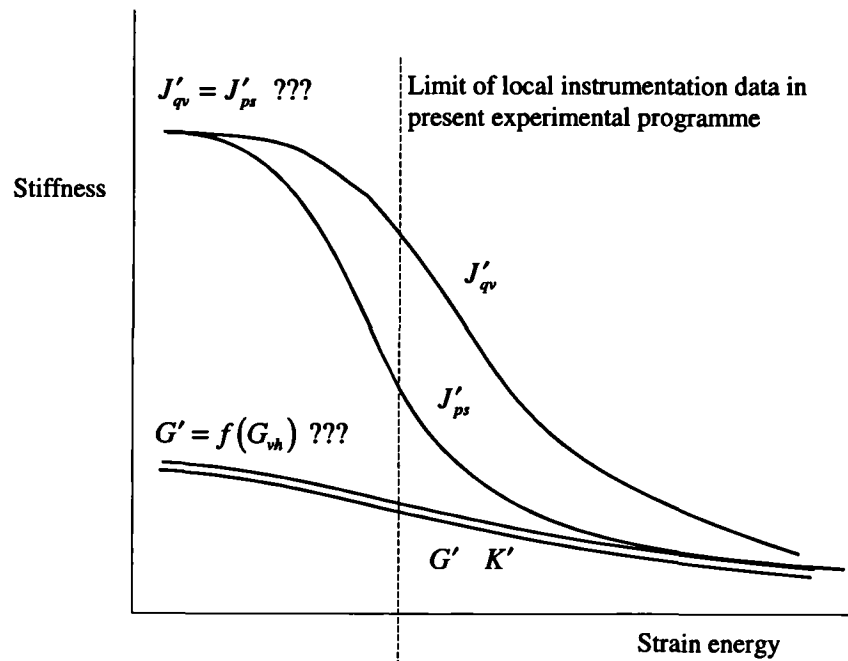


Figure 9.2 - Qualitative possible stiffness response for very small to small strain range

9.5.2 Numerical

Model OC should be validated more extensively by investigating the remaining quadrants of q - p' space that were not investigated in the work described here. This would require further experimental investigations that included suitable diagonal stress paths. It is to be expected that the model will be less effective in the zones closer to the failure surfaces and as plastic straining increases.

The model would perhaps be of greater use in boundary value analyses if a normalised formulation for the stress-strain relations could be derived and if a limiting plastic yield condition was also incorporated.

Further 'predictions' of the Elstow excavation should be carried out using plasticity based constitutive relations.



References

- Abbiss, C.P. (1981), *Shear wave measurements of the elasticity of the ground*, Géotechnique, Vol. 31, No. 1, p91-104.
- Ackerly, S.K., Hellings, J.E., and Jardine, R.J. (1987), *Discussion on 'A new device for measuring local axial strains on triaxial specimens' by Clayton and Khatrush (1986)*, Géotechnique, Vol. 37, pp. 414-415.
- Agarwal, T.K. and Ishibashi, I. (1991), *Multi-directional wave velocity by piezoelectric crystals.*, Geotechnical Special Publication, No. 29, Published by ASCE, New York, New York State, USA, pp. 102-117.
- Aki, K. and Richards P.G. (1980), *Quantitative Seismology Theory and Methods*, Published by Freeman and Company, San Francisco, California, USA.
- Al-Tabbaa, A. and Wood, D.M. (1989), *An experimentally based 'bubble' model for clay*, in Numerical Models in Geomechanics, NUMOG III, edited by S. Pietruszczak and G.N. Pande, Elsevier Applied Science, pp. 91-99.
- Ampadu, S.K. (1991), *Deformation and strength characteristics of clay in triaxial compression and torsional simple shear tests*, D.Eng. thesis, University of Tokyo, Tokyo, Japan.
- Ampadu, S.K. and Tatsuoka, F. (1989), *Automated stress-path control triaxial system*, Geotechnical Testing Journal, Vol. 12, No. 3, pp. 238-243.
- Ampadu, S.K. and Tatsuoka, F. (1993), *A hollow cylinder torsional simple shear apparatus capable of a wide range of shear strain measurement*, Geotechnical Testing Journal, Vol. 16, No. 1, pp. 3-17.
- Arkell, W.J. (1947), *The Geology of Oxford*, Published by Clarendon Press / Oxford University Press.
- Arthur, J.R.F., James, R.G., and Roscoe, K.H. (1964), *The determination of stress fields during plane strain of a sand mass*, Géotechnique, Vol. 14, pp. 283-308.
- Atkinson, J.H. (1973a), *The deformation of undisturbed London Clay*, Ph.D. Thesis, University of London, UK.
- Atkinson, J.H. (1973b), *Elasticity and plasticity in soils*, Géotechnique, Vol. 23, No. 4, pp. 565-571.
- Atkinson, J.H. (1975), *Anisotropic elastic deformations in laboratory test on undisturbed London Clay*, Géotechnique, Vol. 25, No. 2, pp. 357-374.

- Atkinson, J.H. and Bransby, P.L. (1978), *The mechanics of soils. An introduction to critical state soil mechanics*, McGraw-Hill, Maidenhead.
- Atkinson, J.H. and Evans, J.S. (1985), *Discussion on 'The measurement of soil stiffness in the triaxial apparatus'*, Jardine, R.J., Symes, N.J. and Burland, J.B. (1984), Author's reply, *Géotechnique*, Vol. 35, No. 3, pp.378-382.
- Atkinson, J. H., Lau, W.W.H., and Powell, J. J. M. (1989), *Determination of soil stiffness parameters in stress path probing tests*, Proceedings of the International Conference on Soil Mechanics and Foundation Engineering, Vol. 1, Balkema, Rotterdam, Netherlands, pp. 7-10.
- Atkinson, J. H. Richardson, D. (1985), *Elasticity and normality in soil - experimental examinations*, *Géotechnique*, Vol. 35, No. 4, pp. 443-449.
- Atkinson, J.H., Richardson, D. and Stallebrass, S.E. (1990), *Effect of recent stress history on the stiffness of overconsolidated soil*, *Géotechnique*, Vol. 40, No. 4, pp.531-540.
- Atkinson, J.H. and Sällfors, G. (1991), *Experimental determination of stress-strain-time characteristics in laboratory and in-situ tests*, Proceedings 10th ECSMFE, 'Deformation of Soils and Displacements of Structures', Florence, Italy, pp. 915-956.
- Atkinson, J.H. and Stallebrass, S.E. (1991), *A model for recent history and non-linearity in the stress-strain behaviour of overconsolidated soil*, Proceedings 7th IACMAG, Cairns, pp. 555-560.
- Attewell, P.B. and Farmer, I.W. (1974), *Ground deformations resulting from shield tunnelling in London Clay*, *Canadian Geotechnical Journal*, Vol. 11, pp. 380-395.
- Balasubramaniam, A.S. (1976), *Local strains and displacement patterns in triaxial specimens of a saturated clay*, *Soils and Foundations*, Vol. 16, No. 1, pp. 101-114.
- Balla, A. (1960), *Stress conditions in triaxial compression*, *Journal of the Soil Mechanics and Foundations Division*, Vol. 91, No. SM6, ASCE, pp. 1-23.
- Barden, L. and McDermott, R.J.W. (1965), *Use of free ends in triaxial testing of clays*, *Journal of the Soil Mechanics and Foundations Division*, Vol. 91, No. SM6, ASCE, pp. 1-23.
- Bates, C.R. (1989), *Dynamic soil property measurements during triaxial testing*, *Géotechnique*, Vol. 39, No. 4, pp. 721-726.
- Bauer, G.E., Shields, D.H., McRostie, G.C., and Scott, J.D. (1976), *Predicted and observed footing settlements in a fissured clay*, Proceedings of the Conference on Performance of Building Structures, Glasgow, Pentech Press, London, United Kingdom, pp. 287-302.
- Bellotti, R., Jamiolkowski, M., Lo Presti, D.C.F., and O'Neil, D.A. (1996), *Anisotropy of small strain stiffness in Ticino sand*, *Géotechnique*, Vol. 46, No. 1, pp. 115-131.
- Bennell, J.D. (1992), *Personal communication*.
- Bennell, J.D., Taylor-Smith, D., and Davis, A. (1984), *Resonant column testing of marine soils*, Proceedings of the International Conference on Oceanology, Brighton: Society of Underwater Technology, OI1.9.
- Biot, M.A. (1956a), *Theory of elastic waves in a fluid-saturated porous solid. I, low frequency range*, *Journal of Acoustic Society of America*, Vol. 28, pp.168-178.

- Biot, M.A. (1956b), *Theory of elastic waves in a fluid-saturated porous solid. II, high frequency range*, Journal of Acoustic Society of America, Vol. 28, pp. 179-191.
- Bishop, A.W. and Garga, A.W. (1969), *Drained tension tests on London Clay*, Géotechnique, Vol. 19, No. 3, pp. 309-313.
- Bishop, A.W. and Henkel, D.J. (1962), *The measurement of soil properties in the triaxial test*, Published by Edward Arnold (publishers) Ltd., (1st Edition, 1957).
- Bishop, A.W., Webb, D.L. and Lewin, P.I. (1965), *Undisturbed samples of London Clay from the Ashford Common shaft; strength-effective stress relationships*, Géotechnique, Vol. 15, pp. 1-31.
- Bishop, A.W. and Wesley, L.D. (1975), *A hydraulic triaxial apparatus for controlled stress path testing*, Géotechnique, Vol. 25, No. 4, pp.657-670.
- Bjerrum, L. (1967), *7th Rankine Lecture, Engineering geology of Norwegian normally consolidated marine clays as related to settlement of buildings*, Géotechnique, Vol. 17, pp. 81-118.
- Black, D.K. and Lee, K.L. (1973), *Saturating laboratory samples by back pressure*, Journal of Soil Mechanics and Foundation Engineering, ASCE, Vol. 99, No. SM1, pp. 75-93.
- Böese, R. (1992), *The influence of time on the small strain stiffness of overconsolidated clays*, Contribution to 2nd BGS Symposium for Young Geotechnical Engineers, Glasgow, 1992.
- Bond, A.J., and Jardine, R.J. (1995), *Shaft capacity of displacement piles in a high OCR clay*, Géotechnique, Vol. 45, No. 1, pp. 3-23.
- Bordeau, P.L. (1993), *Radiographic visualization in experimental soil mechanics*, Engineering Foundation-National Science Foundation Conference on Digital Image Processing: Techniques and Applications in Civil Engineering, ASCE, New York, USA, pp. 125-134.
- Boyce, J.R. and Brown, S.F. (1976), *Measurement of elastic strain in granular material*, Géotechnique, Vol. 26, No. 4, pp. 637-640.
- Brignoli, E. and Gotti, M. (1992), *Misure della velocità di onde elastiche di taglio in laboratorio con l'impiego di trasduttori piezoelettrici*, Rivista Italiana di Geotecnica, Vol. 26, No. 1, pp. 5-16 (reported in Viggiani, 1992).
- British Geological Survey (1994), *Personal communication*.
- Britto, A.M. and Gunn, M.J. (1987), *Critical State Soil Mechanics via Finite Elements*, Ellis Horwood Limited, England.
- Brown, S.F., Austin, G., and Overy, R.F. (1980), *An instrumented triaxial cell for cyclic loading of clays*, Geotechnical Testing Journal, GTJODJ, Vol. 3, No. 4, pp. 145-152.
- Brown, S.F. and Snaith, M.S. (1974), *The measurement of recoverable and irrecoverable deformations in the repeated load triaxial test*, Géotechnique, Vol. 24, No. 2, pp. 255-259.
- Burghignoli, A. Pane and V. Cavalera, L. (1991), *Monotonic loading*, Proceedings 10th ECSMFE, 'Deformation of Soils and Displacements of Structures', Vol. 3, Published by Balkema, Rotterdam, Netherlands, pp. 961-979.

- Burland, J. B. Georgiannou, V. N. (1991), *Small strain stiffness under generalised stress changes*, Proceedings 10th ECSMFE, 'Deformation of Soils and Displacements of Structures', Vol. 1, Published by Balkema, Rotterdam, Netherlands, pp. 41-44.
- Burland, J.B. (1989), 9th *Laurits Bjerrum Memorial Lecture: "Small is beautiful" - the stiffness of soils at small strains*, Canadian Geotechnical Journal, Vol. 26, pp. 499-516.
- Burland, J.B. and Hancock (1977), *Underground car park at the House of Commons, London: geotechnical aspects*, The Structural Engineer, Vol. 55, pp. 87-100.
- Burland, J.B., Longworth, T.I. and Moore, J.F.A. (1977), *A study of ground movement and progressive failure caused by a deep excavation in Oxford Clay*, Géotechnique, Vol. 27, No. 4, pp. 557-591.
- Burland, J.B. and Maswoswe, J. (1982), *Discussion on 'In situ measurement of horizontal stress in overconsolidated clay'*, Géotechnique, Vol. 32, No. 3, pp. 285-286.
- Burland, J.B. and Moore, J.F.A. (1973), *The measurement of ground displacement around deep excavations*, Proceedings of the Symposium on Field Instrumentation, British Geotechnical Society, London, pp. 70-84.
- Burland, J.B., Moore, J.F.A. and Smith, P.D.K. (1972), *A simple and precise borehole extensometer*, Géotechnique, Vol. 22, No. 1, pp. 174-177.
- Burland, J.B. and Roscoe, K.H. (1969), *Derivation of strains from radiographs*, Appendix to 'Local strains and pore pressures in a normally consolidated clay layer during one-dimensional consolidation', Géotechnique, Vol. 19, No. 3, pp. 335-356.
- Burland, J.B., Simpson, B., and St. John, H.D. (1979), *Movements around excavation in London Clay*, Proceedings 7th ECSMFE, Brighton, UK, Vol. 1, pp. 13-30
- Burland, J.B. and Symes, M. (1982), *A simple axial displacement gauge for use in the triaxial apparatus*, Géotechnique, Vol. 32, No. 1, pp. 62-65.
- Butterfield, R., (1979), *A natural compression law for soils (an advance on e -log p')*, Géotechnique, Vol. 29, No. 4, pp. 469-480.
- Callomon, J.H. (1968), *The Kellaways Beds and the Oxford Clay*, from 'The Geology of the East Midlands' edited by P.C. Sylvester-Bradley and T.D. Ford, Chapter 14, p264-290, Leicester University Press.
- Campanella, R.G. and Stewart, W.P. (1991), *Seismic cone analysis using digital signal processing*, Proceedings 2nd International Conference on Recent Advances in Geotechnics, Earthquake Engineering and Soil Dynamics, St. Louis, USA, Vol. 1, pp. 77-82.
- Campanella, R.G., Baziw, E.J. and Sully, J.P. (1989), *Interpretation of seismic cone data using digital filtering techniques*, Proceedings 12th ICSMFE, Rio de Janeiro, Brazil, Vol. 1, pp. 195-198, Published by Balkema, Rotterdam.
- Carter, J.P. (1982), *Predictions of the non-homogeneous behaviour of clay in the triaxial test*, Géotechnique, Vol. 32, No. 1, pp. 55-8.
- Chamberlain, E.J., Cole, D.M., and Johnson, T.C. (1979), *Resilient response of two frozen and thawed soils*, Journal of Soil Mechanics and Foundation Engineering, ASCE, Vol. 105, 257-.

- Cheney, J.E. (1973), *Technique's and equipment using the surveyor's level for accurate measurement of building level*, Proceedings of the Symposium of Field Instrumentation, British Geotechnical Society, London, pp. 85-99.
- Chandler, R.J., Crilly, M.S., and Montgomery-Smith, G. (1992), *A low-cost method of assessing clay desiccation for low-rise buildings*, Proceedings of ICE, Civil Engineering, Vol. 92, May, pp. 82-89.
- Chandler, R. J. Gutierrez, C. I. (1986), *The filter-paper method of suction measurement*, Géotechnique, Vol. 36, No. 2, pp. 265-268.
- Cherrill, H.E. (1990), *The influence of loading rate on excess pore pressures in triaxial test*, Ph.D. thesis, City University, London, UK.
- Clayton, C. R. I. Hight, D. W. Hopper, R. J. (1992), *Progressive destructuring of Bothkennar clay: Implications for sampling and reconsolidation procedures*, Géotechnique, Vol. 42, No. 2, pp. 219-239.
- Clayton, C.R.I. and Khatrush, S.A. (1986), *A new device for measuring local axial strains on triaxial specimens*, Géotechnique, Vol. 36, No. 4, pp. 593-597.
- Clayton, C.R.I., Khatrush, S.A., Bica, A.V.D., and Siddique, A. (1989), *Use of Hall Effect semiconductors in geotechnical instrumentation*, Geotechnical Testing Journal, Vol. 12, No. 1, pp. 69-76.
- Cole, D.M. (1978), *A technique for measuring radial deformation during repeated load triaxial testing*, Canadian Geotechnical Journal, Vol. 15, pp. 426-429.
- Cole, K.W. and Burland, J.B. (1972), *Observation of retaining wall movements associated with a large excavation*, Proceedings 5th ECSMFE, Madrid, Spain, Vol. 1, pp. 445-453.
- Cooke, R.W. and Price, G. (1973), *Horizontal inclinometers for the measurement of vertical displacement in the soil around experimental foundations*, Proceedings of the Symposium on Field Instrumentation, British Geotechnical Society, London, pp. 112-125, also published as Building Research Establishment Current Paper, CP 26/73, pp. 23-31.
- Costa Filho, L. de M. (1984), *A note on the influence of fissures on the deformation characteristics of London Clay*, Géotechnique, Vol. 34. No. 2, pp. 264-268.
- Costa Filho, L. de M. (1985), *Measurement of axial strains in triaxial tests on London Clay*, Geotechnical Testing Journal, Vol. 8, No. 1, pp. 3-13.
- Costa Filho, L. de M. (1986), *A laboratory investigation of the undrained small strain behaviour of London Clay*, Proceedings of symposium on 'Geotechnical Aspects of Stiff and Hard Clays', Seattle, Washington, Editors Raj P. Khera and C.W. Lovell, Geotechnical Special Publication No. 2, ASCE, pp. 14-27.
- Costa Filho, L. de M. and Vaughan, P.R. (1980), *Discussion on 'A computer model for the analysis of ground movements' by Simpson et al. (1979)*, Géotechnique, Vol. 30, pp.336-339.
- Crabb, G.I. and Atkinson, J.H. (1991), *Determination of soil strength parameters for the analysis of highway slope failures*, Slope stability engineering: developments and applications, Proceedings of the International Conference on Slope Stability organised by the Institute of Civil Engineers, Isle of Wight, Edited by R. Chandler, pp.13-18.

- Cripps, J.C. and Taylor, R.K. (1981), *The engineering properties of mudrocks*, Quarterly Journal of Engineering Geology, Vol. 14, pp. 325-346.
- Crouch, R.S. (1996), *Personal communication*.
- Crouch, R.S. and Wolf, J.P. (1994a), *Unified 3D critical state bounding-surface plasticity model for soil incorporating continuous plastic loading under cyclic paths. Part I: Constitutive relations*, International Journal for Numerical and Analytical Methods in Geomechanics, Vol. 18, pp. 735-758.
- Crouch, R.S. and Wolf, J.P. (1994b), *Unified 3D critical state bounding-surface plasticity model for soil incorporating continuous plastic loading under cyclic paths. Part II: Calibrations and simulations*, International Journal for Numerical and Analytical Methods in Geomechanics, Vol. 18, pp. 759-784.
- Crouch, R.S., Wolf, J.P. and Dafalias, Y.F. (1994), *Unified critical-state bounding-surface plasticity model for soil*, Journal of Engineering Mechanics, Vol. 120, No. 11, pp. 2251-2270
- Dafalias, Y.F. (1986), *Bounding surface plasticity, I: Mathematical formulation and hypoplasticity*, Journal Engineering Mechanics, ASCE, Vol. 112, No. 9, pp. 1263-1291.
- Dafalias, Y.F. and Herrmann, L.R. (1980), *A bounding surface soil plasticity model*, Soils Under Cyclic and Transient Loading, edited by G.N. Pande and O.C. Zienkiewicz, A.A. Balkema, pp. 335-345.
- Dafalias, Y.F. and Herrman, L.R. (1982a), *Bounding surface formulation of soil plasticity*, Soil Mechanics - Transient and Cyclic Loads, Edited by G.N. Pande, and O.C Zienkiewicz, Published by Wiley, New York, USA.
- Dafalias, Y.F. and Herrman, L.R. (1982b), *A generalised bounding surface constitutive model for clays*, Application of plasticity and generalised stress-strain in Geotechnical Engineering, Edited by R.N. Yong, and E.T. Selig, ASCE, New York, USA.
- Dafalias, Y.F. and Herrmann, L.R. (1986), *Bounding surface plasticity II: Application to isotropic cohesive soils*, Journal of Engineering Mechanics, ASCE, Vol. 112, No. 12, pp. 1263-1291.
- Dafalias, Y.F. and Popov, E.P. (1975), *A model of nonlinearly hardening materials for complex loading*, Acta Mechanica, Vol. 21, pp. 173-192.
- Daramola, O. (1978), *The influence of stress-history on the deformation of a sand*, Ph.D. Thesis, University of London, UK.
- Dasari, G.R., Bolton, M.D. and Ng, C.W.W.N. (1995), *Small strain measurement using modified LDTs*, Technical Report CUED/D-SOILS/TR275, Department of Engineering, University of Cambridge, UK.
- Davis, A., (1993), Speaker at 'Measurement of Stiffness of Soils and Rocks Using Dynamic Methods', reported by M.A. Gordon and S.E. Stallebrass, Geoscientist, Vol. 4, No. 6, pp. 26-28.
- Davis, E.H. and Poulos, H.G. (1968), *The use of elasticity theory for settlement and predictions under three-dimensional conditions*, Géotechnique, Vol. 18, No. 1, pp. 67-91.

- de Alba, P. and Baldwin, K.C. (1991), *Use of bender elements in soil dynamics experiments*, Geotechnical Special Publication, No. 29, Published by ASCE, New York, NY, USA, pp. 86-101.
- Desai, C.S. (1971), *Non linear analysis using spline functions*, Journal of the Soil Mechanics and Foundations Division, ASCE, Vol. 97, pp. 1461-1480.
- Drnevich, V.P. (1977), *Resonant column testing - problems and solutions*, Dynamic Geotechnical Testing, ASTM STP 654, pp. 384-398.
- Drucker, D.C., Gibson, R.E., and Henkel, D.J. (1957), *Soil mechanics and work-hardening theories of plasticity*, Transactions of the American Society of Civil Engineers, Vol. 122, pp. 338-346.
- Duffy, S.M. Wheeler, S.J. Bennell, J.D. (1994), *Shear modulus of kaolin containing methane bubbles*, Journal of Geotechnical Engineering, Vol. 120, pp. 781-796.
- Duncan, J.M. and Chang, C.-Y. (1970), *Non-linear analysis of stress and strain in soils*, Journal of the soil mechanics and foundations division, ASCE, Vol. 96, pp. 1629-1653
- Dupas, J.-M., Pecker, A., Bozetto, P., and Fry, J.-J. (1988), *A 300mm diameter triaxial cell with a double measuring device*, Advanced Triaxial Testing of Soil and Rock, ASTM STP 977, Edited by R.T. Danaghe, R.C. Chaney, and M.L. Silver, pp. 132-142.
- Dyvik, R. and Madshus, C. (1985), *Laboratory measurements of G_{max} using bender elements*, 'Advances in the Art of Testing Soils Under Cyclic Conditions', ASCE annual convention 1985, Detroit, p186-196.
- Dyvik, R. and Olsen, T.S., (1989), *G_{max} measured in oedometer and DSS tests using bender elements*, Proceedings 12th ICSMFE, Rio de Janeiro, Brazil, pp. 39-42.
- El-Ruwayih, A.A. (1975), *Stress strain characteristics of rock fill, and of clays under high pore pressure tension*, Ph.D. thesis, University of London, UK.
- El-Ruwayih, A.A. (1976), *Design, manufacture and performance of a lateral strain device*, Géotechnique, Vol. 26, No. 1, pp. 215-216.
- El-Rimawi, J.A.A. (1989), *The behaviour of flexural members under fire conditions*, Ph.D. thesis, University of Sheffield, UK.
- Femsys (1992), Femgen / Femview finite element pre- and post-processing software, Leicester.
- Fourie, A.B., Potts, D.M. and Jardine, R.J. (1986), *The determination of appropriate soil stiffness parameters for use in finite element analyses of geotechnical problems*, Proceedings 2nd International Symposium on Numerical Models in Geomechanics, Ghent, pp.227-235.
- Gardner, R. (1937), *A method of measuring the capillary tension of soil moisture over a wide moisture range*, Soil Science, Vol. 43, pp.277-283.
- Georgiannou (1988), V.N., *The behaviour of clayey sands under monotonic and cyclic loading*, Ph.D. thesis, University of London, UK.
- Gibson, R.E. (1974), *14th Rankine Lecture: The analytical method in soil mechanics*, Géotechnique, Vol. 24, No. 1, pp. 115-140.

- Gohl W.B. (1990), *Response of pile foundations to simulated earthquake loading: experimental and analytical results*, Ph.D. thesis, University of British Columbia, Vancouver, Canada.
- Gohl, W. B. and Finn, W. D. L. (1991), *Use of piezoceramic bender elements in soil dynamics testing*, Geotechnical Special Publication, No. 29. Published by ASCE, New York, New York State, USA, pp. 118-133.
- Goodwin, A. (1991), *The behaviour of unsaturated soils at low stress levels*, Ph.D. thesis, University of Sheffield, UK.
- Goto, S., Tatsuoka, F., Shibuya, S., Kim, Y.S., and Sato, T. (1991), *Simple gauge for local small strain measurements in the laboratory*, Soils and Foundations, Vol. 31, No. 1, pp. 169-180.
- Graham, G. and Houlsby, G.T. (1983), *Anisotropic elasticity of a natural clay*, Géotechnique, Vol. 33, No. 2, pp. 165-180.
- Gunn, M. (1992), *The prediction of surface settlement profiles due to tunnelling*, Proceedings of the Wroth Memorial Symposium, St. Catherine's College, Oxford, pp. 204-215.
- Hajj, A.R. (1990), *The simulation of sampling disturbance and its effects on the deformation behaviour of clays*, Ph.D. thesis, University of Sheffield, UK.
- Hamdi, F. and Taylor-Smith, D. (1982), *The influence of permeability on compressional wave velocity in marine sediments*, Geophysical Prospecting, Vol. 30, pp. 622-640.
- Hashiguchi, K. (1985), *Two-and three-surface models of plasticity*, Proceedings of the 5th International Conference on Numerical Methods in Geomechanics, Vol. 1. Published by Balkema, Rotterdam, Netherlands and Boston, MA, USA, pp. 285-292.
- Head, K.H. (1985), *Manual of Soil Laboratory Testing: Vol. 3 - Effective Stress Tests*, Pentech Press, London.
- Hight, D.W. (1982), *A simple piezometer probe for the routine measurement of pore pressure in triaxial tests on saturated specimens*, Géotechnique, Vol. 32, No. 4, pp. 396-401.
- Hight, D.W. (1983), *Laboratory investigation of sea bed clays*, Ph.D. thesis, University of London, UK.
- Hight, D.W., Böese, R., Butcher, A.P., Clayton, C.R.I., and Smith, P.R. (1992), *Disturbance of the Bothkennar clay prior to laboratory testing*, Géotechnique, Vol. 42, No. 2, pp. 199-217.
- Hight, D.W., Gens, A., and Jardine, R.J. (1985), *Evaluation of geotechnical parameters from triaxial tests on offshore clay*, Proceedings of the International Conference on Offshore Site Investigation, Society for Underwater Technology, London, pp. 253-268.
- Hight, D.W., Jardine, R.J., and Gens, A., (1987), *The behaviour of soft clays*, Embankment on soft clays, Public works research centre, Athens, Chapter 2, pp. 33-158.
- Hight, D.W., Pickles, A.R., De Moor, E.K., Higgins, K.G., Jardine, R.J., Potts, D.M., and Nyirenda, Z.M. (1992), *Predicted and measured tunnel distortions associated with construction of Waterloo International Terminal*, 'Predictive Soil Mechanics', Proceedings of the Wroth Memorial Symposium, St. Catherine's College, Oxford, 27-29 July, pp. 216-234.

- Hird, C.C, Osborne, P.L. and Yung, P. (1987), *Nirex Elstow site investigation - triaxial tests with small strain measurements*, University of Sheffield report for Mott MacDonald Consulting Engineers.
- Hird, C.C. and Pierpoint, N.D. (1994), *A non-linear anisotropic elastic model for overconsolidated clay based on strain energy*, Proceedings 3rd European Conference on Numerical Methods in Geotechnical Engineering, Manchester, UK, Published by Balkema, Rotterdam, pp. 67-74.
- Hird, C.C. and Yung, P.C.Y. (1989), *Use of proximity transducers for local strain measurements in triaxial tests*, Geotechnical Testing Journal, Vol. 12, No. 4, pp. 292-296.
- Hird, C.C. and Hajj, A.R. (1995), *Simulation of tube sampling effects on the stiffness of clays*, Geotechnical Testing Journal, Vol. 18, No. 1, pp. 3-14.
- Hooke, R. (1676), *A description of helioscopes, and some other instruments*, De Potentia restitutiva, London.
- Horn, I.W. (1980), *Some laboratory experiments on shear wave propagation in unconsolidated sands*, Marine Geotechnolgy, Vol. 4, No. 1, pp. 31-54.
- Horton, A., Shephard-Thorn, E.R. and Thurrell, R.G. (1974), *The geology of the new town of Milton Keynes: explanation of 1:25000 Special Geological Sheet SP 83 with parts SP 73, 74, 84, 93 and 94*, Report of the Institute of Geological Sciences, No. 74/16 102pp.
- Houlbec, I. and Finn, P.J. (1969), *A lateral deformation transducer for triaxial testing*, Canadian Geotechnical Journal, Vol. 6, pp. 353-356.
- Houlsby, G.T. (1985), *The use of a variable shear modulus in elastic-plastic models for clays*, Computers and Geotechnics, Vol. 1, pp. 3-13.
- Howarth, D.F. (1985), *Development and evaluation of ultrasonic piezoelectric transducers for the determination of dynamic Young's modulus of triaxially loaded rock cores*, Geotechnical Testing Journal, Vol. 8, No. 2, pp. 59-65.
- Isenhower, W.M. (1979), *Torsional simple shear / resonant column properties of San Francisco Bay mud*, M.Sc. thesis, University of Texas at Austin, USA.
- Iwai, S. and Irobe, M. (1986), *Measurement of dynamic properties of the homogeneous viscoelastic ground*, National Conference Publication - Institution of Engineers, Australia n 86/8. Publ by Inst of Engineers, Australia, Barton, Australia, pp. 76-79.
- Iwasaki, T., Tatsuoka, F., and Takagi, Y. (1978), *Shear moduli of sands under cyclic torsional shear loading*, Soils and Foundations, Vol. 18, No. 1, pp. 39-56.
- Jackson, J.O. (1973), *The alteration characteristics of the Lower Oxford Clay*, Clay Minerals, Vol. 10, pp. 113-126.
- Jackson, J.O. and Fookes, P.G. (1974), *Relationship of the estimated former burial depth of Lower Oxford Clay to some soil properties*, Quarterly Journal of Engineering Geology, Vol. 7, pp. 137-179.
- Jamiolkowski, M., Lancellotta, R., Lo Presti, D.C.F., Pallara, O. (1994), *Stiffness of Toyoura Sand at small and intermediate strain*, Proceedings 13th ICSMFE, New Delhi, India, Vol. 1, pp.169-172.

- Jardine, R.J. (1985), *Investigations of pile-soil behaviour with special reference to offshore structures*, Ph.D. thesis, City University, London, UK.
- Jardine, R.J. (1992), *Some observations on the kinematic nature of soil stiffness*, Soils and Foundations, Vol. 32, No. 2, pp. 111-124.
- Jardine, R.J., Brooks, N.J. and Smith, P.R. (1985b), *The use of electrolevel transducers for strain measurements in triaxial tests on weak rocks*, International Journal of Rock Mechanics, Mineral Science and Geomechanics Abstracts, Vol. 22, No. 5, pp.331-337.
- Jardine, R.J., Fourie, A., Maswoswe, J. and Burland, J.B. (1985a), *Field and laboratory measurements of soil stiffness*, Proceedings 11th ICSMFE, San Francisco, USA, Vol. 2, pp. 511-514.
- Jardine, R.J., Potts, D.M., Fourie, A.B. and Burland, J.B. (1986), *Studies of the influence of non-linear stress-strain characteristics in soil-structure interaction*, Géotechnique, Vol. 36, No. 3, pp. 377-396.
- Jardine, R.J., Potts, D.M., St. John, H.D. and Hight, D.W. (1991), *Some practical applications of a non-linear ground model*, Proceedings 10th ECSMFE, 'Deformation of Soils and Displacements of Structures', Florence, pp. 223-228.
- Jardine, R. J., Symes, M. J., and Burland, J. B. (1984), *Measurement of soil stiffness in the triaxial apparatus*, Géotechnique, Vol. 34, No. 3, pp. 323-340.
- Johnson, K.L. (1985), *Contact Mechanics*, Cambridge University Press
- Jovicic, V., Coop, M.R., and Simic, M. (1996), *Objective criteria for determining G_{max} from bender element tests*, Géotechnique, Vol. 46, No. 2, pp. 357-362.
- Kadri, A. (1984), *An experimental study of piles in soft rocks*, Ph.D. thesis, University of Sheffield, UK.
- Keller, R.W., and Anderson, M.E. (1964), *Development of a soil strain gage for laboratory dynamic tests*, Research report, AFWL-TDR-63-3.
- Khan, M.H. and Hoag, D.L. (1979), *A non-contacting transducer for measurement of lateral strains*, Canadian Geotechnical Journal, Vol. 16, No. 2, pp. 409-411.
- Kim, Y.-S. Tatsuoka, F. Ochi, K. (1994), *Deformation characteristics at small strains of sedimentary soft rocks by triaxial compression tests*, Géotechnique, Vol. 44, No. 3, pp. 461-478.
- Kirkpatrick, W.M. and Belshaw, D.J. (1968), *On the interpretation of the triaxial test*, Géotechnique, Vol. 18, pp. 336-350.
- Kirkpatrick, W.M. and Younger, J.S. (1970), *Strain conditions in a compression cylinder*, Journal of the Soil Mechanics and Foundation Engineering, ASCE, Vol. 96, SM5, pp. 1683-1695.
- Kondner, R.L. and Zelasco, J.S. (1963), *A hyperbolic stress-strain relation for sands*, Proceedings of the Pan American Conference on Soil Mechanics and Foundation Engineering, Brazil, Vol. 1, pp.289-324.
- Kreigel, H.J. and Weisner, H.H. (1973), *Problems of stress-strain conditions in subsoil*, Proceedings 8th ICSMFE, Vol. 1.3, pp. 133-141.

- Lade, P.V. and Nelson, R.B. (1987), *Modelling the elastic behaviour of granular materials*, International Journal of Numerical and Analytical Methods in Geomechanics, Vol. 11, pp. 521-542.
- Lambe, T.W. (1973), *13th Rankine Lecture: Predictions in soil engineering*, Géotechnique, Vol. 23, No. 2, pp. 149-202.
- Lawrence, F.V., Jr. (1963), *Propagation of ultrasonic waves through sand*, Research Report R63-8, Massachusetts Institute of Technology, Cambridge, Massachusetts, USA.
- Lawrence, F.V., Jr. (1965), *Ultrasonic shear wave velocities in sand and clay*, Research Report R63-8, Massachusetts Institute of Technology, Cambridge, Massachusetts, USA.
- Lekhnitskii, S.G. (1963), *Theory of Elasticity of an Anisotropic Elastic Body* (translated from Russian by P. Fern), Holden Day, San Francisco, 1963. Originally published as *Teoriia Uprugosti Anisotropnovo Tela*, Government Publishing House for Technical-Theoretical Works, Moscow and Leningrad, 1950.
- Lewin, P.I. (1970), *Stress deformation characteristics of a saturated soil*, M.Sc. thesis, University of London, UK.
- Lo Presti, D.C.F., Pallara, O., Lancellotta, R., Armandi, M., and Maniscalco, R. (1993), *Monotonic and cyclic loading behaviour of two sands at small strains*, Geotechnical Testing Journal, ASTM, Vol. 16, No. 4, pp. 409-425.
- Lo Presti, D.C.F. Pallara, O. Puci, I. (1995), *Modified commercial triaxial testing system for small strain measurements: preliminary results on Pisa Clay*, Geotechnical Testing Journal, Vol. 18, No. 1, pp. 15-31.
- Love, A.E.H. (1927) *A Treatise on the Mathematical Theory of Elasticity*, Cambridge University Press.
- Mair, R.J. and Wood, D.M., (1987), *Pressuremeter testing - methods and interpretation*, CIRIA, London.
- Marsland, A. (1971), *Laboratory and in-situ measurements of the deformation moduli of London Clay*, Proceedings, The Interaction of Structure and Foundation, Midland Soil Mechanics and Foundation Engineering Society, Department of Civil Engineering, University of Birmingham, 12-14 July, pp. 7-17. Also published as Building Research Establishment Current Paper CP 24/73.
- Mayne, P.W. and Kulhawy, F.H., (1982), *K_0 -OCR relationships in soil*, Journal of Geotechnical Engineering, ASCE, Vol. 108, pp. 851-872.
- Menzies, B.K. (1976), *Discussion on 'Design, manufacture and performance of a lateral strain device'*, Géotechnique, Vol. 26, No. 3, pp. 542-544.
- Mesri, G., Feng, T.W., and Benak, J.M. (1990), *Postdensification penetration resistance of clean sands*, Journal of Geotechnical Engineering Division, ASCE, Vol. 116, No. 7, pp. 1095-1115.
- Milodowski, A.E., Bloodworth, A.J. and Wilmot, R.D. (1985), *Long term effects on potential repository sites: the alteration of the Lower Oxford Clay during weathering*, Report of the Fluid Processes Research Group, British Geological Survey, FLP 85-13 (3rd in series).

- Mitchell, J.K. (1960), *Fundamental aspects of thixotropy in soils*, Journal of Soil Mechanics and Foundation Engineering, ASCE, Vol. 86, No. 3, pp. 19-52.
- Mott MacDonald (1987), *Finite Element Modelling of Elstow Excavation*, Mott, Hay and Anderson, Geotechnical Division Internal Report by M.A. White, GEO231, November 1987.
- Mott MacDonald (1989), *NIREX Storage Vaults pre application site study Elstow Site - consulting engineers report*, Mott, Hay and Anderson, Geotechnical Division Report, January 1989.
- Mroz, Z. (1967), *On the description of anisotropic work hardening*, Journal of the mechanics of physical solids, Vol. 15, pp. 163-175.
- Mroz, Z., Norris, V.A. and Zienkiewicz, O.C. (1978), *An anisotropic hardening model for soil and its application to cyclic loading*, International Journal of Numerical and Analytical Methods in Geomechanics, Vol. 2, pp. 203-221.
- Mroz, Z., Norris, V.A. and Zienkiewicz, O.C. (1979), *Application of an anisotropic hardening model in the analysis of elasto-plastic deformation of soils*, Géotechnique, Vol. 29, pp. 1-34.
- Mukabi, J.N., Ampadu, S.K., Tatsuoka, F., Sato, T., and Hirose, K. (1991), *Small strain stiffness and elasticity of clays in monotonic loading triaxial compression*, Proceedings, Symposium on Triaxial Testing Methods, JSSMFE, Tokyo, pp. 257-264.
- Mukabi, J.N., Tatsuoka, F., and Hirose, K. (1991b), *Effect of strain rate on small strain stiffness of kaolin in CU triaxial compression*, Proceedings 26th Japan National Conference on Soil Mechanics and Foundation Engineering, Nagano, Japan, pp.659-662.
- Mukabi, J.N., Tatsuoka, F., Kohata, Y. and Akino, N., (1994a), *Stiffness and effects of sample disturbance of stiff clays by triaxial tests*, Proceedings 29th Japan National Conference on SMFE, JSSMFE, Morioka, Vol. 1, pp. 577-580.
- Mukabi, J.N., Tatsuoka, F., Kohata, Y. and Akino, N., (1994b), *Small strain stiffness of Pleistocene clays in triaxial compression*, Proceedings International Symposium on Prefailure Deformation Characteristics of Geomaterials, IS-Hokkaido '94, Balkema, Vol. 1, pp. 189-195.
- Nair, K. and Chang, C.-Y. (1973), *Flexible pavement design and management: materials characterization*, National Cooperative Highway Research Program Report 140, National Highway Research Board, Washington, D.C., USA.
- Nataatmadja, A. and Parkin, A.K. (1990), *Axial deformation measurement in repeated load triaxial testing*, Geotechnical Testing Journal, Vol. 13, No. 1, pp. 45-48.
- Nazarian, S. and Stokoe, K.H., II, (1984), *In situ shear wave velocities from spectral analysis of surface waves*, Proceedings of the 8th World Conference on Earthquake Engineering, San Francisco, USA, Vol. 3, pp. 31-38.
- Ng, C.W.W.N. (1992), *An evaluation of soil-structure interaction associated with a multi-propped excavation*, Ph.D. thesis, University of Bristol, UK.

- Ng, C.W.W.N. and Lings, M.L. (1995), *Effects of modelling soil nonlinearity and wall installation on back-analysis of deep excavation in stiff clay*, Journal of Geotechnical Engineering, Vol. 121, pp.687-695.
- Nirex (1985), *Preliminary assessment of the geology and the hydrogeology of the proposed site investigation at Elstow Storage Depot, Bedfordshire*, Nirex Report No. 22, UK Nirex Ltd. Prepared for Nirex by G.M. Williams of the British Geological Survey, January 1985.
- Noma, T. and Ishii, T. (1986), *On the measuring method of axial strain in triaxial test on rock*, Proceedings 41st Annual Conference of Japanese Society of Civil Engineers, Vol. 3, pp. 657-658 (reported in Tatsuoka and Shibuya, 1992).
- Norwest Holst Soil Engineering Limited (1988), *Elstow site investigation (1986-87) for UK Nirex Ltd. - final factual report*, Report No. MWO/SM/F7044, February 1988.
- O'Brien, A.S., Forbes-King, C.J., Gildea, P.A. and Sharp, P. (1992), *In situ stress and stiffness at seven overconsolidated clay and weak rock sites*, published in three parts in Ground Engineering, Vol. 25, No. 8, pp. 26-34, No. 9, pp. 26-33, No. 10, pp. 24-28.
- O'Reilly, M.P. and Brown, S.F. (1992), *Observations on the resilient shear stiffness of granular materials*, Géotechnique, Vol. 42, No. 4, pp. 631-633.
- Parry, R.H.G., *Some properties of heavily overconsolidated Oxford Clay at a site near Bedford*, Géotechnique, Vol. 22, No. 3, pp. 485-507.
- Pennington (1995), *Personal communication*.
- Pierpoint, N.D. (1996a), *'Model OC' - the implementation of a non-linear cross-anisotropic elastic model into the finite element program CRISP*, Geotechnics Research Group Internal Report, Department of Civil and Structural Engineering, University of Sheffield, UK.
- Pierpoint, N.D. (1996b), *Elstow site investigation instrumentation data*, Geotechnical Research Group Internal Report, Department of Civil and Structural Engineering, University of Sheffield, UK.
- Pierpoint, N.D. (1996c), *StressPath*, Geotechnical Research Group Internal Report, Department of Civil and Structural Engineering, University of Sheffield, UK.
- Poulos, H.G. and Davis, E.H. (1974), *Elastic solutions for soil and rock mechanics*, John Wiley & Sons, New York.
- Rice, M.H. and Walsh, J.M. (1957), *Equation of state of water to 250 kilobars*, Journal of Chemical Physics, Vol. 26, No. 4, pp. 824-830.
- Richardson, D. (1988), *Investigations of threshold effects in soil deformations*, Ph.D. thesis, City University, London, UK.
- Richart, F.E., Hall, J.R., Woods, R.D. (1970), *Vibration of Soil and Foundations*, Published by Prentice-Hall Inc., Englewood Cliffs, New Jersey, USA, 414pp.
- Richart, F.E., Hall, J.R., Woods, R.D. (1970), *Vibration of soil and foundations*, Prentice-Hall Inc., Englewood Cliffs, NJ, USA, 414pp.
- Robertson, P.K., Campanella, R.G., Gillespie, D., and Rice, A. (1984), *Seismic CPT to measure in situ shear wave velocity*, Proceedings of Measurement and Use of Shear Wave Velocity for Evaluating Dynamic Soil Properties, Geotechnical Engineering Division, ASCE, Denver, CO, USA, April 1984.

- Roscoe, K.H. and Burland, J.B. (1968), *On the generalised stress-strain behaviour of 'wet' clay*, Engineering Plasticity, Editors J. Heyman and F.A. Leckie, Cambridge University Press, pp. 535-609.
- Roscoe, K.H., Arthur, J.R.F. and James, R.G. (1963), *The determination of strains in soils by an x-ray method*, Civil Engineering and Public Works Review, Vol. 53, pp. 873-876 and pp. 1009-1012.
- Rowe, P.W. and Barden, L. (1964), *The importance of free-ends in the triaxial test*, Journal of the Soil Mechanics and Foundation Engineering Division, ASCE, Vol. 90, SM1, pp. 1-27.
- Rudrum, D.M. (1990), *The short term behaviour of a trial excavation in Oxford Clay*, MSc Dissertation, Imperial College of Science Technology and Medicine, London, UK.
- Russell, D.J., Denness, B. and McCann, D.M. (1978), *Shear-strength anisotropy variations in weathered Oxford Clay*, Engineering Geology, Vol. 12, pp. 337-344.
- Saada, A.S. (1970), *Testing for anisotropic clay soils*, Journal of the Soil Mechanics and Foundation Division, ASCE, Vol. 96, pp. 1847-1852.
- Salman, T.H. (1994), *Triaxial behaviour of partially saturated granular soils at low stress levels*, Ph.D. thesis, University of Sheffield, UK.
- Sánchez-Salineró, A., Roesset, J.M. and Stokoe II, K.H. (1986), *Analytical studies of body wave propagation and attenuation*, Geotechnical Engineering Report GR86-15, Geotechnical Engineering Centre, Civil Engineering Department, University of Texas at Austin, USA.
- Santamarina, J.C., Wakim, T.N., Tallin, A.G., Rab, F., and Wong, J. (1991), *Piezo film technology and applications in geotechnical testing*, Geotechnical Testing Journal, Vol. 14, No. 4, December, pp. 363-370.
- Schmertmann, J.H. (1991), *The mechanical aging of soils*, Journal of Geotechnical Engineering, ASCE, Vol. 117, No. 9, pp. 1288-1330.
- Schofield, A.N. and Wroth, C.P. (1968), *Critical State Soil Mechanics*, McGraw-Hill, London, UK.
- Scholey, G.K., Frost, J.D., Lo Presti, D.C.F., Jamiolkowski, M. (1995), *A review of instrumentation for measuring small strains during triaxial testing of soil specimens*, Geotechnical Testing Journal, ASTM, Vol. 18, No. 2, pp.137-156.
- Schultheiss, P.J. (1981a), *Development of seismic shear wave devices*, Marine Science Laboratories, Gwynedd, UK Report.
- Schultheiss, P.J. (1981b), *Simultaneous measurements of p and s wave velocities during conventional laboratory soil testing procedures*, Marine Geotechnology, Vol. 4, No. 4, pp. 343-367.
- Schultheiss, P.J. (1982), *Influence of packing structure on seismic wave velocities in sediments*, Ph.D. thesis, University College of North Wales.
- Schultheiss, P.J. (1983), *The influence of packing structure and effective stress on v_s , v_p and the calculated dynamic and static moduli in sediments*, Proceedings of 'Acoustics and the Sea-Bed', pp. 19-27.

- Shibuya, S, Park, C.-S., Tatsuoka, F., Abe, F., Teachavorasinskun, S., Kohata, Y. and Sato, T. (1994), *The significance of local lateral strain measurement of soil specimens for a wide range of strains*, Soils and Foundations, Vol. 34, No. 2, pp. 95-105.
- Shibuya, S., Tatsuoka, F., Abe, F., Kim, Y.-S., Park, C.-S. and Mukabi, J.N. (1991b), *A new look into stress and strain relation of soils and rocks*, Proceedings 9th Asian Regional Conference on Soil Mechanics and Foundation Engineering, Bangkok, Vol. 1.
- Shibuya, S., Tatsuoka, F., Teachavorasinskun, S., Park, C.-S., Abe, F. (1991a), *Elastic properties of granular materials measured in the laboratory*, Proceedings 10th ECSMFE, 'Deformation of Soils and Displacements of Structures', Florence, Italy, pp.163-166.
- Shirley, D.J. (1978), *An improved shear wave transducer*, Journal of the Acoustical Society of America, Vol. 63, No. 5, pp. 1643-1645.
- Shirley, D.J. and Anderson, A.L. (1975), *Acoustic and engineering properties of sediments*, Report No. ARL-TR-75-58, Applied Research Laboratory, University of Texas at Austin, USA.
- Shirley, D.J. and Anderson, A.L. (1978), *Acoustics of in situ and laboratory sediments*, Report No. ARL-TR-78-36, Applied Research Laboratory, University of Texas at Austin, USA.
- Shirley, D.J. and Hampton, L.D. (1977), *Shear wave measurements in laboratory sediments*, Journal of the Acoustical Society of America, Vol. 63, No. 2, February, pp.607-613.
- Simpson, B. (1992), *32nd Rankine Lecture: Retaining structures: displacement and design*, Géotechnique, Vol. 42, No. 4, pp. 541-576.
- Simpson, B., Atkinson, A.H., and Jovicic, V. (1996), *The influence of anisotropy on calculations of ground settlements above tunnels*, Proceedings of 'Geotechnical Aspects of Underground Construction in Soft Ground', City University, pp. 511-514.
- Simpson, B, Calabresi, G, Sommer, H and Wallays, M. (1981), *Design parameters for stiff clays-state of the art report*, Session 4, Proceedings 7th ECSMFE, Brighton, Vol. 5, pp. 91-125.
- Simpson, B., O'Riordan, N.J. and Croft, D.D. (1979), *A computer model for the analysis of ground movements in London Clay*, Géotechnique, Vol. 29, No. 2, pp. 149-175.
- Sivakumar, V. (1993), *A critical state framework for unsaturated soil*, Ph.D. thesis, University of Sheffield, UK.
- Skempton, A.W. (1954), *The pore pressure coefficients A and B*, Géotechnique, Vol. 4, pp. 143-147.
- Skempton, A.W. and Sowa, V.A. (1963), *The behaviour of saturated clays during sampling and testing*, Géotechnique, Vol. 13, No. 4, pp.269-290.
- Skinner, A.E. (1975), *The effect of high pore water pressures on the mechanical behaviour of sediments*, Ph.D. thesis, University of London, UK.
- Smith, P.D.K. and Burland, J.B. (1976), *Performance of a high precision multi-point borehole extensometer in soft rock*, Canadian Geotechnical Journal, Vol. 13, No. 2, pp. 172-176.
- Som, N.N. (1968), *The effect of stress path on the deformation and consolidation of London Clay*, Ph.D. thesis, University of London, UK.

- St. John, H.D. (1975), *Field and theoretical studies of the behaviour of ground around deep excavations in London Clay*, Ph.D. thesis, University of Cambridge, Cambridge, United Kingdom.
- St. John, H.D., Potts, D.M., Jardine, R.J. and Higgins, K.G. (1992), *Prediction and performance of ground response due to construction of a deep basement at 60 Victoria Embankment*, Proceedings Wroth Memorial Symposium, pp. 449-465.
- Stallebrass, S.E. (1990a), *Modelling the effect of recent stress history on the deformation of overconsolidated soils*, Ph.D. thesis, City University, London, UK.
- Stallebrass, S.E. (1990b), *Modelling small strains for analysis in geotechnical engineering*, Ground Engineering, Vol. 23, pp. 26-29.
- Stallebrass, S.E. (1994), *Personal communication*
- Stallebrass, S.E., Jovicic, V. and Taylor, R.N. (1994), *The influence of recent stress history on ground movements around tunnels*, Proceedings of the International Symposium on Pre-Failure Deformation Characteristics of Geomaterials, Sapporo, Japan, pp.615-620.
- Stokoe, K.H., II and Hoar, R.J. (1978), *Variables affecting in situ seismic measurements*, Proceedings of Earthquake Engineering and Soil Dynamics, ASCE, Pasadena, USA, June 19-21, 1978, Vol. 2, pp. 919-939.
- Stokoe, K.H., II, (1989), *In situ seismic testing with surface waves*, Proceedings of the 12th International Conference on Soil Mechanics and Foundation Engineering, Rio de Janeiro, Brazil, Vol. 1, published by Balkema, Rotterdam, Netherlands, pp. 331- 334.
- Stokoe, K.H., II, and Woods, R.D. (1972), *In situ shear wave velocity by cross-hole method*, Journal of the Soil Mechanics and Foundation Division, ASCE, Vol. 98, No. SM5, pp. 443-360.
- Stoll, R.D. (1989), *Sediment Acoustics*, Lecture Notes in Earth Sciences, Published by Springer-Verlag.
- Sully, J.P. and Campanella, R.G. (1995), *Evaluation of in situ anisotropy from crosshole and downhole shear wave velocity measurements*, Géotechnique, Vol. 45, No. 2, June, pp. 267-282.
- Tatsuoka, F. (1988), *Some recent developments in triaxial testing systems for cohesionless soils*, State-of-the-art paper, ASTM STP 977, Advanced Triaxial Testing of Soil and Rock, pp. 7-67.
- Tatsuoka, F. (1993), *Personal communication*.
- Tatsuoka, F. and Kohata, Y. (1995), *Stiffness of hard soils and soft rocks in engineering applications*, Report of the institute of industrial science, Vol. 38, No. 5, March 1995, University of Tokyo, Tokyo, Japan.
- Tatsuoka, F. and Shibuya, S. (1992), *Deformation characteristics of soils and rocks from field and laboratory tests*, Report of the Institute of Industrial Science, Vol. 37, No. 1, March 1992, University of Tokyo, Tokyo, Japan.
- Tatsuoka, F., Teachavorasinskun, S.D., Kohata, J., Sato, Y., and Takeshi (1994), *Importance of measuring local strains in cyclic triaxial tests on granular materials*, ASTM Special Technical Publication No. 1213, ASTM, Philadelphia, PA, USA. pp. 288-302.

- Thomann, T.G. and Hryciw, R.D. (1990), *Laboratory measurement of small strain shear modulus under K_0 conditions*, Geotechnical Testing Journal, Vol. 13, No. 2, June, pp. 97-105.
- Timoshenko, S. and Goodier, J.N. (1951), *Theory of elasticity*, 2nd edition, McGraw Hill.
- Truesdale, W.B. (1963), *Development of a small soil strain gage*, Research report, AFWL-TDR-63-3, IIT Research Institute, Chicago, Illinois.
- Truesdale, W.B. (1964), *Strain variation in a triaxial soil test*, Research report, AFWL-TDR-64-47, IIT Research Institute, Chicago, Illinois.
- Truesdale, W.B. and Anderson, M.E. (1964), *A new device for soil strain measurement*, Proceedings of the Symposium on Soil-Structure Interaction, University of Arizona, Tucson, Arizona, USA, pp.129-137.
- Truesdale, W.B. and Schwab, R.B. (1966), *Soil strain gage instrumentation*, Research report, AFWL-TDR-65-207, IIT Research Institute, Chicago, Illinois.
- Truesdale, W.B. and Schwab, R.B. (1967), *Soil strain gage instrumentation*, Proceedings of the International Symposium on Wave Propagation and Dynamic Properties of Earth Materials, University of New Mexico, New Mexico, USA, pp.931-941.
- Viggiani, G (1992), *Small strain stiffness of fine grained soils*, Ph.D. thesis, City University, London, UK.
- Viggiani, G. and Atkinson, J.H. (1995a), *Interpretation of bender element tests*, Géotechnique, Vol. 45, No. 1, March, pp. 149-154.
- Viggiani, G. and Atkinson, J.H. (1995b), *Stiffness of fine-grained soil at very small strains*, Géotechnique, Vol. 45, No. 2, June 1995, pp. 249-265.
- Webb, (1966), *The mechanical properties of undisturbed samples of London Clay and Pierre Shale*, Ph.D. thesis, University of London, UK.
- White, J.E. (1983), *Underground sound, application of seismic waves*, published by Elsevier.
- Whittle, A.J. (1993), *Evaluation of a constitutive model for overconsolidated clays*, Géotechnique, Vol. 43, No. 2, pp. 289-213.
- Whittle, A.J., DeGroot, D.J. Ladd, C.C. Seah, T.-H. (1994), *Model prediction of anisotropic behaviour of Boston blue clay*, Journal of Geotechnical Engineering, Vol. 120, No. 1, pp. 199-224.
- Whittle, A.J., Hashash, Y.M.A. and Whitman, R.V. (1993), *Analysis of deep excavation in Boston*, Journal of Geotechnical Engineering, Vol. 119, No. 1, pp. 69-90.
- Whittle, A.J., Kavvas, M.J. (1994), *Formulation of MIT-E3 constitutive model for overconsolidated clays*, Journal of Geotechnical Engineering, Vol. 120, No. 1 pp. 173-198.
- Wood, D.M. (1990), *Soil Behaviour and Critical State Soil Mechanics*, Cambridge University Press.
- Woods, R.D. (1978), *Measurement of dynamic soil properties*, Proceedings of ASCE Speciality Conference on Earthquake Engineering and Soil Dynamics, Pasadena, USA.

- Wroth, C.P. (1971), *Some aspects of the elastic behaviour of overconsolidated clay*, Proceedings of the Roscoe Memorial Symposium on the Stress Strain Behaviour of Soils, Cambridge University, Published by Foulis, pp. 347-361.
- Wroth, C.P. (1975), *In situ measurement of initial stresses and deformation characteristics*, Proceedings Speciality Conference in *In situ* Measurement of Soil Properties, ASCE, Raleigh, North Carolina, pp. 181-230.
- Wroth, C.P. and Houlsby, G.T. (1985), *Soil mechanics - property characterisation and analysis procedures*, Proceedings 11th ICSMFE, San Francisco, USA, Vol. 1, pp. 1-55.
- Yan, L., Byrne, P.M. (1990), *Simulation of downhole and crosshole seismic tests on sand using the hydraulic gradient similitude method*, Canadian Geotechnical Journal, Vol. 27, No. 4, pp. 441-460.
- Yoshimi, Y., Richart Jr., F.E., Prakash, S., Barkan, D.D., Ilyichev, V.A. (1977), *Soil dynamics and its application to foundation engineering*, Proceedings of IX ICSMFE, Tokyo, Japan, Vol. 2, pp. 605-650.
- Yuen, C.M.K., Lo, K.Y., Palmer, J.H.L., and Leonards, G.A. (1978), *A new apparatus for measuring the principal strains in anisotropic clays*, Geotechnical testing journal, GTJODJ, Vol. 1, No. 1, pp.24-33.
- Yudhbir and Khan, K.K. (1980), *Testing for evaluation of stress-strain behaviour of clays*, Geotechnical Testing Journal, GTJODJ, Vol. 3, No. 1, pp. 18-29.
- Yung, P. (1987), *The measurement of the deformation properties of Cowden Till at small strains*, Ph.D. Thesis, University of Sheffield, UK.
- Zakaria, I. (1994), *Yielding of unsaturated soils*, Ph.D. thesis, University of Sheffield, UK.
- Zytinski, M., Randolph, M.F., Nova, R., and Wroth, C.P. (1978), *On modelling the unloading reloading behaviour of soils*, International Journal of Analytical and Numerical Methods in Geomechanics, Vol. 2, pp. 87-94.

Notation:

- ASCE - American Society of Civil Engineers
- CIRIA - Construction Industry Research and Information Association
- ECSMFE - European Conference of Soil Mechanics and Foundation Engineering
- ICE - Institute of Civil Engineers
- ICSMFE - International Conference of Soil Mechanics and Foundation Engineering
- JSSMFE - Japanese Society of Soil Mechanics and Foundation Engineering



Appendix A - Elstow excavation logging profiles

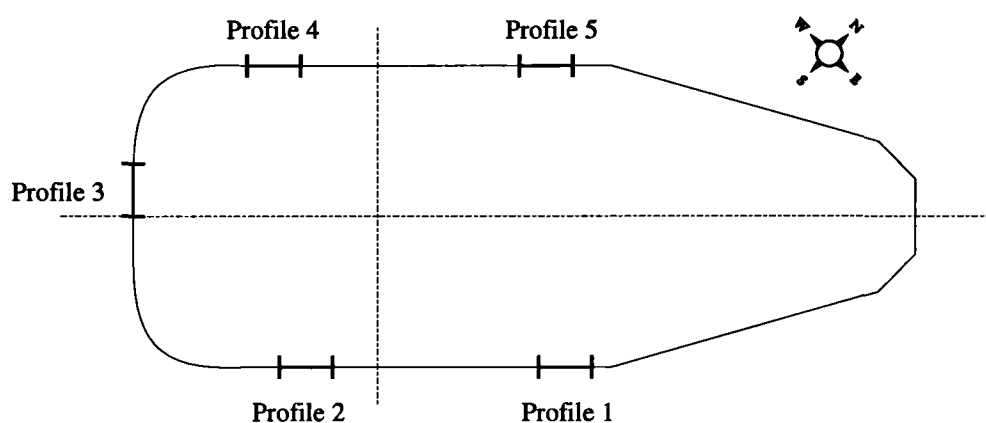


Figure A.1 - Location of logging profiles in relation to excavation plan

The logging profiles taken of the excavation sides during construction provide an essential investigation of the structure and composition of the ground. The location of the five logging profiles is shown in Figure A.1 and their descriptions are presented below as follows: Profile 1 in Figure A.2 and Table A.1; Profile 3 in Figure A.3 and Table A.2; Profile 4 in Figure A.4 and Table A.3; Profile 5 in Figure A.5 and Table A.4 (NB: Profile 2 not shown). The faces shown for each profile are horizontally offset, and not aligned one above the other. Figure A.6 shows a typical view of the unweathered Oxford Clay.

The main strata were numbered in sequence from ground level and a standard lettering scheme was used:

- *A - Made ground*
- *B - Top soil*
- *C - Head deposits/subsoil*
- *D - Head deposits (granular)*
- *E - Head deposits (clay)*
- *F - Weathered Oxford Clay*
- *G - Slightly weathered Oxford Clay*
- *H - Oxford Clay*

Due to significant variation within the nature of these main strata the standardisation was not carried through to the numbered sub-divisions. Therefore H7 on one profile does not carry through to H7 on another profile.

Table A.1 - Soil description for excavation logging profile 1

| Strata | Description |
|--------|---|
| A | Firm to stiff brown and black slightly sandy, slightly gravelly CLAY, some roots and rootlets (MADE GROUND). Black due to ash content. Fine to coarse angular to subrounded, predominantly lint, some sandstone, brick and clinker, gravel. Occasional brick cobbles. |
| C | Firm brown mottled orange brown, slightly sandy slightly gravelly CLAY, some roots and rootlets (SUBSOIL/HEAD DEPOSITS). Fine and medium occasionally coarse angular to subrounded predominantly flint and some sandstone gravel |
| D | Orange brown indistinctly thinly bedded often slightly clayey very sandy GRAVEL, some rootlets (HEAD DEPOSITS). Orange brown due to ferruginous staining. Fine, medium and occasionally coarse angular to subrounded occasionally rounded, predominantly flint, some sandstone and occasional chalk gravel. Indistinct horizontal bedding. |
| D1 | Approximately 100mm thick band of firm to stiff light grey, mottled brown, very sandy slightly gravelly CLAY with occasional rootlets. Fine to medium angular to subrounded predominantly flint and some sandstone gravel. |
| D2 | Variable zone of firm to stiff light grey mottled orange brown very sandy slightly gravelly CLAY, with occasional rootlets and light brown very clayey slightly gravelly SAND. Fine to medium, angular to subrounded predominantly flint and some sandstone gravel. |
| E | Firm light grey mottled light brown CLAY, occasional shells, numerous desiccation cracks. (HEAD DEPOSITS). Shells scattered throughout. Subvertical to vertical closely spaced desiccation cracks, smooth to rough, irregular and planar gleyed up to 5mm occasionally 10mm, some roots, rootlets and rootlet traces. At contact with strata D, zone 50 to 150mm wide slightly gravelly. Fine medium occasionally coarse angular to rounded predominantly flint occasionally sandstone gravel. |
| E1 | With occasional, locally some, shear surfaces. Subhorizontal and inclined variably closely and medium spaced shear surfaces, smooth irregular and planar, slightly polished, generally gleyed up to 2mm, occasionally ridged down dip. Individual extent 300 to 500mm. Orientation random apart from adjacent to D, surfaces often sub-parallel to the contact |
| E2 | With numerous lithorelicts. Lithorelicts generally up to 2x5mm, occasionally up to 5x10mm, random orientated. Lithorelicts light brown, surrounding material light grey. |
| F | Firm becoming stiff to very stiff, light grey and light brown mottled indistinctly thinly laminated CLAY, with numerous lithorelicts becoming very closely fissured with depth, slightly shelly and shelly, numerous selenite crystals, some desiccation cracks (weathered OXFORD CLAY). Centre of fissure blocks and lithorelicts light brown thinly laminated, margin light grey and destructured. Selenite crystals up to 1mm concentrated on fissures and margins of lithorelicts. Subvertical to vertical, closely to medium spaced desiccation cracks, rough, irregular, planar, gleyed up to 5mm, some roots and rootlets, some selenite crystals and white coating. |
| F1 | Firm light grey mottled light brown, with numerous lithorelicts slightly shelly. Lithorelicts light brown indistinctly thinly laminated at centre with light grey destructured margins. Lithorelicts size 5x10mm becoming 10x20mm with depth, locally variable, horizontally elongated. Shells scattered throughout. Closely to medium spaced desiccation cracks. |
| F2 | Approximately 50mm thick band of orange brown mottled light grey, shelly. Orange brown colouration due to ferruginous staining. Generally shelly, occasionally no shells present |
| F3 | Firm to stiff extremely closely to very closely fissured, slightly shelly. Shells scatter throughout. Desiccation cracks medium to closely spaced, gleying generally 2mm but occasionally up to 5mm. |
| F4 | Stiff, extremely closely to very closely fissured, shelly with some roots and rootlets. Extremely closely fissured becoming very closely fissured with depth. Medium to closely spaced desiccation cracks. Shells distributed evenly throughout |
| F5 | 70-100mm band of stiff light brown mottled light grey, indistinctly very closely fissured, very shelly. Orange brown colouring due to ferruginous staining. Fissuring locally absent due to shellyness. Numerous selenite crystals up to 1mm, scattered throughout. |
| F6 | Stiff to very stiff, light brown mottled light grey, very closely fissured slightly shelly, occasional desiccation cracks. Subhorizontal to vertical generally very closely, locally extremely closely spaced fissures, smooth and planar with numerous selenite crystals. Shells evenly distributed. Widely spaced desiccation cracks with roots and rootlet traces, gleyed up to 2mm and with white coating. |
| F7 | Stiff to very stiff light brown mottled light grey very closely fissured, shelly. Light grey at margins of fissure blocks. Subhorizontal to vertical generally very closely, locally extremely closely fissured, smooth planar and irregular. Fissures indistinct due to shellyness. Selenite crystals restricted to fissures, some to numerous. Shells evenly distributed throughout. Desiccation cracks widely spaced. |
| F8 | Stiff to very stiff brown very closely to closely fissured, some selenite, desiccation cracks absent. Subhorizontal to vertical very closely to closely spaced fissures rough irregular, planar, fissures very indistinct due to shellyness. |
| G | Very stiff, grey and brown mottled thinly laminated clay, very locally extremely locally fissured CLAY, shelly, selenite absent (slightly weathered OXFORD CLAY). Grey at centre of fissure blocks, brown at margins. Mainly brown at top of stratum, mainly grey at base. Subhorizontal to vertical very locally extremely closely spaced fissures, smooth irregular and planar. Locally indistinct due to shellyness. Shells scatter throughout. |
| H | Very stiff green grey, thinly laminated, closely to very closely fissured CLAY, with occasional shells (OXFORD CLAY). Fissures generally closely to very closely spaced locally closely spaced and locally very to extremely closely spaced. Fissure blocks elongated horizontally in ratio of 2 or 3:1. Horizontal bedding fissures smooth and planar, occasionally stepped. Occasionally subhorizontal, generally inclined to subvertical fissures, smooth, occasionally slightly rough, generally slightly curved and curved, often stepped, occasionally planar. Subvertical to vertical fissures smooth and planar occasionally slightly curved and occasionally stepped. Prominent subvertical to vertical fissures generally smooth and planar and stepped, with locally up to 5mm comminuted clay. Shells scattered throughout. |
| H1 | Grey, very to extremely closely fissured, shelly. Subhorizontal to vertical, very to extremely closely fissured, indistinct due to shell content, smooth and rough, planar |
| H2 | Green grey, very to extremely closely fissured, very shelly. Subhorizontal to vertical, very to extremely closely spaced fissures very indistinct, very indistinct due to shellyness, rough, irregular and planar. Band contains single pyritic shell 200mm long and 40mm high, 0.80m long. With some lenses up to 10mm thick, 25mm long of grey slightly shelly clay |
| H3 | Closely to very closely, locally very to extremely closely fissured, shelly and slightly shelly. Increasing shellyness with depth, locally very shelly at base. Up to 20mm thick pyritic and slightly pyritic discontinuous band. Fissures locally indistinct due to shellyness. Prominent fissures widely spaced |
| H4 | As main description. Subvertical to vertical dominant over inclined to subvertical fissures. Prominent fissures generally medium spaced, locally closely and widely spaced. Individual prominent fissures over 0.50m exposed extent recorded individually. |
| H5 | 80mm thick band as H4 but shelly and contain discontinuous pyritic and slightly pyritic band up to 5mm thick |
| H6 | 80mm thick very shelly band containing continuous pyritic and slightly pyritic band up to 20mm thick, with occasional carbonaceous material. Subhorizontal to vertical very to extremely closely spaced fissures, rough irregular, indistinct due to shell content. |
| H6a | Band up to 80mm thick of green grey calcareous MUDSTONE, with numerous shells, moderately weak to moderately strong pyritic and slightly pyritic band continuing through it. Extends from 2.50 to 3.90m across face. |
| H7 | Close to medium fissured. Inclined to vertical closely to medium, locally closely to very closely spaced fissures, smooth planar, occasionally stepped, occasionally slightly curved. Other fissures absent. Locally slightly shelly |
| H8 | 100-150mm thick very to extremely closely fissured, very shelly band with continuous pyritic and slightly pyritic band generally 20mm locally up to 35mm thick. Subhorizontal to vertical very to extremely closely spaced fissures, rough to irregular, indistinct due to shellyness and pyritisation. |
| H9 | Slightly shelly. Subvertical to vertical fissures in equal proportions to inclined to subvertical fissures. Prominent fissures; generally medium spaced, occasionally close to medium spaced, occasionally wide. Individual prominent fissures over 0.50m exposed extent recorded individually. |
| H10 | Closely to very closely fissured, locally closely, locally very closely. Inclined to subvertical fissures dominant over subvertical to vertical fissures. Prominent fissures, generally medium spaced, occasionally close to medium spaced, occasionally wide. Individual prominent fissures over 0.50m exposed extent recorded individually. |

Table A.2 - Soil description for excavation logging profile 3

| Strata | Description |
|--------|---|
| A | Firm to stiff black and brown slightly sandy slightly gravelly CLAY, with some roots and rootlets and occasional layers of ash sand (MADE GROUND). Fine to medium and occasionally coarse subangular to subrounded predominantly flint, some sandstone, brick and clinker gravel. Occasional brick cobbles. 50mm thick band of black slightly clayey gravelly ash sand towards base of A |
| C | Firm to stiff brown and grey sandy slightly gravelly CLAY (SUBSOIL/HEAD DEPOSITS). Fine to medium angular to subrounded predominantly flint with some sandstone gravel. |
| C1 | Firm brown mottled orange brown, slightly sandy to sandy. Locally mottled red brown or grey. Fine to medium, angular to subrounded, predominantly flint and some sandstone gravel. |
| C2 | Stiff green grey with numerous desiccation cracks. Vertical to subvertical very closely spaced desiccation cracks, smooth, planar and irregular discontinuous, locally coated with red brown material (cracks recent in origin) |
| D | Orange brown, often slightly clayey very sandy GRAVEL, some rootlets (HEAD DEPOSITS). Orange brown due to ferruginous staining. Fine to medium, occasionally coarse, angular to subrounded, predominantly flint and sandstone occasionally chalk gravel. |
| D1 | Discontinuous 30mm thick band at contact with E of firm to stiff light brown occasionally mottled orange brown, very sandy occasionally gravelly CLAY, occasional rootlets. Fine to medium angular to subrounded, predominantly flint and some sandstone gravel. |
| E | Firm to stiff, light grey mottled light brown CLAY, with occasional shells, some to numerous desiccation cracks, some to numerous disseminated white amorphous material (HEAD DEPOSITS). Shells scatter throughout. Vertical to subvertical closely spaced desiccation cracks, smooth to rough, irregular, planar, gleyed up to 5mm with some roots and rootlets an white amorphous coating. Occasional carbonaceous material. |
| E1 | As E2 but numerous desiccation cracks, numerous disseminated white mineral and occasional orange brown lenses. Desiccation cracks closely to very closely spaced. Occasional orange brown stained lenses, up to 50mm of selenite crystals. |
| E2 | With numerous lithorelicts. Lithorelicts generally 2x5mm, occasionally up to 5x10mm randomly orientated, generally stiff, but firm adjacent to desiccation cracks. Lithorelicts light brown surrounded by light grey. |
| E3 | Numerous desiccation cracks, no white material, some shear surfaces, locally some gravel occasionally some rootlets. Desiccation cracks closely to very closely spaced. Shear surfaces generally some, locally numerous subhorizontal to inclined closely spaced, smooth irregular and planar, gleyed <2mm. Slightly polished, sometimes ridged down dip, extent generally 100-400mm, locally longer as shown on log. Orientation random except close to D contact where 1 to 3 shear surfaces, subparallel to D contact contained in a band up to 50mm thick. Locally, with some gravel, increasing in quantity to D, fine to coarse subrounded predominantly flint gravel. Shear surface: 1): 260-300/20-30 - subhorizontal, smooth and planar, slightly polished, gleyed = <2mm. |
| F | Stiff light grey to light brown mottled indistinctly thinly laminated closely fissured with depth, with occasional shells, some to numerous selenite crystals, with some desiccation cracks, some roots and rootlets (WEATHERED OXFORD CLAY). Lithorelicts and centres of fissured blocks, light brown and thinly laminated, margins light grey and destructured. Selenite crystals (<1mm) concentrated on fissures and between lithorelicts. Subvertical to vertical medium to closely spaced desiccation cracks, rough, irregular, gleyed up to 4mm with amorphous white coating, with roots and rootlets. |
| F1 | Light grey mottled light brown, with numerous lithorelicts, slightly shelly, numerous selenite crystals. Lithorelicts light brown, indistinctly thinly laminated, horizontally aligned, Light grey destructured margins and between lithorelicts. Locally numerous disseminated amorphous white material desiccation cracks closely to medium spaced. |
| F2 | Light brown mottled light grey, very to extremely closely fissured with occasional shells, numerous selenite crystals. Subhorizontal extremely closely spaced fissures, rough, planar. Subvertical very closely spaced fissures, smooth, planar, irregular. Desiccation cracks medium spaced. |
| F3 | Light brown mottled light grey, indistinctly very to extremely closely fissured, shelly, numerous selenite crystals. Locally orange brown due to ferruginous staining. Fissuring indistinct due to shell content. Selenite crystals concentrated to orange brown areas. Medium spaced desiccation cracks. |
| F4 | Indistinct discontinuous, 100mm band of stiff light brown mottled light grey, indistinctly very to extremely closely fissured, shelly. Occasional lenses of stiff orange brown ferruginous stained selenite, generally up to 50x50mm, occasionally up to 300x40mm. Medium spaced desiccation cracks. |
| F5 | Light brown mottled light grey, very to extremely closely fissured shelly, with some selenite. Light grey restricted to the centres of fissure blocks. Subhorizontal extremely closely spaced fissures, rough, planar. Subvertical very closely spaced fissures, smooth, planar, irregular. |
| F6 | Continuous 100 to 150mm band of light brown mottled light grey indistinctly very closely fissures, very shelly, some selenite. Occasional lenses of light grey thinly laminated clay up to 150x10mm. |
| F7 | Light brown mottled light grey, generally very closely fissured, occasional shells, with numerous selenite crystals. Fissure blocks light brown with occasional dark brown centres, grey confined to fissure block margins. Subhorizontal and subvertical generally very closely, occasionally closely to extremely closely spaced fissures, smooth, planar. Desiccation cracks, medium spaced, white coating absent. |
| F8 | Light brown mottled light grey, very closely to extremely closely fissured, shelly, numerous selenite crystals. Fissure block centres light brown thinly laminated, margins light grey, occasionally destructured. Subhorizontal to vertical, very to extremely closely spaced fissures, rough, planar and irregular. Desiccation cracks, medium to widely spaced. |
| F9 | Brown very closely to extremely closely fissured, very shelly, some selenite crystals with numerous lenses up to 5x30mm of light brown slightly shelly clay. Subhorizontal to vertical to extremely closely spaced fissures, rough, planar and irregular, indistinct due to shell content. Fissure blocks brown and thinly laminated. Occasional lenses up to 400x100mm of stiff orange brown clay with numerous selenite crystals >2mm, and some tyritic shells (degraded ammonite). Desiccation cracks widely spaced. |
| G | Stiff, becoming very stiff with depth, grey and light brown mottled thinly laminated, very to extremely closely fissured CLAY, shelly, occasional selenite (slightly weathered OXFORD CLAY). Fissure blocks grey at centre, light brown at margins, mainly light brown at top of stratum becoming mainly light grey at base. Subhorizontal to vertical, very to extremely closely spaced fissures, rough, occasionally smooth, irregular and planar. Shells scattered through. Occasional selenite crystals up to 1mm concentrated on fissures, mainly at top of stratum. |
| H | Very stiff, green grey, thinly laminated closely to very closely fissured CLAY, with occasional shells (OXFORD CLAY). Fissures generally closely to very closely spaced, locally closely spaced, locally very to extremely closely spaced. Fissure blocks elongated horizontally in the ratio of 2 or 3:1. Horizontal bedding fissures, smooth, planar, occasionally stepped. Occasionally subhorizontal, generally inclined to subvertical fissures, smooth to slightly rough, generally slightly curved to curved, occasionally conchoidal, occasionally planar. Subvertical to vertical fissures, smooth, planar, occasionally stepped, occasionally slightly curved. Prominent subvertical to vertical fissures, generally smooth as planar, or slightly curved, occasionally stepped, locally with up to 2mm comminuted clay. Shells scattered throughout. |
| H1 | Grey, very to extremely closely fissured, shelly. Subhorizontal to vertical, very to extremely closely spaced fissures, rough, occasionally smooth, irregular and planar. Prominent fissures absent. |
| H2 | Green grey mottled grey, indistinctly closely to very closely fissures very shelly. Numerous lenses up to 10x40mm of grey clay with occasional shells. Subhorizontal to vertical to extremely closely spaced fissures, rough and irregular. Fissures indistinct due to shellyness. |
| H3 | Shelly. Slightly shelly becoming shelly at base. |
| H4 | Discontinuous slightly pyritic to pyritic shell band up to 10mm thick at base of H3 |
| H5 | As main description. Inclined to subvertical fissures dominant over subvertical to vertical fissures. Prominent fissures, medium to widely spaced. Individual prominent fissures greater than 0.5m. |
| H6 | Continuous shelly to very shelly and 30 to 50mm thick, as H5 except fissures more irregular due to shellyness. |
| H7 | As main description. Prominent fissures medium to widely spaced. Individual prominent fissures greater than 0.5m exposed extent. |
| H8 | Medium fissures, slightly shelly. Subvertical to vertical medium spaced fissures, smooth, locally slightly rough, planar, occasionally irregular and stepped, locally curved. Other fissuring and prominent fissures absent. Slightly shelly throughout. |
| H9 | Very shelly band up to 60mm thick, indistinctly thinly laminated. Fissuring indistinct and absent, containing pyritic band. Pyritic band up to 15mm thick, continuous, locally indistinct. Slightly pyritic and pyritic. |
| H10 | Very shelly band indistinctly thinly laminated, fissuring very indistinct or absent, containing pyritic band. Pyritic band 20-30mm thick continuous. |
| H11 | Generally very closely fissures, slightly shelly. Subhorizontal to vertical, very closely spaced fissures, smooth and irregular, locally curved, locally planar. Occasionally up to 2mm of comminuted clay on vertical fissures. Prominent fissures medium spaced, locally closely, locally widely spaced. Individual prominent fissures >0.5m exposed extent. Slightly shelly throughout. |
| H12 | As main description. Prominent fissures medium spaces locally closely, locally widely spaced. Individual prominent fissures greater than 0.5m. |
| H13 | Very closely to closely fissures. Fissures generally very closely spaced, locally very closely to extremely closely spaced, occasionally closely spaced. Inclined to subvertical fissures dominant over subvertical to vertical fissures. Prominent fissures medium to widely spaced with up to 2mm, occasionally up to 5mm comminuted clay infill. Individual prominent fissures greater than 0.5m. |
| H14 | Slightly shelly. Inclined to subvertical fissures dominant over subvertical to vertical fissures. Prominent fissures medium to widely spaced, locally medium spaced, smooth, stepped, planar, up to 2mm occasionally up to 5mm comminuted clay infill. Individual prominent fissures greater than 0.5m. Shells scattered throughout. |

Table A.3 - Soil description for excavation logging profile 4

| Strata | Description |
|--------|---|
| A | Variable brown sandy slightly gravelly CLAY and black gravelly SAND (MADE GROUND) |
| A1 | Black gravelly SAND, with occasionally plastic bags, bricks, wood and grass. Fine to coarse, angular to subrounded ash, sand and gravel. |
| A2 | Firm to stiff, brown sandy slightly gravelly CLAY. Occasional brick cobbles, roots and rootlets. Fine to medium occasionally coarse, angular to subrounded glint ash and chalk gravel. |
| A3 | As A2 but with occasional inclusions of stratum E clay up to 700c300mm. |
| A4 | 150mm diameter field grain trending 280 degrees, locally subrounded by 200mm land drain. Overlain by medium to coarse angular to subrounded predominantly flint gravel. |
| D | Variably orange brown and brown, often slightly clayey very sandy GRAVEL and light grey and brown gravelly CLAY and brown gravelly SAND. Some roots and rootlets (HEAD DEPOSITS). Fine to medium angular to subrounded, predominantly flint, some sandstone occasionally chalk, gravel |
| D1 | Brown sandy GRAVEL. In the upper part, with irregular 10 to 50mm thick bands of gravelly clay. In the lower part, indistinctly interbedded with orange brown gravelly SAND. |
| D2 | Discontinuous band up to 100mm thick of firm light grey mottled orange brown, gravelly CLAY with some roots and rootlets. Fine to medium, angular to subrounded, predominantly glint some chalk gravel. |
| D3 | Orange brown sand GRAVEL. Fine to medium occasionally coarse gravel. |
| D4 | Firm orange brown, gravelly very sandy CLAY, gravel content increasing at base. |
| E | Firm light brown mottled light grey CLAY, with occasional shells some to numerous desiccation cracks, and some shear surfaces (HEAD DEPOSITS). Shells scattered throughout. Vertical to subvertical closely to very closely spaced, smooth to rough irregular and planar desiccation cracks, gleyed up to 2-3mm, with occasional roots and rootlets. |
| E1 | Brown mottled light grey, locally mottled orange, with numerous lithorelicts and numerous desiccation cracks. Lithorelicts 2 to 5mm across, randomly orientated. Desiccation cracks, closely to very closely spaced, occasionally ferruginous stained, with rot traces. |
| E2 | With some lithorelicts, slightly shelly and occasionally shear surfaces. Lithorelicts 3mm across, randomly orientated. Shear surfaces, nature as E3. |
| E3 | Numerous shear surfaces, locally some gravel, some roots and rootlets. Subhorizontal to inclined very closely to closely spaced shear surfaces, smooth irregular and planar, slightly polished gleyed 2 to 5mm extent 50-600mm orientations random. Towards base of stratum extent less than 100mm, closely spaced, often slickensided down dip. Band 50mm wide at contact with stratum D has extremely closely spaced shear surfaces subparallel to the D contact. Slightly gravelly next to D contact in band is less than 50mm wide. Nature of gravel as D. Shear surfaces 1: 200-215/18-20: smooth, planar, slightly polished, gleying up to 5mm. |
| F | Firm to stiff, light grey and light brown mottled, indistinctly thinly laminated CLAY, with numerous lithorelicts, becoming very to extremely closely fissured, with occasional shells and shelly some to numerous desiccation cracks, and some roots and rootlets (weathered OXFORD CLAY). Lithorelicts and centre of fissure blocks light brown thinly laminated, margins light grey and destructured. Selenite crystals <1mm concentrated on fissures and between lithorelicts. Subvertical to vertical desiccation cracks, rough, irregular with some amorphous white coating, generally gleyed 2-5mm, occasionally up to 15mm. |
| F1 | Light brown mottled light grey, very to extremely closely fissured shelly with some selenite crystals. Light grey restricted to margins of fissure blocks. Subhorizontal extremely closely spaced fissures, rough, planar. Subvertical very closely spaced fissures; smooth, planar, irregular. Medium spaced desiccation cracks, smooth, planar, irregular |
| F2 | Light brown mottled light grey, very to extremely closely fissured, occasionally shells, numerous selenite crystals. Fissures as F1. Medium spaced desiccation cracks. |
| F3 | Continuous 30-70mm band, thinning to east end of profile of stiff locally firm, orange brown, very to extremely closely fissured, shelly, numerous orange brown selenite crystals. Fissures indistinct rough and irregular. |
| F4 | Light grey mottled light brown, extremely to very closely fissured, shelly, numerous selenite. Subhorizontal to vertical extremely to very closely spaced fissures, smooth and planar. Desiccation cracks medium spaced with some roots and rootlets. |
| F5 | Light grey mottled light brown, numerous lithorelicts, slightly shelly to shelly. Lithorelicts light brown indistinctly laminate at centre, light grey destructured at margins and between the lithorelicts. Size up to 5x10mm becoming 10x40mm with depth. Locally numerous selenite crystals. Desiccation cracks medium spaced with some roots and rootlets. Occasional stiff orange brown lenses, up to 70x40mm, of ferruginous selenite crystals in 50mm band. |
| F6 | As F5 but light brown mottled light grey. Shelly becoming slightly shelly with depth. |
| F7 | Stiff brown, indistinctly thinly laminated very to extremely closely fissured, very shelly, selenite absent, desiccation cracks absent. Subhorizontal to subvertical very to extremely closely spaced fissures, rough and irregular, planar. Fissuring indistinct due to shell content. |
| G | Stiff to very stiff, light grey an light brown mottled, thinly laminated, very closely fissured CLAY, shelly numerous selenite (slightly weathered OXFORD CLAY). Light grey at centre of fissure blocks, light brown at margins. Subhorizontal to vertical very closely, occasionally extremely closely spaced fissures, smooth, rough and planar. Generally shelly, occasionally slightly shelly. Selenite crystals restricted to fissure surfaces. |
| G1 | Very stiff indistinctly thinly laminated, very to extremely closely fissured, very shelly, selenite absent. Localised areas of light grey mottled light brown and light brown mottled light grey. Subhorizontal to vertical very to extremely closely spaced fissures, rough, irregular and planar, fissuring indistinct due to shellyness. Shells scattered throughout. |
| G2 | Very stiff grey mottled light brown, very to extremely closely fissured, selenite absent. |
| H | Very stiff green grey laminated closely to very closely fissured CLAY with occasional shells. (OXFORD CLAY). Fissures generally closely to very closely spaced, locally closely spaced, locally very to extremely closely spaced. Fissure blocks elongated horizontally in ratio of 2 or 3:1. Horizontal bedding fissures smooth and planar, occasionally stepped. Occasionally subhorizontal, generally inclined to subvertical fissures, smooth or slightly rough, generally slightly curved and curved, occasionally stepped, occasionally conchoidal, occasionally planar. Subvertical to vertical fissures, generally smooth and planar, occasionally stepped, occasionally slightly curved. Prominent subvertical to vertical fissures, generally smooth and planar or slightly curved, occasionally stepped, often with up to 2mm of comminuted clay. Shells scattered throughout. |
| H1 | Grey, very to extremely closely fissured, shelly. Subhorizontal to vertical very to extremely closely spaced fissures, indistinct due to shell content, smooth and rough, planar. Prominent fissures absent. Locally slightly shelly. |
| H2 | As H1 but containing discontinuous slightly pyritic band up to 10mm thick. |
| H3 | Green grey mottled grey, indistinctly very to extremely closely fissured, very shelly. Numerous lenses of grey slightly shelly clay up to 50mm long, 10mm thick. Subhorizontal to vertical very to extremely closely spaced fissures, rough, irregular and planar. Fissures indistinct due to shellyness. |
| H4 | Continuous shelly band 100mm thick, as H5 except fissures indistinct due to shellyness. |
| H5 | As main description. Inclined to subvertical and subvertical to vertical fissures in approximately equal proportions. Prominent fissures medium to widely spaced. Individual prominent fissures greater than 0.50m exposed extent. |
| H6 | 70mm thick very to extremely closely fissured, very shelly band containing generally continuous, locally discontinuous pyritic and slightly pyritic band up to 20mm thick. Subhorizontal to vertical very to extremely closely spaced fissures. Indistinct due to shell content, rough and irregular. |
| H7 | Close to medium fissured. Subvertical to vertical close to medium spaced, locally close to very closely spaced fissures, generally smooth and planar, occasionally stepped. Other fissuring absent. |
| H8 | 100-150mm thick very to extremely closely fissured, very shelly band containing continuous pyritic band, generally 15mm thick, locally up to 30mm thick. Subhorizontal to vertical very to extremely closely spaced fissures, rough and irregular, indistinct due to shellyness and pyritisation. |
| H9 | Very closely fissured, slightly shelly. Fissures very closely spaced, locally very closely to closely and locally very to extremely closely spaced. Inclined to subvertical fissures dominant over subvertical to vertical fissures. Prominent fissures, generally medium spaced, locally closely, locally widely spaced, often with up to 5mm comminuted clay. Individual prominent fissures greater than 0.50m exposed extent. Shells scattered throughout. |
| H10 | As H9 but occasionally closely fissured. Occasional shells |
| H11 | Very closely to closely fissured. Fissure generally very closely to closely spaced, locally very closely to extremely closely spaced, occasionally closely spaced. Inclined to subvertical fissures dominant over subvertical to vertical fissures. Prominent fissures medium to widely spaced with up to 2mm occasionally up to 5mm comminuted clay infill. Individual prominent fissures of greater than 0.50m exposed extent. |
| H12 | Slightly shelly. Inclined to subvertical fissures dominant over subvertical to vertical fissures. Prominent fissures medium to widely spaced locally medium to widely spaced locally medium spaced, up to 2mm occasionally up to 5mm comminuted clay infill. Individual prominent fissures of greater than 0.5m exposed extent shown. Shells scattered throughout. |

Table A.4 - Soil description for excavation logging profile 5

| Strata | Description |
|--------|---|
| C | Firm to stiff orange brown slightly sandy, slightly gravelly CLAY, some roots and rootlets, occasional desiccation cracks (HEAD DEPOSITS/SUBSOIL). Becomes gravelly and sandy towards base. Fine to medium occasionally coarse subangular to rounded, predominantly flint some quartzite and sandstone gravel. Subvertical to vertical medium spaced desiccation cracks, indistinct very rough and irregular with some roots and rootlets, (recent desiccation cracks) |
| C1 | Rare brick fragments (reworked C backfill to the pipe, boundaries with C indistinct) Land drain: 3 inch clay pipe, trending 050 degrees, blocked |
| D | Light brown and orange brown very sandy GRAVEL, with some rootlets (HEAD DEPOSITS). Fine to medium occasionally coarse, subangular to rounded, predominantly flint with some quartzite and sandstone and occasional chalk gravel. |
| D1 | With indistinct subhorizontal bedding - beds approximately 50-250mm thick. |
| D2 | With occasional irregular and contorted bands of very gravelly clay. Clay bands up to 50mm thick. Gravel is structureless. |
| E | Firm to stiff light grey mottled light brown CLAY, with occasional shells and numerous desiccation cracks (HEAD DEPOSITS). Shells scattered throughout. Subvertical to vertical closely spaced desiccation cracks, rough, irregular and planar, gleyed up to 2mm, some roots and rootlets and root and rootlet traces. |
| E1 | With occasional shear surfaces. Horizontal and subhorizontal possibly closely spaced shear surfaces, smooth irregular and planar, slightly polished, gleyed up to 2mm. Individual surfaces 100-300mm extent. Surfaces commonly parallel to the interface with stratum D in a zone up to 100mm wide, and are locally very closely spaced/ |
| E2 | Light brown mottled light grey with some lithorelicts. Lithorelicts 2-5mm across, randomly orientated. Desiccation cracks closely to medium spaced. |
| E3 | Gravelly and very gravelly. Fine to coarse, subangular to rounded, predominantly flint, occasionally quartzite gravel. |
| F | Firm to stiff becoming stiff to very stiff, light brown and light grey mottled indistinctly thinly laminated CLAY, with numerous lithorelicts becoming very closely fissured, slightly shelly and shelly, numerous selenite crystals, some desiccation cracks (weathered OXFORD CLAY). Centre of fissure blocks and lithorelicts light brown indistinctly thinly laminated, margins light grey and destructured. Selenite crystals up to 1mm concentrated on fissures and around margins of lithorelicts up to 1mm thick. Subvertical to vertical medium spaced desiccation cracks, rough, irregular and planar, gleyed up to 2mm, some roots and rootlets, some selenite crystals, often white coated. |
| F1 | Firm to stiff, with numerous lithorelicts variably slightly shelly and shelly. Lithorelicts light brown indistinctly thinly laminated, surrounding material light grey destructured. Lithorelicts approximately 2x5mm becoming 10x20mm with depth elongated horizontally. Generally shelly with local areas (about 2.00m high and up to 1.00m across) slightly shelly. Shells scattered throughout. |
| F2 | Stiff to very stiff, extremely becoming very closely indistinctly fissured, slightly shelly. Centre of fissure blocks light brown and indistinctly thinly laminated, margins light grey and destructured. Subhorizontal to vertical extremely closely, becoming very to extremely closely spaced with depth, fissures, smooth and planar with numerous selenite crystals. Shells scattered throughout. |
| F3 | As F2 but shelly. Shells scattered throughout. |
| F4 | Stiff to very stiff light brown mottled light grey very closely fissured with occasional shells, desiccation cracks absent. Traces of light grey on fissures. Subhorizontal to vertical generally very closely, locally extremely to very closely spaced fissures smooth and planar with numerous selenite crystals. Shells scattered throughout. |
| F5 | 20-30mm thick band of firm to stiff orange brown clay. |
| F6 | Lens of very stiff orange brown clay with inclusions of shell (probably weathered ammonite) |
| F7 | As F4 but very to extremely closely fissured and shelly. Desiccation cracks close to medium spaced. |
| F8 | Very to extremely closely fissured, slightly shelly to shelly. Desiccation cracks close to medium spaced. Occasionally the very centre of the fissure blocks light grey. Subhorizontal to vertical very to extremely closely spaced fissures smooth and planar with numerous selenite crystals. Shells scattered throughout. |
| F9 | Brown, very shelly, some selenite crystals and occasional orange brown lenses. Occasionally lenses up to 10x40mm of light brown and light grey slightly shelly clay. Occasional orange brown stained lenses up to 70x50mm of selenite crystals up to 1mm. Occasional lenses of carbonaceous material up to 60x15mm. |
| G | Stiff becoming very stiff with depth, light grey and brown mottled thinly laminated, very closely to extremely closely fissures CLAY, slightly shelly and shelly (slightly weathered OXFORD CLAY). Fissure blocks light grey at centre, light brown at margins. Mainly light brown at top of stratum becoming mainly light grey at base. Fissure blocks thinly laminated, margins occasionally destructured. Subhorizontal to vertical very closely to extremely closely spaced fissures, smooth and planar. Generally slightly shelly, locally shelly. |
| G1 | Brown and grey mottled very shelly. Fissure blocks grey at centre, brown at margins. Fissures indistinct due to shell content, rough, irregular and planar. Shells occasionally pyritic. |
| H | Very stiff green grey thinly laminated closely to very closely fissured CLAY with occasional shells (OXFORD CLAY). Fissures generally closely to very closely spaced, locally closely spaced and locally very to extremely closely spaced. Fissure blocks elongated horizontally in a ratio of 2 or 3:1. Horizontal bedding fissures smooth and planar, occasionally stepped. Inclined to subvertical fissures, smooth or slightly rough, generally slightly curved and curved, occasionally stepped or conchoidal, occasionally planar. Subvertical to vertical fissures generally smooth and planar. Prominent subvertical to vertical fissures generally smooth and planar or slightly curved, occasionally stepped locally with up to 2mm comminuted clay. Shells scattered throughout. |
| H1 | As main description. Subvertical to vertical fissures dominant over inclined to subvertical fissures. Prominent fissures medium spaced, none over 0.50m exposed extent. |
| H2 | 100mm thick shelly band containing discontinuous slightly pyritic and pyritic band up to 10mm thick. Subhorizontal to vertical extremely to very closely spaced fissures rough, irregular and planar, indistinctly due to shell content. |
| H3 | 150mm thick band as H1 but slightly shelly occasionally slightly pyritic or pyritic. |
| H4 | 50mm thick very shelly band containing discontinuous slightly pyritic and pyritic band up to 20mm thick. Subhorizontal to vertical extremely closely spaced fissures, rough and irregular, indistinct due to shellyness. |
| H5 | Close to medium spaced fissures. Subvertical to vertical, close to medium spaced fissures smooth and planar occasionally stepped. Other fissures absent. Individual prominent fissures greater than 0.50m exposed extent. |
| H6 | 100mm thick very shelly band containing continuous pyritic band up to 30mm thick. Subhorizontal to vertical very to extremely closely spaced fissures, rough and irregular, indistinct due to shell content. |
| H7 | As main description. Inclined to subvertical fissures dominant over vertical to subvertical fissures. Prominent fissures medium spaced. Individual prominent fissures greater than 0.50m exposed extent. |
| H8 | As main description. Fissure becoming closely spaced with depth. Prominent fissures medium spaced. Individual prominent fissures greater than 0.50m exposed extent. |
| H9 | As main description. Prominent fissures spaced. Individual prominent fissures greater than 0.50m exposed extent. Shells scattered throughout. |

Appendix A: Elstow excavation logging profiles

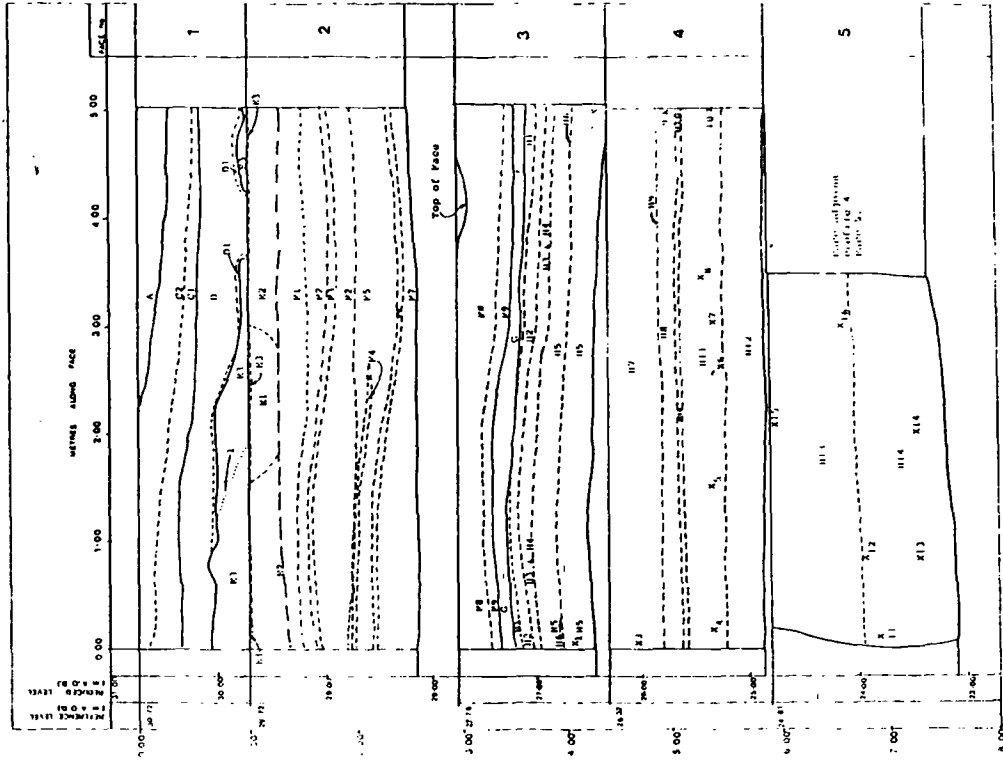


Figure A.3 - Logging profile 3

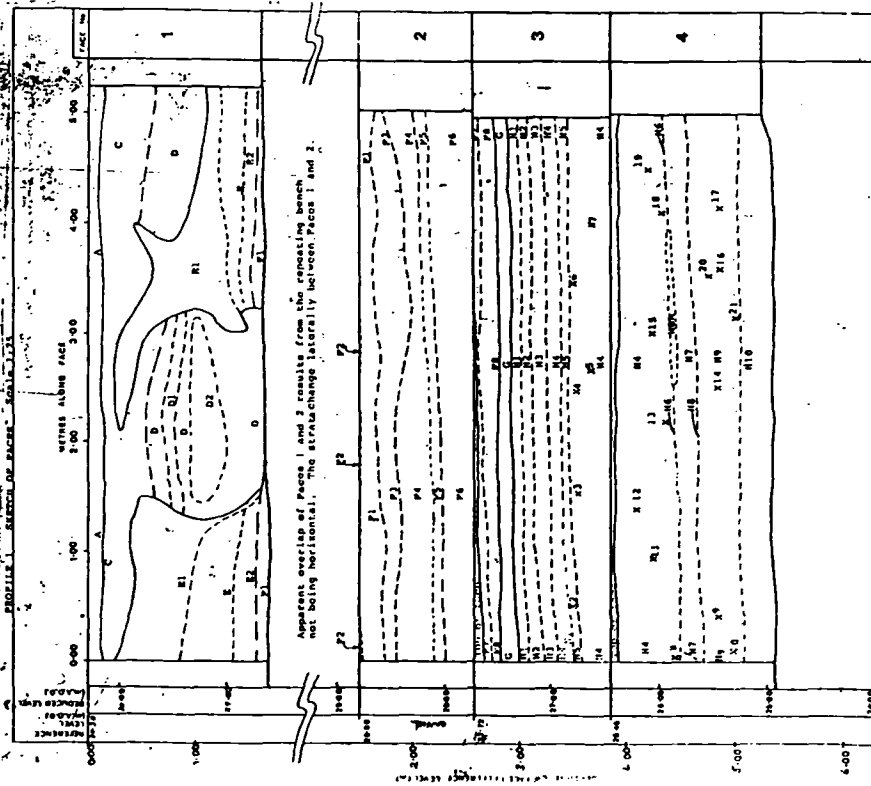


Figure A.2 - Logging profile 1

Appendix A: Elstow excavation logging profiles

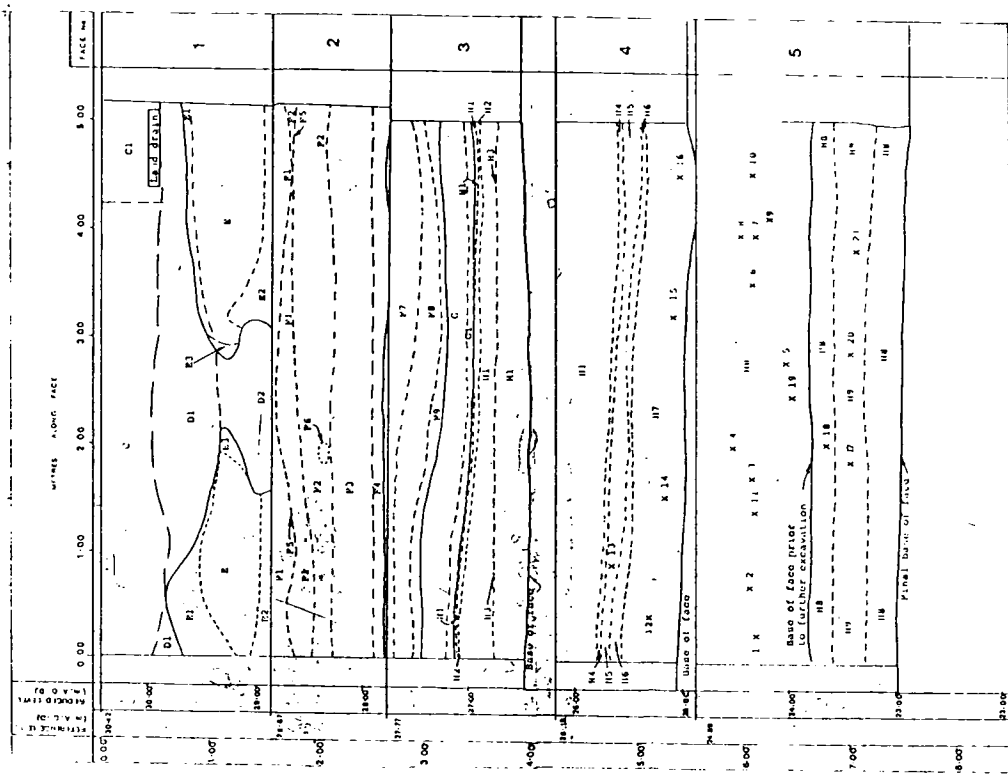


Figure A.5 - Logging profile 5

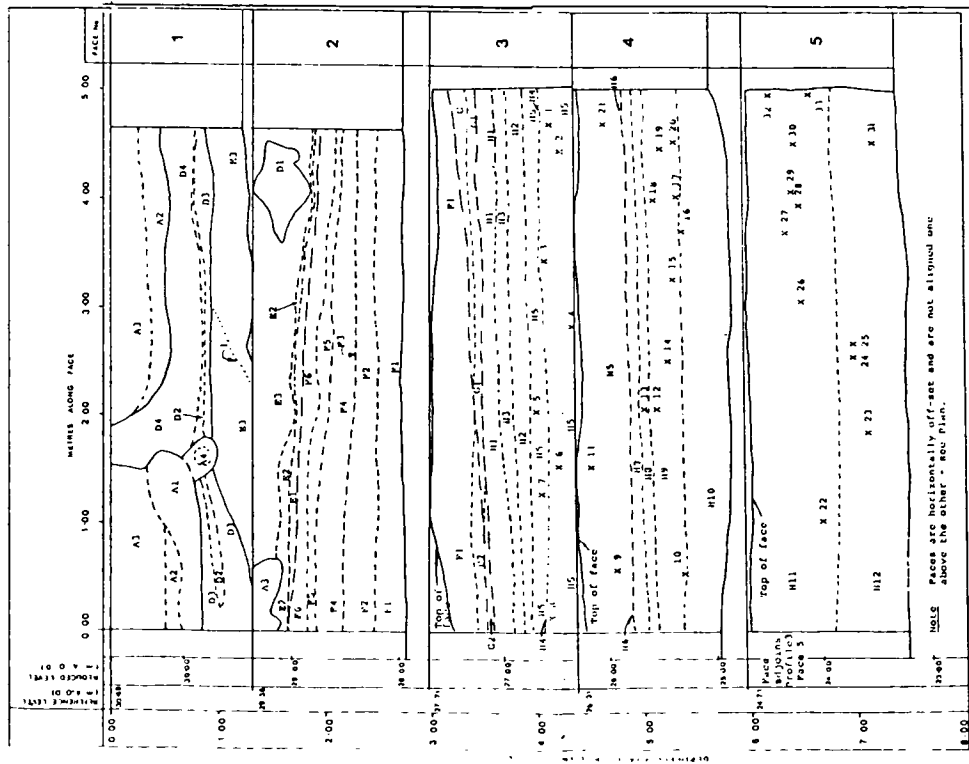


Figure A.4 - Logging profile 4

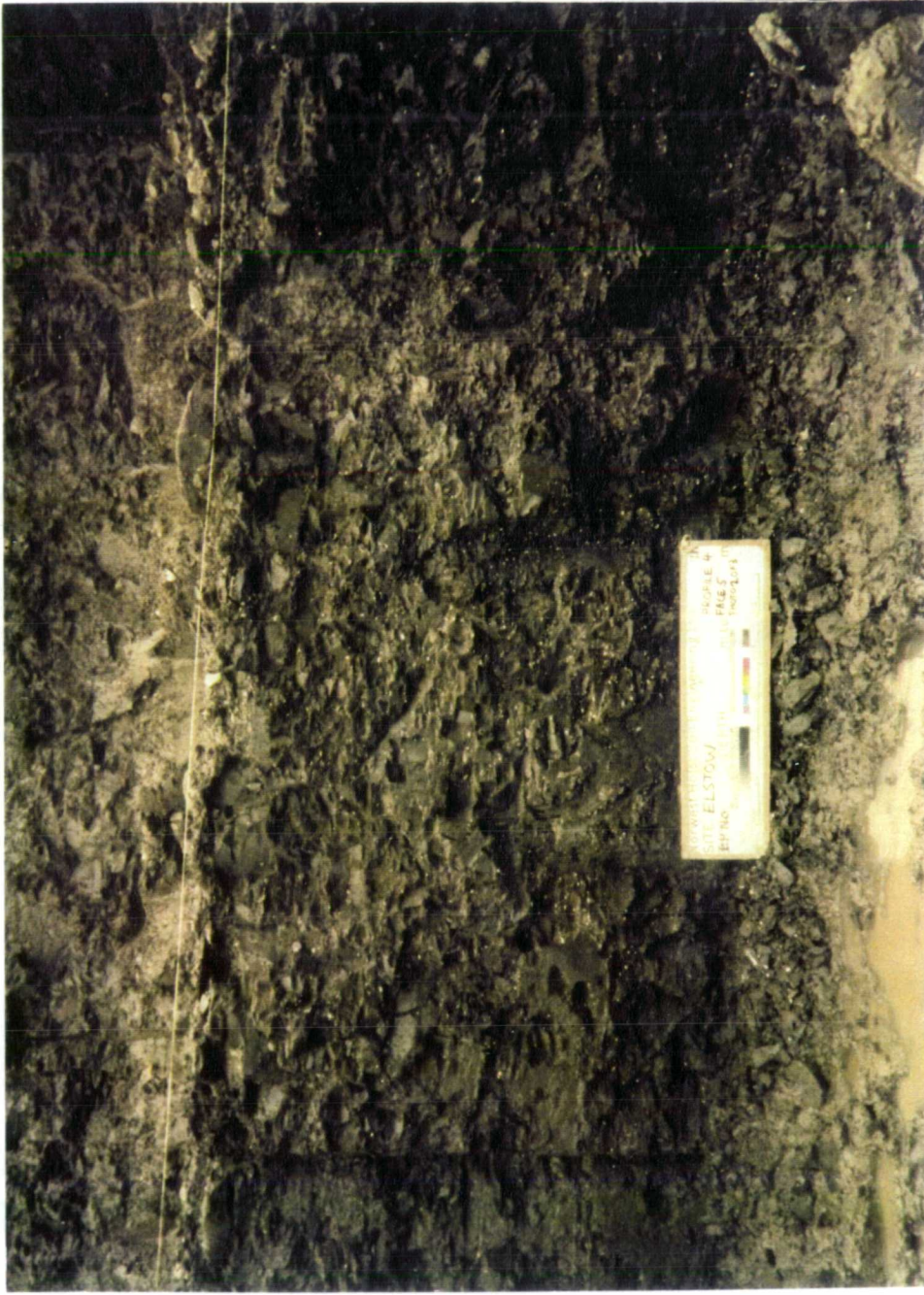


Figure A.6 - View of face 5 of logging profile 4 showing unweathered Oxford Clay